# ADVANCES IN NUCLEAR POWER ENGINEERING

EDITED BY: Zhaoming Meng, Jun Wang, Kaiyi Shi and Shripad T. Revankar
PUBLISHED IN: Frontiers in Energy Research

frontiers Research Topics

# frontiers



ISSN 1664-8714
ISBN 978-2-88966-516-7
DOI 10.3389/978-2-88966-516-7

## About Frontiers

Frontiers is more than just an open-access publisher of scholarly articles: it is a pioneering approach to the world of academia, radically improving the way scholarly research is managed. The grand vision of Frontiers is a world where all people have an equal opportunity to seek, share and generate knowledge. Frontiers provides immediate and permanent online open access to all its publications, but this alone is not enough to realize our grand goals.

## Frontiers Journal Series

The Frontiers Journal Series is a multi-tier and interdisciplinary set of open-access, online journals, promising a paradigm shift from the current review, selection and dissemination processes in academic publishing. All Frontiers journals are driven by researchers for researchers; therefore, they constitute a service to the scholarly community. At the same time, the Frontiers Journal Series operates on a revolutionary invention, the tiered publishing system, initially addressing specific communities of scholars, and gradually climbing up to broader public understanding, thus serving the interests of the lay society, too.

## Dedication to Quality

Each Frontiers article is a landmark of the highest quality, thanks to genuinely collaborative interactions between authors and review editors, who include some of the world's best academicians. Research must be certified by peers before entering a stream of knowledge that may eventually reach the public - and shape society; therefore, Frontiers only applies the most rigorous and unbiased reviews.
Frontiers revolutionizes research publishing by freely delivering the most outstanding research, evaluated with no bias from both the academic and social point of view. By applying the most advanced information technologies, Frontiers is catapulting scholarly publishing into a new generation.

## What are Frontiers Research Topics?

Frontiers Research Topics are very popular trademarks of the Frontiers Journals Series: they are collections of at least ten articles, all centered on a particular subject. With their unique mix of varied contributions from Original Research to Review Articles, Frontiers Research Topics unify the most influential researchers, the latest key findings and historical advances in a hot research area! Find out more on how to host your own Frontiers Research Topic or contribute to one as an author by contacting the Frontiers Editorial Office: frontiersin.org/about/contact

# ADVANCES IN NUCLEAR POWER ENGINEERING

Topic Editors:
**Zhaoming Meng,** Harbin Engineering University, China
**Jun Wang,** University of Wisconsin-Madison, United States
**Kaiyi Shi,** Liupanshui Normal University, China
**Shripad T. Revankar,** Purdue University, United States

**Citation:** Meng, Z., Wang, J., Shi, K., Revankar, S. T., eds. (2021). Advances in Nuclear Power Engineering. Lausanne: Frontiers Media SA.
doi: 10.3389/978-2-88966-516-7

# Table of Contents

frontiers in Energy Research

EDITORIAL
published: 26 January 2021
doi: 10.3389/fenrg.2020.629655

# Editorial: Advances in Nuclear Power Engineering

*Zhaoming Meng[1], Jun Wang[2]*, Kaiyi Shi[2] and Shripad T. Revankar[3]*

*[1]College of Nuclear Science and Technology, Harbin Engineering University, Harbin, China, [2]Department of Engineering Physics, University of Wisconsin-Madison, Madison, WI, United States, [3]Department of Nuclear Engineering, Purdue University, West Lafayette, IN, United States*

**Keywords: gen IV reactor, small modular reactor, thermal hydraulic, neutronic, containment**

## Editorial on the Research Topic

## Advances in Nuclear Power Engineering

Nuclear power has been used widely around the world and is considered a highly efficient and clean energy source (Kim and Alameri, 2020). Many organizations around the globe are leading the efforts to develop new technologies to improve the economy and safety (Openshaw 2019). The research topic "Advances in Nuclear Power Engineering" aims to publish the most advanced and timely research results. The articles include research results on Gen IV reactors, small modular reactors, reactor physics, reactor thermal hydraulics, advanced safety technologies, and related topics. Variety of important areas are covered in these topics including theoretical, computational, and experimental thermal-hydraulics, multiphase heat transfer, neutronics, uncertainty analysis, aerosol transport, and scaling considerations.

Zhang et al. discuss on the Gen IV sodium-cooled fast reactor heat transfer in their article "Theoretical Investigation on the Fully Developed Turbulent Heat Transfer Characteristics of Liquid Sodium." In the article "Numerical Analysis of FLiBe Laminar Convective Heat Transfer Characteristics in Tubes Fitted with Coaxial Cross Twisted Tape Inserts," Yang et al. present computational heat transfer results on Gen IV molten salt reactor. Zhang et al. discuss design of the small modular reactors in the article "Comparisons of Reduced Moderation Small Modular Reactors with Heavy Water Coolant." Those works provide an insight view of the next-generation reactor design include not only high temperature Gen IV reactors but also small modular light water reactor.

Song et al. share their results of computational studies in the article "GPU Based Two-Level CMFD Accelerating Two-Dimensional MOC Neutron Transport Calculation." The neutronic work shows the multidimensional neutronic and thermal information in the reactor core.

The results on thermal-hydraulics experimental work are given by Li et al. in the article "The Effect of Different Branch Angles and Different Branch Pipe Sizes on the Onset Law of Liquid Entrainment"; Gao et al. in the article "Influence of the Size and the Angle of Branches Connected to the Main Horizontal Pipe on the Onset of Gas Entrainment"; Mao et al. in the article "Natural Convection Heat Transfer of the Horizontal Rod-Bundle in a Semi-closed Rectangular Cavity"; Ren et al. in the article "Visualization Experiment of Bubble Coalescence in a Narrow Vertical Rectangular Channel"; and by Wang et al. in the article "Study on the Breakdown Mechanism of Water Film on Corrugated Plate Wall Under the Horizontal Shear of Airflow: A Short Communication." The experimental thermal-hydraulics work aims at the improvement of the heat transfer coefficient and reactor safety.

Other thermal-hydraulics related works include the work of Wang et al. in the article "Review and Prospect of the Measurement Technology of the Thickness of the Liquid Film on the Wall of the Corrugated Plate Dryer"; Saeed et al. in the article "Sensitivity Analysis of Some Key Factors on Turbulence Models for Hydrogen Diffusion Using HYDRAGON Code"; Zhou et al. in the article



***Edited by:***
*Muhammad Zubair, University of Sharjah, United Arab Emirates*

***Reviewed by:***
*Marco Colombo, University of Leeds, United Kingdom*

****Correspondence:***
*Jun Wang*
*jwang564@wisc.edu*

***Specialty section:***
*This article was submitted to Nuclear Energy, a section of the journal Frontiers in Energy Research*

***Received:*** *15 November 2020*
***Accepted:*** *17 December 2020*
***Published:*** *26 January 2021*

***Citation:***
*Meng Z, Wang J, Shi K and Revankar ST (2021) Editorial: Advances in Nuclear Power Engineering. Front. Energy Res. 8:629655. doi: 10.3389/fenrg.2020.629655*

"Analysis of Measuring Characteristics of the Differential Pressure Water-Level Measurement System Under Depressurization Condition"; Zhou et al. in the article "Numerical Study of the Influence of Tube Arrangement on the Flow Distribution Inside the Heat Exchanger in the PCCS"; Wang et al. in the article "Numerical Study on Laminar-Turbulent Transition Flow in Rectangular Channels of a Nuclear Reactor"; Huang et al. in the article "Study on Typical Design Basis Conditions of HPR1000 With Nuclear Safety Analysis Code ATHLET"; Sun et al. in the article "An Improved Best Estimate Plus Uncertainty Method for Small-Break Loss-of-Coolant Accident in Pressurized Water Reactor"; and Zhang et al. in the article "Uncertainty analysis on k-ε turbulence model in the prediction of subcooled boiling in vertical pipes." The theoretical and numerical thermal-hydraulics work expands the boundary of experimental work.

Reactor containment is the final safety boundary of the nuclear power plant. Articles related to reactor containment include articles by Liu et al. "Scaling Design of the Pressure Response Experimental Facility for Pressure Suppression Containment" and Tao et al., "Experimental study on natural deposition characteristics of aerosol in the containment". Those works are important to help containment integrity during beyond design basic accident conditions.

This research topic received good response from authors and successfully attracted dozens of submissions. After the peer-review and editor's efforts, this research topic finally published nineteen articles. We want to thank all the reviewers, authors, and support from the editor office of Frontiers in Energy Research.

## AUTHOR CONTRIBUTIONS

ZM is the leading editor; JW is the contact editor; KS and SR are senior people.

## REFERENCES

Kim, J. H., and Alameri, S. A. (2020). Harmonizing nuclear and renewable energy: case studies. *Int. J. Energy Res.* 44 (10), 8053–8061. doi:10.1002/er.4987

Openshaw, S. (2019). *Nuclear power: siting and safety*. Abingdon, United Kingdom: Routledge.

**Conflict of Interest:** The authors declare that the research was conducted in the absence of any commercial or financial relationships that could be construed as a potential conflict of interest.

frontiers in Energy Research

ORIGINAL RESEARCH
published: 14 February 2020
doi: 10.3389/fenrg.2020.00012

# Sensitivity Analysis of Some Key Factors on Turbulence Models for Hydrogen Diffusion Using HYDRAGON Code

*Muhammad Saeed*[1,2*†], *Xianping Zhong*[1*†], *Jiyang Yu*[1], *Xiaolong Zhang*[1] and *Aniseh Ahmed Atef Abdalla*[1]

[1] Department of Engineering Physics, Tsinghua University, Beijing, China, [2] College of Nuclear Science and Engineering, East China University of Technology, Nanchang, China

OPEN ACCESS

**Edited by:**
Jun Wang,
University of Wisconsin-Madison,
United States

**Reviewed by:**
Mohammad Alrwashdeh,
Khalifa University,
United Arab Emirates
Arun Nissimagoudar,
Ulsan National Institute of Science and Technology, South Korea

***Correspondence:**
Muhammad Saeed
saeedphysics96@gmail.com
Xianping Zhong
zxp15@tsinghua.org.cn

[†] These authors have contributed equally to this work

**Specialty section:**
This article was submitted to Nuclear Energy, a section of the journal Frontiers in Energy Research

**Received:** 08 December 2019
**Accepted:** 20 January 2020
**Published:** 14 February 2020

**Citation:**
Saeed M, Zhong X, Yu J, Zhang X and Abdalla AAA (2020) Sensitivity Analysis of Some Key Factors on Turbulence Models for Hydrogen Diffusion Using HYDRAGON Code. Front. Energy Res. 8:12. doi: 10.3389/fenrg.2020.00012

In this paper, we have investigated the influence of air-fountain injection to study the hydrogen diffusion behavior with the help of 3-Dimensional code, HYDRAGON. Three different turbulence models i. e., Standard k −, model, Re-Normalized Group $k - m$ model and Realizable $k - e$ model have been studied carefully and the comparison of simulated data with experimental data were performed. The effect of air-injection was examined using three different velocities i.e., 0.411, 2.803, and 5.143 m/s to evaluate the phenomena of stratification break-up. When we kept the velocity of the air-injection as low as 0.411 m/s, the simulated results obtained through these three turbulence models were very close to experimental data. As the velocity was set to 5.143 m/s, the simulated data captured the experimental data well. But, when the velocity of air-injection was kept 2.803 m/s, the two turbulence models i.e., SKE and RNG turbulence models gave satisfactory results. However, when we added the turbulent diffusivity coefficient to RNG and RLZ turbulence models in the HYDRAGON code, a minor influence was investigated in these simulation results.

**Keywords: nuclear power plant, air-injection, diffusivity coefficient, HYDRAGON code, turbulence models**

## INTRODUCTION

Due to oxidation and core degradation, a large amount of hydrogen is generated and released into the reactor containment during a severe accidental scenario in the nuclear power plant (NPP). The density of air is 14 times higher than hydrogen, and the flammability range of hydrogen is much higher. These distinct properties show that hydrogen may disperse tremendously faster during accidental conditions, and detonation or deflagration may be initiated inevitably by the potential ignition source. This may threaten the integrity and safety system of the reactor containment. The possible risk related to hydrogen was initially observed during the accident which occurred in Three Mile Island (TMI) in 1979. This was the first well-known example where combustion of hydrogen took place, and where an enormous quantity of hydrogen was generated as a consequence of steam-zirconium interaction in the fuel cladding (Abdalla et al., 2014; Saeed et al., 2016, 2017a,b; Huanga et al., 2017). The hydrogen detonation in the Fukushima Dai-ichi Nuclear Power Plant (NPP) accident (2011) was another example which compelled scientists to explore the risk of hydrogen detonation during a severe accident. Both of these accidents indicate that modeling

the gas behavior is an important subject of interest. To evaluate the combustion that would be detrimental to the reactor, hydrogen distribution must be modeled precisely to measure the initial conditions following combustion (Visser et al., 2012; Abdalla et al., 2015; Yang et al., 2017).

It is quite necessary to keep an eye on the hydrogen concentration during an accident scenario in the containment of an NPP to investigate the probable hydrogen risk and efficiency of the mitigation systems which are fixed in the containment of the NPP (Saeed et al., 2017a). In previous decades, scientists have developed two thermal-hydraulics approaches i.e., Lumped parameters (LP) and computational fluid dynamics (CFD) codes to simulate the related problems in the reactor core (Prabhudharwadkar et al., 2011; Xiao and Travis, 2013). In the beginning, LP codes such as MAAP and CONTAIN were used to predict the hydrogen safety behavior in the NPP (Kanzleiter and Fischer, 1994). For predicting the average hydrogen concentration in the containment, the LP method is more effective for predicting a longer duration of simulation because of its fast estimation for the hydrogen distribution. This method was more effective to investigate the average hydrogen concentration and it could not provide any estimation about the local distribution inside a compartment. Therefore, high-resolution CFD codes were presented for predicting the distribution of hydrogen at low spatial scales. The CFD largely has enhanced the precision, accuracy and analysis of the release of the hydrogen (Kanzleiter and Fischer, 1994; Heck et al., 1995; Bart et al., 2002; Visser et al., 2012).

Recently, 3D CFD codes such as ADREA-HF, CFD-ACE GOTHIC, REACFLOW, TONUS, CFX-5.7, GASFLOW, ROMs, and FLCAS etc. have been used for containment and industrial analyses. GOTHIC either deals with the LP computations or other systematic multidimensional assessment. Royl et al. (2000) used GASFLOW to predict the influence of combustion and hydrogen-steam distribution analysis in the konvoi-type NPP (Royl et al., 2000; Analytis, 2003; Grunloh and Manera, 2016). Houkema et al. (2008) performed a detail comparison between simulation results obtained from the LP code and commercial CFD code CFX and it was observed that a comprehensive three-dimensional analysis was necessary to get a local hydrogen distribution concentration (Houkema et al., 2008). A Russian type Water-Water-Energy-Reactor, VVER 440-213, was designed to perform simulations. Although these codes provided a certain degree of hydrogen mitigation, precise comparison of local hydrogen concentration was still unavailable (Kim et al., 2007).

The development of computational tools that precisely measure the hydrogen mixed gases inside the containment is still an unsolved issue. The precise measurement of the behavior of these gas species was a major concern for nuclear safety experts (Studer et al., 2012). Turbulence modeling is one of the important components to simulate gas mixing and transport equations. Different turbulence models (i.e., standard $k-\varepsilon$ (hereafter SKE) turbulence model, re-normalization group $k-\varepsilon$ (hereafter RNG) turbulence model, realizable $k-\varepsilon$ (hereafter RLZ) turbulence model etc.) were used (Xiao and Travis, 2013; Zhang et al., 2015).

We studied the experimental work from Deri et al. (2010), and compared their experimental data with our simulation results obtained from HYDRAGON code (Abdalla, 2015; Abdalla et al., 2015; Saeed et al., 2016, 2017a,b; Zhang et al., 2017). For the current paper, the published data of the air-fountain case (air-fountain in the erosion of gaseous stratification) performed by Deri et al. was selected as a benchmark. To prevent the hydrogen risk combustion, helium was used during the experiment.

This work assesses the capability of the HYDRAGOON code to simulate the hydrogen distribution which is released during an accidental scenario in the containment of the NPP. In addition, this work is an important framework for assessment of hydrogen risk and risk reduction in the scenario of a severe accident at NPP. The major application of the HYDRAGON code is predicting the hydrogen behavior and multiple gas species inside the containment of NPP during a severe accident.

## NUMERICAL METHODOLOGY

The 3D HYDRAGON code was used for numerical simulation in this manuscript. The next sections of our report introduce the governing equations, various $k-\varepsilon$ turbulence models i.e., SKE, RNG, and RLZ turbulence models, facility description and the initial and boundary conditions, in sequence.

### Governing Equations

The governing equations used in this article are the viva unsteady average Navier-Stokes equations having mass and momentum conservation equations with turbulence transport equations. It is important to mention that the Navier-Stokes equations embody the physics of all types of fluid flows, including turbulent flow. The computations were initiated with three-dimensional transient simulations. The fluid properties such as velocity, pressure, temperature, etc. for the multicomponent fluid have been resolved by using the transport equations (Abdalla et al., 2015; Zhang et al., 2015, 2017; Saeed et al., 2016).

The transport equation is given as under:

$$\frac{\partial(\rho Y_i)}{\partial t} + \nabla \cdot (\rho_\alpha U Y_i) = -\nabla \cdot \vec{J}_i + S_i \tag{1}$$

where $\rho$ represents the fluid density, $\vec{J}_i$ represent the diffusion flux, $Y$ denotes mass fraction of gas species, $U$ is used for the fluid velocity vector and $S_i$ represents the conserved mass. Summation of mass fraction for each mixture component $i$ is obtained as following.

$$\sum_i^{NC} Y_i = 1 \tag{2}$$

where NC represents the number of components $i$.

Diffusion flux:

$$\vec{J}_i = -\rho D_i \vec{\nabla} Y_i - \frac{\mu_t}{sc_t} \vec{\nabla} Y_i \tag{3}$$

where $\vec{J}_i$ represents the diffusion flux, $\rho$ and $D_i$ denote the fluid density of mixture of gas and mass diffusion, respectively. The term $Y_i$ is the mass fraction for gas species $i$.

Continuity mass equation:

$$\frac{\partial \rho}{\partial t} + \nabla.(\rho U) = 0 \tag{4}$$

Conservation of momentum:

$$\frac{\partial (\rho U)}{\partial t} + \nabla.(\rho UU) = -\nabla P + \nabla.\tau + \rho g \tag{5}$$

where $U$ and $\rho g$ represent the velocity vector and gravitational body force, respectively.

Stress tensor:

$$\tau = \mu_{eff}\left(\nabla U - \frac{2}{3}\rho k I\right) \tag{6}$$

Effective turbulence viscosity:

$$\mu_{eff} = \mu + \mu_T \tag{7}$$

where $\mu_{eff}$ is the effective turbulence viscosity, $\mu$ is the molecular viscosity and $\mu_T$ represents the turbulent viscosity.

Thermodynamic equation:

$$p = z(\rho, T)\,\rho\frac{R}{M}T \tag{8}$$

where R and M represent the universal gas constant and fluid molecular weight, respectively. The term z represents the compressibility; T represents the fluid absolute temperature and $p$ represents pressure.

Density of the gas mixture:

$$\frac{1}{\rho} = \frac{Y_{air}}{\rho_{air}} + \frac{Y_{helium}}{\rho_{helium}} \tag{9}$$

Molecular viscosity:

$$\mu(T) = c_1\left(\frac{T}{c_2}\right)^{1.5} \times \frac{c_2 + 110.4}{T + 110.4} \tag{10}$$

## Turbulence Models

The two characteristic equations of N-S models i.e., mass, momentum, and energy equations are not closed. The process of closing the system of mean flow equations during computational system is known as turbulence modeling. Turbulence models are used to close the Reynolds stress term in the system of non-linear equations (Xie et al., 2008; Latif et al., 2013).

Turbulent kinetic energy:

$$k = \frac{1}{2}\left(\overline{U'.U'}\right) \tag{11}$$

Dissipation rate:

$$\varepsilon = \nabla.\left(\upsilon U'U'\right) \tag{12}$$

Turbulent Production:

$$p_k = \mu_t\left[\frac{\partial u_i}{\partial x_j}\left(\frac{\partial u_i}{\partial x_j} + \frac{\partial u_j}{\partial x_i}\right)\right] \tag{13}$$

Turbulent production of due to buoyancy effect:

$$G_k = -g_i\frac{\mu_t}{\rho \mathrm{Pr}_t}\frac{\partial \rho}{\partial x_i} \tag{14}$$

In the above equations, $\mu_t$ represents eddy viscosity, $\rho$ is the density and $p_{r_t}$ is the turbulent Prandtl number. The vaule of turbulent Prandtl number was kept as 0.9.

The Standard $k-\varepsilon$ turbulence model (Abdalla et al., 2014; Saeed et al., 2016)

Eddy viscosity:

$$\mu_t = C_\mu \rho\frac{k^2}{\varepsilon} \tag{15}$$

Transport equations of the SKE turbulence model:

$$\frac{\partial (\rho k)}{\partial t} + \frac{\partial}{\partial x_i}(\rho k u_i) = \frac{\partial}{\partial x_j}\left[\left(\mu + \frac{\mu_t}{\sigma_k}\right)\frac{\partial k}{\partial x_j}\right] + P_k + G_k - \rho\varepsilon \tag{16}$$

$$\frac{\partial (\rho\varepsilon)}{\partial t} + \frac{\partial}{\partial x_i}(\rho\varepsilon u_i) = \frac{\partial}{\partial x_j}\left[\left(\mu + \frac{\mu_t}{\sigma_\varepsilon}\right)\frac{\partial \varepsilon}{\partial x_j}\right] + C_1\frac{\varepsilon}{k}(P_k + G_k) - C_2\rho\frac{\varepsilon^2}{k} \tag{17}$$

The model constants determined from simple benchmark are

$C_u = 0.0$, $\sigma_k = 1.0$, $\mathrm{Pr} = 0.85$, $C_{\varepsilon 1} = 1.44$, $C_{\varepsilon 2} = 1.92$, $\sigma_\varepsilon = 1.3$

The RNG $k-\varepsilon$ model equations are given as (Abdalla et al., 2014; Saeed et al., 2016).

Eddy viscosity:

$$\mu_t = C_\mu \rho\frac{k^2}{\varepsilon} \tag{18}$$

Transport equations of the RNG turbulence model:

$$\frac{\partial (\rho k)}{\partial t} + \frac{\partial}{\partial x_i}(\rho k u_i) = \frac{\partial}{\partial x_j}\left[\sigma_k(\mu + \mu_t)\frac{\partial k}{\partial x_j}\right] + P_k + G_k - \rho\varepsilon \tag{19}$$

$$\frac{\partial(\rho\varepsilon)}{\partial t} + \frac{\partial(\rho\varepsilon u_i)}{\partial x_i} = \frac{\partial}{\partial x_j}\left[(\mu + \mu_t)\sigma_\varepsilon\frac{\partial \varepsilon}{\partial x_j}\right] + C_{1RNG}\frac{\varepsilon}{k}(P_k + G_k) - C_2\rho\frac{\varepsilon^2}{k} \tag{20}$$

The model constants determined from simple benchmark are

$C_u = 0.0$, $\sigma_k = 1.0$, $\mathrm{Pr} = 0.85$, $C_{\varepsilon 1} = 1.44$, $C_{\varepsilon 2} = 1.92$, $\sigma_\varepsilon = 1.3$

The Realizable $k-\varepsilon$ model equations are (Abdalla et al., 2014; Saeed et al., 2016).

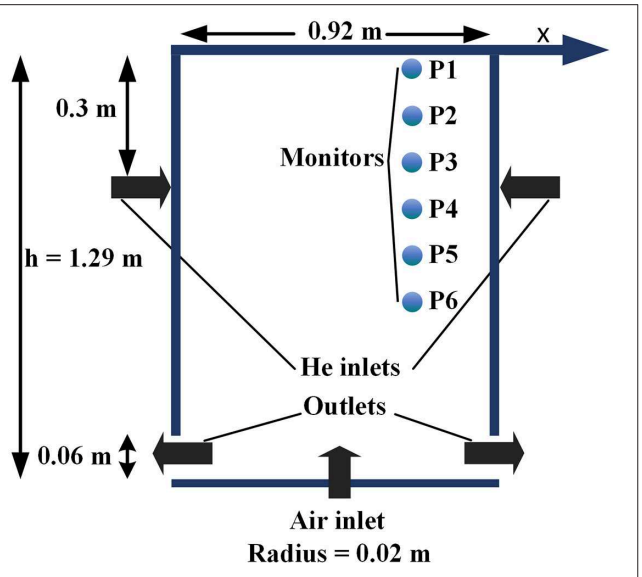


**FIGURE 1 |** Sketch of the experimental layout.

Transport equations of the RLZ turbulence model:

$$\frac{\partial(\rho k)}{\partial t}+\frac{\partial}{\partial x_i}(\rho k u_i)= \frac{\partial}{\partial x_j}\left[\left(\mu+\frac{\mu_t}{\sigma_k}\right)\frac{\partial k}{\partial x_j}\right]+P_k+G_k-\rho\varepsilon \quad (21)$$

$$\frac{\partial(\rho\varepsilon)}{\partial t}+\frac{\partial(\rho\varepsilon u_i)}{\partial x_i}= \frac{\partial}{\partial x_j}\left[\left(\mu+\frac{\mu_t}{\sigma_\varepsilon}\right)\frac{\partial \varepsilon}{\partial x_j}\right]+C_1\rho S\varepsilon+C_{1\varepsilon}\frac{\varepsilon}{k}P_k -C_2\rho\frac{\varepsilon^2}{k+\sqrt{\upsilon\varepsilon}} \quad (22)$$

The model constants are

$\sigma_\varepsilon = 1.2, C_{1\varepsilon} = 1.44,\ C_2 = 1.9.$

## Facility Description

The facility consisted of a parallelepiped, whose dimensions are 1.92 × 0.92 × 0.92 m (Height, length, and width) as shown in **Figure 1**. The inlet is located exactly in the middle of the bottom of the facility, and the outlet measuring 0.06 m is positioned at the bottom of the facility as shown in **Figure 1**. Initially, the facility was filled with air, and 9.1 g of helium was injected in via two upper inlets that were facing horizontally into the facility, during the initial 300 s of the simulation beginning. The air-injection was also started 1 min after the helium injection via the vertical nozzles that were positioned at 0.3 m from the roof on the lateral edges. The injection of air was continued for 300 s. To keep the pressure constant, the surpassing gas flowed out of the facility during the air-fountain. The sensor probes P1, P2, P3, P4, P5, and P6 were located 1.29, 1.09, 0.96, 0.83, 0.69, and 0.49 m, respectively from bottom of the enclosure as shown in **Figure 1**.

**TABLE 1 |** Design parameters of the layout.

| | |
|---|---|
| Inlet diameter for helium | 0.004 m |
| Inlet nozzle diameter for air | 0.02 m |
| Height of the containment | 1.29 m |
| Square area of the containment | 0.92 × 0.92 m |
| Air-injection time | 300 s |
| Pressure | 101,235 pa |
| Temperature | 20°C |
| Air-fountain velocity | 0.411 $ms^{-1}$, −2.803 $ms^{-1}$, 5.11$ms^{-1}$ |
| Froude numbers (Fr) | 0.16,1.09, 2.0 |
| Monitor elevations; P1, P2, P3, P4, and P6 | 1.29 m, 1.09 m, 0.96 m, 0.83 m, 0.69 m, 0.49 m |

Various Froude numbers (Fr) i.e., 0.16, 1.09, and 2.0 were applied to the experiment work to check the behavior of the penetrating jet deal during the experiment. The corresponding air-injections were 0.411, 2.803, and 5.143 m/s (Deri et al., 2010). Local Froude numbers were derived as a function of air-fountain reference velocity $U_{reff}$ = 0.126 $U_e$m/s, length scale of air-fountain $L$ = 0.162 m, Brunt-Vaisala frequency N and stratification thickness $H$ = 0.4 m. Design parameters of the layout is shown in **Table 1**.

$$Fr = \frac{U_{reff}}{NL} \quad (23)$$

$$N = \left[\frac{2g}{\rho_1+\rho_2}\frac{\rho_1-\rho_2}{H}\right]^{0.5} = 2[s^{-1}] \quad (24)$$

where, $N$ is known as Brunt-Vaisala frequency, used to define the initial condition for the stratification, $\rho_1$ is the density of the bottom zone, $\rho_2$ is the density of the upper zone, $U_e$ is the air-fountain velocity and g is the gravity force.

## Initial and Boundary Conditions

To decrease the simulation duration and simplify the computation, we have simplified the geometry as a 3D quarter size. We have imposed a symmetry condition for the entire area and we have performed similar simulations in the other area. During the simulation, an adiabatic heat transfer with an isotropic system was applied. The air was injected through a square inlet whose dimension was 0.0088226917 × 0.0088226917 m. The whole simulations were divided into two different time steps. The duration of air-injection was 150–450 s following the start of the simulations. During the air-injection phase of simulation, when the velocity was high and constant, small time steps were adopted for solving the transient equation because of the higher turbulence intensity closer to the air-fountain source. In the latter phase, variable time steps were used as variation occurred in the velocity and became uncertain. Moreover, "time step maximal variation" was set at low levels.

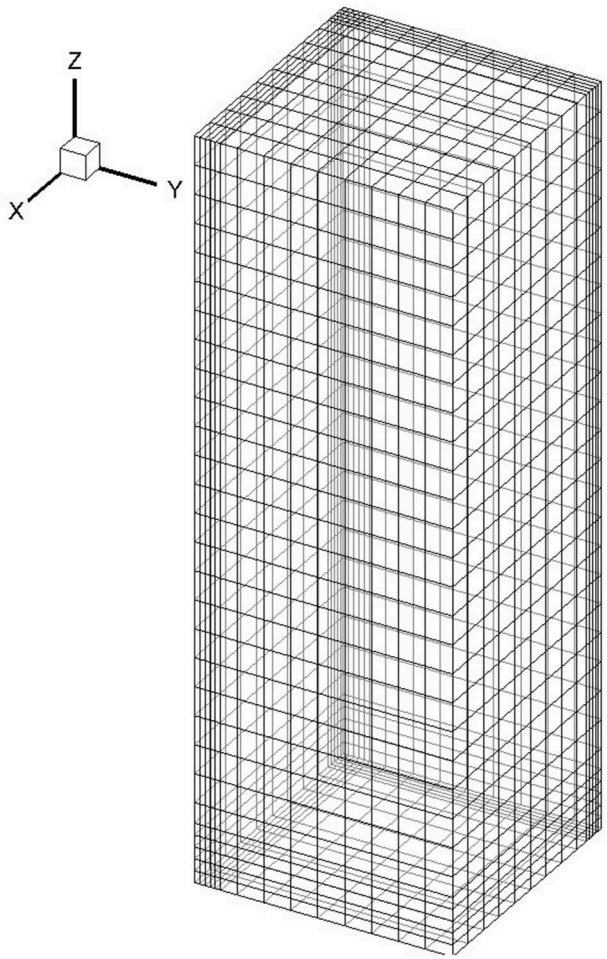


**FIGURE 2 |** Cartesian mesh used for the computation of air-fountain experimental benchmark.

The simulations were performed with a structure of Cartesian coarse mesh, and three different grids conducted for the sensitive analysis were as 6,750, 40,500, and 54,000. An average mesh size of 1.8 × 1.8 × 3.1, 1.8 × 1.8 × 2.3 and 4.5 × 4.5 × 5 cm were tested and it was observed that the coarse mesh (4.5 × 4.5 × 5 cm having a total number of 6,750 grids) was sufficient to capture the gas mixture flow phenomena.

To reduce the simulation time, all the simulation results presented in the paper were computed by using 4.5 × 4.5 × 5 cm average mesh size. The computational domain cells were 15 cells along both the x- and y-axis, and 30 cells along the z-axis. For capturing the rapid variation in the density gradient, the highest mesh density was employed near the air-fountain region during the air-injection. **Figure 2** illustrates the grid system for the computational domain obtained by using HYDRAGON code to solve Navier-Stocks equations. In this article, three different velocities for air-injection were used i.e., 0.411, 2.83, and 5.11 m/s. The helium mass diffusion coefficient for the mixture was $7.35 \times 10^{-5}$. The fully inlet flow was assumed having values calculated with flow physical properties as under (Prabhudharwadkar et al., 2011).

$$k_{in} = 0.001{U_{in}}^2 \tag{25}$$

$$\varepsilon_{in} = \frac{c_\mu {k_{in}}^{3/2}}{l_{in}} \tag{26}$$

$$l_{in} = 0.42 y_p \tag{27}$$

## RESULTS AND DISCUSSION

As the density of helium is lower, so the helium molecules were constantly diffused inside the facility. These helium molecules are consistently deposited on the upper part of the enclosure inside the containment. The air-injection was started after 150 s following the initiation of the simulation. After 450 s, the helium-injection was cut off following the initiation of the simulation. The air injection mixed the atmospheric components of the enclosure and the excess gases were able to exit through the outlet which maintained the thermodynamic pressure on the enclosure. According to the flow type, whole simulations were performed in two different steps. During the air-fountain and helium injection, we have used closely timed steps to solve the transient equations because of the turbulence intensity closer to the air fountain source. So, during the release phase, a longer simulation time was needed for the air fountain. After the release phase, variable time steps were used. The maximal variation for the time steps was kept at lower levels. The simulated data presented in this paper are dimensionless density $\rho_{ref} - \rho/\rho_{ref}$ vs. time for the six monitors i.e., P1, P2, P3, P4 P5, and P6.

### Effect of Velocity Injection Parameters

The simulations were performed by using three different air-injection velocities 0.411, 2.83, and 5.11 m/s to analyze stratification break-up phenomena. To study the interaction between the three different air-fountain velocities and the stratification helium layer, the simulated data was compared with the experimental results calculated at various air-injection velocities mentioned earlier for the three turbulence models.

When the air-injection velocities were set to 0.411 m/s, the results achieved by using the HYDRAGON code for the three turbulence models were in better agreement as shown in **Figures 3**, **4**. The simulation results of the monitors P1 and P2 were close to the experimental data for all the turbulence models during the initial stage of the simulation and a small over prediction was observed after 600 s following the initiation of the simulation. Similarly, for all the remaining three monitors, the simulation results obtained by using HYDRAGON code captured the experimental trend during the initial stage of simulations and a small over prediction was observed at the latter phase of the simulation due to lower density of the helium as shown in **Figures 3**, **4**. The simulation results illustrate that the injected momentum had an influence on the mixing regimes. Mixing

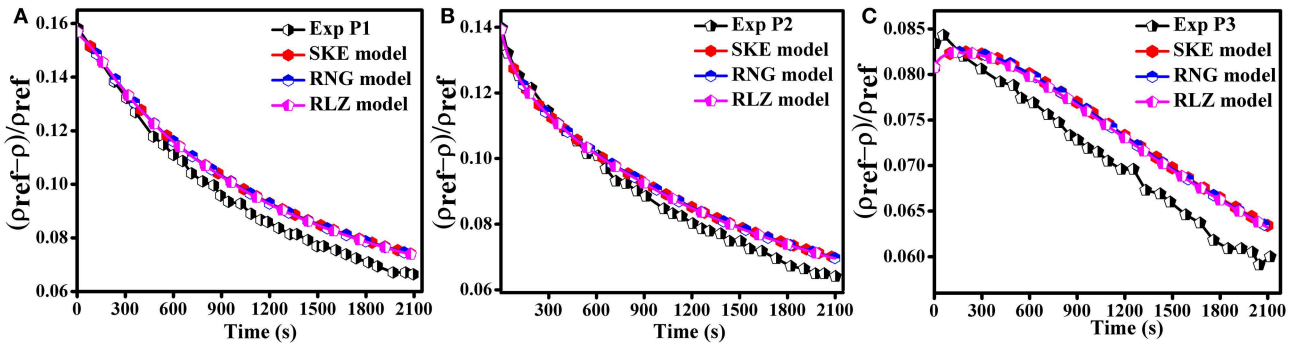


**FIGURE 3 |** Effect of air-injection velocity 0.411 m/s on the simulation results for monitors **(A)** P1, **(B)** P2, and **(C)** P3.

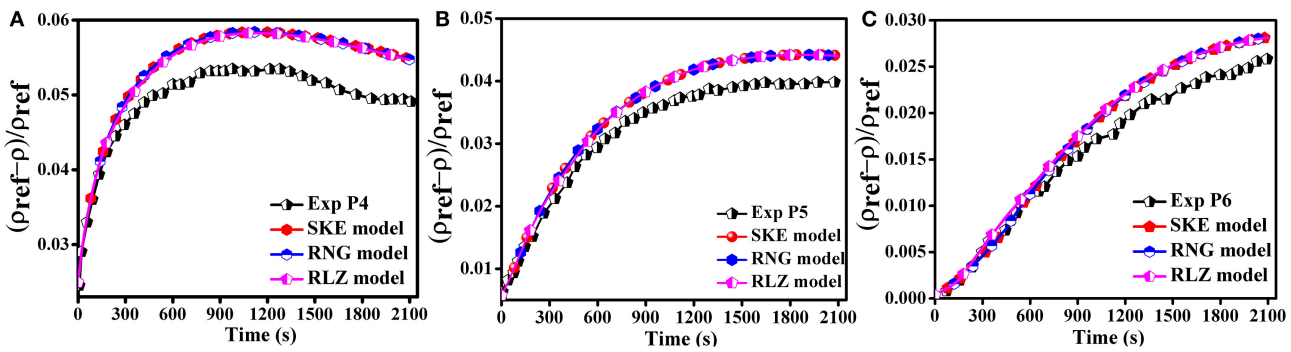


**FIGURE 4 |** Effect of air-injection velocity 0.411 m/s on the simulation results for monitors **(A)** P4, **(B)** P5, and **(C)** P6.

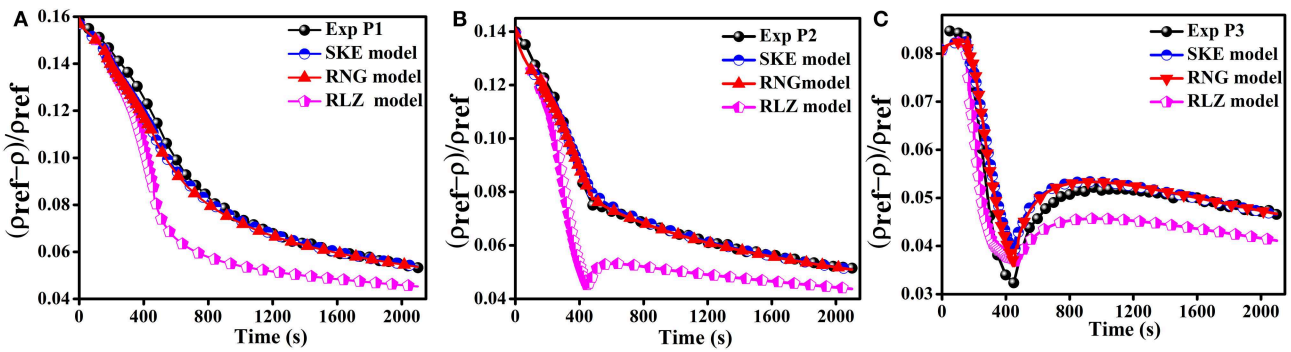


**FIGURE 5 |** Effect of air-injection velocity 2.83 m/s on the simulation results for monitors **(A)** P1, **(B)** P2 and **(C)** P3.

process was dominated by molecular diffusion when air-injection velocity was set to 0.411 m/s.

When the air-injection velocities were set to 2.83 m/s, the turbulence models choice had an influence on the simulation results.

The results obtained for the SKE and RNG turbulence models were closed to the experimental data, while discrepancies for the RLZ turbulence model were observed as shown in **Figures 5**, **6**. The computational results of the RLZ turbulence model varied locally. The results of the RLZ turbulence model were underestimated for P1 and P2 and were improved for P3, P4, and P5, respectively.

The computational data achieved using SKE and RNG models were close to the experimental trend as compared to RLZ turbulence model at any area in the enclosure. **Figures 5**, **6** illustrate that the influence of the upward air fountain flow distance varied for all the three turbulence models. It was observed that the flow simulated by using the RLZ turbulence model reached a better trend than the other two turbulence models, and the horizontal spreading rate was

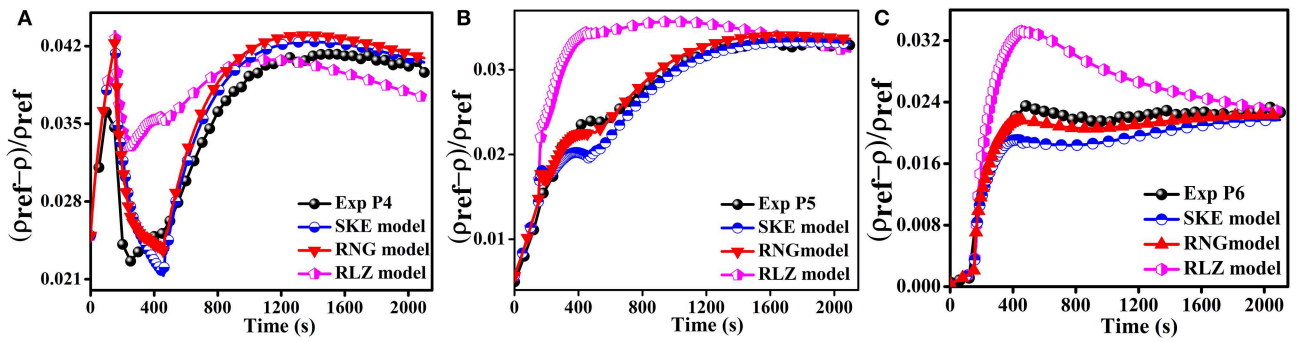


**FIGURE 6 |** Effect of air-injection velocity 2.83 m/s on the simulation results for monitors **(A)** P4, **(B)** P5, and **(C)** P6.

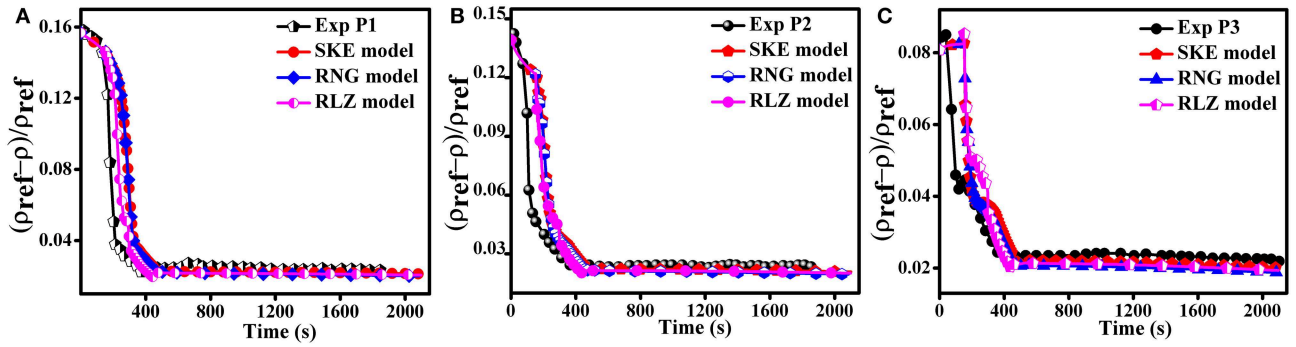


**FIGURE 7 |** Effect of air-injection velocity 5.143 m/s on the simulation results for monitors **(A)** P1, **(B)** P2, and **(C)** P3.

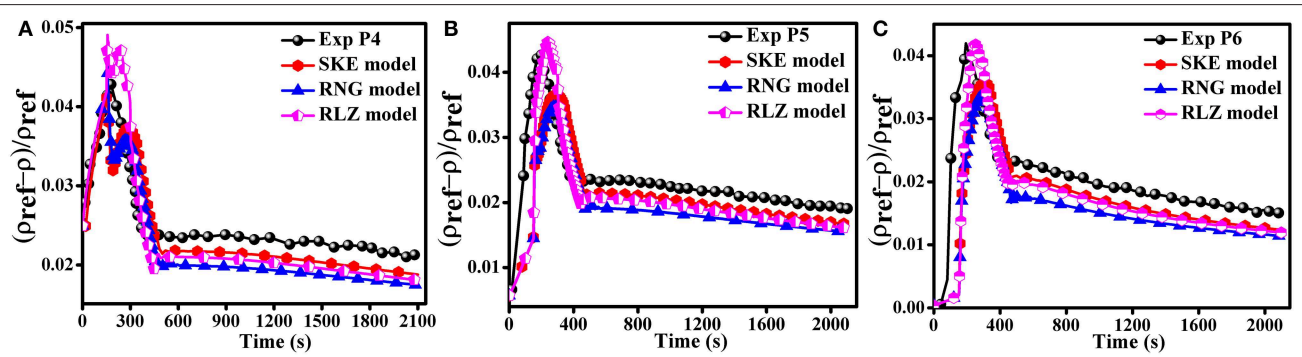


**FIGURE 8 |** Effect of air-injection velocity 5.143 m/s on the simulation results for monitors **(A)** P4, **(B)** P5, and **(C)** P6.

also underestimated for the RLZ turbulence model. The SKE and RNG turbulence models generally better presented the predictions for the density stratification breakup phenomena.

The numerical results calculated when the air-injection was increased to 5.143 m/s for the three turbulence models are shown in **Figures 7**, **8**. The momentum force derived the mixing when the air-injection was set to 5.143 m/s. When the air-injection velocity was set to 5.143 m/s, the simulation results obtained by the SKE turbulence model were similar to the simulation results obtained by RNG and RLZ turbulence models. In general, when air-injection velocity was set to 5.143 m/s, the three different turbulence models were in better agreement with experimental data as shown in **Figures 7**, **8**.

**Figure 9** compares the instantaneous mixture density distribution inside the containment for the SKE, RNG, and RLZ turbulence models computed by three various air-injection velocities, and the instantaneous results presented at 200 s. When air-injection velocity was very small, i.e., 0.411 m/s, the stratification layers were formed in-between the region where the helium concentration varied, as the helium concentrated

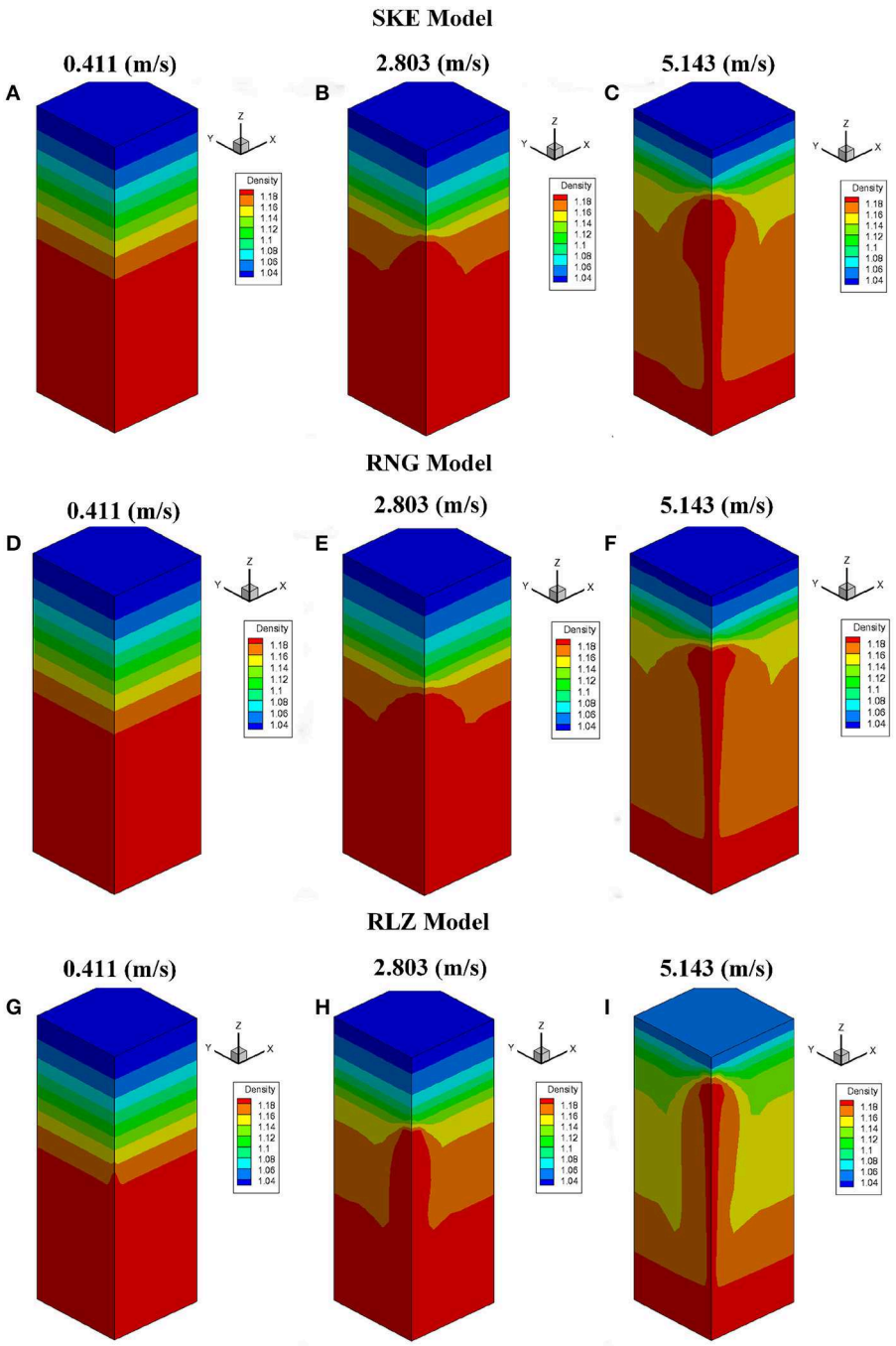


**FIGURE 9 |** Comparison of instantaneous mixture density (kg/m$^3$) calculated by three various air-injection velocities at 200 (s) for SKE **(A)** 0.411 m/s **(B)** 2.803 m/s **(C)** 5.143 m/s, RNG **(D)** 0.411 m/s **(E)** 2.803 m/s **(F)** 5.143 m/s, and RLZ **(G)** 0.411 m/s **(H)** 2.803 m/s **(I)** 5.143 m/s.

at the upper part of the containment. When the air-injection velocity was increased to 2.803 m/s, stratification breakup was observed which was mainly caused by gravity driven force during the air-injection. If air-injection velocity was increased more up to 5.143 m/s, it suddenly penetrated the stratification layers and reached a higher distance but still was unable to penetrate helium stratification layer completely.

The comparison between the gravity-dominated and momentum-dominated regimes were observed by means of the interaction Froude number (Fr), which was set to 1 as a discriminating value. When Fr $<$ 1, the momentum was overcome by the buoyancy and the air-injection was thus unable to penetrate the stratification. Actually, the air flow impinged

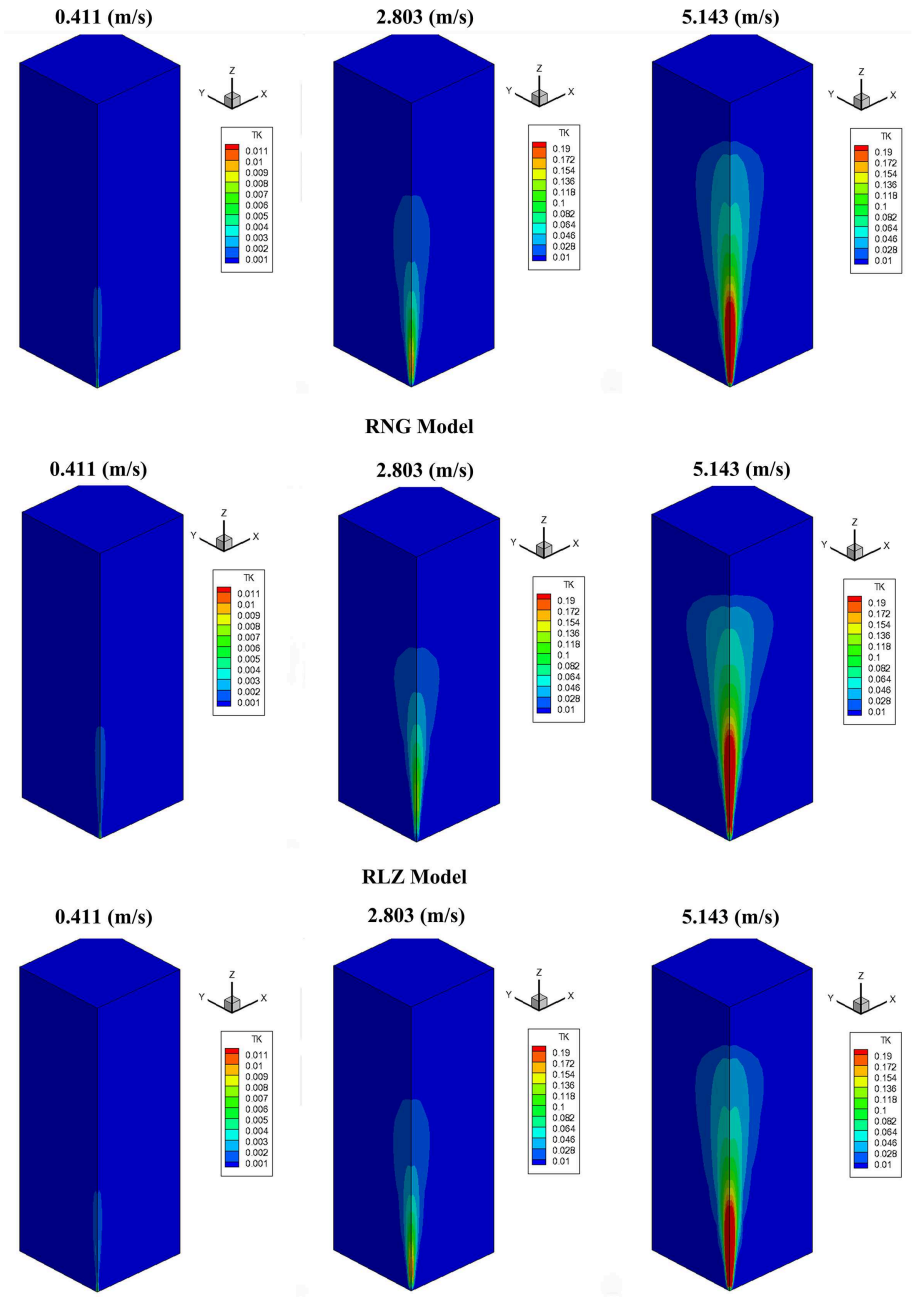


**FIGURE 10 |** Comparison of instantaneous turbulence kinetic energy ($m^2/s^2$) calculated by three various air-injection velocities for SKE, RNG, and RLZ at 200 (s).

over density surface and deflected downward with a fountain behavior.

**Figures 10**, **11** compared the instantaneous turbulence kinetic energy and dissipation rate, respectively for the SKE, RNG, and RLZ turbulence models calculated by three various air-injection velocities and the instantaneous results presented at 200 s. The simulation results illustrated that the air-injection momentum had large influence on the turbulence kinetic energy and dissipation rate. Largest turbulence kinetic energy and dissipation rate were observed when the air-injection velocity was increased to 5.143 m/s.

When, the injection was small, the molecular diffusion dominated the mixing. A buoyancy dominated mixing was observed, as the fountain flow rate was increased. When the value of Fr was set more than 1, the flow regime was momentum dominated and a rapid stratification break-up was observed.

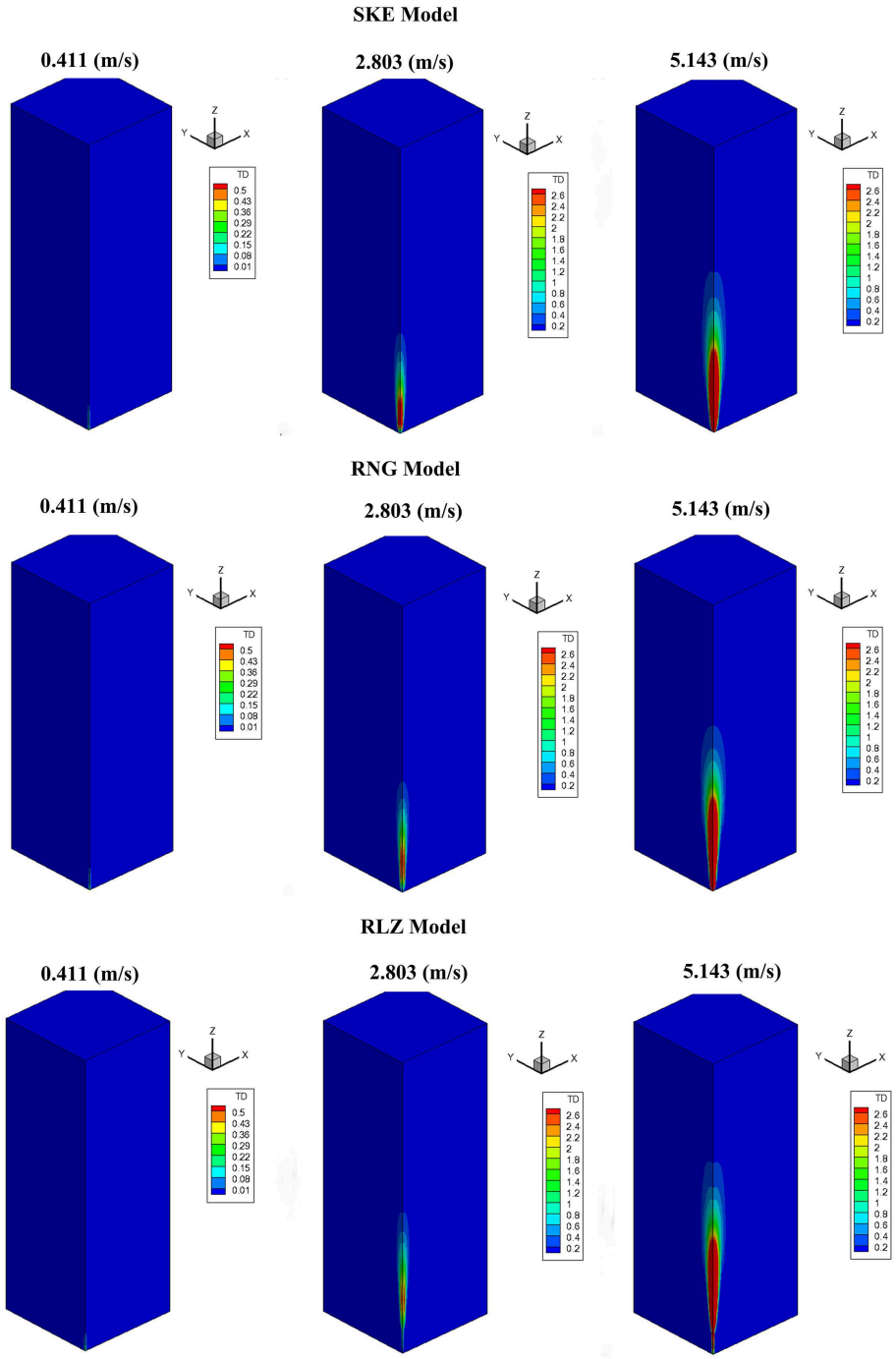


**FIGURE 11 |** Comparison of instantaneous turbulence dissipation rate ($m^2/s^3$) calculated by three various air-injection velocities for SKE, RNG, and RLZ at 200 (s).

## Effect of Turbulent Diffusivity Term

The effect of the turbulent diffusivity was analyzed. The value of the turbulent Schmidt number $Sc_t$ was set to 0.7 (Sanders et al., 1997) and the air-injection velocity was set to 2.83 m/s. Xiao and Travis (2013) suggested that value for the turbulent Schmidt number $Sc_t$ can be selected in the range of 0.5–1.0 value. **Figure 12** illustrates the comparison of simulation results calculated when turbulent diffusivity coefficient was included with the three turbulence models at P5 and P6 regions. Only the region near the air-fountain source was investigated, because it was the region where the turbulent diffusivity affected the most.

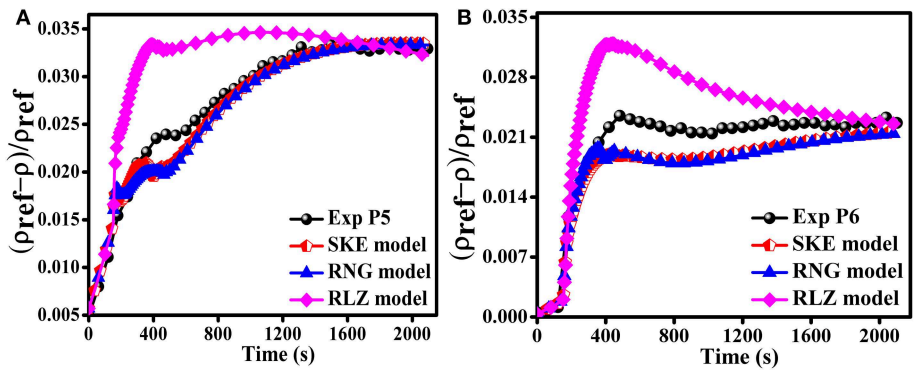


**FIGURE 12 |** Effect of turbulent diffusivity on numerical results calculated for SKE, RNG, and RLZ for monitors **(A)** P5 and **(B)** P6, at inlet velocity 2.803 (m/s).

The simulation results illustrated that the turbulent diffusivity had a small effect on the simulation results at the region near air-fountain source i.e., P5 and P6, for the RNG and RLZ models and it did not have any noticeable effect on the SKE turbulence model as **Figure 12**. By including turbulent diffusivity term to the RNG model, it was observed that the simulation results agreed well with the simulation results obtained by RNG and RLZ model at the region near air-fountain source P6. The curves for the RNG and RLZ turbulence models were closer to the experimental trend when turbulent diffusivity was included to the HYDRAGON code. Moreover, turbulent diffusivity had no noticeable effect on the computed results obtained by SKE model as shown in **Figure 12**.

## CONCLUSION

We have used three different velocities to investigate the stratification break-up phenomena. The molecular diffusion force caused the mixing process when the value of the velocity was 0.411 m/s. The gravity force was responsible for the mixing when the value of the air-injection was 2.803 m/s. The momentum forces derived from the mixing process as the air-injection was set to 5.143 m/s. The simulation results obtained by using various turbulence models showed that maximum penetration distance of the injected air-fountain varied for different turbulence models. It was observed that an air-injection did not have enough momentum to penetrate the helium stratification layer completely, where the injected air density was much heavier than the containment mixture. When the values of the air-injection velocities were 0.411 and 5.143 m/s, respectively, then the results achieved by these three turbulence models were closer to the experimental data. However, when 2.803 m/s velocity used, the results of SKE and RNG turbulence models were very close to the experimental trends at different points as compared to RLZ model. Furthermore, RNG model captured experimental trend better than SKE and RLZ models near the air-fountain source.

Furthermore, the effect of the turbulent diffusivity coefficient term was included to the k and $\varepsilon$ equations. When we added the turbulent diffusivity coefficient term in the HYDRAGON code for RNG and RLZ turbulence models, a minor influence was observed in the results.

## DATA AVAILABILITY STATEMENT

All datasets generated for this study are included in the article/supplementary material.

## AUTHOR CONTRIBUTIONS

MS run simulations. XZho and JY have added turbulence models to the HYDRAGON code while XZha and AA helped in writing the paper.

## REFERENCES

Abdalla, A. (2015). *Validation of Turbulance Models for Gas Distribution Analysis Code* (dissertation). Tsinghua University Beijing, Beijing, BJ, USA.

Abdalla, A., Yu, J., and Alrwashdeh, M. (2014). "Application of some turbulence models to simulate buoyancy-driven flow," in *Proceedings of the 2014 22nd International Conference on Nuclear Engineering* (Prague: ASME Press).

Abdalla, A., Yu, J., Chunhai, Z., Hou, B., and Saeed, M. (2015). "Investigation of the influence of turbulencemodels on the simulation of the gas distribution," in *Proceedings of the 23rd International Conference on Nuclear Engineering* (Chiba: ASME Press).

Analytis G. Th. (2003). Implementation of the renormalization group (RNG) k-ε turbulence model in GOTHIC/6.lb: solution methods and assessment. *Ann. Nucl. Energy* 30, 349–387. doi: 10.1016/S0306-4549(02)00061-0

Bart, M., Dick, E., and Langhe, C. D. (2002). Application of an improved ε equation to a pilot jet diffusion flame. *Combust Flame* 131, 465–468. doi: 10.1016/S0010-2180(02)00420-0

Deri, E., Cariteau, B., and Abdo, D. (2010). Air fountain in the erosion of gaseous stratification. *Int. J. Heat Fluid Fl.* 31:935. doi: 10.1016/j.ijheatfluidflow.2010.05.003

Grunloh, T. P., and Manera, A. (2016). A novel domain overlapping strategy for the multiscale coupling of CFD with 1D system codes with applications to transient flows. *Ann. Nucl. Energy* 90, 442–432. doi: 10.1016/j.anucene.2015.12.027

Heck, R., Kelber, G., Schmidt, K., and Zimmer, H. J. (1995). Hydrogen reduction following severe accidents using the dual recombiner-igniter concept. *Nucl. Eng. Des*. 157, 311–319. doi: 10.1016/0029-5493(95)01009-7

Houkema, M., Siccama, N. B., Nijeholt, J. A., and Komen, E. M. J. (2008). Validation of the CFX4 CFD code for containment thermalhydraulics. *Nucl. Eng. Des*. 238, 590–599. doi: 10.1016/j.nucengdes.2007.02.033

Huanga, T., Zhanga, Y., Tiana, W. X., Sua, G., and Qiua, S. Z. (2017). A 3-D simulation tool for hydrogen detonation during severe accident and its application. *Ann. Nucl. Energy* 104, 113–123. doi: 10.1016/j.anucene.2017.02.011

Kanzleiter, T. F., and Fischer, K. O. (1994). Multi-compartment hydrogen deflagration experiments and model development. *Nucl. Eng. Des*. 146, 417–426. doi: 10.1016/0029-5493(94)90347-6

Kim, J., Hong, S. W., Kim, S. B., and Kim, H. D. (2007). Three-dimensional behaviors of the hydrogen and steam in the APR1400 containment during a hypothetical loss of feed water accident. *Ann. Nucl. Energy* 34, 992–1001. doi: 10.1016/j.anucene.2007.05.003

Latif, M., Masson, C., and Stathopoulos, T. (2013). Comparison of various types of k-ε models for pollutant emissions around a two-building configuration. *J. Wind Eng. IndAerodyn*. 115, 9–21. doi: 10.1016/j.jweia.2013.01.001

Prabhudharwadkar, D. M., Iyer, K. N., and Mohan, N. (2011). Simulation of hydrogen distribution in an Indian nuclear reactor containment. *Nucl. Eng. Des*. 241, 832–842. doi: 10.1016/j.nucengdes.2010.11.012

Royl, P., Rochholz, H., Breitung, W., Travis, J. R., and Necker, G. (2000). Analysis of steam and hydrogen distribution with PARmitigation in NPP containments. *Nucl. Eng. Des*. 202, 231–248. doi: 10.1016/S0029-5493(00)00332-0

Saeed, M., Yu, J., Abdalla, A., Hou, B., Hussain, G., and Zhong, X. (2017b). The effect of turbulence modeling on hydrogen jet dispersion inside a compartment space using the HYDRAGON code. *J. Nucl. Sci. Technol*. 54, 725–732. doi: 10.1080/00223131.2017.1299645

Saeed, M., Yu, J., Abdalla, A., Zhong, X., and Ghazanfar, M. (2017a). An assessment of k-ε turbulence models for gas distribution analysis. *Nucl. Sci. Tech*. 28:146. doi: 10.1007/s41365-017-0304-x

Saeed, M., Yu, J., Hou, B., Abdalla, A., and Chunhai, Z. (2016). "Numerical simulation of hydrogen dispersion inside a compartment using HYDRAGON code," in *Proceedings of the 2016 24th International Conference on Nuclear Engineering* (North Carolina: ASME Press). doi: 10.1115/ICONE24-60610

Sanders, J. P. H., Sarh, B., and Gokalp, I. (1997). Variable density effects in axisymmetric isothermal turbulence jet: a comperison between a first and second oder turbulence model. *Int. J. Heat Mass Transf*. 40, 823–842. doi: 10.1016/0017-9310(96)00151-2

Studer, E., Brinster, J., Tkatschenko, I., Mignot, I., and Paladino, G. D. (2012). Interaction of a light gas stratified layer with an air jet coming from below: large scale experiments and scaling issues. *Nucl. Eng. Des*. 253, 406–412. doi: 10.1016/j.nucengdes.2012.10.009

Visser, D. C., Houkema, M., Siccama, N. B., and Komen, E. M. J. (2012). Validation of a FLUENT CFD model for hydrogen distribution in containment. *Nucl. Eng. Des*. 245, 161–171. doi: 10.1016/j.nucengdes.2012.01.025

Xiao, J., and Travis, J. R. (2013). How critical is turbulence modeling in gas distribution simulations of large-scale complex nuclear reactor containments? *Ann. Nucl. Energy* 56, 227–242. doi: 10.1016/j.anucene.2013.01.016

Xie, Z., Yang, Y., Gu, H., and Cheng, X. (2008). Numerical analysis of turbulent mixed convection air flow in inclined plane channel with k-ε type turbulence model. *J. Nucl. Sci. Tech*. 19:121. doi: 10.1016/S1001-8042(08)60036-6

Yang, J., Liang, R., Lin, Z., Huang, X., and Wang, T. (2017). Transient analysis of AP1000 NPP under the similar Fukushima accident conditions. *Ann. Nucl. Energy* 109, 529–537. doi: 10.1016/j.anucene.2017.04.026

Zhang, X., Tseng, P., Saeed, M., and Yu, J. (2017). A CFD-based simulation of fluid flow and heat transfer in the intermediate heat exchanger of sodium-cooled fast reactor. *Ann. Nucl. Energy* 108, 181–187. doi: 10.1016/j.anucene.2017.05.063

Zhang, Y., Lu, D., Du, Z., Fu, X., and Wu, G. (2015). Numerical and experimental investigation on the transient heat transfer characteristics of C-shape rod bundles used in passive residual heat removal heat exchangers. *Ann. Nucl. Energy* 83, 147–160. doi: 10.1016/j.anucene.2015.04.022

**Conflict of Interest:** The authors declare that the research was conducted in the absence of any commercial or financial relationships that could be construed as a potential conflict of interest.

frontiers in Energy Research

BRIEF RESEARCH REPORT
published: 20 February 2020
doi: 10.3389/fenrg.2020.00008

# Influence of the Size and the Angle of Branches Connected to the Main Horizontal Pipe on the Onset of Gas Entrainment

*Jinchen Gao [1,2], Yanwei Yue [3], Zhaoming Meng [1]*, Xiaoyu Li [1,2] and Geyu Shen [1]*

[1] Fundamental Science on Nuclear Safety and Simulation Technology Laboratory, Harbin Engineering University, Harbin, China, [2] School of Energy and Power Engineering, Xi'an Jiaotong University, Xi'an, China, [3] Research and Development Center, China Nuclear Power Engineering Co., Ltd., Beijing, China

The influence of the size and the angle of the branch on the onset of gas entrainment is explored in the present study. Since previous studies were performed on small-sized branches and the angles of the branches were specific (0° or −90°), it is difficult to apply them to arbitrary-angled branches. So we conducted a series of experiments in a different direction of −30°, −45°, −60°, and −90° angles with the main pipe of 80-mm diameter and a branch of 31-mm diameter (T-tube). A new correlation is developed and can predict the most experimental data well within the error range of ±20%. And the new correlation can predict the onset of gas entrainment at arbitrary-angled branch and is not constrained by the angle of branches; that is, it has good versatility. We also gained some meaningful conclusions by analyzing experimental data and the entrainment phenomenon: gas is entrained by a vortex flow, and the size of the branch and the angle of the branch have little effect on the form of entrainment at a given $h_b/d$. The critical Froude number ($Fr_L$) gradually increases as the angle of the branch changes from −90° to −30°. When this is compared with previous models, it can be found that the correlation of the onset of gas entrainment based on small-sized branches is not suitable for large-scale branches. But we have defined a new critical liquid level ($h_b^*$) to successfully expand the scope of application of the correlation.

**Keywords: T-tube, onset of gas entrainment, size of branch, angle of branch, the onset of phenomenon**

OPEN ACCESS

***Edited by:***
*Bruno Panella,*
*Politecnico di Torino, Italy*

***Reviewed by:***
*Keyou S. Mao,*
*Purdue University, United States*
*Yacine Addad,*
*Khalifa University,*
*United Arab Emirates*

***Correspondence:**
*Zhaoming Meng*
*mengzhaoming@hrbeu.edu.cn*

***Specialty section:***
*This article was submitted to Nuclear Energy, a section of the journal Frontiers in Energy Research*

***Received:*** *20 October 2019*
***Accepted:*** *13 January 2020*
***Published:*** *20 February 2020*

***Citation:***
*Gao J, Yue Y, Meng Z, Li X and Shen G (2020) Influence of the Size and the Angle of Branches Connected to the Main Horizontal Pipe on the Onset of Gas Entrainment. Front. Energy Res. 8:8. doi: 10.3389/fenrg.2020.00008*

## INTRODUCTION

In the AP1000 reactor of the third-generation nuclear power plant, the T-tube structure is widely used in the pipeline of the fourth-stage automatic depressurization system (ADS-4) and the passive residual heat removal system (PRHRS) (Schulz, 2008; Lin, 2010). Zuber (1980) pointed out that for the T-tube structure, when the gas–liquid stratified flow exists in the horizontal main pipe, the relative position of the branch/break and the gas–liquid interface will cause two different entrainment phenomena. If the branch/break location is below the gas–water interface, the gas may be entrained by the continuous liquid stream through the branch/break, causing gas entrainment. Conversely, if the branch/break location is above the interface, the liquid may be entrained by the continuous gas stream through the branch/break, causing liquid entrainment. During loss-of-coolant accidents (LOCAs), gas entrainment may occur at the location of the break below the

horizontal interface. In a pressurized water reactor (PWR), gas entrainment may cause failure of residual heat removal pump (Guide, 1989). Therefore, it is of great engineering value to study the gas entrainment phenomenon.

In the previous work, numerous models of onset of gas entrainment were used in various analytical procedures for analyzing PWR safety accidents. According to the relevant parameters, Zuber (1980) established a simplified correlation for the entrainment through the top, bottom, and side branches:

$$\frac{h_b}{d} = C_1 \left(Fr_b\right)^{C_2} \tag{1}$$

where $Fr_b = [(4/\pi)W_b]/[gd^5\rho_b(\rho_L - \rho_G)]^{0.5}$, $W_b$ is the continuous phase mass flow in the branch, $\rho_L$ is the density of the liquid, $\rho_G$ is the density of the gas, $d$ is the inner diameter of the branch/break, and the coefficients $C_1$ and $C_2$ are determined by experimental data. Smoglie C. from KfK (Smoglie and Reimann, 1984) used point-sink analysis to establish a model that predicts the onset of entrainment at the top, bottom, and side branches, ignoring the effects of liquid viscosity and surface tension.

$$h_b = \frac{KW_{3b}^{0.4}}{\left[g\rho_b\left(\rho_L - \rho_G\right)\right]^{0.2}} \tag{2}$$

where $K$ is obtained by fitting the experimental data. However, the direction of the branch/break is not limited to three (top, bottom, and side). Based on the assumption of inertial force and gravity balance, Lee et al. (2006) developed a correlation that can predict the onset of gas entrainment at arbitrary-angled branches ($-30°$, $-45°$, $-60°$, and $-90°$):

$$Fr_L\left(\frac{\rho_L}{\Delta\rho}\right)^{0.5} = C_{OGE(\theta)}\left[\left(\frac{h_{OGE}}{d}\right) + \frac{1}{2}\left(\frac{D}{d}\right)(1 - \sin\theta)\right]^{0.25} \tag{3}$$

where $\Delta\rho = \rho_L - \rho_G$, $C_{OGE(\theta)}$ is determined by the value of $\theta$, and the Froude number ($Fr_L$) is defined by the volume flow rate ($Q$) at the branch entrance.

$$Fr_L = Q/(\pi\sqrt{\mathrm{gd}}\left(\frac{\mathrm{d}}{2}\right)^2) \tag{4}$$

Since the coefficient $C_{OGE(\theta)}$ is a function of $\theta$, the model is not very versatile. Taking into account the influence of the size of the branches on gas entrainment, Shen et al. (2018) performed a gas entrainment experiment for large-sized ($d/D = 0.625$) and small-sized ($d/D = 0.125$) vertical downward branches; in addition, a new correlation has been established:

$$\frac{h_b}{d} = CFr^{0.2} \tag{5}$$

where the value $C = 1.17$ was obtained by fitting the experimental data. Most of the above models are for small-sized branches. However, some researchers have found that models used to predict liquid entrainment through small-scale branches are not suitable for large-scale branches (Riemke et al., 2006; Welter et al., 2014). Therefore, we have reason to doubt whether the model used to predict gas entrainment through small-scale branches is suitable for large-scale branches.

For the onset of gas entrainment, the above studies, except Lee's, are only for vertical downward branches/break. However, in practice, the branch/break may appear anywhere (below the horizontal). Therefore, to meet the engineering needs and also to verify whether Lee's model is suitable for this experiment, the experiment of onset of gas entrainment through large-sized branches at an arbitrary angle ($-90°$, $-60°$, $-45°$, and $-30°$) is carried out in this paper. The angle of the branch ($\theta$) is defined as the angle between the branch and the horizontal plane (below the horizontal). Using visualization equipment, this paper aims to investigate the effect of the size of the branch and the angle of the branch on the onset of gas entrainment and develop a more universal correlation for the prediction of onset of gas entrainment.

# EXPERIMENTAL CONTENT AND FACILITY

## Experimental Facility

The test bench of this experiment includes a water tank, air–water separator, water pump, horizontal pipe with a diameter of 80 mm, and branch pipe with a diameter of 31 mm, as shown in **Figure 1**. The total length of the test section is 2,570 mm, of which the upstream is 1,730 mm and the downstream is 840 mm. At the T-joint, the branch pipe can be disassembled for the convenience of changing the angle of the branch.

Water flow is supplied by a pump and measured by a turbine flow meter (accuracy of 0.2%, measurement range of 0–6 $m^3$/h). At the end of the gas–water separator, the entrained gas is measured by a micro-gas mass flow meter (accuracy of 0.2%, measurement range of 0–5 L/min). In addition, differential pressure transmitters (accuracy of 0.05%, measurement range of 0–0.17 kPa) are installed before and after the T-joint to measure the pressure difference between the two-phase interface and the bottom of the main pipe, to calculate the liquid level height. The temperatures of gas and water are measured by the thermocouple (accuracy of 0.5°C, measurement range of 0–350°C).

## Experimental Content

(1) Open the centrifugal pump water supply, and regulate gate valves 1 and 2 to ensure the liquid mass flow to reach a certain value and to make the level in the horizontal main pipe rise to a certain height.
(2) When gate valve 3 is regulated, the horizontal interface in the main pipe decreases slowly (<1 mm/min). When a vortex is formed in the liquid phase and a very thin tube reaches the branch entrance, the gas entrainment occurs (i.e., OGE). At this time, the liquid phase height in the main pipe is $h_b$.
(3) Change the mass flow rate of liquid, and repeat steps (1) and (2).
(4) Change the angle ($\theta$) between the branch pipe and the horizontal plane, and repeat steps (1)–(3).

By Equation (6), the mass flow rate of the liquid in the branch ($W_{3L}$) can be calculated by the mass flow rate of the liquid in the

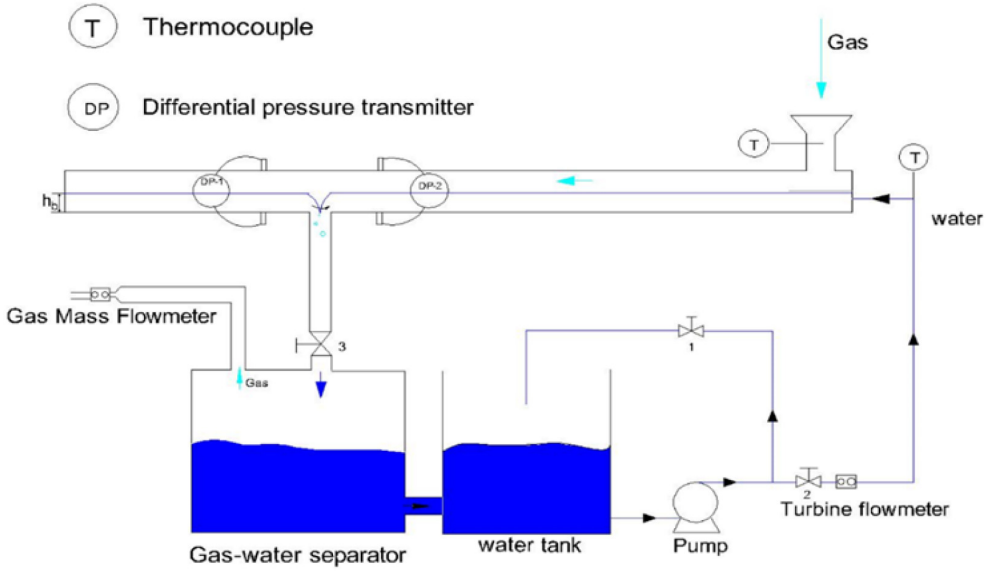


**FIGURE 1 |** Schematic diagram of the test facility.

main pipe ($W_{1L}$) measured by the turbine flow meter.

$$W_{3L} = W_{1L} + \frac{dM}{dt} \tag{6}$$

where $M$ represents the water mass in the main pipe, which is related to main pipe diameter and water level $h$. $dM/dt$ indicates the rate of change in water mass obtained by changing the water level ($h$) in the main pipe. In order to ensure that $W_{1L}$ and $W_{3L}$ are approximately equal, it is necessary to control the water level in the main pipe ($h$) to drop very slowly (<1 mm/min), so it can be assumed that the liquid level in the main pipe is constant during a certain period. Therefore, it can be assumed that the experiment is in a steady state.

## RESULTS AND DISCUSSION

### Onset of Gas Entrainment at Arbitrary-Angled Branch Pipes and Arbitrary-Sized Branch Pipes

The phenomenon of gas entrainment for the bottom branch can be observed as follows: at a given liquid flow rate and water level, a smaller vortex is formed, which will quickly disappear due to buoyancy; after a long time, another large vortex is formed, and the gas tube will gradually become longer, and with the slow decrease of the interface (<1 mm/min), the formation of the vortex becomes more and more frequent. A curved fine gas tube with a big vortex extends to the branch pipe, which is defined as the onset of the gas entrainment.

The development of onset phenomena for the branch with an angle of $-60^\circ$ is the same as that for the bottom branch. Furthermore, for the branches with an angle of $-45^\circ$ and $-30^\circ$, the development of onset phenomena is the same as that for the bottom branch.

In **Figure 2A**, at a given $h_b/d$, the critical Froude number ($Fr_f$) gradually increases as the angle of the branch changes from $-90^\circ$ to $-30^\circ$. On the one hand, according to the mechanism of gas entrainment, the bubble can be entrained into the branch pipe, which is due to the inertial force of the bubble to overcome its buoyancy. At a given $h_b/d$ and Froude number ($Fr_f$), as the angle of the branch increases (from $-90^\circ$ to $-30^\circ$), the component of the inertial force of the bubble reduces in a vertical downward direction (see **Figure 2B**). When the gas entrainment occurs, in order to overcome the buoyancy of the bubble, the inertial force component of the bubble in the vertical downward direction needs to be increased, so the Froude number ($Fr_f$) needs to be increased. On the other hand, the friction on the inner wall surface of the main pipe can hinder the formation of the vortex. At a given $h_b/d$ and Froude number ($Fr_f$), as the angle of the branch increases (from $-90^\circ$ to $-30^\circ$), the position of the vortex gradually approaches to the inner wall surface of the main pipe (see **Figure 2C**), and the formation of vortex is increasingly affected by the friction force (the effect of wall curvature) (Lee et al., 2007; Wang et al., 2011). Hence, when gas entrainment occurs, in order to overcome the buoyancy of the bubble and the wall friction resistance, the liquid velocity ($V_{2L}$) of the horizontal main pipe increases with the gradually increasing angle of the branch pipe, so the liquid velocity ($V_{3L}$) of the branch also increases and the Froude number ($Fr_f$) gradually increases.

In **Figure 2D**, comparing Shen's (Lee et al., 2006) phenomenon of onset entrainment, for the bottom branch, although only the size of the branch is different, the form of onset entrainment all belongs to vortex entrainment, and a thin curved gas tube extends to the branch. Of course, the phenomenon of onset entrainment is still different due to the influence of the

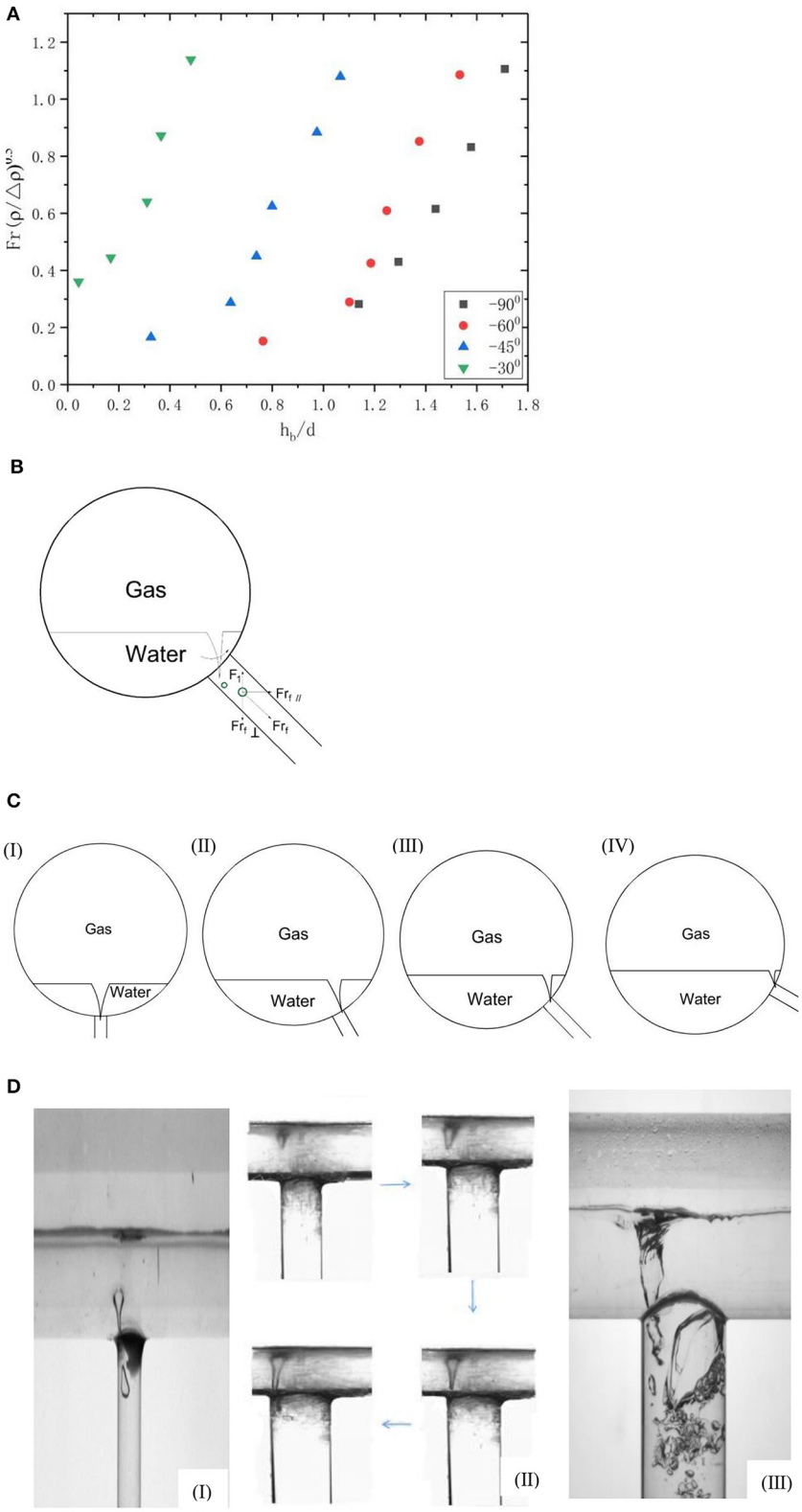


**FIGURE 2 |** Continued

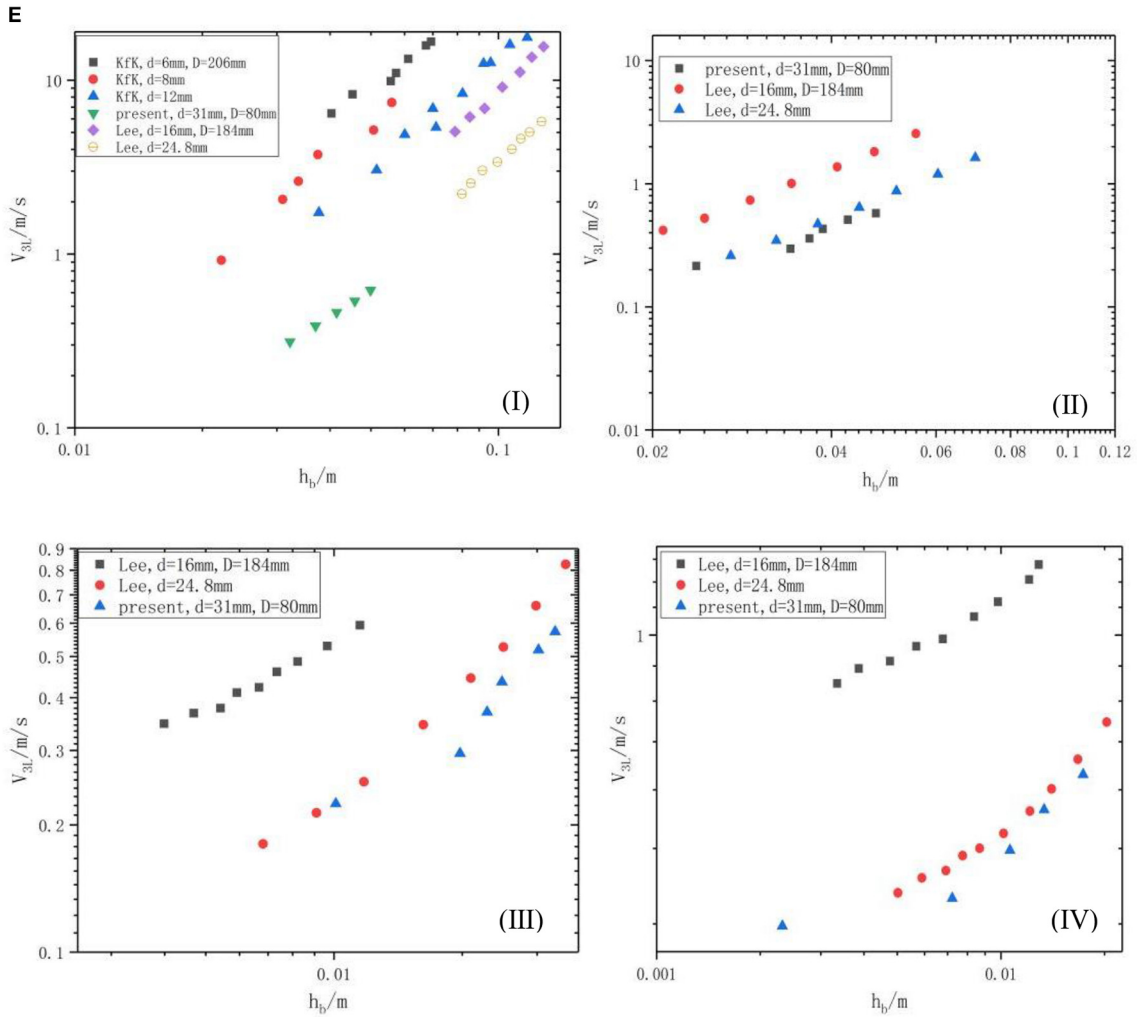


**FIGURE 2 |** The phenomenon and influencing factors of gas entrainment. **(A)** The OGE data at −30°, −45°, −60°, −90° branches. **(B)** Force diagram of bubbles. **(C)** Vortex position, (I) $\theta = -90°$, (II) $\theta = -60°$, (III) $\theta = -45°$, and (IV) $\theta = -30°$. **(D)** Onset phenomenon at arbitrary-sized branches, (I) $d = 10$ mm (Shen et al., 2018), (II) $d = 31$ mm, and (III) $d = 50$ mm (Shen et al., 2018). **(E)** Comparison of present OGE data with KfK and Lee, (I) $\theta = -90°$, (II) $\theta = -60°$, (III) $\theta = -45°$, and (IV) $\theta = -30°$.

geometrical size of the branch. For the branch with a diameter of 50 mm, a distinct gas chamber exists in the entrance of the branch [**Figure 2D** (III)]. The reason is that the shape of the vortex generated at the entrance of the large-sized branch is larger than that generated at the entrance of the small-sized branch. Therefore, for the large-sized branch, when some bubbles with large volume enter the branch, with the effect of the buoyancy force of the bubbles, these bubbles cannot be entrained into the steam–water separator but gather to the entrance of the branch to form a gas chamber.

In **Figure 2E**, the experimental data of Lee, KfK, and Shen are compared with the present experimental data. For arbitrary-angled branch pipes, at a given critical liquid velocity of branch ($V_{3L}$), $h_b$ decreases as the size of branch pipe decreases. The reason is that the local resistance coefficient at the entrance of the small-sized branch pipe is larger than that at the entrance of the large-sized branch pipe. At a given liquid velocity of the branch pipe ($V_{3L}$), the local resistance at the entrance of the small-sized branch is greater than the local resistance at the entrance of the large-sized branch pipe. According to the Bernoulli effect, under a given liquid velocity of the branch pipe ($V_{3L}$), for small-sized branch pipes, the dynamic pressure is greatly affected by the local resistance, which causes the static pressure difference from the inner interface of the main pipe to the branch pipe to reduce. Hence, when gas entrainment occurs, the critical liquid level ($h_b$) is smaller.

## Onset of Gas Entrainment Correlation

Based on the model of Lee et al., we made some modifications to build a more adaptable model. It is assumed that the gas–water in the main pipe is a two-phase stratified flow, and the liquid phase is an incompressible fluid and ignores the viscosity and surface tension of the liquid.

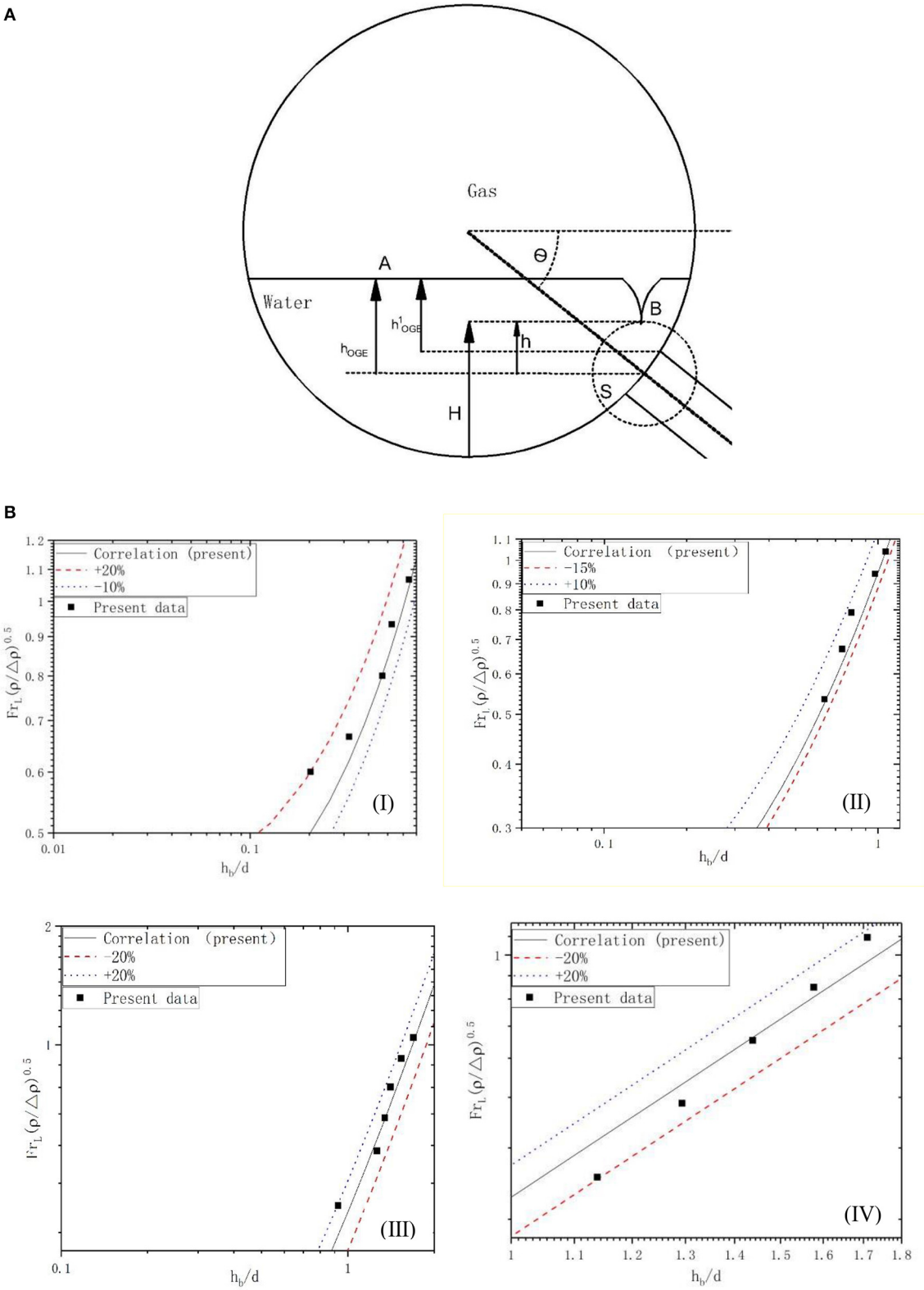


**FIGURE 3 |** Comparison and definition. **(A)** Schematics for the onset of gas entrainment. **(B)** Comparison of present OGE data with KfK and Lee, (I) $\theta = -30°$, (II) $\theta = -45°$, (III) $\theta = -60°$, (IV) $\theta = -90°$.

In **Figure 3A**, schematics for the onset of gas entrainment is shown. For $-90^\circ \leq \theta < 0^\circ$, it is known from the experimental phenomena that when gas entrainment occurs, a fine gas tube always extends to the upper edge of the branch. Hence, in this study, $h^1{}_{OGE}$ is defined as the vertical height between the gas–water interface and the upper edge of the branch, rather than the vertical distance between the gas–water interface and the center of the branch ($h_{OGE}$), which is different from the definition of Lee et al. (2006, 2007).

$$h_{OGE} = h^1_{OGE} + (d\cos\theta)/2 \tag{7}$$

The Froude number used in this study is the same as that of Lee et al.; we can get the following definition of the Froude number:

$$Fr_f = \frac{v}{\sqrt{dg}} = \frac{Q}{\pi(d/2)^2\sqrt{gd}} \tag{8}$$

where $Q$ is the volume flow rate of the liquid.

Inserting Equation (7) into Equation (3), we can get the following correlation:

$$Fr_f\sqrt{\frac{\rho_f}{\Delta\rho}} = C_{OGE(\theta)}\left(\frac{h^1_{OGE}}{d} + \frac{1}{2}\left(\frac{D}{d}\right)(1-\sin\theta) + \frac{\cos\theta}{2}\right)^{2.5} \tag{9}$$

Since $Fr_f$ is nonlinearly related to $h_{OGE}/d$ and is related to the angle of the branch, the correlation is corrected by a sine function. For $-90^\circ \leq \theta < 0^\circ$, we can get the following correlation:

$$Fr_f\sqrt{\frac{\rho_f}{\Delta\rho}} = (\sin(k\theta + n))^m C_{OGE(\theta)}\left(\frac{h^1_{OGE}}{d} + \frac{1}{2}\left(\frac{D}{d}\right)(1-\sin\theta) + \frac{\cos\theta}{2}\right)^{2.5} \tag{10}$$

By fitting Equation (10) with the present experimental data, we can get the optimal solutions for $C_{OGE(\theta)} = 0.283$, $k = 1.149$, $m = 3.224$, and $n = 0.935$.

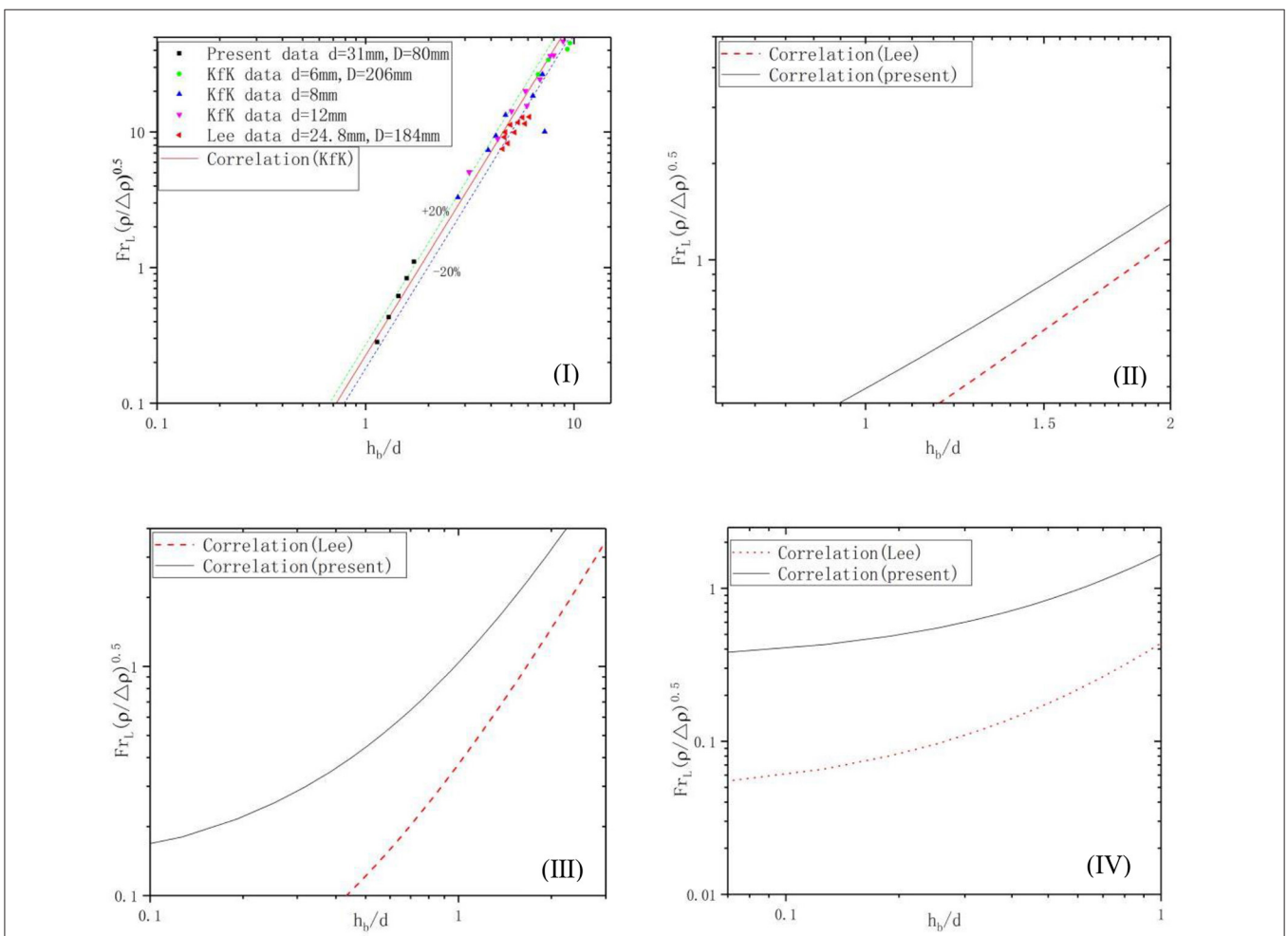


**FIGURE 4 |** Comparison of present data correlation and KfK and Lee correlations, (I) $\theta = -90^\circ$, (II) $\theta = -60^\circ$, (III) $\theta = -45^\circ$, and (IV) $\theta = -30^\circ$.

In **Figure 3B**, the simulated curve and the present experimental data are shown. For arbitrary-sized branches, such as $-90°$, $-60°$, $-45°$, and $-30°$, the experimental data are scattered on both sides of the simulated curve. In general, the correlation of this experiment can well predict the relationship between the critical Froude number ($Fr_f$) and $h_b/d$. Moreover, the experimental data all fall within the error area of $\pm 20\%$.

## Comparative Analysis of the Onset of Gas Entrainment Correlation

For the bottom branch, some studies and correlation predictions were made for the onset of gas entrainment. **Figure 4** (I) represents the comparison of the experimental data and the correlations of previous and present researchers. For the onset of vortex-induced gas pull-through, the correlation of KfK (Equation 2) accurately predicts the data of the onset of gas entrainment for a range of $0.029 < d/D < 0.135$ (Smoglie and Reimann, 1984; Guide, 1989). And for this study, the present data are all within $\pm 20\%$ of the region. In other words, the model of KfK can predict the results of this study well. It is proved that the effective application range of the KfK model can be extended to $0.029 < d/D < 0.388$ for the entrainment through a bottom branch.

**Figure 4** (II, III, and IV) shows the comparison between Lee correlation and present correlation. For other tilted branches, such as $-60°$, $-45°$, and $-30°$, Lee's correlation curve is significantly different from the correlation curve of this experiment. The reason is that the size of branch of this experiment is different from that of Lee. Since $d/D < 0.14$ in Lee's experiment, the effect of the size of the branch on the gas entrainment can be ignored when defining $h_{OGE}$. However, the size of the branch ($d/D = 0.385$) in this experiment is larger than that of Lee, so the influence of the size of the branch pipe on the gas entrainment cannot be ignored. After considering the effect of the size of the branch, we redefine ${h^1}_{OGE}$ as the vertical height between the two-phase interface and the upper edge of the branch, rather than the vertical distance between the two-phase interface and the center of the branch, which explains the difference between our correlation and the correlation of Lee et al.

## CONCLUSION

In this study, the experiment on onset of gas entrainment was carried out in different directions of $-30°$, $-45°$, $-60°$, and $-90°$ through a branch with a diameter of 31 mm. And we have established a new correlation to predict the onset of the gas entrainment in arbitrary directions ($d/D = 0.375$, $\theta = [-30°, -45°, -60°, -90°]$). By analyzing experimental data and experimental phenomena, the main conclusions are as follows:

(1) The gas is entrained by vortex flow, and the size of the branch and the angle of the branch have little effect on the form of entrainment. However, due to the effect of the branch diameter, when the gas is entrained through the 50-mm branch, there is a gas chamber at the inlet of the branch pipe.
(2) The new correlation established in this paper can predict the experimental data well, and the maximum error is $\pm 20\%$.
(3) By comparison with Lee's model, it can be found that the model of onset of gas entrainment based on small-sized branches is not suitable for large-scale branches. This is because the model of Lee does not consider the influence of the diameter of the branch. To solve this problem, we have defined the new critical liquid level (${h^1}_{OGE}$).

## DATA AVAILABILITY STATEMENT

All datasets generated for this study are included in the article/supplementary material.

## AUTHOR CONTRIBUTIONS

JG and ZM participated in the design of this study, and they both contributed significantly to analysis and manuscript preparation. YY and GS helped perform the analysis with constructive discussions. XL and GS carried out the study and collected important background information. JG performed the data analyses and wrote the manuscript. All authors read and approved the final manuscript.

## ACKNOWLEDGMENTS

The financial supports of the National Nature Science Foundation of China (nos. 11605032 and 11605033), the Fundamental Research Funds for Central University of Ministry of Education of China (3072019CF1506), and the Innovation Fund of the Fundamental Research Funds for the Central Universities (3072019GIP1520) are gratefully acknowledged. I would also like to thank YY for his important guidance in this process, whose contribution is equivalent to that of the first author.

## REFERENCES

Guide, R. (1989). *Best Estimate Calculations of Emergency Core Cooling System Performance*. Washington, DC: US Nuclear Regulatory Commission.

Lee, J. Y., Hwang, G. S., Kim, M., and No, H. C. (2006). Experimental analysis of off-take phenomena at the header–feeder system of CANDU. *Ann. Nucl. Energy* 33, 3–8. doi: 10.1016/j.anucene.2005.09.002

Lee, J. Y., Hwang, S. H., Kim, M., and Park, G. C. (2007). Onset condition of gas and liquid entrainment at an inclined branch pipe on a horizontal header. *Nucl. Eng. Des.* 237, 1046–1054. doi: 10.1016/j.nucengdes.2007.01.002

Lin (2010). *Passive Safety Advanced PWR Nuclear Power Technology*. Atomic Energy Press.

Riemke, R. A., Bayless, P. D., and Modro, S. M. (2006). "Recent improvements to the RELAP5-3D code," in *Proceedings of the 2006 International Congress on Advances in Nuclear Power Plants, ICAPP'06*. Reno, NV. 1816–1819.

Schulz, T. L. (2008). Westinghouse AP1000 advanced passive plant. *Nucl. Eng. Des.* 236, 1547–1557. doi: 10.1016/j.nucengdes.2006.03.049

Shen, K., et al. (2018). *Study on Gas Entrainment in Vertical Downward T-tube[D]*. Harbin: Harbin Engineering University, *22–24*. (in Chinese).

Smoglie, C., and Reimann, J. (1984). Two-phase flow through small branches in a horizontal pipe with stratified flow. *Int. J. Multiphase Flow* 12, 609–625. doi: 10.1016/0301-9322(86)90063-7

Wang, W., Su, G., Qiu, S. Z., and Tian, X. W. (2011). Thermal hydraulic phenomena related to small break LOCAs in AP1000. *Prog. Nucl. Energy*. 53, 407–419. doi: 10.1016/j.pnucene.2011.02.007

Welter, K. B., Wu, Q., You, Y., Abel, K., McCreary, D., Bajorek, S., M., et al. (2014). Experimental investigation and theoretical modeling of liquid entrainment in a horizontal tee with a vertical-up branch. *Int. J. Multiphase Flow* 30, 1451–1484. doi: 10.1016/j.ijmultiphaseflow.2004.08.001

Zuber, N. (1980). *Problems in Modeling of Small Break LOCA*. Technial Report, Nuclear Regulatory Commission. Washington, DC: Division of Reactor Safety Research.

**Conflict of Interest:** YY was employed by the company China Nuclear Power Engineering Co.

The remaining authors declare that the research was conducted in the absence of any commercial or financial relationships that could be construed as a potential conflict of interest.

## NOMENCLATURE

| | |
|---|---|
| $d$ | Branch diameter |
| $D$ | Main pipe diameter |
| $Fr$ | Froude number |
| $g$ | Gravitational acceleration |
| $h$ | Distance between interface and branch centerline |
| $h_b$ | Critical liquid level at the onset of gas entrainment |
| $W_{3L}$ | Liquid mass flow rate at branch pipe |
| $V_{3L}$ | Liquid velocity in branch pipe |
| **Greek symbols** | |
| $\theta$ | Branch angle |
| $\rho_f$ | Liquid-phase density |
| $\rho_g$ | Gas-phase density |
| $\Delta\rho$ | Density difference |
| **Subscripts** | |
| $g$ | Gas |
| $l$ | Liquid |
| OGE | Onset of gas entrainment |
| **Abbreviations** | |
| ADS-4 | Fourth-stage automatic depressurization system |
| LOCA | Loss of coolant accident |

frontiers in Energy Research

BRIEF RESEARCH REPORT
published: 25 February 2020
doi: 10.3389/fenrg.2020.00010

# Theoretical Investigation on the Fully Developed Turbulent Heat Transfer Characteristics of Liquid Sodium

*Rui Zhang*[1]*, *Zhenying Wang*[2], *Zhenhong Wang*[1], *Tingting Ren*[1] and *Jiangwu Shi*[1]

[1] College of Nuclear Science and Technology, Harbin Engineering University, Harbin, China, [2] State Key Laboratory of Nuclear Power Safety Monitoring Technology and Equipment, Shenzhen, China

Liquid sodium has been used as the working medium for the high-temperature heat pipe and the generation IV sodium cooled fast reactor due to its extremely high conductivity. The heat transfer characteristics of sodium in a circular pipe is one of the most essential focuses in engineering applications. In this paper, a model to predict the heat transfer coeffcient of fully developed sodium flowing in tube was developed based on universal velocity, turbulent eddy diffusivity, and the linear law inside the thermal boundary layer. The Kays correlation for turbulent Prandtl number was used to predict the turbulent Prandtl in the bulk flow with y + larger than 60. This model was validated by experiment data of Hg, NaK, and sodium, showing superior accuracy than existing models. Besides, the dependence of the accuracy on the model parameters was also analyzed, demonstrating the universal applicability of the current model.

**Keywords: turbulent heat transfer, liquid metal, liquid sodium, heat transfer coefficient, fully developed heat transfer**

OPEN ACCESS

***Edited by:***
*Jun Wang,*
*University of Wisconsin-Madison,*
*United States*

***Reviewed by:***
*Xianping Zhong,*
*Tsinghua University, China*
*Josua Petrus Meyer,*
*University of Pretoria, South Africa*

***Correspondence:**
*Rui Zhang*
*rzhang@hrbeu.edu.cn*

***Specialty section:***
*This article was submitted to Nuclear Energy, a section of the journal Frontiers in Energy Research*

***Received:*** *11 December 2019*
***Accepted:*** *17 January 2020*
***Published:*** *25 February 2020*

***Citation:***
*Zhang R, Wang Z, Wang Z, Ren T and Shi J (2020) Theoretical Investigation on the Fully Developed Turbulent Heat Transfer Characteristics of Liquid Sodium. Front. Energy Res. 8:10. doi: 10.3389/fenrg.2020.00010*

## INTRODUCTION

Liquid metals, especially liquid sodium, have been widely used in high-temperature heat transfer process in industry and power applications, such as sodium cooled fast reactors in France, China, and Russia, and the high temperature heat pipe used in space facilities. To ensure the safety of the facilities, the heat transfer coefficient should be accurately estimated in the thermal design process of industrial applications. However, the heat transfer characteristics of liquid metal are quite different from traditional fluids. The molecular Prandtl numbers of traditional fluids vary from 1 to 10, while the Prandtl numbers of liquid metals are always <0.1, even 0.01. Furthermore, as for liquid sodium, the Prandtl number is in the range of 0.01–0.001 due to extremely large thermal conductivities. The difference in Prandtl number changes the heat transfer characteristics in the near wall and bulk regions. The thermal boundary layers of liquid metal are much thicker than the momentum boundary layer, resulting in the failure of correlations for heat transfer of traditional fluids in the applications of liquid metals. Besides, the discrepancy in the thermal and momentum boundary layers leads to the failure of Reynolds analogy. Thus, the traditional computational fluids dynamics treatment on the energy equation based on Reynolds analogy and the unit turbulent Prandtl number is not validated in liquid metals.

In the past few decades, researchers have devoted themselves to theoretical and experimental investigations. Lyon (1951) proposed the first empirical correlation for turbulent heat transfer of liquid sodium. Then Lubarsky and Kaufman (1955) corrected the Lyon correlation based on experiment data and published a new correlation for channels with specified geometry.

Schleisiek (1970) carried out a series of experiments on liquid sodium heat transfer in a 9-mm inner diameter pipe and derived a formula for Nusselt number based on 24 sets of data. Shi et al. (1981) also gave correlations for liquid sodium, but these correlations have limited applicable range of Peclet number <3,000. Except for the correlations aiming at liquid sodium heat transfer, several correlations were also proposed based on data from other liquid metals, such as mercury (Hg) (Chang and Akins, 1972), sodium–potassium (NaK) eutectic (Sleicher et al., 1973), and lead–bismuth eutectic (LBE) (Ibragimov et al., 1961). In addition, Dwyer (1966) proposed a heat transfer correlation for the universal applications of liquid metal. However, these correlations predict the Nusselt number with large differences. Furthermore, the results show a noticeable divergence even for the same working fluid, especially for sodium and NaK eutectic, which means the investigation on the heat transfer characteristics of sodium has still not matured.

In this work, a theoretical model was proposed to predict the turbulent heat transfer coefficient of liquid sodium. This model employed the correlations for universal velocity and eddy diffusivity to predict the distributions of velocity and turbulence. The linear law was used to predict the non-dimensional temperature in the near wall linear sublayer inside the thermal boundary layer. Beyond this sublayer, the turbulent Prandtl number was predicted using the Kays correlation (Kays, 1994), which is only related to the local turbulent parameters. The governing equations for non-dimensional temperature and heat flux can be solved after being discretized on the radial direction. The model was validated by experiment data, showing superior accuracy compared with other available models. The uncertainty from the model parameters was also investigated based on the parametric analysis.

# METHOD

## Governing Equations for Heat Transfer

The governing equation for energy conservation in a fully developed pipe can be simplified into the following format:

$$\rho c_p u_x \frac{\partial T}{\partial x} = \frac{1}{r}\frac{\partial}{\partial r}(rq) \tag{1}$$

Due to the wall heat flux, the temperature in the pipe cannot be described by a fully developed field with zero gradient in the flow direction since the temperature rises along the pipe. However, the temperature increases linearly with the flow direction in a pipe when the flow and thermal parameters are fully developed. Thus, the temperature $T(x, r)$ in the pipe can be divided into two parts plus a fixed wall temperature at the inlet, that is,

$$T(x, r) = T_{w,x=0} + \frac{\partial T}{\partial x}x - \theta(r) \tag{2}$$

where $T_{w,x=0}$ is the wall temperature at the channel inlet; $\theta(r)$ is the temperature along the radial direction, which is independent from the axial location, that is, fully developed just as the velocity field. $\frac{\partial T}{\partial x}x$ is the temperature increase in the pipe, which is linear with the flow distance or heated length, and can be calculated based on the energy balance, i.e.,

$$\frac{\partial T}{\partial x} = \frac{2q_w}{r_w \rho c_p u_m} \tag{3}$$

After substituting Equations (2) and (3) into Equation 1, we can obtain:

$$\frac{2q_w u_x}{r_w u_m} = \frac{1}{r}\frac{\partial}{\partial r}(rq) \tag{4}$$

Let $R = \frac{r}{r_w}$ and $q^+ = \frac{q}{q_w}$. Then Equation 4 can be transformed into:

$$\frac{1}{R}\frac{d}{dR}(Rq^+) = \frac{2u_x}{u_m} \tag{5}$$

According to Fourier's law on heat transfer, the radial heat flux at any radial location can be written as

$$q = k_{eff}\frac{\partial T}{\partial r} = k_{eff}\frac{d\theta}{dr} \tag{6}$$

where

$$k_{eff} = k_l + k_t = k_l + \rho c_p \varepsilon_q \tag{7}$$

Given $\mathrm{Pr} = \frac{c_p \mu}{k_l}$ and $\mathrm{Pr}_t = \frac{\varepsilon_m}{\varepsilon_q}$, Equation 6 can be changed into:

$$\frac{d\theta}{dR} = \frac{q r_w}{k_l(1 + \frac{\mathrm{Pr}}{\mathrm{Pr}_t}\frac{\varepsilon_m}{\nu})} \tag{8}$$

Define the following non-dimensional parameters:

$$\begin{cases} u^+ = \frac{u_x}{u_\tau} \\ u_m^+ = \frac{u_m}{u_\tau} \\ \theta^+ = \frac{\theta_w - \theta}{\theta_\tau} = -\frac{\theta}{\theta_\tau} \\ r_w^+ = \frac{r_w u_\tau}{\nu} \end{cases} \tag{9}$$

where $u_\tau = \sqrt{\tau_w/\rho}$ and $\theta_\tau = q_w/\rho c_p u_\tau$.
Then, Equations (5) and (8) can be written as:

$$\frac{1}{R}\frac{d}{dR}(Rq^+) = \frac{2u^+}{u_m^+} \tag{10}$$

$$\frac{d\theta^+}{dR} = -\frac{q^+ r_w^+ \mathrm{Pr}}{(1 + \frac{\mathrm{Pr}}{\mathrm{Pr}_t}\frac{\varepsilon_m}{\nu})} \tag{11}$$

The boundary conditions for Equations (10) and (11) are listed as follows:

$$q^+|_{R=1} = 1 \tag{12}$$

$$q^+|_{R=0} = 0 \tag{13}$$

$$\theta^+|_{R=1} = 0 \tag{14}$$

$$\frac{d\theta^+}{dR}|_{R=0} = 0 \tag{15}$$

Until now, we obtained the governing equations and boundary conditions for the dimensionless temperature and heat flux along the radial direction. These equations can be solved numerically by the finite difference method with limited discrete grid along the radius of the pipe. The total length of the radius can be divided into $n-1$ identical intervals with $n$ points, including the points at the pipe center ($i = 0$) and on the wall ($i = n$). Thus, the interval is:

$$\Delta R = 1/(n-1) \tag{16}$$

and the radial location referred from the center of the tube is:

$$R_i = (i-1)\Delta R, \quad i = 1-n \tag{17}$$

The discrete format for Equations (10) and (11) on the $n$ grid in the radial direction of the pipe can be written as:

$$q_i^+ = \left(\frac{u_i^+}{u_m^+}R_i + \frac{u_{i-1}^+}{u_m^+}R_{i-1}\right)\frac{\Delta R}{R_i} + \frac{R_{i-1}}{R_i}q_{i-1}^+ \tag{18}$$

and

$$\theta_{i-1}^+ = \theta_i^+ + \frac{\Delta R \mathrm{Pr} r_w^+}{2}\left[\frac{q_i^+}{1+\frac{\mathrm{Pr}}{\mathrm{Pr}_{t,i}}\left(\frac{\varepsilon_m}{\nu}\right)_i} + \frac{q_{i-1}^+}{1+\frac{\mathrm{Pr}}{\mathrm{Pr}_{t,i-1}}\left(\frac{\varepsilon_m}{\nu}\right)_{i-1}}\right] \tag{19}$$

where the mean universal velocity $u_m^+$ is calculated by:

$$\begin{aligned} u_m^+ &= \frac{\int_0^{R_w} 2\pi u^+ R dR}{\pi R_w^2} \\ &= \int_0^1 2u^+ R dR \\ &= \Delta R \sum_{i=1}^{n}\left(R_{i-1}u_{i-1}^+ + R_i u_i^+\right) \end{aligned} \tag{20}$$

Theoretically, Equations (18) and (19) can be solved iteratively under the following conditions:

$$q_1^+ = 0 \tag{21}$$

$$\theta_n^+ = 0 \tag{22}$$

## Auxiliary Models and Strategy to Solve the Governing Equations

As mentioned earlier, the numerical solutions for governing equations (Equations 10, 11) for energy balance in the radial direction could be obtained by solving Equations (18) and (19) with the boundary conditions of Equations (21) and (22). However, the radial profiles for the velocity, turbulent eddy diffusivity, and turbulent Prandtl number are still unknown and should be given to solve the above governing equations.

### Universal Velocity and Eddy Diffusivity

As for the fully developed turbulent flow in the circular tube, various non-dimensional universal velocity profiles have been proposed in the last century, such as Prandtl's linear law for the sublayer (Johnson, 2016) and Taylor's logarithmic law for the logarithmic regime beyond the buffer layer (Taylor, 1916). Most of these correlations were only validated for the boundary layer, except the universal velocity correlation proposed by Reichardt (1957), that is,

$$\begin{aligned} u^+ = &\frac{1}{\kappa}\ln\left[\left(1+0.4y^+\right)\frac{1.5(1+R)}{1+2R^2}\right] + \\ &\left(5.5-\frac{\ln\kappa}{\kappa}\right)\left[1-\exp\left(-\frac{y^+}{11}\right)-\frac{y^+}{11}\exp\left(-\frac{y^+}{3}\right)\right] \end{aligned} \tag{23}$$

where the non-dimensional radial $R$ locates in the range $0 \le R \le 1$. The non-dimensional distance to the wall is calculated by

$$y^+ = yu_\tau/\nu = (1-R)r_w^+ \tag{24}$$

Reichardt (1957) also proposed an empirical correlation for the eddy diffusivity for the momentum transfer caused by the stochastic movement of fluid from the wall to the center of the duct, which can be expressed in terms of the fraction of eddy diffusivity and kinematic viscosity, that is,

$$\frac{\varepsilon_\tau}{\nu} = \begin{cases} \kappa\left[y^+ - 11\tanh\left(\frac{y^+}{11}\right)\right] & \text{for\$y}^+ \le 50\$ \\ \frac{\kappa}{3}y^+(1+R)\left(0.5+R^2\right) & \text{for\$50} < \text{y}^+ \le \text{r}_\text{w}^+\$ \end{cases} \tag{25}$$

where $\kappa = 0.4$.

### Turbulent Prandtl Number

As for the liquid metal with the molecular Prandtl number much <1, the velocity boundary layer is much thinner than the thermal boundary layer, which means the Reynolds analogy with the turbulent Prandtl number near to unit is not validated under these conditions. Researchers proposed several correlations for the turbulent Prandtl number ($\mathrm{Pr}_t$) with a different molecular Prandtl number for the prediction of heat transfer characteristics. These correlations are only related to the Reynolds number, the molecular Prandtl number, the Peclet number, or the maximum eddy diffusivity in the tube, which means the calculated turbulent Prandtl number is kept as a constant along the radial direction. However, the essential laminar law for the non-dimensional temperature ($\theta^+ = \mathrm{Pr}\cdot y^+$) in the laminar regime inside the thermal boundary layer cannot be satisfied if Equation 19 is directly solved with a constant turbulent Prandtl number. This discrepancy is caused by the improper assumption of a uniform turbulent Prandtl number in the radial direction. As a matter of fact, the turbulent Prandtl number is highly associated to $y^+$, especially in the near wall region with $y^+$ less than about 100 (Kawamura et al., 1999; Duponcheel et al., 2014). Thus, the turbulent Prandtl number relevant to the local $y^+$ should be specified for an exact prediction of the temperature profile in the radial direction. However, as can be noted from the limited DNS and LES simulations (Kawamura et al., 1998, 1999; Tiselj and Cizelj, 2012; Duponcheel et al., 2014), the turbulent Prandtl

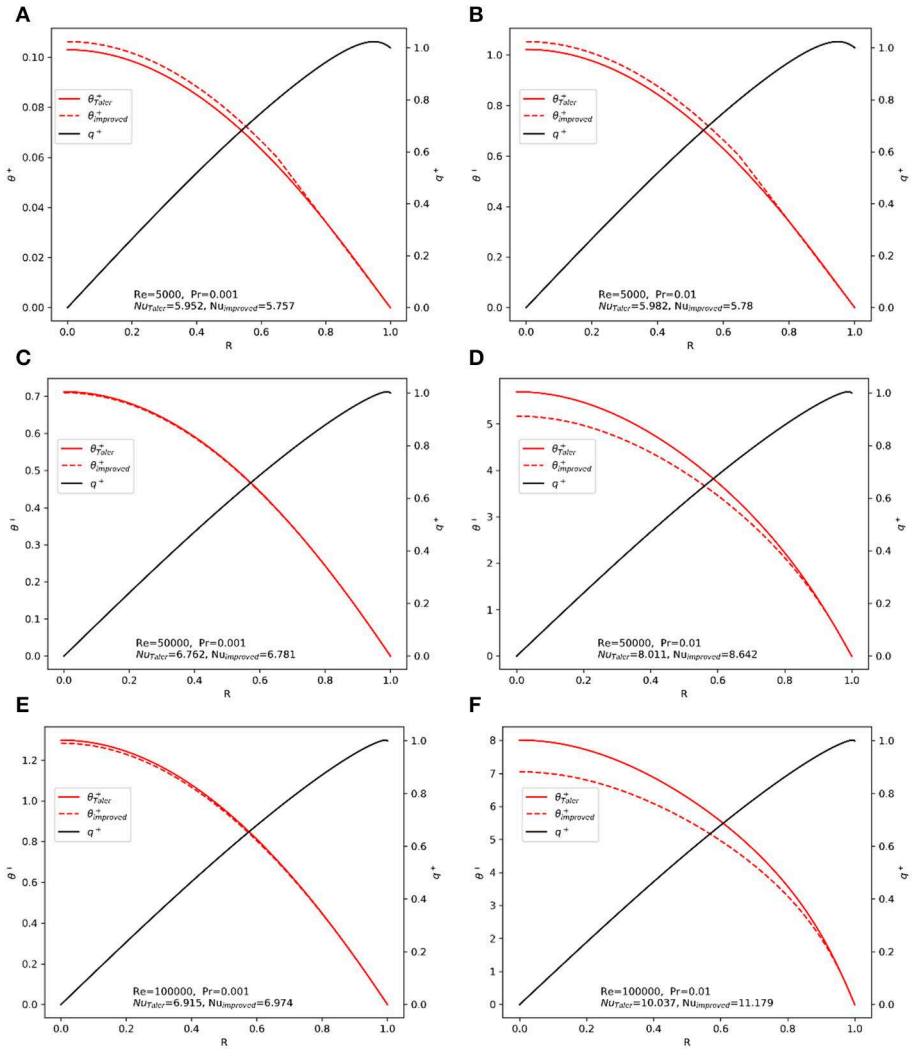


**FIGURE 1 | (A–F)** Non-dimensional heat flux and temperature along the radial direction.

number in the near wall region is highly related to the local turbulent Peclet number non-linearly (Kawamura et al., 1999; Tiselj and Cizelj, 2012; Duponcheel et al., 2014), and there is no universal correlation for the localized turbulent Prandtl number in the near wall region so far (Grötzbach, 2013; Roelofs et al., 2015).

As for the bulk flow region, Bricteux et al. (2012) assessed the DNS and LES data and pointed out that the turbulent Prandtl number should be about 2 for the bulk regime with $y^+$ larger than 200. Duponcheel et al. (2014) assessed the available models with results from large eddy simulation (LES) and found that the Kays correlation (Kays, 1994) is capable of predicting the turbulent Prandtl number in the bulk region, that is,

$$\mathrm{Pr}_t = 0.85 + \frac{0.7}{\mathrm{Pe}_t} \tag{26}$$

where $\mathrm{Pe}_t$ is the turbulent Peclet number defined as

$$\mathrm{Pe}_t = \frac{\nu_t}{\nu}\mathrm{Pr}$$

In Duponcheel et al. (2014), it is claimed that the Kays correlation (Kays, 1994) is validated for y+ < 100; nevertheless, it can be noted from the comparison between the Kays correlation and the LES data that the Kays correlation agrees well with the LES data for y+ < 65, which fortunately gives the opportunity to model the heat transfer of the low Prandtl number liquid metal by using the approach introduced in the next section.

## Treatment on the Near Wall Heat Transfer Without Turbulent Prandtl Number in the Thermal Boundary Layer

As noted in the investigations on the universal velocity profile vs. the non-dimensional wall distance $y^+$, linear, and logarithmic

laws are universal for all kinds of flow conditions in the turbulent flow regime, independent from the Reynolds number of the flow. The non-dimensional temperature, $\theta^+$, which is defined in Equation 9, also satisfies the linear law and the logarithmic law in the boundary layer. Thus, we can use the conception of the wall function to calculate $\theta^+$ in the thermal boundary layer. The near wall profile of $\theta^+$ could be solved by the wall function based on $y^+$, instead of the governing equation in the thermal boundary layer if the wall function for temperature is known priorly. However, due to the failure of the Reynolds analogy in the temperature distribution and the velocity distribution, the universal wall function for temperature in liquid metal with a low molecular Prandtl number is unknown. Besides, the thickness of the thermal boundary layer is much larger than that of the momentum boundary layer. The node in the velocity logarithmic regime may still be in the linear regime for energy transfer. Thus, the approach to set the first node in both the thermal and momentum logarithmic regimes, which is commonly used when dealing with water flow and heat transfer, is not validated.

Fortunately, from the DNS and LES studies on the heat transfer of liquid metal with a low Prandtl number, it can be observed that the thickness of the linear regime in the thermal boundary layer increases with decreasing the molecular Prandtl number (Kader, 1981; Kawamura lab, 2008; Duponcheel et al., 2014). Besides, the thermal linear regime is beyond $y^+$ of 60 when the molecular Prandtl number is <0.01, as noted by Bricteux et al. (2012). As for the liquid sodium, the molecular Prandtl number is <0.01 for most of the conditions. That means, the thickness of the thermal linear regime should be larger than about 60. The non-dimensional temperature $\theta^+$ could be predicted by the linear law in the thermal linear regime. Thus, the radial non-dimensional temperature distribution $\theta^+$ could be calculated by:

$$\theta^+ = \mathrm{Pr} \cdot y^+ \tag{27}$$

if $y^+$ is $<y_c^+$, and by Equation 19 if $y^+$ is larger than $y_c^+$, where $y_c^+$ is the critical non-dimensional wall distance set to be 60 in this work.

# RESULTS AND DISCUSSION

## Analysis on the Non-dimensional Parameters Along the Radial Direction

After solving the governing equations for non-dimensional heat flux and temperature (Equations 18, 19, 30), the non-dimensional heat transfer coefficient can be obtained by:

$$\mathrm{Nu} = \frac{hd}{k_l} = \frac{2\mathrm{Pr} \cdot r_w^+}{\theta_m^+} \tag{28}$$

The non-dimensional temperature and heat flux distributions for liquid metal with a different molecular Prandtl number under various flow conditions can be obtained. First, the dimensionless heat flux is obtained by solving Equation 18 with the boundary condition from heated surface, i.e., Equation 13. Then, the non-dimensional temperature can be solved by Equations (30) or (19) based on $y^+$ of the corresponding node. Results for six typical conditions are presented in **Figure 1**, including Reynolds numbers of 5,000, 50,000, and 100,000 and molecular Prandtl numbers of 0.001 and 0.01 for sodium under different thermal conditions. The results from the model proposed by Taler (2016) are presented as references. For low Reynolds number conditions, the effects of the molecular Prandtl number are quite small, and our model predicts higher non-dimensional temperature than Taler's model, which means a lower heat transfer coefficient. Under the conditions with a moderate to high Reynolds number, our model will present a higher Nusselt number than Taler's model, and the difference between these two models increases with the molecular Prandtl number. It should be mentioned that the linear approach on the near wall temperature distribution affects the temperature distribution not only in the linear regime but also in the bulk regime, since our model will degenerate into Taler's model if the critical $y^+$ for the upper limit of the linear regime is set to be zero.

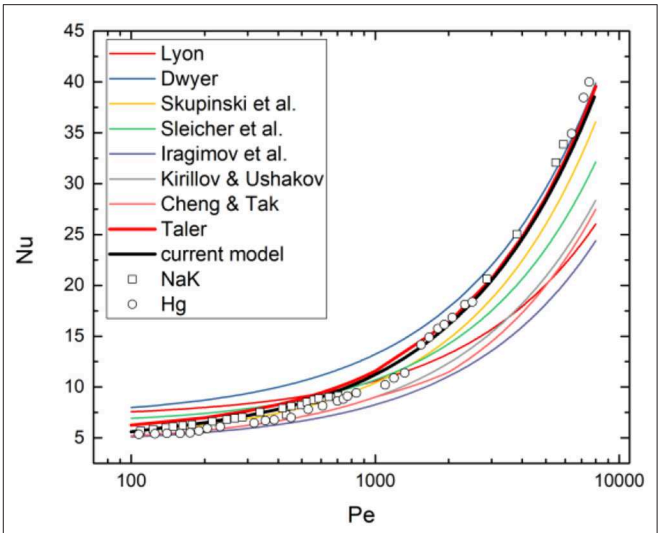


**FIGURE 2 |** Comparison of the Nusselt number with a different Peclet number.

## Model Validation With Experiment Data

In this section, the Nusselt number predicted by Equations (18) and (19) based on the turbulent Prandtl number given by Kays (1994) is compared with the experiment data to validate the accuracy of the models. First, the heat transfer data from Hg and NaK (Skupinski et al., 1965) were used as the benchmark database. Besides, the results predicted by correlations for liquid metal heat transfer are also given as references. As can be noted from the comparisons in **Figure 2**, the Nusselt number predicted by Taler correlation (Taler, 2016) and the current model with $\mathrm{Pr}_t$ obtained from Kays correlation (Kays, 1994) shows superior agreement with the experiment data. The heat transfer coefficient

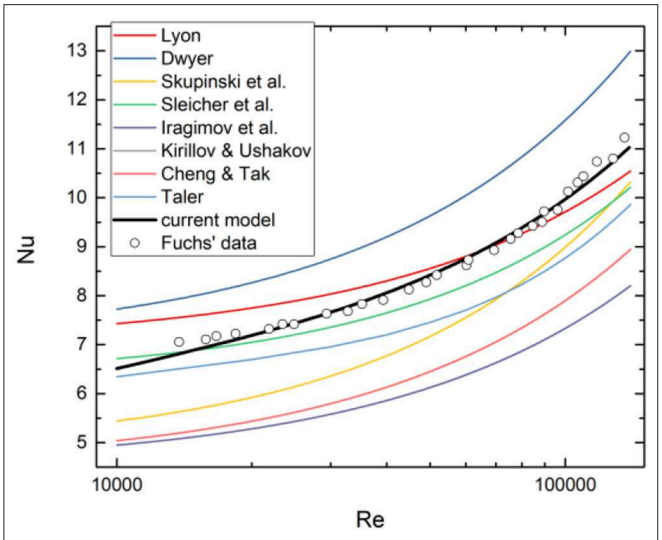


**FIGURE 3 |** Comparison of the Nusselt number for liquid sodium.

data for liquid sodium (Fuchs, 1974) are also used to validate the model. As can be noted from **Figure 3**, the accuracy of the current model is much better than any other models when predicting the liquid metal with an extremely low molecular Prandtl number.

## Parameter Sensitivity Analysis on the Critical $y^+$ for Linear Sublayer

As mentioned above, the upper limit $y^+$ of the linear regime in the thermal boundary layer is set to be 60 in the current model. However, the validation region of the Kays correlation (Kays, 1994) is beyond $y^+$of about 65. Besides, the upper limit of the linear regime may vary with the molecular Prandtl number. Thus, it is necessary to analyze the effects of critical $y^+$ (denoted as $y^+_{crit}$) on the model accuracy. In this section, $y^+_{crit}$ varies from 50 to 70, and the results are analyzed to measure the potential uncertainties introduced by the selection of $y^+_{crit}$. The results are shown in **Figure 4**, which demonstrates negligible effects of $y^+_{crit}$ on the predicted Nusselt number, especially for flow with a high Reynolds number.

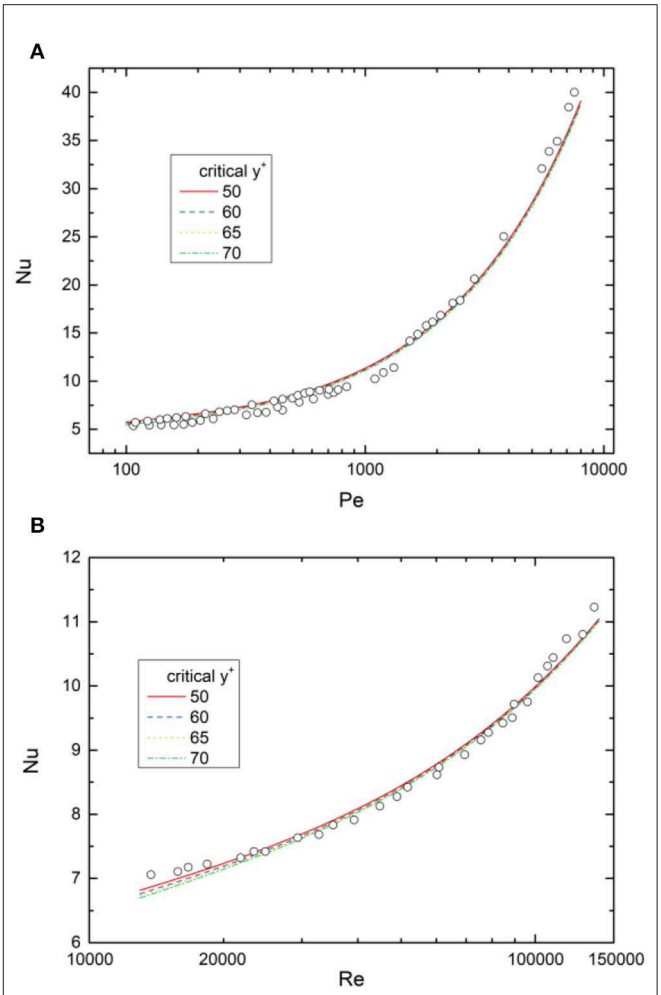


**FIGURE 4 |** Effects of $y^+_{crit}$ on prediction of Nusselt number. **(A)** Nusselt vs. Peclet number. **(B)** Nusselt vs. Reynolds number.

## CONCLUSIONS

In this paper, a new model for turbulent heat transfer of liquid sodium in a circular pipe was proposed. This model was developed based on the universal profiles for velocity and eddy diffusivity, generally applicable for turbulent flow in pipes. The Kays correlation was employed to predict the turbulent Prandtl number in the bulk flow region with non-dimensional wall distance $y^+$ larger than 60. In the near wall region with $y^+$ <60, the linear law was used instead of the turbulent Prandtl number to predict the temperature distribution. The profiles of non-dimensional temperature and heat flux can be obtained by solving the governing equations for temperature and heat flux. The selection of $y^+$ equaling to 60 as the upper limit of the linear regime has little effects on the heat transfer characteristics, which is proved by a sensitivity study related to the influences of critical $y^+$ on the predicted Nusselt number. The new model developed in this paper has superior accuracy when compared with other available correlations by the validation with the experiment data.

## DATA AVAILABILITY STATEMENT

All datasets generated for this study are included in the article/supplementary files.

## AUTHOR CONTRIBUTIONS

RZ contributed significantly to the analysis and manuscript preparation. ZhenyW performed the data analysis and wrote the manuscript. ZhenhW checked

the English writing thoroughly. TR and JS approved the final version.

## FUNDING

The authors greatly appreciate support from the Natural Science Foundation of Heilongjiang Province, China (Grant No. LH2019A009) and the Open Fund Program of the State Key Laboratory of Nuclear Power Safety Monitoring Technology and Equipment (K-A2019.414).

## ACKNOWLEDGMENTS

The authors are thankful for the support from the Fundamental Science on Nuclear Safety and Simulation Technology Laboratory, Harbin Engineering University, China.

## REFERENCES

Bricteux, L., Duponcheel, M., Winckelmans, G., Tiselj, I., and Bartosiewicz, Y. (2012). Direct and large eddy simulation of turbulent heat transfer at very low 22Prandtl number: application to lead–bismuth flows. *Nucl. Eng. Des.* 246, 91–97. doi: 10.1016/j.nucengdes.2011.07.010

Chang, B. H., and Akins, R. (1972). An experimental investigation of natural convection in mercury at low grashof numbers. *Int. J. Heat Mass Transf.* 15, 513–525. doi: 10.1016/0017-9310(72)90214-1

Duponcheel, M., Bricteux, L., Manconi, M., Winckelmans, G., and Bar tosiewicz, Y. (2014). Assessment of RANS and improved near-wall modeling for forced convection at low Prandtl numbers based on LES up to Re $\tau$ =2,000. *Int. J. Heat Mass Transf.* 75, 470–482. doi: 10.1016/j.ijheatmasstransfer.2014.03.080

Dwyer, O. (1966). Recent developments in liquid-metal heat transfer. *Atom. Energy Rev.* 4, 84–95.

Fuchs, H. (1974). *Heat transfer to liquid sodium: theoretical and experimental in vestigations on temperature profiles and turbulent temperature fluctuations in a circular tube* (Ph.D. thesis). ETH Zurich, Zurich, Switzerland.

Grötzbach, G. (2013). Challenges in low-prandtl number heat transfer simulation and modelling. *Nucl. Eng. Des.* 264, 41–55. doi: 10.1016/j.nucengdes.2012.09.039

Ibragimov, M. K., Subbotin, V., and Ushakov, P. (1961). Investigation of heat transfer in the turbulent flow of liquid metals in tubes. *Sov. J. At. Energy* 8, 48–50. doi: 10.1007/BF01491235

Johnson, R. W. (2016). *Handbook of Fluid Dynamics*. Florida City, FL: CRC Press. doi: 10.1201/b19031

Kader, B. (1981). Temperature and concentration profiles in fully turbulent bound ary layers. *Int. J. Heat Mass Transf.* 24, 1541–1544. doi: 10.1016/0017-9310(81)90220-9

Kawamura lab (2008). *DNS Database of Wall Turbulence and Heat Transfer*. Available online at: https://www.rs.tus.ac.jp/t2lab/db/ (accessed September 27, 2018).

Kawamura, H., Abe, H., and Matsuo, Y. (1999). DNS of turbulent heat transfer in channel flow with respect to reynolds and prandtl number effects. *Int. J. Heat Fluid Fl.* 20, 196–207. doi: 10.1016/S0142-727X(99)00014-4

Kawamura, H., Ohsaka, K., Abe, H., and Yamamoto, K. (1998). DNS of turbulent heat transfer in channel flow with low to medium-high Prandtl number fluids. *Int. J. Heat Fluid Fl.* 19, 482–491. doi: 10.1016/S0142-727X(98)10026-7

Kays, W. M. (1994). Turbulent Prandtl number—where are we *J. Heat Transf.* 116, 284–295. doi: 10.1115/1.2911398

Lubarsky, B., and Kaufman, S. J. (1955). *Review of Experimental Investigations of Liquid-Metal Heat Transfer*. Technical Report, Lewis Flight Propulsion Lab.

Lyon, R. N. (1951). Liquid metal heat transfer coefficients. *Chem. Eng. Prog.* 47, 75–79.

Reichardt, H. (1957). *The Principles of Turbulent Heat Transfer*. NACA-TM-1408, Technical Report, NASA.

Roelofs, F., Shams, A., Otic, I. M., Bottcher, Duponcheel, M. Y., Bartosiewicz, Y., et al. (2015). Status and perspective of turbulence heat transfer modelling for the industrial appli cation of liquid metal flows. *Nucl. Eng. Des.* 290, 99–106. doi: 10.1016/j.nucengdes.2014.11.006

Schleisiek, K. (1970). Heat transfer and boiling during forced convection of sodium in an induction-heated tube. *Nucl. Eng. Des.* 14, 60–68. doi: 10.1016/0029-5493(70)90084-1

Shi, S., Zhang, Z., Zhang, J., and Li, J. (1981). Experimental study on the heat tranfer to liquid metal sodium flowing in circular tube and annuli (in chinese). *J. Eng. Thermopys.* 2, 173–180.

Skupinski, E., Tortel, J., and Vautrey, L. (1965). Determination des coefficients de con vection d'un alliage sodium-potassium dans un tube circulaire. *Int. J. Heat Mass Transf.* 8, 937–951. doi: 10.1016/0017-9310(65)90077-3

Sleicher, C., Awad, A., and Notter, R. (1973). Temperature and eddy diffusivity profiles in nak. *Int. J. Heat Mass Transf.* 16, 1565–1575. doi: 10.1016/0017-9310(73)90184-1

Taler, D. (2016). Heat transfer in turbulent tube flow of liquid metals. *Procedia Eng.* 157, 148–157. doi: 10.1016/j.proeng.2016.08.350

Taylor, G. (1916). Conditions at the surface of a hot body exposed to the wind. *Brit. Adv. Com. Aero. Rep. Memor.* 272, 423–429.

Tiselj, I., and Cizelj, L. (2012). DNS of turbulent channel flow with conjugate heat transfer at prandtl number 0.01. *Nucl. Eng. Des.* 253, 153–160. doi: 10.1016/j.nucengdes.2012.08.008

**Conflict of Interest:** The authors declare that the research was conducted in the absence of any commercial or financial relationships that could be construed as a potential conflict of interest.

## NOMENCLATURE

| | |
|---|---|
| $k_{eff}$ | effective conductivity |
| $\theta_w$ | temperature at the wall |
| $u$ | velocity |
| $y$ | wall distance at y direction |
| $\varepsilon_\tau$ | eddy diffusivity |
| $Pe_t$ | turbulent Peclet number |
| $h$ | heat transfer coefficient |
| $d$ | hydraulic diameter |

frontiers in Energy Research

ORIGINAL RESEARCH
published: 03 March 2020
doi: 10.3389/fenrg.2020.00027

# Comparisons of Reduced Moderation Small Modular Reactors With Heavy Water Coolant

*Tengfei Zhang*[1]*, *Xiaojing Liu*[1], *Jinbiao Xiong*[1] and *Xu Cheng*[2]

[1] School of Nuclear Science and Engineering, Shanghai Jiao Tong University, Shanghai, China, [2] Institute of Fusion and Nuclear Technology, Karlsruhe Institute of Technology, Karlsruhe, Germany

This article presents the comparison of two reduced moderation small modular reactor concepts with heavy water coolant. Two reduced moderation small modular reactors, RMSMR-Th and RMSMR-MOX, are proposed for the sustainable utilization of nuclear resources. The design concepts are established on modifications of the well-experienced pressurized water reactor technology. Tightly packed lattice and heavy water coolant are employed to yield a hard neutron spectrum, which proved advantageous for increasing the conversion ratio, as well as lowering the burn-up reactivity swing between beginning of cycle and end of cycle. Thorium–uranium dioxide fuel and MOX fuel are compared using the same core arrangement, and the small modular reactor concept is adopted to reduce void coefficients. Radial blanket region and axial blanket region are adopted to enhance the fissile breeding, and a three-zone fuel configuration is adopted to flatten the power distribution. Core burn-up calculations were carried out to investigate the available cycle length, the conversion ratio, the power peaking factors, reactivity coefficients, etc. Light-water–based thermal–hydraulic models were employed to examine the safety features of the concepts. Numerical simulations indicate that both RMSMR-Th and RMSMR-MOX can sustain the power generation of 100 MWe by 7 years without refueling. Compared with thorium–uranium dioxide fuel, MOX fuel is helpful in reducing the burn-up reactivity swing, increasing the conversion ratio, and increasing the minimum departure from nuclear boiling ratio value. However, the positive void coefficient becomes a problem making RMSMR-MOX less attractive than the RMSMR-Th concept.

**Keywords: nuclear reactor design, reduced moderation, small modular reactor, heavy water coolant, epithermal-to-fast neutron spectrum**

OPEN ACCESS

***Edited by:***
*Jun Wang,*
*University of Wisconsin-Madison, United States*

***Reviewed by:***
*Youqi Zheng,*
*Xi'an Jiaotong University, China*
*Zhuo Li,*
*Sun Yat-sen University, China*
*Qian Zhang,*
*Harbin Engineering University, China*

***Correspondence:**
*Tengfei Zhang*
*zhangtengfei@sjtu.edu.cn*

***Specialty section:***
*This article was submitted to Nuclear Energy, a section of the journal Frontiers in Energy Research*

***Received:*** *17 January 2020*
***Accepted:*** *11 February 2020*
***Published:*** *03 March 2020*

***Citation:***
*Zhang T, Liu X, Xiong J and Cheng X (2020) Comparisons of Reduced Moderation Small Modular Reactors With Heavy Water Coolant. Front. Energy Res. 8:27. doi: 10.3389/fenrg.2020.00027*

## INTRODUCTION

Over the years, research interests in liquid metal fast reactors (LMFRs) have kept increasing because of their prominent features of uranium resources utilization and nuclear waste reduction. Due to the fast neutron spectra, the fission-to-capture ratio produced per fission in LMFRs is increased (Yang, 2012), leading to more fissile nuclear material production. A fast neutron spectrum can be achieved by employing coolants with small scattering cross sections (XSs) such as sodium, lead, or lead–bismuth eutectic (LBE). Although in recent years the fast reactor technology has progressed extensively, problems in the mainstream fast reactors (i.e., LMFRs) are still delaying the rapid spread of this technology. For example, the sodium coolant reacts with water and air, which requires caution while handling sodium to avoid leakage from the reactor. In contrast, lead and LBE are stable from the chemical perspective, but LBE produces non-negligible amount of the radiotoxic isotope $^{210}$Po.

Moreover, both lead and LBE are corrosive, posing risks to structural materials (Cacuci, 2010).

Besides, lowering the moderator quantity by reducing the moderator-to-fuel ratio (MFR) is also beneficial in achieving a hard neutron spectrum, such as using a tightly packed fuel pins layout (tight lattice). Therefore, the reduced-moderation water-cooled reactor was proposed (Okubo et al., 2003; Lindley et al., 2014), aiming for two design targets: an over-unity conversion ratio (CR) and maintaining negative void coefficients (VCs) during the whole cycle. It was found that boiling water reactor loaded with triangular lattices to reduce the coolant volume ratio effectively increases the CR, and a proper design of the core can sustain a whole-cycle negative VC. A pan-like short configuration is generally preferred to increase the axial neutron leakage by which to reduce the VC, and radial and axial blanket regions were employed to increase the CR. Aside from employing boiling water and tightening the lattice configuration, the neutron spectrum hardening is also achievable by using heavy water ($D_2O$). Although $D_2O$ is more expensive than light water ($H_2O$) and produces radioactive products (tritium) by irradiation, the elastic scattering XS of deuterium is 1/5 that of hydrogen. Consequently, a $D_2O$-cooled nuclear reactor with a small coolant volume ratio significantly hardens the neutron spectrum. The potential of this concept is two-fold: $D_2O$ is neither chemically active nor corrosive (as for liquid metal coolants); its similar thermal–physical properties as $H_2O$ enable the use of well-established LWR techniques as the nuclear industry has already accumulated extensive experience in maintaining and operating water-cooled reactors.

A few nuclear reactor concepts have been proposed based on the heavy water coolant. As an example, Hiruta and Youinou (2012, 2013a,b) at Idaho National Laboratory conducted analysis of tightly packed $D_2O$ high-conversion PWRs to shoot for near-breeder or break-even reactor concepts with negative whole-cycle void reactivity. The study was performed based on hexagonal MOX fuel assemblies and revealed important mechanisms such as the relation between MFRs and spectrum hardening, influences of blankets to the breeding effect and the coolant VC, and so on. In previous research, we undertook the conceptual design of a reduced moderation heavy water cooled reactor using thorium–uranium dioxide fuel (Zhang et al., 2019). The concept results in an epithermal-to-fast neutron spectrum and 7 years' operation time with 100-MWe power output. It indicated better utilization of nuclear resources based on the well-experienced water reactor technology. Besides, the epithermal-to-fast neutron spectrum will suppress the production of minor actinides compared to a thermal spectrum, which lowers the waste management pressure and the radiotoxicity hazard of minor actinides. It was pointed out that in a thorium nuclear reactor $^{232}U$ emits high-energy gamma ray that brings risks to the $^{232}Th/^{233}U$ recycling compared to the plutonium nuclear reactor, and the reduced plutonium production is beneficial to the spent fuel proliferation resistance. $^{232}U$ poses a radiation hazard for terrorists who would extract the uranium due to the 2.6-MeV gamma decay of its decay daughter, $^{208}Tl$; only 1 ppm of $^{232}U/U$ poses a similar risk as reactor-grade Pu (Zhang et al., 2019). However, the $^{233}U$-based fuel appears less practical than $^{235}U$- or $^{239}Pu$-based ones (i.e., $UO_2$ or MOX fuels), because the $^{233}U$ isotope does not exist in nature. It is worthwhile to exploit the possibility of more conventional nuclear fuel types. Therefore, in this research, we substitute the fuel type of RMSMR with MOX and offer comparisons of neutronics and thermal–hydraulics features between MOX-fueled concept and thorium–uranium–fueled concept.

The remainder of this article is organized as follows. As the foundation of this research, in *Description of Reactor Core*, the three-dimensional RMSMR core design is discussed in retrospect. In *Comparisons Between RMSMR-TH and RMSMR-MOX*, the RMSMR employing MOX fuel (RMSMR-MOX) is introduced and compared with the RMSMR-Th. The *Conclusions* gives conclusions and points to possible directions for future research.

## DESCRIPTION OF REACTOR CORE

Like most small modular reactors, the RMSMR is designed to be applicable for the deployment in outlying areas such as mountain area and islands. A 100-MWe power rating with a longer than 5 years' operational period is anticipated here to meet the power demand for the practical industrial application of interest, and the small core size has the expected advantages of serial production and incremental deployment, as well as the match to electric grid sitting opportunities. In addition, the fuel conversion phenomenon caused by the epithermal-to-fast neutron spectrum in RMSMR renders longer operational time than current PWR-type SMRs.

The RMSMR design is established within the framework of the traditional PWR technology, that is, adopting a 17 × 17 PWR assembly with a pin pitch of 1.26 cm. The MFR is evaluated as the ratio of the coolant volume to the fuel volume inside each square pin cell, and an MFR of 0.65 was selected considering the trade-off between maximizing CR, as well as reducing the VC. **Figure 1** shows the two-dimensional schematic view of the fuel assembly employed in the RMSMR.

Two fuel types are considered in this research, that is, $^{233}U$–$ThO_2$ fuel and MOX fuel. The reactor concepts are named RMSMR-Th and RMSMR-MOX, respectively. In both concepts,

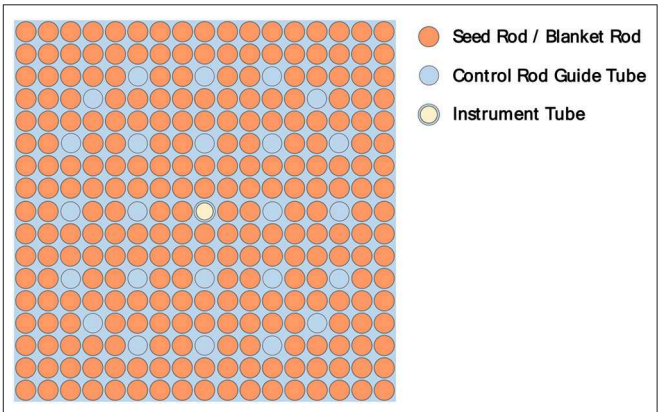


**FIGURE 1 |** Schematic of seed and blanket assemblies.

the flattening of the radial power distribution is achieved by the three-zone out-in assembly configuration. To achieve the expected 7-year operation period, the fissile isotope enrichments of RMSMR-Th seed assemblies are 11.0, 12.5, and 14.0%, as shown in **Figure 2**. In contrast, the molecular fractions of $PuO_2$ [weapon-grade plutonium dioxide (Bortot et al., 2011)] in RMSMR-MOX seed assemblies are 13.0, 14.0, and 15.0%, respectively. The blanket assemblies are designed to employ the same geometry as seed assemblies loaded with $ThO_2$ or depleted uranium (Bortot et al., 2011). To increase the reactor's CR, radial and axial blankets are adopted, as illustrated in **Figure 3**. The core is loaded with a seed fuel region of 100-cm in the middle of the core, and 10-cm blanket regions at the top and the bottom to enhance the leakage effect upon coolant voiding whereby achieving the negative VC. A 40-cm upper plenum is also considered to account for the fission gas release during irradiation. The excess reactivity could be suppressed by $B_4C$ control rods with 90% enrichment of $^{10}B$ (Zhang et al., 2019).

## COMPARISONS BETWEEN RMSMR-TH AND RMSMR-MOX

**Figure 4** presents $k_{eff}$ and CR variations vs. time modeled with OpenMC. Calculations are performed using 250 particle histories among which 100 are set at inactive, with 100,000 particles per history. The over-unity CR of RMSMR-Th and RMSMR-MOX at the beginning of cycle incurred the increase of $k_{eff}$. The $k_{eff}$ and the CR values for both RMSMR-Th and RMSMR-MOX begin to drop at the second year because of the counteraction between the accumulation of fission products and the fissile breeding. Both concepts can sustain the operation period of 7 years. Additionally, it can be observed that the RMSMR-MOX outperforms RMSMR-Th in terms of the reactor control, because the reactivity swing during the cycle is smaller. However, the slightly larger reactivity swing of RMSMR-Th can also be controlled by control rods or burnable poisons. **Figure 5** compares the neutron spectrum of RMSMR-Th, RMSMR-MOX, SFR, and PWR. It can be observed that the use of $D_2O$ shifts the neutron spectrum to epithermal-to-fast energy range, and the hardening of neutron spectrum with MOX fuel appears more pronounced than with thorium–uranium–based fuel. Therefore, the CR of RMSMR-MOX is slightly higher than that of RMSMR-Th, for example, 0.88 vs. 0.86 at End of Cycle (EOC). Because of the larger CR, the burn-up reactivity swing of RMSMR-MOX is smaller than that of RMSMR-Th. RMSMR-MOX has a reactivity change of +1$ during the whole operational period, which facilitates the reactivity control. In comparison, the reactivity change of RMSMR-Th is −3.7$.

The blanket assemblies cause a local power dip in the core center (i.e., a high-power peaking factor) at Beginning of Cycle (BOC), whereas with fuel conversion the peaking factor rapidly decreases with time, as shown in **Table 1**. Some important design parameters of RMSMRs are tabulated in **Table 2**. The

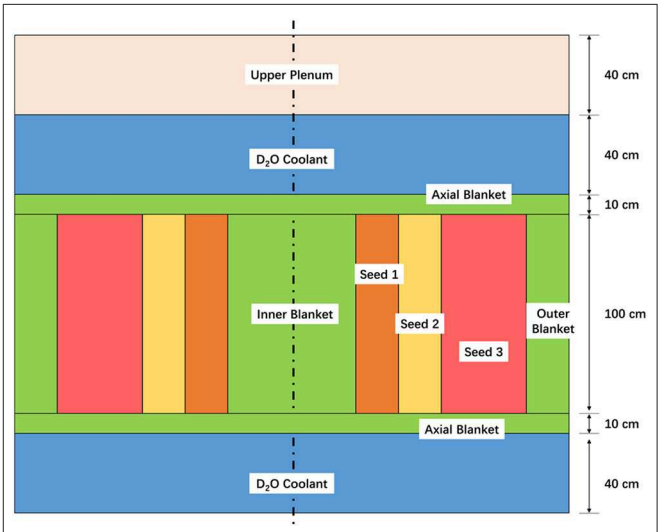


**FIGURE 3 |** Axial schematic view of RMSMR-Th.

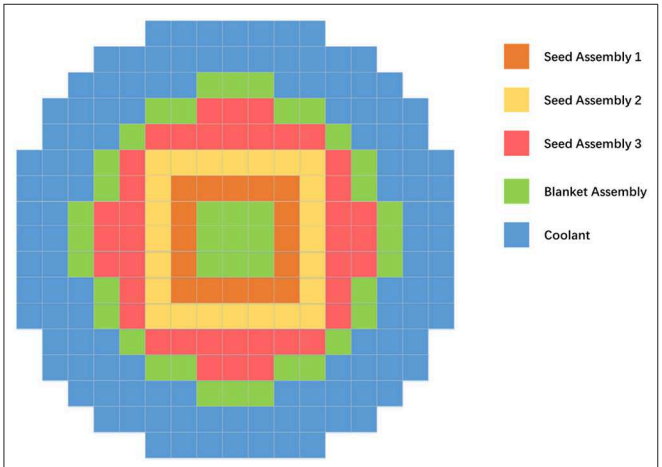


**FIGURE 2 |** Radial schematic view of RMSMR-Th.

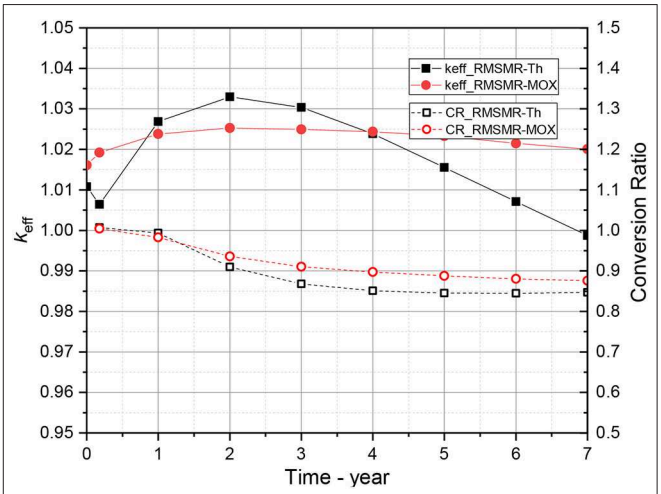


**FIGURE 4 |** $k_{eff}$ and CR variations of RMSMR-Th and RMSMR-MOX.

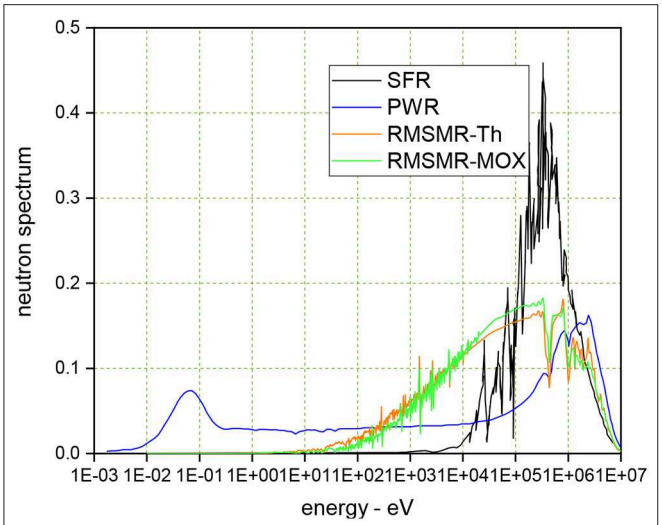


**FIGURE 5 |** Neutron spectrum comparisons.

**TABLE 1 |** Power peaking factors.

| | RMSMR-Th | | RMSMR-MOX | |
|---|---|---|---|---|
| | **Radial** | **Axial** | **Radial** | **Axial** |
| BOC | 1.90 | 1.44 | 1.84 | 1.35 |
| MOC | 1.43 | 1.07 | 1.60 | 1.17 |
| EOC | 1.40 | 1.15 | 1.53 | 1.14 |

**TABLE 2 |** Basic reactor design parameters of RMSMR.

| **Items** | **RMSMR-Th** | **RMSMR-MOX** |
|---|---|---|
| Thermal power/electric power (MW) | 300/100 | |
| Pressure (MPa) | 15.5 | |
| Pressure drop (kPa) | 4.9 | 5.9 |
| Core lifetime (years) | 7 | |
| Core height (cm) | 120 | |
| Equivalent diameter (cm) | 364 | |
| Number of seed fuel assemblies | 80 | |
| Number of blanket assemblies | 41 | |
| Coolant type | Heavy water ($D_2O$) | |
| Fuel type | $^{233}U$–$^{232}Th$ dioxide | MOX |
| Enrichment (%) | 11.0/12.5/14.0, 3 radial zones | 13.0/15.0/18.0, 3 radial zones |
| Core $^{233}U/^{239}Pu$ inventory (tHM) | 1.5 | 2.3 |
| Core $^{232}Th/^{238}U$ inventory (tHM) | 12.4 | 20.0 |
| Average discharged burn-up (MWd/tHM) | 55.2 | 32.4 |
| Core inlet/outlet temperatures (°C) | 285/315 | |
| Coolant flow rate (kg/s) | ≈1,960 | |
| Power density (W/cm$^3$) | ≈82 | |
| Assembly geometry | | |
| Fuel pellet diameter (cm) | 1.0455 | |
| Fuel pin diameter (cm) | 1.1455 | |
| Number of pins/assembly | 264 (17 × 17) | |
| Moderator to fuel ratio | 0.65 | |

power outputs of the two concepts are both 300 MWth/100 MWe, and the operating pressures are both 15.5 MPa. The coolant temperatures are referenced from commercial PWRs, with the inlet/outlet temperatures of 285°C/315°C. The coolant mass flow rate is set at around 1,960 kg/s for both RMSMR. Resultantly, pressure drops are estimated to be 4.9 and 5.9 kPa, respectively, for RMSMR-Th and RMSMR-MOX based on the Blasius correlation.

It should also be noted that the tight lattice core tends to reduce the critical heat flux and increase the pressure drop, which brings concerns to the thermal–hydraulic safety. To look into the thermal–hydraulics features, the W-3 formula widely used for PWRs is adopted to estimate the minimum departure from nuclear boiling ratio (mDNBR), thanks to the similar thermal properties of $D_2O$ and $H_2O$. Based on the power peaking factors in **Table 1**, total powers of hot fuel pins are 33.7 kW for RMSMR-Th and 32.7 kW for RMSMR-MOX. Correspondingly, enthalpy rises are 362.7 kJ/kg and 333.4 kJ/kg, respectively, based on the conservative uniform coolant flow distribution. The slight differences in thermal–hydraulic parameters between RMSMR-Th and RMSMR-MOX are caused by different pin power distributions. Eventually, the calculation with the W-3 formula yielded mDNBR values of 2.84 and 3.22 for RMSMR-Th and RMSMR-MOX, respectively. As indicated, the thermal–hydraulics safety margin for RMSMR-MOX is larger than that for RMSMR-Th.

**TABLE 3 |** Reactor safety characteristics of RMSMR.

| **Items** | **RMSMR-Th** | **RMSMR-MOX** |
|---|---|---|
| Effective delayed neutron fraction (pcm) | | |
| BOC | 319.0 ± 21.0 | 372.0 ± 31.0 |
| EOC | 307.0 ± 23.0 | 353.0 ± 30.0 |
| Prompt neutron generation time ($\mu$S) | | |
| BOC | 12.1 ± 0.7 | 168.2 ± 1.0 |
| EOC | 174.4 ± 2.7 | 250.5 ± 1.8 |
| FTC (pcm/K) | −6.4 ± 0.1 | −3.6 ± 0.2 |
| Coolant temperature coefficient (pcm/K) | −22.7 ± 0.1 | −3.4 ± 0.3 |
| Void reactivity coefficient (pcm/%void) | | |
| BOC | −211.7 ± 0.4 | +736.5 ± 0.6 |
| EOC | −105.8 ± 0.4 | +487.9 ± 0.5 |

Last but not least, key reactivity coefficients are evaluated, that is, the VC, the fuel temperature coefficient (FTC), and the coolant temperature coefficient (CTC). To obtain the VC, a 5% reduction in the coolant density is considered to simulate a 5% coolant voiding. The FTC is evaluated based on the reactivity/Kelvin between 900 and 600 K fuel temperatures. The CTC is computed as the reactivity/Kelvin between 600 and 300 K coolant temperatures. **Table 3** compares reactor safety characteristics of RMSMR-Th and RMSMR-MOX. It can be

observed that incorporations of $^{233}$U and $^{239}$Pu lead to smaller effective delayed neutron fractions ($\beta_{eff}$) than a conventional $^{235}$U-fueled reactor (Kazimi et al., 1999), although the MOX fuel results in larger $\beta_{eff}$ values and longer prompt neutron generation time than thorium–uranium–based fuel. The smaller $\beta_{eff}$ of the RMSMR-Th than the RMSMR-MOX implies an issue upon reactivity-induced transients, but can be somewhat mitigated by the faster Doppler feedback response because the harder neutron spectrum yields much shorter neutron lifetime. The FTC and CTC values of RMSMR-MOX are smaller than those of RMSMR-Th, but still within the required negative range. One crucial problem with MOX fuel would be the increased void reactivity coefficient, which is remarkably positive throughout the whole operation cycle, with a value of $+736 \pm 0.6$ pcm/%void at BOC. To tackle with this problem, several measures can possibly be taken, such as compaction of the core to enhance the neutron leakage upon coolant voiding, or increasing the MFR to soften the neutron spectrum, and so on. Also, it is noted in Hibi et al. (2001) work that a triangular lattice configuration with heterogeneous internal blanket yields an over-unity CR with negative void reactivity coefficient.

## CONCLUSIONS

This article presents comparisons of two reduced moderation small modular reactors, RMSMR-Th and RMSMR-MOX. The design concepts are established on modifications of the pressurized water reactor technology. For increasing the CR for better utilization of uranium resources and for reducing the burn-up reactivity swing to simplify the reactivity control, reduced-moderation lattice and heavy water coolant are employed. Thorium–uranium dioxide fuel and MOX fuel are compared using the same core arrangement. Compared with thorium–uranium dioxide fuel, MOX fuel reduces the burn-up reactivity swing and increases the CR and the mDNBR value while preserving negative FTC and CTC. However, MOX fuel incurs the coolant VC to become positive. This becomes a serious problem, making the current RMSMR-MOX less attractive than the RMSMR-Th concept. Further studies are required to optimize the core size, the MFR, and the layout of assemblies in order to reduce the VC of RMSMR-MOX.

## DATA AVAILABILITY STATEMENT

The datasets generated for this study are available on request to the corresponding author.

## AUTHOR CONTRIBUTIONS

All authors listed have made a substantial, direct and intellectual contribution to the work, and approved it for publication.

## FUNDING

This research was supported by the National Natural Science Foundation of China (Grant Nos. 11805122 and 11922505) and Startup Fund for Youngman Research at SJTU.

## REFERENCES

Bortot, S., Moisseytsev, A., Sienickib, J. J., and Artioli, C. (2011). Core design investigation for a SUPERSTAR small modular lead-cooled fast reactor demonstrator. *Nuclear Eng. Design*. 241, 3021–3031. doi: 10.1016/j.nucengdes.2011.04.012

Cacuci, D. G. (ed.). (2010). *Handbook of Nuclear Engineering: Vol. 1: Nuclear Engineering Fundamentals; Vol. 2: Reactor Design; Vol. 3: Reactor Analysis; Vol. 4: Reactors of Generations III and IV; Vol. 5: Fuel Cycles, Decommissioning, Waste Disposal and Safeguards*. Springer Science & Business Media

Hibi, K., Shimadab, S., Okubob, T., Iwamurab, T., and Wada, S. (2001). Conceptual designing of reduced-moderation water reactor with heavy water coolant. *Nuclear Eng. Design* 210, 9–19. doi: 10.1016/S0029-5493(01)00420-4

Hiruta, H., and Youinou, G. (2012). *Preliminary Neutronics Design and Analysis of $D_2O$ Cooled High Conversion PWRs*. Idaho National Laboratory. doi: 10.2172/1060965

Hiruta, H., and Youinou, G. (2013a). *Preliminary Neutronic Study of $D_2O$-cooled High Conversion PWRs*. Idaho National Laboratory.

Hiruta, H., and Youinou, G. (2013b). *Investigation of the Performance of $D_2O$-Cooled High-Conversion Reactors for Fuel Cycle Calculations*. Idaho National Laboratory. doi: 10.2172/1115609

Kazimi, M. S., Czerwinski, K. R., Driscoll, M. J., Hejzla, P., and Meyer, J. E. (1999). *On the Use of Thorium in Light Water Reactors*. Department of Nuclear Engineering, MIT, MIT-NFCTR-016.

Lindley, B. A., Franceschini, F., and Parks, G. T. (2014). The closed thorium–transuranic fuel cycle in reduced-moderation PWRs and BWRs. *Ann. Nuclear Energy* 63, 241–254. doi: 10.1016/j.anucene.2013.07.052

Okubo, T., Takamichi, I., Renzo, T., Toyoaki, Y., and Hiroyuki, O. (2003). "Design study on reduced-moderation water reactor (RMWR) core for plutonium multiple recycling," *Proceedings of GENES4/ANP2003* (Kyoto), 1145.

Yang, W. S. (2012). Fast reactor physics and computational methods. *Nuclear Eng. Technol.* 44, 177–198. doi: 10.5516/NET.01.2012.504

Zhang, T., Xiong, J., Liu X., Chai, X., Li, W., and Cheng, X. (2019). Conceptual design of an innovative reduced moderation thorium-fueled small modular reactor with heavy-water coolant. *Int. J. Energy Res.* 43, 8286–8298. doi: 10.1002/er.4827

**Conflict of Interest:** The authors declare that the research was conducted in the absence of any commercial or financial relationships that could be construed as a potential conflict of interest.

frontiers in Energy Research

BRIEF RESEARCH REPORT
published: 05 May 2020
doi: 10.3389/fenrg.2020.00074

# Natural Convection Heat Transfer of the Horizontal Rod-Bundle in a Semi-closed Rectangular Cavity

*Xi-dao Mao*[1,2]* *and Hong Xia*[1]

[1] College of Nuclear Science and Technology, Harbin Engineering University, Harbin, China, [2] China Nuclear Power Engineering Co., Ltd., Beijing, China

During the refueling of PWR, the spent fuel assemblies are transferred from the reactor building to the fuel building through an underwater tube. The heat transfer characteristics of the spent fuel assembly in the top-corner area of the carrier with poor heat transfer conditions is important for the safety design. Experiments were carried out and single phase natural convection and pool boiling heat transfer coefficients of the three fuel rods in the top-corner area of the carrier under different heat flux was measured and obtained. The new correlations were presented. The results can provide a reference for evaluating the thermal safety state and the maximum surface temperature of the fuel assembly during the transportation process in future engineering applications.

**Keywords: fuel transfer tube, fuel assembly, natural convection, pool boiling heat transfer, horizontal bundle**

OPEN ACCESS

***Edited by:***
*Jun Wang,*
*University of Wisconsin-Madison, United States*

***Reviewed by:***
*Mingjun Wang,*
*Xi'an Jiaotong University, China*
*Claudio Tenreiro,*
*University of Talca, Chile*

***Correspondence:**
*Xi-dao Mao*
*maoxidao@126.com*

***Specialty section:***
*This article was submitted to Nuclear Energy, a section of the journal Frontiers in Energy Research*

***Received:*** *25 February 2020*
***Accepted:*** *14 April 2020*
***Published:*** *05 May 2020*

***Citation:***
*Mao X and Xia H (2020) Natural Convection Heat Transfer of the Horizontal Rod-Bundle in a Semi-closed Rectangular Cavity. Front. Energy Res. 8:74. doi: 10.3389/fenrg.2020.00074*

## INTRODUCTION

During a refueling of the light water reactor, the spent fuel assemblies are transferred from the reactor building to the fuel building through an underwater tube, as shown in **Figure 1A**. When the fuel assembly is transferred horizontally through the transfer tube, it is carried and protected by the perforated carrier and the transport trolley (Guo and Wang, 2013), as shown in **Figure 1B**. It is important for the design of a fuel transfer device to consider the hypothetical accidents such as the mechanical failure and loss of power supply. In this situation, the spent fuel assembly may be trapped in the transfer tube. Therefore, to avoid the overheating of the assembly, it is necessary to study the heat transfer of the fuel assembly in the transfer tube to find out that whether the decay heat of the fuel assembly can be removed only rely on natural convection cooling.

The driving force of natural circulation in the transfer tube comes from the density difference of hot and cold fluids. The cold water from the pool flows from the lower part of the tube to the fuel assembly. The water flows into the fuel assembly through the circular holes on both sides of the carrier. The cooling water is heated in the fuel assembly and then flows out of the assembly through the top holes of the carrier due to the buoyancy. The water flows back to the pool through the upper part of the tube.

In the previous analysis, the flow field in the transfer tube can be decomposed into two directions: longitudinal flow along the transfer tube and crosswise flow in the cross section of the transfer tube, respectively (Xi-dao et al., 2018). The flow of cooling water in the cross section of the fuel assembly in the transfer tube is shown in **Figure 1B**. The natural convection in the cross section is more complicated compared with the longitudinal flow along the transfer tube. It is a key factor affecting the cladding temperature of the fuel assembly.

The fuel assembly usually employs an arrangement of $17 \times 17$. The core of the cooling problem of the fuel assembly in the transfer channel is the natural convection heat transfer of the horizontal

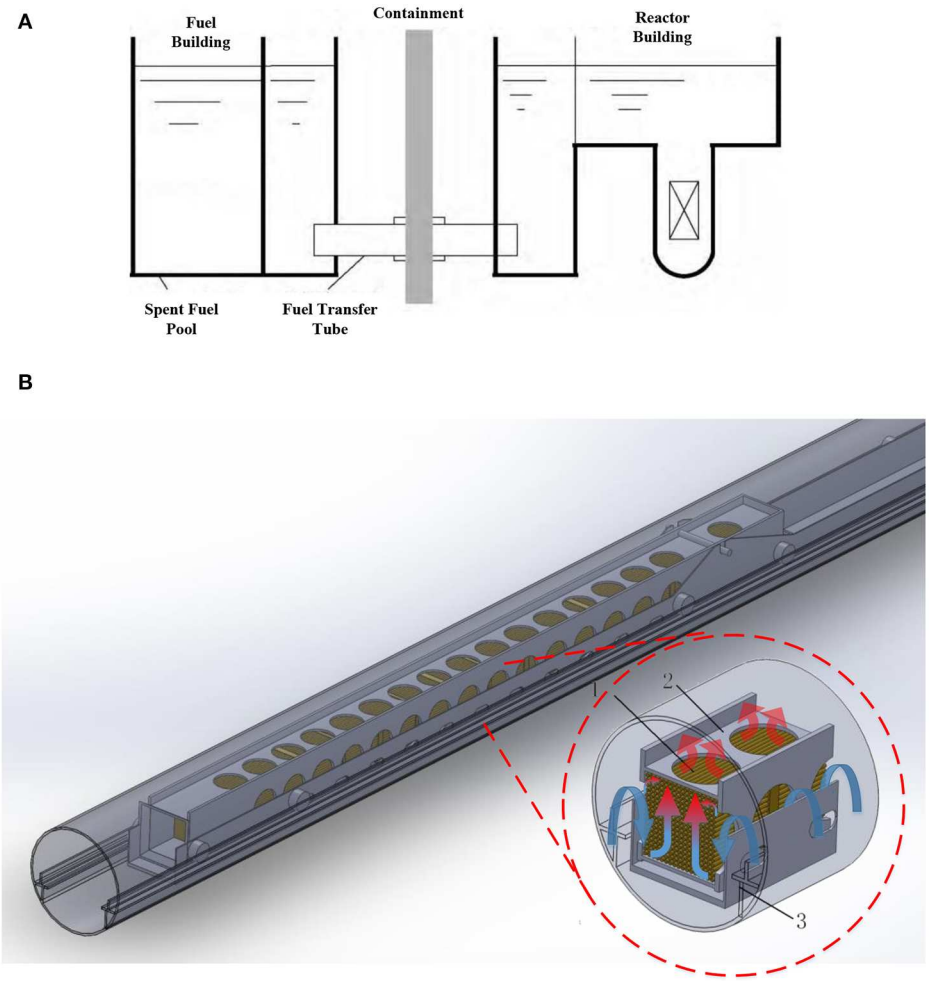


**FIGURE 1 |** Schematic of fuel transfer system. **(A)** Schematic of fuel transfer system. **(B)** Schematic of carrier and transport trolley in the transfer tube. The symbol "1" refers to fuel assembly; the symbol "2" refers to carrier; the symbol "3" refers to transport trolley.

rod bundle. However, the fuel assembly is located in the carrier in the transfer tube, which is a semi-closed rectangular cavity. This would result to a weakened heat exchange. Therefore, the natural convection heat transfer of the fuel assembly in the carrier is different from the natural convection in an infinite space or in enclosure.

When the temperature of cooling water is low, the flow in the tube bundles is single-phase natural convection. The disturbance and the pre-heating effects of the lower tube will enhance and weaken the heat transfer ability of the upper tube bundles, respectively. The natural convective heat transfer characteristics of the tube bundles are very different from a single rod. There are some researches focused on the heat transfer of the tube bundle and the single tube under different conditions, respectively.

Studies of the steady state free convection heat transfer from horizontal isothermal cylinders with low Rayleigh numbers were presented, such as Sadeghipour and Asheghi (1994) and Tokanai et al. (1997). The correlations were presented to calculate the Nusselt numbers in terms of Rayleigh numbers in these studies, which are in the condition of infinite space. The pitch-to-diameter ratio has a significant influence on the heat transfer behavior.

There are some results of the natural convection of the tube bundles in enclosure too. Keyhani and Dalton (1996) studied the natural convection heat transfer in enclosed horizontal 3 × 3, 5 × 5, and 7 × 7 rods with a pitch-to-diameter ratio of 1.35. Each array was positioned in an isothermal square enclosure with a width-to-diameter ratio of 20.6. The experimental results show that the heat transfer behavior is related to the relative size of the closed boundary and the position of the tube bundles. A two-dimensional solution for natural convection in an enclosure with 2 × 2 tube bundles was obtained by Park et al. (2015). The numerical results show the similar conclusions with Keyhani that locations of the cylinders affect the heat transfer in the enclosure.

Ashjaee et al. (2008) studied the steady two-dimensional free convection heat transfer from a horizontal, isothermal cylinder located underneath an adiabatic ceiling using a Mach–Zehnder interferometer. When the Rayleigh number is 14,500 to 40,000,

and the ratio of the height of the rod top and the plate to the diameter (L/D) of the rod ranges from 0.5 to 1.5, the local Nusselt number at the rod top is the minimum value of the entire rod surface. Sebastian (Sebastian and Shine, 2015) developed a two-dimensional model for natural convection heat transfer of a single rod with a horizontal confinement at the top. The calculation results are in good agreement with the experimental results. The results show that the local Nusselt number at the top of the rod is the minimum value of the entire rod surface within a certain L/D range. However, the boundary conditions studied by Ashjaee and Sebastian are oversimplified compared to the boundary conditions of the fuel assembly in the carrier. The difference in heat transfer characteristics between single rods and rod bundles is also very big, and it is difficult to directly use their results to evaluate safety of fuel assembly.

On the other side, when the temperature reaches the saturation temperature, the single-phase convection in the fuel assembly will turn into the pool boiling. There are many results present to study the different factors affecting boiling, such as wall materials, surface characteristics, and physical properties of working fluids. The Rohsenow pool boiling model is widely used for heat transfer calculation of the flat plate and the single tube. However, the model error of Rohsenow is as much as ±50% in some conditions due to the complexity of the boiling (Pioro et al., 2004a,b). Therefore, different specialized experiments are developed to get better estimates for different conditions.

The pool boiling of the horizontal bundle is more complicated than the condition of a single tube. The heat transfer of the upper parts of the bundles can be enhanced or weaken under different conditions. Kang studied the 2 × 1 tube bundle to reveal the buddle effect (Kang, 2015, 2016). Zhang studied the multiple tube bundles to reveal the nucleate pool boiling (Zhang et al., 2018). These studies have similar results that the heat transfer of the upper part is enhanced when the bubbles generated from the lower parts of the bundles scour the upper parts and thin the liquid film as well as the bubbles gathered and fallen. Under the condition of high heat flux, experimental results show that the upper tube will be coated by the bubbles generated in the lower part of the tube bundle, which can weaken the heat transfer of the upper tube (Swain and Das, 2018).

The pool boiling of the fuel bundle in the transfer tube is different with the bundle in the reboiler or the steam generator. The carrier influences the inflow and outflow of the fluid. Some of the fuel elements on the top-corner of the fuel assembly are in a semi-closed state, and bubbles are likely to accumulate at this position and affect heat transfer.

The heat transfer of the fuel assembly in the transfer tube under natural convection is different with the regular horizontal tube bundle, including the single-phase condition and the two-phase condition. The natural convection heat transfer of fuel assembly in the transfer tube is a key factor to effect the temperature of the spent fuel and the cladding integrity. However, the heat transfer of the fuel assembly in the carrier of the fuel transfer tube is not specially studied yet. This paper present an experiment to study the natural convection heat transfer on the cross-section which is affected by the carrier. New correlations are also presented both for single-phase and the two-phase conditions.

## EXPERIMENTAL SETUP

The experiment of full-scale ratio is not realistic due to the expensiveness and long-period. Therefore, a simplified test facility is developed based on the similar rules and the theoretical analysis (Xi-dao et al., 2018).

A set of electrical heating rods is used to simulate the fuel assembly. The heat flux of the heating rod is uniform. Considering the heating uniformity of the real fuel element, 1.65 or 2.62 multiply the power density in the test with the mean heat flux of the fuel element conservatively.

The test facility is shown in **Figure 2A**. The symbol A in this figure refers to an electric heating rod with a length of 750mm, which is used to simulate the fuel assembly near the central symmetry plane. The symbol B refers to the carrier. The symbol C refers to the transfer trolley. The symbol D refers to the cooler, which is used to simulate the heat exchange of at the inlet of the transfer tube. A mesh resistance element was added between the heating rod and the cooler to simulate the pressure loss caused by the transshipment tube and the transfer device out of the experimental section. The main geometric parameters of the test facility is listed in **Table 1**.

According to the previous research results (Guo and Wang, 2013), the maximum temperature of the cladding of the fuel assembly is located on the top of the fuel rod at the top corner of the carrier. In order to reduce the interference to the flow field of the top-corner area of the carrier, thermocouples are only fixed on the top of 1#, 3#, and 5# heating rod at intervals, as shown in **Figure 2B**.

### Experimental Parameters for Single-Phase Natural Convection

The temperature of inlet of the fuel assembly is controlled as 60, 70, and 80°C, respectively. The heat flux of the heating rod is controlled as 3900, 4300, 6200, and 6800 W/m$^2$. T-Type thermocouples and pressure gauges with high precision were employed. The instruments were calibrated. The overall error of the temperature measurement is about ±1.5°C, and the over error of the pressure measurement is about ±0.14%. The data acquisition system was Solartron IMP 35951C.

In the test, the power of the heating rod is set to a fixed value, and then the temperatures of the both sides of the fuel assembly simulated are adjusted by controlling the cooler. The data are acquired when the system and all the measurement are stable.

### Parameters for Pool Boiling Test

During the pool boiling experiment, the pressure is controlled at 0.1MPa. The inlet subcooled temperatures of the assembly are controlled under 0.5°C. The range of heat flux on the surface of the heating rod is 2,400–20,000 W/m$^2$. The heating rod is made of polished 316L stainless steel with a surface roughness Ra≈0.8 μm. Thermocouples were fixed on top of 1#, 3#, and 5# heating rods as before.

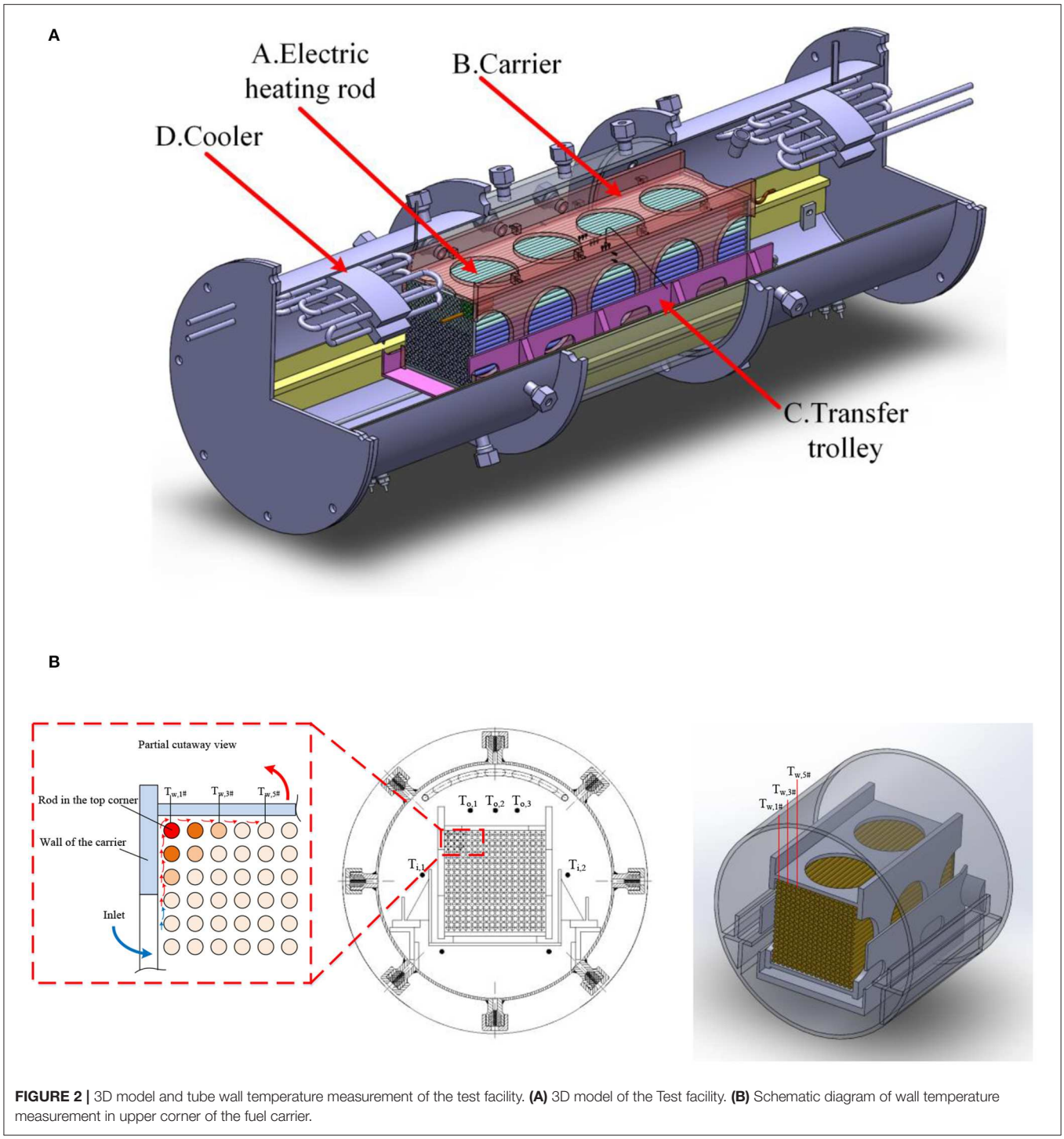


**FIGURE 2 |** 3D model and tube wall temperature measurement of the test facility. **(A)** 3D model of the Test facility. **(B)** Schematic diagram of wall temperature measurement in upper corner of the fuel carrier.

In order to exclude the influence of the unstable vaporized core on the wall surface of the heating pipe on the test results, the surface aging of the heating pipe was carried out before the formal test. The tests were performed from low heat flux to high heat flux. The power of the heating rod and the temperature of each thermocouple were recorded when the condition is stable.

# EXPERIMENTAL RESULTS AND DISCUSSION

## Single Phase Experimental Results

In the data processing, the local Nusselt number $Nu_{top}$ on the top corner of the fuel rod in the natural convection is calculated from the following:

**TABLE 1 |** The main geometric parameters of the test facility.

| Item | Unit | Test facility |
|---|---|---|
| Heating rod OD | mm | 9.5 |
| Pitch | mm | 12.6 |
| Heating rod length | mm | 750 |
| Length of the fuel transfer tube | m | ~2 |
| Diameter of the fuel transfer tube | mm | 508 |
| The diameter of the hole in the carrier | mm | 160 |

$$Nu_{\text{top}} = \frac{h_{\text{top}} D}{\lambda_{\text{f}}} \quad (1)$$

The temperature used to define the physical property parameters is defined as $t_{\text{m}} = (t_{\text{w}} + t_{\text{in}})/2$, where the $t_{\text{w}}$ is the top wall temperature of the rod in the top-corner of the carrier, and the $t_{\text{in}}$ is the temperature of cooling water at the inlet of the carrier. $\lambda_{\text{f}}$ is the thermal conductivity of water evaluated at the temperature $t_{\text{m}}$. The characteristic length $D$ employs the hydraulic diameter of the fuel rod.

A series of experiments were conducted on the test facility to get the local heat transfer data on the top of the rod at the top-corner of the carrier. **Figure 3A** shows a comparison of the heat transfer coefficient for the different rod location. For the same Rayleigh Number (Ra number), the $Nu_{\text{top}}$ at the top of the 1 # rod is the smallest, and the Nu number at the top of the 5 # rod is the largest.

From the experiment data, it is found that the heat transfer coefficient is relative with heating power and distance from the top-corner of the carrier. When the heat flux of fuel rod and water temperature at the inlet of the carrier are the same, the closer the rod to the top-corner of the carrier, the smaller the natural convective heat transfer coefficient.

## Pooling Boiling Experimental Results

In the test, the system pressure is atmospheric pressure. The characteristic temperature is the saturation temperature of the water at the test pressure. The characteristic length of the pool boiling is defined as: $l_* = \sigma/[g(\rho_{\text{l}} - \rho_{\text{g}})]$. where $\sigma$ is the surface tension, with the unit of $\text{N} \cdot \text{m}^{-1}$, $\rho_{\text{g}}$ is the density in gaseous phase, $\rho_{\text{l}}$ is the density in liquid phase. The unit of the density is $\text{kg} \cdot \text{m}^{-3}$.

**Figure 3B** shows the pool boiling heat transfer coefficients at the top of 1 #, 3 #, and 5 # rods. The solid black line in the figure is the single-rod pool boiling heat transfer coefficient calculated by the Rohsenow correlation (Rohsenow, 1952), which is used to compare with the fuel assembly test results. Although the bubble movement is hindered by the carrier, it can be seen that the boiling heat transfer coefficient at the top of the fuel assembly 1 #, 3 #, and 5 # heating rods is still higher than that of a single rod.

With the increase of heat flux density, the rod bundle effect of boiling heat transfer coefficient of 1 #, 3 #, and 5 # rods gradually weakened. Under the condition of heat flux about $2 \times 10^4 W/m^2$, the boiling heat transfer coefficient of 1 # rod closest to the top corner of the carrier is almost equal to that of a single rod.

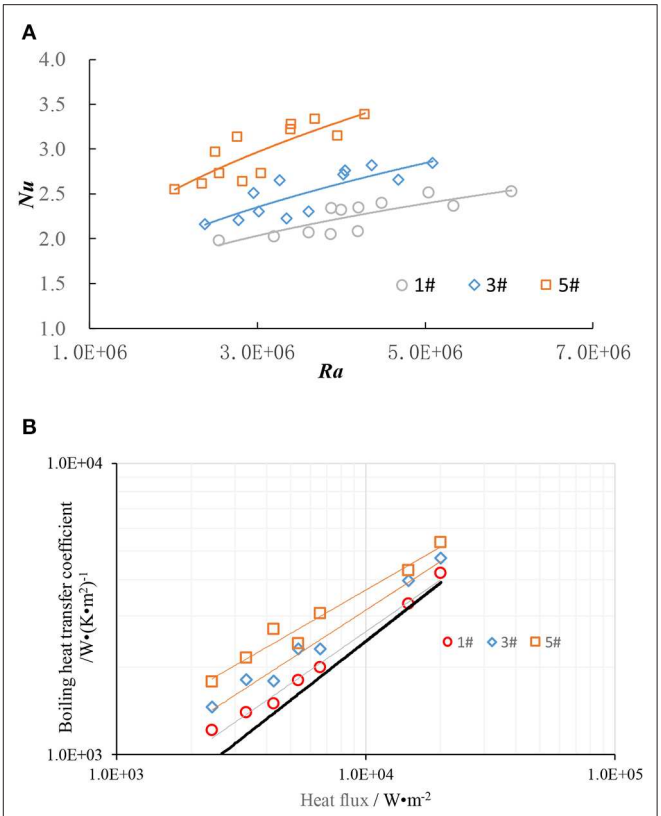


**FIGURE 3 |** Heat transfer characteristics of fuel assemblies in transfer tube. **(A)** The Nusselt number of single-phase natural convection. **(B)** The pool boiling heat transfer coefficient.

# NEW CORRELATIONS FOR LOCAL HEAT TRANSFER COEFFICIENTS

The published correlations were developed using the data for plates, wires, and outside surfaces of tubes (Pioro et al., 2004b; Shah, 2017). Since the correlations do not contain the effects of the semi-closed rectangular cavity and the lower tube heat flux, the calculated heat transfer coefficients does not agree with the present experimental data. Therefore, it is not reasonable to use the correlation equations available on the literature to predict the present experimental data.

## Single-Phase Heat Transfer Correlations

The Nusselt Number of the top corner of the fuel element in the natural convection can be expressed with a function of Rayleigh Number *Ra*. Through the regression analysis of the experimental data with the help of a computer program (which uses the least square method as a regression technique) three correlations were determined as follows:

$$\text{Nu}_{1,top} = 0.0176(\text{Ra})^{0.319} \; 2.54 \times 10^6 \leq \text{Ra} \leq 6.03 \times 10^6 \quad (2)$$

$$\text{Nu}_{3,\text{top}} = 0.0091(\text{Ra})^{0.372} \; 2.38 \times 10^6 \leq \text{Ra} \leq 5.09 \times 10^6 \quad (3)$$

$$\text{Nu}_{5,\text{top}} = 0.0099(\text{Ra})^{0.382} \; 2.02 \times 10^6 \leq \text{Ra} \leq 4.28 \times 10^6 \quad (4)$$

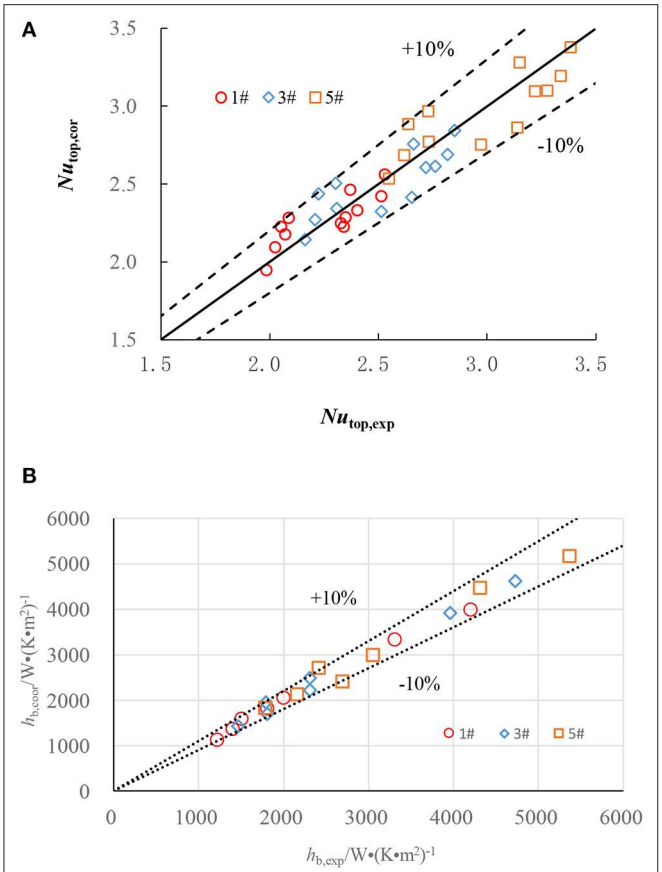


**FIGURE 4 |** Comparison of calculated data with experimental data. **(A)** Comparison of calculated heat transfer coefficients with single phase experimental data. **(B)** Comparison of calculated heat transfer coefficients with pool boiling experimental data.

A comparison between the measured Nusselt and the calculated values by Equation (2) to (4) is shown in **Figure 4A**. The newly developed correlation predicts the present experimental data within ±10%.

## Pooling Boiling Heat Transfer Correlations

A Pioro -type (Pioro et al., 2004b) correlation is introduced here to predict local pool boiling heat transfer coefficients.

$$h_{\text{top}} = C\frac{k}{l_*}\left\{\frac{q}{h_{\text{fg}}\rho_{\text{g}}^{0.5}[\sigma g(\rho_{\text{l}}-\rho_{\text{g}})]^{0.25}}\right\}^{n}\text{Pr}^{m} \quad (5)$$

where $h_{\text{top}}$ is the boiling heat transfer coefficient of the top corner of the fuel elements with unit of $\text{W}\cdot\text{m}^{-2}\cdot\text{K}^{-1}$; $q$ is the heat flux of the heating rod surface with the unit of $\text{W}\cdot\text{m}^{-2}$; $k$ is liquid heat transfer coefficient with the unit of $\text{W}\cdot\text{m}^{-1}\cdot\text{K}^{-1}$; $h_{\text{fg}}$ is the latent heat of vaporization with the unit of $\text{J}\cdot\text{kg}^{-1}$;Pr is the Prandtl Number;$l_*$ is the characteristic length. $C$, $n$ and $m$ are to be solved.

$h_{\text{top}}$, $q$, $Pr$ and the physical property parameters can be calculated based on the experiment data, and then the coefficient $C$, $n$ and $m$ can be solved by multiple regression. The coefficient $C$, $n$ and $m$are solved, and the boiling heat transfer coefficient can be expressed by the equation of (6)–(8) for the position of 1#, 3#, and 5#, respectively:

$$h_{1,\text{top}} = 984.5\frac{k}{l_*}\left\{\frac{q}{h_{\text{fg}}\rho_{\text{g}}^{0.5}[\sigma g(\rho_{\text{l}}-\rho_{\text{g}})]^{0.25}}\right\}^{0.593}\text{Pr}^{-1.1} \quad (6)$$

$$h_{3,\text{top}} = 909.9\frac{k}{l_*}\left\{\frac{q}{h_{\text{fg}}\rho_{\text{g}}^{0.5}[\sigma g(\rho_{\text{l}}-\rho_{\text{g}})]^{0.25}}\right\}^{0.556}\text{Pr}^{-1.1} \quad (7)$$

$$h_{5,\text{top}} = 697.8\frac{k}{l_*}\left\{\frac{q}{h_{\text{fg}}\rho_{\text{g}}^{0.5}[\sigma g(\rho_{\text{l}}-\rho_{\text{g}})]^{0.25}}\right\}^{0.493}\text{Pr}^{-1.1} \quad (8)$$

**Figure 4B** plots the error range of the fitted equations of (6) to (8). As shown in the figure, the errors of the predicted quantities from these equations are <10%, which means that the precision of the fitting process of these equations was good.

## CONCLUSIONS

An experimental heat transfer investigation for the horizontal rod-bundle in a semi-closed rectangular cavity submerged in the cooling water tube was conducted to find the characteristics of the fuel transfer device under natural circulation conditions. The major conclusions of the present study are as follows:

In the single-phase natural convection test and the pool-boiling test, the heat transfer coefficient of the 1# heating rod closest to the top corner of the carrier was the smallest.

Within the parameters of the pool-boiling test, the heating rod in the upper row of the heating rod is affected by the steam generated from the lower heating tube, and the boiling heat transfer coefficient is higher than that of the single tube pool boiling heat transfer coefficient. As the heating power increases, the boiling heat transfer coefficient of the 1 # heating rod is closer to that of a single rod.

Through the regression analysis of the experimental data, new empirical correlations suitable for single-phase and pool boiling heat transfer were developed, which can provide a reference for evaluating the thermal safety status and maximum surface temperature of fuel assembly during transfer.

## DATA AVAILABILITY STATEMENT

All datasets generated for this study are included in the article/supplementary material.

## AUTHOR CONTRIBUTIONS

HX is graduate advisor of XM.

## FUNDING

This work was supported by China Nuclear Power Engineering Co Ltd.

## REFERENCES


Ashjaee, M., Eshtiaghi, A.H, Yaghoubi, M., and Yousefi, T. (2008). Experimental investigation on free convection from a horizontal cylinder beneath an adiabatic ceiling. *Exp. Therm. Fluid Sci.* 32, 614–623. doi: 10.1016/j.expthermflusci.2007.07.004

Guo, Q., and Wang, H. (2013). "Numerical simulation on 3D flow in the fuel transfer canal and local flow field analysis," in *ASME Proceedings of the 21th International Conference on Nuclear Engineering* (Chengdu: ASME).

Kang, M. G. (2015). Effects of elevation angle on pool boiling heat transfer of tandem tubes. *Int. J. Heat Mass Transf.* 85, 918–923. doi: 10.1016/j.ijheatmasstransfer.2015.02.041

Kang, M. G. (2016). Pool boiling heat transfer from an inclined tube bundle. *Int. J. Heat Mass Transf.* 101, 445–451. doi: 10.1016/j.ijheatmasstransfer.2016.05.099

Keyhani, M., and Dalton, T. (1996). Natural convection heat transfer in horizontal rod-bundle enclosures. *J. Heat Transfer* 118, 598–605. doi: 10.1115/1.2822674

Park, Y. G., Ha, M. Y., and Park, J. (2015). Natural convection in a square enclosure with four circular cylinders positioned at different rectangular locations. *Int. J. Heat Mass Transf.* 81, 490–511. doi: 10.1016/j.ijheatmasstransfer.2014.10.065

Pioro, I. L., Rohsenow, W., and Doerffer, S. S. (2004a). Nucleate pool-boiling heat transfer, I: Review of parametric effects of boiling surface. *Int. J. Heat Mass Transf.* 47, 5033–5044. doi: 10.1016/j.ijheatmasstransfer.2004.06.019

Pioro, I. l., Rohsenow, W., and Doerffer, S. S. (2004b). Nucleate pool-boiling heat transfer, II: Assessment of prediction methods. *Int. J. Heat Mass Transf.* 47, 5045–5057. doi: 10.1016/j.ijheatmasstransfer.2004.06.020

Rohsenow, W. M. (1952). A method of correlating heat transfer data for surface boiling of liquids. *Transac. ASME*. 74, 969–976.

Sadeghipour, M. S., and Asheghi, M. (1994). Free convection heat transfer from arrays of vertically separated horizontal cylinders at low Rayleigh numbers. *Int. J. Heat Mass Transf.* 37, 103–109. doi: 10.1016/0017-9310(94)90165-1

Sebastian, G., and Shine, S. R. (2015). Natural convection from horizontal heated cylinder with and without horizontal confinement. *Int. J. Heat Mass Transf.* 82, 325–334. doi: 10.1016/j.ijheatmasstransfer.2014.11.063

Shah, M. M. (2017). A correlation for heat transfer during boiling on bundles of horizontal plain and enhanced tubes. *Int. J. Refrigerat*. 78, 47–59. doi: 10.1016/j.ijrefrig.2017.03.010

Swain, A., and Das, M. K. (2018). Performance of porous coated 5×3 staggered horizontal tube bundle under flow boiling. *Appl. Therm. Eng.* 128, 444–452. doi: 10.1016/j.applthermaleng.2017.09.038

Tokanai, H., Kuriyama, M., Harada, E., Konno, H. (1997). Natural convection heat transfer from vertical and inclined arrays of horizontal cylinders to air. *J. Chem. Eng. Japan* 30, 728–734. doi: 10.1252/jcej.30.728

Xi-dao, M., Yang, L., Hai-jun, J., and Qiang, G. (2018). "Design and distortion analysis of thermal-hydraulics test facility for the fuel transfer tube," in *ASME Proceedings of the 26th International Conference on Nuclear Engineering* (London: ASME).

Zhang, K., Hou, Y. D., Tian, W. X., Zhang, Y. P., Su, G. H., and Qiu, S. Z. (2018). Experimental investigation on steam-water two-phase flow boiling heat transfer in a staggered horizontal rod bundle under cross-flow condition. *Exp. Therm. Fluid Sci.* 96, 192–204. doi: 10.1016/j.expthermflusci.2018.03.009


**Conflict of Interest:** XM was employed by the company China Nuclear Power Engineering Co., Ltd.

The authors declare that this study received funding from China Nuclear Power Engineering Co., Ltd. The funder had the following involvement with the study: Experimental study of thermo-hydraulic characteristics in the transfer channel of double pressure containment (No. KY514).

frontiers in Energy Research

BRIEF RESEARCH REPORT
published: 27 May 2020
doi: 10.3389/fenrg.2020.00067

# Numerical Study on Laminar-Turbulent Transition Flow in Rectangular Channels of a Nuclear Reactor

*Zhenying Wang[1]*, Rui Zhang[2], Ting Yu[2], Zhiyun Liu[1], Yu Huang[1], Jianjun Wang[2] and Tenglong Cong[2]*

[1] State Key Laboratory of Nuclear Power Safety Monitoring Technology and Equipment, China Nuclear Power Engineering Co., Ltd, Shenzhen, China, [2] College of Nuclear Science and Technology, Harbin Engineering University, Harbin, China

Laminar-turbulent transition flow can be observed in thermal engineering applications, but the flow resistance and heat transfer characteristics are not fully understood. In this work, flow and heat transfer for the laminar-turbulent transition in a rectangular channel were predicted by a four-equation transition turbulent model. A set of correlations for the heat transfer coefficient in a rectangular channel were developed and implemented in the RELAP5/MOD3.1 code to make it capable of analyzing a plate-type fuel assembly with rectangular coolant channels. The improved RELAP5/MOD3.1 code was employed to analyze the SBLOCA along with the SBO scenario for an integrated pressurized reactor, illustrating the effects of model modification on the evolution of the accident.

**Keywords: laminar-turbulent transition, rectangular channel, RELAP5 code, station blockout, CFD simulation**

OPEN ACCESS

***Edited by:***
*Jun Wang,*
*University of Wisconsin-Madison, United States*

***Reviewed by:***
*Guanyi Wang,*
*Purdue University, United States*
*Zhu Rongsheng,*
*Jiangsu University, China*

****Correspondence:***
*Zhenying Wang*
*wangzhenying@cgnpc.com.cn*

***Specialty section:***
*This article was submitted to Nuclear Energy, a section of the journal Frontiers in Energy Research*

***Received:*** *29 January 2020*
***Accepted:*** *03 April 2020*
***Published:*** *27 May 2020*

***Citation:***
*Wang Z, Zhang R, Yu T, Liu Z, Huang Y, Wang J and Cong T (2020) Numerical Study on Laminar-Turbulent Transition Flow in Rectangular Channels of a Nuclear Reactor. Front. Energy Res. 8:67. doi: 10.3389/fenrg.2020.00067*

## 1. INTRODUCTION

Rectangular channels have been widely used in thermal engineering applications, such as nuclear reactors with a plate-type fuel element (Tian et al., 2018) and high-efficiency heat exchangers (Xu et al., 2018), due to their characteristics of high heat transfer capacity and easy manufacture. The height of the channel is generally smaller than 3 mm, which can increase the heat transfer capacity. Furthermore, the wetted area concentrations for heat transfer in heat exchange facilities with rectangular channels are greater than for those with circular channels, resulting in a high volumetric energy density, which will benefit the miniaturization of heat-exchanger equipment.

Most heat exchangers operate in the regime of turbulent flow to reach a high heat transfer coefficient; however, there are still many heat exchangers that operate in the laminar-turbulent transition regime. In the startup period or accident scenario of a nuclear power plant, the coolant experiences flow regimes from laminar to turbulent flow with the transition regime between them (Shi et al., 2016). Besides, a power plant may experience the transition flow regime when updating it from the laminar regime (Silin et al., 2010a). For the internal flow in circular tubes, the transition regime refers to the state with a Reynolds number between 2,300 and 4,000. Experimental investigations have been carried out to evaluate the heat transfer coefficient and pressure drop for internal and external transition flow (Whan and Rothfus, 1959). Cioncolini and Santini (2006) obtained the heat transfer coefficient for transition flow in helically coiled pipes. Draad et al. (1998) compared the heat transfer characteristics of the laminar-turbulent transition for Newtonian and non-Newtonian fluids by experiment. Bertsche et al. (2016) investigated the heat transfer coefficients for liquid in a circular tube with Prandtl numbers varying from 7 to 41, finding that the Gnielinski correlation was of high accuracy for a Reynolds number between 1,000

and 4,000. Silin et al. (2010a,b) carried out experimental work to study the heat transfer characteristics in the laminar to turbulent transition regime for water flowing in a rectangular channel.

Based on these experimental and theoretical investigations, the heat transfer and flow resistance correlations can be developed. Gnielinski (1976) proposed a correlation with satisfactory accuracy in the Reynolds number range between 3,000 and $10^6$. Interpolation functions were proposed to satisfy the requirement of continuity in code development (Churchill, 1977). In the safety analysis codes for nuclear power plants, such as RELAP5 and TRACE, the heat transfer and resistance coefficients were obtained by data interpolation from the laminar and fully turbulent regimes. In general, the mechanisms for the laminar-turbulent transition were not well-resolved from the experimental work, and the current system analysis codes cannot predict the heat transfer and flow resistance characteristics for laminar-turbulent transition flow, although they are significant for the design and safety analysis of nuclear power plants.

Recently, with the development of CFD technology and of knowledge on the mechanisms of transition intermittency, which is defined as the ratio of the mean duration of turbulent flow to the total duration, Abraham et al. (2011) investigated the characteristics of laminar-turbulent transition flow by using CFD technology. In these works, mechanical models for the intermittency and the transition onset criteria were proposed to model the transition intermittency along with the traditional two-equation SST k-$\omega$ model.

In our previous paper, the concept for an integrated modular reactor was proposed for the application of a submarine, where there were strong demands for miniaturization and volumetric energy density (Jiang et al., 2018). To obtain a high rate of volumetric heat release, plate-type fuels were employed in the fuel assembly. During the design and safety analysis, it was found that the current system codes, RELAP5, just employed a linear interpolation to tackle the flow resistance and heat transfer coefficient in the transition regime, which is oversimplified. Furthermore, there is no model to consider the effects of a rectangular channel geometry on the flow and heat transfer characteristics in RELAP5, which would also introduce high deviations and uncertainties in the safety analysis procedure. In the current work, the transition SST model was employed to predict the heat transfer and flow resistance of transition flow in rectangular channels. An empirical formula was developed based on the CFD results and was used to improve the reactor system code, RELAP5. A typical scenario, an accident involving a small break loss of coolant with station blockout, for an integrated small modular reactor was simulated by using the improved RELAP5 code to show the improvement offered by and necessity of model improvement.

## 2. METHOD

### 2.1. Numerical Models for a Transition SST Model

The most commonly used turbulent model is the Reynolds Averaged Navier-Stokes (RANS) model, due to its high robustness and economy. However, it cannot predict the laminar-turbulent transition since it does not consider transition intermittency. Abraham et al. (2011) carried out a series of studies on the development and validation of a transition SST turbulent model for transition flow in a circular channel. In the transition SST model, the intermittency and the momentum-thickness Reynolds number were modeled by two additional partial differential equations along with the modified SST k-$\omega$ equations. In the current work, this model was employed to predict the flow and heat transfer characteristics in rectangular channels. Here we introduce this model briefly. The governing equations for the transition SST turbulent model are given as (ANSYS Inc., 2017):

$$\frac{\partial}{\partial t}(\rho\gamma)+\frac{\partial}{\partial x_i}(\rho u_i\gamma)=\frac{\partial}{\partial x_j}((\mu+\frac{\mu_t}{\sigma_\gamma})\frac{\partial\gamma}{\partial x_j})+P_\gamma \quad (1)$$

$$\frac{\partial}{\partial t}(\rho \mathrm{Re}_{\theta t})+\frac{\partial}{\partial x_i}(\rho u_i \mathrm{Re}_{\theta t})=\frac{\partial}{\partial x_j}(\sigma_{\theta t}(\mu+\mu_t)\frac{\partial \mathrm{Re}_{\theta t}}{\partial x_j})+P_{\theta t} \quad (2)$$

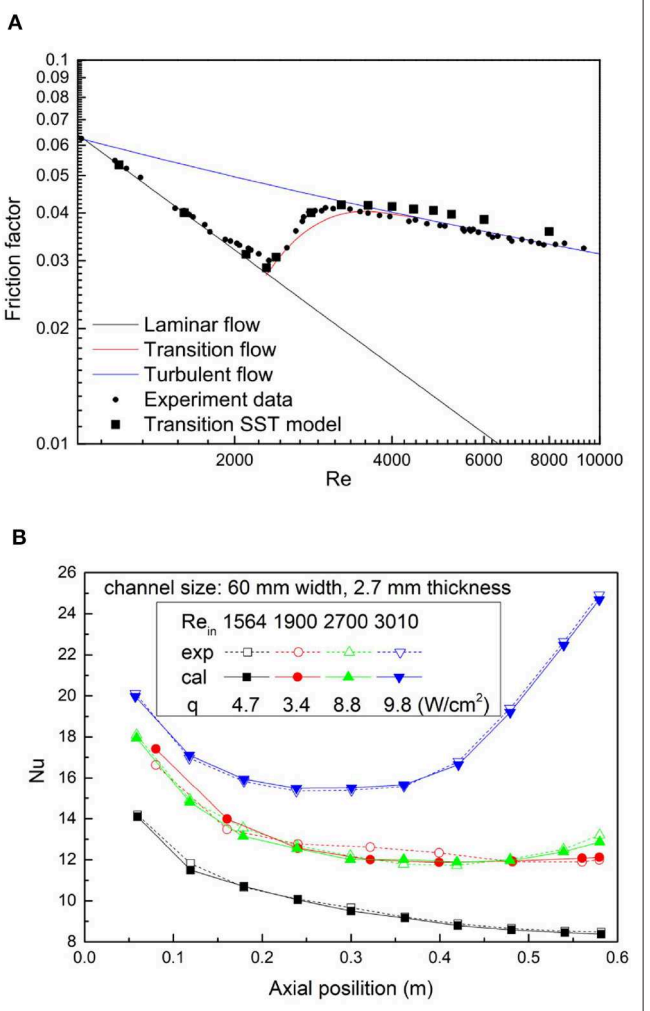


**FIGURE 1 |** Model validation. **(A)** Validation of the friction factor. **(B)** Validation of the heat transfer coefficient.

$$\frac{\partial}{\partial t}(\rho k)+\frac{\partial}{\partial x_i}(\rho k u_i) = \frac{\partial}{\partial x_j}(\Gamma_k \frac{\partial k}{\partial x_j})+S_k+\gamma G_k - \min\left(\max\left(\gamma, 0.1\right), 1.0\right) Y_k \quad (3)$$

$$\frac{\partial}{\partial t}(\rho \omega)+\frac{\partial}{\partial x_i}(\rho \omega u_i) = \frac{\partial}{\partial x_j}(\Gamma_\omega \frac{\partial \omega}{\partial x_j})+S_\omega+G_\omega-Y_\omega \quad (4)$$

The definitions of the parameters used in these equations can be found in the nomenclature.

To ensure the numerical stability of the iteration process, the transition SST models were solved alternately along with the governing equations for mass, momentum, and energy by using the coupled strategy (ANSYS Inc., 2017). The grid thickness of the first layer in the wall direction is about 0.006 mm, and the grid expansion ratio in the wall-normal direction is carefully controlled to be $< 1.05$. The grid size along the flow direction is kept at 0.06 mm. The selected mesh is carefully checked to make sure that the calculated result is mesh-independent. In this condition, the $y^+$ values for the near-wall cells were $< 1.0$ for all Reynolds numbers, which met the calculation standard. All these equations were solved using the commercial CFD code ANSYS Fluent 18.1.

## 2.2. Model Validation

The capacity of the transition SST model for predicting the flow and heat transfer characteristics in the transition intermittency regime was validated by the experimental data of Cioncolini and Santini (2006) and Silin et al. (2010a,b). In Cioncolini and Santini's experiment, the friction factors for fully developed flow from laminar to turbulent regimes in a circular tube with an inner diameter of 6.06 mm were measured. In Silin et al.'s work, the local heat transfer coefficients for transition flow in a rectangular channel of 60 mm width and 2.7 mm thickness were measured. The boundary condition is set as the experiment. The inlet is set as the velocity inlet with the corresponding Reynold number ranging from 1,564 to 3,010. The outlet is set as the pressure outlet. A uniform heat flux is given at the wall. A comparison between the results calculated by the transition SST model and the experimental data are shown in **Figure 1**.

## 2.3. Development of Correlations for Transition Flow in a Rectangular Channel

In RELAP5 code, three flow regimes are considered in the estimation of single-phase flow resistance and the heat transfer coefficient, including the laminar, laminar-turbulent transition, and turbulent flow regimes. The Darcy-Weisbach friction factor is used to compute the flow resistance in tubes (Colebrook, 1939).

$$f=\begin{cases}\frac{64}{\mathrm{Re}} & 0\le \mathrm{Re}\le 2200\\ \left\{-2\log_{10}\left[\frac{\epsilon}{3.7d_h}+\frac{2.51}{\mathrm{Re}}\left(1.14-2\log_{10}\left(\frac{\epsilon}{d_h}-\frac{21.25}{\mathrm{Re}^{0.9}}\right)\right)\right]\right\}^{-2} & \mathrm{Re}\ge 3000\end{cases} \quad (5)$$

For the transition regime with Reynolds number between 2,200 and 3,000, an interpolation strategy is used, that is,

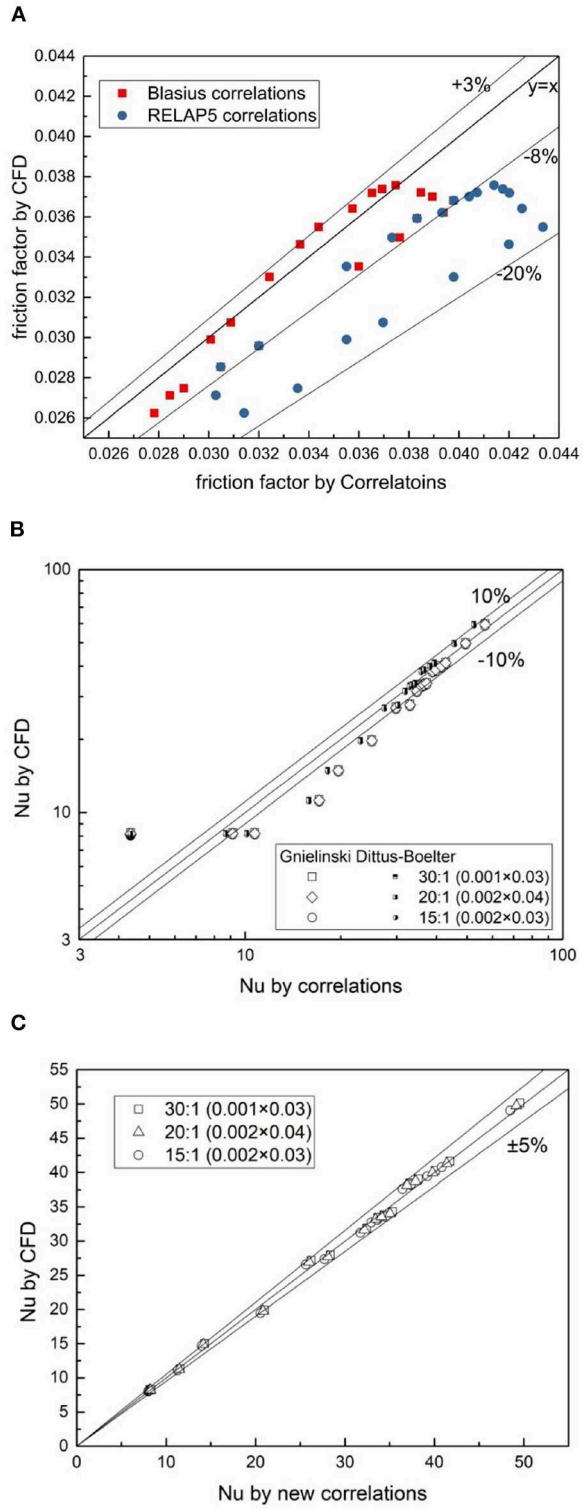


**FIGURE 2 |** Assessments of friction factor and heat transfer correlations. **(A)** Assess the RELAPS5 and Blasius correlation for friction transfer. **(B)** Assess the RELAPS5 and Gnielinski correlation for heat transfer. **(C)** Assess the new developed correlation for heat transfer.

$$f = \left(3.75 - \frac{8250}{\mathrm{Re}}\right)\left(f_{T,3000} - f_{L,2200}\right) + f_{L,2200} \tag{6}$$

where $f_{T,3000}$ and $f_{L,2200}$ are the friction factor at Reynolds numbers of 3,000 and 2,200, calculated by turbulent and laminar models, respectively. As for the heat transfer coefficient, RELAP5 employs the Dittus-Boelter equation when Re > 3,000 (Dittus and Boelter, 1985) and a constant laminar heat transfer coefficient at Re < 2,100. In the transition regime with $2,100 \leq \mathrm{Re} \leq 3,000$, linear interpolation is employed to obtain the heat transfer coefficient.

The accuracy of the correlations used in RELAP5 for the friction factor and heat transfer coefficient should be estimated before being utilized to the conditions of a rectangular channel. The friction factor and Nusselt number obtained from CFD simulations are compared with the RELAP5 correlations, as shown in **Figures 2A,B**. Other than the RELAP5 correlations, the Gnielinski equation and the Blasius equation (Trinh, 2010) for the heat transfer coefficient and friction factor in the turbulent regime, respectively, are also employed as references. The deviations between the reference data from CFD and the data from the RELAP5 equations are significant, which means that the original empirical correlations for flow resistance and heat transfer in RELAP5 are not applicable for a rectangular channel under the transition condition. The set of Blasius equations (using the Blasius equation for Re ≥ 3,000, the laminar model for Re ≤ 2,200, and linear interpolation otherwise) can give good accuracy with a largest deviation of < 8 %, which means that the set of Blasius equations are qualified to predict the friction factor in rectangular channels with acceptable accuracy. Dittus-Boelter and Gnielinski correlations predict similar results when the Nusselt number is larger than 30; however, they both fail in the transition regime. Thus, a new set of heat transfer correlations should be developed.

It can be obtained from the analytical solution for laminar flow heat transfer in the rectangular channel that the Nusselt number equals 4.32 for a rectangular channel with a unit aspect ratio and equals 8.23 for a channel with an infinite aspect ratio (infinite plate). Besides, the Nusselt number in the laminar regime is independent of the Reynolds number and Prandtl number; thus, from data fitting, the correlation for the laminar Nusselt number can be obtained, which is

$$\mathrm{Nu} = 8.23\left(1 + 10^3\alpha^{-2.97}\right)^{-0.0933} \tag{7}$$

For the fully turbulent regime, the heat transfer correlation is

$$\mathrm{Nu} = 0.007\mathrm{Re}^{0.95}\mathrm{Pr}^{0.4}\left(1 + 10^3\alpha^{-2.97}\right)^{-0.0933} \tag{8}$$

For the transition regime, it is

$$\mathrm{Nu} = \left[-0.04255\left(\frac{\mathrm{Re}}{100}\right)^3 + 3.433\left(\frac{\mathrm{Re}}{100}\right)^2 - 90.47\left(\frac{\mathrm{Re}}{100}\right) + 786.2\right]\mathrm{Pr}^{0.4}\left(1 + 10^3\alpha^{-2.97}\right)^{-0.0933} \tag{9}$$

The demarcation point between the transition and laminar regimes is determined by the largest intersection point of Equations (7) and (9); while the discreteness point between the transition and turbulent regimes is determined by the smallest intersection point of Equations (8) and (9). The applicable range of the proposed correlations covers an aspect ratio from 15:1 to 30:1 and a channel height from 1 to 2 mm. The newly developed heat transfer correlations were also assessed against the CFD data and showed a maximum deviation of < 5% (**Figure 2C**).

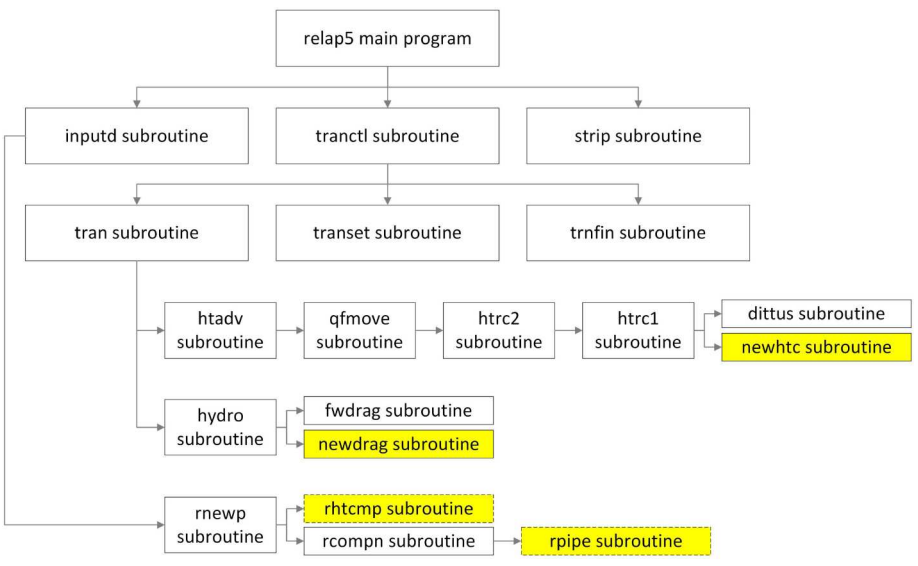


**FIGURE 3 |** Structure of the RELAP5/MOD3.1 code.

# 3. RESULTS

## 3.1. Structure of the RELAP5/MOD3.1 Code and Model Modification

The RELAP5/MOD3.1 code is written in the FORTRAN language with more than 600 subroutines with a top-down structure, as illustrated in **Figure 3**. The main program, "relap5," calls the "inputd" and "tranctl" subroutines to read the input cards and to perform the transient calculation, respectively. Among the subroutines called by the "tran" subroutine, the "dittus" subroutine is used to calculate the single-phase heat transfer coefficients for the regimes from laminar to turbulent. The "fwdrag" subroutine is called to compute the wall drag force. By default, the correlations for a circular tube are used in these subroutines. As is already known, these correlations for a circular tube are not applicable for the rectangular channel. However, these subroutines should not be replaced since they will still be used in other circular components, such as heat exchangers and pipes. Thus, two new subroutines for heat transfer and flow resistance in the rectangular channel are added to the RELAP5 code and are named "dittusrectangular" and "fwdragrectangular."

The rectangular channel is modeled by the pipe component in RELAP5 even though the cross-section is not circular. One more word is added to the pipe card to identify the shape of the pipe cross-section. Besides, a word describing the geometry information is also added to the boundary condition card for the heat structure to help to select the correlations for heat transfer; that is, the thermal boundary of the heat structure is circular or rectangular. The "inputd" subroutine is called by the main program to read the input cards of the problem. Among the subroutines called by "inputd," the "rhtcmp" and "rpipe" subroutines are used to read the information for the heat structure and pipe components, respectively. Thus, these two subroutines were modified to make them applicable to the new cards of the heat structure and pipe with one additional word for geometry information. After the above modification to the source code and the input card, the RELAP5/MOD3.1 code can be used to analyze a reactor with rectangular channels.

## 3.2. Application of RELAP5/MOD3.1 Code to an SBLOCA With SBO Scenario for an Integrated Modular Reactor

IP200 is an integrated pressurized water reactor with its main facilities in the reactor pressure vessel (RPV) to minimize the length of connecting pipes and to enhance the inherent safety. Plate-type fuel assemblies are placed at the bottom of the RPV, and once-through steam generators are installed in the upper part of the RPV around the core, symmetrically. The rising section above the active zone and the downcomer below the steam generators are used as the hot leg and cold leg, respectively. A plenum is built by the steam at the top of the RPV, working as the pressurizer. Compared with other traditional reactors used on land, such as AP1000 and EPR1000, IP200 has the advantages of small size and high volumetric rate of heat release. The schematic diagram and main design parameters of IP200

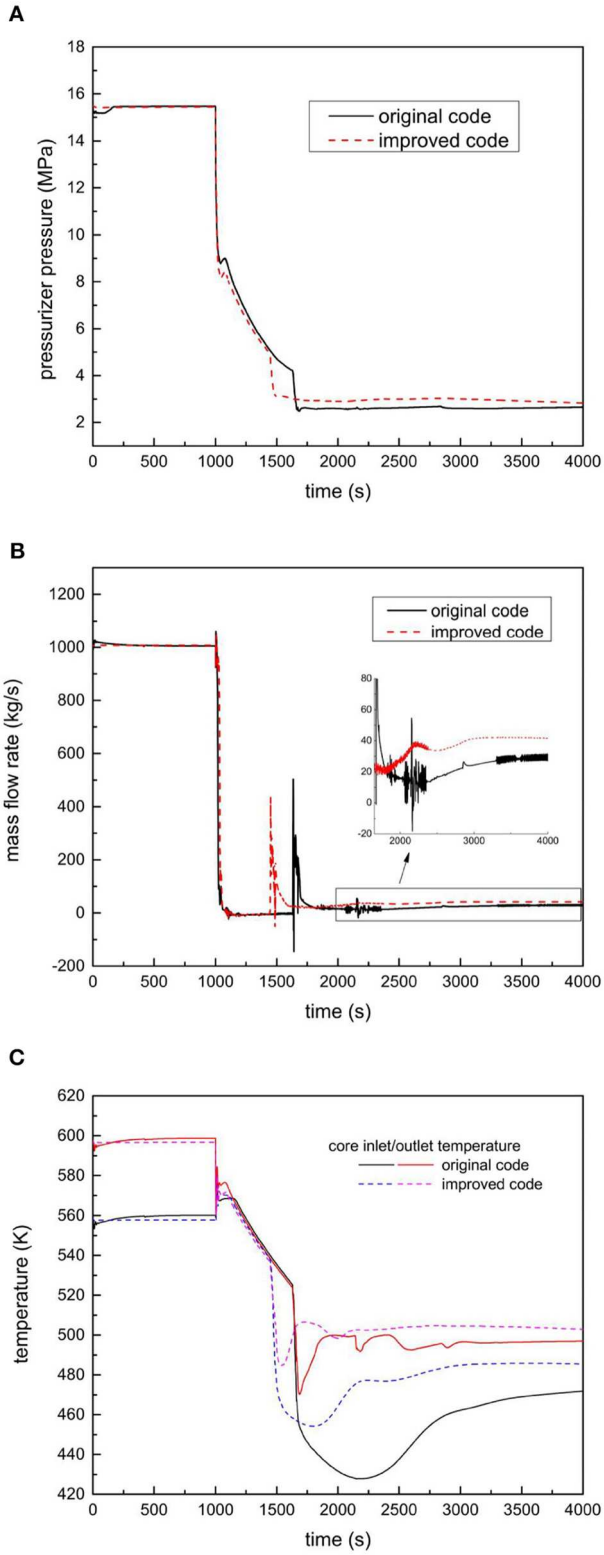


**FIGURE 4 |** Comparisons between the original and improved RELAP5/MOD3.1 codes. **(A)** Pressure in pressurizer. **(B)** Mass flow rate in the core. **(C)** Coolant temperature at core inlet and outlet.

can be found in Jiang et al. (2018). The passive safety system (PSS) is critical for the safety of IP200 since the volumetric heat release is significantly high, especially under accident conditions. However, in the safety analysis related to the PSS of IP200, RELAP5 code with correlations for a circular tube and rod bundle were employed in the simulations (Jiang et al., 2018). In this work, the improved RELAP5/MOD3.1 code was used to assess the PSS of IP200. The typical accident scenario, a small break loss of coolant accident (SBLOCA) along with Station Blockout (SBO), was applied to evaluate the performance of the PSS.

The RELAP5 nodalization model for the IP200 PSS can be found in our previous paper on the safety analysis of the IP200 reactor (Jiang et al., 2018). In the current work, the SBLOCA with SBO accident was analyzed with the improved RELAP5/MOD3.1 code to evaluate the effectiveness and performance of the PSS. In the first 1000.0 s, the reactor operates in the full-power steady state. At the 1000.0 s, the valve on the vent pipe of the pressurizer is opened by accident, and the station blockout occurs. Meanwhile, the reactor scrams, and both the coolant pumps and feedwater pumps shut down. During the accident, there are three different flow regimes in a rectangular channel in the core: the turbulent, transition, and laminar flow regimes. The core cooling and the residual heat removal fully depend on the PSS. The accident sequences of the SBLOCA plus SBO scenario were modeled by the original RELAP5/MOD3.1 code and by the improved code with new heat transfer and flow resistance models for rectangular channels. The results are compared in **Figure 4**. The comparison shows that the modifications on the heat transfer and flow resistance models make significant differences to the accident evolution after SBLOCA and SBO.

After the initiation of SBLOCA, the pressure in the RPV plunges sharply due to the leakage of vapor from the break. The rate of depressurization then decreases when the two-phase blowdown begins. Meanwhile, the pressure in the containment increases. The valves on the vent pipe and on the sump pipe open when the pressure difference between the RPV and the containment reaches 0.2 and 0.02 MPa, respectively. After that, the natural circulation for the fluid in the RPV and containment can be built. The pressure in the RPV decreases with the injection of cold water from the containment, while the coolant temperature at the inlet of the core plummets since the cold water injection will flow past the primary side of the steam generator to the inlet of the core. The discharged vapor and two-phase mixture from the RPV to the containment will be cooled by the ultimate heat exchanger, by which long-term cooling can be established.

It can be seen that there are significant differences between the results from the original RELAP5/MOD3.1 code and the improved code; these are caused by the changes in the models for flow resistance and heat transfer. In general, as can be observed from **Figures 2A,B**, the models in the original RELAP5 code over-estimated the friction factor for all flow regimes and over-estimated the heat transfer coefficient in the transition flow regime. The over-prediction of heat transfer would affect the temperature in the fuel but has negligible effects on the total energy released to the coolant, especially in the quasi-steady long-term cooling stage. However, the over-estimation of the friction factor would increase the flow resistance in a core with rectangular channels, which would reduce the coolant flow rate, especially under the natural circulation period. This conclusion can be obtained from **Figure 4B**; the mass flow rate in the core predicted by the improved code is larger than that by the original code, which leads to a decline in the temperature increase in the core, as shown in **Figure 4C**. From the above application of the improved RELAP5/MOD3.1 code, we find that the improved code can predict the accident evolution more reasonably. Quantitative assessment of this improved code is not presented in this paper since there are no experimental data for IP200 or other types of reactors with a plate-type fuel assembly available.

## 4. DISCUSSION

In this work, the flow and heat transfer characteristics for the laminar-turbulent transition were predicted by a CFD methodology with a four-equation transition turbulent model. A set of heat transfer coefficient correlations were developed. The models for the friction factor and heat transfer coefficient in RELAP5/MOD3.1 code were modified to make it applicable for the safety analysis of a reactor with a plate-type fuel assembly. After the modification to the code, it was applied to analyze the SBLOCA with SBO scenario in an integrated pressurized reactor. The following conclusions can be drawn.

1. A combination of the Blasius equation and the laminar friction factor model can predict the flow resistance in rectangular channels with satisfactory accuracy.
2. A set of heat transfer correlations for coolant flow in a rectangular channel under all flow regimes was proposed and compiled into the RELAP5/MOD3.1 code to extend the applicability and accuracy of this code for safety analysis for a reactor with a plate-type fuel assembly.
3. The SBLOCA with SBO accident for an integrated pressurized reactor was analyzed by the improved RELAP5/MOD3.1 code to demonstrate the impacts of model modification on accident evolution.

## DATA AVAILABILITY STATEMENT

All datasets generated for this study are included in the article/supplementary material.

## AUTHOR CONTRIBUTIONS

ZW and RZ carried out the CFD simulation. TY, ZL, and YH developed the correlations. JW and TC improved the RELAP5 code and wrote the manuscript.

## FUNDING

The authors greatly appreciate support from the National Natural Science Foundation of China (No. 11705035), the Natural Science Foundation of Heilongjiang Province, China (No. LH2019A009), and the Open Fund Program of the State Key Laboratory of Nuclear Power Safety Monitoring Technology and Equipment (No. K-A2019.414).

## REFERENCES


Abraham, J. P., Sparrow, E. M., and Minkowycz, W. J. (2011). Internal-flow Nusselt numbers for the low-Reynolds-number end of the laminar-to-turbulent transition regime. *Int. J. Heat Mass Transfer* 54, 584–588. doi: 10.1016/j.ijheatmasstransfer.2010.09.012

ANSYS Inc. (2017). *ANSYS Fluent Theory Guide v18.1*. ANSYS Inc.

Bertsche, D., Knipper, P., and Wetzel, T. (2016). Experimental investigation on heat transfer in laminar, transitional and turbulent circular pipe flow. *Int. J. Heat Mass Transfer* 95, 1008–1018. doi: 10.1016/j.ijheatmasstransfer.2016.01.009

Churchill, S. W. (1977). Comprehensive correlating equations for heat, mass and momentum transfer in fully developed flow in smooth tubes. *Indus. Eng. Chem. Fundament*. 16, 109–116. doi: 10.1021/i160061a021

Cioncolini, A., and Santini, L. (2006). An experimental investigation regarding the laminar to turbulent flow transition in helically coiled pipes. *Exp. Thermal Fluid Sci.* 30, 367–380. doi: 10.1016/j.expthermflusci.2005.08.005

Colebrook, C. F. (1939). Turbulent flow in pipes, with particular reference to the transition region between the smooth and rough pipe laws. *J. Instit. Civil Eng.* 11, 133–156. doi: 10.1680/ijoti.1939.13150

Dittus, F. W., and Boelter, L. M. K. (1985). Heat transfer in automobile radiators of the tubular type. *Int. Commun. Heat Mass Transfer* 12, 3–22. doi: 10.1016/0735-1933(85)90003-X

Draad, A. A., Kuiken, G. D. C., and Nieuwstadt, F. T. M. (1998). Laminar-turbulent transition in pipe flow for Newtonian and non-Newtonian fluids. *J. Fluid Mech.* 377, 267–312. doi: 10.1017/S0022112098003139

Gnielinski, V. (1976). New equations for heat and mass transfer in turbulent pipe and channel flow. *Int. Chem. Eng.* 16, 359–368.

Jiang, N., Peng, M., and Cong, T. (2018). Simulation analysis of an open natural circulation for the passive residual heat removal in IPWR. *Ann. Nuclear Energ.* 117, 223–233. doi: 10.1016/j.anucene.2018.03.037

Shi, S., Hibiki, T., and Ishii, M. (2016). Startup instability in natural circulation driven nuclear reactors. *Prog. Nuclear Energ.* 90, 140–150. doi: 10.1016/j.pnucene.2016.03.016

Silin, N., Masson, V., Osorio, D., and Converti, J. (2010a). Hydrodynamic transition delay in rectangular channels under high heat flux. *Ann. Nuclear Energ.* 37, 615–620. doi: 10.1016/j.anucene.2009.12.013

Silin, N., Masson, V. P., and Garcia, J. C. (2010b). Convection in a rectangular channel with a flow of water in laminar-turbulent transition with high heat fluxes. *Latin Am. Appl. Res.* 40, 125–130.

Tian, C., Wang, J., Cao, X., Yan, C., and Ala, A. A. (2018). Experimental study on mixed convection in an asymmetrically heated, inclined, narrow, rectangular channel. *Int. J. Heat Mass Transfer* 116, 1074–1084. doi: 10.1016/j.ijheatmasstransfer.2017.09.099

Trinh, K. T. (2010). On the blasius correlation for friction factors. *arXiv preprint arXiv:1007.2466*.

Whan, G. A., and Rothfus, R. R. (1959). Characteristics of transition flow between parallel plates. *AIChE J.* 5, 204–208. doi: 10.1002/aic.690050215

Xu, Z., Han, Z., Wang, J., and Liu, Z. (2018). The characteristics of heat transfer and flow resistance in a rectangular channel with vortex generators. *Int. J. Heat Mass Transfer* 116, 61–72. doi: 10.1016/j.ijheatmasstransfer.2017.08.083


**Conflict of Interest:** ZW, ZL, and YH were employed by company China Nuclear Power Engineering Co., Ltd.

The remaining authors declare that the research was conducted in the absence of any commercial or financial relationships that could be construed as a potential conflict of interest.

## NOMENCLATURE

| | |
|---|---|
| $\epsilon$ | Turbulent eddy diffusivity for momentun transfer |
| $\gamma$ | Transition intermittency |
| $\rho$ | Density |
| $\mu$ | Dynamic viscosity |
| $\mu_t$ | Turbulent dynamic viscosity |
| $\mathrm{Re}_{\theta t}$ | Momentum-thickness Reynolds number |
| $k$ | Turbulence kinetic energy |
| $\omega$ | Specific dissipation rate |
| $P_i$ | Source term for $\gamma$ and $\mathrm{Re}_{\theta t}$, $i = \gamma, \theta t$ |
| $u_i$ | Velocity component, $i$=1, 2, 3 |
| $G_i$ | Generation terms for $k$ and $\omega$, $i = k, \omega$ |
| $Y_i$ | Dissipation terms for $k$ and $\omega$, $i = k, \omega$ |
| $S_i$ | Source terms for $k$ and $\omega$, $i = k, \omega$ |
| $\Gamma_i$ | Effective diffusivity $k$ and $\omega$, $i = k, \omega$ |
| $\sigma_i$ | Turbulent Prandtl number for $\gamma$, $\mathrm{Re}_\theta t$, $i = \gamma, \theta t$ |
| $f$ | Fraction factor |
| Nu | Nusselt number |
| Re | Reynolds number |
| Pr | Prandtl number |
| $\epsilon$ | Surface roughness |
| $d_h$ | Hydraulic diameter |
| $\alpha$ | Width-height ratio of the rectangular channel |
| OTSG | Once-Through Steam Generator |
| SBLOCA | Small-Break Loss Of Coolant Accident |
| SBO | Station Blockout |
| HX | Heat exchanger |
| $y^+$ | Non-dimensional wall distance |
| $T$ | Temperature |
| $\lambda$ | Thermal conductivity |
| $p$ | Pressure |
| LES | Large Eddy Simulation |
| PSS | Passive Safety System |
| SRS | Scale-Resolved Simulation |
| RANS | Reynolds Averaged Navier-Stokes |

frontiers in Energy Research

BRIEF RESEARCH REPORT
published: 02 June 2020
doi: 10.3389/fenrg.2020.00096

# Visualization Experiment of Bubble Coalescence in a Narrow Vertical Rectangular Channel

*Tingting Ren*[1], *Zhiqiang Zhu*[2], *Rui Zhang*[1]*, *Jiangwu Shi*[1] and *Changqi Yan*[1]

[1] Fundamental Science on Nuclear Safety and Simulation Technology Laboratory, Harbin Engineering University, Harbin, China, [2] Wuhan Second Ship Design and Research Institute, Wuhan, China

Visualization experiments were carried out and sliding bubble coalescence behaviors were observed for subcooled flow boiling in a narrow rectangular channel. The results show that the consecutive coalescence process is composed of four steps based on the bubble morphological change: approaching, merging, adjustment, and stabilization, in which the more important are the merging and adjustment of the bubble. Bubble always slides along the heating surface and does not lift off in coalescence process. Bubble diameter and sliding velocity increase first, then decrease and finally stabilize. Bubble shape also oscillates from an irregular ellipse to a stable circle. In addition, a new small bubble may be induced in the coalescence process.

**Keywords: bubble coalescence, narrow rectangular channel, subcooled flow boiling, sliding bubble, visualization experiment**

OPEN ACCESS

***Edited by:***
*Shripad T. Revankar, Purdue University, United States*

***Reviewed by:***
*Boštjan Končar, Institut JoŽef Stefan (IJS), Slovenia*
*Jiankai Yu, Massachusetts Institute of Technology, United States*

***Correspondence:**
*Rui Zhang*
*rzhang@hrbeu.edu.cn*

***Specialty section:***
*This article was submitted to Nuclear Energy, a section of the journal Frontiers in Energy Research*

***Received:*** *01 March 2020*
***Accepted:*** *04 May 2020*
***Published:*** *02 June 2020*

***Citation:***
*Ren T, Zhu Z, Zhang R, Shi J and Yan C (2020) Visualization Experiment of Bubble Coalescence in a Narrow Vertical Rectangular Channel. Front. Energy Res. 8:96. doi: 10.3389/fenrg.2020.00096*

## INTRODUCTION

The narrow rectangular channel has been widely used in engineering because of its characteristics of heat transfer enchantment and its ability to meet the requirements of small volume but high power. Bubble dynamics is the basis of boiling heat transfer research. Present research on the bubble behavior in narrow channels mainly focus on the behavior characteristics of individual bubbles, such as bubble nucleation, departure, growth and condensation. Ren et al. (2019, 2020) studied the effects of thermal parameters on the bubble nucleation, departure, growth, and sliding velocity in the previous work. Xu et al. (2013) has found in a visualization experiment that typical bubble sliding behavior exists in the narrow rectangular channel at low heat flux conditions. Li et al. (2013) also has found that most bubbles in the narrow channel slip along the heating wall instead of lifting off as in the conventional large channel. The distribution of bubble sliding velocity was obtained by statistical method. In fact, nucleate boiling is a complex process that involves the motion of individual bubbles and the interactions between them. In the former studies, many researchers experimentally or numerically investigated the bubble coalescence in the large space or channel, while few studies on bubble interaction in a narrow channel have been reported.

Bonjour et al. (2000) experimentally studied three types of bubble coalescence in pool nucleate boiling: (1) bubble coalescence away from the heating surface; (2) vertical bubble coalescence near the heating surface; (3) horizontal bubble coalescence near the heating surface. Liu et al. (2006) proposed to divide bubble coalescence into three types including vertical coalescence, horizontal coalescence and the mixtures of them. Feng et al. (2016) proposed that there were two forms of bubble coalescence, namely, connectionless coalescence and connected coalescence. In the study of Nguyen et al. (2013), the connected coalescence process includes the following steps: the approach and collision of bubbles, the formation and discharge of a liquid film, the rupture of the film when it

reaches a critical thickness. Zhang and Shoji (2003) has found that the coalescence of bubbles had a great effect on the bubble departure frequency. Mukherjee and Dhir (2004) has numerically found that the lateral bubbles enhanced the heat transfer by trapping liquid layers during coalescence process. It has been found from Chen and Chung's (2002) experiment that the deformation caused by bubble coalescence increased the contact time between the cold liquid and the heating wall, thereby enhancing the heat transfer. According to Coulibaly et al.'s (2014) work, increasing liquid subcooling reduced the size and the departure frequency of coalesced bubble. Compared with the single-bubble boiling, the heat flux fluctuated more significantly during bubble coalescence process.

The above studies do not consider the limitations of space. In a narrow channel, the influence of flow resistance, surface tension and significantly enhances wall boundary constraints. The characteristics of bubble coalescence is different from those in the large channel (Lu et al., 2017). The bubbles grow to the narrow channel size and the distance between bubbles decrease, which enhance the bubble coalescence. However, sufficient research has not been conducted on the characteristics of bubble coalescence in narrow channels. In this work, visualization experiments were carried out to investigate the sliding bubble coalescence in an isolated bubble region in a narrow rectangular channel. The vapor-liquid interface evolution during bubble coalescence process and the change of characteristic parameters before and after coalescence were studied.

## Experimental Method

**Figure 1** shows the schematic diagram of the experimental equipment. The experimental loop mainly consists of a major circulation loop and a cooling loop. In order to intuitively study the characteristics of bubble coalescence, a visualization test section is designed and constructed. The main instruments in the circuit include a preheater, a test section, a condenser, a pressurizer, two pumps, an electromagnetic flowmeter, and some pipe valves. Before the formal experiment, water is heated by preheater and test section to reduce the solubility of the non-condensable gas in order to avoid the effect on the experimental phenomenon. In the experiment, deionized water is heated to boiling when flowing through the test section and then flows into the condenser through the riser. The condensed water flows to the preheater through the downcomer and is heated to a required temperature by the preheater. Then the water with a certain degree of subcooling flows into the test section and is heated again to boiling. In the cooling loop, the condenser is cooled by an air cooling tower and a large water tank. The circulation pumps are used to adjust the circulation flow and the pressurizer is used to maintain the system pressure.

The vertical visualization test section details are shown in **Figures 1B,C**. A narrow rectangular flow channel of 700 mm × 40 mm × 2 mm is constructed by a quartz glass and a stainless steel heating plate, sealed by an O-shape ring. Two copper electrodes are welded to the stainless steel plate, connecting to a 50V/2000A DC (Direct Current) power. The heating length is 550 mm. The bubble coalescence behaviors are recorded by a high-speed camera equipped with a macro lens and the lens has a focal length of 105 mm and an aperture specification of F2.8. The camera is placed on a two-dimensional guide rail which can be movable in vertical and horizontal direction. Two adjustable fiber lights facing the test section are used to provide sufficient light.

Six N-type sheathed thermocouples are arranged at the inlets and outlets of the preheater, test section and condenser to measure fluid temperature. Eleven horizontal rows and three vertical rows K-type sheathed thermocouples are uniformly welded on the back of heating plate to measure the outer wall temperature at different positions. Additionally, the circulation flow is obtained by the electromagnetic flowmeter. In order to capture clear bubble images, the camera frame rate and resolution are, respectively, set to 4,300 frames per second and 1,024 × 1,024 pixels. Thus, the time interval between two adjacent images is 0.23 ms. A clear scale is taken for each experiment and the actual observation area is approximately 10.28 × 10.28 $mm^2$. All instruments are connected with an NI (National Instruments) acquisition system to record the experimental data. When parameters, i.e., fluid temperature, wall temperature and flow rate reach stable, corresponding bubble images and thermal data are recorded simultaneously. The relevant parameters in the experiment are: the system pressure is 0.4 MPa, wall heat flux in test section is 114–212 $kW{\cdot}m^{-2}$, inlet fluid subcooling is 31°C, mass flow rate is 333–619 $kg{\cdot}m^{-2}{\cdot}s^{-1}$.

The determination of the bubble diameter and sliding velocity is described in the previous study (Ren et al., 2020). The N-type and K-type sheathed thermocouples respectively have accuracies of ±0.5°C and ±1°C. The heating power has an accuracy of 0.55%. The accuracies for bubble diameter and position are ±2 pixel. Based on the Kine and Mcclintock (1953) uncertainties analysis method, the relative uncertainty range for heat flux and inner wall temperature are, respectively, 1.8–4.2% and ±1°C. The relative uncertainty for bubble diameter and bubble velocity are, respectively, ±0.02 mm and ±0.08 m/s.

$$U_F = \pm \sqrt{\sum_{i=1}^{n} \left( \frac{\partial F}{\partial p_i} u_{p_i} \right)^2} \tag{1}$$

where $F$ is a function of variables $p_1$, $p_2$, … $p_n$; $U_F$ is the uncertainty for $F$ and $u_{pi}$ is the uncertainty for the variable $p_i$. The relative uncertainty for the friction factor λ can be calculated as.

$$\frac{U_\lambda}{\lambda} = \pm \sqrt{\sum_{i=1}^{n} \left( \frac{u_{p_i}}{p_i} \right)^2} \tag{2}$$

# RESULTS AND DISCUSSION

## Morphology Changes During Bubble Coalescence

**Figure 2** shows three different groups of bubble coalescence images: (a) the coalescence of two bubbles with similar size in the flow direction, (b) the coalescence of two bubbles with different size in the flow direction, (c) the coalescence of two bubbles in the horizontal direction. Based on Zheng et al.'s (2014) work,

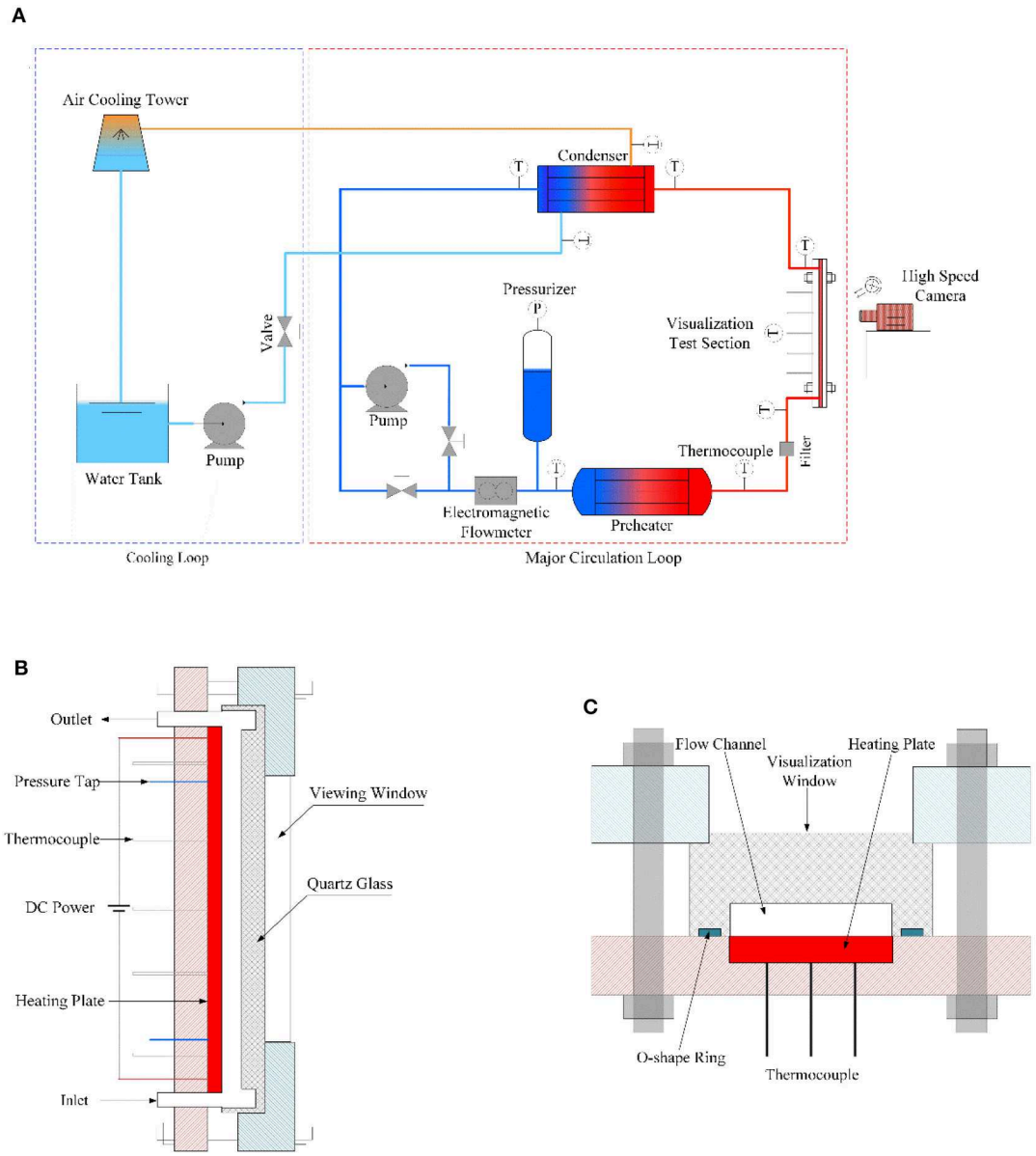


**FIGURE 1 |** Schematic diagram of experimental equipment. **(A)** Schematic diagram of the experimental loop, **(B)** side section of the visualization test section, and **(C)** cross section of the visualization test section.

the consecutive coalescence process is composed of the following four steps according to the bubble morphological change: (1) approaching, (2) merging, (3) adjustment and (4) stabilization. In step (1), the two bubbles approach each other until the phase interfaces begin to contact; in step (2), the two bubble phase interfaces merge to form an irregularly shaped bubble; in step (3), the shape of new bubble is constantly adjusted and the oscillation gradually weakens; in step (4), the new bubble reaches stability and continues to slide. Among of those steps, step (2) and (3) are more important.

Group (a) shows the coalescence process of two bubbles in the flow direction. At 0 ms, the two bubbles slide along the heating wall, then the distance between two bubbles decreases due to the different sliding velocities. At about 7.28 ms, the two bubble phase interfaces contacts each other and begin to merge. A new bubble is formed at 8.28 ms. In the long period adjustment process, the shape of bubble constantly changes. The oscillation gradually weakens and the bubble shape stabilizes at 17.02 ms. From the bubble images, there is a clear contact circle in the center of the bubble, which is represented by red lines in **Figure 2B**. This is caused by the contact between the bottom of the bubble and the heating surface. Therefore, it can be judged that the bubble always contact the wall surface in this process and no lifting off occurs.

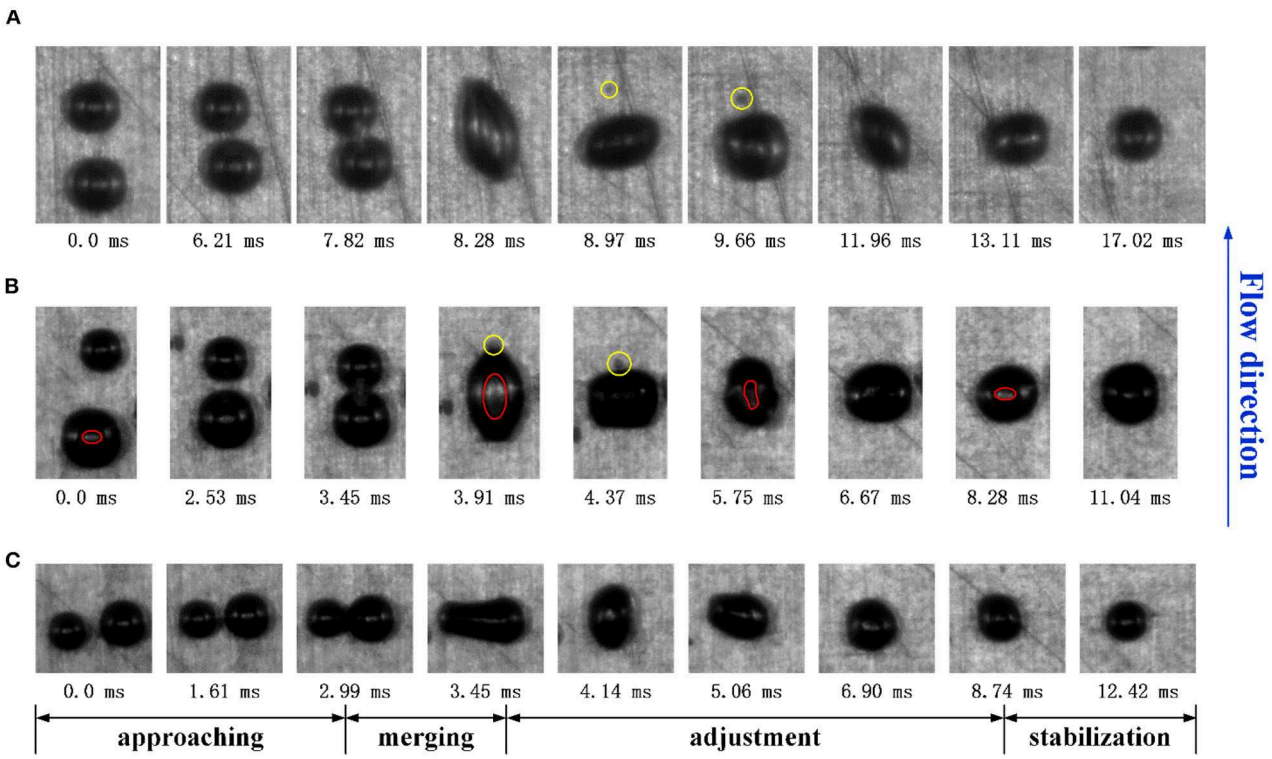


**FIGURE 2 |** Bubble coalescence image. **(A)** $q = 114.3$ kW·m$^{-2}$; $\Delta T_{sub,in} = 31°C$; $G = 333.9$ kg·m$^{-2}$·s$^{-1}$, **(B)** $q = 212.2$ kW·m$^{-2}$; $\Delta T_{sub,in} = 30.8°C$; $G = 619.6$ kg·m$^{-2}$·s$^{-1}$, and **(C)** $q = 212.2$ kW·m$^{-2}$; $\Delta T_{sub,in} = 30.8°C$; $G = 619.6$ kg·m$^{-2}$·s$^{-1}$.

Group (b) shows the coalescence process of two sliding bubbles with large size difference in the flow direction. In 0∼3.45 ms, two bubbles get close to each other, the lower bubble gradually catches up with the upper one, and the diameter of the lower bubble decreases slightly. Then the bubble phase interfaces contact and coalesce, forming a new bubble. The time of bubble merging stage lasts about 0.5 ms and the time of bubble adjustment stage lasts about 7 ms. It is found in the experiment that if two bubble sizes differ greatly before coalescence, the oscillation during coalescence is small. If the size difference is small and both are large bubbles, there is a more severe oscillation and a longer adjustment period.

Group (c) shows the horizontal coalescence process of two sliding bubbles. Coalescence in horizontal direction is more difficult compared to that in vertical direction. However, the two bubbles in the figure are relatively close and the lateral position of two bubbles is shifted due to the growth of bubbles or the disturbance of the fluid. At 2.99 ms, the two bubble interfaces contact each other. After about 0.55 ms merging and 8.5 ms adjustment, a stable new bubble is formed. Similarly, the bubble always slides along the heating surface and does not lift off.

In addition, a small new bubble is generated in the coalescence process, which is reflected in **Figures 2A,B**. At 8.29 ms in **Figure 2A**, the length of the merging bubble in the vertical direction reaches the maximum value and then begins to shorten. A small amount of gas separates from the main bubble at the upper end because of inertia, which is then absorbed by the merging bubble during the movement. Similarly, the generation of a small bubble in **Figure 2B** occurs at 3.91 ms and also occurs at the top. If the small bubble is generated on the side, it may absorb heat energy to form a separate bubble, which is more likely to occur in the coalescence process of two larger bubbles.

## Diameter Changes Before and After Bubble Coalescence

Based on coalescence process of sliding bubbles in **Figures 2**, **3** shows the bubble mean diameter and the ratio of the maximum diameter to minimum diameter variation with the time before and after coalescence. Considering the effects of light and flow heat transfer, the bubble may appear in various shapes. Bubble mean diameter is used to describe the bubble equivalent diameter, which is defined as the average diameter in all directions through the centroid. The ratio of bubble maximum diameter to the minimum diameter could approximately describe the bubble shape.

It can be seen from **Figures 3A,B**, for the coalescence occurring in the vertical flow direction, the bubble at the bottom tends to be larger, while the upper bubble is smaller. The bubble growth rate is relatively small in the sliding process. Before the interaction, a single bubble basically shows a stable state and the

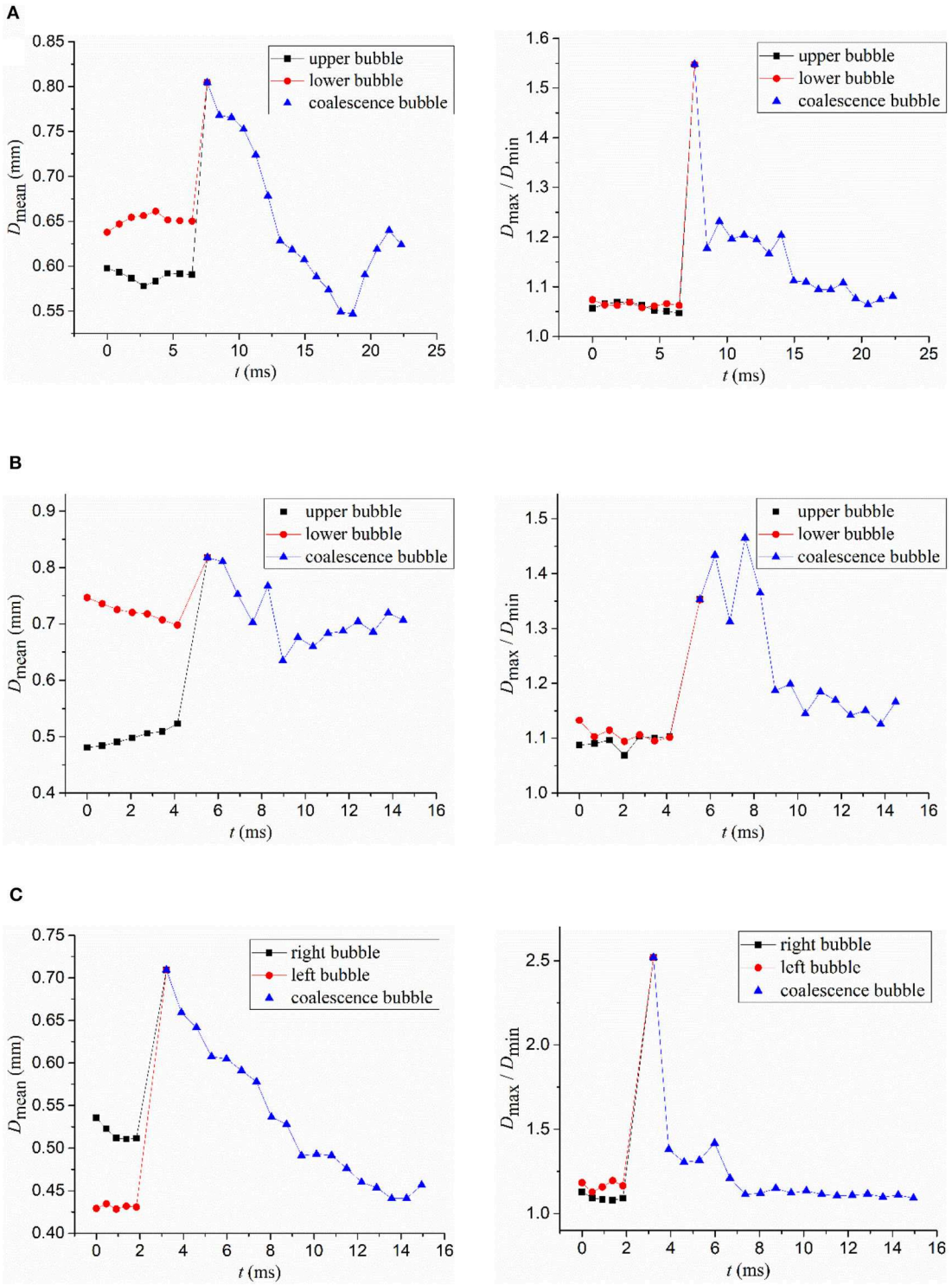


**FIGURE 3 |** Bubble diameter and shape variation with time. **(A)** $q = 114.3$ kW·m$^{-2}$; $\Delta T_{sub,in} = 31$°C; $G = 333.9$ kg·m$^{-2}$·s$^{-1}$, **(B)** $q = 212.2$ kW·m$^{-2}$; $\Delta T_{sub,in} = 30.8$°C; $G = 619.6$ kg·m$^{-2}$·s$^{-1}$, and **(C)** $q = 212.2$ kW·m$^{-2}$; $\Delta T_{sub,in} = 30.8$°C; $G = 619.6$ kg·m$^{-2}$·s$^{-1}$.

bubble diameter remains constant. When two bubbles are close to each other, they begin to interact by affecting the flow field and the bubble diameters and shapes are also disturbed to varying degrees. For example in group (b), the upper bubble diameter increases slightly, while the lower bubble diameter decreases. In the coalescence process, the bubble mean diameters for three

groups increase at first, then decrease and finally stabilize. Later the new bubbles begin to absorb heat and grow like any other stable bubbles. The diameter of the final stable bubble is similar to the diameter of any bubble before coalescence, and its volume is less than the sum of the two bubble volumes before coalescence. This is because in subcooled boiling, the bubble size increases at the beginning of coalescence, increasing the contact area with the subcooled fluid. Moreover, the turbulence in the coalescence process further strengthens the disturbance of the fluid, resulting in greater condensation heat flux than evaporation heat flux. Therefore, the bubble volume decreases after coalescence.

According to Xu et al.'s (2013) work, the stable bubble is approximately spherical when it is sliding along the heating surface before coalescence. In this experiment, the front view is approximately circular. Hence, the ratio of the maximum diameter to the minimum diameter is about 1. It can be found from the bubble image that an irregular ellipse appears when the two bubbles first contact. At this time, the bubble maximum diameter is the largest and the minimum diameter is the smallest. In the subsequent adjustment stage, the bubble continuously trembles, while the degree of tremor weakens. The ratio of the maximum diameter to the minimum diameter gradually decreases until it finally stabilizes.

## Velocity Changes Before and After Bubble Coalescence

**Figure 4** shows the bubble velocity in the vertical direction variation with time before and after bubble coalescence. Compared to the vertical velocity, the horizontal velocity of the sliding bubble is very small and negligible. From the figure, a single sliding bubble moves at a uniform speed before the bubbles interaction. For two bubbles in the vertical flow direction, as shown in **Figures 4A,B**, the sliding velocity of the larger lower bubble is bigger than the velocity of the smaller upper bubble. In **Figure 4C**, the sliding velocities of the two bubbles with the same lateral position are similar. After bubble coalescence, the velocity of the new bubble formed increases first and then decreases with some fluctuations, which is the same as the bubble diameter change.

Xu et al. (2011) pointed out in the research that the influence distance of the initial interaction between two sliding bubbles was about twice times of the average diameter. The coalescence between bubbles is a positive effect, which increases the bubble sliding velocity and is beneficial to the improvement of the heat transfer near the region. In the study, the sliding velocities of the two bubbles in group (a) increases slightly before coalescence, since the lower bubble is in the wake region of the upper bubble and is accelerated by the wake. At the same time, the acceleration promotes the movement of the upper bubble, so the velocities of two bubbles increase. However, the bubble sliding velocity is not only affected by coalescence, but also by the mainstream velocity, flow field disturbance and bubble size. It is known from previous study that the bubble sliding velocity is positively related to the bubble size (Ren et al., 2020). From **Figure 3**, the size of the upper bubble in group (b) decreases before coalescence and the velocity decreases as well. Bubble velocity in group (c) is basically unchanged. Therefore, Xu's conclusion is not applicable to this study, which might due to the limitation of the image window size. At 0 ms, the two bubbles are close to each other and at the end of the interaction, the acceleration is not obvious. In addition, the combined effects of bubble interaction,

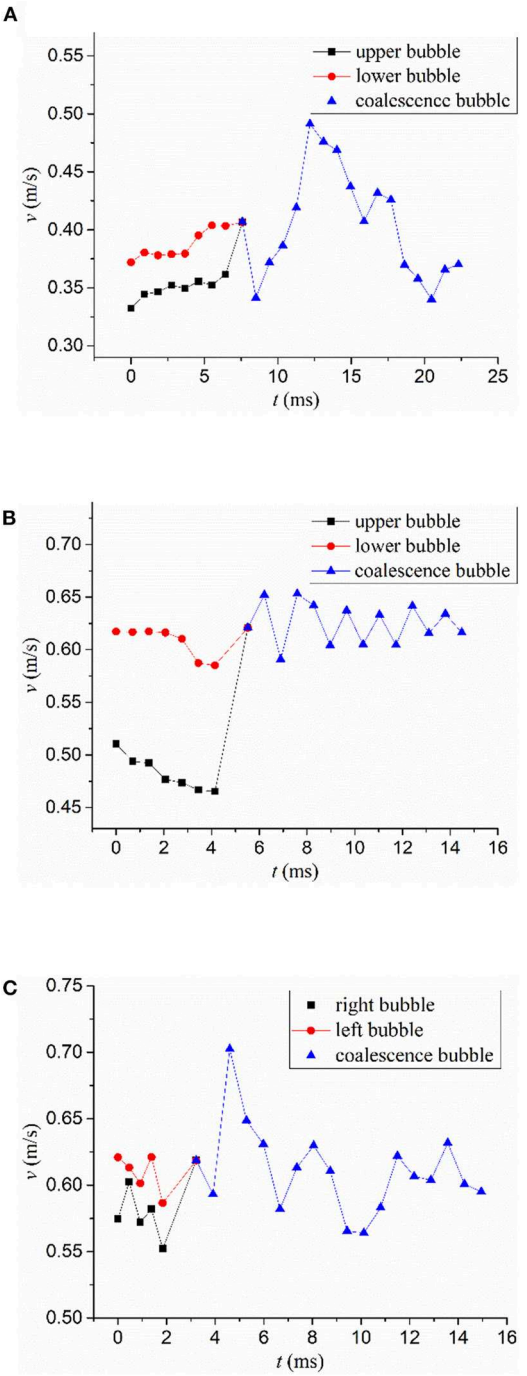


**FIGURE 4 |** Bubble velocity variation with time. **(A)** $q = 114.3$ kW·m$^{-2}$; $\Delta T_{sub,in} = 31°C$; $G = 333.9$ kg·m$^{-2}$·s$^{-1}$, **(B)** $q = 212.2$ kW·m$^{-2}$; $\Delta T_{sub,in} = 30.8°C$; $G = 619.6$ kg·m$^{-2}$·s$^{-1}$, and **(C)** $q = 212.2$ kW·m$^{-2}$; $\Delta T_{sub,in} = 30.8°C$; $G = 619.6$ kg·m$^{-2}$·s$^{-1}$.

flow field disturbances and size change of bubbles may also lead to different results. If the bubble wake effect is greater, bubble velocity increases before coalescence. If other factors have greater influence, bubble velocity decreases or remain unchanged before coalescence.

## CONCLUSIONS

In this paper, visualization experiments were carried out and sliding bubble coalescence behaviors were observed for subcooled flow boiling in a narrow vertical rectangular channel. The changes of morphology diameter and velocity before and after bubble coalescence were studied and analyzed. The main conclusions of the present work can be expressed as:

(1) The consecutive coalescence process is composed of four steps based on the bubble morphological change: approaching, merging, adjustment, and stabilization, in which the more important are the merging and adjustment of the bubble. If the size difference for two bubbles is small and both are large bubbles, there is a more severe oscillation and a longer adjustment period. In coalescence process, the bubble always slides along the heating surface and does not lift off.

(2) Bubble diameter increases first, then decreases and finally stabilizes in coalescence process. The new bubble volume is less than the sum of two bubble volumes before coalescence. Bubble shape also oscillates from an irregular ellipse to a stable circle. The change in bubble sliding velocity is the same as that in diameter.

(3) A new small bubble is generated next to the main bubble in the coalescence process, which is then absorbed by the main bubble during the movement or it may absorb heat energy to form a separate bubble.

Intuitive information is obtained about the interaction of bubbles in a narrow channel, which provides theoretical support for the study of boiling heat transfer. However, more quantitative analysis needs to be completed in future work.

## DATA AVAILABILITY STATEMENT

The datasets generated for this study are available on request to the corresponding author.

## AUTHOR CONTRIBUTIONS

TR contributed significantly to the analysis and manuscript preparation, performed the data analysis, and wrote the manuscript. ZZ and JS checked the English writing thoroughly. CY and RZ approved the final version.

## FUNDING

The authors greatly appreciate support from Natural Science Foundation of China (Grant No. 11675045), support from the Natural Science Foundation of Heilongjiang Province, China (Grant No. LH2019A009), and the Open Fund Program of the State Key Laboratory of Nuclear Power Safety Monitoring Technology and Equipment (K-A2019.414).

## ACKNOWLEDGMENTS

The authors are thankful for support from the Fundamental Science on Nuclear Safety and Simulation Technology Laboratory, Harbin Engineering University, China.

## REFERENCES

Bonjour, J., Clausse, M., and Lallemand, M. (2000). Experimental study of the coalescence phenomenon during nucleate pool boiling. *Exp. Thermal Fluid Sci.* 20, 180–187. doi: 10.1016/S0894-1777(99)00044-8

Chen, T., and Chung, J. N. (2002). Coalescence of bubbles in nucleate boiling on microheaters. *Int. J. Heat Mass Transfer* 45, 2329–2341. doi: 10.1016/S0017-9310(01)00334-9

Coulibaly, A., Bi, J., Lin, X., and Christopher, D. M. (2014). Effect of bubble coalescence on the wall heat transfer during subcooled pool boiling. *Int. J. Thermal Sci.* 76, 101–109. doi: 10.1016/j.ijthermalsci.2013.08.019

Feng, J., Li, X., Bao, Y., Cai, Z., and Gao, Z. (2016). Coalescence and conjunction of two in-line bubbles at low Reynolds numbers. *Chem. Eng. Sci.* 141, 261–270. doi: 10.1016/j.ces.2015.11.014

Kine, S. J., and Mcclintock, F. A. (1953). Describing uncertainties in single-sample experiments. *Mech. Eng.* 75, 3–8.

Li, S., Tan, S., Xu, C., Gao, P., and Sun, L. (2013). An experimental study of bubble sliding characteristics in narrow channel. *Int. J. Heat Mass Transfer* 57, 89–99. doi: 10.1016/j.ijheatmasstransfer.2012.10.002

Liu, Z., Herman, C., and Mewes, D. (2006). Visualization of bubble detachment and coalescence under the influence of a nonuniform electric field. *Exp. Thermal Fluid Sci.* 31, 151–163. doi: 10.1016/j.expthermflusci.2006.03.025

Lu, Q., Chen, D., Huang, Y., Yuan, D., and He, X. (2017). Visual investigation on the coalescence process and the thermal-hydraulic characteristics of the two-phase interface morphology in narrow vertical channel. *Int. J. Heat Mass Transfer* 115, 537–550. doi: 10.1016/j.ijheatmasstransfer.2017.08.052

Mukherjee, A., and Dhir, V. K. (2004). Study of lateral merger of vapor bubbles during nucleate pool boiling. *J. Heat Transfer* 126, 1023–1039. doi: 10.1115/1.1834614

Nguyen, V. T., Songab, C. H., Baeb, B. U., and Euh, D. J. (2013). Modeling of bubble coalescence and break-up considering turbulent suppression phenomena in bubbly two-phase flow. *Int. J. Multiphase Flow* 54, 31–42. doi: 10.1016/j.ijmultiphaseflow.2013.03.001

Ren, T., Zhu, Z., Yana, M., Shia, J., and Yan, C. (2019). Experimental study on bubble nucleation and departure for subcooled flow boiling in a narrow rectangular channel. *Int. J. Heat Mass Transfer* 144, 118670. doi: 10.1016/j.ijheatmasstransfer.2019.118670

Ren, T., Zhub, Z., Shia, J., Yana, C., and Zhang, R. (2020). Experimental study on bubble sliding for upward subcooled flow boiling in a narrow rectangular channel. *Int. J. Heat Mass Transfer* 152:119489. doi: 10.1016/j.ijheatmasstransfer.2020.119489

Xu, J., Chen, B. D., Huang, Y. P., Yan, X., and Yuan, D. (2013). Experimental visualization of sliding bubble dynamics in a vertical narrow rectangular channel. *Nuclear Eng. Des.* 261, 156–164. doi: 10.1016/j.nucengdes.2013.02.055

Xu, J., Chen, B. D., and Wang, X. J. (2011). Experimental visualization coalesced interaction of sliding bubble near wall in vertical narrow rectangular channel. *Yuanzineng Kexue Jishu/Atomic Energy Sci. Technol.* 45, 548–553. doi: 10.1007/s12264-011-1035-3

Zhang, L., and Shoji, M. (2003). Nucleation site interaction in pool boiling on the artificial surface. *Int. J. Heat Mass Transfer* 46, 513–522. doi: 10.1016/S0017-9310(02)00291-0

Zheng, Q., Gao, P. Z., Xu, C., Feng, G., and Jian, H. (2014). Research on bubble coalescence in narrow rectangular channel. *Yuanzineng Kexue Jishu/Atomic Energy Sci. Technol.* 48, 1015–1019. doi: 10.7538/yzk.2014.48.06.1015

**Conflict of Interest:** The authors declare that the research was conducted in the absence of any commercial or financial relationships that could be construed as a potential conflict of interest.

## NOMENCLATURE

$P$ System pressure, MPa
$q$ Wall heat flux, $kW \cdot m^{-2}$
$G$ Mass flow rate, $kg \cdot m^{-2} \cdot s^{-1}$
$\Delta T_{sub,in}$ Inlet subcooling, °C
$D$ Diameter, mm
$v$ Velocity, m/s.

frontiers in Energy Research

BRIEF RESEARCH REPORT
published: 02 June 2020
doi: 10.3389/fenrg.2020.00095

# The Effect of Different Branch Angles and Different Branch Pipe Sizes on the Onset Law of Liquid Entrainment

*Xiaoyu Li*[1,2], *Geyu Shen*[1], *Ping Liu*[1], *Jinchen Gao*[1], *Ningxin Gu*[1] *and Zhaoming Meng*[1]*

[1] *Fundamental Science on Nuclear Safety and Simulation Technology Laboratory, Harbin Engineering University, Harbin, China,* [2] *Energy and Power Engineering College, Xi'an Jiaotong University, X'ian, China*

The T-junction has been extensively employed in nuclear power plant systems. To ensure the normal operation of nuclear power plant, the onset point of T-junction liquid entrainment requires in-depth studies. Existing studies have been conducted on the onset point of liquid entrainment, whereas most of them are for small branch pipes. This study primarily discussed the onset law of large branch pipe. Moreover, the effects of branch angle and size on the onset point of liquid entrainment were analyzed by comparing it with other branch pipe sizes in this study. This study demonstrated that the effect of branch angle on the onset point of entrainment complies with that of other sizes, i.e., because that the decrease in the inertial force in the vertical direction acting on the liquid phase by the gas phase with the decrease in the angle, hence, the onset requires larger $Fr_g$ under the identical $h_b$with the decrease in the angle between the branch pipe and the horizontal direction. Moreover, by comparing the onset point law of liquid entrainment exhibiting different branch pipe sizes, the effect of branch pipe size on the onset was reported in this study that the smaller branch pipe requires the greater gas velocity in the presence of onset. We found that there is different flow resistance of different sizes of branch pipe, small branch has larger flow resistance, in order to remedy the flow resistance, the gas dynamic head decreases, thereby causing the Bernoulli effect weaker; the onset of liquid entrainment requires larger $V_{3g}$.

**Keywords: the onset of liquid entrainment, the effect of branch angle, the effect of branch pipe size, the air chamber height, the froude number**

OPEN ACCESS

***Edited by:***
*Muhammad Zubair, University of Sharjah, United Arab Emirates*

***Reviewed by:***
*Yago Rivera, Polytechnic University of Valencia, Spain*
*Muhammad Zeeshan Khalid, University of Engineering and Technology Taxila, Pakistan*

***Correspondence:**
*Zhaoming Meng*
*mengzhaoming@hrbeu.edu.cn*

***Specialty section:***
*This article was submitted to Nuclear Energy, a section of the journal Frontiers in Energy Research*

***Received:*** *25 May 2019*
***Accepted:*** *04 May 2020*
***Published:*** *02 June 2020*

***Citation:***
*Li X, Shen G, Liu P, Gao J, Gu N and Meng Z (2020) The Effect of Different Branch Angles and Different Branch Pipe Sizes on the Onset Law of Liquid Entrainment. Front. Energy Res. 8:95. doi: 10.3389/fenrg.2020.00095*

## INTRODUCTION

The T-junction has been broadly applied in the industry, and it is also critical to the nuclear industry. Two examples of this technology are the inlet piping of the Fourth Stage Automatic Depressurization System (ADS-4) of the AP1000 (Schulz, 2006) and the header-feeder system of CANDU (Kowalski and Hanna, 1989). On the whole, the T-junction refers to a major horizontal pipe with an inclined branch pipe. The liquid entrainment is that liquid phase acts as the discontinuous phase, while gas phase serves as the continuous phase; liquid phase can be entrained into the branch pipe by the gas phase (Zuber, 1980). In 1980, Zuber (Zuber, 1980) published a technical report on a small break water loss accident, suggesting that in the occurrence of the reactor LOCA accident, liquid entrainment is more likely to occur; due to the effect of gravity, the gas-liquid two-phase flows in the major horizontal pipe exhibits stratified flow. In the presence of the liquid entrainment, it is more likely to cause the nuclear reactor meltdown. The more liquid

phase is entrained, the less coolant will be left in the core (Wang et al., 2011). Accordingly, the study on liquid entrainment is critical to engineering.

Liquid phase entrainment reflects the Bernoulli effect. When there exists a pressure difference between the gas phase in the branch pipe and in the main pipe, then, the liquid phase overcomes gravity by the action of the gas phase pressure difference (Smoglie and Reimann, 1986; Smoglie et al., 1987) and is carried out of the branch pipe.

The study on liquid phase entrainment complies with the onset of liquid entrainment. Thus, the study on onset point of liquid entrainment appears to be essential. Numerous scholars have long conducted a lot of studies on the liquid entrainment onset phenomenon, they have made several achievements. Different scholars have conducted a series of studies on the onset, there is exhibiting two parts, one is different branch pipe sizes and another one is different branch pipe angles.

In the study on onset, the size of branch pipe is defined below. On the whole, a branch pipe with the diameter to main pipe diameter ratio <0.2 is defined as a small branch pipe, while the ratio over or =0.2 is defined as a large branch pipe (Meng, 2015). Moreover, branch pipe angle refers to the angle between the branch pipe and the horizontal direction (Lee et al., 2007).

The studied conducted by Yonomoto and Tasaka (1991) and Lee et al. (2007) suggested that the entrainment onset phenomenon is associated with the vortex of the branch pipe entrance. Lee et al. (2007) and Lee et al. (2006) analyzed the onset phenomenon of the liquid entrainment of small branch pipes (the branch pipe diameter $d$: 16 mm and 24.8 mm, the horizontal main pipe diameter $D$: 184 mm). Besides, Lee et al. obtained the law of small branch pipes with different angles (the angle $\theta$: 30°, 60°, 90°). The study by Lee et al. suggested that onset of liquid entrainment is primarily correlated with the gas phase, Froude number and the dimensionless air chamber height $h_b/d$. Besides, the air chamber height $h_b$ of onset point rises with the increase in gas phase Froude number. Many other scholars have built some mathematical models that have been successfully applied for various analysis programs (e.g., RELAP5 Ransom et al., 2001 and CATHARE Maciaszek and Micaelli, 1990). However, Bartley et al. (2008) studied the entrainment process of the inclined branch pipe on the flat wall surface; he found that the onset point of the liquid phase entrainment was independent of the inclination angle. Wang et al. (2011) and Smoglie et al. (1987) assessed the entrainment onset of small branch pipes with horizontal, vertical upward and vertical downward directions by ignoring the viscosity and surface tension of the fluid. Furthermore, Cho et al. (2004), Cho and Jeun (2004), Cho and Jeun (2007), and Welter et al. (2004) also made outstanding contributions to the study on the onset of liquid entrainment.

Lu et al. (2018) have conducted a study on large branch pipe ($D = 80$ mm, $d = 56$ mm) with different angles. In the research conducted by Lu et al., the entrainment onset correlation was developed. They demonstrated that the gas phase $Fr$ at the onset of liquid entrainment decreases with an increase in the branch angle $\theta$ (Lu et al., 2018).

There are considerable studies on the onset of liquid entrainment, whereas most of the studies are about small branch pipe. Many researchers (Welter et al., 2004; Meng et al., 2014a,b) found that the onset entrainment of small branch pipes is different from large branch pipes, whereas the study on large branch pipes remains rare. Also, fewer studies have been conducted on the effect of size and angle on the onset of liquid entrainment, but branch pipes of different sizes and different angles are ubiquitous in engineering. Accordingly, it is necessary to study large branch pipes and the effect of size and angle on the onset of liquid entrainment.

# METHOD

## Experimental Content

As shown in **Figure 1**, when gas-liquid two-phase flows in the pipeline, the distance between the interface of the gas-liquid two-phase and the entrance center of branch pipe refers to $h$. Under the regulated liquid level and gas flow in the major horizontal pipe, when the liquid level and the gas flow rate reach the certain value, the gas phase begins to carry the liquid phase into the branch pipe, at which time $h$ is equated with a critical value $h_b$, and the $h_b$ denotes the height of the onset of entrainment. If the liquid level continues to be elevated, $h$ will decrease, and the amount of liquid phase carried by the gas phase will increase. The test section used throughout this study is a T-junction with a main pipe inner diameter of 80 mm and a branch pipe inner diameter of 31 mm. The total length of the test bench is 2,570 mm, of which the upstream is 1,730 mm and the downstream is 840 mm. In the experimental pipeline, the working medium of the gas phase is air, and liquid working medium is water. For stratified flow inside the major horizontal pipe, the means of visualization were combined with quantitative and qualitative methods to analyze the liquid entrainment of different branch pipe ($d/D = 0.3875$) angles.

The study on this experiment is about that onset entrainment of large branch pipe and the effect of branch angle and branch pipe size on the onset of liquid entrainment. The study on the onset point of liquid entrainment involves: When the onset entrainment occurs at different angles, analyzing the flow condition and corresponding parameters of two-phase working medium, and ascertaining the effects of various factors (air chamber height, gas velocity, branch pipe angle, etc.) on the onset point of liquid entrainment according to the experimental data; compared with previous study on the onset point of liquid entrainment exhibiting different branch pipe sizes to analyze the effect of different branch pipe sizes on the onset point of liquid entrainment with certain parameters.

## Experimental Facility

The schematic diagram of the experimental facility used in this study is illustrated in **Figure 1**. The experimental facility primarily consists of three sub-systems: (1) water supply system, (2) gas supply system, and (3) Experimental section.

The water supply system: the water supply system consists of a centrifugal pump with a maximum flow rate of 4 $m^3$/h and turbine flowmeter (Model: LWGY-15C, Shanghai Automation Instrumentation Co., Ltd., China, Accuracy: 1.0%) with a measurement range of 0–5 $m^3$/h. The water flowed

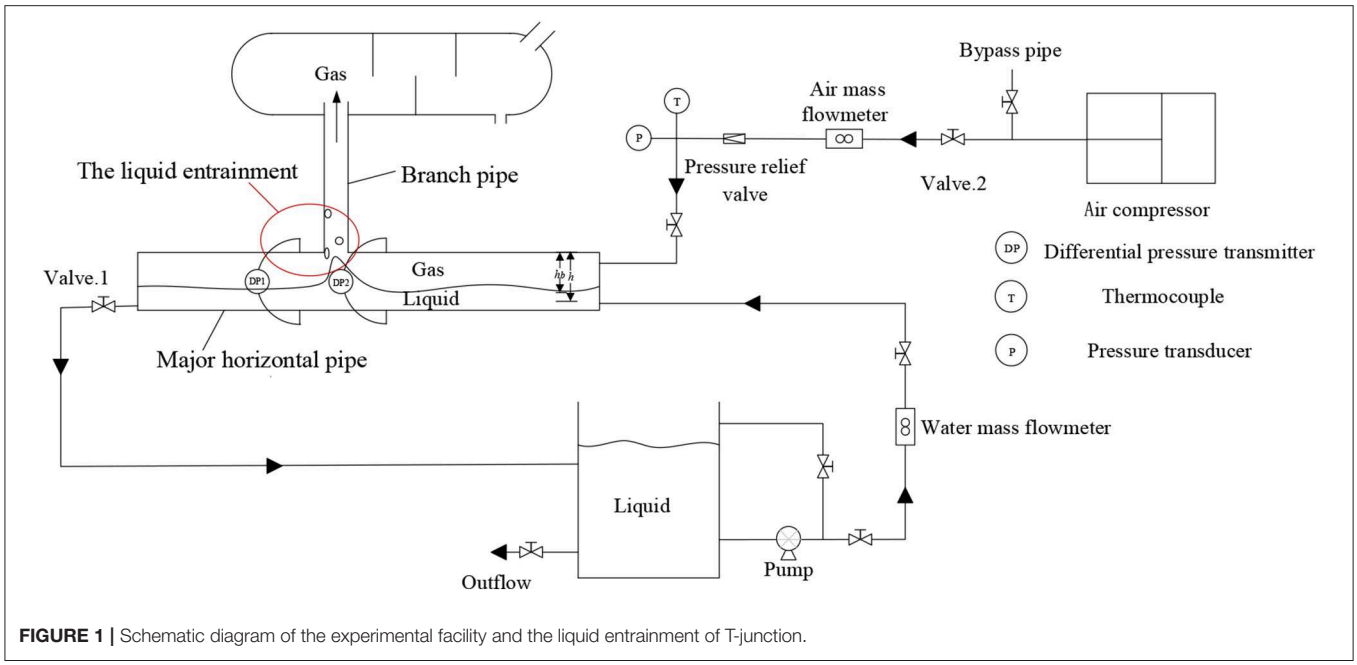


**FIGURE 1 |** Schematic diagram of the experimental facility and the liquid entrainment of T-junction.

into the T-junction experimental section via a 40 mm diameter stainless steel pipeline. The gas supply system: the gas supply system consists of a roots blower. A vortex flowmeter (Model: Prowirl200, Endress+Hauser AG, Switzerland, Accuracy: 0.5%) exhibits a measurement range of 0–200 kg/h. The gas was transported into the T-junction test section via a 40 mm diameter stainless steel pipeline. The experimental section: the length of horizontal upstream pipe is 1,730 mm, the length of horizontal downstream pipe is 840 mm, and the length of branch pipe reaches 700 mm. The T-junction experimental section took polymethyl methacrylate (PMMA) acrylic plastic as the material to more effectively observe the onset point of liquid entrainment and analysis of the onset point of entrainment mechanism. Other experimental facilities: the pressure difference transmitter (Accuracy: 0.05%) with a measurement range of 0–0.17 kPa is used to measure the water level in the major horizontal pipe. The temperature was measured by K-Thermocouple (Accuracy: 0.5°C) with a measurement range of 0–350°C. The entrance of the experimental section was provided with a partition board to ensure that the gas-liquid two-phase flow in the pipeline is stratified. During the experiment, the water level in the major horizontal pipe was regulated by adjusting the valve at downstream of the experiment section.

In this study, the thermocouple was adopted to measure the gas temperature and get the density of the gas based on the gas temperature. The pressure difference between the bottom of the main pipe and the two phases interface was measured with a pressure difference sensor. Based on this pressure difference, the liquid phase height of the pipeline was obtained, and then the air chamber height was calculated. A vortex flowmeter was adopted to measure the gas phase flow. For the analysis of uncertainty, the following formula was adopted (Liu, 2000; Hu, 2002; Liang et al., 2005; Luo, 2007; Ni, 2009):

$$U_B = \frac{\Delta_{ins}}{C} \tag{1}$$

Where $\Delta_{ins}$ is the measurement error, $C = \sqrt{3}$. $\Delta_{ins}$ includes both $\Delta_{mea}$ and $\Delta_{NI}$, $\Delta_{mea}$ is the instrumentation measurement error, $\Delta_{NI}$ is the error in NI acquisition systems. After calculation, three types of uncertainty were obtained (gas temperature 0.3°C, pressure difference 0.07 Pa, gas flow 0.6 $m^3$/h). The primary analysis parameter in the experiment is the Froude number, the formula for Froude number is expressed as:

$$Fr_g = \frac{V_{3g}}{\sqrt{gd}} \tag{2}$$

Where $V_{3g}$(the gas phase velocity at the branch pipe entrance) denotes the gas flow. Thus, the relative uncertainty of the Froude number is 0.015.

The experimental process:

(1). Opening the pump and blower to make the gas-liquid two-phase fluid enter the experimental section.
(2). Regulating the valve1 to make the water level in the major horizontal pipe reaches the level at which the onset of liquid entrainment can occur.
(3). Recording the experimental data (the water level in major horizontal pipe, the gas flow) then.
(4). Keeping the liquid flow constant, altering the gas flow by regulating the valve2 and repeating the experiment step (2)-(3).
(5). Turning off the pump and blower when sufficient experimental data were obtained.
(6). Changing the branch angle, repeating the experiment step (1)-(5).

Data processing:

Key parameters of existing studies about the onset point of liquid entrainment were almost the same ($\theta$: the branch pipe angle, $h_b$: the air chamber height of liquid entrainment onset, $d$: the inner diameter of branch pipe, $V$: the gas flow rate, etc.). Accordingly, the experimental data were also processed here according to these parameters.

During the experiment, the effect of branch angle on onset entrainment was found correlated with the water level and the balance of gravity and inertial forces. The $Fr$ denotes a dimensionless number that represents the ratio of inertial force to gravity. Besides, the air chamber height $h_b$ can represent the water level. Thus, the experimental parameters used in the research regarding the effect of branch angle on the onset point of liquid entrainment are $Fr_g$ and the dimensionless air chamber height $h_b/d$ of the branch pipe. Moreover, the effect of branch size on onset entrainment was found correlated with the water level and the gas phase velocity. The experimental parameters in the research regarding the effect of branch size on the onset point of liquid entrainment used are the gas phase velocity $V_{3g}$ at the branch pipe entrance and the air chamber height $h_b$.

# RESULTS

Based on the study of Lee et al. (2007) and Lu et al. (2018), we obtained the experimental data of other pipe sizes. As shown in Table 1 of the **Appendix**, we presented our experimental data and the data of other pipe sizes. Our analysis is based on these data.

## The Effect of Branch Angle

We analyze the effect of branch angle on the onset of liquid phase entrainment by drawing upon the comparison of the results of Lee et al. (2007) and Lu et al. (2018). As shown in **Figure 2C**, given the experimental data acquired, $Fr_g\ (\rho_g/\Delta\rho)^{0.5}$ with $h_b/d$ relationship curves were plotted in this study. As showed in the experimental data: at constant $\theta$ value, the air chamber height $h_b$ of the onset of liquid entrainment increases with $Fr_g$ increase; under the identical air chamber height, the onset of liquid entrainment requires larger $Fr_g$ when the angle of the branch decreases in the horizontal direction.

As shown in **Figures 2A,B,D**, there are experimental data to curves of the other three branches. By comparing the experimental data, the onset point law of liquid entrainment of all branch sizes with the variation of angle is consistent. At constant $\theta$, the Bernoulli effect increases with $Fr_g$ increase, and therefore the gas phase exerts a greater inertial force on the liquid phase in the presence of the onset. Besides, the water level requirement in the main pipe will be reduced, accordingly, the air chamber height $h_b$ of the onset of liquid entrainment increases with $Fr_g$ increase.

As shown in **Figure 2E**, under the identical water level, the component of the inertial force in vertical direction will be smaller with the same $Fr_g$ when the angle of the branch decreases. According to the balance of forces, to achieve the presence of the onset of liquid entrainment, a greater inertial force is required to overcome gravity; thus, it requires larger $Fr_g$. Lastly, the result presents that the $h_b$ of the onset increases with $Fr_g$ increase.

## The Effect of Branch Pipe Size

As shown in **Figures 3A–D**, respectively, under the fixed angle, the relationship curves of the gas phase velocity $V_{3g}$ with the air chamber height $h_b$ were plotted. The data indicate the laws as follows: the air chamber height $h_b$at the onset of liquid entrainment increases with the increase in gas velocity $V_{3g}$; at the identical air chamber height, the smaller the branch pipe diameter, the greater the gas phase velocity will be generally required for the onset. The explanation for the law that $h_b$ rises with the increase in $V_{3g}$ has been stated in the previous section and will not be repeated here. Under the identical air chamber height, the gas phase velocity at the onset of liquid entrainment increases with the decrease in branch pipe diameter, the explanation for which are as follows:

In accordance with fluid mechanics, the flow resistance of a pipe is inversely proportional to the diameter of the pipe; accordingly, the smaller the pipe diameter, the greater the flow resistance will be (Kong, 1992). Moreover, the force exploited to balance the flow resistance is exerted by the dynamic head of the gas. When the flow resistance of a fluid under the identical entrance conditions in the pipe is greater, the dynamic head loss of the gas will be comparatively larger, the Bernoulli's equation is expressed as

$$P_1 + \rho g h_1 + \frac{\rho {v_1}^2}{2} = P_2 + \rho g h_2 + \frac{\rho {v_2}^2}{2} = C \tag{3}$$

where $P$ denotes the fluid static pressure, $\rho$ is the fluid density, $v$ is the fluid velocity and $\frac{\rho v^2}{2}$is the dynamic pressure, and $h$ is the fluid location. In this study, $h$ exerts almost no effect; thus, the Bernoulli's equation is expressed as:

$$P_1 + \frac{\rho {v_1}^2}{2} = P_2 + \frac{\rho {v_2}^2}{2} = C \tag{4}$$

The Bernoulli's equation reveals that when the smaller the dynamic pressure, the larger the static pressure will be. In this study, under the same branch pipe entrance air velocity, the flow resistance of the gas-phase fluid varies with branch diameter, the diameter of is 16 mm leads to the maximum flow resistance, and the diameter of 56 mm leads to the minimum flow resistance. According to the mentioned principle, under the identical air chamber height and the identical entrance air velocity, when the branch pipe is smaller, the fluid resistance will be larger, the loss of dynamic pressure will rise, the static pressure $P$ will increase; as a result, the pressure difference between the gas-liquid interface and the branch pipe will decrease. Accordingly, the liquid entrainment onset is difficult to occur, and the onset point of liquid entrainment requires higher gas phase velocity $V_{3g}$.

# CONCLUSION

In this study, the mechanism of onset was observed by a visualized experimental facility.

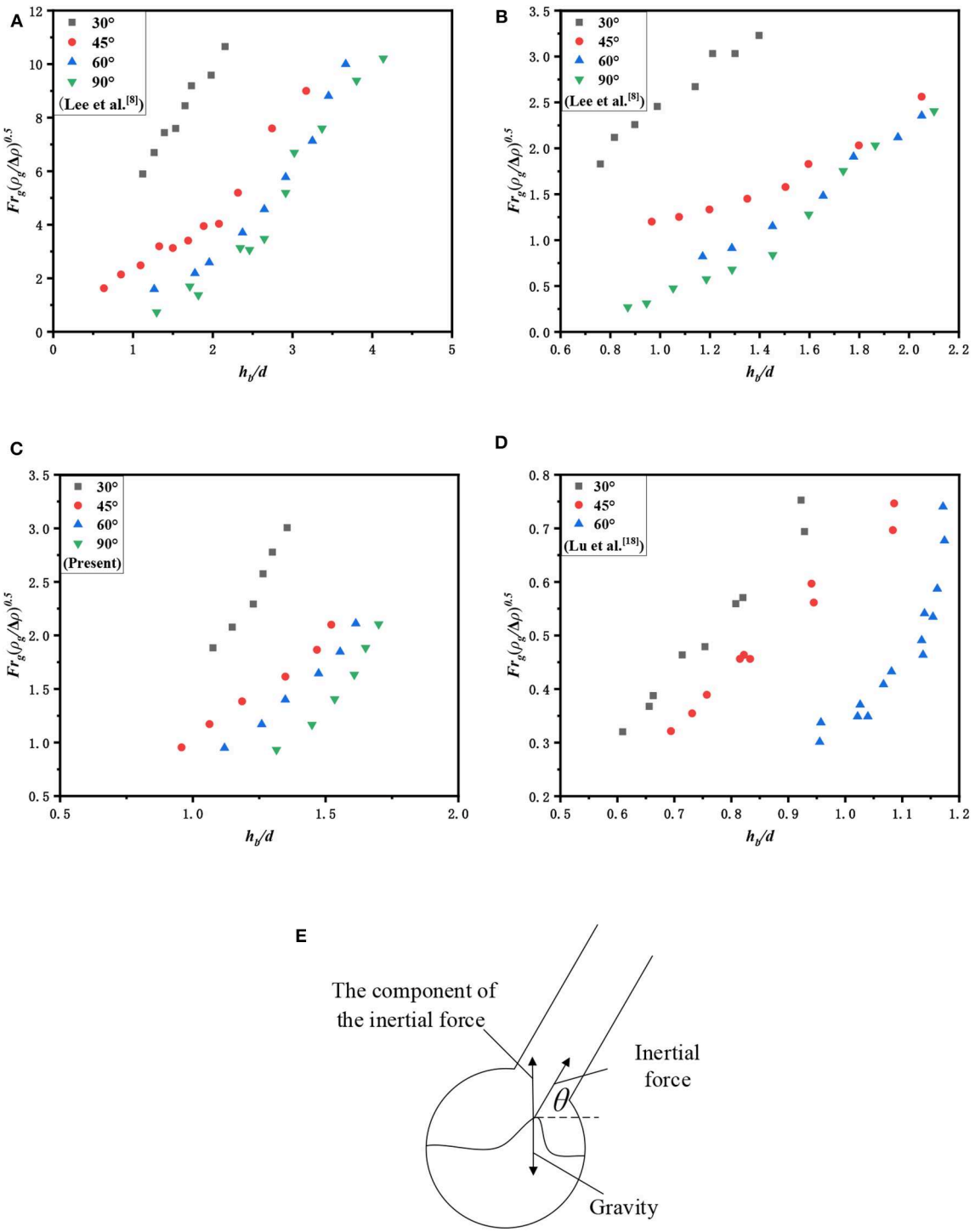


**FIGURE 2 |** Comparison of entrainment onset data at different branch angles (Lee et al., 2007; Lu et al., 2018) **(A)** $d = 16$ mm, **(B)** $d = 24.8$ mm, **(C)** $d = 31$ mm, and **(D)** $d = 56$ mm **(E)** diagram of force balance.

The effect of branch angle on the law of onset is studied in this paper. This study found that the onset point law of entrainment with the angle change is consistent. With the decrease in the angle between the branch pipe and the horizontal direction, the onset requires larger $Fr_g$ under the identical $h_b$. The component of the inertial force in the vertical direction will be smaller with the same $Fr_g$ when the angle of the branch becomes smaller, according to the balance of forces, to make the onset of liquid entrainment occur there must have a greater $Fr_g$.

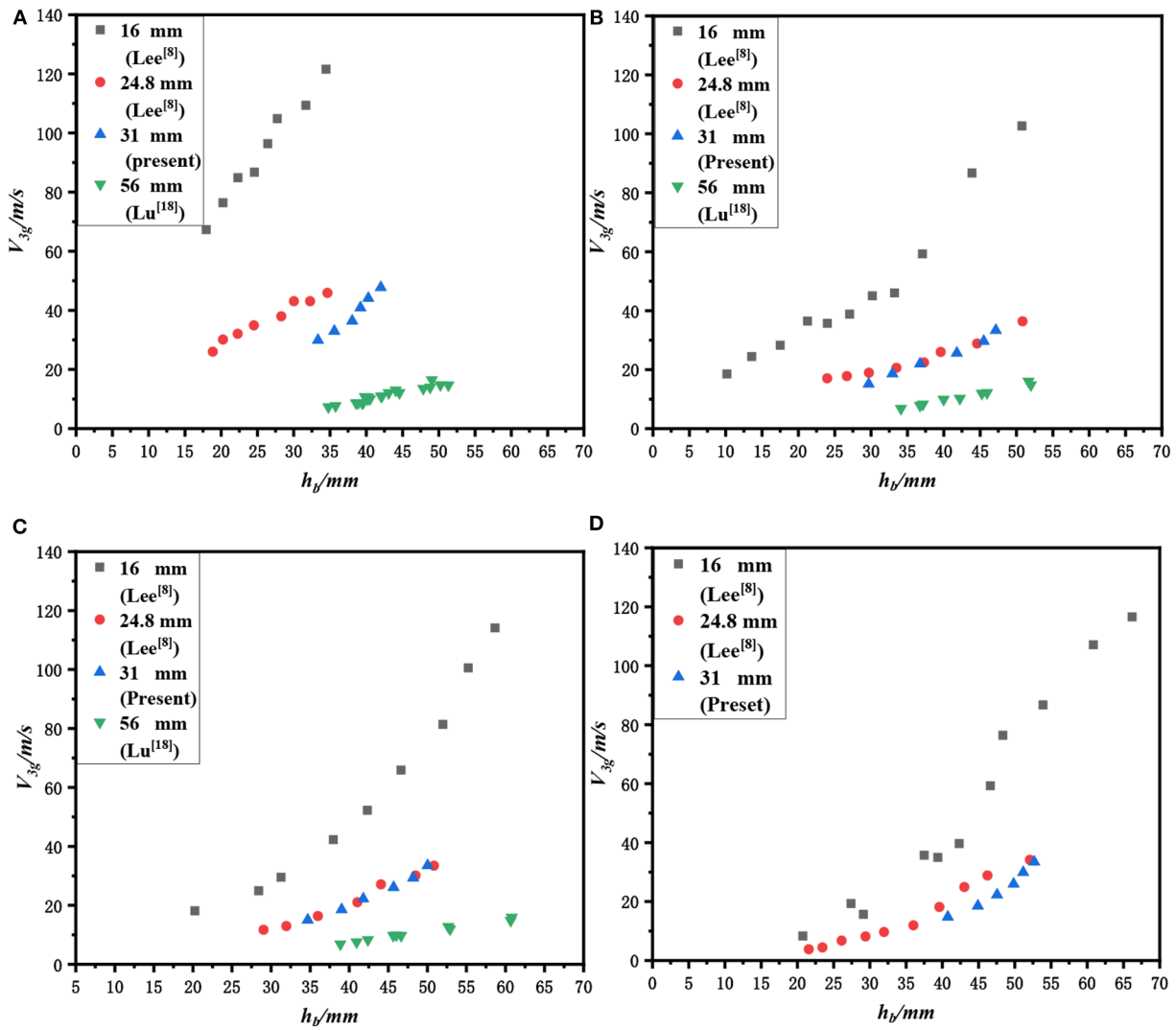


**FIGURE 3 |** Comparison of entrainment onset data at different branch sizes (Lee et al., 2007; Lu et al., 2018) **(A)** Branch angle: 30°, **(B)** Branch angle: 45°, **(C)** Branch angle: 60°, and **(D)** Branch angle: 90°.

Under $\theta$ as a constant value, the study regarding the effect of the branch pipe size on the onset of liquid entrainment reported that the onset of smaller branch pipe requires larger $V_{3g}$ with the identical air chamber height. Since the flow resistance of different branches is different, the smaller branch has greater flow resistance, and the gas dynamic head helps remedy the flow resistance, thereby causing the Bernoulli effect weaker; subsequently, the onset of liquid entrainment requires larger $V_{3g}$.

## DATA AVAILABILITY STATEMENT

The datasets generated for this study are available on request to the corresponding author.

## AUTHOR CONTRIBUTIONS

XL participated in the experimental process, and he processed and analyzed the experimental data to sum up the law. GS sorted out the material and provided some useful opinions on the experimental process and data processing. PL, JG, and NG helped to build the experimental facility and carried out the experiment. ZM guided the whole process of the research and provided suggestions for experiments and data processing.

## FUNDING

The work was financed by a grant from the National Natural Science Foundation of China (No. 11605032).

## SUPPLEMENTARY MATERIAL

The Supplementary Material for this article can be found online at: https://www.frontiersin.org/articles/10.3389/fenrg.2020.00095/full#supplementary-material

## REFERENCES


Bartley, J. T., Soliman, H. M., and Sims, G. E. (2008). Experimental investigation of the onsets of gas and liquid entrainment from a small branch mounted on an inclined wall. *Int. J. Multiph. Flow* 34, 905–915. doi: 10.1016/j.ijmultiphaseflow.2008.04.003

Cho, Y. J., Ahn, S.-H., and In-Goo Kim/KINS. (2004). *Development of Horizontal Off-Take Model for Application to Reactor Headers of CANDU Type Reactors*. Karlsruhe: US Nuclear Regulatory Commission.

Cho, Y. J., and Jeun, G. D. (2004). Modeling of liquid entrainment and vapor pull-through in header-feeder pipes of CANDU. *Nucl. Eng. Technol.* 36, 142–152.

Cho, Y. J., and Jeun, G. D. (2007). A study of the liquid entrainment and vapor pull-through in an angled branch line. *Nucl Technol.* 158, 366–377. doi: 10.13182/NT07-A3848

Hu, X. (2002). On the uncertainty of measurement. *Phys. Testing Chem. Analysis B Chem. Analysis* 38, 406– 409.

Kong, L. (1992). Engineering fluid mechanics. Beijing: China Electric Power Press. 84–85. (in Chinese).

Kowalski, J., and Hanna, B. (1989). "Studies of two-phase flow distribution in a CANDU-type header/feeder system," in *Fourth international topical meeting on nuclear reactor thermal-hydraulics (NURETH-4). Proceedings. Vol. 1*. Washington, DC.

Lee, J. Y., Hwang, G. S., Kim, M., and No, H. C. (2006). Experimental analysis of off-take phenomena at the header–feeder system of CANDU. *Ann. Nuclear Energy* 33, 1–12. doi: 10.1016/j.anucene.2005.09.002

Lee, J. Y., Hwang, S. H., Kim, M., and Park, G. C. (2007). Onset condition of gas and liquid entrainment at an inclined branch pipe on a horizontal header. *Nucl. Eng. Design* 237, 1046–1054. doi: 10.1016/j.nucengdes.2007.01.002

Liang, K., Jiao, T., Li, S., Luo, X., Chen, J., Liu, W., et al. (2005). Measurement uncertainty in analytical data processing. *Anal. Testing Technol.* 11, 149–152.

Liu, Z. (2000). *Uncertainty and Its Practice*. Beijing: Standards Press of China.

Lu, Z., Meng, Z., Gu, N., Wang, J., Nian, F., Wang, J., et al. (2018). Development of correlations for liquid entrainment through a large-scale inclined branch pipe connected to the main horizontal pipe. *Exp. Thermal Fluid Sci.* 96, 128–136. doi: 10.1016/j.expthermflusci.2018.03.007

Luo, G. (2007). Serches of the uncertainty A and the uncertainty B. *Metrol. Measur. Technique* 34, 42-43.

Maciaszek, T., and Micaelli, J. (1990). CATHARE phase separation modeling for small breaks in horizontal pipes with stratified flow. *Nuclear Eng. Design* 124, 247–256. doi: 10.1016/0029-5493(90)90295-9

Meng, Z. (2015). *Research of entrainment at t-junction in large advanced PWR* (doctoral thesis). Xi'an Jiaotong University, Xian, China.

Meng, Z., Dong, B., Wang, L., Fu, X., Tian, W., Yang, Y., Su, G., et al. (2014a). Experimental research of liquid entrainment through ADS-4 in AP1000. *Ann. Nuclear Energy* 72, 428–437. doi: 10.1016/j.anucene.2014.06.012

Meng, Z., Dong, B., Wang, L., Fu, X., Tian, W., Yang, Y., Su, G., et al. (2014b). Experimental and theoretical investigation of liquid entrainment through small-scaled ADS-4 in AP1000. *Exp. Thermal Fluid Sci.* 57, 177–187. doi: 10.1016/j.expthermflusci.2014.04.022

Ni, Y. (2009). *Evaluation of Practical Measurement Uncertainty*. Beijing: China Metrology Press.

Ransom, V. H. J., Trapp, J., and Wagner, R. (2001). "RELAP5/MOD3. 3 code manual volume IV: models and correlations," in *Information Systems Laboratories* (Washington, DC: Division of Systems Research Office of Nuclear Regulatory Research).

Schulz, T. L. (2006). Westinghouse AP1000 advanced passive plant. *Nucl. Eng. Design* 236, 1547–1557. doi: 10.1016/j.nucengdes.2006.03.049

Smoglie, C., and Reimann, J. (1986). Two-phase flow through small branches in a horizontal pipe with stratified flow. *Int. J. Multiphase Flow* 12, 609–625. doi: 10.1016/0301-9322(86)90063-7

Smoglie, C., Reimann, J., and Müller, U. (1987). Two phase flow through small breaks in a horizontal pipe with stratified flow. *Nucl. Eng. Design* 99, 117–130. doi: 10.1016/0029-5493(87)90114-2

Wang, W., Su, G. H., Qiu, S. Z., and Tian, W. X. (2011). Thermal hydraulic phenomena related to small break LOCAs in AP1000. *Progress in Nuclear Energy*53, 407–419. doi: 10.1016/j.pnucene.2011.02.007

Welter, K., Wu, Q., You, Y., Abel, K., McCreary, D., Bajorek, S. M., et al. (2004). Experimental investigation and theoretical modeling of liquid entrainment in a horizontal tee with a vertical-up branch. *Int. J. Mult. Flow* 30, 1451–1484. doi: 10.1016/j.ijmultiphaseflow.2004.08.001

Yonomoto, T., and Tasaka, K. (1991). Liquid and gas entrainment to a small break hole from a stratified two-phase region. *Int. J. Mult. Flow* 17, 745–765. doi: 10.1016/0301-9322(91)90054-7

Zuber, N. (1980). *Problems in Modeling of Small Break LOCA*. Technical Report. Washington, DC: Nuclear Regulatory Commission, Div. of Reactor Safety Research. doi: 10.1615/ICHMT.1982.AdvCourHeatTransfNucReactSaf.20


**Conflict of Interest:** The authors declare that the research was conducted in the absence of any commercial or financial relationships that could be construed as a potential conflict of interest.

## NOMENCLATURE

| | |
|---|---|
| *D* | *Diameter of main horizontal pipe* |
| *d* | *Diameter of branch pipe* |
| *Fr* | *Froude number* |
| *g* | *Gravitational acceleration* |
| *h* | *Distance between two-phase interface and branch centerline* |
| *V* | *Gas phase velocity* |
| *Greek symbols* | |
| $\Delta\rho$ | *Gas-liquid density difference* |
| $\rho_g$ | *Gas phase density* |
| $\theta$ | *Branch angle* |
| *Subscripts* | |
| *g* | *Gas* |
| *b* | *the onset point of liquid entrainment* |
| *3g* | *gas phase at the branch entrance* |
| *Abbreviations* | |
| *LOCA* | *Loss of coolant accident* |

frontiers in Energy Research

ORIGINAL RESEARCH
published: 02 July 2020
doi: 10.3389/fenrg.2020.00127

# Study on Typical Design Basis Conditions of HPR1000 With Nuclear Safety Analysis Code ATHLET

*Xi Huang[1]*, Weixin Zong[1], Ting Wang[2], Zhikang Lin[2], Zhihao Ren[2], Chubin Lin[1] and Yuan Yin[1]*

*[1] Advanced Nuclear Energy Research Team, College of Physics and Optoelectronic Engineering, Shenzhen University, Shenzhen, China, [2] China Nuclear Power Technology Research Institute, Shenzhen, China*

The third-generation nuclear power plant Hua-long Pressurized Reactor (HPR1000) is developed based on the experience of Chinese commercial Nuclear Power Plant (NPP) designs, construction, operation and maintenance. It improves the concept of defense in depth and strengthens severe accident prevention and mitigation strategies. The HPR1000 has implemented a number of active and passive innovative safety systems and accident management procedures for design basis conditions, e.g., the employment of Medium Pressure Rapid Cooldown (MCD) and Atmospheric Steam Dump System (ASDS) for the activation of Middle Head Safety Injection (MHSI), the application of Secondary Passive Residual Heat Removal System (SPRHR) for the residual heat removal. In the article, calculations are carried out for HPR1000 nuclear power plant with nuclear system safety analysis code ATHLET (Analysis of Thermal-Hydraulics of Leaks and Transient) 3.1 (Lerchl et al., 2016). By means of conservative deterministic safety analysis approach, transient analyses concerning selected typical design basis conditions, i.e., Large Break Loss-Of-Coolant Accident (LB-LOCA), Small Break Loss-Of-Coolant Accident (SB-LOCA), Steam Generator Tube Rupture accident (SGTR), and Feed water Line Break (FLB) are performed. The ATHLET results are also compared with the results performed by CGN-CNPTRI (China General Nuclear—China Nuclear Power Technology Research Institute) with their own code LOCUST with similar assumptions. The comparisons indicate that, although some discrepancies are detected, the trends of system responses predicted by the two codes are generally in agreement with each other for different accident scenarios. The results also demonstrate that the acceptance criteria for each accident can be met with significant safety margin. Thus, the effectiveness of safety system configuration and accident management procedures is guaranteed.

**Keywords: design basis conditions, LOCA, SGTR, FLB, HPR1000, ATHLET**

OPEN ACCESS

***Edited by:***
*Jun Wang,*
*University of Wisconsin-Madison, United States*

***Reviewed by:***
*Mingjun Wang,*
*Xi'an Jiaotong University, China*
*Xianping Zhong,*
*University of Pittsburgh, United States*
*Han Bao,*
*Idaho National Laboratory (DOE), United States*

****Correspondence:***
*Xi Huang*
*xi.huang@szu.edu.cn*

***Specialty section:***
*This article was submitted to Nuclear Energy, a section of the journal Frontiers in Energy Research*

***Received:*** *10 February 2020*
***Accepted:*** *27 May 2020*
***Published:*** *02 July 2020*

***Citation:***
*Huang X, Zong W, Wang T, Lin Z, Ren Z, Lin C and Yin Y (2020) Study on Typical Design Basis Conditions of HPR1000 With Nuclear Safety Analysis Code ATHLET. Front. Energy Res. 8:127. doi: 10.3389/fenrg.2020.00127*

## HIGHLIGHTS

- Application of ATHLET 3.1 for the typical Design Basis Conditions (DBCs) transient analysis of a Generation III nuclear reactor design.
- Comparison between results of different nuclear system analysis codes.
- Demonstration of the effectiveness of the safety system configuration of a Generation III nuclear reactor design.

## INTRODUCTION

The Hua-long Pressurized Reactor (HPR1000) technology is developed based on experiences of Chinese commercial Nuclear Power Plant (NPP) designs, construction, operations, and maintenance (General Nuclear System Ltd., 2018a). By considering operational experience from similar nuclear power plants and the lessons learned from the Fukushima accident, as well as applying new proven technologies, a series of modifications were implemented. The third-generation nuclear power plant HPR1000 improves the design of defense in depth, and strengthens severe accident prevention and mitigation. HPR1000 design proposed by CGN is implemented in FCG (Fang Cheng Gang) Units 3&4 which are under construction (Nian, 2017).

The HPR1000 is a third-generation 3-loop Pressurized Water Reactor (PWR), which has a design life of 60 years and a nominal electrical power output of 1,180 MW (General Nuclear System Ltd., 2018a). The system layout of nuclear island is shown in **Figure 1** and the main technical characteristics are summarized in **Table 1**. The HPR1000 design employs three separate safety systems. It incorporates active and passive safety systems and severe accident prevention and mitigation measures. The "safety redundancy" is put into practice for HPR1000 by means of multiple levels of protection that work independently from each other, and some of the key features include: Safety Injection System; Emergency Boration System; Emergency Water Supply System; Secondary Passive Residual Heat Removal System and In-vessel Retention System (IVR) (General Nuclear System Ltd., 2018a). HPR1000 has also employed an innovative accident management procedure for LOCA and SGTR accidents, i.e., the Medium Pressure Rapid Cooldown (MCD). This cooldown procedure is working by discharging the steam through the ASDS from the top of SGs. Both primary pressure and second pressure are reduced at a specific rate corresponding to $-250^{\circ}$C/h as the residual heat is removed via ASDS, so that the middle head safety injection (MHSI) can be activated. The adoption of MCD and MHSI can reduce the primary pressure faster and more actively at the early stages of the transients and therefore can reduce the break flow compared to traditional PWRs, for which the high-pressure head injection (HHSI) systems are commonly used. The effectiveness of the innovative safety system configurations and accident management strategies of the third-generation nuclear power plant ought to be evaluated.

The article aims to evaluate the arrangement and capacity of various safety systems of the newly developed third generation nuclear reactor, e.g., the Medium Head Safety Injection system (MHSI), the Low Head Safety Injection system (LHSI), the accumulator (ACC), Atmospheric Steam Dump System (ASDS), safety valve of pressurizer for depressurization and the capability of the innovative Medium Pressure Rapid Cooldown (MCD), as well as to assess the mitigation strategies of specific accident/event, e.g., the mitigation strategies and the operator actions in the event of Steam

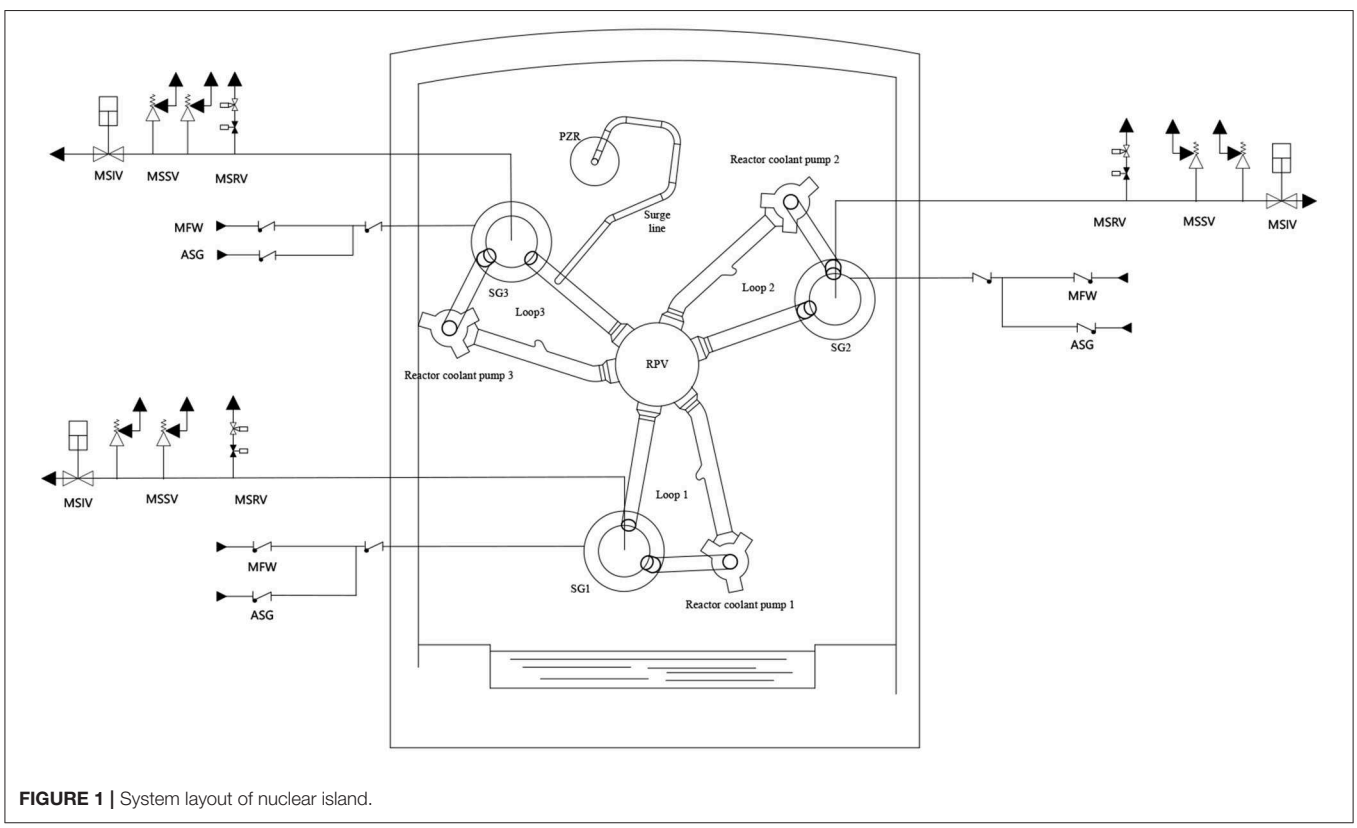


**FIGURE 1 |** System layout of nuclear island.

**TABLE 1 |** HPR1000 main technical parameters (General Nuclear System Ltd., 2018a).

| Parameters | Unit | Values |
|---|---|---|
| Reactor type | – | 3-loop PWR |
| Layout | – | Single unit |
| Design life | Year | 60 |
| Nominal power output | $MW_e$ | 1,180 |
| Core related thermal power | $MW_{th}$ | 3,150 |
| RPV coolant average temperature (full power) | °C | 307.0 |
| Primary pressure | MPa abs | 15.5 |
| Primary flow rate | $m^3/h$ | 25,450 |
| Containment free volume | $m^3$ | 73,500 |

Generator Tube Rupture (SGTR). For this purpose, several typical design basis conditions (DBC) of HPR1000, i.e., LB-LOCA, SB-LOCA, SGTR, and FLB are selected. The German nuclear systematic code ATHLET 3.1 for the nuclear system safety evaluation is used to carry out the analysis. Furthermore, the results of ATHLET are then compared with those performed by CGN code LOCUST with similar assumptions. Thus, the effectiveness of the safety system configurations and the accident management strategies are demonstrated as the similar results of both codes show that the safety criteria for different accidents can be met with considerable margins.

## SIMULATION TOOLS USED FOR HPR1000

In the past few decades, plenty of projects were launched for the studies on system transients of nuclear power plants in the events of various accidents. The LOCAs, SGTR and other design basis transients have attracted more attentions for nuclear safety analysis since the Three Mile Island (TMI) nuclear power plant accident. Plenty of institutions have contributed a lot on the Design Basis Condition transients with different simulation tools such as ATHLET, RETRAN, TRAC, CATHARE, RELAP5, and TRACE for di?erent reactor types for the variations of reactor thermal hydraulic parameters. A large amount of knowledge about thermohydraulic processes in the reactor cooling systems under different operational statuses and accident conditions has been gained based on a vast number of experimental and analytical studies (Aksan, 2008; Umminger et al., 2010; Kozmenkov and Rohde, 2013; Asmolov et al., 2014; Wang et al., 2015; Bestion, 2017). The recent studies focus more on the performance of passive safety systems and the increased safety margins of newly developed reactors, as well as the code to code comparisons (Nevo et al., 2012; Wang et al., 2012; Hu et al., 2013, 2014; Salehi and Jahanfarnia, 2016; Yousif et al., 2017). In the article ATHLET 3.1A is employed for the transient analysis of LB-LOCA, SB-LOCA, SGTR, and FLB (350 s transient for LB-LOCA, 5,000 s for SB-LOCA, 12,000 s for SGTR, and 3,000 s for FLB), and the results predicted with LOCUST by CGN-CNPTRI are captured for comparison.

## Nuclear System Thermal Hydraulic Code ATHLET

In the study the German nuclear system thermal hydraulic code ATHLET 3.1A is employed for the DBC analysis of HPR1000. The code is developed by the GRS (Gesellschaft für Anlagen-und Reaktorsicherheit-a German institute for nuclear plant and reactor safety) to describe the reactor coolant system thermal-hydraulic response during various operating conditions including LOCA accidents (Lerchl et al., 2016; Austregesilo and Deitenbeck, 2017). For all working fluids, the system of differential equations used in ATHLET is based on the following general conservation equations for the liquid and vapor phases (Austregesilo et al., 2016):

**Liquid Mass**

$$\frac{\partial((1-\alpha)\rho_L)}{\partial t} + \nabla\cdot((1-\alpha)\rho_L \vec{w}_L) = -\psi \tag{1}$$

**Vapor Mass**

$$\frac{\partial(\alpha\rho_V)}{\partial t} + \nabla\cdot(\alpha\rho_V \vec{w}_V) = \psi \tag{2}$$

**Liquid Momentum**

$$\frac{\partial\left((1-\alpha)\,\rho_L \vec{w}_L\right)}{\partial t} + \nabla\cdot\left((1-\alpha)\,\rho_L \vec{w}_L \vec{w}_L\right) + \nabla((1-\alpha)\,\rho) = \tag{3}$$

$$\begin{aligned}
&+\vec{\tau_i} && \textit{Interfacial friction}\\
&-(1-\alpha)\,\vec{f_w} && \textit{Wall friction}\\
&+\psi\,\vec{w} && \textit{Momentumfluxduetophase change}\\
&-(1-\alpha)\,\rho_L\,\vec{g} && \textit{Gravitation}\\
&+\alpha\,(1-\alpha)\,(\rho_L-\rho_V)\,\vec{g}\,D_h\nabla\alpha && \textit{Waterlevel force}\\
&+\alpha\,(1-\alpha)\,\rho_m\left(\frac{\partial \vec{w}_R}{\partial t} + \nabla \vec{w}_R\right) && \textit{Virtual mass}\\
&+S_{I,L} && \textit{Externalmomentumsourceterms}\ (\textit{e.g., pumps})
\end{aligned}$$

**Vapor Momentum**

$$\frac{\partial\left(\alpha\rho_V \vec{w}_V\right)}{\partial t} + \nabla\cdot\left(\alpha\rho_V \vec{w}_V \vec{w}_V\right) + \nabla(\alpha\rho) = \tag{4}$$

$$\begin{aligned}
&-\vec{\tau_i} && \textit{Interfacial friction}\\
&-\alpha\,\vec{f}_W && \textit{Wall friction}\\
&+\psi\,\vec{w} && \textit{Momentumfluxduetophase change}\\
&-\alpha\rho_V\,\vec{g} && \textit{Gravitation}\\
&-\alpha\,(1-\alpha)\,(\rho_L-\rho_V)\,\vec{g}\,D_h\nabla\alpha && \textit{Waterlevel force}\\
&-\alpha\,(1-\alpha)\,\rho_m\left(\frac{\partial \vec{w}_R}{\partial t} + \nabla \vec{w}_R\right) && \textit{Virtual mass}\\
&+S_{L,V} && \textit{Externalmomentumsourceterms}\ (\textit{e.g. pumps})
\end{aligned}$$

**Liquid Energy**

$$\frac{\partial[(1-\alpha)\rho_L(h_L+\frac{1}{2}\vec{w}_L\vec{w}_L-\frac{\rho}{\rho_L})]}{\partial t} +\nabla\cdot\left[(1-\alpha)\rho_L\vec{w}_L(h_L+\frac{1}{2}\vec{w}_L\vec{w}_L\right]= \quad (5)$$

$$\begin{aligned}
&-p\frac{\partial(1-\alpha)}{\partial t}\\
&+\vec{\tau_i}\vec{w_L} && \textit{Shearworkatthephase interface}\\
&+(1-\alpha)\,\vec{\tau_i}(\vec{w}_V-\vec{w}_L) && \textit{Dissipationduetointerfacial shear}\\
&+(1-\alpha)\,\rho_L\vec{g}\,\vec{w}_L && \textit{Gravitational work}\\
&+\dot{q}_{WL} && \textit{Heatflowthrough structures}\\
&+\dot{q}_i && \textit{Heatflowatthephase interface}\\
&+\psi\left(h_{\psi,L}+\frac{1}{2}\vec{w}_\psi\vec{w}_\psi\right) && \textit{Energyflowduetophase change}\\
&+S_{E,L} && \textit{Externalsource terms}
\end{aligned}$$

**Vapor Energy**

$$\frac{\partial\left[\alpha\rho_V\left(h_V+\frac{1}{2}\vec{w}_V\vec{w}_V-\frac{p}{\rho_V}\right)\right]}{\partial t} +\nabla\cdot\left[\alpha\rho_V\vec{w}_V(h_V+\frac{1}{2}\vec{w}_V\vec{w}_V)\right]= \quad (6)$$

$$\begin{aligned}
&-p\frac{\partial\alpha}{\partial t}\\
&-\vec{\tau_i}\vec{w}_V && \textit{Shearworkatthephase interface}\\
&+\alpha\vec{\tau}_i\left(\vec{w}_V-\vec{w}_L\right) && \textit{Dissipationduetointerfacial shear}\\
&+\alpha\rho_V\vec{g}\,\vec{w}_V && \textit{Gravitational work}\\
&+\dot{q}_{WV} && \textit{Heatflowthrough structures}\\
&+\dot{q}_i && \textit{Heatflowatthephase interface}\\
&+\psi\left(h_{\psi,V}+\frac{1}{2}\vec{w}_\psi\vec{w}_\psi\right) && \textit{Energyflowduetophase change}\\
&+S_{E,V} && \textit{Externalsource terms}
\end{aligned}$$

After spatial integration, the above conservation equations lead to a set of first order differential equations. For solving the equation systems, certain additional parameters are determined with closure equations or constitutive models. The code comprises of the following main constitutive models: (1) The wall mass and heat transfer model; (2) The Fluid properties; (3) Liquid-vapor interphase mass and energy transfer model; (4) The drift-flux model providing a one-dimensional description of the velocity differences between liquid and vapor phases taking into consideration the void fraction across the flow channel; (5) The form pressure loss and the wall friction pressure loss determining the irreversible pressure loss in a flow channel.

ATHLET has incorporated a large spectrum of models as illustrated in **Figure 2A** (Di Marcello et al., 2015; Wielenberg et al., 2019). With user's interfaces, the other independent modules like the GRS containment code COCOSYS and the Computational Fluid Dynamics (CFD) codes can be coupled. The extended ATHLET-CD code can be applied for the analysis of the beyond design basis conditions considering core degradation. Moreover, as illustrated in **Figure 2B**, with the GRS analysis simulator ATLAS, the visualization and interactive controls of the above-mentioned codes are enabled.

A systematic validation process based on separate effect tests and integrated experiments of the OECD/NEA/CSNI code validation matrices ensures the capability and quality of the code (Hollands et al., 2019; Wielenberg et al., 2019). The ATHLET has been successfully applied in the case of pre and post-test calculations of both large and small-scale experiments in the frame of International Standard Problems (ISPs), benchmarks and various international and national projects, e.g., the LSTF, PKL, and UPTF test facilities (Yousif et al., 2017; Hollands et al., 2019). The code's capabilities were investigated with the experimental data of test facilities named ATLAS and INKA (Di Marcello et al., 2015). Moreover, the code is validated is against the experimental data of facilities like MYHRRA, KASOLA, and TALL for the Accelerator-Driven Subcritical (ADS) systems and the future Generation IV nuclear applications (Hollands et al., 2019).

## The Nuclear System Thermal Hydraulic Code LOCUST

In the article, the results of selected HPR1000 DBC scenarios simulated with LOCUST are captured from the literature (China Nuclear Power Design Co., Ltd., 2018a,b,c,d) and presented in the following chapter for comparison. LOCUST is a system thermal-hydraulic code developed by CGN and it has the capability of performing the analysis of LB-LOCA, IB/SB-LOCA, SGTR, etc. **Figure 3** demonstrates the modular structure of LOCUST, the physical models implemented in the code can cover the key phenomena of HPR1000 within the application scope (China Nuclear Power Technology Research Institute, 2019).

The code is used to simulate two-fluid, non-equilibrium, and heterogeneous hydrodynamic conditions in various NPP transients. A six-equation two-phase flow model is employed in hydrodynamics model. These equations represent the balance of mass, momentum and energy for gas phase and liquid phase, as expressed by Equations (1)–(6) (China Nuclear Power Technology Research Institute, 2019).

Continuity equations for gas and liquid phase:

$$\frac{\partial}{\partial t}\left(\alpha_g\rho_g\right)+\frac{1}{A}\frac{\partial}{\partial x}\left(\alpha_g\rho_g v_g A\right)=\Gamma_g \quad (7)$$

$$\frac{\partial}{\partial t}\left(\alpha_f\rho_f\right)+\frac{1}{A}\frac{\partial}{\partial x}\left(\alpha_f\rho_f v_f A\right)=\Gamma_f \quad (8)$$

Momentum equations for gas and liquid phase:

$$\begin{aligned}
&\alpha_g\rho_g A\frac{\partial v_g}{\partial t}+\frac{1}{2}\alpha_g\rho_g A\frac{\partial v_g^2}{\partial x}=-\alpha_g A\frac{\partial P}{\partial x}+\alpha_g\rho_g B_x A\\
&-\left(C_{gw}v_g+C_{gI}v_g-C_{gI}v_f\right)\left(\alpha_g\rho_g A\right)+\Gamma_g A\left(v_{gI}-v_g\right)\\
&-C_{\text{virtual}}\alpha_g\alpha_f\rho_m A\left[\frac{\partial\left(v_g-v_f\right)}{\partial t}+v_f\frac{\partial v_g}{\partial x}-v_g\frac{\partial v_f}{\partial x}\right] \quad (9)
\end{aligned}$$

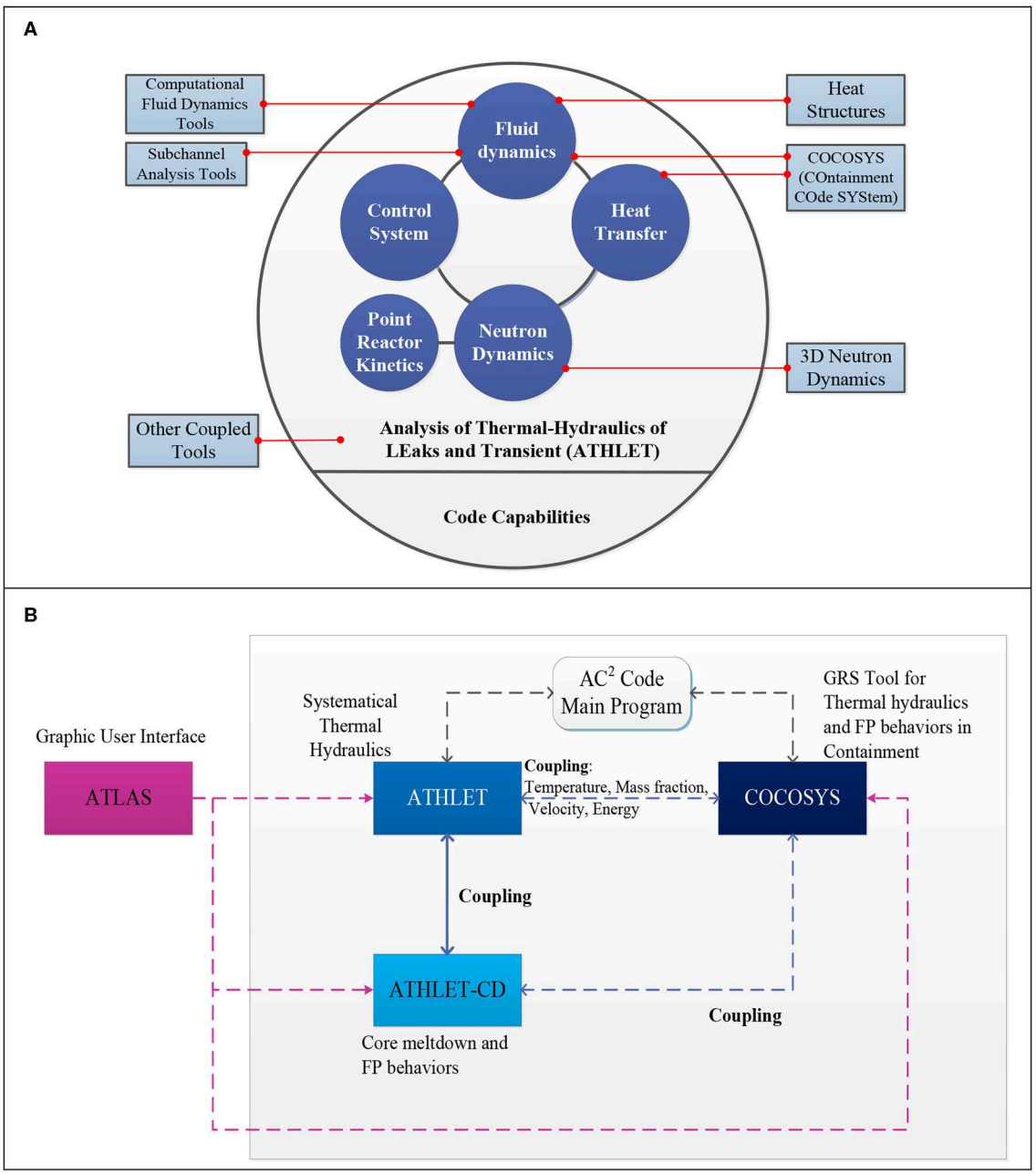


**FIGURE 2 |** ATHLET code capabilities and structures (Hu et al., 2013). **(A)** ATHLET code capabilities. **(B)** Connection between ATHLET and other GRS codes.

$$\alpha_f \rho_f A \frac{\partial v_f}{\partial t} + \frac{1}{2}\alpha_f \rho_f A \frac{\partial v_f^2}{\partial x} = -\alpha_f A \frac{\partial P}{\partial x} + \alpha_f \rho_f B_x A - \left(C_{fw} v_f + C_{fl} v_f - C_{fl} v_g\right)\left(\alpha_f \rho_f A\right) - \Gamma_g A \left(v_{fl} - v_f\right) - C\alpha_f \alpha_g \rho_m A \left[\frac{\partial \left(v_f - v_g\right)}{\partial t} + v_g \frac{\partial v_f}{\partial x} - v_f \frac{\partial v_g}{\partial x}\right] \quad (10)$$

Thermal energy equations for gas and liquid phase:

$$\frac{\partial}{\partial t}\left(\alpha_g \rho_g U_g\right) + \frac{1}{A}\frac{\partial}{\partial x}\left(\alpha_g \rho_g U_g v_g A\right) = -P\frac{\partial \alpha_g}{\partial t} - \frac{P}{A}\frac{\partial}{\partial x}\left(\alpha_g v_g A\right) + Q_{gw} + Q_{gI} + \Gamma_{gI} h_g + \Gamma_w h_g^s + \alpha_g \rho_g C_{gw} {v_g}^2 \quad (11)$$

$$\frac{\partial}{\partial t}\left(\alpha_f \rho_f U_f\right) + \frac{1}{A}\frac{\partial}{\partial x}\left(\alpha_f \rho_f U_f v_f A\right) = -P\frac{\partial \alpha_f}{\partial t} - \frac{P}{A}\frac{\partial}{\partial x}\left(\alpha_f v_f A\right) + Q_{fw} + Q_{fI} - \Gamma_{gI} h_f^s - \Gamma_w h_f + \alpha_f \rho_f C_{fw} {v_f}^2 \quad (12)$$

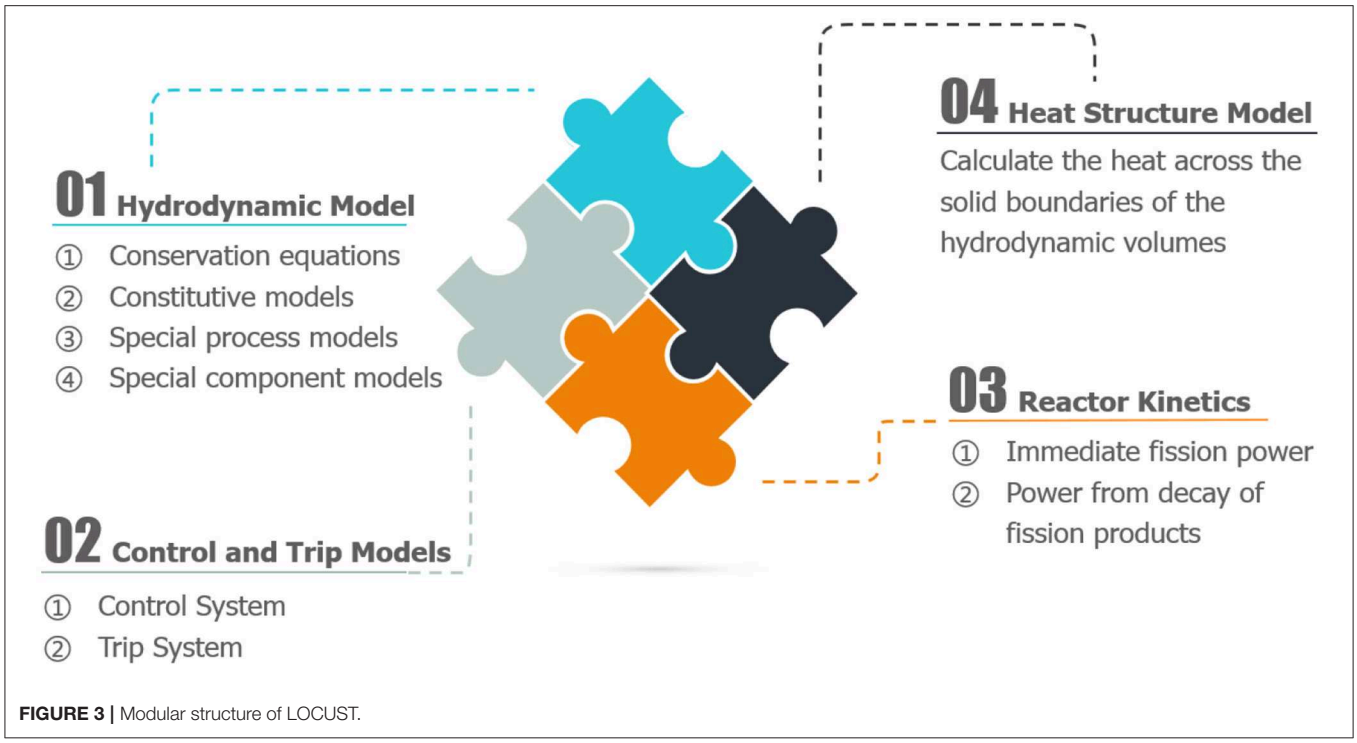


**FIGURE 3 |** Modular structure of LOCUST.

**TABLE 2 |** Summary of specific models developed for LOCUST (China Nuclear Power Technology Research Institute, 2019).

| Special process | Default model |
|---|---|
| Critical flow model | Ransom-Trapp model |
| Countercurrent flow limitation model | G. B. Wallis model |
| Entrainment model | Ardron-Bryce model |
| Reflood model | Paul Scherrer Institute model |
| Abrupt area change model | Borda-Carnot formulation |

The constitutive models, e.g., the water state equations, heat transfer properties on the liquid-steam interphase or wall-fluid interface, interphase friction force in different flow regime, are used to solve the conservation equations. Plenty of types of constitutive correlations are built into LOCUST including interphase friction; interphase mass transfer; virtual mass force; wall friction; wall-fluid heat transfer; and direct heating between the gas and liquid. Some models describing special process are developed in the code as summarized in **Table 2**.

The most important features of LOCUST are the flexible nodalization, capability to analyze two-fluid, thermal non-equilibrium in all fluid volumes. The code is incorporated with models to simulate special processes such as choked flow, thermal stratification, and counter-current flooding limitations. LB-LOCA and SB-LOCA are analyzed using conservative evaluation models, and some of optional physical models in LOCUST are modified according to the requirements of 10 CFR 50 Appendix K (US Nuclear Regulatory Commission, 1974).

## SIMULATION OF HPR1000 UNDER SELECTED DBC CONDITIONS

A Design-Basis Accident/Condition (DBA/DBC) refers to the postulated event/condition that a nuclear facility must be designed and built to withstand without loss to the systems, structures, and components that are necessary to ensure public health and safety. The HPR1000 design has groups PIE (Postulated Initial Events) into four categories (DBC-1 to 4) according to their anticipated frequency of occurrence and potential radiological consequences to the public. DBC-1 and DBC-2 indicate normal operation and anticipated operational occurrences. DBC-3 refers to conditions that may occur once during the lifetime of an operating plants and may result in the failure of a small fraction of the fuel rods, while DBC-4 indicates the limiting conditions considered in the design which are unlikely to happen but considered since their consequences might lead to the release of radioactive material in significant quantities (General Nuclear System Ltd., 2018b).

The study aims to investigate four typical DBC-3/4 conditions, i.e., LB-LOCA (DBC-4), SB-LOCA (DBC-3), SGTR (one tube) (DBC-3), and FLB (DBC-3) scenarios, which may result in relatively serious consequences and involve complicated thermal hydraulic phenomena e.g., the two phase critical break flow and two phase phenomena in reactor core. These selected events can also activate various safety systems, e.g., the Medium Pressure Rapid Cooldown (MCD) and may require further actions by the operators, and therefore are of great concern for nuclear safety analysis and pertinent simulation tools.

## HPR1000 System Nodalization With ATHLET

ATHLET nodalization scheme of HPR1000 is presented in **Figure 4A**. The plant model contains 555 control volumes and sub-control volumes, 623 junctions or sub-junctions, and 66 heat structures. The RPV (Reactor Pressure Vessel) and three cooling loops in parallel make up for the basic thermal-hydraulic model of HPR1000. The tube side of the steam generators, the cold legs, the hot legs, the surge-line with the pressurizer, and the RPV comprise the primary side of the RCS. The cold legs are connected to the passive water Accumulators (ACC). The secondary side of SGs, the steam link tank, the Main Steam Lines (MSL), along with the Feed Water (FW) lines, the Emergency Feed Water (EFW), and the Main Steam Isolation Valves (MSIV), form the components of secondary side. The Atmospheric Steam Dump System (ASDS) connects the SGs to the environment. As indicated in **Figure 4B**, the ATHLET Input Graphics Program (AIG) is applied to create a graphical representation of an ATHLET input data set. It displays the general schematic representation of all control volumes, i.e., the Thermo Fluid dynamic Object (TFOs) and their interconnections. This supports the examination and documentation of the geometry and nodalization of the input data set.

## LB-LOCA Simulation

The Large Break Loss of Coolant Accident (LB-LOCA) is considered as a DBC-4 accident for HPR1000 (General Nuclear System Ltd., 2018b). It is imperative for the modern reactor designs to ensure the safety of the public and the environment in the event of LB-LOCA without potential substantial core damage. The passive accumulators and active low-pressure injection systems (activated in case of large break LOCA) are designed as part of the important safety systems to ensure this purpose (General Nuclear System Ltd., 2018a). When RCS pressure falls below a set point, the passive accumulators start to inject coolant passively from the elevated tanks due to the pressure difference and the gravity. The low-pressure injection systems, which are driven by electricity, pump cooling water to the RCS when the system pressure drops to a lower setpoint. Sufficient time margin is guaranteed for further actions since the safety systems transfer water in large quantities into the reactor core after depressurization. With the availability of a proper heat sink and the startup of an active system injection, the ultimate core cooling is ensured.

The study conducted with LOCUST has identified the worst case against acceptance criteria for LB-LOCA of HPR1000 (China Nuclear Power Design Co., Ltd., 2018a). The configuration of the ATHLET model in the article for simulation is therefore in line with these findings. Important penalizing parameters used in the analysis are presented as follows: the break size used for simulation is 0.7 times of double-ended loop leg break. The break is assumed to be on the cold leg between main pump and the reactor pressure vessel inlet. Safety injection in the broken loop is failed. Important initial conditions are: the initial operating power is full power plus the maximum uncertainty; the initial primary temperature is the rated value at power minus the maximum uncertainty; the initial pressure of the pressurizer is the rated value plus the maximum uncertainty to postpone the reactor trip and safety injection signals; low containment pressure is assumed to increase the break flow during the blowdown, and to decrease the core reflood rate. For the safety systems, the main assumptions are: the minimum safety injection flowrate. Safety injection water of broken loop leaks to the containment directly. It is assumed that the SI injects at full flowrate after a delay due to LOOP as SI signal is generated. The ACCs are postulated with fast discharge rate which is conservative for the reflood peaking cladding temperature. Emergency feedwater system (EFWS) is actuated by the SI signal with Loss of Offsite Power (LOOP). The single failure (SF) criterion is assumed to occur on the Emergency Diesel Generator (EDG). Consequently, one RIS train (one MHSI pump and one LHSI pump) and one EFWS train are unavailable. Regarding the LOOP, it's assumed all the coolant pumps begin to coast down at 0 s, leading to a faster depressurization of primary system. The initial conditions of ATHLET simulation are presented in **Table 3**.

The typical LB-LOCA scenario of HPR1000 can be divided into 4 phases based on relatively independent phenomena, i.e., the blowdown, the core refill, early stage of reflooding, and the late stage of reflooding. The fuel cladding temperature can exhibit 3 peaks in the meantime in accordance with the progression of accident scenario. During the blowdown phase, the fast depressurization leads to the instant vaporization of the coolant in the RCS. The departure from nucleate boiling (DNB) occurs at the high-power region of the reactor core which results in the sharp increase of fuel cladding temperature. Thereafter, the coolant from intact coolant trains and reverse flow of coolant from upper plenum of RPV moisten the core and reduce the cladding temperature. The above-mentioned process causes the first peak cladding temperature (PCT1). During the refill, due to the bypass of coolant injected from accumulator (ACC), only a small amount of coolant flows through the core and cladding temperature rises again. This temperature increase stops at the early stage of reflooding when the safety injection water enters the core in the form of steam after vaporization and this leads to the second peak cladding temperature (PCT2). In the late phase of reflooding, the upper core region may experience a temperature rise again, but the trend is moderate due to the cooling of steam flow and entrained liquid droplets and this results in the third peak cladding temperature (PCT3).

**Figures 5A–E** present the results of AHTLET for LB-LOCA with the assumptions described above. The LOCUST results are shown with dashed curves for comparison. **Figure 5A** demonstrates the peak cladding temperature calculated with ATHLET and LOCUST. The two curves exhibit similar timings of three PCTs. However, LOCUST gives a higher overall peak cladding temperature (PCT1) while ATHLET predicts a higher PCT3 during reflooding.

The initial peak cladding temperature (PCT1) is related to the blowdown process after break. However, slight difference of pressure drops in the reactor core in the first a few seconds after break leads to the difference of predicted initial cladding

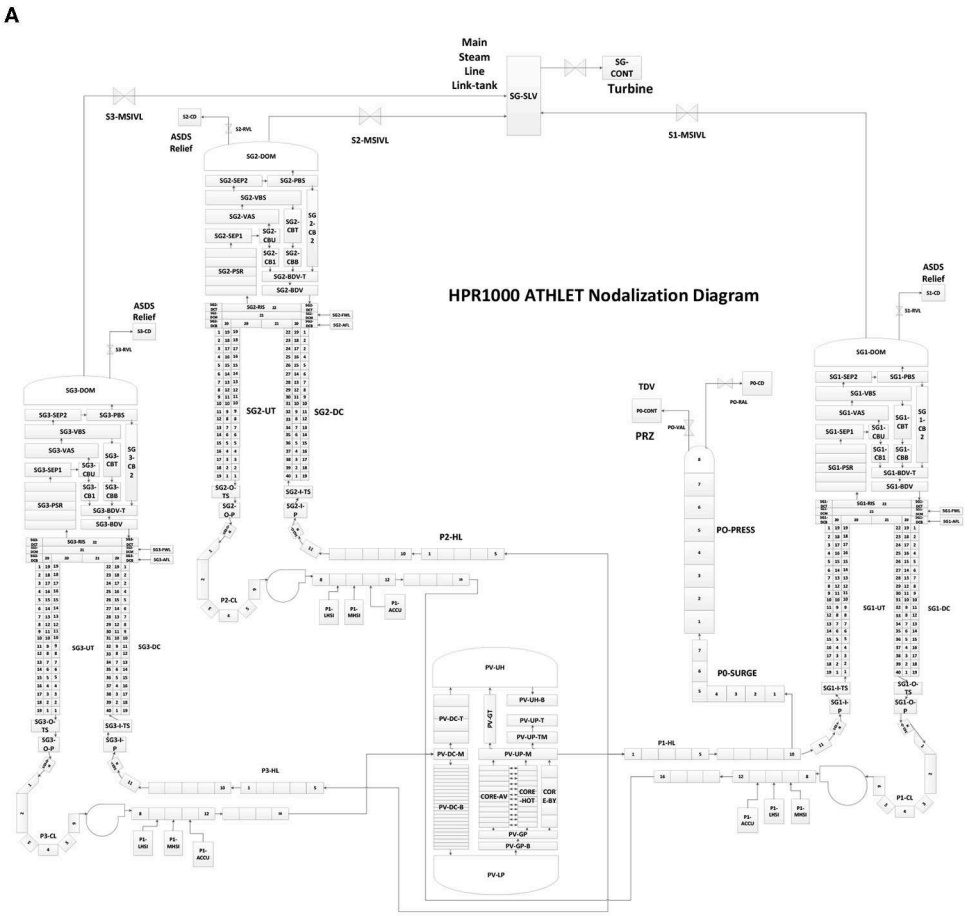


**FIGURE 4 | (A)** Nodalization diagram for HPR1000 with ATHLET. **(B)** Graphical representation of HPR1000 ATHLET input data.

**TABLE 3 |** Key parameters of initial conditions of ATHLET 3.1 simulations.

| Key parameters (LB/SB LOCA) | Unit | LB-LOCA | SB-LOCA |
|---|---|---|---|
| Core power | MW | 1.02 × 3,150 | 1.02 × 3,150 |
| Flow rate of one circuit | $m^3/h$ | 24,003 | 24,003 |
| Averaged coolant temperature | °C | 305 | 310 |
| Core bypass | % | 6.5 | 6.1 |
| Pressurizer pressure | MPa | 15.75 | 15.75 |
| Pressurizer level | % | 49 | 49 |
| **Key parameters (SGTR and FLB)** | **Unit** | **SGTR** | **FLB** |
| Core power | MW | 1.02 × 3,150 | 1.02 × 3,150 |
| Flow rate of one circuit | $m^3/h$ | 23,568 | 24,003 |
| Core bypass | % | 6.1 | 6.1 |
| Pressurizer pressure | MPa | 15.75 | 15.75 |
| Pressurizer level | % | 40 | 44 |

temperature. It is noteworthy that the cladding temperature drops considerably earlier according to the result of ATHLET than that of LOCUST. This is caused by a slightly higher collapse level in the RPV calculated by ATHLET and resultant earlier completion of reflooding, as indicated in **Figure 5B**. **Figure 5C** shows the overall safety injection rate history including the medium/low head safety injection and accumulator discharge rate. The peak injection rate as shown in the figure in the early stage is mainly resulted by the accumulator discharge. The ATHLET gives a higher overall injection rate in the early stage while in the later phase, both curves present similar values. **Figures 5D,E** present the break flow rate and pressure history predicted by both codes, which are consistent with each other. The time sequence of key events during the LB-LOCA transient predicted with ATHLET is shown in **Table 4**.

The analysis performed for LB-LOCA, as described above, indicates that the peak cladding temperature during the transient predicted with AHTLET, which is 1,016°C, meet the important acceptance criteria of DBC-4 that the PCTs should not exceed 1,204°C. Additionally, by considering similar initial conditions and assumptions for the simulation, the results performed with ATHLET are generally in good agreement with those predicted by LOCUST.

## SB-LOCA Simulation

The SB-LOCA is classified as a DBC-3 event for HPR1000 (China Nuclear Power Design Co., Ltd., 2018b). The small break LOCAs are characterized by longer period of transient after the break, compared to LB-LOCAs. During the SB-LOCA transient the core remains covered by the coolant at the beginning and the primary system remains at a high pressure relatively. Different break locations, break sizes, the ECCS set points, reactor designs, and the various operator actions, lead to various sequence of events following a small break LOCA in contrast to the large break LOCAs. Therefore, the integral system behavior during a small break LOCA ought to be carefully investigated.

As a significant safety-related system, the Atmospheric Steam Dump System (ASDS) is designed for HPR1000 to eliminate the high-pressure head safety injection. In the event of SB-LOCA and SGTRs, Medium Pressure Rapid Cooldown (MCD) shall be carried out through the ASDS by releasing the steam into the atmosphere to remove the decay heat if the turbine bypass is unavailable. The primary pressure can be reduced accordingly and injection pressure of the middle head safety injection (MHSI) will be reached. In addition, during SB-LOCA with complete loss of MHSI, Low Pressure Full Cooldown (LCD) shall be carried out through the operation of the ASDS, thus the RCS pressure and temperature can be reduced to the injection conditions of the LHSI.

For the simulation performed with ATHLET, the break is assumed to be at the cold leg of the reactor coolant system. A break with an equivalent diameter of 5.0 cm is considered according to the sensitivity study based on LOCUST (China Nuclear Power Design Co., Ltd., 2018b). The initial conditions are chosen to maximize the primary heat and to minimize water inventory. Important assumptions for the initial condition are summarized as follows: initial reactor power is the nominal power plus maximum uncertainty; the average temperature of the coolant is the rated value plus maximum uncertainty; the initial pressure of the pressurizer is the rated value plus the maximum uncertainty to delay the reactor trip and safety injection signals. The single failure is assumed occur on the emergency diesel generator. Consequently, one safety injection system train, one emergency feedwater system for one intact loop are unavailable. This assumption penalizes the water inventory and heat removal for primary side. It is assumed that LOOP occurs at the time of turbine trip. LOOP leads to the coolant pumps trip and maximize time delay of emergency feedwater system and safety injection system startup. The initial conditions of ATHLET simulation for SB-LOCA are presented in **Table 3**.

The SB-LOCA results in a potential decrease of primary pressure and possible radioactive release to the environment, as well as the decrease of reactor coolant inventory and potential core overheating. SB-LOCAs are mainly gravity-driven accidents, in which the reactor coolant system discharges slowly with the formation of mixing layers in primary system. The reactor core can be heated up at the beginning and the engineered safety systems, e.g., the Medium Head Safety Injection (MHSI), Accumulators (ACC), and Low Head Safety Injection (LHSI) for HPR1000, will be activated to inject coolant through core and prevent further increase of fuel cladding temperature. The time sequence of key events during the SB-LOCA transient simulated with ATHLET is shown in **Table 4**.

**Figures 6A–E** demonstrate the important results of SB-LOCA calculated with AHTLET, the LOCUST results are displayed for comparison. **Figure 6A** demonstrates the pressure variation during the transient. As shown in the figure, shortly after the break, the reactor core is scrammed as the primary pressure drops to the setpoint. Main feedwater flow is isolated, and the turbine is tripped. This leads to an increase of the secondary pressure and the ASDS is activated subsequently to maintain the secondary pressure at the setpoint of 8.6 MPa. As the primary pressure decreases to pressurizer pressure low 3 setpoint, the Medium Pressure Rapid Cooldown (MCD) is triggered through the ASDS by discharging the steam from the top of SGs. Both primary pressure and second pressure are

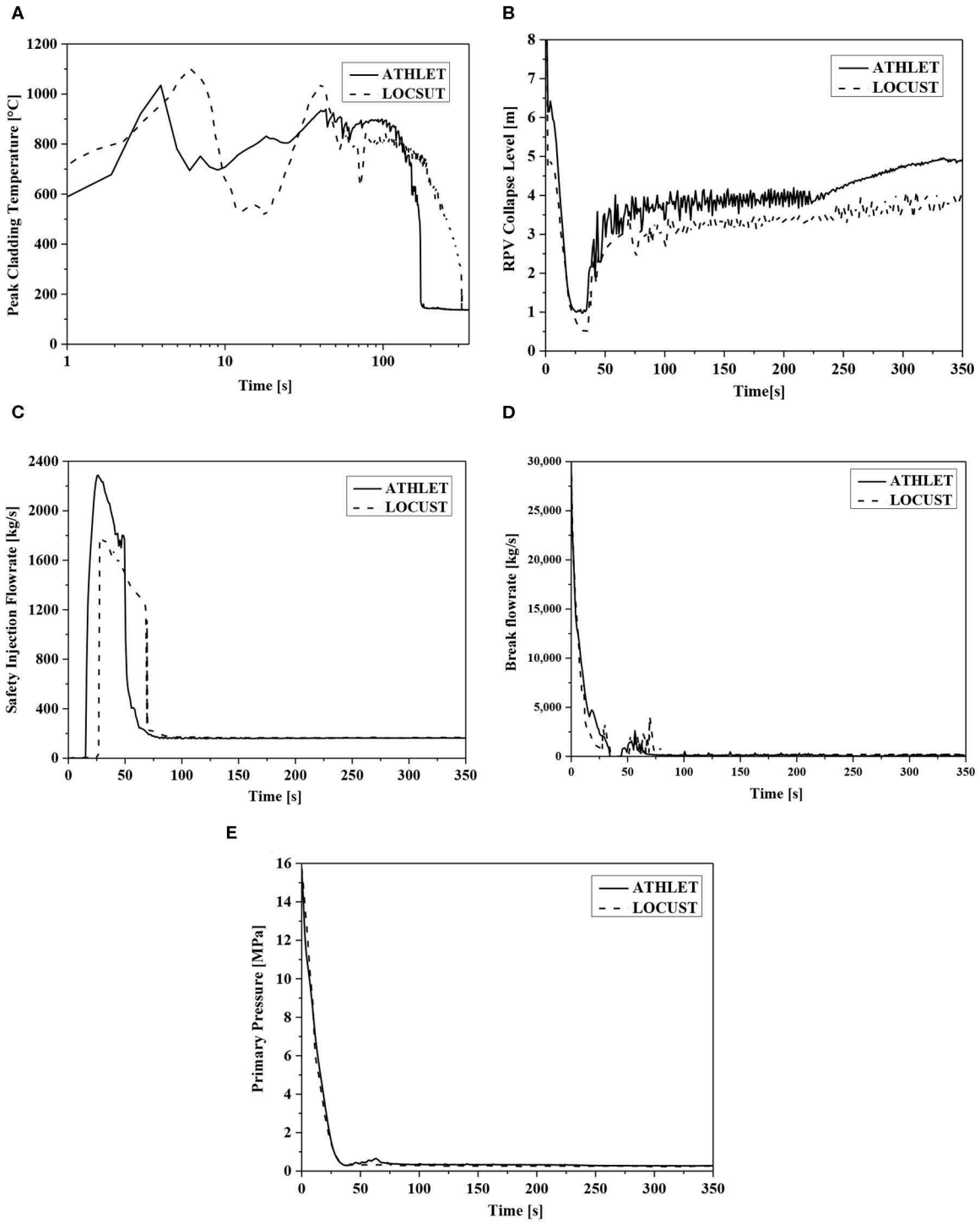


**FIGURE 5 |** Simulation results of LB-LOCA for HPR1000. **(A)** Peak cladding temperature (PCT) change. **(B)** The change of RPV collapse level. **(C)** The change of safety injection flowrate. **(D)** The change of break flowrate. **(E)** The change of primary pressure.

reduced at a rate corresponding to −250°C/h as the residual heat is removed via ASDS, so that the middle head safety injection (MHSI), as shown in **Figure 6B**, is activated. Both codes exhibit same trend of pressure history but ATHLET gives a faster pressure decrease and accordingly early activation of ASDS. **Figures 6C,D** present the change of the break flow rate, RPV collapse level and SG wide range level over time, respectively.

**TABLE 4 |** Time sequence of key events predicted with ATHLET 3.1.

| Events | Time/s | Events | Time/s |
|---|---|---|---|
| **LB-LOCA** | **SB-LOCA** | | |
| Reactor trip signal | 3.1 | Break | 0.0 |
| SI signal | 4.6 | Reactor trip signal | 28.3 |
| ACC injection | 15.2 | Turbine trip | 31.3 |
| Reflood starts | 48.6 | Reactor trip | 34.3 |
| SI activated | 39.5 | Main feedwater stops | 35.3 |
| ACC exhausted | 131.3 | SI injection signal | 45.6 |
| Auxiliary feedwater activated | 56.7 | Pressure Rapid Cooldown starts | 45.8 |
| End of Simulation | 350.0 | Pressure Rapid Cooldown ends | 395.8 |
| | | Auxiliary feedwater activated | 2146.1 |
| **SGTR** | **FLB** | | |
| SG 1 tube break | 0.0 | Main feedwater line break | 0.0 |
| Pressurizer low-low pressure signal | 248.0 | Control rods drop | 43.1 |
| Pressure Rapid Cooldown activates | 255.6 | Turbine trips | 45.3 |
| Auxiliary feedwater activated | 557.4 | Main steam isolation valves close | 64.9 |
| Pressure Rapid Cooldown ends | 859.3 | Steam dumping system of unaffected SG activated | 193.2 |
| Operator action starts | 1800.0 | Pressurizer safety valve opened | 577.8 |
| Critical boron condensation reaches, RBS stops | 4032.0 | Pressurizer safety valve closed | 587.6 |
| ACC isolated | 11689.1 | Pressurizer safety valve opened again | 2379.1 |
| $T_{ric}$ <180°C, the last MHSI pump stops | 11229.1 | | |
| Steam dumping system at SGa activated for depressurization | 11229.1 | | |
| Thermal hydraulic conditions meet the criteria for RHR mode | 13207.0 | | |

It is noteworthy that for ATHLET simulation, the core level experienced a considerable drop between 2,500 and 3,000 s. At around 2700 s, the primary side experienced a pressure drop, as indicated in **Figure 6A**. This results in a slight increase of safety injection rate and therefore leads to a water level increase in the core. On the other hand, the pressure decrease also results in further evaporation, which can cause level decrease. The overall change of the water level depends on the combine effect of these two phenomena. For ATHLET, the core level exhibits a considerable drop for a short period. However, for LOCUST, the water level also experienced significant oscillation, but the pressure drop is not obvious.

It can be inferred from these simulation results that for the SB-LOCA with above described penalizing assumptions, the configuration and operation strategy of the safety system ensures that the plant can be brought plant into a safe status, that the safety injection can be introduced into the primary system in time and it provides sufficient flow rate to guarantee the core to be covered. Thus, no significant core heat-up would occur. Moreover, the comparison between the results predicted by ATHLET and LOCUST also indicates that, though discrepancies are exhibited, both codes give similar trend of the variations of various parameters.

## SGTR Simulation

For PWRs, the performance and reliability of the steam generator are of crucial importance. The steam generator tube rupture accidents may result in the leak of radionuclides from the primary circuit to the secondary side and finally to the environment with the containment being bypassed. More involvement of the operator's actions before the primary loop comes to the Residual Heat Removal (RHR) operation modes, makes SGTR accidents different from other LOCAs. For HPR1000, one SG tube rupture condition (One tube SGTR) is classified as a DBC-3 event.

In case of an SGTR event of HPR1000, the radioactivity could be released by steam or liquid discharge through Main Steam Relief Control Valve (MSRCV) of Atmospheric Steam Dump System (ASDS) or Main Steam Safety Valve (MSSV) and this will lead to a direct discharge of activity to the atmosphere. The typical transient of SGTR event of HPR1000 can be divided into two phases, i.e., the short-term phase until leak elimination and the long-term phase to the safe state.

At the beginning of the event, primary coolant leaks to the secondary side through the break, the primary pressure decreases. The reactor trip signal is triggered. Turbine trip and isolation of Main Feedwater Flow Control System full load lines for all SGs are initiated. Thereafter, the secondary pressure increases and rapidly reaches the setpoint of ASDS. Contaminated steam is thus released to the environment and decay heat is removed. The continuous leakage to secondary side and the decrease of decay heat lead to a primary depressurization. Then the Medium Pressure Rapid Cooldown (MCD) is actuated. The MCD is carried out by reducing the ASDS setpoint in order to cool the Reactor Coolant System with a specific rate of 250°C/h. The Medium Head Safety Injection (MHSI) pumps are actuated on Safety Injection (SI) signal and start injecting when the primary pressure is lower than their injection head. The MHSI injection flow can compensate the leak flow and

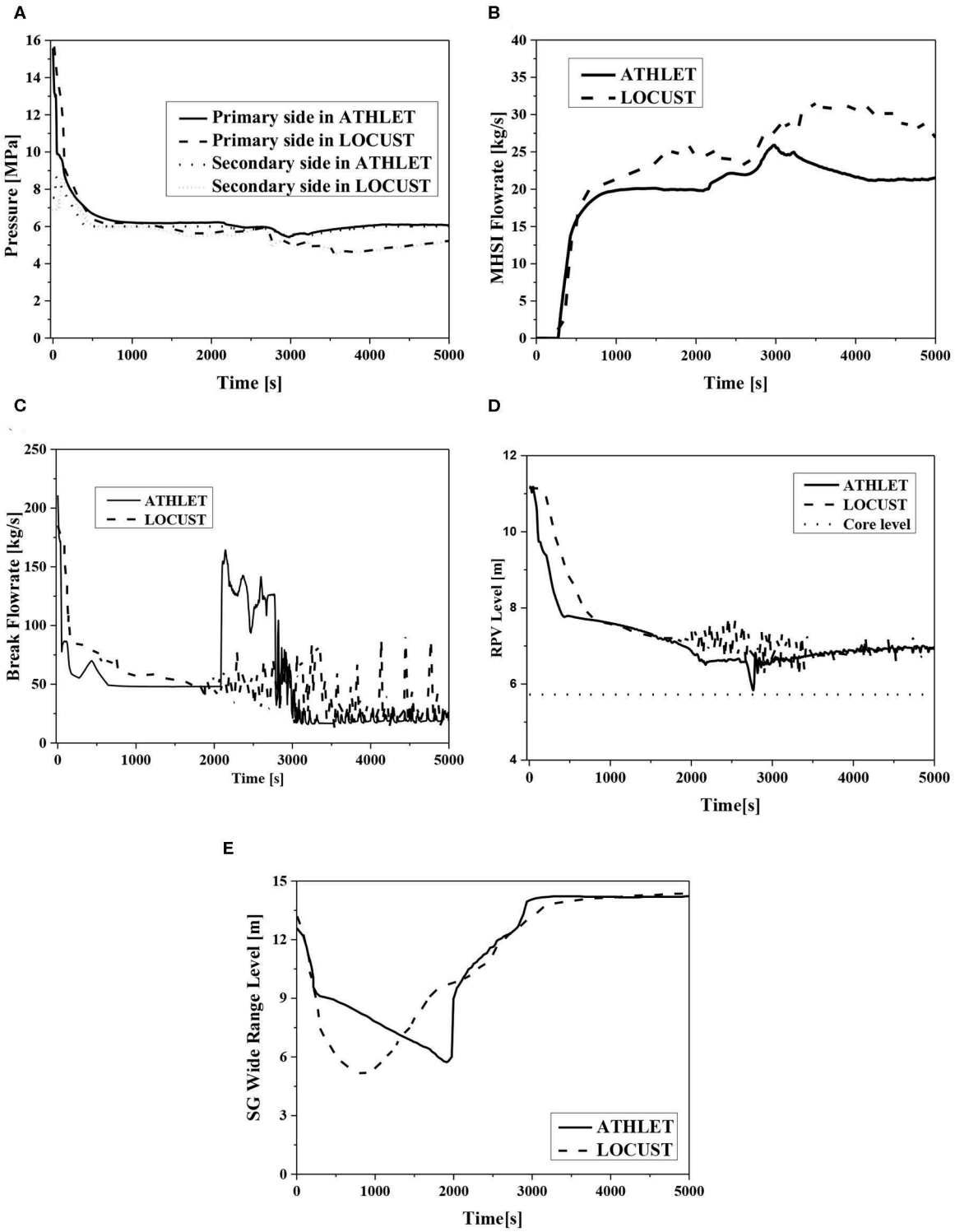


**FIGURE 6 |** Simulation results of SB-LOCA for HPR1000. **(A)** The pressure change. **(B)** The change of MHSI injection rate. **(C)** The change of break flowrate. **(D)** The change of RPV level. **(E)** The change of SG wide range level.

thus the controlled state is reached. To eliminate the leak, the operator isolates the affected steam generator from both the steam side and feed side. The injection of MHSI maintains the primary pressure at a stable level. To reduce the leakage flow, the operator can shut down two of the three MHSI pumps. Due to the isolation of the SGa, the pressure of SGa

increases until it reaches primary pressure level and the leak is eliminated.

During the RCS cooldown, to ensure the core sub-criticality, the operator uses Emergency Boration System (EBS) to compensate the reactivity insertion resulting from the RCS cooldown. Unaffected Steam Generators and MHSI are used to cool the primary at a rate of 56°C/h with two or three EBS trains. The SIS in RHR mode can finally be connected and the safe state is reached. The SGTR nodalization is shown in **Figure 7**. When SGTR occurs, the valve simulating the tube rupture is open and the coolant leaks from primary circuit to the secondary circuit via the valve.

The initial conditions for SGTR event are chosen to maximize the primary heat and to penalize the tube uncovery of SGa (the affected Steam Generator). The initial core power is 102% FP (Full Power). The primary pressure is maximized to increase the difference between primary and secondary pressure. The initial SG level is minimized to penalize the SG tube uncovery. The single failure is assumed at the EFWS train applied to the SGa. This penalizes the steam release and tube uncovery in SGa. The

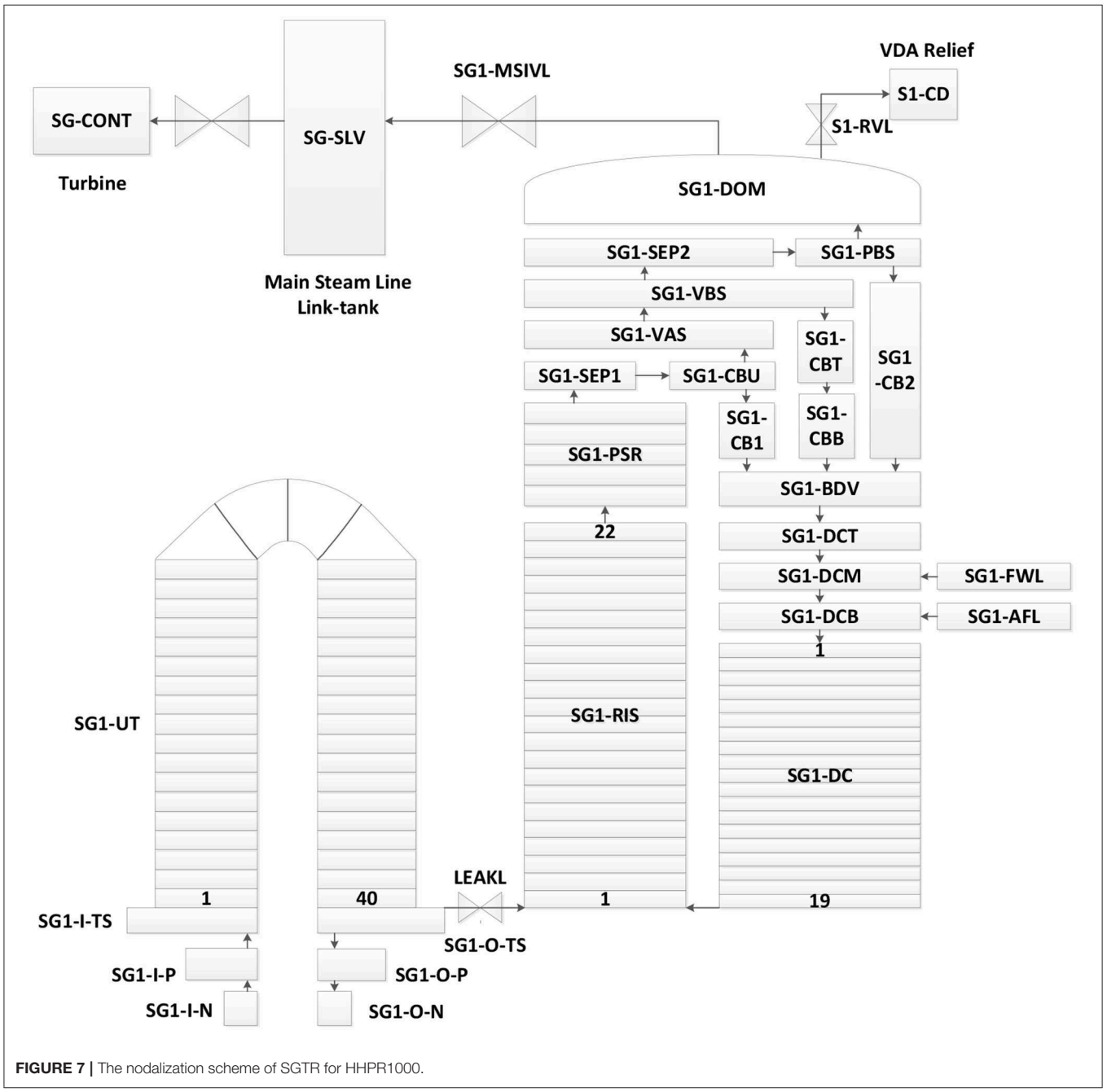


**FIGURE 7 |** The nodalization scheme of SGTR for HHPR1000.

initial conditions of ATHLET simulation for SGTR are presented in **Table 3**.

The transient of selected SGTR case with ATHLET is presented in **Figures 8A–E**. The time sequence of key events during the SGTR transient calculated with ATHLET is shown in **Table 4**. **Figures 8A,B** demonstrate the pressure history of primary and secondary side and the coolant temperature change of an intact loop in the transient of SGTR. **Figures 8C,D** show the break flowrate and safety injection rate over time. These results indicate that the leak elimination and safe state of the plant can be successfully achieved by automatic accident management strategy. For the safety injection rate, as indicated in **Figure 8D**, a valley of flow rate is exhibited in LOCUST result at about 4800 s which is not shown in ATHLET result. The MHSI injection rate is quite sensitive to the primary pressure depending on the SG tube break flow rate. As shown in **Figure 8B**, the break flow rate predicted by AHTLET is slightly higher than that of LOCUST, this results in generally larger MHSI injection rate and thus the valley of injection rate doesn't appear in ATHLET result.

**Figure 8E** shows the prediction of integrated steam mass release via the Atmospheric Steam Dump System (ASDS). According to the study with LOCUST (China Nuclear Power Design Co., Ltd., 2018c), the total steam release from ASDS of SGa is calculated to be slightly more than 100 tons, including about 88 tons released during the short-term phase. The radiological consequences are within the limit of acceptance criteria. As shown in **Figure 8E**, ATHLET gives a prediction of about 57 tons released during the short-term phase and the total steam release is slightly lower than the result of LOCUST. Therefore, it can be inferred that ATHLET results can reach similar conclusion, since both codes exhibit similar prediction results of total steam release from ASDS of SGa.

Nevertheless, remarkable discrepancies can still be observed between the results of ATHLET and LOCUST for the SGTR accident transient. For instance, the ATHLET calculated primary pressure decreases faster than the prediction of LOCUST shortly after the occurrence of SG tube rupture. This results in the difference in the activation time of MCD, and therefore the difference of pressure responses in secondary side. This could be attributed to the discrepancies of the modeling details between the two codes due to the lack of detailed information, e.g., the possible difference of rupture nodalization, the possible discrepancy of Chemical and Volume Control System (CVCS) charging and letdown rate in the early stage of the transient.

## FLB Simulation

A large feedwater system piping break is selected as one of key DBCs to be analyzed in the article. It is defined as a Feedwater Line Break (FLB) which is large enough to prevent the feed water from reaching the SGs. The fluid in corresponding SG may be discharged through the break, resulting in depressurization and a reversal of steam flow from the two intact SGs to the affected SG. The event could result in the overheating of primary loop. Therefore, the primary system heat-up effects of the FLB are evaluated in the study. The initial conditions of ATHLET simulation for FLB are presented in **Table 3**.

The feedwater system piping break is classified as a DBC-4 event for HPR1000 (General Nuclear System Ltd., 2018b). A feedwater line rupture impairs heat removal from the RCS. This is due to the reduction of flow rate of the main feedwater to the SGs, and the fluid discharged through the break with low enthalpy is not available for heat removal, this reduction of heat removal capability results in the increase of RCS pressure and temperature.

Automatic and manual actions are required during a typical sequence of this event. The current study only addresses the transient from the initial event to the controlled state. After the feedwater line break, the water level in the intact SGs will decrease before the isolation of the affected SG, leading to the primary heat up. After the "Reactor Trip," the primary temperature and pressure continue to increase due to the decay heat. Then bulk boiling may occur and the pressurizer may be filled. The RCS pressure can be limited by opening PSVs. Then the main steam line will be isolated, and the emergency feed water system will be actuated. Therefore, the residual heat can be continuously removed.

For the ATHLET simulation, the boundary and initial conditions are considered in accordance with LOCST calculation (China Nuclear Power Design Co., Ltd., 2018d). The break is assumed to occur between SG feedwater inlet nozzle and check valve. The size of break is assumed to be corresponding to the area of the SG feedwater inlet nozzle. Main feedwater to all SGs is assumed to be lost after the break occurs. LOOP is assumed to occur at the time of turbine trip. For the initial conditions, the core power is 102% of the full power. Coolant temperature is nominal value plus 2.5°C uncertainty. The pressurizer pressure is nominal value minus 0.25 MPa uncertainty, and pressurizer level is nominal value minus 7% uncertainty.

The current study only addresses the transient from the initial event to the controlled state. Operators can take actions to achieve the final safe state from controlled state by performing primary cooldown and depressurization via EFWS, ASDS, pressurizer spray and the PSVs. Accordingly, before the operator actions, which is assumed to be about 30 min after the occurrence of the event, the controlled state ought to be ensured, i.e., the RCS pressure can be limited by PSVs, the main steam line will be isolated and the emergency feed water system will be actuated. The system responses of HPR1000 after a typical FLB accident are shown in **Figures 9A–C**. The time sequence of key events during the FLB transient predicted with ATHLET is recorded in **Table 4**. The transient time duration of ATHLET results are rescaled as indicated by the labels at the top of the figures, in order to be compared to the results of LOCUST, since considerable discrepancies of time frames of the transients predicted with the two codes are found. As indicated in these figures, for both transients predicted by ATHLET and LOCUST, the RCS pressure is limited by PSVs, the pressurizer dose not overfill, a sufficient subcooling of the hot leg coolant is maintained and there is no risk of core uncovery before the operator action time which is ∼1800 s after the occurrence of the event. Consequently, the controlled state of the plant after

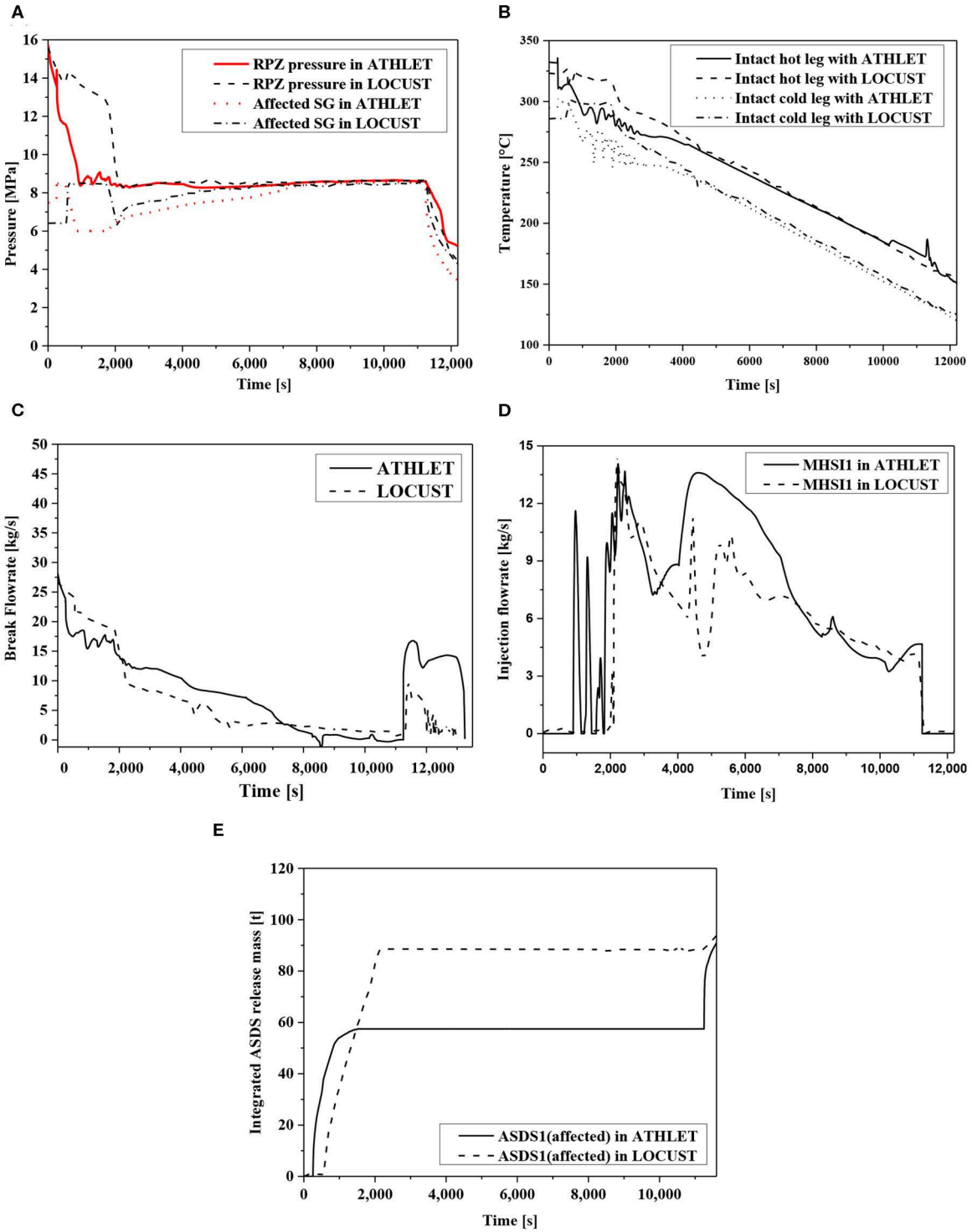


**FIGURE 8 |** Simulation results of SGTR for HPR1000. **(A)** The pressure change of primary and secondary side. **(B)** The change of cold leg and hot leg temperature. **(C)** The SGTR break flowrate. **(D)** The MHSI injection rate. **(E)** The integrated mass released via ASDS.

FLB is successfully reached. Although discrepancies are detected between the results of ATHLET and LOCUST, the trends of system responses predicted by the two codes are generally in correspondence with each other.

## CONCLUDING REMARKS

In the article, calculations are carried out with reference to the HPR1000 nuclear power plant, utilizing a qualified nodalization

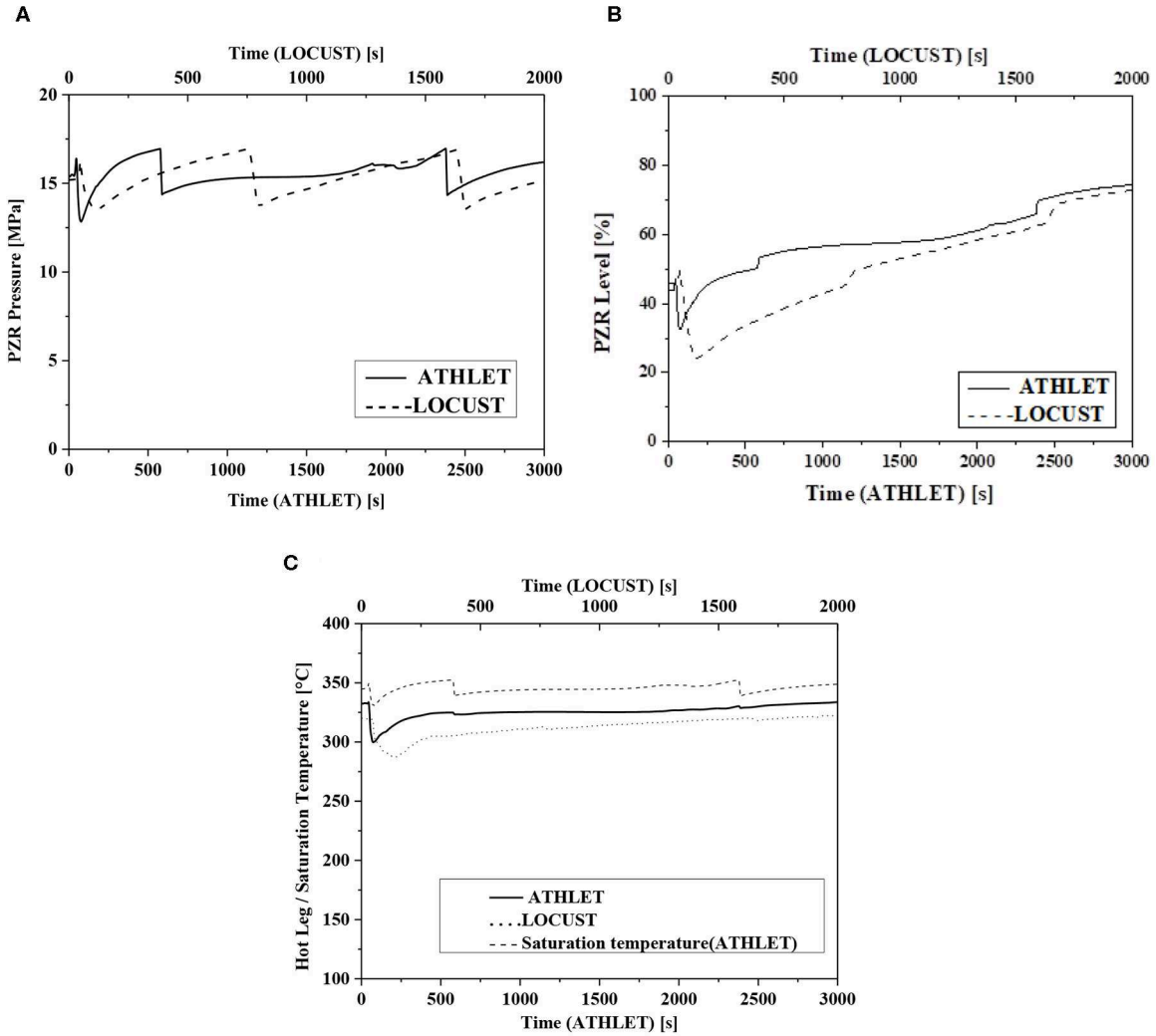


**FIGURE 9 |** Simulation results of FLB for HPR1000. **(A)** PZR pressure history. **(B)** The change of PZR level. **(C)** The change of hot-leg temperature.

of the geometry model for the nuclear system safety analysis code ATHLET 3.1. In order to evaluate the arrangement and capacity of various safety systems, e.g., the Medium Head Safety Injection system (MHSI), the Low Head Safety Injection system (LHSI), the accumulator (ACC), Atmospheric Steam Dump System (ASDS), and safety valve of pressurizer for depressurization, as well as to assess the mitigation strategies of specific accident/event, several typical design basis conditions (DBC) of HPR1000, i.e., LB-LOCA, SB-LOCA, SGTR, and FLB are selected in the article for the transient analysis. The results of ATHLET are also compared with those performed by LOCUST with similar conservative assumptions. The noteworthy findings are summarized as follows.

For the analysis performed for LB-LOCA, it can be concluded that the peak cladding temperature during the transient predicted with AHTLET, which is 1,016°C, meet the important acceptance criteria of DBC-4. Additionally, by considering similar initial conditions and assumptions for the simulation, the results performed with ATHLET are generally in good agreement with those predicted by LOCUST.

For the SB-LOCA with penalizing assumptions, the configuration and operation strategy of the safety system ensures that the plant can be brought into a safe status, that the safety injection can be introduced into the primary system in time and it provides sufficient flow rate to guarantee the core to be covered. Thus, no significant core heat-up would occur. Moreover, the comparison between the results predicted by ATHLET and LOCUST also indicates that, though discrepancies are exhibited, both codes give the similar trend of the variations of various parameters during the transient.

For SGTR events of HPR1000, according to the study with ATHLET, the total steam release from ASDS of SGa is calculated to be slightly less than the result of LOCUST. Accordingly, the radiological consequences are within the limit of acceptance

criteria. Both ATHLET and LOCUST code exhibit similar prediction results of total steam release from ASDS of SGa, though discrepancies can still be observed between the results of both codes.

Regarding the FLB accidents, for both transients predicted by ATHLET and LOCUST, the RCS pressure is limited by PSVs, the pressurizer dose not overfill, a sufficient subcooling of the hot leg coolant is maintained and there is no risk of core uncovery before the operator action time, which is supposed to be about 1800 s after the occurrence of the break. Therefore, the controlled state of the plant after FLB can be reached successfully. Although considerable discrepancies are detected, the trends of system responses predicted by the two codes are generally in correspondence with each other.

Based on the transient analyses and comparison carried out in the study, it can be inferred that, the discrepancies between the results predicted with the two codes might be attributed to the discrepancies of the modeling details between the model of AHTLET and that of LOCUST due to the lack of detailed information, the different nodalization schemes as well as the differences of physical models incorporated into the codes. Further investigations in detail concerning these discrepancies are foreseen in near future. Nevertheless, the results indicate that the acceptance criteria for each accident taken into account can be met with significant safety margin, and both codes present similar trends of system response for different accident scenarios.

## DATA AVAILABILITY STATEMENT

The datasets presented in this article are not readily available for reasons of confidentiality. Please contact the corresponding author for the requests to access the datasets.

## AUTHOR CONTRIBUTIONS

XH has written and organized the structure of the article, and has performed some of the calculations presented in the article. WZ and CL have performed some of the calculations in the article. YY has given some advice about the article. All authors contributed to the article and approved the submitted version.

## FUNDING

This work was supported by Science and Technology Program of Shenzhen, Guangdong province, China (JCYJ20180305124244969).

## REFERENCES

Aksan, N. (2008). International standard problems and small break loss-of-coolant accident (SBLOCA). *Sci. Technol. Nuclear Install.* 2008:814572. doi: 10.1155/2008/814572

Asmolov, V. G. E., Blinkov, V. N., Melikhov, V. I., Melikhov, O. I., Parfenov, Y. V., Emelyanov, D. A., et al. (2014). Current state of system thermohydraulic codes and trends in their development abroad. *High Temp.* 52, 98–109. doi: 10.1134/S0018151X14010027

Austregesilo, H., Bals, C., Hora, A., Lerchl, G., and Romstedt, P. (2016). *ATHLET, 3.1A, Models and Methods*. Cologne: Gesellschaft für Anlagen und Reaktorsicherheit (GRS) mbH, GRS-P-1, 4.

Austregesilo, H., and Deitenbeck, H. (2017). *ATHLET Mod 3.1A Programmer's Manual*. Cologne: Gesellschaft für Anlagen und Reaktorsicherheit (GRS) mbH, GRS-P-1, 2.

Bestion, D. (2017). System thermalhydraulics for design basis accident analysis and simulation: Status of tools and methods and direction for future R&D. *Nuclear Eng. Design* 312, 12–29. doi: 10.1016/j.nucengdes.2016.11.010

China Nuclear Power Design Co., Ltd. (2018a). *Large Break (Loss of Coolant Accident) (LB-LOCA) (Up to Double-Ended Break) (State A)*. Technical Report, Generic Design Assessment (GDA) for UK HPR1000.

China Nuclear Power Design Co., Ltd. (2018b). *Small Break (Loss of Coolant Accident) (SB-LOCA) (at Power) Including a Break in the Emergency Boration System (RBS [EBS]) Injection Line (State A)*. Technical Report, Generic Design Assessment (GDA) for UK HPR1000.

China Nuclear Power Design Co., Ltd. (2018c). *SG Tube Rupture (SGTR) (One Tube) (State A)*. Technical Report, Generic Design Assessment (GDA) for UK HPR1000.

China Nuclear Power Design Co., Ltd. (2018d). *Large Feedwater System Piping Break (State AB)*. Technical Report, Generic Design Assessment (GDA) for UK HPR1000.

China Nuclear Power Technology Research Institute (2019). *Introduction to the Thermal-Hydraulic System Analysis Code: LOCUST*. Internal Technical Report.

Di Marcello, V., Escalante, J. J., and Espinoza, V. S. (2015). Validation of the thermal-hydraulic system code ATHLET based on selected pressure drop and void fraction BFBT tests. *Nuclear Eng. Design* 288, 183–194. doi: 10.1016/j.nucengdes.2015.04.003

General Nuclear System Ltd. (2018a). *PCSR-Chapter-1-Introduction*. Technical Report HPR-GDA-PCSR-0001, UK-HPR1000 GDA Project.

General Nuclear System Ltd. (2018b). *PCSR-Chapter-12-Design Basis Condition Analysis*. Technical Report HPR-GDA-PCSR-0012, UK-HPR1000 GDA Project.

Hollands, T., Buchholz, S., and Wielenberg, A. (2019). Validation of the AC2 codes ATHLET and ATHLET-CD. *Kerntechnik* 84, 397–405. doi: 10.3139/124.190069

Hu, H., Shan, J., Gou, J., Cao, J., Shen, Y., and Fu, X. (2014). Simulation of advanced accumulator and its application in cpr1000 LBLOCA analysis. *Ann. Nuclear Energy* 69, 183–195. doi: 10.1016/j.anucene.2014.01.037

Hu, H., Shan, J., Gou, J., Zhang, B., Wang, H., and Yang, Z. (2013). "LBLOCA analysis of CPR1000 NPP with advanced accumulator," in *2013 21st International Conference on Nuclear Engineering* (Chengdu: American Society of Mechanical Engineers Digital Collection). doi: 10.1115/ICONE21-16480

Kozmenkov, Y., and Rohde, U. (2013). Application of statistical uncertainty and sensitivity evaluations to a PWR LBLOCA analysis calculated with the code ATHLET. Part 1: uncertainty analysis. *Kerntechnik* 78, 354–361. doi: 10.3139/124.110379

Lerchl, G., Austregesilo, H., Schöffel, P., von der Cron, D., and Weyermann, F. (2016). *ATHLET 3.1 A User's Manual*. Cologne: Gesellschaft für Anlagenund.

Nevo, A. D., Adorni, M., D'Auria, F., Melikhov, O. I., and Benčík, M. (2012). Validation of advanced computer codes for VVER technology: LB-LOCA transient in PSB-VVER facility. *Sci. Technol. Nuclear Install.* 2012:480948. doi: 10.1155/2012/480948

Nian, V. (2017). "Progress in nuclear power technology," in *Encyclopedia Sustainable Technologies*, ed M. A. Abraham (Singapore: Elsevier Inc.), 87–106. doi: 10.1016/B978-0-12-409548-9.10103-4

Salehi, M., and Jahanfarnia, G. (2016). Small break LOCA analysis without emergency core cooling systems using the RELAP5/SCDAP code in VVER-1000 reactor. *Ann. Nuclear Energy* 87, 299–307. doi: 10.1016/j.anucene.2015.09.009

Umminger, K., Schollenberger, S. P., Cornille, S., Agnoux, C., Quintin, D., and Freydier, P. (2010). "PKL tests on heterogeneous inherent boron dilution following SB-LOCA: applicability to reactor scale," in *18th International Conference on Nuclear Engineering* (Xi'an: American Society of Mechanical Engineers Digital Collection), 433–439. doi: 10.1115/ICONE18-29400

US Nuclear Regulatory Commission (1974). *Appendix K to Part 50-ECCS Evaluation Models*.

Wang, M., Zhao, H., Zhang, Y., Su, G., Tian, W., and Qiu, S. (2012). Research on the designed emergency passive residual heat removal system during the station blackout scenario for CPR1000. *Ann. Nuclear Energy* 45, 86–93. doi: 10.1016/j.anucene.2012.03.004

Wang, W., Meng, Z., Tian, W., Su, G., Qiu, S., Liu, L., et al. (2015). Analysis of characteristics for liquid entrainment through ADS-4 during a small break LOCA in AP1000. *Nuclear Power Eng.* 3, 178–183. doi: 10.1016/j.anucene.2013.05.006

Wielenberg, A., Lovasz, L., Pandazis, P., Papukchiev, A., Tiborcz, L., Schöffel, P. J., et al. (2019). Recent improvements in the system code package AC2 2019 for the safety analysis of nuclear reactors. *Nuclear Eng. Design* 354:110211. doi: 10.1016/j.nucengdes.2019.110211

Yousif, E., Zhang, Z., Tian, Z., and Ju, H. R. (2017). Simulation and analysis of small break LOCA for AP1000 using RELAP5-MV and its comparison with NOTRUMP code. *Sci. Technol. Nuclear Install.* 2017:4762709. doi: 10.1155/2017/4762709

**Conflict of Interest:** The authors declare that the research was conducted in the absence of any commercial or financial relationships that could be construed as a potential conflict of interest.

# NOMENCLATURE

**ABBREVIATIONS**

| | |
|---|---|
| ACC | ACCumulator |
| ADS | Accelerator-Driven Subcritical |
| AIG | Input Graphics Program |
| ASDS | Atmospheric Steam Dump System |
| ATHLET | Analysis of Thermal-Hydraulics of Leaks and Transient |
| CGN | China General Nuclear |
| CNPTRI | China Nuclear Power Technology Research Institute |
| COCOSYS | Containment Code System |
| CVCS | Chemical and Volume Control System |
| DBC | Design Basis Conditions |
| DNB | Departure from Nucleate Boiling |
| EBS | Emergency Boration System |
| ECCS | Emergent Core Cooling System |
| EDG | Emergency Diesel Generator |
| EFW | Emergency Feed Water |
| FLB | Feed water Line Break |
| FW | Feed Water |
| GRS | Gesellschaft für Anlagen- und Reaktorsicherheit (a German institute for nuclear plant and reactor safety) |
| HPR | Hua-long Pressurized Reactor |
| ISPs | International Standard Problems |
| IVR | In-vessel Retention System |
| LBE | Lead-Bismuth Eutectic |
| LB-LOCA | Large Break Loss-Of-Coolant Accident |
| LCD | Low Pressure Full Cooldown |
| LHSI | Low Head Safety Injection system |
| LOOP | Loss of Offsite Power |
| MCD | Pressure Rapid Cooldown |
| MHSI | Medium Head Safety Injection system |
| MSIV | Main Steam Isolation Valves |
| MSL | Main Steam Lines |
| MSLB | Main Steam Line Piping Break |
| MSRCV | Main Steam Relief Control Valve |
| MSSV | Main Steam Safety Valve |
| NEA | Nuclear Energy Agency |
| NEUKIN | Neutron Kinetics |
| NPP | Nuclear Power Plant |
| OECD | Organization for Economic Cooperation and Development |
| PCT | Peak Cladding Temperature |
| PIE | Postulated Initial Events |
| PSV | Pressurizer Safety Valves |
| RCS | Reactor Coolant System |
| RHR | Residual Heat Removal |
| RT | Reactor Trip |
| SB-LOCA | Small Break Loss-of-Coolant Accident |
| SF | single failure |
| SG | Steam Generator |
| SGTR | Steam Generator Tube Rupture accident |
| SI | Safety Injection |
| SIS | Safety Injection System |
| TFD | Thermo-Fluid Dynamics |

**ROMAN LETTERS**

| | |
|---|---|
| $A$ | Cross-sectional area |
| $B_x$ | Body force in x coordinate direction |
| $C$ | Drag coefficient |
| $f$ | Vector for liquid |
| $g$ | Vector for gas |
| $h$ | Specific enthalpy |
| $I$ | Interface |
| $m$ | Mixture |
| $P$ | Pressure |
| $Q$ | Volumetric heat transfer rate |
| $U$ | Specific internal energy |
| $v$ | Liquid velocity |
| $w$ | Wall |

**GREEK SYMBOLS**

| | |
|---|---|
| $\alpha$ | Void fraction |
| $\Gamma$ | Volumetric mass exchange rate |
| $\rho$ | Density |

frontiers in Energy Research

ORIGINAL RESEARCH
published: 07 July 2020
doi: 10.3389/fenrg.2020.00124

# GPU Based Two-Level CMFD Accelerating Two-Dimensional MOC Neutron Transport Calculation

*Peitao Song, Qian Zhang*, Liang Liang, Zhijian Zhang and Qiang Zhao*

*Fundamental Science on Nuclear Safety and Simulation Technology Laboratory, College of Nuclear Science and Technology, Harbin Engineering University, Harbin, China*

The Graphics Processing Units (GPUs) are increasingly becoming the primary computational platform in the scientific fields, due to its cost-effectiveness and massively parallel processing capability. On the other hand, the coarse mesh finite difference (CMFD) method has been one of the most popular techniques to accelerate the neutron transport calculation. The GPU is employed into the method of characteristics (MOC) accelerated by two-level CMFD to solve the neutron transport equation. In this work, the Jacobi method, the successive over-relaxation (SOR) method with red-black ordering, and the preconditioned generalized minimum residual (PGMRES) method are applied to solve the linear system under the framework of CMFD. The performance of these linear system solvers is characterized on both CPU (Central Processing Unit) and GPU. The two-dimensional (2-D) C5G7 benchmark problem and an extended mock quarter-core problem are tested to verify the accuracy and efficiency of the algorithm with double precision, as well as the feasibility of massive parallelization. Numerical results demonstrate that the desired accuracy is maintained. Moreover, the results show that the few-group CMFD acceleration is effective to accelerate the multi-group CMFD calculation. The PGMRES method shows remarkable convergence characteristics compared to the Jacobi and the SOR methods. However, the SOR method shows better performance on GPU for solving the linear system of CMFD calculation, which reaches about 2,400x speedup on GPU with two-level CMFD acceleration compared to the CPU-based MOC calculation.

**Keywords: MOC, GPU, CUDA, CMFD acceleration, PGMRES**

OPEN ACCESS

***Edited by:***
*Jun Wang,*
*University of Wisconsin-Madison, United States*

***Reviewed by:***
*Kees Vuik,*
*Delft University of Technology, Netherlands*
*Jiankai Yu,*
*Massachusetts Institute of Technology, United States*

****Correspondence:***
*Qian Zhang*
*qianzhang@hrbeu.edu.cn*

***Specialty section:***
*This article was submitted to Nuclear Energy, a section of the journal Frontiers in Energy Research*

***Received:*** *22 November 2019*
***Accepted:*** *25 May 2020*
***Published:*** *07 July 2020*

***Citation:***
*Song P, Zhang Q, Liang L, Zhang Z and Zhao Q (2020) GPU Based Two-Level CMFD Accelerating Two-Dimensional MOC Neutron Transport Calculation. Front. Energy Res. 8:124. doi: 10.3389/fenrg.2020.00124*

## INTRODUCTION

Significant advances in high-performance computing (HPC) systems enable the computational feasibility of high-fidelity, three-dimensional (3-D) whole-core neutron transport calculation. Several applications have been developed and deployed on the HPC systems based on the method of characteristics (MOC) (Askew, 1972). These applications employ the MOC as their routine 2-D or 3-D neutron transport method for practical whole-core simulations. The MOC code nTRACER (Jung et al., 2013) was developed as direct whole-core simulator by Seoul National University. Meanwhile, the University of Michigan developed the MPACT code (Kochunas et al., 2013) to perform the 3-D neutron simulation. And then followed by OpenMOC (Boyd et al., 2014) and NECP-X (Chen et al., 2018). However, many researches show that the MOC suffers from the slow

convergence rate especially for the large heterogeneous whole-core simulation. Hence, various numerical acceleration techniques and parallel algorithms have been employed to accelerate the MOC calculation.

Considerable research has been performed to accelerate the convergence of MOC neutron transport calculation. The non-linear acceleration technique is appropriate when considering that the steady-state problem of interest for a reactor is an eigenvalue problem. The coarse mesh finite difference (CMFD) method (Smith, 1984), has been widely used with pronounced success for reactor analysis for the last several decades. As a low-order acceleration scheme, CMFD solves the diffusion-like equation on a coarse mesh and it is very effective at accelerating the MOC calculation (Liu et al., 2011; Kochunas et al., 2013). However, CMFD can introduce numerical instabilities in optically thick regions which results in a degradation in performance or even a failure to convergence. As a result, several specific techniques such as the partial-current CMFD (pCMFD) method (Cho et al., 2003), the odCMFD method (Zhu et al., 2016) and lpCMFD method (Wang and Xiao, 2018) have been studied for stabilizing CMFD acceleration of neutron transport problems.

Moreover, massively parallel computing has been applied successfully to whole-core analysis based on the HPC systems which deploys CPU as their computational units (Kochunas et al., 2013; Godfrey et al., 2016). However, the cost of high-fidelity whole-core simulation is still unacceptable, even the large scale, parallel computing hardware is used (Kochunas et al., 2015; Ryu et al., 2015). Recently, CPUs/GPUs heterogeneous computing systems have increasingly come to the forefront of state-of-the-art supercomputers. As reported by the top supercomputer rankings in June 2019, 122 heterogeneous systems equips the NVIDIA GPUs are their main computing resources (TOP500 official site, 2019).

Massively parallel architecture of GPUs allows more powerful, more energy-efficient and higher throughput than CPUs. Therefore, the inclusion of GPU and heterogeneous computing in the neutron transport calculation is increasingly explored. Boyd et al. (2013) and Han et al. (2014) developed the GPU-accelerated 2-D MOC code which shows that the GPU is suitable to accelerate the MOC neutron transport calculation. Also Tramm et al. (2016) implemented a formulation of 3-D MOC neutron transport simulation. In our former research, a GPU-accelerated 2-D MOC parallel algorithm was implemented and the performance of the algorithm is investigated by a performance analysis model (Song et al., 2019). Meanwhile, efforts have been focused on implementing the MOC neutron transport calculation on multi-GPUs. The ray parallel scheme was introduced into the 3-D MOC simulation with intra-node multi-GPUs parallelization by Zhang et al. (2013). A CPU-GPU hybrid parallel MOC neutron transport calculation was implemented with a dynamic workload assignment (Liang et al., 2020; Song et al., 2020).

Since the feasibility of GPU acceleration of MOC calculation had been explored, the GPU-accelerated CMFD calculation is required to keep up with the enhanced performance of GPU-based MOC. Several researches has been conducted to accelerate the CMFD calculation on GPU. Kang and Joo, 2018) implemented the GPU-based preconditioned BiConjugate Gradient Stabilized solver (pBiCGSTAB) in nTRACER. Furthermore, the performance of several linear system solvers on GPU under the CMFD framework has been studied based on the nTRACER code (Choi et al., 2018). Since the core work of CMFD calculation is solving the linear system which is conducted by the CMFD equation, the researched and experience of solving linear systems on GPU can be used as reference to deploy the CMFD calculation on GPU. Li and Saad (2012) developed the high-performance iterative linear solvers on GPU. They speeded up the sparse matrix-vector product (SpMV) operations and discussed the suitable preconditioning methods. Jong et al. (2017) presented the GPU-accelerated RRB-solver, which is a PCG-type solver based on the Repeated Red-Black (RRB) method and the incomplete Cholesky factorization. And it shown good performance on GPU for solving 5-/9-point stencils problems.

In this work, for the solution of the large sparse linear system involved in the CMFD formulation, the performance of the Jacobi method, the successive over-relaxation (SOR) method, and the preconditioned generalized minimum residual (PGMRES) method are implemented on GPU. Especially, the numerical performance of these linear system solvers on both CPU and GPU under the CMFD framework is compared. Afterward, the effectiveness of the CMFD is examined.

The rest of the paper is organized as follows. Section Background gives the required background about the MOC and the CMFD framework. Then the parallelization of MOC and several liner system solvers on GPU are introduced in section Implementation on GPU. Section Numerical resultsshows the numerical tests and related analysis. Then the conclusions and discussions are presented in section Conclusion.

# BACKGROUND

## Method of Characteristics (MOC)

The method of characteristics is a general mathematical technique for solving the partial differential equations. The characteristic form of the multi-group neutron transport equation in steady-state is given by Equation (1):

$$\frac{d\varphi_g(s)}{ds} + \Sigma_{t,g}(s)\,\varphi_g(s) = Q_g(s) \tag{1}$$

where $s$ is the coordinate which represents both the reference position and the flight direction of the neutron, $\varphi_g(s)$, $\Sigma_{t,g}(s)$ represent the angular neutron flux, and total cross-section, respectively. $Q_g(s)$ is the source term. And $g$ represents the index of energy group.

With the isotropic scattering approximation and the flat source region approximation, the source term $Q_g(s)$ includes the fission and scattering sources and it can be expressed in terms of scalar neutron flux $\phi_g$:

$$Q_g(s) = \frac{1}{4\pi}\left[\frac{\chi_g}{k_{eff}}\sum_{g'}\nu\Sigma_{f,g'}(s)\,\phi_{g'}(s) + \sum_{g'}\Sigma_{s,g'\to g}(s)\,\phi_{g'}(s)\right] \tag{2}$$

$\Sigma$ denotes the cross-section, and the subscript $f$ and $s$ represent different reaction types, which are fission and scattering, respectively. $\chi_g$ is the normalized fission spectrum, and $k_{eff}$ represents the effective neutron multiplication factor or eigenvalue of the system.

Equation (1) can be integrated along the characteristic line within a flat source region. And the angular flux along the characteristic line can be expressed as Equation (3). The average angular flux along a specific segment is calculated by Equation (4).

$$\varphi_{out}^{s} = \varphi_{in}^{s} e^{-\Sigma_t l^s} + \frac{\overline{Q}}{\Sigma_t}(1 - e^{-\Sigma_t l^s}) \tag{3}$$

$$\overline{\varphi}^{s} = \frac{\overline{Q}}{\Sigma_t} + \frac{\varphi_{in}^{s} - \varphi_{out}^{s}}{\Sigma_t l^s} + \frac{\overline{Q}}{\Sigma_t} \tag{4}$$

where $\varphi_{in}^{s}$ and $\varphi_{out}^{s}$ are the incoming and outgoing angular neutron flux of segment, respectively. $\overline{\varphi}^{s}$ represents the average angular neutron flux, and $l^s$ is the length of current segment along $s$. The subscript $g$ is omitted for simplicity in Equation (3) and Equation (4).

For a given direction, a set of characteristic rays must be tracked through a discretized spatial domain and the transport sweep is performed along with those rays during the calculation. Then the scalar flux is integrated over discretized angles, as expressed in Equation (5).

$$\phi = \sum\nolimits_p \omega_p \frac{\sum_{s \in n} \overline{\varphi}^{s} l^s d^p}{\sum_{s \in n} l^s d^p} \tag{5}$$

where the quadrature weights $\omega_p$ are introduced for each of the quadrature points $\Omega_p$. $d^p$ is the ray spacing in $\Omega_p$ direction.

In order to obtain the scalar flux distribution over the space and all energy groups, an iteration scheme is applied to solve the source in Equation (2) and finally the scalar flux in Equation (5). The quadrature proposed by Yamamoto et al. (2007) is used for the polar angles and weights by default. Another well-known optimization of MOC calculation is to tabulate the exponential function or more specifically, $1 - e^{-\Sigma_t l^s}$, which is actually time-consuming in Equation (3). For the evaluation of the exponential function, the table with linear interpolation is used in this work.

## Two-Level CMFD Formulation

The MOC provides a framework for solving the neutron transport equation in heterogeneous geometries. However, challenges arise when whole-core problems are encountered. To reduce this computational burden, numerous acceleration methods are developed. The coarse mesh finite difference method (CMFD) is a popular method for accelerating the neutron transport calculation.

### Multi-Group CMFD Formulation (MG CMFD)

CMFD defines a diffusion equation on a coarse mesh with a correction to the diffusion coefficient that preserves the current between the cells from the transport solution. The neutron balance equation on coarse-mesh is derived as:

$$\frac{1}{V_i}\sum\nolimits_{is} A_i^{is} J_{is,i}^{G} + \Sigma_{t,i}^{G}\phi_i^{G} = \sum\nolimits_{G'} \Sigma_{s,i}^{G' \to G}\phi_i^{G'} + \frac{\chi_G}{k_{eff}}\sum\nolimits_{G'} \nu\Sigma_{f,i}^{G'}\phi_i^{G'} \tag{6}$$

where $i$ is the index of the coarse-mesh cell, $is$ is the index of the surface of cell $i$, $G$ represents the CMFD group index. $J_{is,i}^{G}$ represents the surface-averaged net current across the surface $is$. $A_i^{is}$ is the area of surface $is$ and $V_i$ is the volume of cell $i$, $\phi_i^{G}$ is the cell-averaged scalar flux on the coarse mesh. And the coarse-mesh cross-sections are generated by energy-condensation and area-averaging from the MOC fine-mesh cross-sections. The homogenized cross-section for cell $i$ is

$$\Sigma_{x,i}^{G} = \frac{\sum_{\substack{g \in G \\ r \in i}} \Sigma_{x,r}^{g}\phi_r^{g} V_r}{\sum_{\substack{g \in G \\ r \in i}} \phi_r^{g} V_r} \tag{7}$$

In order to conserve the neutron balance between the CMFD and MOC problems, a non-linear diffusion coefficient term is introduced to correct the difference between the inter-cell current calculated by the transport solution and approximated by the Fick's Law. The net current across the surface $is$ is expressed as:

$$J_{is,i}^{G} = -\hat{D}_{is,i}^{G}\left(\phi_{i+1}^{G} - \phi_i^{G}\right) - \tilde{D}_{is,i}^{G}\left(\phi_{i+1}^{G} + \phi_i^{G}\right) \tag{8}$$

where $is$ is the surface between cell $i$ and cell $i+1$. $J_{is,i}^{G}$ is the actual net current produced from the MOC solution. The parameter $\hat{D}_{is,i}^{G}$ is the coupling coefficient determined by the ordinary finite difference method and expressed in Equation (9-a), and $\tilde{D}_{is,i}^{G}$ is the non-linear diffusion coefficient correction factor as shown in Equation (9-b)

$$\hat{D}_{is,i}^{G} = \frac{2D_i^{G} D_{i+1}^{G}}{D_i^{G} h_{is}^{i+1} + D_{i+1}^{G} h_{is}^{i}} \tag{9a}$$

$$\tilde{D}_{is,i}^{G} = \frac{-\hat{D}_{is,i}^{G}\left(\phi_{i+1}^{G} - \phi_i^{G}\right) - J_{is,i}^{G}}{\left(\phi_{i+1}^{G} + \phi_i^{G}\right)} \tag{9b}$$

where $D_i^{G}$ is the diffusion coefficient of cell $i$, and $h_{is}^{i}$ is the thickness of cell $i$ along the surface $is$.

Going back to Equation (6) and inserting the surface net current $J_{is}^{G}$ illustrated in Equation (8), the finite difference form of the CMFD diffusion equation can be condensed down matrix form to get the generalized eigenvalue problem:

$$M\phi = \frac{1}{k_{eff}}\chi F\phi \tag{10}$$

where $M$ represents neutron migration by diffusion and scattering. $F$ represents the neutron generation by fission. The CMFD equations in 2-D form a five-stripe sparse linear system which is usually solved using the iterative methods.

Then the multi-group CMFD can be solved numerically. Upon convergence of the CMFD eigenvalue problem, a prolongation is performed by scaling the scalar flux of MOC fine mesh and the angular fluxes at the core boundaries with the ratio of the converged scalar flux $\phi^G_{i,cmfd}$ to the scalar flux $\phi^G_{i,\,moc}$ which is generated from the MOC solution:

$$\phi^g_r = \phi^g_r \times \frac{\phi^G_{i,cmfd}}{\phi^G_{i,\,moc}},\ \forall\, r \in i \tag{11a}$$

$$\varphi^g_l = \varphi^g_l \times \frac{\phi^G_{i,cmfd}}{\phi^G_{i,\,moc}},\ \forall\, l \in \textit{surface of } i \tag{11b}$$

where $\varphi^g_l$ is the boundary angular flux of track $l$.

### Two-Level CMFD

For large scale problems, the multi-group CMFD is still time-consuming. As a result, the few-group based CMFD (FG CMFD) formulation has been successfully applied to accelerate the multi-group CMFD calculation (Cho et al., 2002; Joo et al., 2004). Hence, the multi-group MOC calculation can be accelerated by the two-level CMFD technique. The multi-group CMFD (MG CMFD) calculation is directly accelerated by the few-group CMFD (FG CMFD) calculation. The FG CMFD is the group-condensed CMFD which has the same coarse mesh geometry as MG CMFD.

The FG CMFD has a similar formulation as illustrated in Equation (6) and the few-group constants are simply calculated using multi-group constants and multi-group spectra as:

$$\Sigma^{FG}_{x,i} = \frac{\sum_{G\in FG} \Sigma^G_{x,i}\phi^G_i}{\sum_{G\in FG} \phi^G_i} \tag{12}$$

where $FG$ is the energy group index in the FG CMFD equation.

In order to obtain the non-linear diffusion coefficient correction factor, condensed few-group surface currents are calculated as:

$$J^{FG}_{is,i} = \sum\nolimits_{G\in FG} J^G_{is,i} \tag{13}$$

Here, the multi-group currents are calculated using the MG CMFD solution and Equation (8). Then the coupling coefficient and the nonlinear diffusion coefficient correction factor of FG CMFD can be calculated by Equation (9) in which the multi-group quantities are replaced by that of few-group.

With the group-condensed constants, FG CMFD calculation which is also an eigenvalue problem as shown in Equation (10) can be performed. Once the desired FG CMFD solution is obtained, an additional update is needed for the MG CMFD scalar flux before the subsequent MG CMFD calculation. The multi-group scalar flux prolongation can be achieved simply by multiplying the ratio of the converged few-group scalar flux $\phi^{FG}_{i,cmfd}$ to the few-group scalar flux $\phi^{MG\to FG}_{i,cmfd}$ generated by the MG CMFD solution:

$$\phi^G_i = \phi^G_i \times \frac{\phi^{FG}_{i,cmfd}}{\phi^{MG\to FG}_{i,cmfd}} \tag{14}$$

## Iteration Algorithm

The iteration algorithm of MOC neutron transport calculation with two-level CMFD acceleration is illustrated in **Figure 1**. First, the homogenized multi-group constants for all cells and all the cell surfaces are calculated. The few-group constants are determined from the multi-group constants. The CMFD calculation begins from the few-group calculation and moves to the multi-group calculation if FG CMFD converges or the number of iterations meets the user setting. Then the multi-group scalar fluxes are updated by the converged few-group scalar flux, as shown in Equation (14). The multi-group iteration continues until the MG CMFD converges or the maximum number of iterations is reached. After the multi-group CMFD calculation is completed, the scalar fluxes of MOC fine mesh and the angular fluxes at the domain boundaries need to be scaled using the MG CMFD solution. Then the MOC neutron transport calculation is performed after the evaluation of the total source. When the MOC neutron transport calculation is finished, the overall convergence is checked using the $k_{eff}$ and the MOC scalar flux.

# IMPLEMENTATION ON GPU

## MOC Parallelization on GPU

The GPU is designed to perform the compute-intensive and highly parallel computations. Hence, the basic idea of GPU programming is transferring the compute-intensive parts of the application to the GPU, and the sophisticated flow control parts still remain at CPU. For the MOC neutron transport calculation, there is an enormous amount of parallel rays tracing across the computational domain. These relatively independent rays quite suitable for massive parallelization. Therefore, the ray parallelization is involved to implement the MOC neutron transport calculation on GPU.

**Figure 2** illustrates the flowchart of the GPU-based MOC neutron transport calculation. The initialization which includes the preparation of cross-section and track information is performed on the CPU. Then those information is copied to the GPU global memory. Then the total source which including the fission source and scattering source is evaluated on GPU. And each of the GPU threads handles the source evaluation of one energy group for one fine-mesh. After the source evaluation, the transport sweep is performed. In order to reach the optimal performance on GPU, our former research (Song et al., 2019) recommends to deploy the loop over rays and the loop over energy groups onto the GPU threads, as illustrated in **Figure 2**.

## CMFD Parallelization on GPU

As shown in **Figure 1**, the group constants condensation, the linear system construction and linear system solving are three main parts which can be parallelized on GPU for CMFD calculation. It is quite direct to parallelize the group constants condensation, the evaluation of group constants of coarse mesh $i$ and CMFD group $G$ is assigned to a GPU thread. Hence the groups constants for all coarse meshes and all CMFD groups are evaluated simultaneously and independently. As for the linear system which is constructed explicitly, the generation of elements

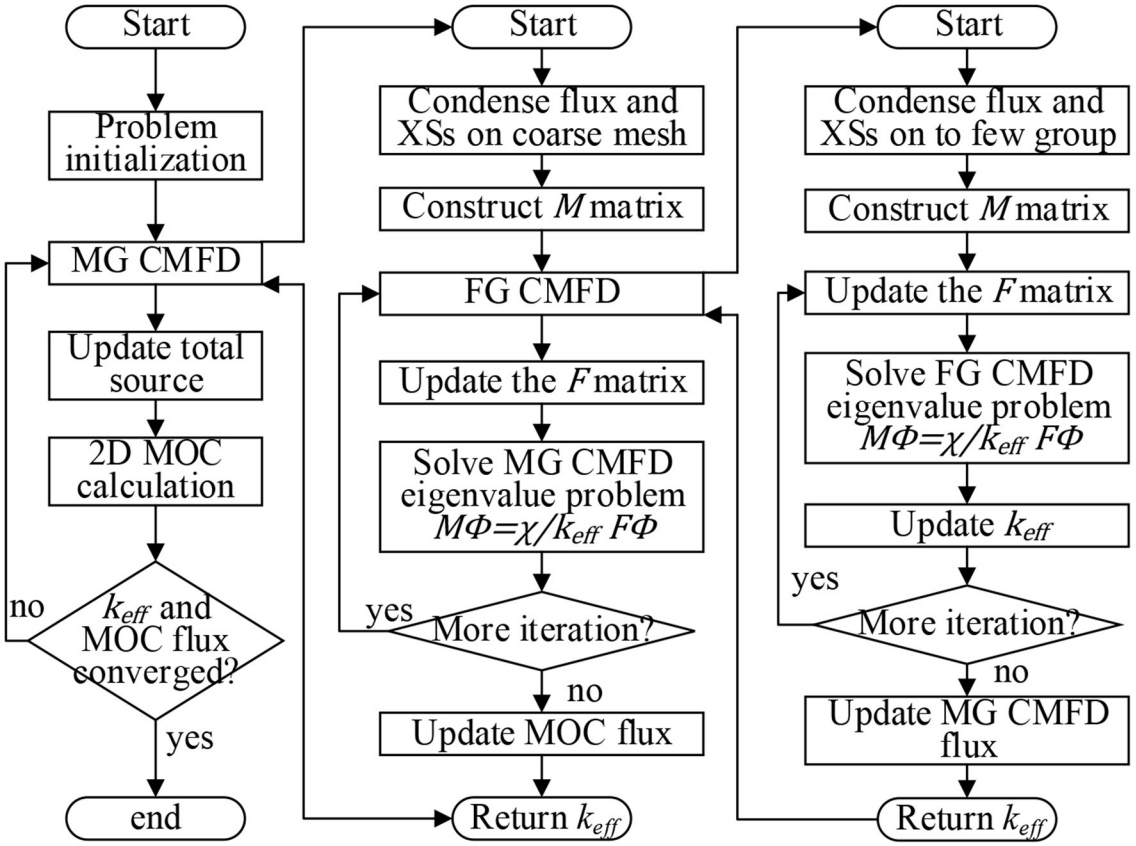


**FIGURE 1 |** The solution procedure for two-level CMFD accelerated MOC.

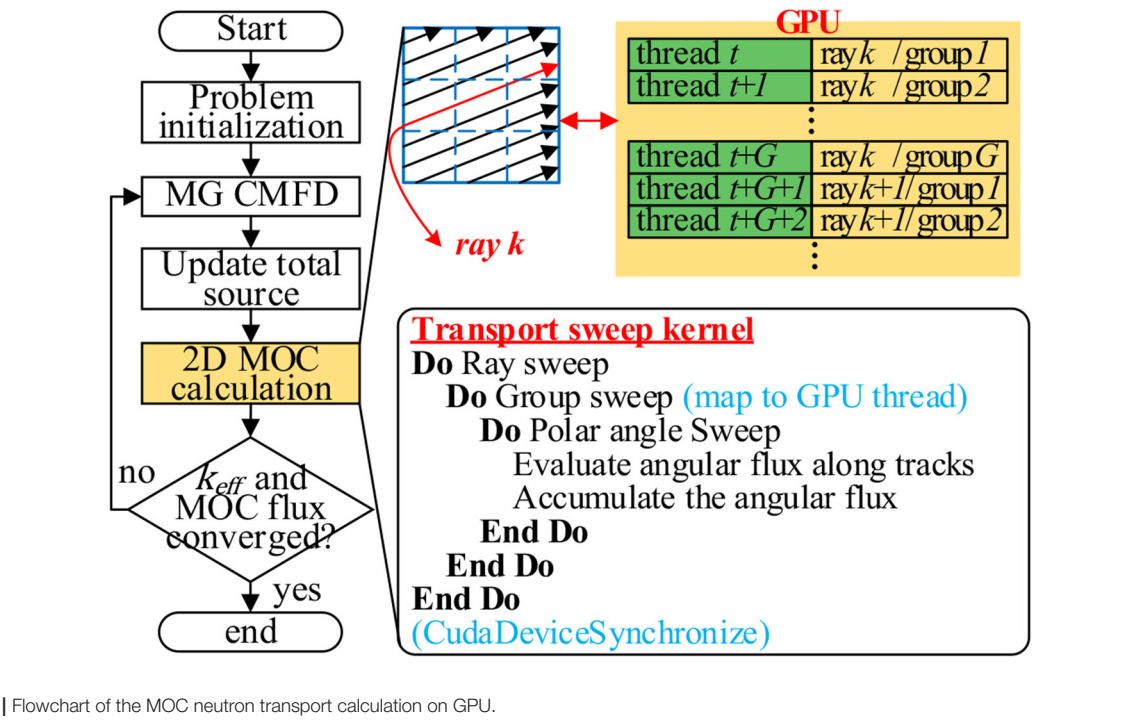


**FIGURE 2 |** Flowchart of the MOC neutron transport calculation on GPU.

in each row of matrix $M$ and vector $F$ is assigned to each GPU thread.

The third main part is to solve the sparse linear system, as shown in Equation (10). And the power iteration is used in this study for obtaining the eigenvalue and its corresponding normalized eigenvectors. However, for the problems we are primarily interested in, solving the linear system directly is prohibitively costly, since the directed inversion of matrix $M$ is expensive. Hence, it is replaced by solving the linear system using the iterative method:

$$M\phi^{(n)} = \frac{1}{k_{eff}{}^{(n-1)}}\chi F\phi^{(n-1)} \tag{15}$$

where $n$ is the power iteration index.

The goal of a linear system solver is to solve for $\boldsymbol{x}$ in the linear system:

$$\boldsymbol{Ax}=\boldsymbol{b} \tag{16}$$

Here, $\boldsymbol{x},\boldsymbol{b} \in \mathbb{R}^n$, $\boldsymbol{A} \in \mathbb{R}^{n\times n}$.

In this study, we applied three methods to solve the linear system iteratively: the Jacobi method, the successive over-relaxation (SOR) method, and the preconditioned generalized minimum residual (PGMRES) method. These three linear system solvers are implemented on both CPU and GPU, and the performance of these solvers are compared and analyzed.

## Jacobi Method

For the linear system of equations described by Equation (16), the diagonal elements, $a_{ii}$, of $\boldsymbol{A}$ are all non-zero. It starts with the decomposition of matrix $\boldsymbol{A}$.

$$\boldsymbol{A}=\boldsymbol{L}+\boldsymbol{D}+\boldsymbol{U} \tag{17}$$

where, $\boldsymbol{D}=diag\left(a_{11},\cdots,a_{nn}\right)$ is the diagonal matrix containing the diagonal elements of $\boldsymbol{A}$, $\boldsymbol{L}$ is the strict lower part, and $\boldsymbol{U}$ is the strict upper part.

Then the Jacobi method can be organized as following matrix form:

$$\boldsymbol{x}^{(k+1)}=\boldsymbol{G_J x}^{(k)}+\boldsymbol{g_J},\boldsymbol{G_J}=-\boldsymbol{D}^{-1}\left(\boldsymbol{L}+\boldsymbol{U}\right),\boldsymbol{g_J}=\boldsymbol{D}^{-1}\boldsymbol{b} \tag{18}$$

where the superscript indicates the iteration number.

The parallelization of the Jacobi method on GPU is straightforward because the Jacobi scheme is naturally parallelizable. As a result, $n$ GPU threads are invoked and each of the threads performs the calculation of one $x$ in vector $\boldsymbol{x}$, namely:

$$x_i^{(k+1)} = \frac{1}{a_{ii}}\left(-\sum\nolimits_{j\neq i} a_{ij}x_j^{(k)} + b_i\right),\ \ i=1,\cdots,n \tag{19}$$

## Successive Over-relaxation (SOR)

The successive over-relaxation (SOR) method is one of the well-known iterative methods. The SOR formulation can be defined by introducing the over-relaxation factor $\omega$:

$$\boldsymbol{x}^{(k+1)}=\boldsymbol{G_s x}^{(k)}+\boldsymbol{g_s},\boldsymbol{G_s}=\left(\boldsymbol{D}+\boldsymbol{\omega L}\right)^{-1}\left[\left(1-\boldsymbol{\omega}\right)\boldsymbol{D}-\boldsymbol{\omega U}\right],\boldsymbol{g_s}=\left(\boldsymbol{D}+\boldsymbol{\omega L}\right)^{-1}\boldsymbol{b} \tag{20}$$

A necessary condition for the SOR method to be convergent is that $0<\omega<2$. Choosing $\omega<1$ results in under-relaxation, which can help stabilize a divergent of this method. Choosing $\omega>1$ results in over-relaxation, which can accelerate the convergence in certain situations.

For the parallelization of SOR, a red-black ordering strategy is used. In Equation (10), the solution estimated at iteration $\left(k+1\right)$ of cell $i$ is only depends on the solution of its six immediate neighbors at iteration $\left(k\right)$. If all the cells in a computational domain are colored in a checkerboard-like manner, then, during the calculation, the red cells only need data from the black cells. Thus, red-black SOR is a high parallelizable algorithm. At a given step, half of the cells can be updated simultaneously.

## Preconditioned Generalized Minimum Residual (PGMRES) Method

The preconditioned generalized minimum residual (PGMRES) method (Saad and Schultz, 1986) is one of the most popular Krylov methods for solving the non-symmetric linear system. The basic idea of PGMRES is to produce a $n\times n$ Hessenberg matrix and the corresponding basis $\boldsymbol{V}$, then the approximate solution $\boldsymbol{x}^{(n)}$ is found by minimizing the residual norm $\|\boldsymbol{r}\|_2 = \left\|\boldsymbol{b}-\boldsymbol{Ax}^{(n)}\right\|_2$. The methodology and fundamental properties of PGMRES method can be found in many literatures (Van der Vorst and Vuik, 1993).

The performance of the GMRES method is usually improved significantly via preconditioning. A preconditioner $\boldsymbol{M}$ whose inverse satisfies $\boldsymbol{M}^{-1}\approx\boldsymbol{A}^{-1}$ in some sense should be relatively inexpensive to apply. The preconditioner is designed to improve the spectral properties of $\boldsymbol{A}$, making the system converge faster. In this study, the left preconditioning technique is utilized in the GMRES method, which is based on solving the linear system as $\boldsymbol{M}^{-1}\boldsymbol{Ax}=\boldsymbol{M}^{-1}\boldsymbol{b}$. A preconditioner applied to Algorithm 1 would appear in lines 1 and 4. The preconditioner investigated in this work is the Jacobi preconditioner. The Jacobi preconditioner is the diagonal matrix which contains the diagonal elements of the sparse matrix $\boldsymbol{A}$. The inversion of the Jacobi preconditioner can be easily performed done with a small computation burden.

The main computational components in the PGMRES method are: (1) Sparse matrix-vector product; (2) Vector operations; (3) Preconditioning operation; (4) Solving the least-square problem. The implementation of these four parts on GPU is discussed as follows.

In this study, the sparse matrix $\boldsymbol{A}$ and the preconditioner $\boldsymbol{M}$ are stored with the compressed sparse row (CSR) format which is widely used as a general-purpose sparse matrix storage format. As illustrated in Algorithm 1, the sparse matrix-vector product (SpMV) is one of the major components which are highly parallelizable in the PGMRES method. To parallel the SpMV for a matrix with the CSR format, the multiplication of one row of the matrix with the vector is simply assigned to one thread. As a result, the computation of all threads is independent.

There exist several other GPU-friendly operations in the PGMRES method, such as the vector addition, dot production of two vectors, and vector scaling. These procedures can be easily

parallelized by assigning the operation of elements of vectors to the GPU threads. The reduction is involved when calculating the 2-norm of the vector and performing the dot product of two vectors. The reduction operation is also performed on GPU by utilizing the shared memory. The parallel reduction is performed to sum up all partial results which are saved into the shared memory by the GPU threads.

One important aspect of the PGMRES method is the preconditioning operation. The incomplete-LU preconditioning technique is implemented to provide an incomplete factorization of the coefficient matrix. It requires a solution of lower and upper triangular linear system in every iteration of PGMRES method. In order to implement the preconditioning operation, the sparse triangular solve implemented in the cuSPARSE library (NVIDIA cu SPARSE Library) is used.

The least-square problem is solved by the QR factorization of the Hessenberg matrix. Since this procedure is naturally serial, a series of Givens rotation is performed to solve the least-square problem on GPU with serial execution.

## NUMERICAL RESULTS

The numerical tests were conducted on a workstation with Intel Core i9-7900X Processor (3.30 GHz, 10-core) and an NVIDIA GeForce GTX 1080Ti (1.5 GHz, 3584 CUDA cores, 11GB memory) running 64-bit Linux systems. All tests are performed with double-precision arithmetic.

### Accuracy of the Implementation

The 2-D C5G7 benchmark (Lewis et al., 2003) is usually used to verify the accuracy of the algorithm. **Figures 3A–C** illustrate the assembly and core configuration of this benchmark with the boundary conditions. The fuel assembly is constructed with 17 by 17 of square pins. And the geometry of fuel pin is shown in **Figure 3B**. Seven-group macroscopic cross-sections are specified. For spatial discretization, the whole computing domain is divided into 51 by 51 pins. Each pin is subdivided into 5 radial subdivision and 8 azimuthal divisions, as illustrated in **Figure 3B**. All tests are performed with the 0.03 cm ray spacing and 56 azimuthal angles. Tabuchi-Yamamoto (Yamamoto et al., 2007) polar quadrature sets are used. The stopping criteria for convergence are $\varepsilon_{keff} < 10^{-6}$ and $\varepsilon_{flux} < 10^{-5}$.

The computations are performed with and without two-level CMFD acceleration. **Table 1** shows the eigenvalue and power distribution of the benchmark, along with the reference Monte Carlo solution. Compared to the reference results, the absolute difference of eigenvalue is 6 pcm which is under the stochastic uncertainty of the reference. The power distribution shows good agreement. And the maximum relative pin power error is <1.4%. The results demonstrate desired agreement for both eigenvalue and the power distribution. Moreover, the CMFD acceleration maintains the desired accuracy compared to the MOC calculation.

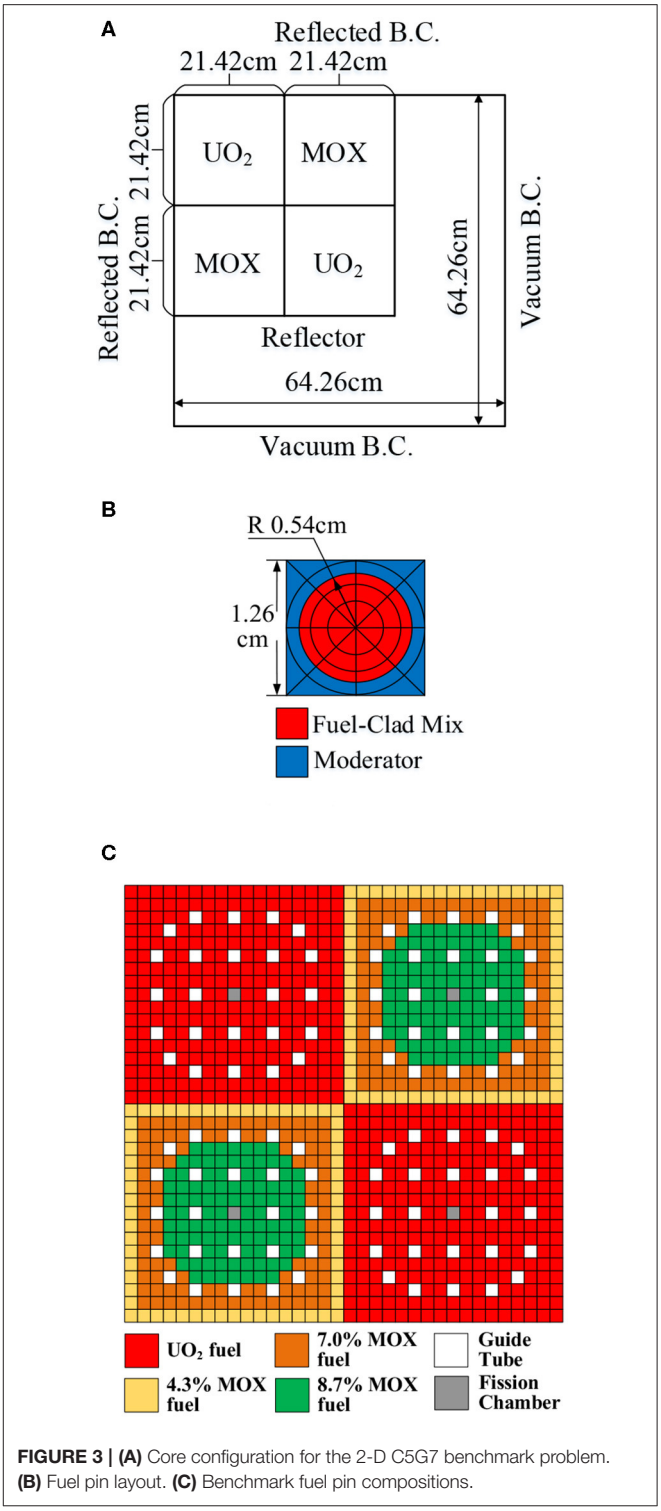


**FIGURE 3 | (A)** Core configuration for the 2-D C5G7 benchmark problem. **(B)** Fuel pin layout. **(C)** Benchmark fuel pin compositions.

### Overall Performance of Two-Level CMFD and GPU Acceleration

In this section, the overall performance of two-level CMFD and GPU acceleration is studied. In order to exploit the full computing power of GPU, a series of cases are performed with a fictitious quarter-core problem. The quarter core contains 21 $UO_2$ fuel assemblies and 20 MOX fuel assemblies from the 2-D C5G7 benchmark problem. Those assemblies are aligned in a checkerboard pattern as illustrated in **Figure 4**. The mesh division and computing parameters maintain the same as the

**TABLE 1 |** Runtime, Eigenvalue, and Power Distribution Results for 2-D C5G7 Benchmark.

| Metric | value | | |
|---|---|---|---|
| | Reference | MOC | MOC with two-level CMFD |
| Eigenvalue $k_{eff}$ ($\Delta k_{eff}$. pcm) | 1.18655 ± 9.5 pcm | 1.18648 −6 pcm | 1.18648 −6 pcm |
| **Pin power data** | | | |
| Max. pin power | 2.498 | 2.496 | 2.496 |
| (relative error) | ±0.16% | 0.08% | 0.08% |
| Min. pin power | 0.232 | 0.234 | 0.234 |
| (relative error) | ±0.58% | 1.16% | 1.16% |
| **Assembly power** | | | |
| Inner $UO_2$ Assy | 492.8 | 492.4 | 492.4 |
| (relative error) | ±0.10% | 0.07% | 0.07% |
| MOX Assy | 211.7 | 211.8 | 211.8 |
| (relative error) | ±0.18% | 0.06% | 0.06% |
| Outer $UO_2$ Assy | 139.8 | 139.8 | 139.8 |
| (relative error) | ±0.20% | 0.11% | 0.11% |
| **Pin power distribution** | | | |
| MAX error | ------- | 1.38% | 1.38% |
| AVG error | 0.32% | 0.22% | 0.22% |
| RMS error | 0.34% | 0.01% | 0.01% |
| MRE error | 0.27% | 0.17% | 0.17% |

*MAX error, Maximum relative pin power percent error.*
*AVG error, Average pin power percent error.*
*RMS error, Root mean square of the pin power percent error distribution.*
*MRE error, Mean relative pin power percent error.*

aforementioned 2-D C5G7 benchmark problem, except the overall convergence criterion of flux which is set to be $10^{-4}$. The convergence criteria for $k_{eff}$ and flux of MG CMFD calculation are $\varepsilon_{keff}<5 \times 10^{-7}$ and $\varepsilon_{flux}<5 \times 10^{-5}$. And the related convergence criteria of FG CMFD are $\varepsilon_{keff}<2.5 \times 10^{-7}$ and $\varepsilon_{flux}<2.5 \times 10^{-5}$.

## Convergence Performance of Different Linear System Solvers

In order to characterize the convergence performance of different linear system solvers, Three cases are executed with MG CMFD acceleration on GPU. Based on a series of tests, the maximum number of iterations of MG CMFD and the maximum number of linear iterations per CMFD calculation are both set to be 30. The Krylov subspace dimension of the PGMRES solvers is set to 2. Then **Figure 5** illustrates the overall convergence history of the $k_{eff}$ with the Jacobi, SOR, and PGMRES solvers. As shown in **Figure 5**, the PGMRES solver shows a better convergence rate. Moreover, the SOR solver has a medium rate of convergence, and it needs more iterations to achieve convergence when the Jacobi solver is involved.

## Overall Performance of Two-Level CMFD on GPU

A series of runs are performed to evaluate the overall performance of two-level CMFD and GPU acceleration. The sensitivity study has been performed with varied upper limits of the number of CMFD iterations and the number of linear solver

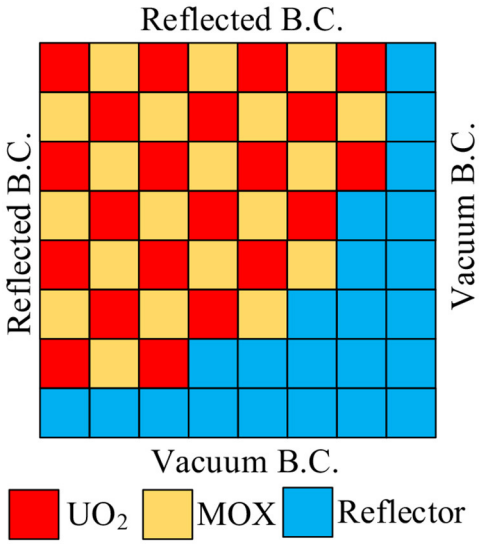


**FIGURE 4 |** A mock PWR quarter core.

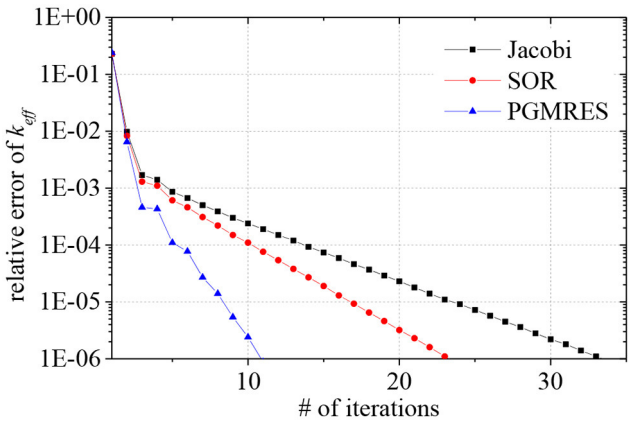


**FIGURE 5 |** Convergence history of $k_{eff}$ of the different linear system solvers for the mock quarter-core problem.

iterations. Moreover, the impact of different Krylov subspace dimensions to the overall performance is also examined and it is set to 2. After the sensitivity study, the best results for each execution are listed in **Table 2**.

From **Table 2**, the following observations can be made based on the numerical results:

(1) The GPU shows great performance advantages compared to the CPU. The comparison of the case (0a) and case (0b) shows that the GPU-based MOC calculation achieves about 25x speedup compared to the serial CPU-based calculation. This observation is consistent with the results drawn in our former research (Song et al., 2019).
(2) The CMFD acceleration can significantly reduce the number of iterations. For both CPU-based and GPU-based calculation, about 100x speedup is provided by two-level

**TABLE 2 |** Results of the mock quarter-core problem with or without CMFD and GPU acceleration.

| Cases | # of iter. | Overall runtime (s) | MOC runtime (s) | CMFD runtime (s) | # of MG CMFD iter. | # of FG CMFD iter. | Speedup |
|---|---|---|---|---|---|---|---|
| (0a) CPU_MOC | 1640 | 40035.6 | ------ | ------ | ------ | ------- | Ref. |
| (0b) GPU_MOC | 1640 | 1615.7 | ------ | ------ | ------ | ------- | 25 |
| (1a) CPU_MG_Jacobi[(a)] | 12 | 358.2 | 306.8 | 48.7 | 516 | ------ | 112 |
| (1b) CPU_MG_SOR | 12 | 344.1 | 308.8 | 32.4 | 356 | ------ | 116 |
| (1c) CPU_MG_PGMRES | 12 | 361.8 | 306.6 | 52.6 | 250 | ------ | 111 |
| (1d) CPU_2L_Jacobi[(a)] | 12 | 329.1 | 308.2 | 18.0 | 178 | 1,780 | 122 |
| (1e) CPU_2L_SOR | 12 | 325.9 | 308.3 | 14.9 | 108 | 916 | 123 |
| (1f) CPU_2L_PGMRES | 12 | 327.8 | 306.4 | 18.6 | 103 | 717 | 122 |
| (2a) GPU_MG_Jacobi | 12 | 21.1 | 12.2 | 5.5 | 720 | ------ | 1,897 |
| (2b) GPU_MG_SOR | 12 | 21.5 | 12.5 | 5.7 | 600 | ------ | 1,864 |
| (2c) GPU_MG_PGMRES | 12 | 26.6 | 12.3 | 11.0 | 324 | ------ | 1,503 |
| (2d) GPU_2L_Jacobi | 12 | 16.9 | 12.2 | 1.3 | 240 | 3,600 | 2,376 |
| (2e) GPU_2L_SOR | 12 | 16.7 | 12.2 | 1.1 | 180 | 1,800 | 2,402 |
| (2f) GPU_2L_PGMRES | 12 | 18.7 | 12.3 | 3.2 | 120 | 960 | 2,141 |

[(a)] *MG and 2L represent the multi-group and two-level CMFD acceleration, respectively.*

CMFD acceleration. Moreover, the GPU acceleration for CMFD calculation is about 13x [case (1d) vs. case (2d) and case (1e) vs. case (2e)] for cases using Jacobi solver and SOR solver. While the GPU acceleration for CMFD calculation is about 5.8x [case (1f) vs. case (2f)] when PGMRES solver is used. Compared to the serial CPU-based MOC calculation (case (0a)], the overall speedup of case (2e) is contributed by 3 aspects: (1) the speedup provided by the CMFD acceleration which can significantly reduce the number of iterations (about 100x), (2) GPU acceleration on MOC neutron transport calculation (about 25x), (3) GPU acceleration on CMFD calculation (about 13x). And in case (2e), the CMFD calculation contributes about 7% of overall runtime. As a result, over 2,400x [case (0a) vs. case (2e)] speedup is obtained when the two-level CMFD and GPU accelerations are applied simultaneously.

(3) Although the Jacobi method has the maximum degree of parallelism on GPU, a relatively large number of CMFD iterations is needed because of the poor convergence performance of the Jacobi method, as illustrated in **Figure 5**. However, the SOR method can maintain the desired parallelism by adopting the red-black ordering strategy. On the other hand, it also can keep the relative high convergence rate compared to the Jacobi method, which results in a reduction in the number of CMFD iterations. Hence, the SOR-based calculations show better performance than the Jacobi-based calculations. The number of CMFD iterations is relatively reduced when the PGMRES solver is involved. And the overall performance of PGMRES-based calculations on CPU is comparable to the Jacobi-based and SOR-based calculations. Nevertheless, the performance degradation of PGMRES-based calculations is observed on GPU. The detailed analysis is discussed in the following sections. As a result, the SOR-based calculations show better performance compared against other cases with the Jacobi and PGMRES solver in the same group [such as the comparison of the cases (1a), (1b), and (1c)].

(4) The FG CMFD is effective to accelerate the CMFD calculation. Compared to the cases with MG CMFD calculations, over 50% improvement in 2 L CMFD calculations is observed by comparing the execution time of CMFD calculations.

## Detailed Execution Time of CMFD Calculation

The execution time of CMFD calculation is contributed by three parts, (1) cross-sections generation (xs_gene), (2) linear system construction (linSys_cons), (3) linear system solving ($Ax = b$). **Figure 6** shows the execution time of different partitions of CMFD calculation for the cases listed in **Table 2**. As shown, for CPU calculation, the generation of multi-group cross-sections contributes a considerable part to the overall CMFD calculation, especially for the two-level CMFD calculation. However, since the xs_gene procedure is performed with thread parallelization on GPU, the execution time of xs_gene is significantly reduced to $<0.2$ s on GPU. For all cases, the execution time for constructing the linear system is $<0.1$ s. Moreover, **Figure 6** indicates that the FG CMFD acceleration can significantly reduce the execution time of solving the linear system in 2 L CMFD calculation. When applying the PGMRES method on GPU, the performance improvement for linear system solving is about 3.7 x which is relatively small compared to the other two methods. The detailed performance analysis of the linear solvers will be performed in future work.

Current work is focused on the 2-D CMFD calculation on GPU. However, simulation of practical problem is usually focused on 3-D calculations. The CMFD equations in 2-D form a five-stripe sparse linear system, while it is a seven-stripe sparse linear system on the 3-D geometry. Since the iterative methods applied in this work are general methods for

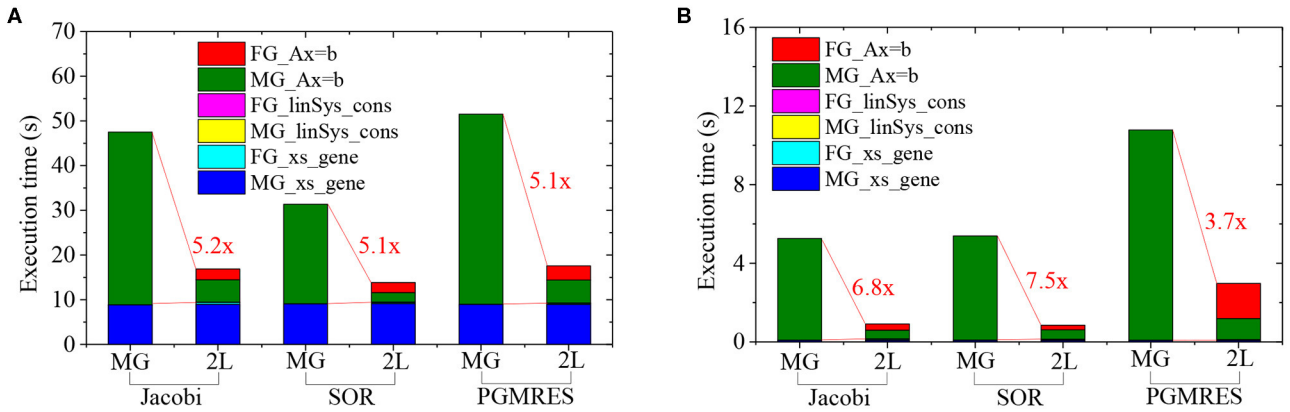


**FIGURE 6 | (A)** Time break down of CMFD calculations on CPU. **(B)** Time break down of CMFD calculations on GPU.

solving the CMFD linear systems. Hence, the related linear system solvers can be directly applied to solve the 3-D CMFD problems. And the performance is supposed to be consistent in 3-D cases.

In addition, the large-scale problems usually need to be solved with parallel strategy such as spatial domain decomposition. The scalability and efficiency to computing the large-scale problems with multiple GPUs need to be examined.

As for the further performance optimization, the MOC calculation contributes the majority of runtime for the simulation of 2-D neutron transport calculations on GPU. This observation is supposed to be consistent in 3-D simulations. Hence, in order to improving the overall performance, more efforts should be focused on the optimization of GPU-based MOC calculation in 3-D situation. In addition, when the spatial domain decomposition and multiple GPUs are involved, the performance of 3-D CMFD calculation may be impacted by the communication between decomposed domains. And it may further impact the overall performance.

## CONCLUSION

In this work, a two-level CMFD acceleration technique was implemented on both CPU and GPU to accelerate the 2-D MOC neutron transport calculation. In the two-level CMFD scheme, a few-group CMFD problem is used as a lower-order accelerator to the standard pinwise multi-group CMFD problem. Several linear system solvers, i.e., Jacobi solver, SOR solver with red-black ordering, and the PGMRES solver, are applied and the performance was examined under the CMFD framework. The overall performance of CMFD acceleration on both CPU and GPU is compared to evaluate the effectiveness of CMFD and GPU acceleration.

The numerical calculations are performed with 2-D C5G7 benchmark problem and an extended 2-D mock quarter-core problem and the following conclusions can be drown:

(1) For the 2-D C5G7 benchmark, the difference of eigenvalue is 6 pcm and the power distribution shows good agreement compared against the reference solution. The results of calculations with and without two-level CMFD acceleration provide desired accuracy in both eigenvalue and power distribution.

(2) As a linear system solver, the PGMRES solver shows a better convergence rate with minimum number of iterations. While the number of iterations of Jacobi solver is tripled compared to the PGMRES solver at the same convergence level. And the SOR solver has a medium rate of convergence.

(3) It appears that SOR is a suitable method for solving the linear system under the CMFD framework on both CPU and GPU. For CPU-based CMFD calculation, the PGMRES method has comparable performance to the SOR method, because the arithmetic complexity of the PGMRES method can be counteracted by its remarkable convergence characteristics. However, since the Jacobi method and SOR method can reach a relatively high degree of parallelism on GPU, the performance of these two methods is better than the PGMRES method. When the two-level CMFD and GPU accelerations are applied simultaneously, the overall speedup is contributed by 3 aspects: 1) the CMFD acceleration which can significantly reduce the number of iterations (about 100x), 2) GPU acceleration on MOC neutron transport calculation (about 25x), 3) GPU acceleration on CMFD calculation (about 13x for SOR method). As a result, it reaches about 2,400x speedup on GPU with two-level CMFD acceleration compared to the CPU-based MOC calculation.

(4) The CMFD calculation contributes about 7% (for cases with Jacobi and SOR solver) and 17% (for cases with PGMRES solver) of the overall runtime. The procedure for solving the linear system contributes to the majority of the runtime of the CMFD calculation. Moreover, the results show that the FG CMFD acceleration is effective to accelerate the MG CMFD execution.

This work demonstrates the high potential of the two-level CMFD technique and GPUs to accelerate the practical whole-core neutron transport calculation. Based on the numerical results, GPUs provide a high-performance advantage for accelerating both MOC and CMFD calculations. Since the PGMRES method is still preferred in that it can solve various linear systems with a wide range of numerical properties, more efforts need to be concentrated on the performance optimization of the PGMRES method on GPU. Moreover, the main purpose is to perform the 3-D whole-core MOC neutron transport simulation on GPU under CMFD framework. Hence, in the future, more efforts will be focused on the 3-D CMFD calculation on GPU with the detailed performance analysis. In addition, the efficiency comparison of different solvers and the study of the parallelization will be included with practical computational cases. Furthermore, the scalability to computing the large-scale problems on large-scale parallel machines also needs to be examined in the future.

## DATA AVAILABILITY STATEMENT

All datasets generated for this study are included in the article/supplementary material.

## AUTHOR CONTRIBUTIONS

PS, ZZ, and LL contributed to the ideas and designs of this study. PS implemented the algorithm through programming and wrote the first draft of the manuscript. ZZ helped to design and organize the cases for validating the algorithm. LL helped to perform the numerical analysis and organize the database. QZhang and QZhao explained the details of linear algebra used in this work and provided technical support during programming. All authors helped to revise the manuscript and approve the submitted version.

## FUNDING

This work is supported by the funds provided by the following sources: Science and Technology on Reactor System Design Technology Laboratory, Heilongjiang Province Science Foundation for Youths [QC2018003], Nuclear Power Technology Innovation Center, Fundamental Research Funds for the Central Universities [grant number GK2150260178], the Research on Key Technology of Numerical Reactor Engineering [J121217001], and the National Key R&D Program of China [2018YFE0180900].

## REFERENCES

Askew, J. R. (1972). A characteristics formulation of the neutron transport equation in complicated geometries. *AEEWM 38*:1108.

Boyd, W., Shaner, S., Li, L., Forget, B., and Smith, K. (2014). The OpenMOC method of characteristics neutral particle transport code. *Ann. Nucl. Energy* 68, 43–52.

Boyd, W. R., Smith, K., and Forget, B. (2013). "A massively parallel method of characteristics neutral particle transport code for GPUs," in *Proceedings of the International conference on Mathematics and Computational Method Applied To Nuclear Science and Engineering (M&C 2013)*, (Sun Valley).

Chen, J., Liu, Z., Zhao, C., He, Q., Zu, T., Cao, L., et al. (2018). A new high-fidelity neutronics code NECP-X. *Ann. Nucl. Energy* 116, 417–428. doi: 10.1016/j.anucene.2018.02.049

Cho, J. Y., Joo, H. G., Kim, K. S., and Zee, S. Q. (2002). Cell based CMFD formulation for acceleration of whole-core method of characteristics calculations. *J. Korean Nucl. Soc*. 34, 250–258.

Cho, N., Lee, G. S., and Park, C. J. (2003). Partial current-based CMFD acceleration of the 2D/1D fusion method for 3D whole-core transport calculations. *Trans. Am. Nucl. Soc*. 88:594.

Choi, N., Kang, J., and Joo, H. G. (2018). "Performance comparison of linear system solvers for CMFD acceleration on GPU architectures," in *Transactions of the Korean Nuclear Society Spring Meeting* (Jeju).

Godfrey, A., Collins, B., Kim, K. S., Lee, R., Powers, J., Salko, R., et al. (2016). VERA benchmark results for Watts Bar nuclear plant unit 1 cycle 1-12," in *The Physics Reactor Conference (PHYSOR 2016)* (Sun Valley).

Han, Y., Jiang, X., and Wang, D. (2014). CMFD and GPU acceleration on method of characteristics for hexagonal cores. *Nucl. Eng. Des*. 280, 210–222. doi: 10.1016/j.nucengdes.2014.09.038

Jong, M. D., Ploeg, A. V. D., Ditzel, A., and Vulk, K. (2017). Fine-grain parallel RRB-solver for 5-/9-point stencil problems suitable for GPU-type processors. *Electron Transc Numer Ana.* 46, 375–393.

Joo, H. G., Cho, J. Y., Kim, K. S., Lee, C. C., and Zee, S. Q. (2004). "Methods and performance of a threedimensional whole-core transport code DeCART," in *Proceedings of the PHYSOR2004* (Chicago).

Jung, Y. S., Shim, C. B., Lim, C. H., and Joo, H. G. (2013). Practical numerical reactor employing direct whole core neutron transport and subchannel thermal/hydraulic solvers. *Ann. Nucl. Energy* 62, 357–374. doi: 10.1016/j.anucene.2013.06.031

Kang, J., and Joo, H. G. (2018). "GPU-based parallel krylov linear system solver for CMFD calculation in nTRACER," in *Transactions of the Korean Nuclear Society Spring Meeting* (Jeju).

Kochunas, B., Collins, B., Jabaay, D., Downar, T. J., and Martin, W. R. (2013). "Overview of development and design of MPACT: Michigan parallel characteristics transport code," in *International Conference on Mathematics & Computational Methods Applied To Nuclear Science & Technology* (Sun Valley).

Kochunas, B., Collins, B., Jabaay, D., Stimpson, S., Salko, R., Graham, A., et al. (2015). "VERA core simulator methodology for PWR cycle depletion," in *Joint International Conference on Mathematics and Computation (M&C), Supercomputing in Nuclear Applications (SNA) and the Monte Carlo (MC) Method* (Nashville).

Lewis, E. E., Palmiotti, G., Taiwo, T. A., Blomquist, R. N., Smith, M. A., and Tsoulfanidis, N. (2003). *Benchmark Specifications for Deterministic MOX Fuel Assembly Transport Calculations without Spatial Homogenization*. (Organization for Economic Co-operation and Development's Nuclear Energy Agency).

Li, R., and Saad, Y. (2012). GPU-accelerated preconditioned iterative linear solvers. *J Supercomput.* 63, 443–466. doi: 10.1007/s11227-012-0825-3

Liang, L., Zhang, Q., Song, P., Zhang, Z., Zhao, Q., Wu, H., et al. (2020). Overlapping communication and computation of GPU/CPU heterogeneous parallel spatial domain decomposition MOC method. *Ann. Nucl. Energy* 135:106988. doi: 10.1016/j.anucene.2019.106988

Liu, Z., Wu, H., Chen, Q., Cao, L., and Li, Y. (2011). A new three-dimensional method of characteristics for the neutron transport calculation. *Ann. Nucl. Energy* 38, 447–454. doi: 10.1016/j.anucene.2010.09.021

NVIDIA cu SPARSE Library (2019). Avaliable online at: https://docs.nvidia.com/cuda/cusparse/index.html (accessed May 01, 2020).

Ryu, M., Jung, Y. S., Cho, H. H., and Joo, H. G. (2015). Solution of the BEAVRS benchmark using the nTRACER direct whole core calculation code. *J Nuclear Sci Technol.* 52, 961–969. doi: 10.1080/00223131.2015.1038664

Saad, Y., and Schultz, M. H. (1986). GMRES: A generalized minimal residual algorithm for solving nonsymmetric linear systems. *SIAM J. Sci. Stat. Comput.* 7, 856–869. doi: 10.1137/0907058

Smith, K. S. (1984). Nodal method storage reduction by non-linear iteration. *Transac. Am. Nuclear Soc*. 44:265.

Song, P., Zhang, Z., Liang, L., Zhang, Q., and Zhao, Q. (2019). Implementation and performance analysis of the massively parallel method of characteristics based on GPU. *Ann. Nucl. Energy*. 131, 257–272. doi: 10.1016/j.anucene.2019.02.026

Song, P., Zhang, Z., and Zhang, Q. (2020). Implementation of the CPU/GPU hybrid parallel method of characteristics neutron transport calculation using the heterogeneous cluster with dynamic workload assignment. *Ann. Nucl. Energy*. 135:106957. doi: 10.1016/j.anucene.2019.106957

TOP500 official site (2019). Avaliable online at: https://www.top500.org/> (accessed May 11, 2019).

Tramm, J. R., Gunow, G., He, T., Smith, K. S., Forget, B., and Siegel, A. R. (2016). A task-based parallelism and vectorized approach to 3D Method of Characteristics (MOC) reactor simulation for high performance computing architectures. *Comput. Phys. Commun*. 202, 141–150. doi: 10.1016/j.cpc.2016.01.007

Van der Vorst, H. A., and Vuik, C. (1993). The superlinear convergence behaviour of GMRES. *J. Comput. Appl. Math.* 48, 327–341.

Wang, D., and Xiao, S. (2018). A linear prolongation approach to stabilizing CMFD. *Nucl. Sci. Eng*. 190, 45–44. doi: 10.1080/00295639.2017.1417347

Yamamoto, A., Tabuchi, M., Sugimura, N., Ushio, T., and Mori, M. (2007). Derivation of optimum polar angle quadrature set for the method of characteristics based on approximation error for the Bickley function. *J. Nucl. Sci. Eng*. 44, 129–136. doi: 10.1080/18811248.2007.9711266

Zhang, Z., Wang, K., and Li, Q. (2013). Accelerating a three-dimensional MOC calculation using GPU with CUDA and two-level GCMFD method. *Ann. Nucl. Energy* 62, 445–451. doi: 10.1016/j.anucene.2013.06.039

Zhu, A., Jarrett, M., Xu,. Y., Kochunas, B., Larsen, E., Downar, T., et al. (2016). An optimally diffusive Coarse Mesh Finite Difference method to accelerate neutron transport calculations. *Ann. Nucl. Energy* 95, 116–124. doi: 10.1016/j.anucene.2016.05.004

**Conflict of Interest:** The authors declare that the research was conducted in the absence of any commercial or financial relationships that could be construed as a potential conflict of interest.

frontiers in Energy Research

BRIEF RESEARCH REPORT
published: 21 July 2020
doi: 10.3389/fenrg.2020.00164

# Numerical Study of the Influence of Tube Arrangement on the Flow Distribution Inside the Heat Exchanger in the PCCS

*Jian Zhou[1]*, Yanwei Yue[2], Zhaoming Meng[1]* and Zhongning Sun[1]*

*[1] Fundamental Science on Nuclear Safety and Simulation Technology Laboratory, Harbin Engineering University, Harbin, China, [2] Research and Development Center, China Nuclear Power Engineering Co., Ltd., Beijing, China*

OPEN ACCESS

***Edited by:***
*Muhammad Zubair,*
*University of Sharjah,*
*United Arab Emirates*

***Reviewed by:***
*Yen-Shu Chen,*
*Institute of Nuclear Energy Research (INER), Taiwan*
*Luteng Zhang,*
*Chongqing University, China*
*Arash Mirabdolah Lavasani,*
*Islamic Azad University Central Tehran Branch, Iran*
*Xiaowei Li,*
*Tsinghua University, China*

****Correspondence:***
*Jian Zhou*
*zhoujian@hrbeu.edu.cn;*
*18045625729@163.com*
*Zhaoming Meng*
*mengzhaoming@hrbeu.edu.cn;*
*1023240585@qq.com*

***Specialty section:***
*This article was submitted to Nuclear Energy, a section of the journal Frontiers in Energy Research*

***Received:*** *14 October 2019*
***Accepted:*** *29 June 2020*
***Published:*** *21 July 2020*

***Citation:***
*Zhou J, Yue Y, Meng Z and Sun Z (2020) Numerical Study of the Influence of Tube Arrangement on the Flow Distribution Inside the Heat Exchanger in the PCCS. Front. Energy Res. 8:164. doi: 10.3389/fenrg.2020.00164*

Passive containment cooling system (PCCS) is widely applied in a new generation of nuclear power plants. The initial heat exchanger is the most improtant heat transfer device in the PCCS. Past studies show that the flow distribution has a great influence on the heat transfer performance of a heat exchanger. And a lot of work has been done on improving the flow distribution uniformity of the heat exchanger such as the geometry modification, proper choice of the geometry parameters. However, little work has been done on the tube arrangement. For a heat exchanger applied in the industry, the number of tubes are huge, and it is unrealistic to arrange all the tubes in a row on the one side of the heat exchanger. Therefore, more work should be paid on the influence of the tube arrangement on the flow distribution in the heat exchanger. The present study numerically investigated the effect of the tube arrangement on the flow distribution in a Central-type parallel heat exchanger. Six different kinds of tube arrangement have been investigated on the flow distribution and the pressure loss characteristics of the heat exchanger. The obtained results show that the tube arrangement has a great influence on the flow distribution and the staggered tube arrangement provides a better flow distribution than the aligned tube arrangement.

**Keywords: flow distribution, tube arrangement, central-type, compact, pressure loss**

## INTRODUCTION

For the new generation of nuclear power plants, passive containment cooling system (PCCS) is commonly applied in the system. The initial heat exchanger is the most important heat transfer device and it has a great effect on the heat transfer performance of the PCCS. Therefore, it is neccesary to pay more attention on the initial heat exchanger. In the PCCS, the initial heat exchangers are usually compact parallel flow heat exchangers.

Compact parallel flow heat exchanger has been widely used in many industrial systems such as the reheater and electric heater in the power station boiler system, radial flow reactor in chemical applications, plate heat exchanger or plate fin heat exchanger, solar collector, etc.

However, ununiform flow distribution in the heat exchanger always exists and greatly affects the normal operation of the heat exchanger. For example, ununiform flow distribution reduces the performance of the heat exchanger. And for some tubes with very little liquid flow, they may be

more likely to boil under overheating, threatening the safety of the heat exchanger. In addition, due to the ununiform flow distribution, the heat transfer performance is degraded, and the heat exchanger may not meet the design performance requirements in practical applications. Therefore, the attention is focused on the study of the flow distribution in heat exchangers. In this study, the goal was to provide some simple and feasible inlet and header designs numerically, which can significantly reduce the flow maldistribution in the heat exchanger.

There are some works focused on the modification of heat exchanger design for a more uniform flow distribution. Wang et al. (2011) have applied five modified headers to a compact parallel heat exchanger and investigated the characteristics of the flow distribution in the heat exchanger. The results show that the header shape greatly influences the flow distribution and the modified header with baffle tube significantly improve the flow distribution uniformity. In the work of Ye (2017), the cross section of the duct was changed to improve air distribution in duct ventilation. The design principles and corresponding processes are given. The results show that the method has good performance and the air maldistribution coefficient is less than 10%. Shi et al. (2010) optimized the inlet manifold structure of the fin heat exchanger. The results show that after optimization, the heat transfer performance of the heat exchanger is improved by 1.03–3.98%. In addition, numerical and experimental studies have been carried out on the optimization results, and the results show that the temperature and flow distribution are improved. Said et al. (2014) successfully reduced the maldistribution in a central-type heat exchanger with the method of applying orifice approach and nozzle approach in tubes, respectively. Liu et al. (2010) have done the investigation on the multiple structural bifurcations of flow channels. Compared to the typical flow distribution structures of manifolds, this novel method greatly improved the uniformity of flow distribution. For the channel bifurcations, Liu and Li (2013) has done a deeper investigation on the two categories of the bifurcations. Also, some characteristic parameters have been investigated, and results show that the ratio of the length of channels from the end of one bifurcation to the beginning of the next bifurcation to the width of the channel has a significant effect on the flow distribution uniformity. In another investigation made by Liu et al. (2012) on the bifurcation parameters. The design criterion has been given that $f_i/c_i = 0.05\mathrm{Re}_i$. Besides, they found that the Tee-type bifurcation is better than the Circular-type. For the two-phase flow distribution, Yuan et al. (2013) has proposed an two-phase flow distributor to achieve the uniform flow distribution in a plate heat exchanger. The results show that the proposed structure has a better flow distribution compared to the original structure.

Wang and Wang (2015) have done a lot of work on the discrete model for design of the flow distribution in the manifold. Discrete methods for U-type and Z-type manifolds have been developed. The results show that the flow distribution in U-type manifolds is more uniform than that in the Z-type. In addition, the analytical model provides useful tools for evaluating flow distribution in manifolds and provides guidance for geometric design.

For parallel channels, Wei et al. (2015a,b, 2016) have done great work for a uniform flow distribution or a uniform temperature distribution with both method of experiments and CFD simulation. They provide creative modification or design on the channel geometry.

In our previous work (Zhou et al., 2017, 2018). We have done some CFD simulation work on the central-type heat exchanger, and showed the effects of the geometric parameters of the a central-type heat exchanger on the flow distribution. Also, we have done the modification of the geometry for a better flow distribution (Zhou et al., 2019).

In previous studies, a lot of work has been done on the reducing flow maldistribution in parallel manifolds or micro channels, and a lot of valuable results have been obtained. For the PCCS initial heat exchanger, the compact parallel manifolds with two headers are chosen for the basic geometry. Except for the basic part of the geometry, the tube arrangement is one of the most important part of the heat exchanger design. The tube arrangement makes a great influence on the flow distribution in the heat exchanger, and the flow distribution will influence the whole natural circulation of the PCCS. Therefore, a uniform flow distribution will help establish a steady natural circulation of the PCCS. However, little work has been done on tube arrangement. A approritate choice of the tube arrangement will help improve the flow distribution, besides, the tube arrangement is also important for a heat exchanger with large number of tubes because of the limitation of the space occupation and the reduction of the material.

For the Central-type manifolds of heat exchanger, there is still more work to be done on the tube arrangement. With the appropriate tube arrangement, improving the flow distribution may be easier and more convenient. In the present study, six kinds of tube arrangement have been investigated for their effects on the flow distribution through tubes.

## PROBLEM DESCRIPTION

In the present study, the aim is to investigate the influence of the tube arrangement on the flow maldistribution existed in a Central-type heat exchanger. Therefore, six different kinds of tube arrangements have been applied for a central-type heat exchanger and investigated on their influence on the flow maldistribution through tubes. For the configuration model, there are two headers namely dividing header and combining header, respectively, and sixteen C-tubes are connected to the headers. Six different test cases with different tube arrangement have been under investigations, respectively. And three cases are denoted case1, case2, case3,case4, case5, and case6. For the case1, the tube arrangement is a common tube arrangement and all parallel tubes are arranged at one side of the heat exchanger as shown in **Figure 1A**. For the case2, tubes are divided equally into two halves and set on both sides of the heat exchanger, besides, tubes are in aligned arrangement which means that the tube inlet of two parts of tubes are facing to each other as shown in the **Figure 1B**. While for the case3, tube inlets on opposite sides are staggered from each other as shown in **Figure 1C**. For the case4 and case5, tubes are arranged in double rows on one side of the heat exchanger. And differences in the arrangement are shown in

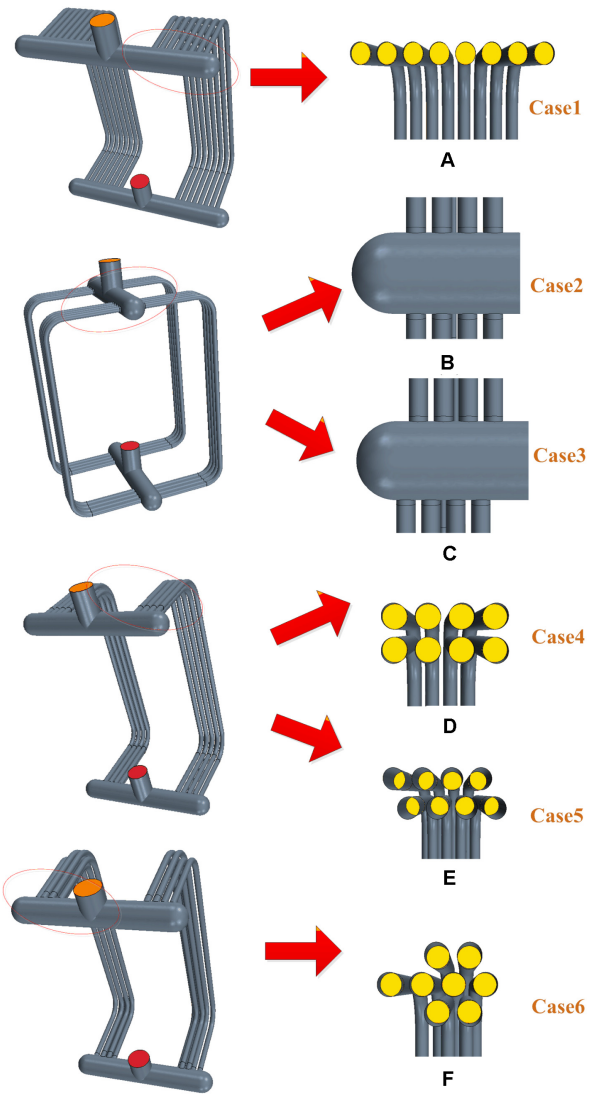


**FIGURE 1 |** The three dimensional geometry of six different tube arrangements for the central-type heat exchanger. **(A–F)** Stands for the number of six different structures.

the **Figures 1D,E**. For the case6, tubes are arranged in three rows on one side as shown in the **Figure 1F**.

For the heat exchanger, the dividing and combining header diameter is 180 mm, the tube diameter is 44 mm, and the height of the heat exchanger is 1.7 m, the tube distance is 0.044 m, the tube length is 1.9 m, and the angles between the tube and the headers is 90 degree.

## SOLVING PROCESS AND BOUNDRY CONDITIONS

The heat exchanger three dimensional model is created by the CAD module in the Star-ccm+. And the grid processing is accomplished by the Star-ccm+.

For the boundary conditions, velocity-inlet is selected for the inlet, the pressure outlet selected for the outlet is set to zero gauge pressure, and the walls are set to no slip condition and rough. The $k$–ε turbulent model is chosen as the turbulence model. When all of the residuals are less than $1 \times 10^{-4}$, solutions are considered to be completely convergent.

For the evaluation of the flow distribution, two dimensionless parameters Φ and β have been utilized.

$$\Phi = \frac{\sqrt{\frac{\sum_{i=1}^{N}(m_i - m_{av})^2}{N}}}{M} \tag{1}$$

$$\beta_i = \frac{m_i}{M} \tag{2}$$

Where the $m_i$ and $m_{av}$ represent the mass flow rate through the *ith* tube and the average mass flow rate, respectively. And the $M$ represents the total flow rate. And the Φ means the flow maldistribution coefficient, the smaller the Φ is, the better the flow distribution is. The $\beta_i$ stands for the ratio of the flow rate through *ith* tube to the total flow rates.

## GOVERNING EQUATIONS AND MODEL VALIDATION

The governing equations are listed below.

The steady-state continuity equation is expressed as

$$\frac{\partial u_i}{\partial x_i} = 0 \tag{3}$$

The steady-state momentum conservation equation is expressed as

$$\rho u_j \frac{\partial u_i}{\partial x_i} = -\frac{\partial p}{\partial x_i} + \frac{\partial}{\partial x_j}\left[\mu_t\left(\frac{\partial u_i}{\partial x_j} + \frac{\partial u_j}{\partial x_i}\right)\right] + \rho\vec{g} \tag{4}$$

The steady-state transport equation for $k$ is expressed as

$$\rho u_j \frac{\partial k}{\partial x_j} = \frac{\partial}{\partial x_j}\left(\frac{\mu_t}{\sigma_k}\frac{\partial k}{\partial x_j}\right) + \mu_t\left(\frac{\partial u_i}{\partial x_j} + \frac{\partial u_j}{\partial x_i}\right)\frac{\partial u_i}{\partial x_j} - \rho\varepsilon \tag{5}$$

The steady-state transport equation for ε is expressed as

$$\rho u_j \frac{\partial \varepsilon}{\partial x_j} = \frac{\partial}{\partial x_j}\left(\frac{\mu}{\sigma_\varepsilon}\frac{\partial \varepsilon}{\partial x_j}\right) + C_1\mu_t\frac{\varepsilon}{k}\left(\frac{\partial u_i}{\partial x_j} + \frac{\partial u_j}{\partial x_i}\right)\frac{\partial u_i}{\partial x_j} - C_2\rho\frac{\varepsilon^2}{k} \tag{6}$$

Where

$K$ stands for turbulent kinetic energy;
ε stands for turbulent energy dissipation rate;
ρ stands for density of the working fluid;
$u$ stands for velocity;
$\mu_t$ stands for turbulent dynamic viscosity.

In this present work, no phase change happens. For the single-phase flow, the flow distribution in the heat exchanger is

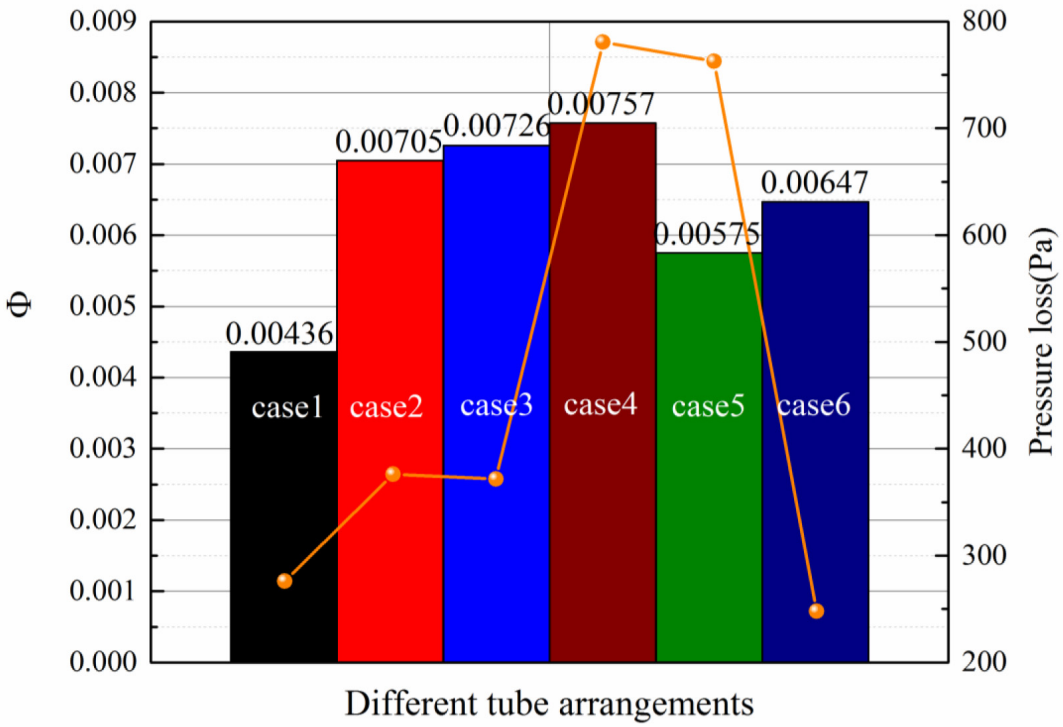


**FIGURE 2 |** The flow distribution cofficient and the pressure loss for different tube arrangements.

determined by the geometry of the heat exchanger and has little relationship with the heat transfer. Therefore, the heat transfer process is beyond the consideration.

For the grid independence test and the model validation, we have done detailed work in our previous study (Zhou et al., 2017). And they will not be illustrated here.

## RESULTS AND DISCUSSION

### The Flow Distribution and the Pressure Loss for Different Tube Arrangement

For six different kinds of tube arrangement, the flow maldistribution coefficient and the pressure loss are shown in **Figure 2**. It shows that the case1 shows the best flow distribution and the least pressure loss, however, it cost the most space occupation and material. For the case2 and case3, both the flow maldistribution coefficient and the pressure loss are very close to each other. It shows that if tubes are arranged in single row at two opposite sides of the heat exchanger, there is no obvious different effect on the flow distribution uniformity and pressure loss for the aligned arrangement and staggered arrangement. However, for the double row arrangement on one side of the heat exchanger, the staggered arrangement shows better in both of the flow distribution uniformity and the pressure loss than aligned arrangement. And, comparing to the case1, the double-row arrangement brings more flow maldistribution and pressure loss. For the case6, three-row arrangement reduces the flow maldistribution and the pressure loss comparing to the double-row arrangement. In the following part, the pressure distribution in the header will be analyzed to figure out the reason behind results of different tube arrangements.

### The Flow Distribution and the Pressure Distribution for Single-Row Arrangement

For the tube arrangement of the case1, case2, and case3. They all belong to the single-row arrangement. Therefore, the flow distribution and the pressure distribution of case1, case2, and case3 will be analyzed together in this part. The **Figure 3A**, shows the flow distribution for the case1, case2, and case3. Firstly it can be seen that the flow distribution for the case2 and case3 are almost the same. And it means that with the single-row arrangement on both sides of the central-type heat exchanger, the staggered arrangement shows little difference from the aligned arrangement. Also, the flow distribution for the case1 shows a lot of difference from that for the case2 and case3. It is because of the difference in the pressure distribution inside the header. The **Figure 3B** shows the pressure distribution in the dividing header for the case1, case2, and case3. In the header, the pressure distribution is mainly controlled by pressure recovery effect and the frictional resistance (Acrivos et al., 1959). The pressure recovery effect increases the pressure and the frictional resistance reduces the pressure. For the compact heat exchanger, the pressure recovery effect is higher than the pressure decrease caused by the frictional resistance, therefore, the pressure will

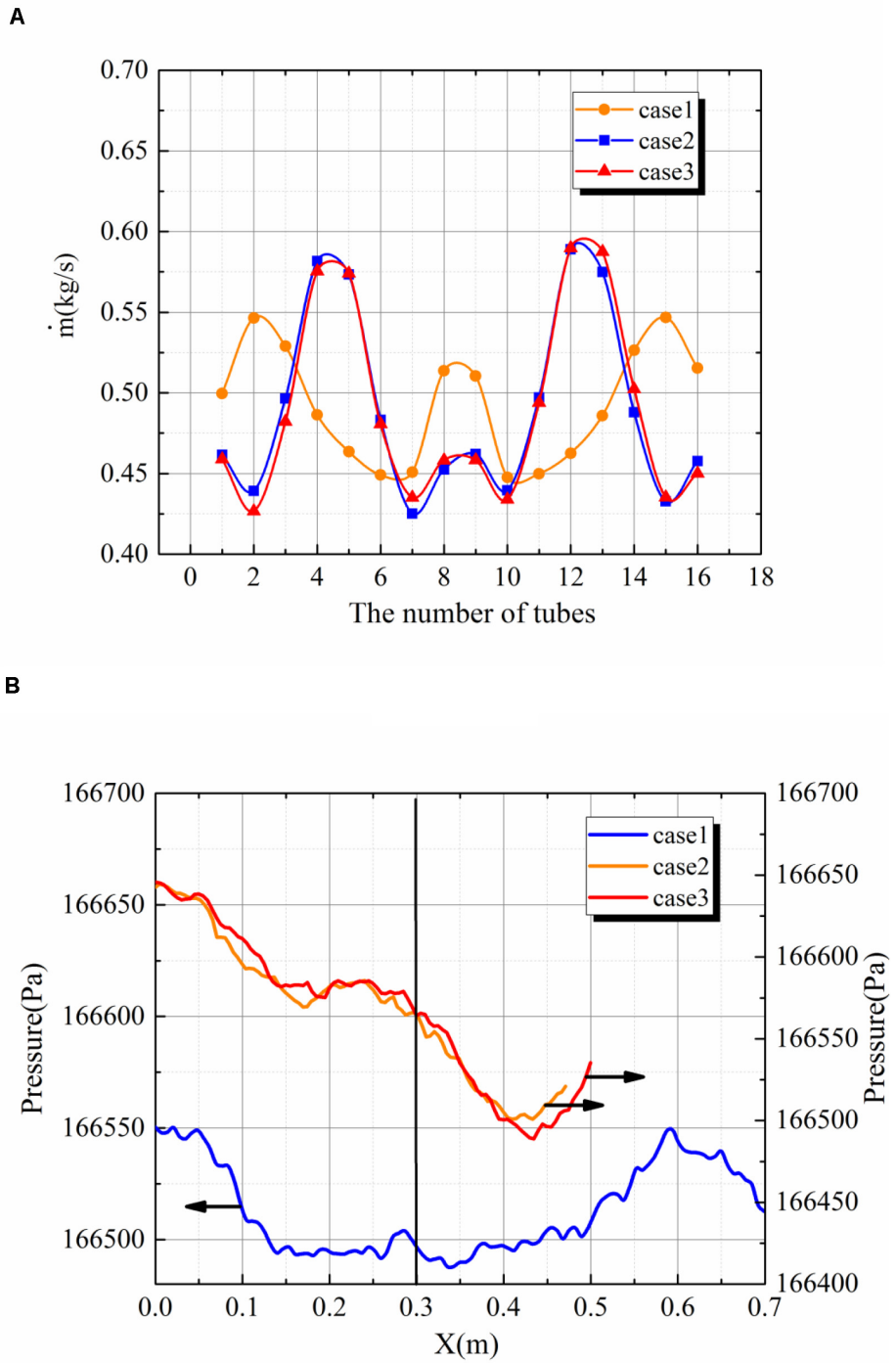


**FIGURE 3 | (A)** The flow distribution in tubes for case1, case2, and case3. **(B)** The pressure distribution in the dividing headers for case1, case2, and case3.

increase along the direction of the main stream as seen in **Figure 3B** for case1. However, for the case2 and case3, the pressure along the main flow direction decrease. Differently from the case1, the main stream is divided into two sides rather than one side as in the case1. And it will bring more local pressure loss, therefore, the pressure decreases along the main stream. This pressure distribution is different from the classic pressure distribution theory for the compact heat exchanger with the tube

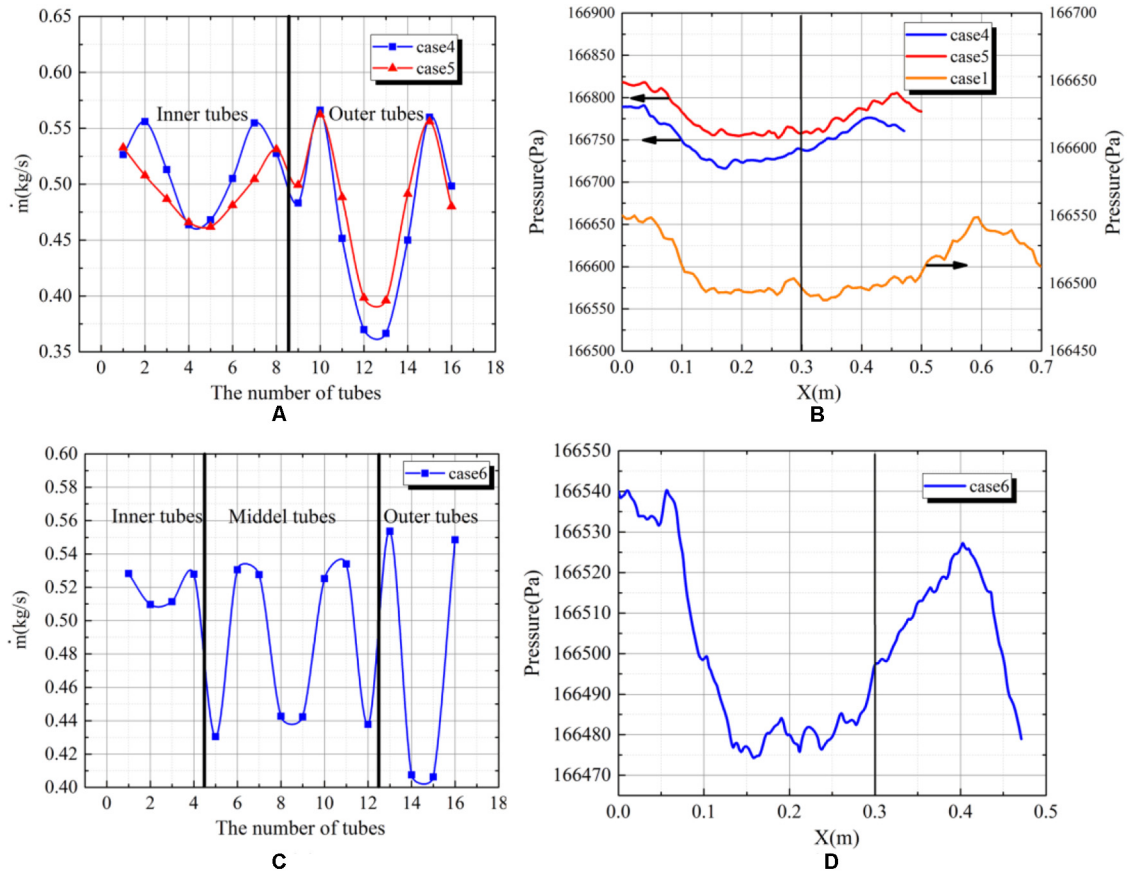


**FIGURE 4 | (A)** The flow distribution in tubes for case4 and case5. **(B)** The pressure distribution in the dividing headers for case1, case4 and case5. **(C)** The flow distribution in tubes for case6. **(D)** The pressure distribution in the dividing headers for case6.

arrangement at one side. And it shows that the discipline of the pressure distribution for compact heat exchanger will change with different tube arrangement.

## The Flow Distribution and the Pressure Distribution for Double-Row Arrangement

The **Figure 4A** shows the flow distribution for the case1, case4 and case5. For these three cases, tubes are all arranged at one side of the heat exchanger. For the case4 and case5, there are two rows of the tube, the length of the inner-row tube is less than that of the outer-row tube. And it is can be seen that the flow distribution in inner tubes are worse than that in outer tubes. Besides, the difference between the maximum flow and the minimum flow in outer tubes is larger than that in inner tubes. It is because that inlets of outer tubes is lower than inlets of inner tubes, therefore, the pressure at the inlet of outer tubes will be higher than inlets of inner tubes. And higher pressure means larger fluctuation in pressure distribution and worse flow distribution.

Comparing to the case1, the increase amplitude in pressure is bigger for the case4 and case5. And the difference in pressure distribution in the dividing header is mainly caused by the tube arrangement. Comparing to the case1, at each position of the tube, there are two tubes instead of one. And it means that the pressure recovery effect is bigger for the case4. For the case5, the staggered arrangement leads to a the smaller tube pitch than that for the case1. It means that along the direction of the main stream, the pressure will increase more quickly over unit distance. And it can be seen that in the **Figure 4B**, that the pressure is rising faster for the case4 and case5 than that for the case1. However, a quicker increase in the pressure contributes to a less uniform pressure distribution, then leads to a worse flow distribution.

## The Flow Distribution and the Pressure Distribution for Three-Row Arrangement

The **Figure 4C** shows the flow distribution for the case6. There are three rows of tubes, namely inner tubes, middle tubes and outer tubes. It can be seen that the flow distribution in outer tubes are more uniform than that in inner and middle tubes. It is similar to that for the case4 and case5. The positions of inlets of outer tubes are lower than that of inner tubes, therefore, the pressure fluctuation will be larger and contribute to a worse flow distribution. The **Figure 4D** shows the pressure distribution along the central line of the dividing header. Due to the more

densely tube arrangement, the pressure along the direction of the main stream rise more quickly. And most water flows into front tubes, therefore, at the area of behind tubes, the pressure recovery effect is small leading to a quick going down in pressure.

### The Pressure Loss for Different Tube Arrangements

Comparing to the case1, the case2 and case3 brings more pressure loss. It is because that the diversion of fluid to both sides bring more local pressure loss. For the case4 and case5. The more densely tube arrangement contributes to a more local pressure loss at the inlet of tubes. Comparing to the case4, the staggered arrangement for the case5 brings less local pressure loss than the aligned arrangement. For the case6, the more densely tube arrangement comparing to the case4 and case5, making a shorter length of the dividing header and the combining header. And the frictional pressure loss is decreased, therefore, the pressure loss for the case6 is less than that in case4 and case5.

## CONCLUSION

This study investigated the effects of six different tube arrangements on the flow distribution characteristics and pressure loss in the central-type heat exchanger. The conclusions are as follows:

1. Under the premise of fixed important geometrical dimensions such as header diameter, tube diameter, inlet and outlet diameter, etc., the tube arrangement has a significant effect on the flow distribution characteristics and resistance characteristics of the heat exchanger tubes.
2. Due to the larger header length for the case1, more frictional pressure drop is introduced to make the static pressure distribution in the header more uniform, and the flow distribution uniformity is the best among all cases.
3. For the single row arrangement on both sides of the heat exchanger, the pressure distribution is different from the classic pressure distribution theory for the compact heat exchanger with the tube arrangement at one side. The increase in pressure caused by the pressure recovery effect is less than the decrease in pressure caused by the local pressure loss. Therefore, the pressure decreases along the direction of the main stream rather than increase as in the classic pressure distribution theory for the compact heat exchanger with the tube arrangement at one side. And it shows that the discipline of the pressure distribution for compact heat exchanger will change with different tube arrangements.
4. For the case2 and the case3, the aligned and staggered tube arrangements show no apparent difference in flow distribution and the pressure loss of the heat exchanger.
5. For the double-row tube arrangement on one side of the heat exchanger such as case4 and case5, the staggered tube arrangement contributes to a more uniform flow distribution and the flow distribution coefficient has been decreased by 24%, comparing to the aligned tube arrangement.
6. For the double-row and three-row tube arrangement, the flow distribution is worse in outer tubes. Besides, the difference between the maximum flow and the minimum flow in outer tubes is larger than that in inner tubes.

**Nomenclature** (Zhou et al., 2017).

| | |
|---|---|
| $\Phi$ | Evaluation parameter of flow maldistribution |
| $k$ | turbulent kinetic energy |
| $\varepsilon$ | turbulent energy dissipation rate |
| $\rho$ | density of the working fluid |
| $u$ | velocity |
| $\sigma_k$, $\sigma_\varepsilon$ | turbulent constants |
| $\mu_t$ | turbulent dynamic viscosity |

## DATA AVAILABILITY STATEMENT

The datasets generated for this study are available on request to the corresponding authors.

## AUTHOR CONTRIBUTIONS

JZ finish this manuscript. ZM give some useful advice. ZS provide the guideline for the manuscript. All authors contributed to the article and approved the submitted version.

## REFERENCES


Acrivos, A., Babcock, B. D., and Pigford, R. L. (1959). Flow distributions in manifolds. *Chem. Eng. Sci.* 10, 112–124. doi: 10.1016/0009-2509(59)80030-0

Liu, H., and Li, P. (2013). Even distribution/dividing of single-phase fluids by symmetric bifurcation of flow channels. *Int. J. Heat Fluid Flow* 40, 165–179. doi: 10.1016/j.ijheatfluidflow.2013.01.011

Liu, H., Li, P., Jon, V. L., and Daniel, J. R. (2012). Experimental study of the flow distribution uniformity in flow distributors having novel flow channel bifurcation structures. *Exp. Therm. Fluid Sci.* 37, 142–153. doi: 10.1016/j.expthermflusci.2011.10.015

Liu, H., Li, P., and Lew, J. V. (2010). CFD study on flow distribution uniformity in fuel distributors having multiple structural bifurcations of flow channels. *Int. J. Hydrogen Energy* 35, 9186–9198. doi: 10.1016/j.ijhydene.2010.06.043

Said, S. A. M., Rached, B. M., Habib, M. A., and Siddiqui, M. U. (2014). Reducing the flow mal-distribution in a heat exchanger. *Comput. Fluids* 107, 1–10. doi: 10.1016/j.compfluid.2014.09.012

Shi, J. Y., Xiao, H. Q., Zhao, G. Q., and Chen, J. P. (2010). Effect of inlet manifold structure on the performance of the heater core in the automobile air-conditioning systems. *Appl. Therm. Eng.* 30, 1016–1021. doi: 10.1016/j.applthermaleng.2010.01.016

Wang, C. C., Yang, K. S., Tsai, J. S., and Ing, Y. C. (2011). Characteristics of flow distribution in compact parallel flow heat exchangers, part II: modified inlet header. *Appl. Therm. Eng.* 31, 3235–3242. doi: 10.1016/j.applthermaleng.2011.06.003

Wang, J., and Wang, H. (2015). Discrete method for design of flow distribution in manifolds. *Appl. Therm. Eng.* 89, 927–945. doi: 10.1016/j.applthermaleng.2015.06.069

Wei, M., Boutin, G., Fan, Y., and Luo, L. (2016). Numerical and experimental investigation on the realization of target flow distribution among parallel mini-channels. *Chem. Eng. Res. Des.* 113, 74–84. doi: 10.1016/j.cherd.2016.06.026

Wei, M., Fan, Y., Luo, L., and Gilles, F. (2015a). CFD-based evolutionary algorithm for the realization of target fluid flow distribution among parallel channels. *Chem. Eng. Res. Design* 100, 341–352. doi: 10.1016/j.cherd.2015.05.031

Wei, M., Fan, Y., Luo, L., and Gilles, F. (2015b). Fluid flow distribution optimization for minimizing the peak temperature of a tubular solar receiver. *Energy* 91, 663–677. doi: 10.1016/j.energy.2015.08.072

Ye, W. B. (2017). Design method and modeling verification for the uniform air flow distribution in the duct ventilation. *Appl. Therm. Eng.* 110, 573–583. doi: 10.1016/j.applthermaleng.2016.08.177

Yuan, P., Jiang, G. B., He, Y. L., Yi, X. L., and Tao, W. Q. (2013). Experimental study on the performance of a novel structure for two-phase flow distribution in parallel vertical channels. *Int. J. Mult. Flow* 53, 65–74. doi: 10.1016/j.ijmultiphaseflow.2012.05.006

Zhou, J., Ding, M., Bian, H., Zhang, Y., and Sun, Z. (2018). CFD simulation for the effect of the header match on the flow distribution in a central-type parallel heat exchanger. *Chem. Eng. Res. Des.* 136, 144–153. doi: 10.1016/j.cherd.2018.04.047

Zhou, J., Ding, M., Bian, H., Zhang, Y., and Sun, Z. (2019). Characteristics of flow distribution in central-type compact parallel flow heat exchangers with modified inlet and header. *Appl. Therm. Eng.* 166:114636. doi: 10.1016/j.applthermaleng.2019.114636

Zhou, J., Sun, Z., Ming, D., Bian, H., Nan, H., and Meng, Z. (2017). CFD simulation for flow distribution in manifolds of central-type compact parallel flow heat exchangers. *Appl. Therm. Eng.* 126, 670–677. doi: 10.1016/j.applthermaleng.2017.07.194

**Conflict of Interest:** YY was employed by company Research and development Center, China Nuclear Power Engineering.

The remaining authors declare that the research was conducted in the absence of any commercial or financial relationships that could be construed as a potential conflict of interest.

frontiers in Energy Research

METHODS
published: 19 August 2020
doi: 10.3389/fenrg.2020.00188

# An Improved Best Estimate Plus Uncertainty Method for Small-Break Loss-of-Coolant Accident in Pressurized Water Reactor

*Dabin Sun, Zhijian Zhang*, Xinyu Li, Lei Li, He Wang, Anqi Xu and Sijuan Chen*

*Fundamental Science on Nuclear Safety and Simulation Technology Laboratory, Harbin Engineering University, Harbin, China*

Best estimate plus uncertainty (BEPU) analysis method has been widely used to analyze various transient accidents of pressurized water reactor (PWR). However, the traditional BEPU method has some limitations: (1) The input parameters are not clearly defined, resulting in inaccurate conclusions in the sensitivity analysis. (2) The uncertainty quantification and sensitivity analysis usually share the same set of samples, but they have different requirements for the sample size. In this work, an improved BEPU method is proposed, which can alleviate the above defects. The improved BEPU method possesses the following two characteristics: (1) The sensitivity analysis is performed for the steady-state and transient calculation, respectively. It provides more comprehensive results than does the traditional BEPU method. (2) The sensitivity analysis is performed before the uncertainty analysis to reduce the number of uncertainty analysis inputs. A small-break loss-of-coolant accident (SBLOCA) is simulated by Reactor Excursion and Leak Analysis Program (RELAP) 5 to verify the accuracy and applicability of the improved BEPU method. By the sensitivity analysis, the coolant pump inlet roughness, main flow rate, core heat channel temperature, break area, and PRZ pressure have moderate or higher relationships with the peak core outlet temperature. The fission product yield factor has a moderate positive relationship with the peak cladding temperature (PCT). The sensitivity analysis by the improved BEPU method shows that the peak core outlet temperature has strong relationships with main flow rate, core heat channel temperature, and PRZ pressure, which is not captured by the traditional BEPU method. As a result, it is more reasonable to take steady-state parameters as inputs in the sensitivity analysis of transient. Only those parameters with high correlation coefficients are sampled for uncertainty analysis. Meanwhile, the results of the uncertainty analysis obtained by the improved BEPU are consistent with the results of the traditional method. Neither the PCT nor the peak core outlet temperature will exceed their limits. The results illustrate that the improved BEPU method can reduce the size of samples but maintains the desired accuracy.

**Keywords: best estimation, sensitivity analysis, uncertainty analysis, small-break loss-of-coolant accident, pressurized water reactor, Reactor Excursion and Leak Analysis Program 5**

OPEN ACCESS

***Edited by:***
*Jun Wang,*
*University of Wisconsin-Madison, United States*

***Reviewed by:***
*Muhammad Saeed,*
*East China University of Technology, China*
*Jiankai Yu,*
*Massachusetts Institute of Technology, United States*

****Correspondence:***
*Zhijian Zhang*
*zhangzhijian_heu@hrbeu.edu.cn*

***Specialty section:***
*This article was submitted to Nuclear Energy, a section of the journal Frontiers in Energy Research*

***Received:*** *29 May 2020*
***Accepted:*** *15 July 2020*
***Published:*** *19 August 2020*

***Citation:***
*Sun D, Zhang Z, Li X, Li L, Wang H, Xu A and Chen S (2020) An Improved Best Estimate Plus Uncertainty Method for Small-Break Loss-of-Coolant Accident in Pressurized Water Reactor. Front. Energy Res. 8:188. doi: 10.3389/fenrg.2020.00188*

## INTRODUCTION

Effective safety analysis of nuclear power plant (NPP) operations and accident scenarios are usually performed by the best estimate (BE) system codes, such as Reactor Excursion and Leak Analysis Program (RELAP) 5 (Martin, 1995; Rockville, 2001), CATHARE (Barre and Bernard, 1990), and TRACE (NR Commisson, 2010; Berar et al., 2013). To ensure sufficient safety margin for the design and operation of NPPs, conservative hypothesis is widely used in this field. However, overconservatism will make the analysis results and safety standard deviate from the actual operating conditions, which seriously impacts the benefits of NPPs (Jamali, 2015). Therefore, in 1988, the US Nuclear Regulatory Commission (NRC) revised the Emergency Core Coolant System (ECCS) guidelines in 10CFR50.46 to allow the use of the "best estimate plus uncertainty" (BEPU) method for safety analysis of NPPs (Ibarra, 1988; Gupta et al., 2013). According to the definition of BEPU given by the International Atomic Energy Agency (IAEA), there are three principles that should be observed (IAEA, 2002). (1) No pessimism is imported into the accident for the selected acceptance criteria; (2) use the best estimation procedure; and (3) perform uncertainty analysis on the calculation results. Following these principles, the BEPU method can obtain results that are very significant for the design and operation of NPPs. The comparison of uncertainty analysis to assess safety margins (Luo, 2012) with other traditional methods is shown in **Figure 1**. The upper limit values of BEPU method can be lower than the results of Appendix K (Wang et al., 2017) and conservative method, which is of benefit to the economics of nuclear power plants.

For the BEPU method, there are many theoretical systems for typical input uncertainty parameters, such as CSAU (Boyack et al., 1990) in the United States, GRS (Glaeser, 2008) in Germany, and KINS-REM (KINS, 2005) in South Korea. The CSAU evaluation method developed by the NRC in 1989 is a systematic and integrated method that integrates accidents, tests, procedures, and power plants. Moreover, it can be used to quantify the uncertainty of complex systems. It provides a complete and logical analysis framework for the BEPU method and establishes an important foundation for the subsequent uncertainty analysis methods. The common process of BEPU is as follows (Helton and Davis, 2003): (1) Latin hypercube sampling (LHS) or other sampling methods are used to generate a set of samples. (2) The system simulations are performed with the above samples to the results. (3) Uncertainty analysis

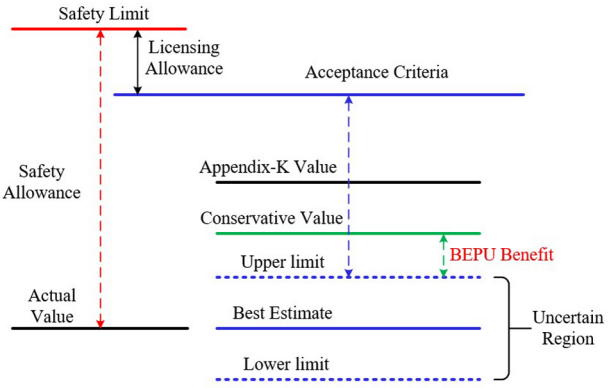


**FIGURE 1 |** Comparison of safety margins in evaluating different methods.

of the results is then performed to obtain the range of the parameters. (4) The relevance between input parameters and output parameters is conducted by the sensitivity study. In procedures (1) and (4), non-parametric sampling and testing based on the Wilks (Wilks, 1941) formula are commonly used, and sensitivity is evaluated with some correlation coefficients such as Pearson's coefficient (Coefficient, 1996) or Spearman's coefficient (Sedgwick, 2014).

Owing to the complexity and particularly serious consequences of the loss-of-coolant accident (LOCA) in pressurized water reactor (PWR), it is necessary to perform a more accurate analysis of the LOCA on the basis of the BEPU method. Ni C (CN, 2011) found that the peak cladding temperature (PCT) in the large-break LOCA (LBLOCA) of the AP1000 was still under the safety limit even with uncertainty. Zhikang et al. (2016) analyzed the LBLOCA of CPR1000, and he showed that although the input uncertainty will make the PCT higher than the best estimate, there is still a large margin to the safety limit. However, it was noted in the classic probabilistic safety assessment (PSA) analysis report WASH-1400 (Rasmussen, 1975) that small-break LOCA (SBLOCA), not LBLOCA, was the main factor resulting in the core melt accident. Many researchers used the BEPU method to analyze SBLOCA. Sanchez-Saez et al. (2017) presented a methodology and the application to G7.1 experiment. They performed uncertainty analysis of PKL SBLOCA G7.1 test simulation using TRACE with Wilks' and GAM surrogate methods and found that for larger sample sizes, GAMPE and Wilks' results present similar performance. Deng et al. (2019) accomplished an uncertainty analysis on the scaled passive system SBLOCA and found that key parameters such as the lowest core level of the reactor core remained above the safety limit.

Although some progress has been made on the SBLOCA uncertainty analysis of NPPs, the previous research still has some imperfections. In the process of researching the uncertainties and sensitivities of the input parameters, many scholars usually first studied the uncertainties and then carried out a sensitivity analysis (Perez et al., 2011; Gupta et al., 2013; Ghione et al., 2017;

**Abbreviations:** ACC, Accumulator; BE, Best Estimate; BEPU, Best estimate plus uncertainty; CSAU, Code scaling, applicability, and uncertainty; ECCS, Emergency core cooling system; FOM, Figure of merit; GRS, Gesselschaft für Anlagen und ReaktorsicherheitmbH; HPIS, High-pressure injection system; IAEA, International Atomic Energy Agency; IRWST, In-containment Refueling Water Storage Tank; KINS, Korea Institute of Nuclear Safety; KINS-REM, KINS-realistic evaluation methodology; LBLOCA, Large-break loss-of-coolant accident; LHS, Latin hypercube sampling; LOCA, Loss-of-coolant accident; LPIS, Low-pressure injection system; NPP, Nuclear power plant; NRC, Nuclear Regulatory Commission; PCT, Peak cladding temperature; PIRT, Phenomena Identification and Ranking Table; PWR, Pressurized water reactor; RCS, Reactor coolant system; RCSS, Reactor containment spray system; RELAP, Reactor Excursion and Leak Analysis Program; SBLOCA, Small-break loss-of-coolant accident; SI, Safety injection.

Sanchez-Saez et al., 2017; Wang et al., 2017, 2019; Sanchez-Saez et al., 2018). This order can share the same set of sampling parameters, which saves the sampling cost. However, there are some disadvantages in terms of computational efficiency and correlation analysis results.

1. The process of debugging in steady-state calculation is complicated, and the fluctuation of parameters may lead to the failure of convergence. The more parameters are changed, the more likely the system simulation program (e.g., RELAP5) will not to converge. This may produce a part number of invalid outputs that will be culled in uncertainty analysis, which wastes the samples and interferes with their statistical properties. Besides, it is difficult to know the distribution and probability density functions (PDFs) of various parameters accurately.
2. The definition of input parameters is not clear in the transient calculation. The "input" parameters of transient calculation are derived from the output of steady state, not directly from the input file. There is a significant difference in the calculation process between the system simulation program (e.g., RELAP5 and SAS-DIF3DK) (Dunn, 1999) and numerical calculation software [e.g., the particle transport code (MCNP) (Briesmeister, 1993)] and the computational fluid dynamics (CFD) software (FLUENT; ANSYS Inc, 2013, etc.). The input parameters, such as boundary conditions (wall temperature, wall heat flux, etc.) in the CFD will not change during the whole calculation process (Dunn et al., 2010; Cutrono Rakhimov et al., 2019; Dubois et al., 2019; Rakhimov et al., 2020). Therefore, CFD-based uncertainty analysis need not consider the change of input parameters. However, the system simulation program will modify the initial parameters to achieve steady-state operating conditions before performing transient calculations. The output of steady state may be introduced into the relationship even if the initial values are independent of each other. Some work only analyzed the initial parameters and the transient output and obtain the relevance between them (Ghione et al., 2017; Deng et al., 2019). Such conclusions only reflect the relevance between inputs and outputs from "user-input" to "transient computations," rather than the relevance between the actual physical process.
3. Relationships between input parameters may be overlooked during sampling. For example, core power and coolant temperature are related in the physical process, but simple random sampling treats them as an independent. However, it should be noticed that the Wilks formula can only be applied to an independent random sample (Porter, 2019).

In summary, the traditional BEPU method, in which uncertainty analysis was followed by the sensitivity analysis, results in lower analysis efficiency. Excessive numbers of samples may increase the number of failed processes in RELAP, which will interfere with the distribution of output. Besides, the definition of input parameters is not clear in the transient calculation, which leads to a misunderstanding of the relationship between input and output parameters.

In this work, the process in steady state and the SBLOCA transient of PWR are analyzed based on an improved BEPU method. To improve the efficiency of the analysis, the sensitivity analysis with small sample size based on Wilks' formula and LHS method is firstly adopted to find the key parameters with strong relationships, Afterward, uncertainty analysis is carried out, and the propagation law of uncertainty in the transient calculation process is illustrated. Furthermore, the traditional BEPU method is used to analyze and compare the results to show the rationality of the improved BEPU method. In this paper, section "Methodologies" establishes the RELAP5 code for a PWR (Yangyu, 2000). Section "Description and Modeling of the Pressurized Water Reactor" accomplishes the analysis of sensitivity and uncertainty with the improved BEPU method. Conclusions and discussions are illustrated in section "Sensitivity Analysis and Uncertainty Analysis."

# METHODOLOGIES

## Improved Best Estimate Plus Uncertainty Method

**Figure 2** shows the main process of the improved BEPU method, which partly referred to Sanchez's work (Sanchez-Saez et al., 2018). The improved BEPU framework consists of 11 steps, in which the order of the sensitivity analysis and uncertainty quantification is swapped.

1. Select the accident scenario and research objects. There are different event sequences and key safety parameters in diverse accidents, which are closely related to a specific power plant system. Therefore, identifying accident scenarios and research objects is a prerequisite for the analysis.
2. Select the figure of merit (FOM). Important output parameters are usually selected as the indicators to evaluate the safety of NPP. The PCT and the peak core outlet temperature are selected as the FOMs.
3. Reference the Phenomena Identification and Ranking Table (PIRT) (Wilson and Boyack, 1998). In the PIRT, the important phenomena and parameters in accident analysis are mainly based on some selective calculations and judgments of experts, which is important guidance for the input parameters in the BEPU method.
4. Identify the key systems. Diverse systems are involved in different accident processes. The key systems under specific accident processes are identified to improve the modeling efficiency and ensure the accuracy of the calculation.
5. Determine the sequence of events. It ensures that the accident process of the model is consistent with that of the nuclear power plant.
6. Complete modeling. A model of NPP that meets the requirements of the simulations is established.

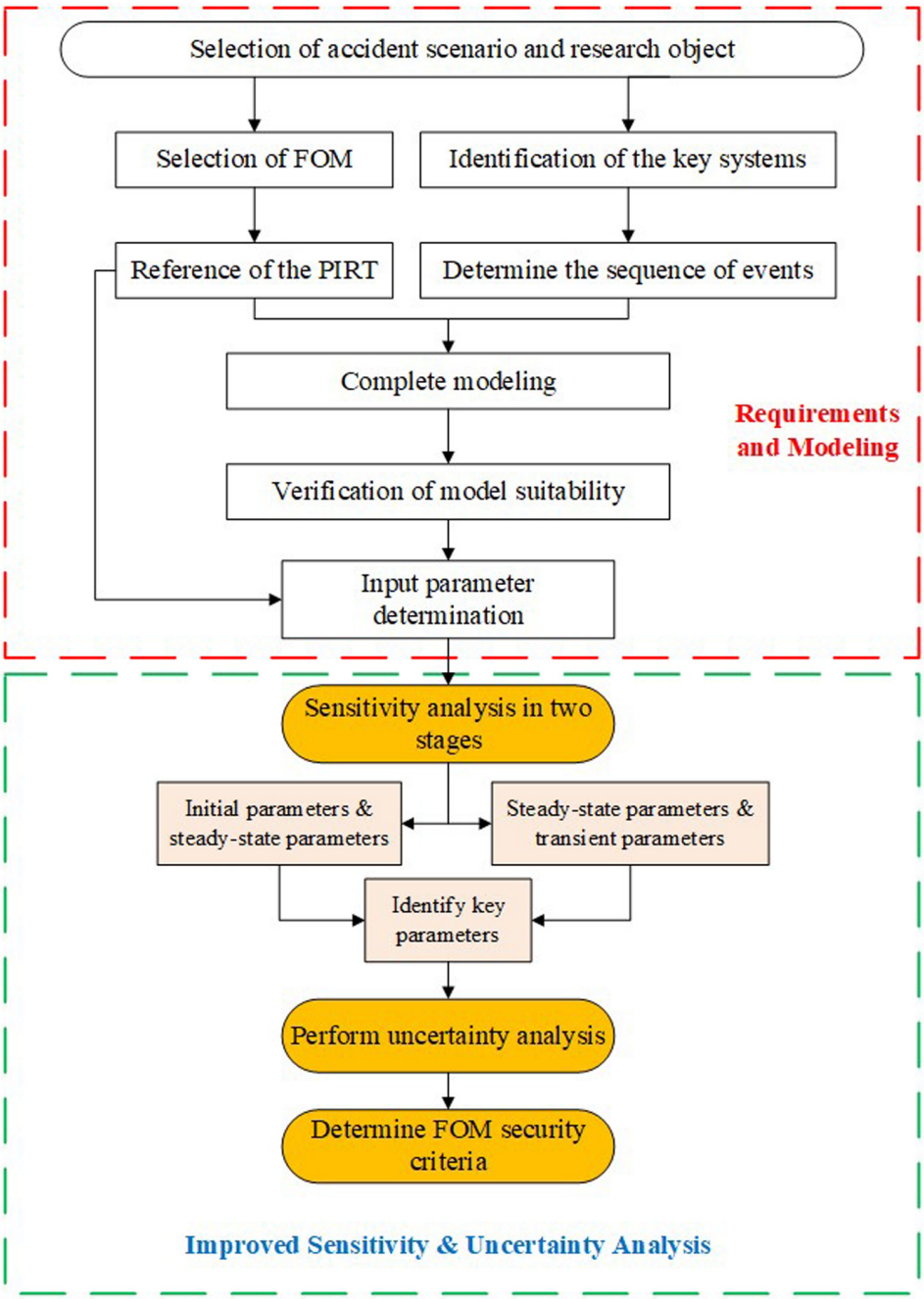


**FIGURE 2 |** The framework of the improved best estimate plus uncertainty analysis (BEPU) method.

7. Verify the applicability of modeling. To ensure the accuracy of the calculation, the model needs to be analyzed in steady-state and transient-state calculations. The results are supposed to be consistent with some nominal values (Zhujian and Shoulv, 1992; Jizhou et al., 2004) to prove that the model is appropriate.
8. Determine the input parameters with uncertainties. This work mainly researches the uncertainty of input parameters, and their distributions are determined through PIRT and related literature research (Zhujian and Shoulv, 1992; Gupta et al., 2013; Sanchez-Saez et al., 2017).
9. Perform the sensitivity analysis to identify the key parameters. There are two stages involved during the sensitivity study in the improved BEPU method: (1) the sensitivity analysis between initial parameters and steady-state parameters and (2) the sensitivity analysis between steady-state parameters and transient parameters. The sensitivity analysis is firstly performed to reduce

the number of inputs. Hence, only the key input parameters that have a significant impact on the calculation results are identified.

10. Perform uncertainty analysis. The range and propagation laws of uncertainties are obtained by analyzing the results.
11. Determine FOM security criteria. The confidence interval of the parameter is generated. The output parameters are verified whether they conform to the FOM.

## Sampling and Statistical Methods

An important part of analyzing the propagation of uncertainty is the application of LHS. LHS is more stable than random sampling to produce distribution in a smaller sample space, which saves costs of computing (Helton and Davis, 2003). The rationality of LHS can be realized when the sample space is greater than 4/3 times the number of inputs (Helton and Davis, 2003; CN, 2011). In this work, 15 input parameters introduced uncertainties. As a result, in the sensitivity analysis, it is only necessary to ensure that the sample space of each parameter is greater than 20(15 * 4/3). The specific numbers of the sample are given in detail below.

However, in the uncertainty analysis, because the non-parametric statistical method based on Wilks' formula is adopted, a certain number of samples must be satisfied (Zhikang et al., 2016). Because this work outputs multiple parameters at the same time, the improved version of Wilks' formula (Guba et al., 2003) is applied as shown in Eq. (1). The formula can be described as follows. For all values of any variable, at least a portion $\gamma$ of them is within the confidence interval, with the probability of $\beta$. "$p$" represents the number of variables and "$N$" represents the size of samples.

$$\beta = \sum_{j=0}^{N-p} \frac{N!}{(N-j)!j!} \gamma^j (1-\gamma)^{N-j} \tag{1}$$

$$\begin{cases} p = 2 \\ \beta = \gamma = 0.95 \end{cases}$$

The output parameters used to analyze the uncertainty include two parameters: the peak core outlet temperature and the lowest core level. Hence, $p$ is equal to 2, and $N$ is equal to 93. The sample space must be at least 93 to make reasonable uncertainty analysis of these two variables. According to Wilks' theory in non-parametric test, 93 samples of output are enough to satisfy the upper boundary at the 95% confidence level with 95% probability, and vice versa.

Spearman's coefficient is used to evaluate the sensitivity as shown in Eq. (2). It evaluates the relationships by rank rather than the original data. $N$ is the number of samples (Sedgwick, 2014),

$$\text{corr}\,(X_i, Y_i) = 1 - \frac{6\sum d_i^2}{N(N^2-1)} \tag{2}$$

$$d_i = X_i - Y_i$$

The closer the correlation coefficient $\text{corr}(x_i, y_i)$ is to $+1$, the greater the positive relationship between the parameters, and vice

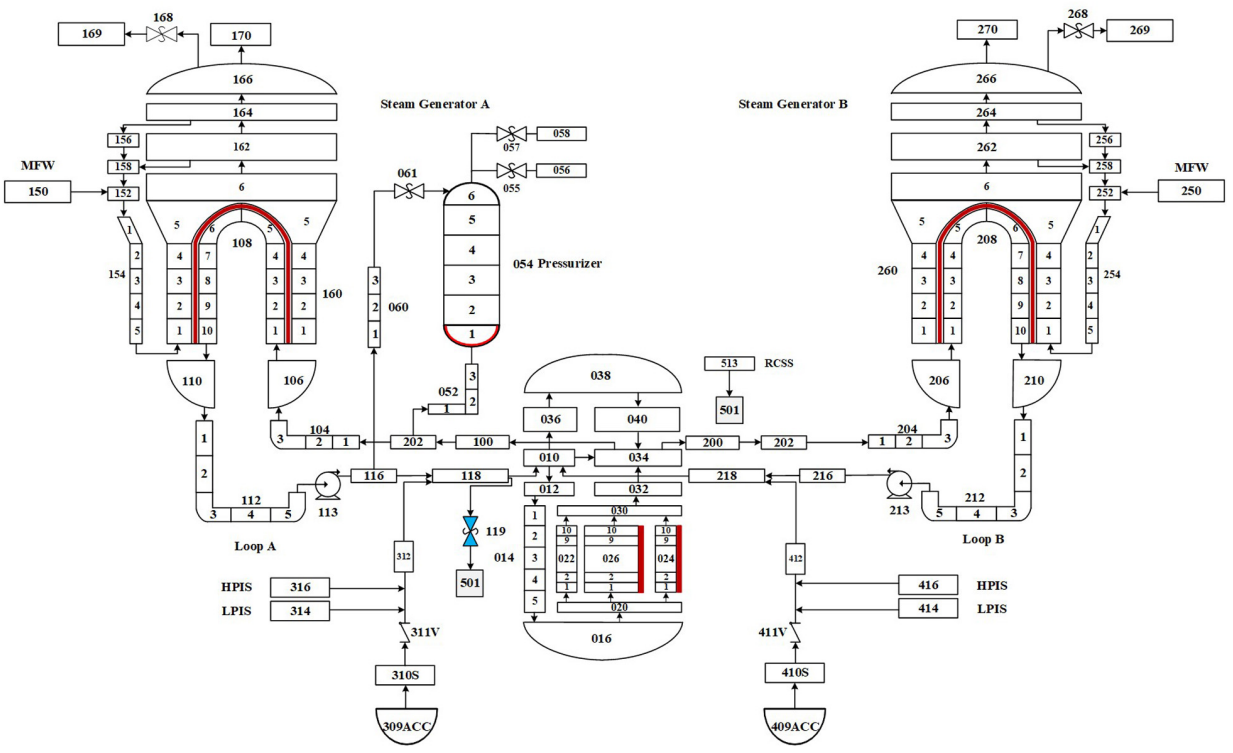


**FIGURE 3 |** The RELAP5 model nodalization.

versa. There are some guidelines for the relationship classification (Pawel and Mesina, 2011).

(1) $|\mathrm{corr}(x_i, y_i)| \in [0.7, 1.0]$ illustrates that the parameters $(x_i, y_i)$ have a strong relationship.
(2) $|\mathrm{corr}(x_i, y_i)| \in [0.3, 0.69]$ illustrates that the parameters $(x_i, y_i)$ have a medium relationship.
(3) $|\mathrm{corr}(x_i, y_i)| \in [0.0, 0.29]$ illustrates that the parameters $(x_i, y_i)$ have a weak relationship.

## DESCRIPTION AND MODELING OF THE PRESSURIZED WATER REACTOR

Based on RELAP5, this work establishes a model for a typical PWR as illustrated in **Figure 3**. The model is composed of the primary loop system, the necessary secondary equipment, and the dedicated safety facilities involved in SBLOCA. The primary loop system adopts a two-inlet–two-outlet layout structure, and each loop consists of one hot leg, one cold leg, one steam generator, and one pump. The high-pressure injection system (HPIS), accumulator (ACC) injection system, low-pressure injection system (LPIS), and reactor containment spray system (RCSS) are installed to perform SBLOCA.

### Best Estimate Calculation of the Steady State

The specific goal of steady-state verification is to ensure that the steady-state value calculated by the simulation is sufficiently close to the nominal operating value of the NPP (Rockville, 2001). To ensure that the deviation between the main steady-state operating values and the target values is small enough, certain parameters (e.g., drag coefficients) are adjusted before the accident simulation. The comparison of the values obtained by RELAP5 in steady state and the nominal value of the NPP is listed in **Table 1**. The results illustrate that the calculated values are anastomotic with the nominal values of the key parameters of NPP operation.

### Best Estimate Calculation of the Small-Break Loss-of-Coolant Accident Transient

For this model, the nominal value of the break area is 0.0085 $m^2$, which is an example to represent a small size break in SBLOCA (Murray, 1987; Jinhan and Fei, 1998). Pressure drop can be limited by isolating the steam generator, isolating the break, or increasing the flow of HPIS. The break is simulated by adding a time-controlled trip valve and a time-dependent control volume connected to the cold leg with the pressurizer.

The transient calculation is performed based on the converged steady-state calculation. **Table 2** shows the sequence of events for the SBLOCA transient simulated by RELAP5. At 0 s, a break appears in the cold leg and an "S" signal is issued simultaneously. After 3 s, the reactor control rods drop. Three more seconds later, the main steam is isolated, and the main feedwater system stopped at the same time. To ensure that the core can be cooled, the HPIS starts when the pressure of the primary loop system drops to 12.25 MPa. The ACC injection is triggered after getting a lower pressure signal. To maintain the integrity of the reactor vessel, when the internal pressure of the vessel rises to 0.147 MPa, the RCSS starts to reduce the pressure. With the consumption of the security system of the cooling water, when the level of the refueling water tank drops to 2.26 m, the water source of the HPIS and the RCSS will be converted into pit water to realize the

**TABLE 1 |** Comparison of calculated and nominal values of the key parameters during the nuclear power plant (NPP) operation.

| System parameters | Calculated values | Nominal values |
|---|---|---|
| Reactor power (MW) | 970 | 966 |
| Core inlet temperature (K) | 559.5 | 562.0 |
| Core outlet temperature (K) | 586.0 | 588.4 |
| PRZ pressure (MPa) | 15.2 | 15.2 |
| Secondary pressure (MPa) | 5.2 | 5.2 |
| Main steam flow rate (kg/s) | 260.4 | 259.9 |
| Main coolant flow rate (kg/s) | 6, 660.8 | 6, 666.7 |

**TABLE 2 |** Event sequence of SBLOCA transient.

| Events | Postulated setpoint | Action time (s) |
|---|---|---|
| Break opens | $t$ = 0 s | $t$ = 0 |
| Reactor stops | PRZ pressure < 12.74 MPa | $t$ = 6 |
| Main pumps stop | Reactor stops | $t$ = 6 |
| Main steam isolates | Reactor stops | $t$ = 6 |
| Main feed water stops | Reactor stops | $t$ = 6 |
| HPIS starts | PRZ pressure < 12.25 MPa | $t$ = 7 |
| RCSS starts | Vessel pressure > 0.147 MPa | $t$ = 53 |
| ACC injection starts | PRZ pressure < 4.90 MPa | $t$ = 429 |
| LPIS starts | PRZ pressure < 0.98 MPa | $t$ = 1,671 |

*SBLOCA, small-break loss-of-coolant accident; HPIS, high-pressure injection system; RCSS, reactor containment spray system; ACC, accumulator; LPIS, low-pressure injection system.*

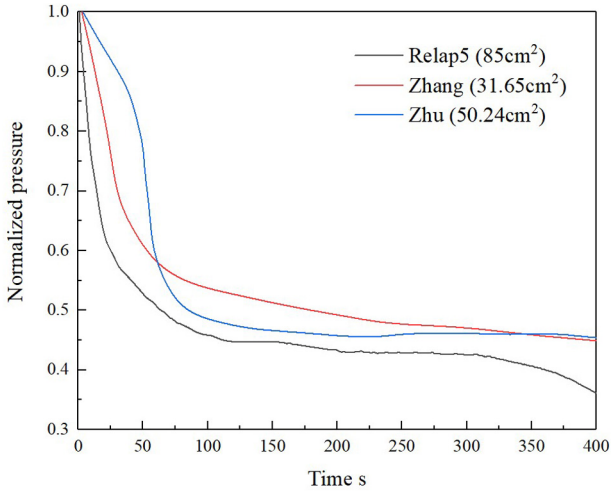


**FIGURE 4 |** PRZ pressure in small-break loss-of-coolant accident (SBLOCA).

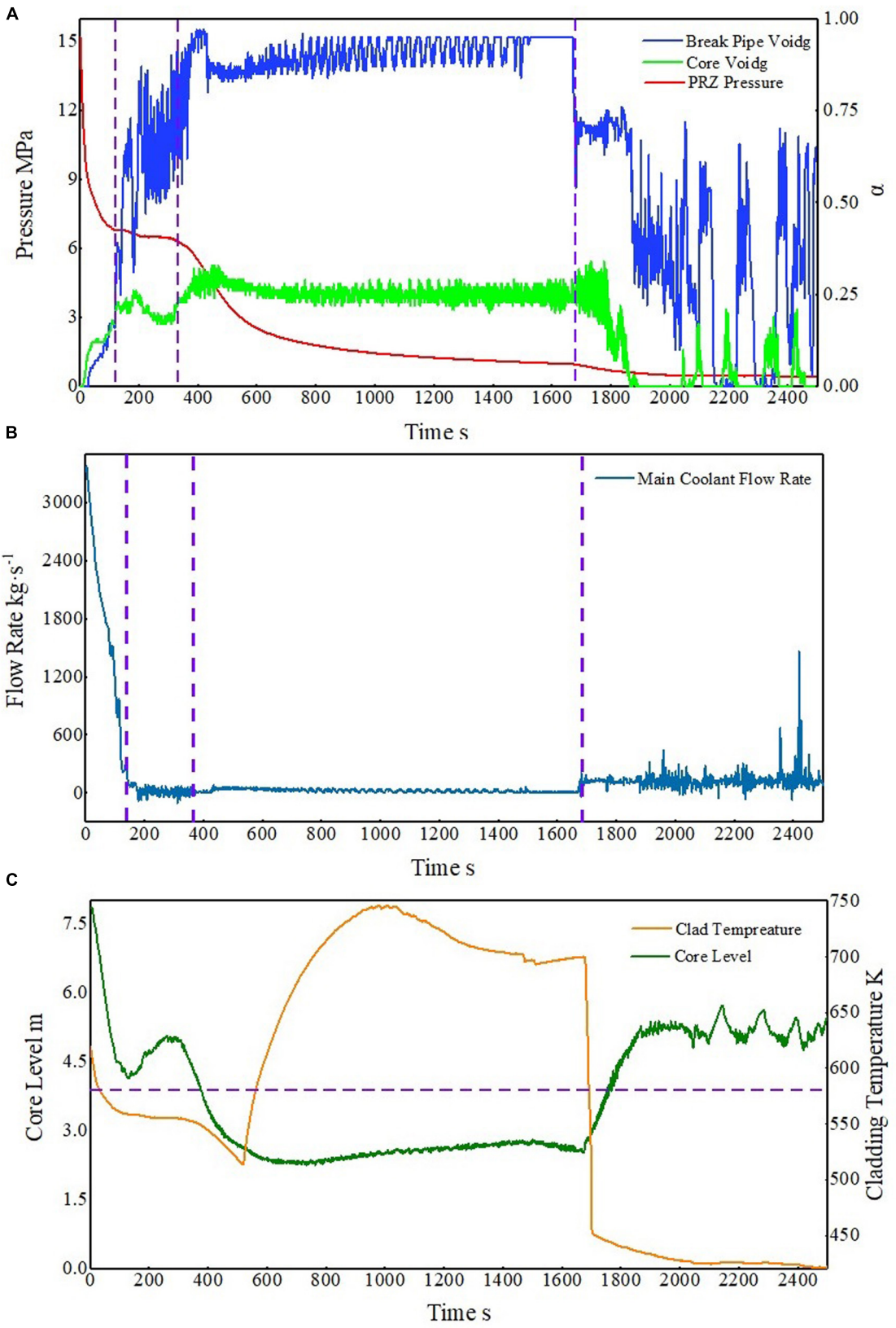


**FIGURE 5 |** The process of small-break loss-of-coolant accident (SBLOCA). **(A)** Trends in pressure and quality of gas mixture. **(B)** Trends in main flow rate. **(C)** Trends in core level and clad temperature.

recycling of cooling water. When the level of the refueling water tank drops to 2.26 m, the water source of the HPIS and RCSS is converted into pit water.

The pressure of the system obtained during the transient simulation is compared with some nominal values (Zhujian and Shoulv, 1992; Jizhou et al., 2004). As illustrated in **Figure 4**, during the transient analysis of SBLOCA simulated by RELAP5 with different sizes of the breaks, the overall trend of pressure drop of the primary loop system is similar for all cases.

The different sizes of the breaks lead to the variation in the pressure drop rate. In the initial stage, the primary loop system pressure drops rapidly owing to the rapid leakage of coolant. The HPIS starts to inject coolant into the primary circuit after a period, which offsets the depressurization. Besides, the increasing pressure inside the containment vessel makes a pressure balance between the inside and outside of the coolant loop.

In this work, the process of SBLOCA is divided into four stages as illustrated in **Figure 5**, which are separated by vertical dashed lines, and the core height is indicated by the horizontal dashed line. They are spray stage, natural cycle stage, coolant seal stage, and long-term cooling stage.

### Spray Stage

At the initial stage of the break, the primary loop pressure drops rapidly owing to the loss of the coolant. This is because the break area is close to 90 $cm^2$, which has reached between the medium-size small break and the large-size small break (Pingan et al., 2002). The effect of underheat pressure relief is more obvious, so the pressure decreases faster but not fast enough for ACC to start in time. As the pressure drops in the primary loop, the reactor and main pump shut down. Owing to the supercooling of the coolant, even if the pressure of the primary loop drops rapidly, the subcooled spray sustains for 26 s. After that, the process enters the saturation spray stage. At this stage, the break flow is so large that the primary loop pressure constantly decreases. Because the break is located between the core and IS, it is difficult for the coolant to be injected into the core. Because of the loss of the injection coolant from the break, the void fraction of the core keeps rising and the water level of the core constantly drops.

### Natural Cycle Stage

The natural cycle stage comes after the spray stage. At this stage, the primary coolant pressure tends to be stable, which is called "pressure platform" (Jizhou et al., 2004), and the break flow decreases. Because of that, a small part of injection coolant can enter the core. The void fraction of the core decreases, and the water level rises caused by the cooling effect of this part of injection coolant.

### Coolant Seal Stage

At this stage, only a small part of the coolant flows into the break loop. The "pressure platform" disappears, and the pressure begins to drop rapidly. At the beginning of this stage, the HPIS flow is less than the break flow, and there is no effective injection coolant entering the core. Nucleate boiling in the core heat channel can effectively discharge the decay heat, which makes the cladding temperature and the core water level decrease simultaneously. Then, owing to the large flow resistance, the steam cannot be discharged from the reactor core in time, which makes the boiling condition change and the deterioration of heat transfer. Because of this process, the cladding temperature rises. With the decrease of the primary loop pressure, the ACC injection system operates. More injection flows into the core, which leads to the core water level gradually stabilizing and increasing. After the lowest core water level, the thermal channel PCT appears, and then it decreases with the injection of the coolant. Because the flow of the ACC injection is driven by differential pressure, after about 1,500 s, the flow rate of the ACC decreases, and the temperature of the cladding begins to rise. After about 1,700 s, the primary loop pressure decreases to 0.98 MPa. Meanwhile, the LPIS operates. A large amount of coolant is injected into the core, and the cladding temperature plunges.

### Long-Term Cooling Stage

A large amount of coolant is injected into the core by LPIS, which quickly submerges the reactor core.

## SENSITIVITY ANALYSIS AND UNCERTAINTY ANALYSIS

## Sensitivity Analysis

There are generally two main stages for accident analysis in RELAP5. Firstly, the steady-state calculation is performed based on the initial parameters to obtain the steady-state

**TABLE 3 |** Input parameters for sensitivity analysis.

| Parameter | Nominal | Distribution | Uncertainty range |
|---|---|---|---|
| **Initial and constant boundary conditions** | | | |
| Fission product yield factor | 1 | Uniform | 1–1.2 |
| ACC initial temperature (K) | 315 | Uniform | 310.5–319.5 |
| ACC initial volume ($m^3$) | 20 | Uniform | 19–21 |
| ACC initial pressure (MPa) | 4.9 | Uniform | 4.8–5.0 |
| Break area ($10^{-3}$ $m^2$) | 8.5 | Uniform | 8.0–9.0 |
| HPIS flow rate (kg/s) | 6.25 | Uniform | 6.1–6.4 |
| **Initial conditions** | | | |
| Initial PRZ pressure (MPa) | 15.2 | Uniform | 14.6–15.8 |
| Initial core power (MW) | 970 | Uniform | 969.5–970.5 |
| Initial main flow rate (kg/s) | 3333 | Uniform | 3300–3366 |
| Initial core heat channel temperature (K) | 600 | Uniform | 580–620 |
| **Hydraulic constants** | | | |
| Coolant pump inlet roughness | 1 | Uniform | 0.92–1.08 |
| Core heat channel roughness ($10^{-6}$) | 1 | Uniform | 0.95–1.05 |
| Core bypass roughness ($10^{-6}$) | 1 | Uniform | 0.95–1.05 |
| ACC roughness | 1 | Uniform | 0.90–1.10 |
| Break roughness | 1 | Uniform | 0.85–1.15 |
| **Properties of the materials** | | | |
| Core fuel gap thermal conductivity [W/(m·K)] | 0.95 | Gaussian | 0.95 ± 0.05 |
| Core fuel gap heat capacity (J/K) | 4.36 | Gaussian | 4.36 ± 0.05 |

*ACC, accumulator; HPIS, high-pressure injection system.*

parameters. Then, the transient calculation is simulated based on the aforementioned steady-state results. The traditional BEPU method usually combines the above two stages to analyze the sensitivity between the initial parameters and the transient results. However, for a more comprehensive analysis of sensitivity, the steady-state and transient analyses is performed individually. As a result, the following two stages are involved during the sensitivity study in the improved BEPU method.

(1) The sensitivity analysis between initial parameters and steady-state parameters.
(2) The sensitivity analysis between steady-state parameters and transient parameters.

In the first stage, the combined effects from RELAP5 and the initial parameters on the steady-state parameters can be researched. Afterward, the relationships between steady-state parameters and transient output parameters can be found in the second stage. Eventually, the third stage is used to study the relationship between initial parameters and the transient parameters.

The safety facilities are put into operation after the accident occurred so that the accident-related parameters listed in **Table 3** do not participate in the first stage, while the hydraulic constants and properties of the materials have been participating in all stages of calculation and analysis.

For the sensitivity analysis, 15 input parameters are adopted and summarized in **Table 3**. For undisclosed parameters, such as configurations of ACC, HPIS, and pump, common values are used and corresponding uncertainties and PDFs are introduced. For the roughness that has been adjusted many times, it is adopted as the expectation, and corresponding uncertainty is introduced. The value of this roughness can make the steady-state parameters conform to the design parameters. Considering fluctuations in actual operation, uncertainties and corresponding PDFs are also introduced for important thermal parameters of the reactor, such as PRZ pressure, core power, main flow rate, and core heat channel temperature.

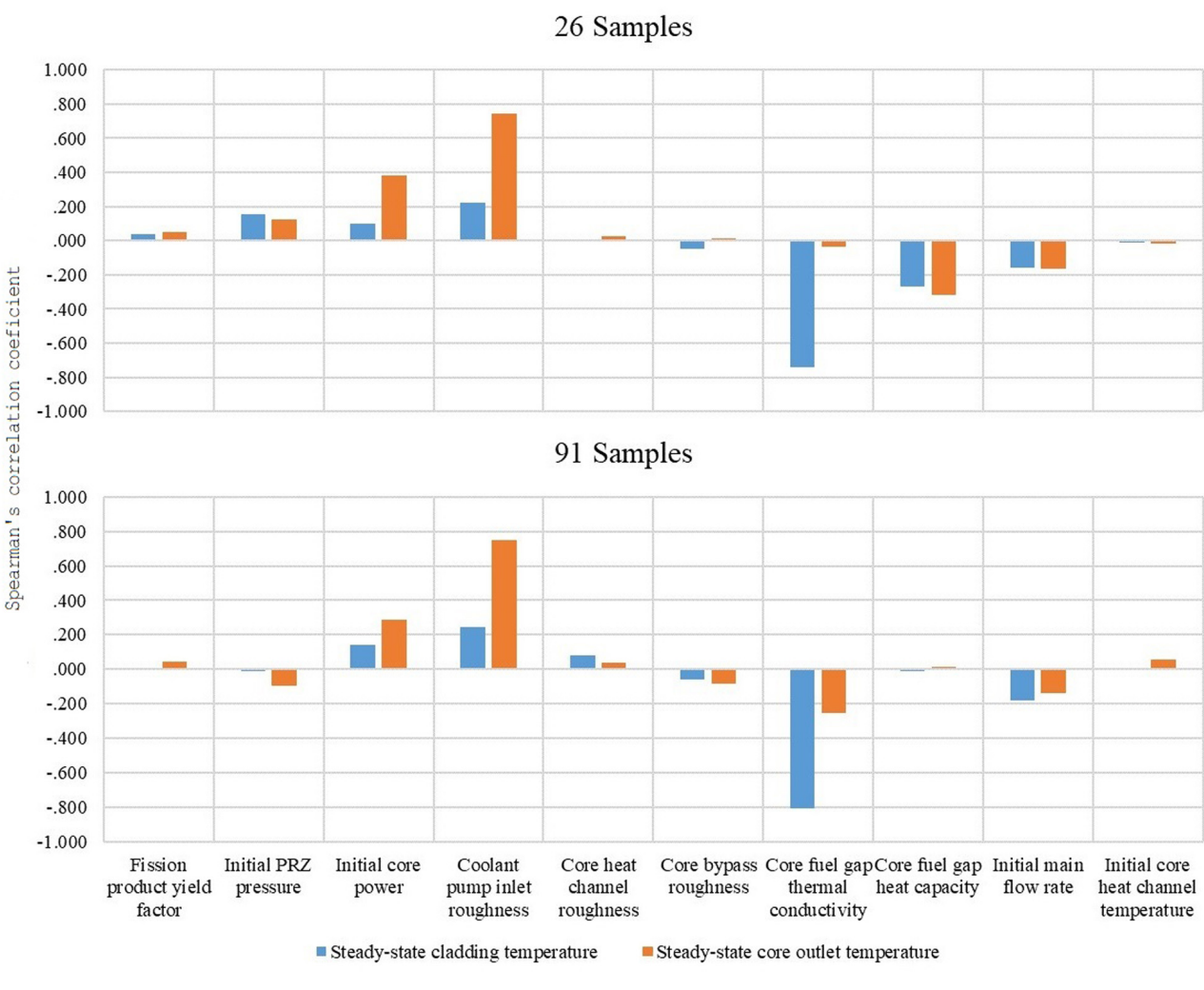


**FIGURE 6 |** Sensitivity between initialization parameters and steady-state core outlet temperature.

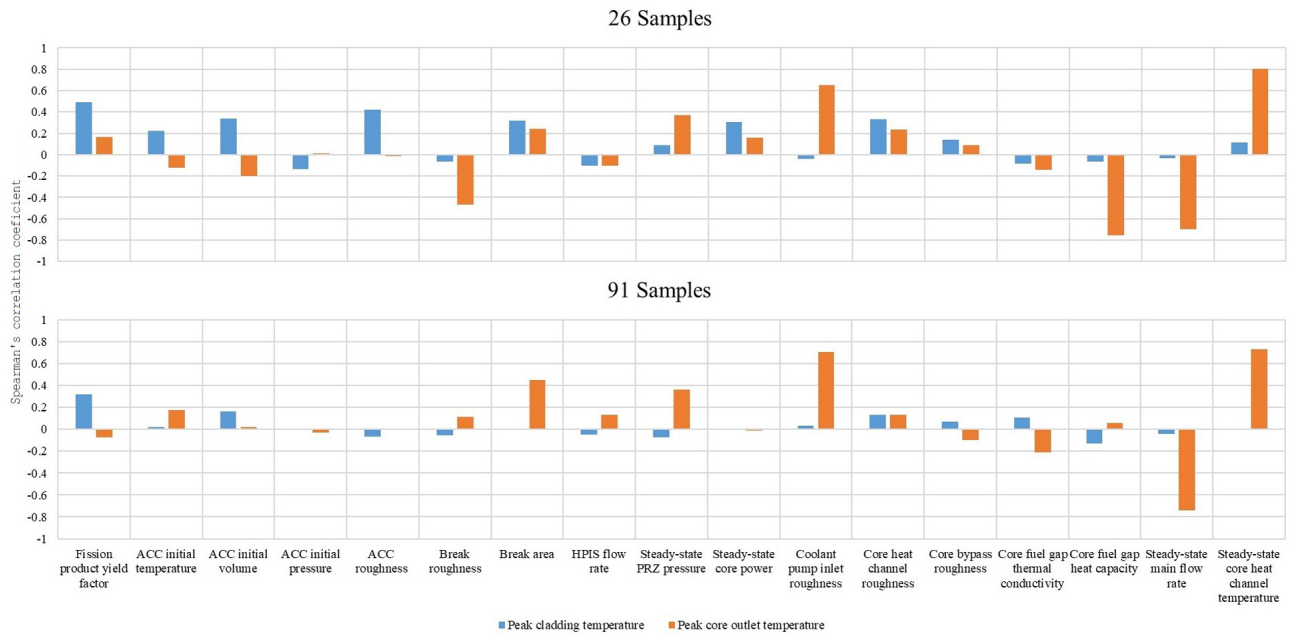


**FIGURE 7 |** Sensitivity between steady-state parameters and figures of merit (FOMs).

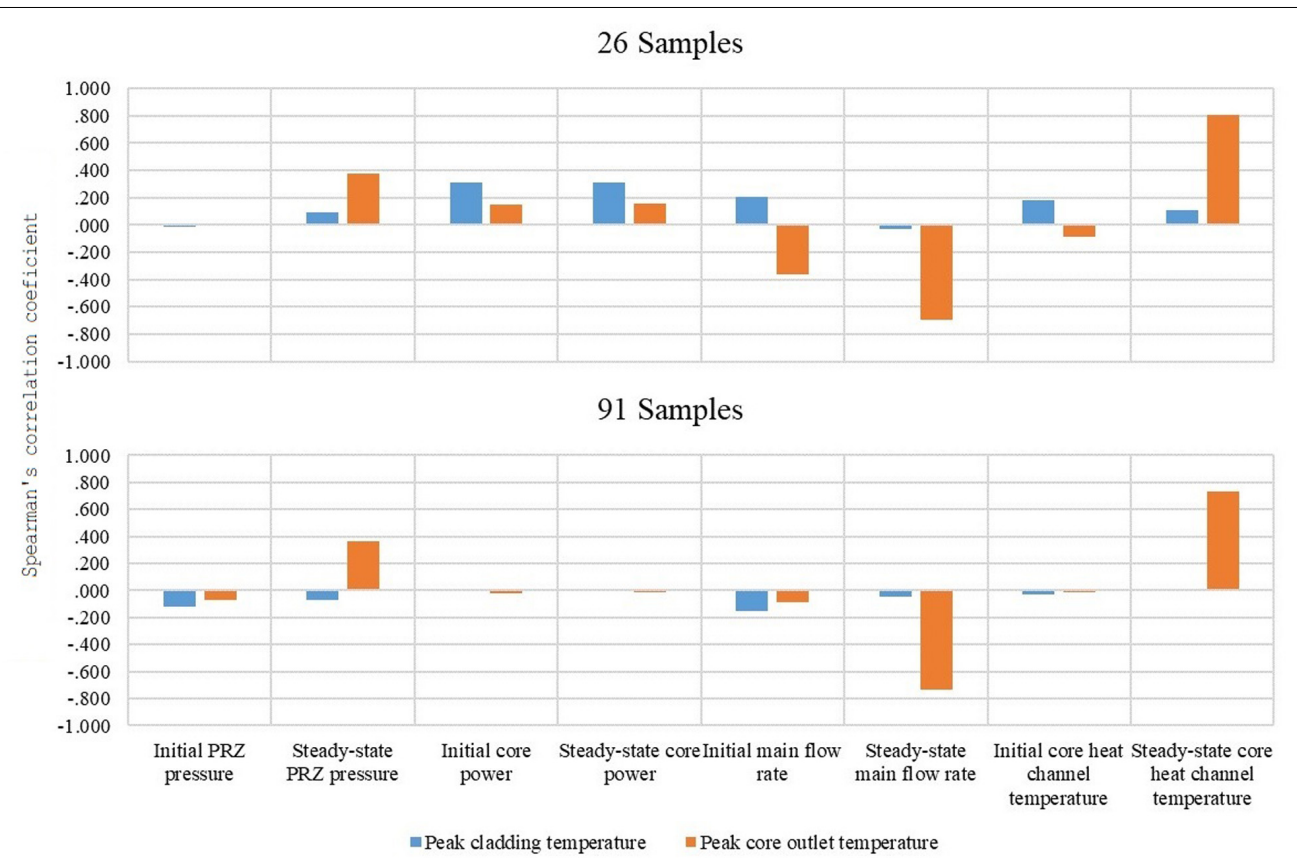


**FIGURE 8 |** The comparison between the initial parameters and the steady-state parameters with the output figures of merit (FOMs).

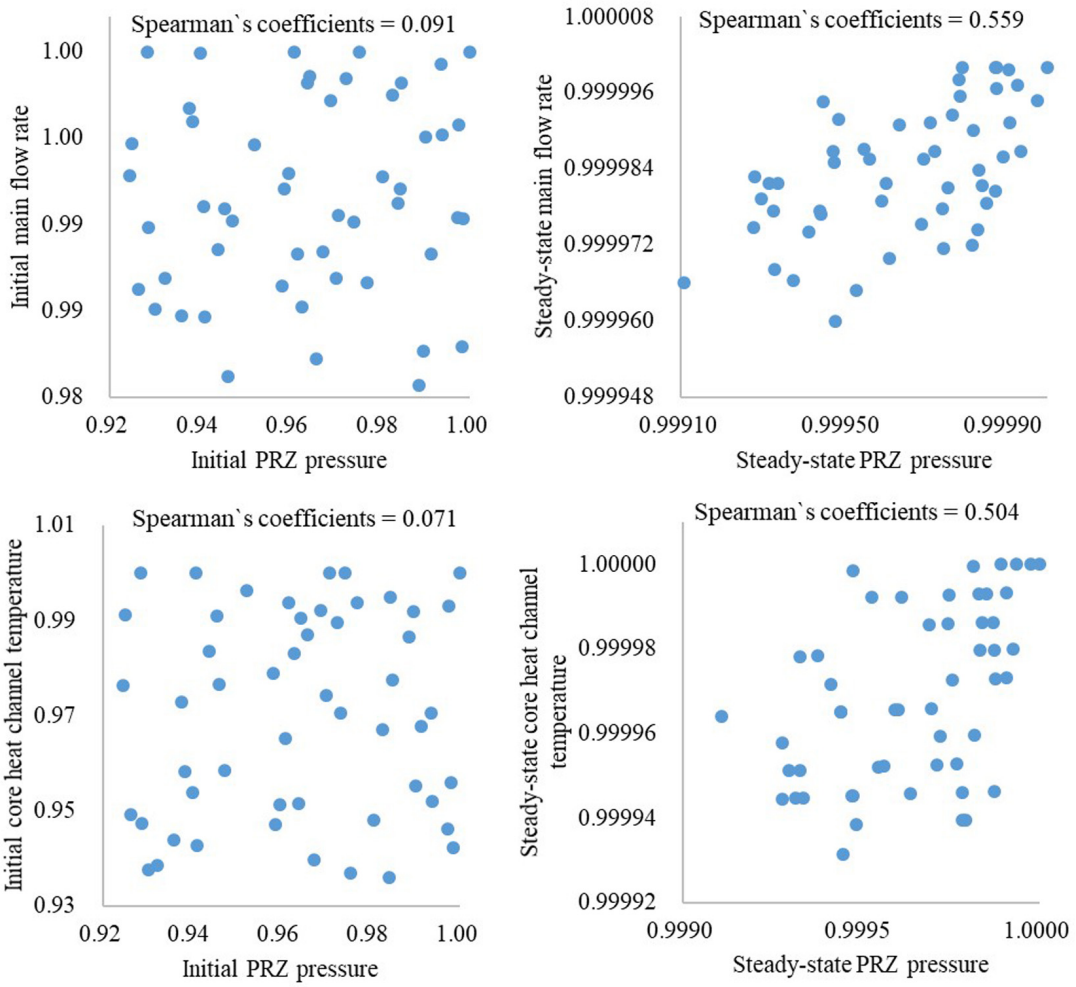


**FIGURE 9 |** The relationship between initial and steady-state input parameters.

Generally, the thermal physical properties of the material, such as core fuel gap thermal conductivity and its heat capacity, can be obtained from the manufacturers. They are usually specified as the Gaussian distributions with mean values and standard deviations (Wang et al., 2017).

As for thermal and hydraulic parameters, there is no definitive uncertainty information existing owing to the fluctuation in actual operation, so a uniform PDF can be adopted without certain mean values.

In theory, the sample size of 4/3 as the number of parameters is enough for the sensitivity analysis, but the comparison in **Figures 5–7** shows that expanding the sample space on the basis of requirement "4/3" can effectively reduce the analysis accuracy caused by insufficient data (CN, 2011). Considering that the sensitivity analysis of large sample space is more accurate, 91 samples are adopted rather than 26 samples.

The number of input parameters selected in this work is 15, so 20 samples are enough for the sensitivity analysis (Helton and Davis, 2003; CN, 2011). Owing to the complex modeling structure of the reactor, the calculations of the remaining four samples failed and were abandoned. After testing, the input parameters of the 26 samples are consistent with those of the original PDF, and the same is true of the 91 selected after testing.

Comparing the two sensitivity analyses as shown in **Figures 6–8**, it can be seen that there are certain differences. Finally, 91 samples are selected for the sensitivity analysis, which has higher accuracy.

**Figure 6** illustrates the sensitivity between initial parameters and steady-state core outlet temperature.

In the first stage, core fuel gap thermal conductivity is significantly negatively correlated with steady-state cladding temperature. This is because the higher thermal conductivity makes the overall thermal resistance of gap and cladding lower, so that heat can be removed in time, which will eventually result in a lower cladding temperature.

Coolant pump inlet roughness and steady-state core outlet temperature are significantly positively related. This is because higher friction results in the decrease of flow in pump, which reduces the heat transport capacity of the coolant and makes its temperature higher.

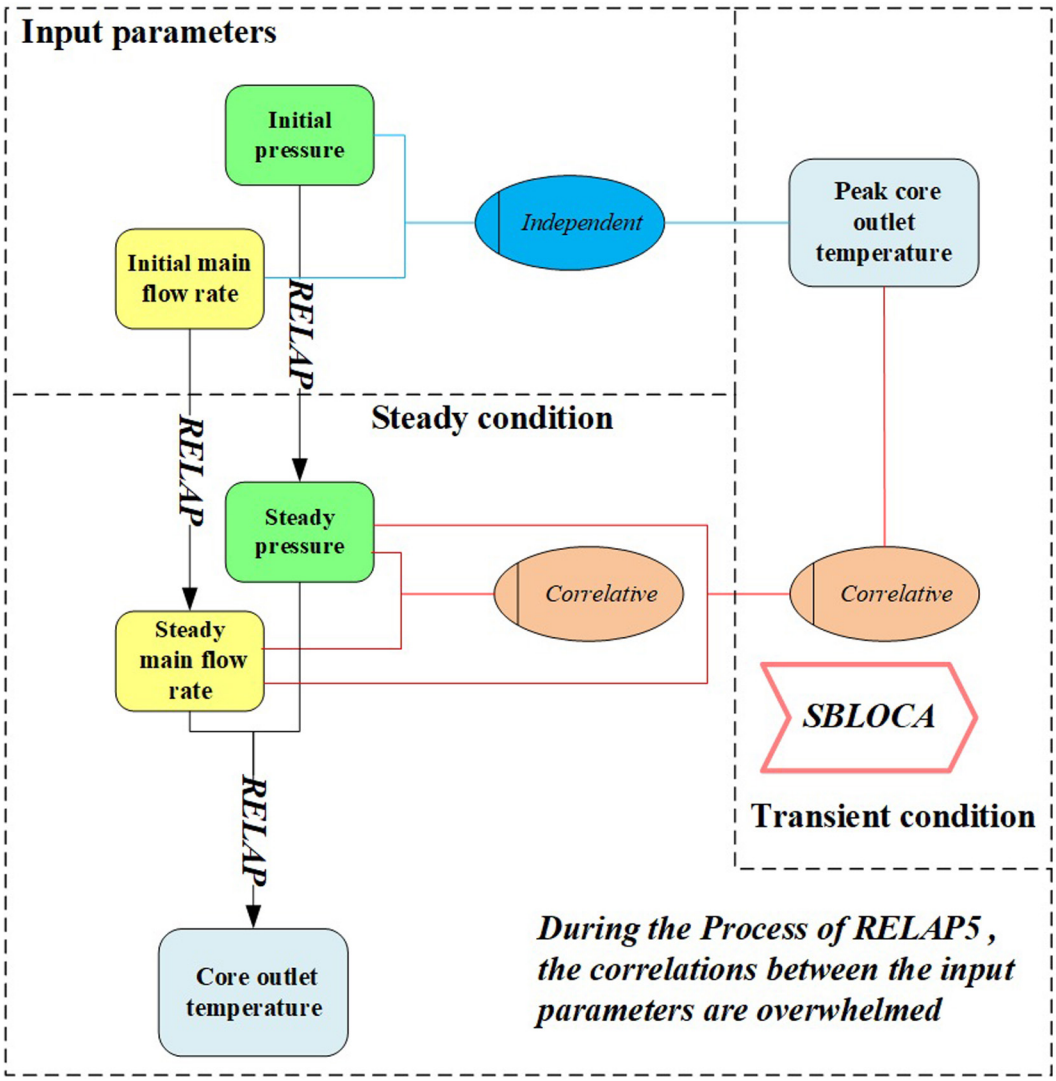


**FIGURE 10 |** The improved sensitivity analysis process.

**TABLE 4 |** Input parameters for uncertainty analysis of the improved BEPU method.

| Parameter | Condition | Nominal | Distribution | Uncertainty range |
|---|---|---|---|---|
| **Initial and constant boundary conditions** | | | | |
| Fission product yield factor | All the time | 1 | Uniform | 1–1.2 |
| Break area ($10^{-3}$ $m^2$) | After small break | 8.5 | Uniform | 8.0–9.0 |
| **Initial conditions** | | | | |
| Initial PRZ pressure (MPa) | All the time | 15.2 | Uniform | 14.6–15.8 |
| Initial main flow rate (kg/s) | | 3333 | Uniform | 3300–3366 |
| Initial core heat channel temperature (K) | | 600 | Uniform | 580–620 |
| **Hydraulic constants** | | | | |
| Coolant pump inlet roughness | All the time | 1 | Uniform | 0.92–1.08 |

Core power and steady-state core outlet temperature are medium positively related. That high power results in high coolant temperatures is reasonable. However, the correlation is not very obvious owing to the feedback of the reaction.

The other correlations with steady-state cladding temperature and steady-state core outlet temperature are weak.

The sensitivity analysis in the second stage is shown in **Figure 7**. This stage strictly reflects the sensitivity between the input parameters and the FOMs.

For PCT, the fission product yield factor is moderately related to it. This is because the high fission product yield factor leads to higher decay power. In the process of calculation, as the source of heat increases (higher decay power), the thermal resistance from the pellet to coolant decreases slightly. This eventually makes their temperatures increase but decreases the positive correlation owing to changes in thermal conductivity. However,

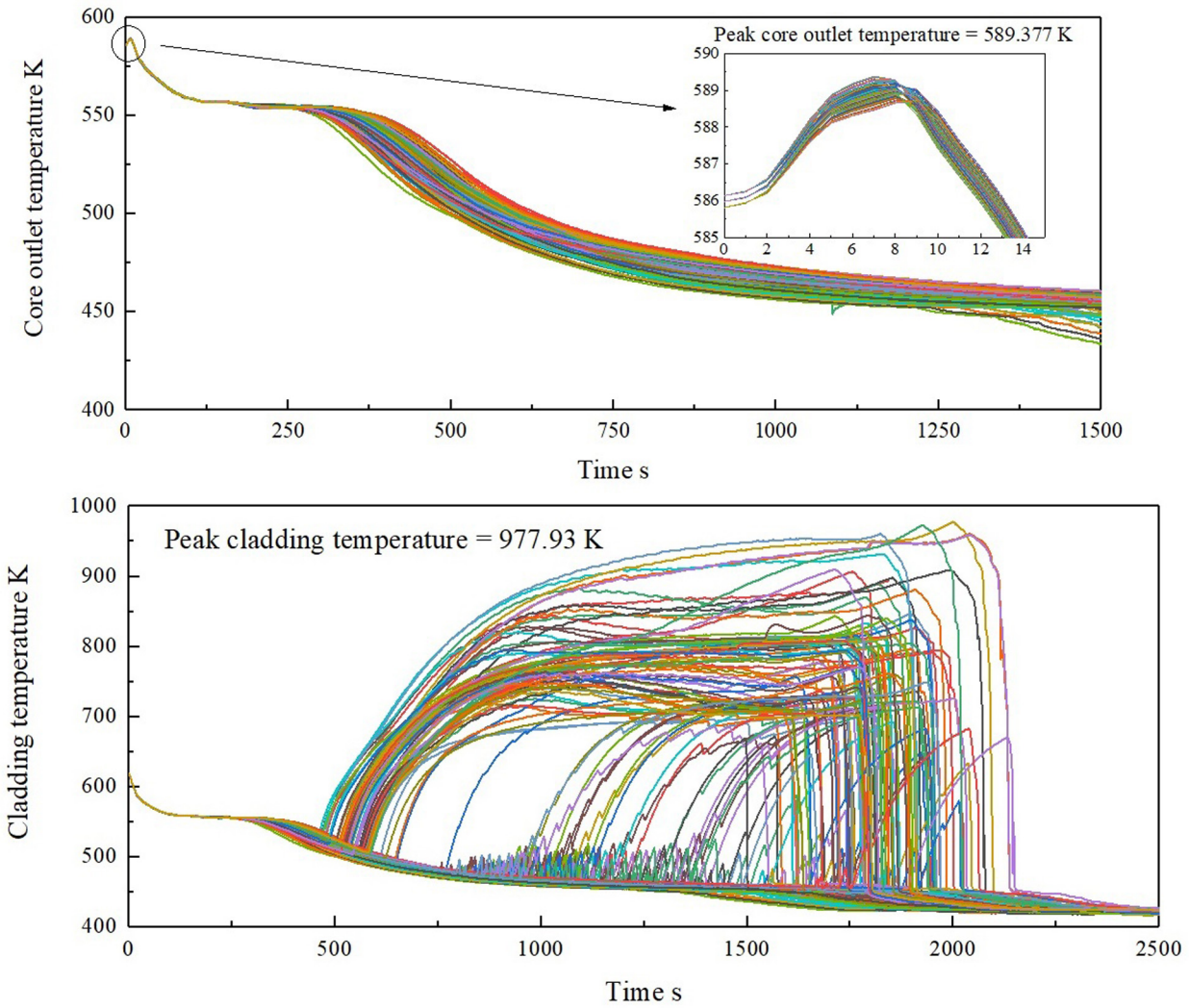


**FIGURE 11 |** Uncertainty results of figures of merit (FOMs) with improved best estimate plus uncertainty (BEPU) method. **(A)** Results of the peak core outlet temperature. **(B)** Results of the peak cladding temperature (PCT).

owing to the decrease in thermal conductivity, the correlation is not very strong.

For peak core outlet temperature, there are three factors of significant relationship – coolant pump inlet roughness, steady-state main flow rate, and steady-state core heat channel temperature. The decrease in flow due to high pump inlet roughness increases the coolant temperature both in the core heat channel and at the core outlet. Both the break area and steady-state PRZ pressure have medium positive relationships with the peak core outlet temperature. This is because high steady-state pressure and larger size of small break can make coolant main flow reduce faster, which raises the core outlet temperature.

The sensitivity results of the traditional BEPU method are shown in **Figure 8**. Meanwhile, the related results of stage (2) are also given as a comparison. As illustrated in **Figure 7**, both the steady-state main flow rate and the steady-state core heat channel temperature have strong relationships with peak core outlet temperature, whereas the relationship with their initial values is very weak. Meanwhile, the steady-state PRZ pressure has a medium relationship with the peak core outlet temperature, which cannot be found in the initial PRZ pressure. To analyze the difference in sensitivity results, the relationship between PRZ pressure, main flow rate, and core heat channel temperature is analyzed in the initial situation and steady state, as shown in **Figure 9**. It illustrates that the PRZ pressure, main flow rate, and core heat channel temperature are tightly related when the reactor is operating in a steady state. However, the traditional sensitivity analysis ignores the relationship by independent sampling, which probably ignores the key factors that affect FOMs. Hence, it is more reasonable to take steady-state parameters as inputs in the sensitivity analysis of transient.

The sensitivity analysis framework of the improved BEPU method is summarized in **Figure 10**. PRZ pressure and

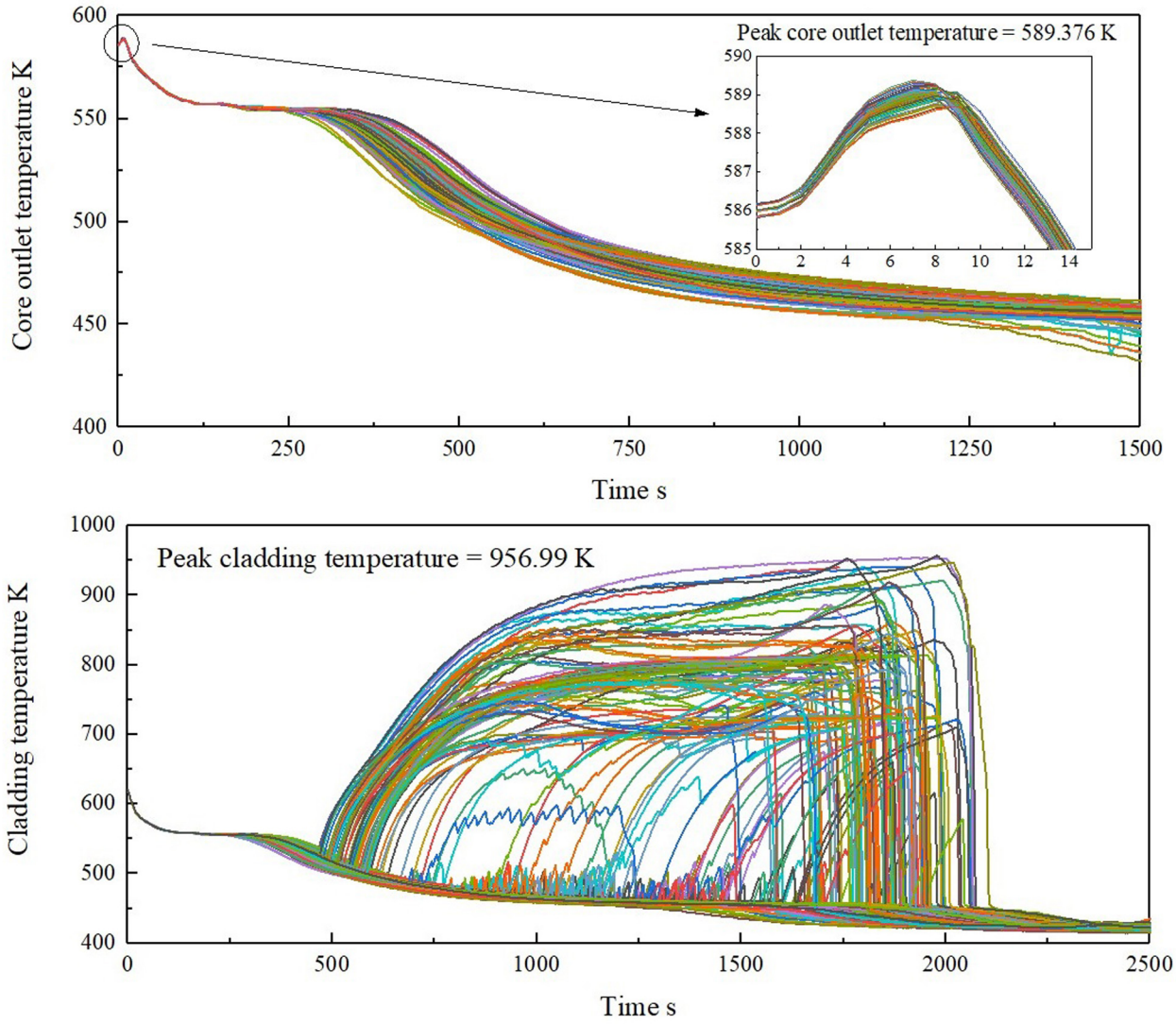


**FIGURE 12 |** Uncertainty results of figures of merit (FOMs) with traditional best estimate plus uncertainty (BEPU) method. **(A)** Results of the peak core outlet temperature. **(B)** Results of the peak cladding temperature (PCT).

main flow rate are selected as inputs for an example. The initial parameters are sampled independently according to the distributions and uncertainty ranges in **Table 3**. However, during the calculation process in RELAP5, all parameters are adjusted to obey the physical laws. Because of that, after the steady-state calculation, the PRZ pressure and main flow rate become highly correlated (illustrated in **Figure 9**). This process can also be considered as a correlative sampling of irrelevant parameters.

## Uncertainty Analysis

Uncertainty analysis is performed for peak core outlet temperature and the PCT of SBLOCA. The parameters with strong relationships are sampled in **Table 4**. Some of the coefficients go to 0, and the others go up to 1 when the sample size goes from 26 to 91. The principle of sampling is to choose the parameters with a correlation coefficient greater than 0.3. Six parameters are selected to perform uncertainty analysis. The results of the improved BEPU method are shown in **Figure 11**. For comparison, **Figure 12** shows the result of the traditional BEPU method.

**TABLE 5 |** Comparison with improved BEPU and traditional BEPU method.

| Calculated value | Improved BEPU | Traditional BEPU | Relative deviation |
|---|---|---|---|
| Peak core outlet temperature (K) | 589.377 | 589.376 | 0.0017‰ |
| Peak cladding temperature (m) | 977.93 | 956.99 | 2.2% |

*BEPU, best estimate plus uncertainty analysis.*

The power of the reactor does not immediately drop when the break occurs at 0 s. Meanwhile, the coolant leaks rapidly. The decrease in flow causes the core outlet temperature to rise to a peak value of 589.377 K. As the reactor stops and safety facilities start, the temperature reduces. As illustrated in **Figure 11A**, the uncertainty of the core outlet temperature increased with time. The PCT goes up at about 500 s, and the maximum value is 977.93 K at about 2,000 s. As shown in **Figure 11B**, the LPIS is started in time so that the temperature does not exceed the limit at 1,447.15 K.

The uncertainty results of the traditional BEPU method are given in **Figure 12** and **Table 5** as a comparison. In the traditional BEPU method, all input parameters are directly sampled for uncertainty analysis. By comparing **Figures 11**, **12**, it is evident that the improved BEPU method shows similar results with the traditional BEPU method. The number of inputs of the improved BEPU method is significantly reduced from 17 to 6, as listed in **Tables 3**, **4**. Meanwhile, as listed in **Table 5**, the deviation of the two FOMs is less than 5%, which indicates that the improved BEPU method maintains the desired accuracy with the smaller size of samples.

## CONCLUSION

In this work, RELAP5 is used to model the PWR and stimulate the steady-state condition and SBLOCA. And the improved BEPU method is proposed to perform the sensitivity and the uncertainty analysis of the FOMs. Compared with the traditional BEPU method, the improved BEPU method possesses the following two characteristics:

(1) Two main stages, that is, steady-state calculation and transient calculation, are usually considered for accident analysis in RELAP5. The sensitivity analysis is performed for both stages in the improved BEPU method to provide more comprehensive results. However, the traditional BEPU method usually combines the above two stages to analyze the sensitivity between the initial parameters and the transient results.
(2) The sensitivity analysis is firstly performed to reduce the number of uncertainty analysis inputs. Only the key input parameters that have a significant impact on the uncertainty analysis are identified.

In this work, a PWR SBLOCA is simulated by RELAP5 to verify the accuracy and applicability of the improved BEPU method. And three main conclusions are drawn as follows:

(1) The sensitivity analysis by the improved BEPU method shows that the peak core outlet temperature has strong relationships with main flow rate, core heat channel temperature, and PRZ pressure, whereas the traditional BEPU method cannot identify the strong relationship among them. Hence, it is more reasonable to take steady-state parameters as inputs in the sensitivity analysis of transient.
(2) By the sensitivity analysis, the coolant pump inlet roughness, main flow rate, and core heat channel temperature have a strong relationship with the peak core outlet temperature. Meanwhile, both the break area and PRZ pressure are medium positive relationships with the peak core outlet temperature. For the PCT, the fission product yield factor is moderately related to it. There are only these parameters sampled for uncertainty analysis.
(3) The results of the uncertainty analysis obtained by the improved BEPU are consistent with the results of the traditional method. Neither the PCT nor the peak core outlet temperature will exceed their limits. The results illustrate that the improved BEPU method can reduce the size of samples and maintains the desired accuracy.

In this work, the improved BEPU method is proposed and tested to capture the detailed features during sensitivity and uncertainty analysis. Because the size of the samples in uncertainty analysis is reduced, it is supposed to reduce the failure rate of the simulation. And the related test will be performed in the future. Moreover, the improved BEPU method will be used to analyze other accidents such as LBLOCA.

## DATA AVAILABILITY STATEMENT

The original contributions presented in the study are included in the article/supplementary material, further inquiries can be directed to the corresponding author.

## AUTHOR CONTRIBUTIONS

DS completed the main content of the work. ZZ directed the important direction of the work. XL completed some relevant data processing of the work. LL and HW assisted some of the technical guidance for the work. AX and SC provided technical guidance for traditional BEPU methods. All authors contributed to the article and approved the submitted version.

## FUNDING

This study was supported by National Key R&D Program of China on Risk-informed Safety Margin Characterization Technology (2018YFB1900302).

## REFERENCES

ANSYS Inc (2013). *ANSYS Fluent Theory Guide*. Canonsburg, PA: ANSYS Inc.

Barre, F., and Bernard, M. (1990). The CATHARE code strategy and assessment. *Nuclear Eng. Design* 124, 257–284. doi: 10.1016/0029-5493(90)90296-a

Berar, O.-A., Prošek, A., and Mavko, B. (2013). RELAP5 and TRACE assessment of the Achilles natural reflood experiment. *Nuclear Eng. Design* 261, 306–316. doi: 10.1016/j.nucengdes.2013.05.007

Boyack, B. E., Catton, I., Duffey, R. B., Griffith, P., Katsma, K. R., Lellouche, G. S., et al. (1990). Quantifying reactor safety margins part 1: an

overview of the code scaling, applicability, and uncertainty evaluation methodology. *Nuclear Eng. Design* 119, 1–15. doi: 10.1016/0029-5493(90)90071-5

Briesmeister, J. F. (1993). *MCNP-A General Monte Carlo N-Particle Transport Code. LA-12625*. Available online at: https://permalink.lanl.gov/object/tr?what=info:lanl-repo/lareport/LA-13709-M

CN (2011). *Reaserch on Modeling and Uncertainty of Optimal Estimation and Analysis of Water Loss Accident in AP1000 Nuclear Power Plant*. Shanghai: Shanghai Jiao Tong University.

Coefficient, P. S. C. (1996). Pearson's correlation coefficient. *New Zealand Med. J.* 109:38.

Cutrono Rakhimov, A., Visser, D. C., and Komen, E. M. J. (2019). Uncertainty Quantification method for CFD applied to the turbulent mixing of two water layers – II: deterministic Sampling for input uncertainty. *Nuclear Eng. Design* 348, 146–158. doi: 10.1016/j.nucengdes.2019.04.016

Deng, C., Chen, L., Yang, J., and Wu, Q. (2019). Best-estimate calculation plus uncertainty analysis of SBLOCA transient for the scale-down passive test facility. *Progr. Nuclear Energy* 112, 191–201. doi: 10.1016/j.pnucene.2018.12.018

Dubois, A., Leong, Z. Q., Nguyen, H. D., and Binns, J. R. (2019). Uncertainty estimation of a CFD-methodology for the performance analysis of a collective and cyclic pitch propeller. *Appl. Ocean Res.* 85, 73–87. doi: 10.1016/j.apor.2019.01.028

Dunn, F. E. (1999). *Comparisons of Steady-State and Transient Thermal Hydraulic Results from SAS-DIF3DK and RELAP5 mod 3.2 for an RBMK reactor*. Oak Ridge: Office of Scientific & Technical Information.

Dunn, M. C., Shotorban, B., and Frendi, A. (2010). "Uncertainty quantification of turbulence model coefficients via latin hypercube sampling method," in *Proceedings of the ASME 2010 3rd Joint US-European Fluids Engineering Summer Meeting: Volume 1, Symposia – Parts A, B, and C2010*, Montreal, 2913–2921.

Ghione, A., Noel, B., Vinai, P., and Demazière, C. (2017). Uncertainty and sensitivity analysis for the simulation of a station blackout scenario in the Jules Horowitz Reactor. *Ann. Nuclear Energy* 104, 28–41. doi: 10.1016/j.anucene.2017.02.008

Glaeser, H. (2008). GRS Method for uncertainty and sensitivity evaluation of code results and applications. *Sci. Technol. Nuclear Instal.* 2008:798901.

Guba, A., Makai, M., and Pál, L. (2003). Statistical aspects of best estimate method—I. *Reliabil Eng. Syst. Safety* 80, 217–232. doi: 10.1016/s0951-8320(03)00022-x

Gupta, S. K., Dubey, S. K., and Rao, R. S. (2013). *Uncertainty Evaluation in Best Estimate Accident Analysis of NPPs*. New Delhi: Springer India.

Helton, J. C., and Davis, F. J. (2003). Latin hypercube sampling and the propagation of uncertainty in analyses of complex systems. *Reliabil. Eng. Syst. Safety* 81, 23–69. doi: 10.1016/s0951-8320(03)00058-9

IAEA (2002). *Accident Analysis for Nuclear Power Plants*. Vienna: IAEA.

Ibarra, J. G. (1988). *Editor Non-Plant Referenced Simulator Methodology to Meet New 10 CFR 55.45 rule*. Piscataway: IEEE.

Jamali, K. (2015). Achieving reasonable conservatism in nuclear safety analyses. *Reliabil. Eng. Syst. Safety* 137, 112–119. doi: 10.1016/j.ress.2015.01.008

Jinhan, B., and Fei, W. (1998). Review of the research on small break loss of coolant accident. *Chin. J. Nuclear Sci. Eng.* 18, 172–179.

Jizhou, Z., Shuren, X., Jianqiang, S., and Bin, Z. (2004). *Nuclear Reactor Safety Analysis*. Shaanxi: Xi'an Jiaotong University Press.

KINS (2005). *Improvement of the ECCS Best Estimate Methodology and Assessment of LOFT L2-5 Experiment. KINS/RR-279*. Daejeon: Korea Institute of Nuclear Safety.

Luo, H. (2012). *Quantified PIRT and Uncertainty Quantification for Computer Code Validation*. Oregon: Oregon State University.

Martin, R. P. (1995). *RELAP5/MOD3 Code Coupling Model*. Vienna: INIS.

Murray, R. L. (1987). Guidebook to Light Water Reactor Safety Analysis. *Nuclear Technol.* 76, 309–310. doi: 10.13182/nt87-a33887

NR Commisson (2010). *TRACE V5.0 User's Manual. U.S*. Washington, DC: NR Commisson.

Pawel, A. J., and Mesina, G. L. (2011). *Uncertainty Analysis for RELAP5-3D Idaho National Laboratory, INL/EXT-12-26182*. Idaho: Idaho National Laboratory.

Perez, M., Reventos, F., Batet, L., Guba, A., Tóth, I., Mieusset, T., et al. (2011). Uncertainty and sensitivity analysis of a LBLOCA in a PWR Nuclear Power Plant: results of the Phase V of the BEMUSE programme. *Nuclear Eng. Design* 241, 4206–4222. doi: 10.1016/j.nucengdes.2011.08.019

Pingan, Y., Ruian, Z., Zhenwan, Y., and Xiuzhong, S. (2002). *Thermal Analysis of Nuclear Reactors*. Shanghai: Shanghai Jiao Tong University Press.

Porter, N. W. (2019). Wilks' formula applied to computational tools: a practical discussion and verification. *Ann. Nuclear Energy* 133, 129–137. doi: 10.1016/j.anucene.2019.05.012

Rakhimov, A. C., Visser, D. C., and Komen, E. M. J. (2020). Uncertainty Quantification method for CFD validated for turbulent mixing experiments from GEMIX. *Nuclear Eng. Design* 358:110444. doi: 10.1016/j.nucengdes.2019.110444

Rasmussen, N. C. (1975). *Der Rasmussen-Bericht (WASH-1400)*. Berlin: Springer.

Rockville, M. (2001). *RELAP5/MOD3.3 Code Manual*. Idaho: Idaho Falls.

Sanchez-Saez, F., Carlos, S., Villanueva, J. F., Sanchez, A. I., and Martorell, S. (2017). Uncertainty analysis of PKL SBLOCA G7.1 test simulation using TRACE with Wilks and GAM surrogate methods. *Nuclear Eng. Design* 319, 61–72. doi: 10.1016/j.nucengdes.2017.04.037

Sanchez-Saez, F., Sánchez, A. I., Villanueva, J. F., Carlos, S., and Martorell, S. (2018). Uncertainty analysis of a large break loss of coolant accident in a pressurized water reactor using non-parametric methods. *Reliabil. Eng. Syst. Safety* 174, 19–28. doi: 10.1016/j.ress.2018.02.005

Sedgwick, P. (2014). Spearman's rank correlation coefficient. *BMJ*. 349:g7327.

Wang, C., Peng, M., Cong, T., and Xia, G. (2019). Uncertainty analysis on natural circulation characteristics under ocean conditions. *Ann. Nuclear Energy* 128, 300–308. doi: 10.1016/j.anucene.2019.01.027

Wang, C., Sun, K., Zhang, D., Tian, W., Qiu, S., and Su, G. H. (2017). Uncertainty analysis of Transportable Fluoride-salt-cooled High-temperature Reactor (TFHR) using coupled DAKOTA with RELAP-3D method. *Nuclear Eng. Design* 324, 269–279. doi: 10.1016/j.nucengdes.2017.08.021

Wilks, S. S. (1941). Determination of sample sizes for setting tolerance limits. *Ann. Math. Stat.* 12, 91–96. doi: 10.1214/aoms/1177731788

Wilson, G. E., and Boyack, B. E. (1998). The role of the PIRT process in experiments, code development and code applications associated with reactor safety analysis. *Nuclear Eng. Design* 186, 23–37. doi: 10.1016/s0029-5493(98)00216-7

Yangyu, O. (2000). *Qinshan Nuclear Power Engineering*. Beijing: Atomic Energy Press.

Zhikang, L., Ting, W., Jianshu, L., Ren, L., and Xianghui, L. (2016). Research on quantitative analysis method of uncertainty in real LOCA analysis. *Nuclear Power Eng.* 37, 75–79.

Zhujian, Z., and Shoulv, X. (1992). Post-Commission Loca Analysis Of Qinshan Npp. *Chin. Nuclear Sci. Technol. Rep.* 00, 316–326.

**Conflict of Interest:** The authors declare that the research was conducted in the absence of any commercial or financial relationships that could be construed as a potential conflict of interest.

frontiers in Energy Research

ORIGINAL RESEARCH
published: 27 August 2020
doi: 10.3389/fenrg.2020.00145

# Analysis of Measuring Characteristics of the Differential Pressure Water-Level Measurement System Under Depressurization Condition

*Xuwei Zhou, Jie Cheng, Luchao She and Guangming Fan**

*Fundamental Science on Nuclear Safety and Simulation Technology Laboratory, Harbin Engineering University, Harbin, China*

OPEN ACCESS

**Edited by:**
*Jun Wang,*
*University of Wisconsin–Madison, United States*

**Reviewed by:**
*Jiankai Yu,*
*Massachusetts Institute of Technology, United States*
*Xingang Zhao,*
*Massachusetts Institute of Technology, United States*

***Correspondence:**
*Guangming Fan*
*fanguangming007@hotmail.com*

**Specialty section:**
*This article was submitted to Nuclear Energy, a section of the journal Frontiers in Energy Research*

**Received:** *25 April 2020*
**Accepted:** *12 June 2020*
**Published:** *27 August 2020*

**Citation:**
*Zhou X, Cheng J, She L and Fan G (2020) Analysis of Measuring Characteristics of the Differential Pressure Water-Level Measurement System Under Depressurization Condition. Front. Energy Res. 8:145. doi: 10.3389/fenrg.2020.00145*

In this paper, RELAP5 code was selected to study the measuring characteristics of the double reference tube level gauge, which is commonly used in high temperature and high pressure vessels on marine nuclear power platforms, under steady and transient depressurization conditions. The response characteristics of water-level gauge, influenced by the reference cup supply water flow rate under the condition of rapid depressurization, is discussed. Measurement error and accuracy of the water-level measuring device are analyzed under both steady and transient conditions. The simulation results indicate that the relative error of the double reference tube level gauge is about 0.79% in steady state, while the measurement error is too large to accurately obtain the level in the vessel under the transient depressurization condition. However, the relative measurement error can reach about 10% under the condition of a small depressurization rate.

**Keywords: the double reference tube level gauge, transient depressurization, measurement error, response characteristics, the measuring characteristics**

## INTRODUCTION

The water-level is crucial for some high temperature and high-pressure equipment of the PWR primary system, such as the steam generator and pressurizer. The water-level control is accomplished by the water-level control system, and the output signal of the water-level measurement system is frequently the input signal of the water-level control system (Zhang and Hu, 2012; Zhang et al., 2012; Salehi et al., 2018). It has been found that the accuracy and dynamic characteristics of the water-level measurement system directly affect the control effect of the water-level control system.

Generally, there are many kinds of water-level measuring devices, including waveguide acoustic water-level meter, ultrasonic water-level meter, capacitance water-level meter, differential pressure water-level gauge, etc. The sound pressure wave generated by water boiling is decomposed by the waveguide acoustic wave water-level meter to obtain the level, but it is limited to the measurement

of the boiling water-level (Singh and Mohanty, 2018). The time interval and energy loss between the transmitted sound wave and the reflected sound wave are used by the ultrasonic water-level meter to obtain the level, but there may be a measurement blind zone in a vessel with a complex shape, and it is greatly affected by temperature and water mist (Soltz, 1984; Melnikov and Khokhlov, 1997; Lee et al., 2005; Mel'nikov et al., 2016). The capacitance of the capacitive water-level meter vary with the change of the water-level. This feature is used to obtain the water-level, but its load capacity is weak. The measurement accuracy is not high enough, because it will be disturbed by parasitic capacitance. The dielectric constant will change with temperature, and it is necessary to perform temperature compensation or reduce the distance between two electrodes (Zhang and Liu, 2013; Jin et al., 2015; Paczesny et al., 2015; Rizi and Abadi, 2017). The difference in heat exchange capacity between liquid and gas can also be used to obtain the level, but this measurement method has a long response time and is still immature (Petrie and Mcduffee, 2018). In addition, the dynamic tube pressure method is mainly used to measure the liquid level of molten salt (Kim et al., 2017).

In view of the limitations of the above liquid level measuring methods in application scenarios and some shortcomings in measurement, the differential pressure measurement system is still applied in nuclear power equipment for water-level measurement. The differential pressure measuring method can be divided into the external water-level measuring method and the internal water-level measuring method according to location of reference tube. The internal water-level measuring method requires two reference tubes; hence it is also called the double reference tube level gauge. When the external water-level measurement method is used for level measurement of marine high temperature and high pressure vessels, there are four influencing factors (1) the distance of the reference tube from the central axis of the vessel; (2) the radius of the vessel; (3) the density of the liquid; and (4) the inclination. The measurement error is very large (Lin, 1986). In order to improve the measurement accuracy of the differential pressure water-level gauge, some scholars have improved the structure of the level measurement device and developed the double reference tube level gauge (CGN Research Institute Co. Ltd., 2018a,b). The new type of water-level gauge can eliminate the influence of inclination angle, radius of vessel, and reduce the influence of density on the measurement results. In recent years, some researchers have found that the existence of gas in the measurement system will cause the fluctuation of the measuring value (Xiong and Zhou, 2016). For a marine steam generator, the load changes frequently and the amplitude is large. The liquid water in the level measuring device may flash evaporation to generate bubbles, which greatly affects the measurement accuracy and requires correction of the water-level measurement value (Li and Sun, 1997; Li and Jiao, 1999; Li et al., 2005).

Obviously, the accuracy of the measurement results will be affected by the existence of bubbles in the water-level measuring device. However, currently, there is no public literature focus on the measurement characteristics of the double reference tube level gauge under transient depressurization. The only related literature, mentioned that the relative error of its steady state measurement is approximately 2.0% (Lin, 1986).

The RELAP5 code has been developed for best-estimate transient simulation of light water reactor coolant systems

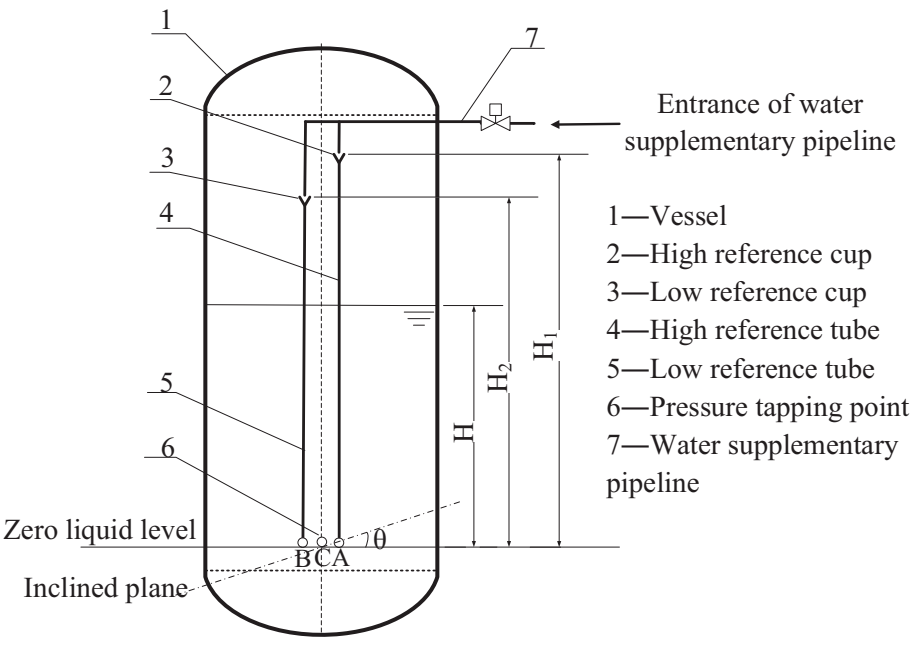


**FIGURE 1 |** Structure diagram of level measurement system.

during postulated accidents. A generic modeling approach is used that permits simulating a variety of thermal hydraulic systems. Nuclear power equipment such as a pressurizer and steam generator are allowed to be modeled using the RELAP5 code. In addition, the flow and heat transfer model in the RELAP5 code is suitable for analyzing the complicated single-phase flow, two-phase flow, and heat transfer process in this study (Wang et al., 2016). Moreover, the RELAP5 code has been used by some researchers to simulate the transient water-level of the AP1000 steam generator, and the results show that it is consistent with the actual situation (Jiang et al., 2013).

Therefore, in this paper, the RELAP5 code was selected to study the measuring characteristics of the double reference tube level gauge under steady state and transient depressurization conditions, and the code was used to explore the influence of changing the supply water flow on the measurement results under transient depressurization conditions as well.

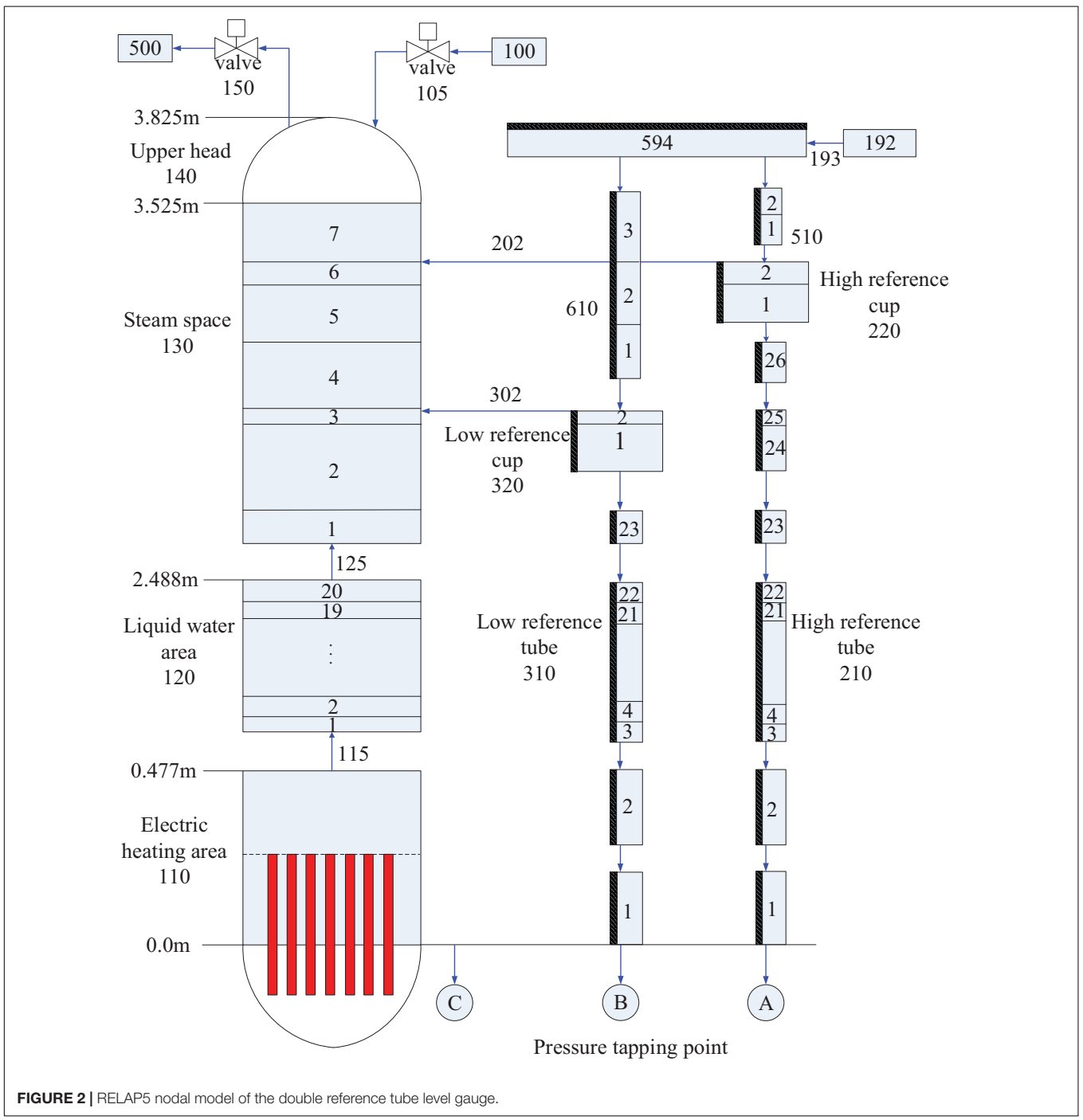


**FIGURE 2 |** RELAP5 nodal model of the double reference tube level gauge.

**TABLE 1 |** Design parameters of the double reference tube level gauge.

| Parameters | Values |
|---|---|
| Power of electric heating rod [kW] | 2.00 |
| Initial pressure of vessel gas space [MPa] | 3.30 |
| Volume of high reference cup [$cm^3$] | 764 |
| Volume of low reference cup [$cm^3$] | 703 |
| Inner diameter of high reference tube [mm] | 16.0 |
| Inner diameter of low reference tube [mm] | 16.0 |
| Length of high reference tube [m] | 2.97 |
| Length of low reference tube [m] | 2.57 |
| Inner diameter of vessel [mm] | 600 |
| Height of vessel [m] | 4.13 |

## NOMENCLATURE

$h$ Real water-level [m].
h* The water-level measured by double reference tube level gauge [m].
$P$ Pressure of gas space in vessel [MPa].
$A$ Valve flow area [$m^2$].
$A_F$ Reynolds number independent forward flow energy loss coefficient.
$A_R$ Reynolds number independent reverse flow energy loss coefficient.
$\Delta P_1$ Pressure difference between pressure points A and B [MPa].
$\Delta P_2$ Pressure difference between pressure points B and C [MPa].
$\rho_1'$ Density of water in the reference tube [$kg/m^3$].
$\rho_2'$ Density of water in measured vessel [$kg/m^3$].
$\rho_2''$ Density of steam in measured vessel [$kg/m^3$].
$g$ Gravity acceleration [$m/s^2$].
$H_1$ Total length of high reference cup and high reference tube [m].
$H_2$ Total length of low reference cup and low reference tube [m].
$H$ Height of liquid water in vessel [m].

**Greek symbols**

$\alpha$ Void fraction.
$\theta$ Inclination angle [rad].

## MEASUREMENT PRINCIPLE AND MODEL

### Measuring Principle

The structure of the double reference tube level gauge is shown in **Figure 1**. The lower part of the vessel is filled with water and the upper one is full of steam. The upper ends of the high and low reference tubes communicate with the high and low reference liquid cups, respectively, and the lower ends are closed. The high reference cup and low reference cup are continuously filled with water by the water injection pipeline to ensure that both the reference cup and the reference tube are full of water. There are two differential pressure transmitters (not shown); the press-leading tube of the first differential pressure transmitter is connected with the pressure tapping point A of the high reference tube and the pressure tapping point B of the low reference tube, respectively, and the press-leading tube of the second differential pressure transmitter is connected with the pressure tapping point B of the low reference tube and the pressure tapping point C of the vessel, respectively. The output signals of the two differential pressure transmitters are calculated by the divider to obtain the corresponding water-level value.

The following assumptions are adopted to derive the relationship between water-level and pressure difference:

(1) The density of steam and liquid water in the vessel remains the same everywhere;
(2) The density of liquid water in the reference tube remains the same everywhere;
(3) The device is inclined;
(4) The height difference between the pressure outlet of the reference tube and the differential pressure transmitter is ignored.

The density difference of liquid water inside and outside the reference tube is very small, which can be approximately regarded as equal, that is,

$$\rho_1' = \rho_2' \tag{1}$$

where $\rho_1'$ and $\rho_2'$ is the density of water in the reference tube and the density of water in the vessel, respectively. Then, the differential pressure of the differential pressure transmitter is $\Delta P_1$ and $\Delta P_2$, respectively.

$$\Delta P_1 = \left(\rho_1' - \rho_2''\right) g \left(H_1 - H_2\right) \cos\theta \tag{2}$$

$$\Delta P_2 = \left(\rho_1' - \rho_2''\right) g \left(H_2 - H\right) \cos\theta \tag{3}$$

where $\rho_2''$ is the density of steam in the vessel. This $g$ is the gravity acceleration. Here, $H_1$, $H_2$, and $H$ are the total length of the high reference cup and high reference tube, total length of the low reference cup and low reference tube, and the height of liquid water in the vessel, respectively.

From the above two formulas, the formula of water-level height $H$ in the vessel can be deduced as follows:

$$H = H_2 - \frac{\Delta P_2}{\Delta P_1}\left(H_1 - H_2\right) \tag{4}$$

According to Eq. (4), the factors affecting the measurement results of the device include the differential pressure $\Delta P_1$ and $\Delta P_2$, and the total height $H_1$ and $H_2$ of the reference cup and the reference tube.

### Simulation Model and Parameters

In order to study the measuring characteristics of the double reference tube level gauge, the structure of the device is divided into nodes according to the RELAP5 modeling requirement.

The external supply water flows into the reference cups (nodes 220 and 320) through channels (nodes 594, 510, and

**TABLE 2 |** Calculation condition parameters.

| Steady state condition No. | Parameters | | | Supply water flow rates |
|---|---|---|---|---|
| C1 | $\alpha = 0$, $P = 3.30$ MPa | | | 0.002 kg/s |
| **Transient condition No.** | **Valve opening time** | **Valve closing time** | **Parameters of pressure relief valve** | |
| C2 | 1000 s | 1300 s | $A = 0.00785$ m$^2$, $A_F = 50.0$, $A_R = 50.0$ | |
| C3 | 1000 s | 1300 s | $A = 0.00589$ m$^2$, $A_F = 50.0$, $A_R = 50.0$ | |
| C4 | 1000 s | 1300 s | $A = 0.00393$ m$^2$, $A_F = 50.0$, $A_R = 50.0$ | |
| C5 | 1000 s | 1300 s | $A = 0.00196$ m$^2$, $A_F = 50.0$, $A_R = 50.0$ | |
| C6 | 1000 s | 1300 s | $A = 0.00196$ m$^2$, $A_F = 400.0$, $A_R = 400.0$ | |
| C7 | 1000 s | 1300 s | $A = 0.00196$ m$^2$, $A_F = 800.0$, $A_R = 800.0$ | |
| C8 | 1000 s | 1300 s | $A = 0.00196$ m$^2$, $A_F = 1200.0$, $A_R = 1200.0$ | |
| C9 | 1000 s | 1300 s | $A = 0.00196$ m$^2$, $A_F = 2000.0$, $A_R = 2000.0$ | |
| C10 | 1000 s | 1300 s | $A = 0.00785$ m$^2$, $A_F = 50.0$, $A_R = 50.0$ | 0.0025 kg/s |
| C11 | 1000 s | 1300 s | $A = 0.00785$ m$^2$, $A_F = 50.0$, $A_R = 50.0$ | 0.005 kg/s |
| C12 | 1000 s | 1300 s | $A = 0.00785$ m$^2$, $A_F = 50.0$, $A_R = 50.0$ | 0.007 kg/s |
| C13 | 1000 s | 1300 s | $A = 0.00785$ m$^2$, $A_F = 50.0$, $A_R = 50.0$ | 0.01 kg/s |

610). The reference cups (nodes 220 and 320) have a certain water storage capacity and can replenish water to the reference tubes (nodes 210 and 310) in time. The outer wall surface of the reference tubes (nodes 210 and 310, numbers 1–26 or 1–23 mean that the node is divided into 26 or 23 control volumes for more accurate calculation of flow and heat transfer) is provided with "heat structures" to simulate the convective heat transfer process with water and steam in the vessel. The heating area (node 110) in the vessel is provided with "heat structures" for simulating electric heating elements. The liquid water area (node 120) in the vessel can adjust the initial water-level by changing the parameters of the control volume. The steam space (node 130) communicates with the reference cups (nodes 220 and 320). The vessel upper head (node 140) is in communication with the pressure relief valve. The detailed RELAP5 node model of the water-level measurement device is shown in **Figure 2**. The detailed parameters of the water-level measurement system are shown in **Table 1**.

## Simulation Conditions

The depressurization rate is determined by adjusting the parameters of the pressure relief valve to study the change of the water-level measuring characteristics under transient conditions. The calculation conditions are shown in **Table 2**. For the double reference tube level gauge, 13 simulation conditions are set, including 1 steady state condition and 12 transient conditions.

# ANALYSIS OF SIMULATION RESULTS

## Measuring Characteristics Under Steady State Condition

During the steady state simulation, the reference cup and its reference tube are in a state of full water, and the time last for 1000–1300 s, as shown in **Figure 3**. Under steady state condition C1, the real water-level value is stable at 2.49 m, the measured value of the water-level meter is stable at 2.47 m, the measured value is always smaller than the real level, and the relative error is basically stable at 0.79%. In deriving formula (4), assuming that the water density in the reference tube is the same as the water density in the vessel, that is, $\rho_1' = \rho_2'$, an error will be introduced. The density at the pressure tapping point of the differential pressure transmitter is shown in **Figure 4**. The density of the pressure tapping point C is slightly smaller than the pressure tapping points A and B since the static pressure of the pressure tapping point C is smaller than the pressure tapping points A and B.

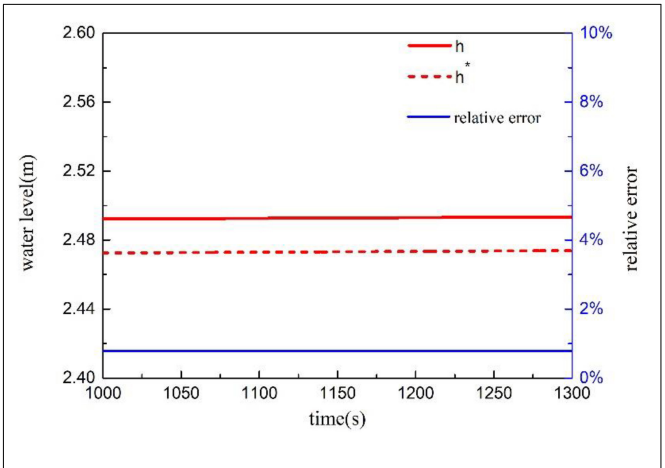


**FIGURE 3 |** The relative measurement error under steady state conditions.

## Measuring Characteristics During Rapid Depressurization

The void fraction at the bottom of the water space of the vessel under transient conditions is shown in **Figure 5**. The results of the RELAP5 code show that a large amount

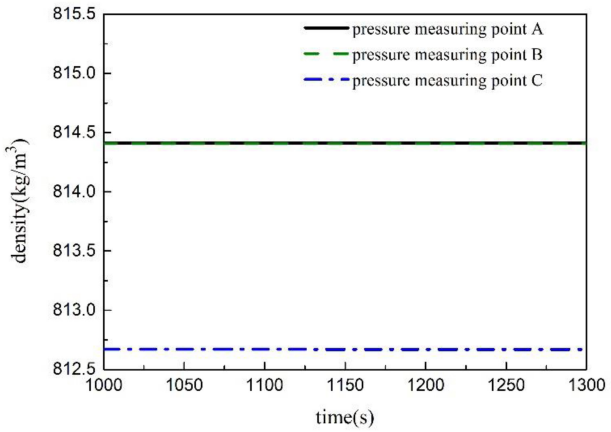


**FIGURE 4 |** The density of pressure tapping point under steady state condition.

of bubbles will be generated in the water space and reach the peak quickly, then the proportion of bubbles will gradually decrease until the normal level is reached after the flashing under transient depressurization condition. The maximum void fraction at the bottom of the vessel will reach about 0.27 under the extreme depressurization condition C2. The peak value of void fraction will reach approximately 0.1 even under C5 condition with low depressurization rate. This will have a significant impact on the pressure measurement at pressure tapping point C, and then affect the measurement value of double reference tube level gauge.

At 1011.8 s, the void fraction of water reaches the peak value, and the void fraction of each water volume at that time is shown in **Figure 6**. It can be found that the void fraction at the bottom is significantly lower than the upper part under transient conditions C4 and C5, a slow rising process is presented.

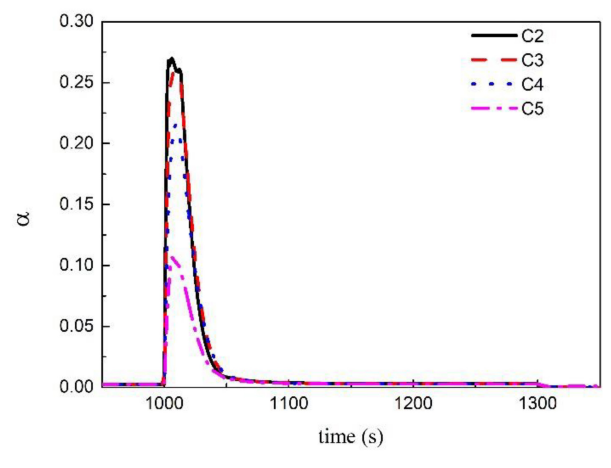


**FIGURE 5 |** Void fraction at the bottom of water space under different conditions.

The bottom of the water of the vessel is less affected by the pressure drop. However, the change of the void fraction in the axial direction is small under transient conditions C2 and C3, indicating that the entire vessel's water space has experienced severe flash evaporation.

It can be found from **Figure 7** that the flash conditions in the high reference tube and the low reference tube are almost the same, and the fluctuation range of the void fraction increases with the increase of the depressurization rate. Under transient conditions C2, the temperature and pressure are in a more severe imbalance state, and the steam is intermittently overheated and saturated. This may result in a mismatch in the proportion of void fraction between the high and low reference tubes.

The void fraction in the reference tube will reach the peak value after the pressure is released for around 8 s. The change of void fraction at different volumes of reference tube at peak time is shown in **Figure 8**. Obviously, the change trend of void

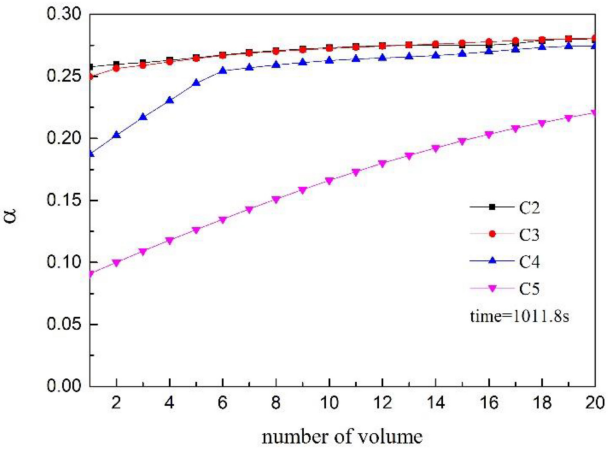


**FIGURE 6 |** The void fraction of different volume in vessel.

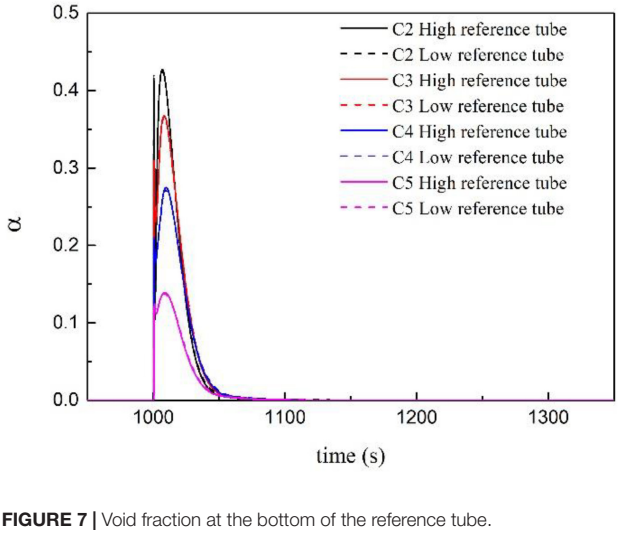


**FIGURE 7 |** Void fraction at the bottom of the reference tube.

fraction under each condition is roughly the same, from bottom to top and rising slowly. However, the void fraction drops sharply when the volume number is large. According to RELAP5 node model **Figure 2**, the volumes 26 and 23 are on top of the reference tubes (nodes 210 and 310), and these volumes communicate with the reference cups. When a large amount of water in the reference tube is flashed, the water in the reference cup penetrates into the volumes at the upper end of the reference tube under the action of gravity, which makes the void fraction in these volumes drop sharply. The void fraction in the reference tube is much higher than that in the water space of the vessel under the same transient depressurization condition. A large number of bubbles produced by flash evaporation are not easily discharged from the reference tube quickly since the inner diameter of the reference tube is extremely small, as a result that there is a bubble accumulation effect in the reference tube, which will affect the measuring accuracy of the level measurement device.

The temperature of the pressure tapping point changes along with time under different pressure reduction rates is shown in **Figure 9**. The temperature at each pressure tapping point will drop sharply, then slowly rise until it recovers after the pressure is released. The pressure at each pressure tapping point is shown in **Figure 10**, and the density at each pressure tapping point is shown in **Figure 11**. The pressure of the whole measurement system will drop rapidly after the valve is opened to relieve pressure, then a severe flash evaporation will occur, resulting a great quantity of bubbles, which will greatly reduce the density of each pressure tapping point in a short time. With the end of flash evaporation and the rise of vapor bubbles into the gas space, the space occupied by the bubbles around the pressure tapping point will be quickly backfilled by liquid water, which will lead to a suddenly density increase, and then gradually decrease to normal values due to the gradual temperature rise. In addition, the fluctuation range of temperature, density, and pressure are all closely related to the decompression rate.

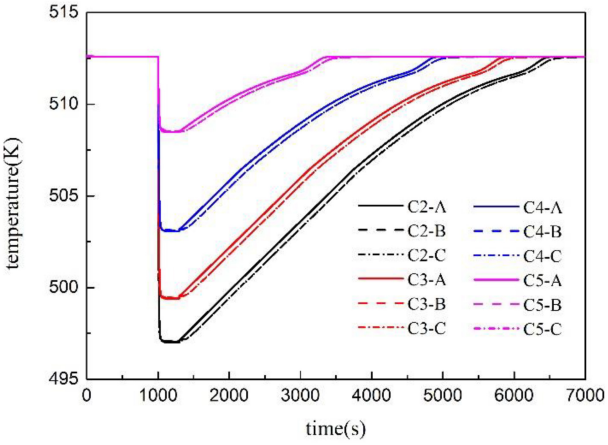


**FIGURE 9 |** Temperature of each pressure measuring point.

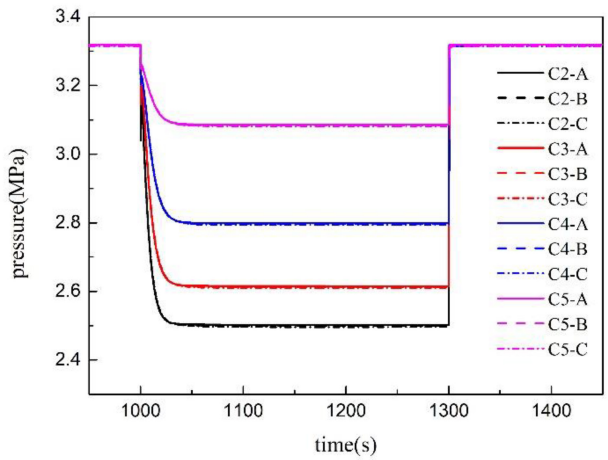


**FIGURE 10 |** Pressure of each pressure measuring point.

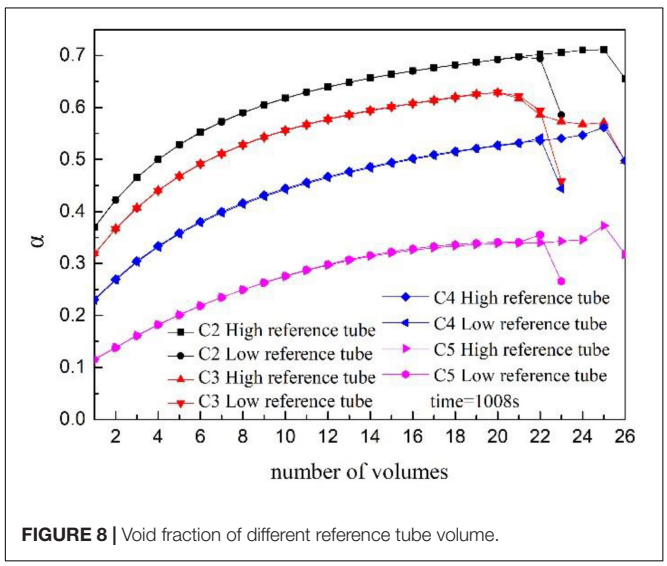


**FIGURE 8 |** Void fraction of different reference tube volume.

The transient water-level of the double reference tube level gauge under the condition of rapid pressure drop is shown in **Figure 12**. The water-level gauge appears to have a false water-level within a short time after the pressure is released. Under the extreme decompression condition C2, the measured value of water-level gauge will have a significant vibration phenomenon, and its water-level display value has far exceeded the real water-level value. During rapid depressurization, the water in the reference tube will flash evaporation violently since the temperature of the water in the reference tube is similar to the temperature of the water in the vessel, resulting in a large number of bubbles, which will cause an inaccurate conversion between the pressure difference value and the water-level value. Therefore, the measurement results of the double reference tube level gauge in the process of rapid depressurization are not ideal. The error is pretty large at least within a few tens of seconds after the pressure is released.

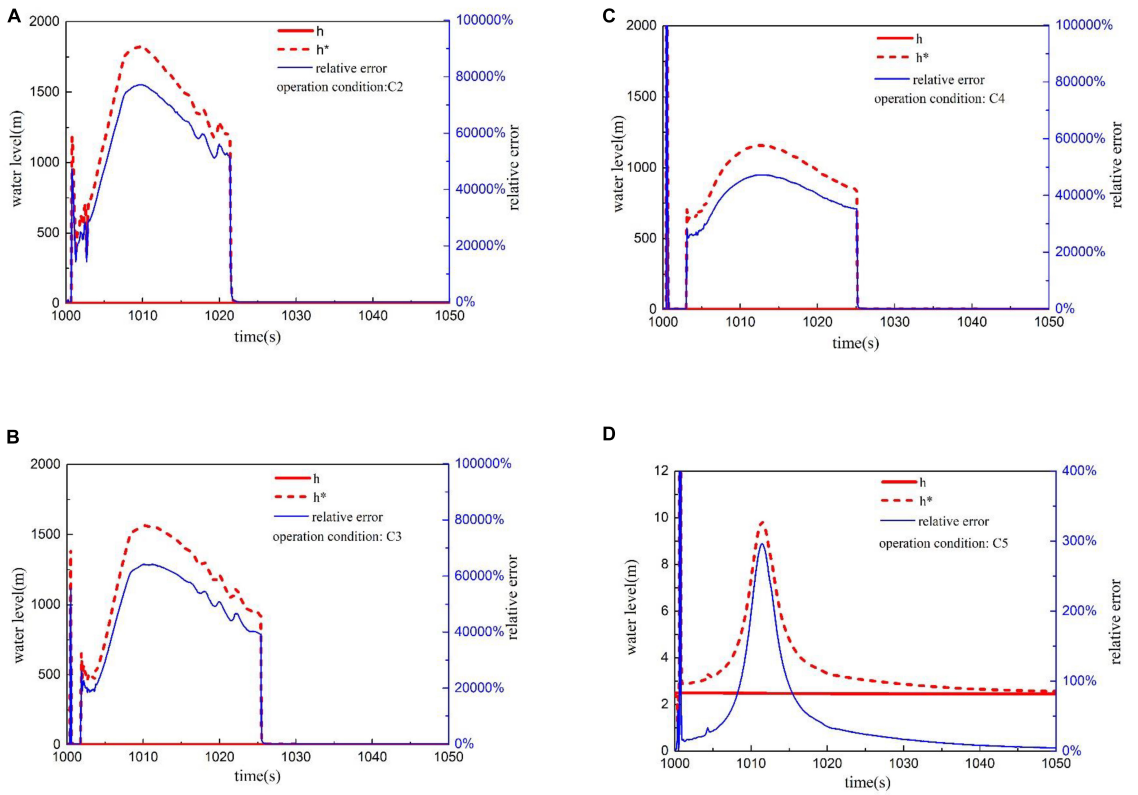


**FIGURE 12 |** Transient water-level and relative error under rapid depressurization. **(A)** Transient water-level under condition C2. **(B)** Transient water-level under condition C3. **(C)** Transient water-level under condition C4. **(D)** Transient water-level under condition C5.

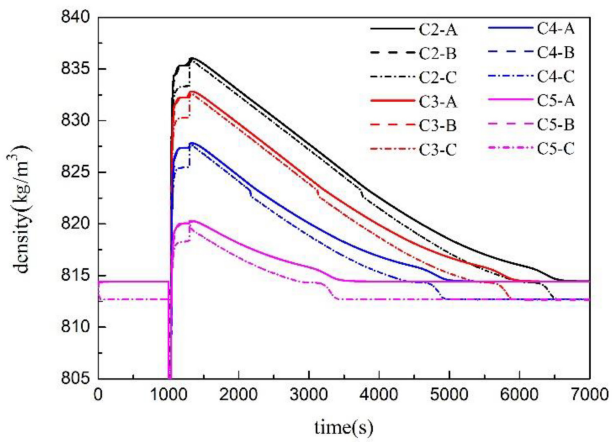


**FIGURE 11 |** Density of each pressure measuring point.

## Measuring Characteristics During Slow Depressurization

The transient water-level under slow depressurization condition is shown in **Figure 13**. A large amount of vapor bubbles will be discharged from the vessel after the pressure is released, causing the real water-level to drop slightly. With the decrease of the depressurization rate, the variation amplitude of the measured level value in the early stage of depressurization will be weakened, and the phenomenon of water-level oscillation will disappear. The flash evaporation phenomenon is not obvious since the pressure change in the vessel during the slow depressurization process is not large. The time for the measured water-level of the water-level gauge to track the real water-level will be slightly shortened. The relative error remains basically below 10.0% in the process of slow depressurization, and a smaller the depressurization rate will lead to a smaller the maximum relative error. The recovery time of relative error below 1.0% will be shortened with decreasing the depressurization rate. The simulation results indicate that the measured water-level of the double reference tube level gauge performs better in the process of slow pressure reduction, and the real water-level can be tracked in tens of seconds.

## Influence of Supply Water Flow Rate

It can be found from the above discussion that there is violent flash evaporation at each critical part of the double reference tube level under the condition of rapid depressurization, which greatly affects the transient measurement accuracy. In order to solve the problem, the section discusses the influence of the supply water flow of the reference cup on

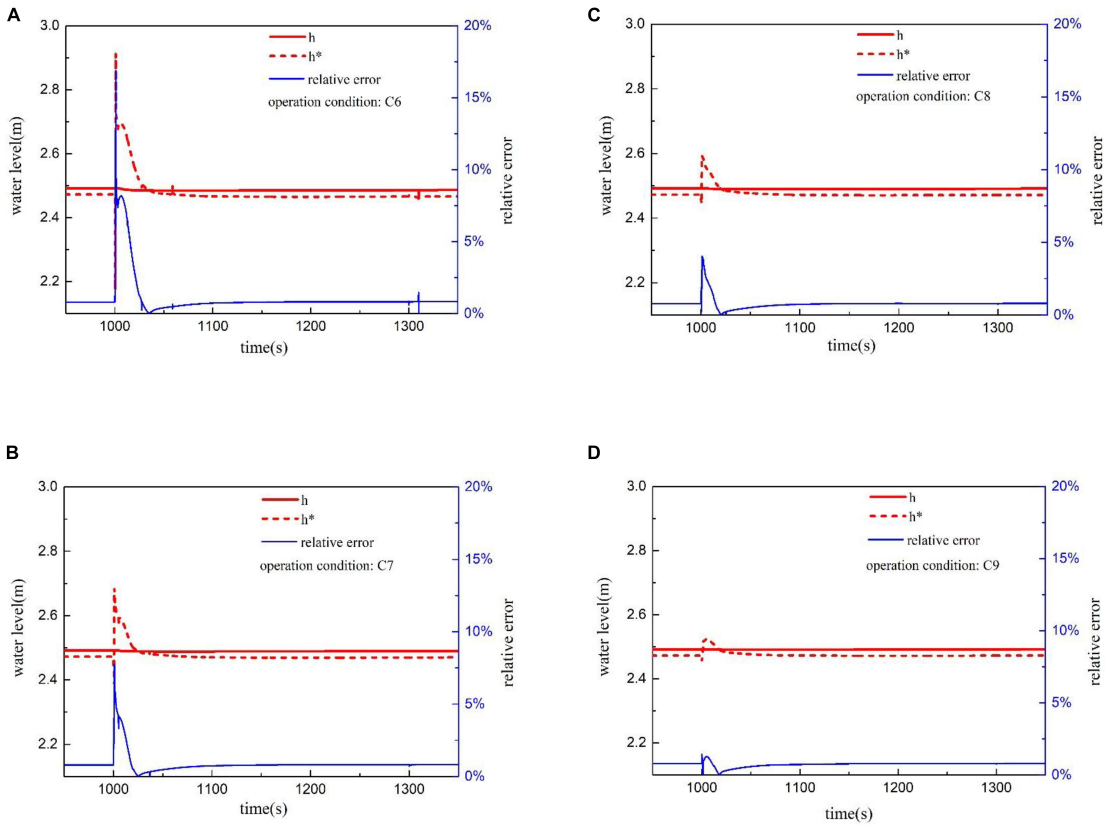


**FIGURE 13 |** Water-level and relative error under slow depressurization. **(A)** Transient water-level under condition C6. **(B)** Transient water-level under condition C7. **(C)** Transient water-level under condition C8. **(D)** Transient water-level under condition C9.

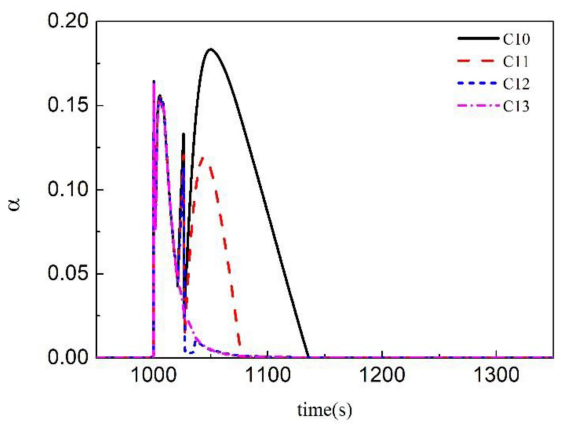


**FIGURE 14 |** Void fraction in low reference cup.

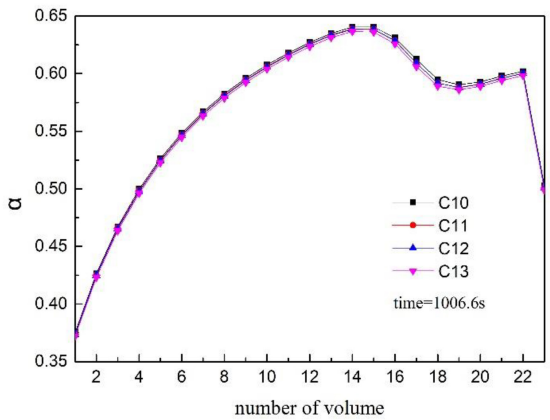


**FIGURE 15 |** Void fraction of different volume of low reference tube.

the measured value of the differential pressure water-level measurement system.

Taking the low reference cup as an example, the void fraction under different supply water flow conditions is shown in **Figure 14**. The vibration of the void fraction gradually weakened with the increase of the reference cup supply water flow, and the time needed to recover the void fraction to the normal level is also decreased. A part of the steam can be condensed by increasing the supply water flow, reducing the severity of the flash in the reference cup.

The void fraction of the different volume in low reference tube under supply water flow rates is shown in **Figure 15**. The void

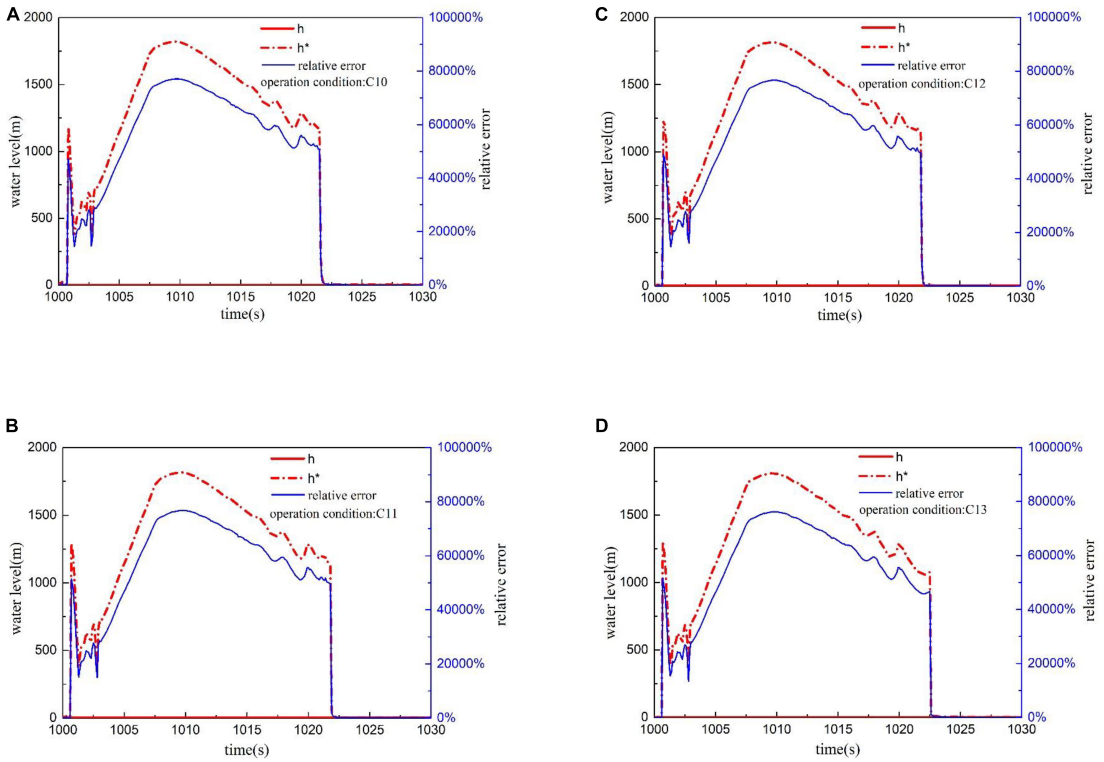


**FIGURE 16 |** Water-level and relative error curve under different supply water flow. **(A)** Transient water-level under condition C10. **(B)** Transient water-level under condition C11. **(C)** Transient water-level under condition C12. **(D)** Transient water-level under condition C13.

fraction inside the reference tube cannot be effectively reduced by increasing the supply water flow. Since the inner diameter of the reference tube is pretty small, a large amount of bubbles cannot be discharged in time under the condition of rapid depressurization, resulting in a short period of bubble blockage. The reason for such a result might be that a large amount of bubbles rushed out from the inlet of the reference tube in an instant, which inhibited the process of supply water into the reference tube, resulting in that most of the supply water overflowed from the reference cup.

As shown in **Figure 16**, there is no significant effect to increase the supply water flow rate in shortening the tracking time and reducing the deviation of the measured water-level. The flash evaporation will occur in both the reference tube and the reference cup under the condition of high depressurization rate, and a large number of bubbles are generated, resulting in that supply water cannot be injected into the reference tube in time.

## CONCLUSION

In this paper, a simulation model of RELAP5 code is established for the double reference tube level gauge. The measuring characteristics of the differential pressure water-level measurement system are analyzed under both steady state condition and transient depressurization condition. The conclusions are as follows:

(1) The measurement error of the double reference tube level gauge can be controlled within 1% under the steady state condition, which can usually meet the accuracy requirements.
(2) There will be violent flash evaporation in the water-level measurement system when the depressurization rate is large, which makes the water density, temperature, and pressure fluctuate sharply in the reference tube and vessel. The measured value of the double reference tube level gauge deviates greatly from the real water-level value in a short time. The measurement error of the double reference tube level gauge can be controlled within 10% when the depressurization rate is small, and the real water-level can be tracked in tens of seconds.
(3) Increasing the supply water flow rate can reduce the flash evaporation intensity in the reference cup under the condition of rapid depressurization rate, but cannot reduce the relative error of the water-level measurement system during the transient measurement, nor shorten the response time of water-level measurement systems.

The research that has been completed so far is mainly about the measuring characteristics of the measurement device in a stationary state. Additionally, the water-level measurement device may work under the conditions of rolling motion and sloshing motion. In the future, we will focus on the ocean

application scenarios to further study the measuring characteristics of the measurement device. Meanwhile, we also hope that researchers can do further experimental research on the double reference tube level gauge under the transient depressurization condition and optimize its structure to improve the measurement accuracy.

## DATA AVAILABILITY STATEMENT

The raw data supporting the conclusions of this article will be made available by the authors, without undue reservation.

## AUTHOR CONTRIBUTIONS

In the course of the completion of this thesis, all authors have substantial contributions to design of the work. GF and JC provided the research direction of the subject. XZ determined the research method and specific parameters such as the working quality. LS and XZ carried out numerical simulation and obtained, collated and analyzed the data, in the process, JC had been instructed and helped. XZ wrote the first draft of the manuscript and was corrected by GF, and JC also gave some suggestions. All authors approved the final version to be published and agreed to be responsible for all aspects of the work.

## FUNDING

The authors greatly appreciate support from the National Natural Science Foundation of China (Grant No. 11875117) and the Fundamental Research Funds for the Central Universities (No. 3072020CFJ1502).

## REFERENCES

CGN Research Institute Co., Ltd. (2018a). *A Device and Method for Measuring Water Level of Pressurizer: China, 201810443517.6*. 2018-05-10 (in Chinese).

CGN Research Institute Co., Ltd. (2018b). *Pressurizer and Liquid Level Measuring Device for Pressurizer of Offshore Floating Platform: China, 201810433077.6*. 2018-05-08 (in Chinese).

Jiang, R. T., Zhou, S. L., and Wei, Y. Q. (2013). Transient analysis for water level of AP1000 steam generator. *Atomic Energy Sci. Technol.* 47, 610–613.

Jin, B., Zhang, Z., and Zhang, H. (2015). Structure design and performance analysis of a coaxial cylindrical capacitive sensor for liquid-level measurement. *Sens. Actuators A Phys.* 223, 84–90. doi: 10.1016/j.sna.2014.12.027

Kim, J. Y., Lee, J. H., Bae, S. E., Paek, S., Kim, S. H., Kim, T. J., et al. (2017). Automated high-temperature liquid level measurement system using a dynamic tube pressure technique. *J. Indus. Eng. Chem.* 49, 30–35. doi: 10.1016/j.jiec.2016.10.041

Lee, D. W., No, H. C., and Song, C. H. (2005). Measurement of two-phase mixture level using an ultrasonic method. *Exp. Ther. Fluid Sci.* 29, 609–614. doi: 10.1016/j.expthermflusci.2004.07.003

Li, D. P., and Jiao, Z. G. (1999). Correction calculation of the double reference tube level gauge for steam generator. *Power Syst. Eng.* 15, 21–23.

Li, D. P., and Sun, F. R. (1997). The improvement of water level measurement system of marine steam generator. *Power Gen. Equip.* 5, 28–30.

Li, D. P., Yang, Z. D., and Zhao, Y. S. (2005). Improvement of soft sensing technology of double reference tube level measurement system of evaporator. *Comput. Meas. Control* 13, 1186–1188.

Lin, J. (1986). The method for measuring level of high temperature and high pressure vessels for marine. *Nucl. Power Eng.* 7, 65–71.

Mel'nikov, V. I., Ivanov, V. V., and Teplyashin, I. A. (2016). The study of ultrasonic reflex-radar waveguide coolant level gage for a nuclear reactor. *Nucl. Energy Technol.* 2, 37–41. doi: 10.1016/j.nucet.2016.03.007

Melnikov, V. I., and Khokhlov, V. N. (1997). Waveguide ultrasonic liquid level transducer for nuclear power plant steam generator. *Nucl. Eng. Design* 176, 225–232. doi: 10.1016/s0029-5493(97)00155-6

Paczesny, D., Tarapata, G., Michał, M., and Jachowicz, R. (2015). The capacitive sensor for liquid level measurement made with ink-jet printing technology. *Proc. Eng.* 120, 731–735. doi: 10.1016/j.proeng.2015.08.776

Petrie, C. M., and Mcduffee, J. L. (2018). Liquid level sensing for harsh environment applications using distributed fiber optic temperature measurements. *Sens. Actuators A Phys.* 282, 114–123. doi: 10.1016/j.sna.2018.09.014

Rizi, M. T., and Abadi, M. H. S. (2017). Analytical modeling of a coaxial cylindrical probe capacitive sensor based on MATLAB/Simulink for conductive liquids level measurements. *Turkish J. Elect. Eng. Comput. Sci.* 25, 3024–3036. doi: 10.3906/elk-1603-259

Salehi, A., Kazemi, M. H., and Safarzadeh, O. (2018). The μ–synthesis and analysis of water level control in steam generators. *Nucl. Eng. Technol.* 51, 163–169. doi: 10.1016/j.net.2018.09.018

Singh, S., and Mohanty, A. R. (2018). Measurement of boiling liquid levels by decomposition of sound waves in a waveguide. *Appl. Acoust.* 129, 248–257. doi: 10.1016/j.apacoust.2017.08.005

Soltz, D. J. (1984). *Ultrasonic Liquid Level Meter*. U.S. Patent No. 4,470,299.

Wang, G. H., Peng, C. H., and Guo, Y. (2016). The preliminary thermal–hydraulic analysis of a water cooled blanket concept design based on RELAP5 code. *Fusion Eng. Design* 109, 489–495. doi: 10.1016/j.fusengdes.2016.02.069

Xiong, F., and Zhou, H. Q. (2016). The optimization of level measurement system for steam generator of CPR1000 Nuclear Power Plant. *Electr. Instrum. Customer* 23, 95–97.

Zhang, G. D., Yang, X. H., Ye, X. L., Xu, H., Lu, D. Q., and Chen, W. (2012). Research on pressurizer water level control of pressurized water reactor nuclear power station. *Energy Procedia* 16(Part–B), 849–855. doi: 10.1016/j.egypro.2012.01.136

Zhang, Y., and Liu, X. Y. (2013). Research on the liquid level in tin bath based on application of capacitance sensor. *Adv. Mater. Res.* 816-817, 429–432. doi: 10.4028/www.scientific.net/amr.816-817.429

Zhang, Z., and Hu, L. S. (2012). Performance assessment for the water level control system in steam generator of the nuclear power plant. *Ann. Nucl. Energy* 45, 94–105. doi: 10.1016/j.anucene.2012.02.012

**Conflict of Interest:** The authors declare that the research was conducted in the absence of any commercial or financial relationships that could be construed as a potential conflict of interest.

frontiers in Energy Research

PERSPECTIVE
published: 03 September 2020
doi: 10.3389/fenrg.2020.00214

# Review and Prospect of the Measurement Technology of the Thickness of the Liquid Film on the Wall of the Corrugated Plate Dryer

*Bo Wang[1]*, Bowen Chen[1], Jiming Wen[1], Chuan Lu[2] and Ruifeng Tian[1]**

*[1] Fundamental Science on Nuclear Safety and Simulation Technology Laboratory, Harbin Engineering University, Harbin, China, [2] Science and Technology on Reactor System Design Technology Laboratory, Nuclear Power Institute of China, Chengdu, China*

OPEN ACCESS

**Edited by:**
*Jun Wang,*
*University of Wisconsin–Madison,*
*United States*

**Reviewed by:**
*Xingang Zhao,*
*Massachusetts Institute of Technology, United States*
*Jiankai Yu,*
*Massachusetts Institute of Technology, United States*
*A. E. Kabeel,*
*Tanta University, Egypt*

***Correspondence:**
*Bo Wang*
*bowang@hrbeu.edu.cn*
*Ruifeng Tian*
*ruifengtian@hrbeu.edu.cn*

**Specialty section:**
*This article was submitted to Nuclear Energy, a section of the journal Frontiers in Energy Research*

**Received:** *10 June 2020*
**Accepted:** *07 August 2020*
**Published:** *03 September 2020*

**Citation:**
*Wang B, Chen B, Wen J, Lu C and Tian R (2020) Review and Prospect of the Measurement Technology of the Thickness of the Liquid Film on the Wall of the Corrugated Plate Dryer. Front. Energy Res. 8:214. doi: 10.3389/fenrg.2020.00214*

The corrugated plate dryer is an important steam-water separation device in the steam generator in the secondary loop of a light water reactor. It is essential to understand its steam-water separation mechanism. Most studies have shown that the separation efficiency of the corrugated plate is related to the thickness of the liquid film on the wall of the corrugated plate. We have studied the relationship between the thickness of the liquid film and the critical airflow velocity of the corrugated plate. At present, scholars mostly use the image method, ultrasonic method, and capacitance method to measure the thickness of thin liquid film. We have analyzed the application of these three methods in liquid film thickness measurement. Some important examples are listed. The results show that the capacitance method is recommended for liquid film thickness measurement experiments, whereas its accuracy is not particularly high. To pursue the higher accuracy, the image method is recommended. Planar laser-induced fluorescence (PLIF) technology is the first choice among image methods. The ultrasonic method is applicable in the case that the measurement data are large.

**Keywords: liquid film thickness, corrugated plate, PLIF, steam-water separation, measurement**

## INTRODUCTION

The corrugated plate dryer is an important steam-water separation device in the steam generator in the secondary loop of the nuclear power plant. It is important to understand its steam-water separation mechanism. The rupture and flow of the liquid film on the wall have a huge impact on the steam-water separation efficiency of the corrugated plate. The current research status of the corrugated plate is detailed in our previous review article in reference (Wang et al., 2019). We will not repeat them here. Most studies have shown that the separation efficiency of the corrugated plate is related to the thickness of the liquid film on the wall of the corrugated plate. We have studied the relationship between the thickness of the liquid film and the critical airflow velocity of the corrugated plate in reference (Wang and Tian, 2019b) [as shown in Eq. (1)]. The Navier-Stokes (N-S) equation and continuity equation of the two-dimensional boundary layer in the curvilinear coordinate system at the corrugated plate corner is established. The dimensionless method is used. Neglecting the higher-order terms, a simplified N-S equation and continuity equation in curvilinear

coordinate system can be obtained. A liquid film breakdown model at the corrugated plate corner is established according to boundary layer theory, thus Eq. (1) is obtained.

$$u_g = 2.4\left(\frac{d\cos\theta\cdot\sigma\mu_{al}^2}{\rho_l\rho_g\mu_g}\right)^{\frac{1}{3}}\frac{1}{h} \quad (1)$$

where, $d$, $\theta$, $\sigma$, $\mu_{al}$, $\rho_l$, $\rho_g$, $\mu_g$, $h$ are linear distance between two plate walls, inflection angle of the corrugated plate corner, surface tension, liquid phase dynamic viscosity, liquid density, air density, dynamic viscosity of the air, and liquid film thickness, respectively.

Considering the important role of the measurement for liquid film thickness, many scholars currently have used the image method, capacitance method, and ultrasonic method to measure the thickness of liquid film. In the following, we analyze the application of these three methods in liquid film thickness measurement. Some important examples are listed. Prospects for future measurement methods of the thickness of the liquid film on the wall surface of the corrugated plate are given.

# MEASUREMENTS METHODS

## Ultrasonic Method

Wei et al. (2020) measured the free-falling film under the large Reynolds number and analyzed the volatility of the liquid film. The ultrasonic method was applied to the measurement the instantaneous thickness of the liquid film left on the wall of the square tube. Then they performed a power spectrum analysis on the curve of the instantaneous thickness of the liquid film (Wei et al., 2020). The ultrasonic method is very common, of which the principle is the doppler effect. During the measurement, the sensor emits ultrasonic waves to the measurement object at a certain Doppler angle. Ultrasound waves change their frequency when they encounter tiny particles (bubbles or solid particles). This makes the time of the reflected wave received by the sensors in different positions different, and the velocity of the liquid can be obtained.

The ultrasonic reflected wave and incident wave of the liquid film can be obtained by using the ultrasonic transducer. Fast Fourier Transform is performed on the two through an oscilloscope to obtain the reflection coefficient spectrogram and frequency, and then to obtain the thickness of the liquid film (Wei et al., 2020). The above measurement process can all be completed by using an oscilloscope and through computer programming, thus achieving the acquisition of liquid film thickness. The above process does not require post-processing. Therefore, the ultrasonic method is suitable for the measurement of large amounts of data. However, the shortcomings of ultrasonic method could be described as follows: The velocity of the fluid particles on the ultrasonic motion path can be obtained based on spectrum analysis. The fluid particle velocity is assumed to be the fluid velocity at that location. Of course, there must be a difference between the speed of a single particle and the speed of fluid. This assumption is accepted by the academic community, and there is currently no very good solution to this.

## Capacitance Method

The basic principle of the capacitance method to measure film thickness is as follows: When the medium or plate distance between two parallel metal electrodes changes, the output voltage changes. Within a certain range, the voltage change of the capacitor has a linear relationship with the change of the liquid film thickness. The thickness of the liquid film can be measured by obtaining the voltage signal.

He et al. (2019) conducted an experimental study on the liquid film behavior of the two-phase circulation on the rod bundle. They conducted cold experiments on the circulation in a 3 × 3 fuel bundle in a pressurized water reactor. Air-water circulation is used to simulate the flow of hot steam. In the test, the local liquid film thickness of the rod bundle needs to be measured. They developed a method for measuring the thickness of the liquid film based on the capacitance method.

When the capacitance method is used for measurement, the liquid film thickness can be automatically measured directly through the combination of capacitance sensors, National Instruments (NI) data collectors, and computers. Thus, the measurement speed is very good.

## Image Method

Ye et al. (2020) conducted an experimental study on the transmission of the liquid surface around the bubbles in the microchannel with cavitation. High-speed cameras are used to capture the shape of bubbles. The gray-scale image of bubbles can be obtained based on the processing of image pixels based on MATLAB (Ye et al., 2020). In the experiment, they needed to measure the thickness of the thin liquid film under Taylor flow (Ye et al., 2020). But in Taylor flow, the bubble keeps in contact with the liquid film. The irregular shape of the bubbles will be irregular in the shape of the liquid film.

Chinnov et al. (2019) also applied the image measurement method. High-speed infrared cameras and fluorescence methods were used to measure the thickness and temperature field of the vertically dropped heated liquid film on the flat plate at a Reynolds number of 50. Liu et al. (2020) conducted an experimental study on the interface fluctuation and liquid film thickness of the swirling gas-liquid flow. Image analysis is used to measure the thickness of the liquid film.

Wang and Tian (2019a; 2019c) and Wang et al. (2020a) measured the thickness of the liquid film on the wall surface of the corrugated plate based on the planar laser-induced fluorescence (PLIF) method. Their measurement accuracy can reach 1 μm. Before the experiment, a few milligrams of rhodamine B was put into the liquid. The narrow-slit method is applied to generate a stable flowing liquid film on the wall surface (Wang and Tian, 2019a; Wang et al., 2020a). The PLIF measurement needs to keep the surrounding environment in a dark state (Wang and Tian, 2019a). The wavelength of the light emitted by the solid-state laser is 532 nm. The maximum absorption wavelength of rhodamine B is 555 nm. Therefore, the rhodamine B particles irradiated by the solid-state laser will be excited. The excited particles are unstable, so they return to the ground state and release visible light. This light can be captured by a high-speed

camera. A liquid film surface profile can be captured through acquisition of the horizontal cross-section image of water film by high-speed camera, thus obtaining average water film thickness by application of liquid film image processing software.

Yang et al. (2020) measured the liquid film thickness based on the diode-laser absorption spectroscopy (DLAS) method. Guo et al. (2020) conducted an experimental measurement of transient liquid film during micro-channel flow boiling based on the laser confocal displacement meter (LFDM) method.

## ANALYSIS AND DISCUSSION

According to He et al. (2019), the capacitance method is a contact measurement method. This will inevitably affect the flow of the liquid film. Therefore, this will affect the accuracy of the measurement.

In reference (Ye et al., 2020), Ye et al. gave a novel calculation method for the thickness of the liquid film. For bubbles with a longer length, the shape of the liquid film in contact therewith is generally more regular. Its shape is mostly rectangular. Its thickness is the width of the rectangle. Measurements can be achieved using optical image methods such as PLIF technology. For irregularly shaped bullet bubbles and short bubbles, they used an integral method to measure the thickness of the liquid film. We have also used the idea of integration to calculate the average liquid film thickness when using the moving particle semi-implicit method to simulate the shape of the liquid film rupture (Wang et al., 2020b).

The study of the volatility of the liquid membrane with such a small Reynolds number is rare in academia because the formation and control of liquid film with a small Reynolds number is difficult. Therefore, the research is very innovative. The experiment in reference (Chinnov et al., 2019) outcomes the results in the case that the Reynolds number is 50. Experiments with a larger range of Reynolds numbers are encouraged. The general conclusion is expected to be presented.

Besides, the PLIF method is different from other image measurement methods in that PLIF uses fluorescent substances, because in general experiments, the boundary of the liquid film and the surrounding environment are not much different under high-speed camera shooting. Therefore, there are difficulties and certain errors for the subsequent image processing. Because all the use of images to measure the thickness of the liquid film needs to identify the boundary of the liquid film. The principle of boundary differentiation is applied. The determination of the boundary threshold is one of the main sources of error. If a fluorescent substance such as rhodamine B is added and the surrounding environment is kept in a dark state, the boundary image of the liquid film is clearer under a high-speed camera. This is very beneficial for reducing errors. Adding a few milligrams of rhodamine B has almost no effect on the physical properties of the liquid film. Therefore, the measurement will not be affected in any way. Obviously, if it is extremely precise measurement, such as the measurement accuracy is about a few nanometers, the fluorescent substance is not recommended to be used. Of course, this kind of high-accuracy measurement is not common for the measurement of the thickness of the liquid film on the wall surface of the corrugated plate.

According to references (Yang et al., 2020) and (Guo et al., 2020), both DLAS and LFDM are optical imaging methods. No fluorescent agent is used in these methods. Therefore, this is not conducive to eliminating the reflected light generated by the high-speed camera shooting the liquid film image.

According to above, the following conclusions can be obtained:

(1) The accuracy of the image method depends on the resolution of the high-speed camera. The measurement accuracy is generally a few microns, but the measurement speed is slow (Wang and Tian, 2019a,c; Wang et al., 2020a), because in the PLIF method, a high-speed camera is required to obtain the image of the liquid film. It is necessary to write a program based on the principle of boundary differentiation to identify the boundary of the liquid film. Finally, the number of pixels corresponding to the thickness of the liquid film is measured by the image processing software, and the thickness of the liquid film is calculated according to the scale.
(2) The capacitance method is a contact measurement. When the capacitance method is used for measurement, the liquid film thickness can be automatically measured directly through the combination of capacitance sensors, NI data collectors, and computers. Thus, the measurement speed is very good. However, the contact measurement will affect the flow field and temperature field of the liquid film, which will inevitably produce measurement errors.
(3) The accuracy ultrasonic method is able to reach tens of microns. The measurement accuracy is not as good as the image method, but it is suitable for the measurement of large amounts of data.

Therefore, for the experiments that do not require very high accuracy, the capacitance method is recommended. For higher measurement accuracy, the image method is recommended. PLIF technology is the first choice among image methods. PLIF can effectively improve the recognition accuracy of liquid film boundary. The ultrasonic method is suitable for measuring the thickness of the liquid film when there are many measurement data.

## CONCLUSION

The corrugated plate dryer is an important steam-water separation device in the steam generator in the secondary loop of the nuclear power plant. Since the separation efficiency of the corrugated plate is related to the thin thickness of the liquid film on the wall surface of the corrugated plate, the measurement methods of the thickness of the thin liquid film such as the image method, the ultrasonic method, and the capacitance method are summarized.

For the experiments that do not require very high accuracy, the capacitance method is recommended. The ultrasonic method is suitable for measurement when the amount of data is large. For higher measurement accuracy, the image method is

recommended. The study is expected to provide reference for liquid film measurement in nuclear engineering.

## DATA AVAILABILITY STATEMENT

The raw data supporting the conclusions of this article will be made available by the authors, without undue reservation.

## AUTHOR CONTRIBUTIONS

BW designed this study. Besides, BW, BC, JW, CL, and RT contributed to the investigation on the related references. BW mainly co-wrote most of the manuscript. All authors contributed to writing the manuscript.

## FUNDING

The authors would like to acknowledge financial support provided by the Ph.D. Student Research and Innovation Fund of the Fundamental Research Funds for the Central Universities (3072020GIP1518), the Fundamental Research Funds for the Central Universities, China Scholarship Council, Chinese Universities Scientific Fund, and the National Natural Science Foundation of China (No. 51676052).

## REFERENCES

Chinnov, E. A., Shatskiy, E. N., and Semionov, V. V. (2019). Effect of thermocapillary instability on liquid film breakdown. *Int. J. Heat Mass Transfer* 145:118692. doi: 10.1016/j.ijheatmasstransfer.2019.118692

Guo, C. H., Tao, J., Jiang, Y. Y., Sun, Y. H., and Wang, T. (2020). Measurement and theoretical analysis of transient liquid film during micro-channel flow boiling. *Int. J. Mult. Flow* 130:103365. doi: 10.1016/j.ijmultiphaseflow.2020.103365

He, H., Pan, L. M., Ren, Q. Y., Ting-pu, Y., and Zhang, D. F. (2019). Local liquid film behavior of annular two-phase flow on rod-bundle geometry-I. Experimental phenomenon and analysis. *Int. J. Heat Mass Transfer* 141, 58–70. doi: 10.1016/j.ijheatmasstransfer.2019.06.032

Liu, L., Wang, K., and Bai, B. F. (2020). Comparative investigation of liquid film thickness and interfacial wave properties of swirling gas-liquid flows. *Chem. Eng. Sci.* 213:115407. doi: 10.1016/j.ces.2019.115407

Wang, B., Chen, B. W., Li, R., and Tian, R. F. (2020a). Analysis of fluctuation and breakdown characteristics of liquid film on corrugated plate wall. *Anna. Nuclear Energy* 135:106946. doi: 10.1016/j.anucene.2019.106946

Wang, B., Chen, B. W., Li, R., and Tian, R. F. (2020a). Analysis of fluctuation and breakdown characteristics of liquid film on corrugated plate wall. *Anna. Nuclear Energy* 135:106946. doi: 10.1016/j.anucene.2019.106946

Wang, B., Chen, B. W., Li, R., and Tian, R. F. (2020b). Study on fracture morphology of water film on the wall of vertical corrugated plate under shear of the air flow. *Ann. Nuclear Energy* 136:107012. doi: 10.1016/j.anucene.2019.107012

Wang, B., Chen, B. W., and Tian, R. F. (2019). Review of research progress on flow and rupture characteristics of liquid film on corrugated plate wall. *Ann. Nuclear Energy* 132, 741–751. doi: 10.1016/j.anucene.2019.06.060

Wang, B., and Tian, R. F. (2019a). Study on characteristics of water film breakdown on the corrugated plate wall under the horizontal shear of airflow. *Nuclear Eng. Des.* 343, 76–84. doi: 10.1016/j.nucengdes.2018.12.018

Wang, B., and Tian, R. F. (2019b). Study on fluctuation feature and breakdown characteristic of water film on the wall of corrugated plate. *Int. J. Heat Mass Transfer* 143:118501. doi: 10.1016/j.ijheatmasstransfer.2019.118501

Wang, B., and Tian, R. F. (2019c). Investigation on flow and breakdown characteristics of water film on vertical corrugated plate wall. *Ann. Nuclear Energy* 127, 120–129. doi: 10.1016/j.anucene.2018.12.001

Wei, Z. Y., Wang, Y. F., Wu, Z. W., Xin, P., and Yu, G. S. (2020). Wave characteristics of the falling liquid film in the development region at high Reynolds numbers. *Chem. Eng. Sci.* 215:115454. doi: 10.1016/j.ces.2019.115454

Yang, H. N., Guo, Y. F., Li, C. L., Tao, J., Zhang, Y., Su, M., et al. (2020). Development of a two-line DLAS sensor for liquid film measurement. *Spectrochim. Acta Part AMo. Biomol. Spectrosc.* 224:117420. doi: 10.1016/j.saa.2019.117420

Ye, X., Hao, T.-T., Chen, Y. S., Ma, X. H., and Rui, J. (2020). Liquid film transport around Taylor bubble in a microchannel with gas cavities. *Chem. Eng. Process. Process Intensificat.* 148:107828.

**Conflict of Interest:** The authors declare that the research was conducted in the absence of any commercial or financial relationships that could be construed as a potential conflict of interest.

frontiers in Energy Research

ORIGINAL RESEARCH
published: 07 September 2020
doi: 10.3389/fenrg.2020.00197

# Study on the Breakdown Mechanism of Water Film on Corrugated Plate Wall Under the Horizontal Shear of Airflow: A Short Communication

*Bo Wang[1]*, Bowen Chen[1], Bingzheng Ke[1], Gongqing Wang[1], Ru Li[1], Jiming Wen[1], Chuan Lu[2] and Ruifeng Tian[1]**

[1] *Fundamental Science on Nuclear Safety and Simulation Technology Laboratory, Harbin Engineering University, Harbin, China,* [2] *Science and Technology on Reactor System Design Technology Laboratory, Nuclear Power Institute of China, Chengdu, China*

OPEN ACCESS

**Edited by:**
*Shripad T. Revankar, Purdue University, United States*

**Reviewed by:**
*Subash Sharma, University of Massachusetts Lowell, United States*
*Mingjun Wang, Xi'an Jiaotong University, China*

***Correspondence:**
*Bo Wang*
*bowang@hrbeu.edu.cn*
*Ruifeng Tian*
*ruifengtian@hrbeu.edu.cn*

**Specialty section:**
*This article was submitted to Nuclear Energy, a section of the journal Frontiers in Energy Research*

**Received:** *05 June 2020*
**Accepted:** *27 July 2020*
**Published:** *07 September 2020*

**Citation:**
*Wang B, Chen B, Ke B, Wang G, Li R, Wen J, Lu C and Tian R (2020) Study on the Breakdown Mechanism of Water Film on Corrugated Plate Wall Under the Horizontal Shear of Airflow: A Short Communication. Front. Energy Res. 8:197. doi: 10.3389/fenrg.2020.00197*

The corrugated plate dryer (CPD) is an important steam-water separation (SWS) equipment in the steam generator in the secondary loop of nuclear power plants (NPPs). Therefore, it is very important to understand the process and mechanism of liquid film rupture (LFR) on the wall surface of the CPD. In this paper, for the first time, the process of rupture of the liquid film (LF) on the surface of the corrugated plate is studied. The mechanism of LFR on the wall surface of a vertical corrugated plate was studied experimentally. A high-speed camera was used to collect the image of the broken liquid film, and an experimental research on the broken position, the broken process, and the broken shape of the liquid film was carried out. The results show that the rupture of the liquid film on the wall surface of the corrugated plate under the horizontal shear of airflow (HSA) mostly occurs at the upper middle position of the main flow of the liquid film. Also, the rupture position moves up with the increase in the Reynolds number of the liquid film. LFR needs to go through the process of stable flow, single strip-shaped liquid film (SSLF) detachment, two strip-shaped liquid film (TSSLF) formation, and finally chaotic disordered rupture. The angle between the two strip-shaped liquid films (ATSSLF) is positively related to the Reynolds number of the liquid film.

**Keywords: nuclear energy, corrugated plate dryer, breakdown mechanism, breakdown position, liquid film, water film rupture process**

## INTRODUCTION

The corrugated plate dryer (CPD) is an important steam-water separation (SWS) equipment in the steam generator in the secondary loop of nuclear power plants (NPPs; Zhang et al., 2015; Huang et al., 2019; Wang and Tian, 2019a,b,c; Wang et al., 2019; Chen et al., 2020a,b; Fang et al., 2020a,b; Wang et al., 2020a,b,c). Therefore, it is very important to understand the process and mechanism of liquid film rupture (LFR) on the wall surface of the CPD. The structural

diagram of the CPD and the distribution of airflow and LF inside the CPD are shown in **Figure 1**.

The LFR due to the horizontal shear of airflow (HSA) has a great influence on the gas–water separation effect of the CPD. As the HSA increases, the stable LF will rupture at a certain instant. The separation mechanism of the LFR is also closely related to the position of the LFR and the movement behavior after the rupture. Zhang et al. (2015) studied the fluctuation of the LF on the wall surface of the CPD. Wang and Tian studied the rupture characteristics of the LF on the surface of the CPD (Wang et al., 2019; Wang and Tian, 2019a,b,c; Wang et al., 2020c). Chen et al. (2020a; 2020b) studied the motion behavior of droplets in the CPD. For the current research status of the LF on CPD, refer to reference (Wang et al., 2019). This article will not repeat them here.

The above studies mainly focused on the study of the volatility of the liquid film and the separation efficiency of the CPD. The current research shows that there is no characteristic frequency for the volatility of the liquid film on CPD wall. When the Reynolds number is small enough, the gravity of the LF will not cause the LF to break. Therefore, based on this, many scholars simplified complex three-dimensional problems into two-dimensional models when studying LFR. Nonetheless, due to the complexity of the LFR process, research on the LFR and morphology under HSA has not been unified. There is not enough research on the phenomenon of two strip-shaped liquid film (TSSLF) accompanied by large airflow velocity. In this paper, the LF on the wall surface of the CPD under the HSA is taken as a research object to study the shape and process of LFR.

## EXPERIMENT ON LFR

An LFR experiment was conducted on a corrugated plate with a plate spacing of 18.2 mm, height of 250 mm, and folding angle of 33 degrees. The schematic diagram of the experimental bench can refer to reference (Wang et al., 2020c), because this article uses the same experimental bench as reference (Wang et al., 2020c). However, the parameters of CPD applied for the article and reference (Wang et al., 2020c) are different. Similarly, the capture of LF and measurement of PLIF can be seen in reference (Wang et al., 2020c). The parameters of the CPD selected in the article are much smaller than those applied in NPPs. This is because these CPD parameters may contribute to small NPPS such as nuclear power ships.

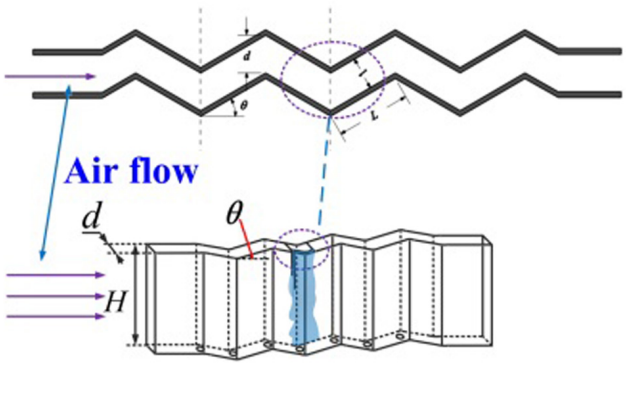


**FIGURE 1 |** Structure of the corrugated plate and the distribution of different phases in the corrugated plate dryer (CPD).

The LF with Rhodamine B fluorescent stain with a maximum absorption wavelength of 555 nm flows from the high-level water tank to the stabilized water tank (Wang et al., 2020c). The level of height of the liquid on the left side of the stabilized water tank will not change, and the excess liquid will flow into the tank, which makes the LF pressure unchanged. The liquid film generated by the LF generator flows stably and uniformly down the wall. The LF flowing through the experiment section flows from the drain water tank at the CPD bottom to collection tank and enters the circulating water tank. In this study, a slit method is applied for the generation of a thin LF, that is, a horizontal slit is set on CPD so that the LF flows smoothly on the wall (Wang and Tian, 2019a). The air flowing from the blower passes through the stable section and enters the experimental section area. In the experiment, the airflow speed was gradually increased. When the LF just broke, it was observed that small droplets flew out from the LF mainstream surface, that is, the LF was considered to have broken. Specific details can be found in reference (Wang and Tian, 2019c). For details of the experimental error analysis, image capture method, and PLIF measurement, please refer to the references (Wang and Tian, 2019c; Wang et al., 2020c).

## RESULTS AND ANALYSIS

### LFR Process

**Figure 2** is the image of the liquid film on the wall surface at the corner of the corrugated plate taken by a high-speed camera, which records the rupture process of the liquid film on the wall surface under the HSA. The rupture process when airflow velocity increases from 0 to 7.5 m/s is as follows:

(1) The liquid film flows stably.
(2) The boundary of the liquid film is inclined to the convex angle position of the bending angle of the corrugated plate.
(3) LFR occurs.
(4) Small droplets splash out on the surface of the liquid film mainstream.
(5) Single strip-shaped liquid membranes are detached.
(6) Double strip-shaped liquid film appears.
(7) The mainstream part of the liquid film becomes disordered and ruptures.

The rupture process and morphology of LF under different LF Reynolds numbers are similar (Wang and Tian, 2019b; Wang et al., 2020a,b). LF flows steadily before rupture, and its distribution on the wall surface is very uniform (**Figures 2A,B**). As airflow speed increases, LF distributed at the center of CPD will move to the corner under HSA (**Figures 2C–E**). When it reaches the edge of the CPD corner, due to the surface tension on the solid–liquid interface, the LF will not immediately rupture, but will form a convex arc curve (**Figures 2F,G**). As the airflow

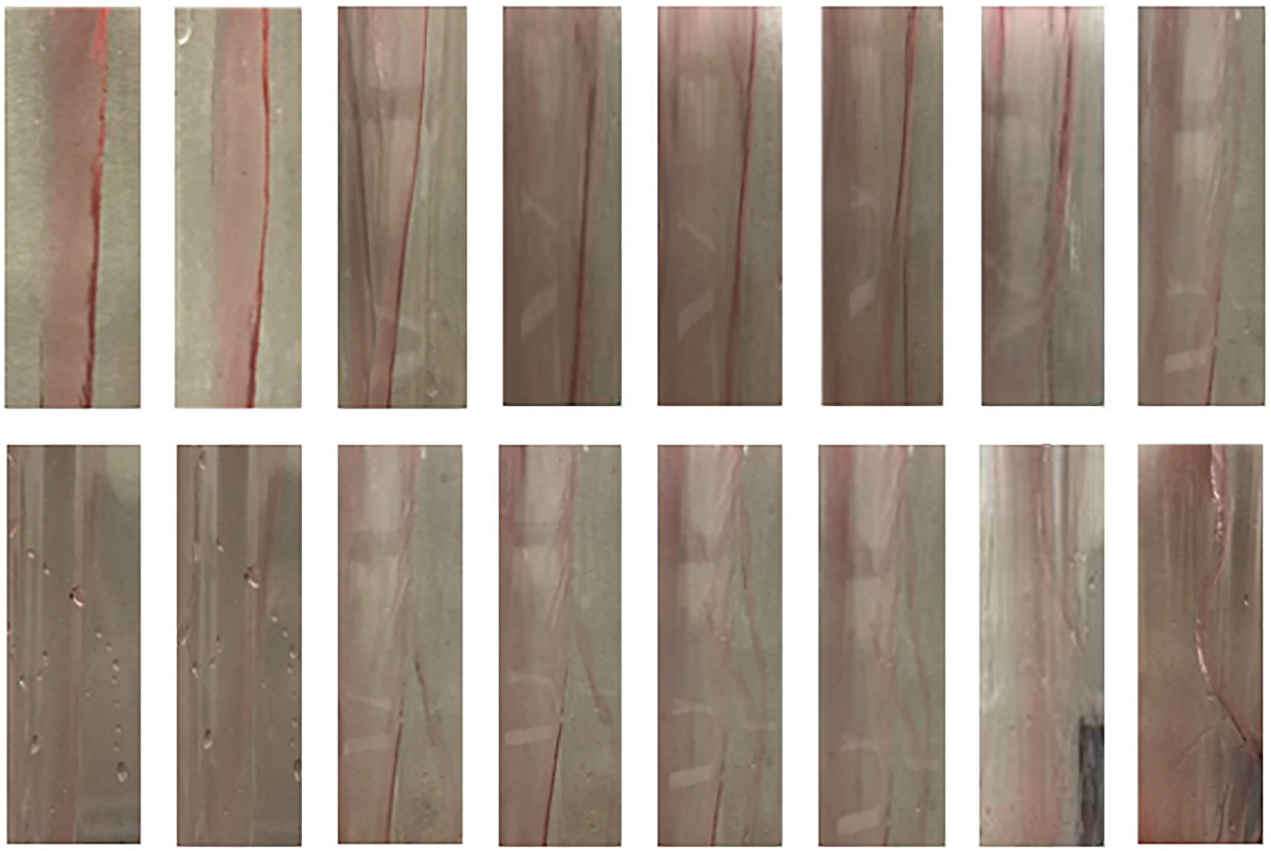

**FIGURE 2 |** Image of liquid film rupture (LFR) characteristics and process on corrugated plate dryer (CPD) wall.

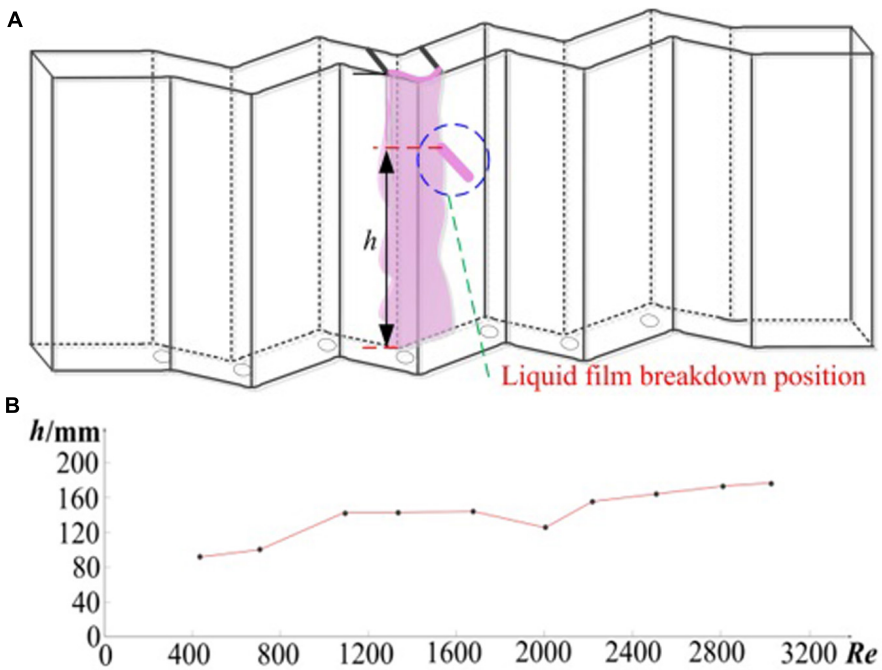


**FIGURE 3 |** Liquid film rupture (LFR) position. **(A)** Schematic diagram of the LFR position. **(B)** Curve of the LFR position for different *Re*.

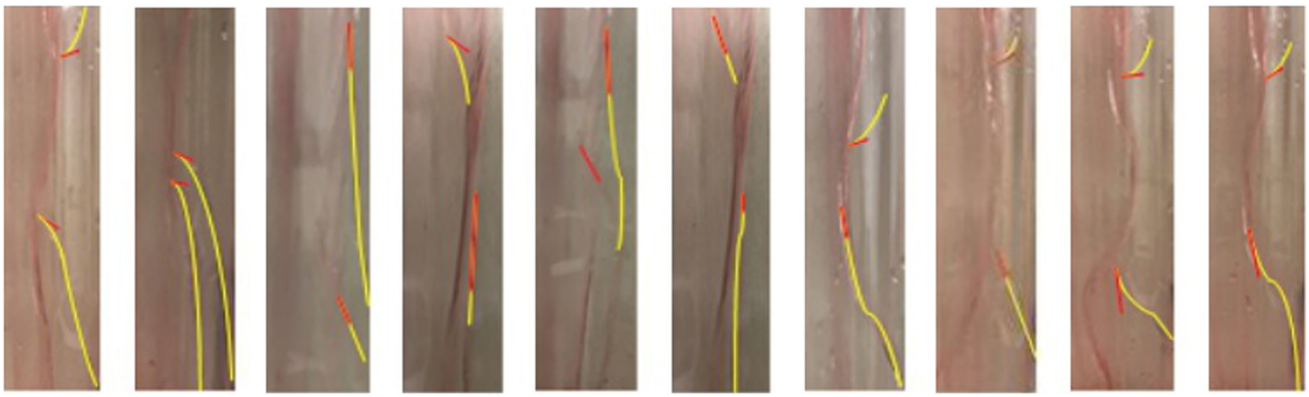

**FIGURE 4 |** Schematic diagram of two strip-shaped liquid film (TSSLF) for different Reynolds numbers.

rate increases further, LF will suddenly break down at the convex corner of the inflection angle. At the moment of rupture, there will be smaller droplets detached from the LF mainstream. Under the joint action of the gravity of the droplet itself and the airflow, it splashes out in a downward direction, which is the starting moment of the LFR (**Figures 2H–J**). The increase in the airflow rate continuing, the LFR gradually changed from a splash of small droplets to detachment of a single SSLF (**Figures 2K,L**). At this time, due to gravity, the flying distance of the SSLF is significantly reduced compared with the flying distance of small droplets flying away from the LF (because SSLF is heavier than the droplet). As airflow speed gradually increases, the single SSLF gradually develops into the phenomenon of double SSLF splashing. One of the relatively thin strip-shaped liquid films flew away from the surface of the main flow of the liquid film in a horizontal direction or in a downward direction. The other relatively thicker liquid film still maintains the flight direction when the airflow rate is low. Therefore, a certain angle will be formed between the two band-shaped liquid films (**Figures 2M,N**). The increase in the airflow speed kept, most of the LF mainstream cracked. The band-shaped LF disappears, and the shape of the LF when flying away from the LF mainstream has no obvious characteristics (**Figures 2O,P**).

## LFR Rupture Position

A schematic diagram of the LFR position and the relationship between LFR position under HSA and *Re* is shown in **Figure 3**.

Most of the LFR occurs in the middle and upper parts of the LF, and the rupture position shows an upward trend with the increase in the Reynolds number of the LF. In the small Reynolds number zone, the rupture position rises faster as the liquid film Reynolds number increases. In the middle Reynolds number zone, the position of the LFR is relatively stable. At high Reynolds numbers, the position of the rupture rises significantly. When the Reynolds number of the LF is large under the same airflow rate, the probability of LFR is relatively high, which will cause the position of the LFR to gradually move up. The phenomenon that the double-strip LF flew away from the wall mainstream LF is due to the fact that when the wind speed is large, an airflow vortex will be formed at the lower part of the LF, causing some LFs to flow back, making the thickness of the upper part of the LF obvious increase (Wang and Tian, 2019a; Wang et al., 2020a). At the same airflow rate, the upper part of the LF is more likely to rupture than the lower half. Therefore, the experiment showed that the LFR mostly occurred in the upper middle part of the mainstream of LF. Moreover, the position of LFR moves up as the Reynolds number increases. In addition, the mass of the reflux of liquid film caused by the vortex is much smaller than the mass of the LF in the lower part of the mainstream; thus, a relatively thin SSLF is formed at the upper part of the LF. The shape of this LF is relatively small, and its gravity is small. It often flew away from the LF surface in a horizontal or slightly downward direction when flying away from the mainstream.

## ATSSLF

In the phenomenon of double-strip LF when it ruptures, a certain angle is formed between the flying directions of the TSSLF, that is, the angle between the two strip-shaped liquid films (ATSSLF; as shown in **Figure 4**). The Reynolds numbers of the LF from

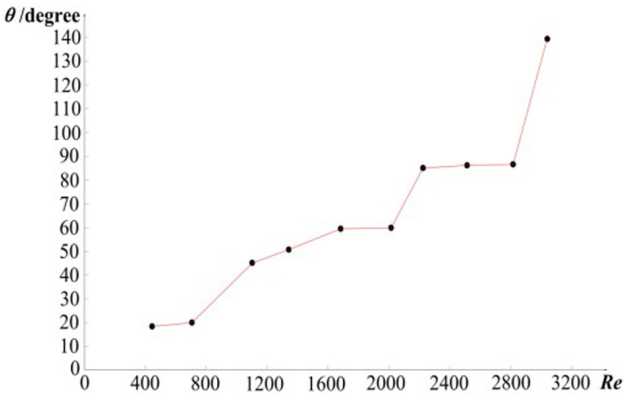


**FIGURE 5 |** Curve of angle between the two strip-shaped liquid films (ATSSLF) and Reynolds numbers.

left to right are 442.4, 706.2, 1088.7, 1330.0, 1684.9, 2014.1, 2213.1, 2509.0, 2818.6, and 3030.5. The curve of the ATSSLF and Reynolds numbers is shown in **Figure 5**.

It reveals that ATSSLF gradually increased with the increase of *Re*. This is because with the increase in *Re*, the gravity of the thicker one of TSSLFs gradually increases, and the flying distance gradually becomes shorter as it escapes from the LF mainstream. In the experiment, it was found that the flight state of another relatively thin SSLF flying away from the surface of the LF mainstream in the horizontal direction or the downward direction will not change significantly with the Reynolds number. Therefore, the angle of the double-strip liquid film gradually increases with the increase in *Re*. The research on the ATSSLF will still be an important prospect in the future.

## CONCLUSION AND PROSPECTS

In this paper, through the experimental study of LFR of the vertical CPD wall under HSA, the following conclusions are drawn.

(1) LFR mostly occurs at the upper middle position of the LF mainstream on the CPD wall surface, and the rupture position generally gradually moves upward as the Reynolds number of the liquid film increases. In the low and high Reynolds numbers, the rupture position increased sharply with the increase in the liquid film Reynolds number. In the middle Reynolds number zone, the position of the rupture did not change significantly.
(2) LFR on the CPD wall surface under HSA passes through the following process.
(a) The LF flows stably.
(b) The LF boundary is inclined to the convex angle position of the CPD dryer.
(c) LFR occurs.
(d) Small droplets splash from the LF mainstream surface.
(e) SSLF is detached.
(f) TSSLF appears.
(g) The mainstream part of the LF becomes disordered and ruptures.

(3) The phenomenon of the TSSLF is caused by the vortex of the airflow generated in the lower part of the experimental section when the airflow rate is large, which causes the upper part of LF to reflux, and the LF is more likely to rupture. Therefore, the angle gradually increases as the Reynolds number of the LF increases. The research on the ATSSLFs will be the prospect research in the future. Nevertheless, due to the difficulty of measurement, our data is relatively small. It is necessary to add experimental data and conduct experiments on CPDs with different parameters in future research. At present, the law of the rupture position of the LF cannot be obtained and unified because the influence of the CPD parameters on the LFR position is great. This is also an important research direction in the future. Many parameters in the LF have non-linear characteristics, which is the future research direction.

## DATA AVAILABILITY STATEMENT

The raw data supporting the conclusions of this article will be made available by the authors, without undue reservation.

## AUTHOR CONTRIBUTIONS

BW designed this study and mainly performed the experiments. BC, GW, RL, BK, JW, CL, and RT contributed to performing the experiments. BW mainly co-wrote most of the manuscript and all authors contributed to writing the manuscript.

## FUNDING

Authors would like to acknowledge the financial support provided by the Ph.D. Student Research and Innovation Fund of the Fundamental Research Funds for the Central Universities (3072020GIP1518), the Fundamental Research Funds for the Central Universities, China Scholarship Council, Chinese Universities Scientific Fund, and the National Natural Science Foundation of China (No. 51676052).

## REFERENCES

Chen, B.-W., Wang, B., Mao, F., Tian, R.-F., and Lu, C. (2020a). Analysis of liquid droplet impacting on liquid film by CLSVOF. *Ann. Nuclear Energy* 143:107468. doi: 10.1016/j.anucene.2020.107468

Chen, B.-W., Wang, B., and Tian, R.-F. (2020b). Experimental study of droplet impacting on inclined wetted wall in corrugated plate separator. *Ann. Nuclear Energy* 137:107155. doi: 10.1016/j.anucene.2019.107155

Fang, D., Li, L.-F., Li, J., Wang, M., Yu, H., Zhang, J., et al. (2020a). Full-scale numerical study on the thermal hydraulic characteristics of steam-water separation system in an advanced PWR UTSG. Part two: droplets separation process. *Prog. Nuclear Energy* 118:103139. doi: 10.1016/j.pnucene.2019.103139

Fang, D., Wang, M.-J., Duan, Y.-G., Li, J., Qiu, G., Tian, W., et al. (2020b). Full-scale numerical study on the flow characteristics and mal-distribution phenomena in SG steam-water separation system of an advanced PWR. *Prog. Nuclear Energy* 118:103075. doi: 10.1016/j.pnucene.2019.103075

Huang, Y., Gao, P.-Z., and Wang, C.-Q. (2019). Experimental and numerical investigation of bubble-bubble interactions during the process of free ascension. *Energies* 12, 1–20. doi: 10.3390/en12101977

Wang, B., Chen, B.-W., Ke, B.-Z., Li, R., and Tian, R. (2020a). Study on strip-shaped liquid film in the corrugated plate dryer. *Ann. Nuclear Energy* 139:107237. doi: 10.1016/j.anucene.2019.107237

Wang, B., Chen, B.-W., Wang, G.-Q., Ke, B., Wen, J., Lu, C., et al. (2020b). Analysis of influencing factors of rupture phenomenon of liquid film on the wall of corrugated plate dryer. *Ann. Nuclear Energy* 147:107694. doi: 10.1016/j.anucene.2020.107694

Wang, B., Ke, B.-Z., Chen, B.-W., Li, R., and Tian, R. (2020c). Study on the size of secondary droplets generated owing to rupture of liquid film on corrugated plate wall. *Intern. J. Heat Mass Transf.* 147:118904. doi: 10.1016/j.ijheatmasstransfer.2019.118904

Wang, B., Chen, B.-W., and Tian, R.-F. (2019). Review of research progress on flow and rupture characteristics of liquid film on corrugated plate wall. *Ann. Nuclear Energy* 132, 741–751. doi: 10.1016/j.anucene.2019.06.060

Wang, B., and Tian, R.-F. (2019a). Investigation on flow and breakdown characteristics of water film on vertical corrugated plate wall. *Ann. Nuclear Energy* 127, 120–129. doi: 10.1016/j.anucene.2018.12.001

Wang, B., and Tian, R.-F. (2019b). Judgement of critical state of water film rupture on corrugated plate wall based on SIFT feature selection algorithm and SVM classification method. *Nuclear Eng. Design* 347, 132–139. doi: 10.1016/j.nucengdes.2019.03.025

Wang, B., and Tian, R.-F. (2019c). Study on fluctuation feature and breakdown characteristic of water film on the wall of corrugated plate. *Intern. J. Heat Mass Transf.* 143:118501. doi: 10.1016/j.ijheatmasstransfer.2019.118501

Zhang, H., Liu, Q., Qin, B., and Bo, H. (2015). Simulating particle collision process based on Monte Carlo method. *J. Nucl. Sci. Technol.* 52, 1393–1401. doi: 10.1080/00223131.2014.1003152

**Conflict of Interest:** The authors declare that the research was conducted in the absence of any commercial or financial relationships that could be construed as a potential conflict of interest.

frontiers in Energy Research

ORIGINAL RESEARCH
published: 28 September 2020
doi: 10.3389/fenrg.2020.00178

# Numerical Analysis of FLiBe Laminar Convective Heat Transfer Characteristics in Tubes Fitted With Coaxial Cross Twisted Tape Inserts

*Zimu Yang[1], Xiaoya Liu[2], Xiaxin Cao[1]*, Zhichao Gao[1] and Ming Ding[1]**

[1] Fundamental Science on Nuclear Safety and Simulation Technology Laboratory, Harbin Engineering University, Harbin, China, [2] College of Nuclear Science and Technology, Naval University of Engineering, Wuhan, China

OPEN ACCESS

**Edited by:**
Shripad T. Revankar,
Purdue University, United States

**Reviewed by:**
Xingang Zhao,
Massachusetts Institute of Technology, United States
Muhammad Saeed,
East China University of Technology, China

***Correspondence:**
Xiaxin Cao
caoxiaxin@hrbeu.edu.cn
Ming Ding
dingming@hrbeu.edu.cn

**Specialty section:**
This article was submitted to Nuclear Energy, a section of the journal Frontiers in Energy Research

**Received:** 15 May 2020
**Accepted:** 09 July 2020
**Published:** 28 September 2020

**Citation:**
Yang Z, Liu X, Cao X, Gao Z and Ding M (2020) Numerical Analysis of FLiBe Laminar Convective Heat Transfer Characteristics in Tubes Fitted With Coaxial Cross Twisted Tape Inserts. Front. Energy Res. 8:178. doi: 10.3389/fenrg.2020.00178

Molten salts are now widely used as heat transfer fluids in solar thermal plants and molten salt nuclear reactors. In order to explore their heat transfer enhancement method, new coaxial cross twisted tapes (CCTTs) are applied to plain tubes with molten salt FLiBe as the working fluid, and the characteristics of pressure drop and heat transfer are numerically investigated by the CFD software STAR-CCM+. Simulations are performed in a laminar flow regime where the Reynolds number ranges from 100 to 1100, and the velocity, temperature profiles, and enhanced performance evaluation criteria (PEC) are analyzed to investigate the heat transfer performance of FLiBe in the tube fitted with CCTTs and typical twisted tape (TT). Research was performed on water and lubricating oil to investigate the effects of fluid thermal-physical properties on the performance of CCTTs. The results show that CCTTs can produce stronger swirl flow and greatly enhance heat transfer. For overall heat transfer performance, the maximum PEC of FLiBe with CCTTs reaches 2.37. The comparison of three different fluids also indicates that CCTTs have better heat transfer performance for higher Prandtl number fluids such as molten salt. The correlations of CCTTs and TT are developed into a unified form for the prediction of friction factors and Nusselt numbers for various Prandtl number fluids.

**Keywords: coaxial cross twisted tapes, twisted tape inserts, numerical simulation, molten salt, heat transfer enhancement**

## HIGHLIGHTS

- Laminar convection of FLiBe with coaxial cross twisted tapes is numerically investigated.
- Coaxial cross twisted tapes greatly enhance the heat transfer of FLiBe and high Prandtl number fluids.
- A general correlation for twisted tapes is proposed based on simulations.

## INTRODUCTION

During the last few decades, molten salts have been widely applied in various industries, including alloy production, thermal storage, and power plants (Kearney et al., 2004; Serrano-López et al., 2013; Sabharwall et al., 2014; Vignarooban et al., 2015; Garbrecht et al., 2017; Romatoski and Hu, 2017). For the last two applications, interest is growing rapidly because of their desirable thermal-physical properties (Serrano-López et al., 2013). Their advantages include higher volumetric heat capacity and thermal stability at high temperatures, and hence molten salts do not need to be pressurized as heat transfer fluids and would significantly reduce the cost of heat exchangers and pumps for a required volume (Sabharwall et al., 2014). More importantly, these attributes enable high-temperature operation which raises the efficiency of thermal conversion. Thus they have been widely used as thermal storage medium (Garbrecht et al., 2017) and heat transfer fluids in solar thermal plants and molten salt nuclear reactors (Kearney et al., 2004; Vignarooban et al., 2015; Romatoski and Hu, 2017). Recently, research conducted using molten salt FLiBe (LiF-$BeF_2$) as a coolant in fluoride-salt-cooled high-temperature reactors (FHR) is a highly focused area (Scarlat and Peterson, 2014).

However, molten salts are generally high Prandtl number fluids with high viscosity and low thermal conductivity, which result in their poor heat transfer performance. To overcome this problem, many heat transfer enhancement techniques have been studied, including heat pipes (Amini et al., 2017), different modified grooved tubes (Jianfeng et al., 2013; Lu et al., 2015; Chen et al., 2018), and various passive inserts (porous medium (Chiba et al., 2001), staggered cylinders (Chiba et al., 2006), sphere-packed insert (Watanabe et al., 2013). Some research on applying FLiBe in typical heat exchangers (Xiao et al., 2015; Chen et al., 2017; Chang et al., 2018), those with internal structures (Du et al., 2017), and reactor coolant systems (Toda et al., 2002; Dave et al., 2018) were also performed to testify the potential usage in industry. These studies showed that passive inserts in tubes or obstruction in heat exchangers could effectively create vortices or secondary flow that mix and uniform the temperature distribution which mitigates the low thermal conductivity. On the other hand, though fair augmentation on the heat transfer coefficient could be achieved, most of the above research only utilizes typical heat transfer enhancement methods and lacks discussion on whether the device is preferable for molten salts with a high Prandtl number. Chen et al. (2018) experimentally studied the effects of Reynolds number and Prandtl number on the thermal-hydraulic behavior of molten salt with a transversely grooved tube heat exchanger in laminar-transition-turbulent regimes ($Re$ = 300–60,000). Results showed that heat transfer enhancement could vary notably with the changing of the Prandtl number ($Pr$ = 11–27) for laminar flow and transition flow, while the enhancement effect is almost independent on the Reynolds number and Prandtl number for the turbulent flow. In the laminar and transition regime, enhancement factor (ratio of Nusselt number from the grooved tube and plain tube) of fluid with $Pr$ = 27 is 30–50% higher than those with $Pr$ = 11 at corresponding Reynolds numbers. Such a small change on the Prandtl number could remarkably affect the performance with viscous fluid, then it is necessary to investigate the effect of larger range Prandtl numbers on heat transfer technique and discuss its applicability on viscous molten salts.

For heat transfer enhancement of high viscosity fluids, the passive device twisted tape (TT) insert is widely used in the heat exchanger as a swirl flow generator (Manglik et al., 1993). The advantages of steady performance, low cost, and simple configuration make it suitable for multiple cases. During the past few decades, a lot of research have been done to investigate the performance of TT with different working fluids, including water, air (Smithberg and Landis, 1964; Thorsen and Landis, 1968), ethyl alcohol (Manglik and Bergles, 1993a,b), and oil (Agarwal and Rao, 1996). The results showed that TT is particularly effective in heat transfer enhancement of laminar flow and viscous fluid, which indicates its potential to improve the laminar convective heat transfer of high viscosity molten salts. Although the swirl flow induced by TT can appreciably enhance the heat transfer by disturbing the flow, it also introduces additional friction resistance and more dissipation of fluid momentum at a cost, which raises the cost of pumps, especially with high viscosity molten salts. Given this contradiction, many new types of TT with different geometries were designed and analyzed (Saha et al., 1989; Promvonge, 2008; Rahimi et al., 2009; Eiamsa-Ard and Promvonge, 2010; Abed et al., 2018; He et al., 2018; Hosseinnezhad et al., 2018; Piriyarungrod et al., 2018; Ruengpayungsak et al., 2019). Research on modified twisted tapes indicate a continuous endeavor in finding the optimal heat transfer enhancement device that obtains higher heat transfer coefficient and retains lower friction resistance in various working conditions.

Recently, a new type of twisted tape named coaxial cross twisted tape (CCTT) was designed, numerically simulated, and analyzed in our previous research (Liu et al., 2017a,b, 2018). Liu et al. (2017b) numerically studied CCTT performance under different clearance ratio, twist ratio (Liu et al., 2017a), and its local thermal-hydraulic behavior (Liu et al., 2018) with oil in laminar flow regime, and reported that the Nusselt number of the pipe equipped with CCTT was enhanced about 151–195% in comparison with TT. The performance evaluation criterion (PEC, defined as Eq.8) is at its highest at 0.077 for clearance ratio, and PEC also increases as the twist ratio decreased. Kunlabud et al. (2017) and Saysroy and Eiamsa-Ard (2017) later performed numerical analysis on a similar CCTT design with various twist ratio and clearance ratio in laminar and turbulent water flow. Results showed that the CCTT design could achieve a thermal performance factor ($f_0^{1/3}Nu/f^{1/3}Nu_0$) of 7.28 in laminar flow, while 1.04 for turbulent flow. Bahiraei et al. (2019) also presented numerical research on employing graphene-based nanofluid and rotating coaxial double-twisted tapes (RCDTT) to enhance heat transfer at $Re$ = 5000. Their research indicated that increasing rotational speed from 0 to 900 rpm at a twisted ratio of 3.5 can obtain 77% improvement in the convective heat transfer coefficient. Khanmohammadi and Mazaheri (2019) conducted a numerical simulation and analysis based on the second law of thermodynamics for CCTT to investigate its performance in water turbulent flow. It showed that CCTT could achieve a higher

heat transfer coefficient and lower entropy generation compared to TT. All the previous research showed that CCTT provides better heat transfer enhancement than TT and it is suitable for laminar flow.

However, these studies of the new twisted tape have been exclusively focusing on common working fluids such as oil and water, and the results with molten salts (e.g., FLiBe) and effect of the Prandtl number on its performance are still unknown. To examine the applicability of CCTT on high viscous molten salt, we chose FLiBe as the main working fluid in this paper and also simulated other fluids (water, lubricating oil) to compare their results and discuss the effect of the Prandtl number. The physical and numerical models are introduced in sections "Physical Model" and " Numerical Simulation and Model." In section "Results and Discussion," the results of heat transfer and pressure drop characteristics of FLiBe in laminar flow regimes with CCTT are numerically analyzed. The water and lubricating oil are also selected as working fluids to investigate CCTTs performance with different Prandtl numbers. Based on the results in the present study range, the correlations of the Nusselt number and friction factor for TT and CCTT are uniformly developed based on numerical results in the studied range. Moreover, this numerical analysis of performance of CCTTs with FLiBe shows its potential application on heat transfer enhancement in secondary coolant heat exchangers of molten salt reactors where the radiation level is acceptable for long term maintenance. The relationship of the Prandtl number with the performance of CCTTs also implies the application of other heat transfer molten salts where a compact heat exchanger is needed, such as parabolic trough (Kearney et al., 2004), thermal storage (Vignarooban et al., 2015), and phase-change systems (Garbrecht et al., 2017).

## PHYSICAL MODEL

According to the field synergy principle (Guo et al., 2005), a better synergy between velocity and temperature gradients can enhance the convective heat transfer rate. The numerical solution (Meng et al., 2005) of heat transfer in a circular tube revealed that having 4–8 vortices in the cross section can optimize the synergy between velocity and temperature field, and therefore the heat transfer is enhanced effectively. Based on this theory, a new type of twisted tape named coaxial cross twisted tape (CCTT) is designed, and a previous study (Liu et al., 2018) has shown prominent enhancement on laminar convective heat transfer of lubricating oil. It implies a potential usage with a high Prandtl number molten salt.

The geometry of CCTT and its cross-section view in the tube are displayed in **Figure 1**. The coaxial cross double twisted tape (CCDTT) and coaxial cross triple twisted tape (CCTTT) are formed by two or three TTs that have the same twist ratios and axis and they are spaced by an angle of mutual 90° or 60°, respectively. The material of the CCTTs is aluminum.

The diameter ($D$) of the tube is 0.012 m, and the length ($L$) is 0.3 m. CCTTs with the thickness ($\delta$) of 0.001 m are fitted in the tube. The twist ratio ($y = H/D$), defined as a ratio of the 180-degree twist pitch to the tube diameter, are 2, 3, 4, and infinity. The clearance ratio ($CR = c/D$), defined as a ratio of the clearance between the edge of the tape and the tube wall to the tube diameter, is set 0 to eliminate its effect on heat transfer. The working fluids are water ($Pr$ = 7–8), 68# lubricating oil ($Pr$ = 870–900), and FLiBe molten salt ($Pr$ = 14–15). Their thermo-physical properties are assumed to be temperature-dependent.

Reynolds number ($Re$), Nusselt number ($Nu$), and friction factor ($f$) are defined as follows:

$$Re = \frac{\rho u D}{\mu} \tag{1}$$

$$f = \frac{\Delta P}{\left(\rho u^2/2\right)\left(L/D\right)} \tag{2}$$

$$Nu = \frac{hD}{\lambda} \tag{3}$$

where $\rho$ is density, $u$ is inlet mean velocity, $D$ is inner tube diameter, $\mu$ is fluid dynamic viscosity, $\lambda$ is fluid thermal conductivity, $h$ is heat transfer coefficient, $L$ is tube length, and $\Delta P$ is pressure drop.

According to our results of the simulation, coaxial cross twisted tapes have a strong mixing effect due to induced swirl flow. The heat transfer coefficient at the wall quickly dropped and became stable at $l$ = 0.03 m. In this case, a 10-times longer tube length is enough to give fully developed laminar flow, and the Nusselt number is calculated from the average heat transfer coefficient of the wall at the fully developed region ($l$ = 0.24 m).

## NUMERICAL SIMULATION AND MODEL

### Simplifying Assumptions

The mathematical model involves the prediction of flow and heat transfer behaviors. Some simplified assumptions are required to apply the conventional flow equations and energy equations to model the heat transfer process in the tube with twisted tape. These major assumptions are: (1) the flow through the tube with twisted tape is laminar and incompressible, (2) the flow is in a steady state, (3) natural convection and thermal radiation are neglected, and (4) the thermo-physical properties of the fluid are temperature dependent. For FLiBe, its physical properties are defined by the correlations in the corresponding temperature range (650–700°C) from the liquid salt database (Sohal et al., 2010).

### Governing Equations

The problem under consideration is assumed to be three-dimensional, laminar, and steady. Heat conduction in the twisted tape is neglected. Equations of continuity, momentum, and energy for the fluid flow are given below in the tensor form,

Continuity equation:

$$\frac{\partial}{\partial x_i}\left(\rho u_i\right) = 0 \tag{4}$$

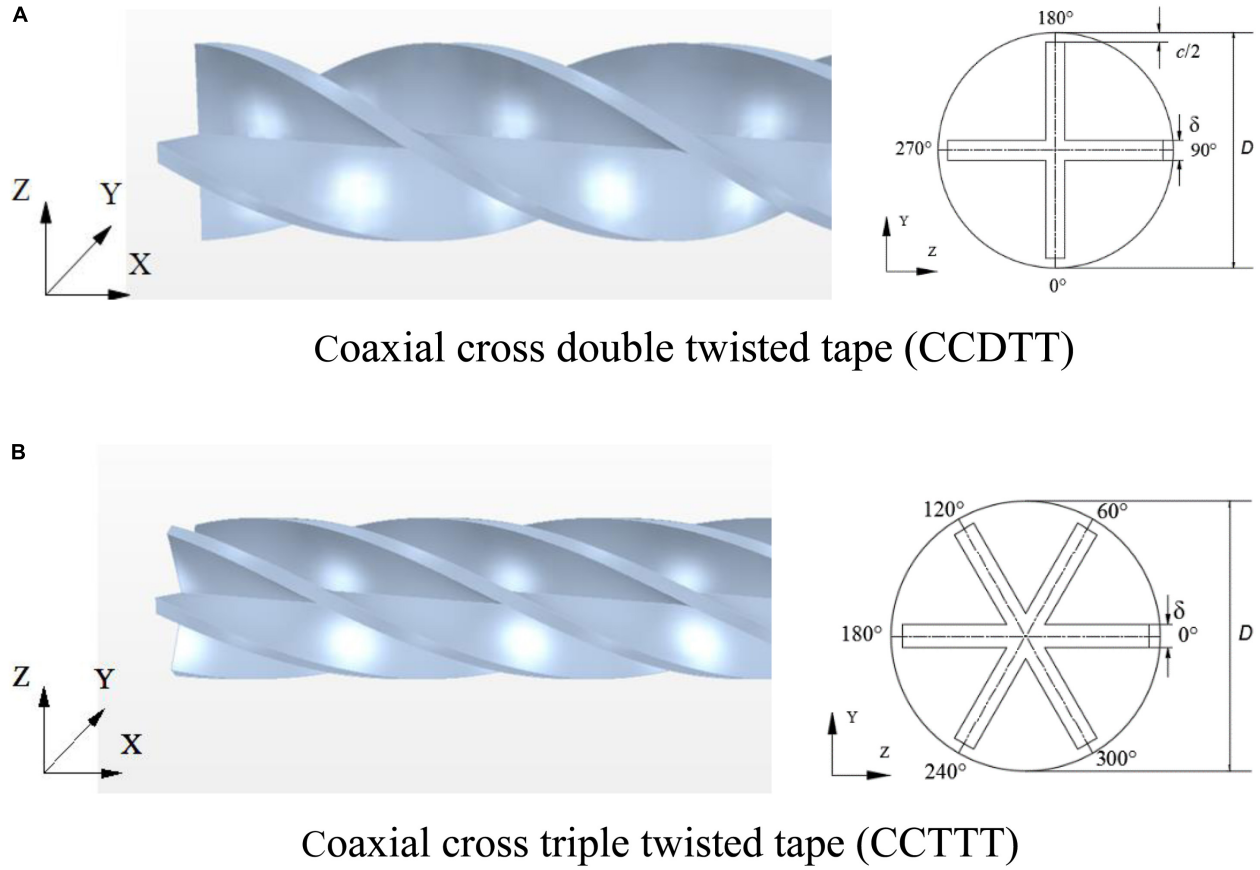


**FIGURE 1 |** The geometry and cross-section view of the tubes with CCTT. **(A)** Coaxial cross double twisted tape (CCDTT). **(B)** Coaxial cross triple twisted tape (CCTTT).

Momentum equations:

$$\frac{\partial}{\partial x_j}\left(\rho u_i u_j\right) = \frac{\partial}{\partial x_j}\left[\mu\left(\frac{\partial u_i}{\partial x_j} + \frac{\partial u_j}{\partial x_i}\right)\right] - \frac{\partial p}{\partial x_i} \tag{5}$$

Energy equation:

$$\frac{\partial}{\partial x_i}\left(\rho u_i C_p T - \lambda \frac{\partial T}{\partial x_i}\right) = 0 \tag{6}$$

## Boundary Conditions

At the inlet, the fully developed profile of velocity is specified in Eq. 7 and the exit is set to pressure outlet.

$$u = 2u_m\left(1 - \frac{r^2}{R^2}\right) \tag{7}$$

where $u_m$ is the mean velocity. $R$ is the tube inner radius, and $r$ is the radial position.

The Reynolds number used in the computation is referred to in the inlet values, which is set from 100 to 1,100. The exit condition is set as a pressure outlet, where the pressure is the same as the reference pressure ($p$ = 101.325 kPa). The constant wall temperature boundary condition is adopted in all simulation calculations. Considering the evident difference among working fluids' industrial applications, the temperature of inlet fluid and inner wall for water, lubricating oil, and FLiBe are set constant at 10, 40, 650°C and 40, 60, 700°C, respectively. The adiabatic thermal boundary condition is adopted on the surface of twisted tape, since its thermal effects can be ignored. On the tube walls and surface of twisted tapes, no-slip conditions are imposed.

## Numerical Method

In this work, the CFD software STAR-CCM+ 10.02 (CD-adapco, 2015) is used for numerical computations and data post-processing. It provides a finite volume method fluid dynamics solution using the common Semi-Implicit Method for Pressure-Linked Equations (SIMPLE) with Rhie-Chow interpolation for pressure-velocity coupling and algebraic multi-grid preconditioning. For mesh generation, STAR-CCM+ provides tetrahedral, polyhedral, and trimmed (hexahedral) meshes. Prism layers of mesh cells can be included for modeling heat transfer and turbulence at important surfaces. For steady incompressible flow simulation, the second-order upwind discretization schemes for momentum and energy equations are employed in the numerical model of this study. Pressure-velocity coupling is handled by the Segregated Flow Model,

**TABLE 1 |** Comparison of the CFD results with experimental results (Wongcharee and Eiamsa-Ard, 2011).

| | | | | | | | | | |
|---|---|---|---|---|---|---|---|---|---|
| | | | | | ***f*** | | | | |
| ***Re*** | **827** | | | **995** | | | **1151** | | |
| ***y*** | **3** | **4** | **5** | **3** | **4** | **5** | **3** | **4** | **5** |
| Exp | 0.410 | 0.335 | 0.290 | 0.386 | 0.316 | 0.274 | 0.368 | 0.302 | 0.261 |
| CFD | 0.415 | 0.348 | 0.310 | 0.378 | 0.309 | 0.277 | 0.341 | 0.283 | 0.252 |
| Error(%) | 1.17 | 4.09 | 6.78 | −2.18 | −2.25 | 1.21 | −7.34 | −6.39 | −3.41 |
| | | | | | ***Nu*** | | | | |
| ***Re*** | **827** | | | **995** | | | **1151** | | |
| ***y*** | **3** | **4** | **5** | **3** | **4** | **5** | **3** | **4** | **5** |
| Exp | 12.3 | 10.0 | 8.61 | 14.9 | 12.6 | 10.9 | 17.6 | 15.1 | 13.3 |
| CFD | 12.8 | 11.2 | 9.66 | 14.5 | 13.0 | 11.4 | 16.7 | 14.5 | 13.9 |
| Error(%) | 4.27 | 12.1 | 12.2 | −3.04 | 3.50 | 4.83 | −5.45 | −3.77 | 4.31 |

**TABLE 2 |** Comparison of the CFD results with empirical correlation (Manglik and Bergles, 1993a).

| ***Re*** | **110** | **212** | **312** | **411** | **510** | **608** | **706** | **804** | **601** | **1000** |
|---|---|---|---|---|---|---|---|---|---|---|
| *f*(correlation) | 2.59 | 1.41 | 1.02 | 0.827 | 0.713 | 0.640 | 0.579 | 0.534 | 0.499 | 0.469 |
| *f*(CFD) | 2.22 | 1.29 | 0.956 | 0.785 | 0.679 | 0.607 | 0.555 | 0.515 | 0.485 | 0.462 |
| Error(%) | −14.2 | −8.49 | −6.01 | −5.09 | −4.75 | −4.48 | −4.09 | −3.56 | −2.80 | −1.33 |
| *Nu*(correlation) | 12.9 | 15.3 | 17.1 | 19.0 | 21.3 | 23.8 | 26.4 | 28.9 | 31.6 | 34.1 |
| *Nu*(CFD) | 12.0 | 14.9 | 17.8 | 20.3 | 22.4 | 24.3 | 26.0 | 27.6 | 29.3 | 31.6 |
| Error(%) | −7.30 | −2.76 | 4.28 | 6.82 | 5.15 | 1.91 | −1.57 | −4.75 | −7.26 | −7.46 |

which is a modified SIMPLE-type algorithm using a collocated grid arrangement.

## Grid Independent Test

The grid independent test has been performed for the physical model to which the polyhedral grid type is applied. To improve the accuracy of the near-wall flow solution, prism layer mesh is applied to the near-wall grid and in the vicinity of the twisted tape. Four grid systems with approximately 1,258,000, 1,658,000, 2,172,500, and 3,170,770 cells are applied to calculate a baseline case of Nusselt number ($Nu$) and friction factor ($f$) in which $Re$ = 1000, $y$ = 3.0. Results show that the difference in Nusselt numbers and friction factors between 2,172,500 and 3,170,770 cells are 0.77 and 0.3%, respectively. Considering both convergent time and solution precision, the grids with 2172500 cells are used for the computational model.

## Validation of the Numerical Model

To validate the accuracy of the numerical model, the simulation results of the Nusselt number and friction factor of the tube inserted with TT are compared with experimental results (Wongcharee and Eiamsa-Ard, 2011). In **Table 1**, simulations are done in a 1,000 mm long, 19 mm diameter tube fitted with 1 mm thickness, 18 mm width typical twisted tape with different twist ratio ($y$ = 3,4,5), which are the same with each experiment. The overall deviations of the calculated $f$ and $Nu$ from the experimental results are found to be within ± 8% and ± 13%, respectively.

The numerical model is also tested by comparing results with the semi-empirical correlation (9), (10) which was developed by Manglik and Bergles (1993a) under fully developed flow conditions. The verifications are conducted for conditions $Re$ = 110–1,000, $y$ = 3. The other dimensions are the same with our physical model. **Table 2** shows that the deviations of the present simulations from correlations were mostly within ± 4.8% and ± 7.3%, respectively. The maximum deviation of $f$ and $Nu$ are 14.2 and 7.5%, respectively. The comparison shows that the numerical model is benchmarked against the previous experiment and empirical correlation. Concerning that CCTT and TT produce similar swirl flow and have the same mechanism of heat transfer enhancement, the numerical model for TT can be also applied to CCTT.

# RESULTS AND DISCUSSION

## Characteristics of Heat Transfer for FLiBe

In this section, simulation results of the velocity profile, friction factor, temperature profile, Nusselt number, and overall heat transfer performance of the plain tube fitted with TT and CCTTs are shown and analyzed. Previous research (Liu et al., 2017a, 2018) on CCTTs have investigated the twist ratio effect on its

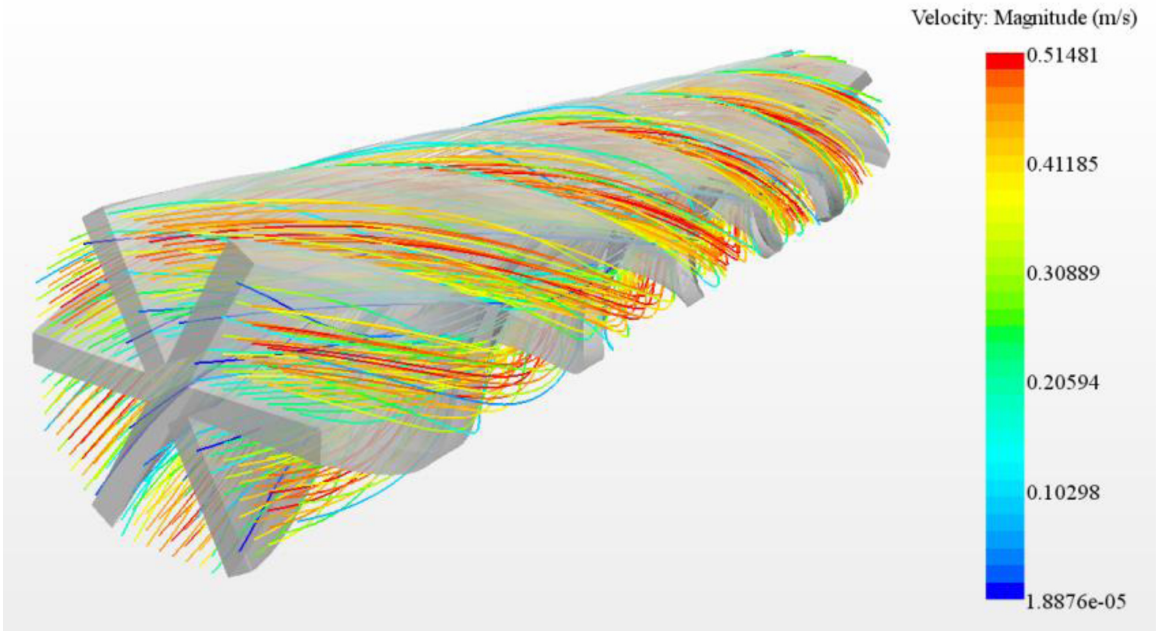


**FIGURE 2 |** The streamline of the tube fitted with CCTTT ($y$ = 3) at $l$ = 0.24 m, $Re$ = 720.

performance, and hence we chose the results of twist ratio $y$ = 3 as a representative case in the following analysis.

## Friction Factor and Effect on Velocity Profiles

With multiple twisted tapes in the tube, CCTTs shall have prominent disturbance on the velocity field. The contour plot of the streamline of FLiBe through the tube fitted with a CCTTT ($y$ = 3) at $l$ = 0.24 m, $Re$ = 720 is displayed in **Figure 2**. It can be seen that six longitudinal vortices are generated around the CCTTT as it twists. These longitudinal vortices would induce considerable centrifugal force which results in the mixing of core flow and boundary flow, and hence effectively disturb the velocity profile and the temperature distribution of the core flow. This result also implies that CCTT has good disturbance on FLiBe even though it has high viscosity.

To make a comparison between disturbance of CCTT and TT on the velocity field, the velocity profiles of FLiBe in the plain tube and the tube fitted with TT, CCDTT, and CCTTT ($y$ = 3, $l$ = 0.24 m, $Re$ = 720) are shown in **Figure 3**. Compared to the plain tube, the TT and CCTTs can all significantly change the velocity distribution of FLiBe. The major difference is that the core flow is accelerated and split into symmetric parts, which is the result of twisted tape's partitioning and the centrifugal force of swirl flow. This can be determined more easily from the streamline in **Figure 2**.

Compared to TT, the CCDTT has a stronger blockage effect and can divide the flow into four swirls, and therefore the velocity profile of FLiBe with CCDTT has a higher value of velocity and the core flow is closer to the wall. Hence, it induces a higher velocity gradient near the tube wall, which can be determined from the steep slope. Such great disturbance on the velocity

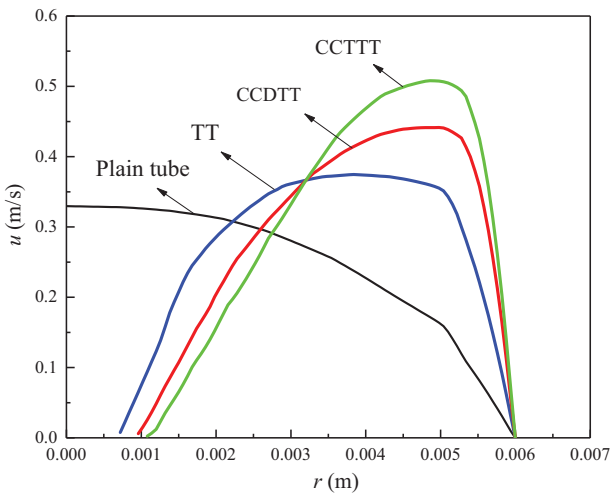


**FIGURE 3 |** The velocity profile of FLiBe in the plain tube and the tube fitted with TT, CCDTT, and CCTTT ($y$ = 3) at $l$ = 0.24 m, $Re$ = 720.

profile is particularly effective for high viscosity fluid like FLiBe which usually has a low inlet velocity. All the above mechanisms show that CCTTT has a stronger effect than CCDTT due to greater partitioning and blockage.

One of the biggest side effects of utilizing the passive device for heat transfer enhancement is the increased pressure drop. **Figure 4** shows the friction factor as a function of the Reynolds number in the flow of FLiBe in the plain tube and the tube fitted with TT, CCDTT, and CCTTT, $y$ = 3. Apparently, the friction

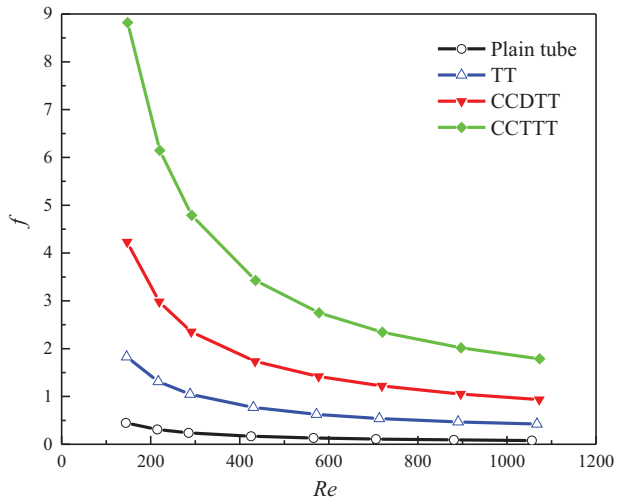


**FIGURE 4 |** Variation of friction factor with the Reynolds number for FLiBe in the plain tube and the tube fitted with TT, CCDTT, and CCTTT ($y$ = 3).

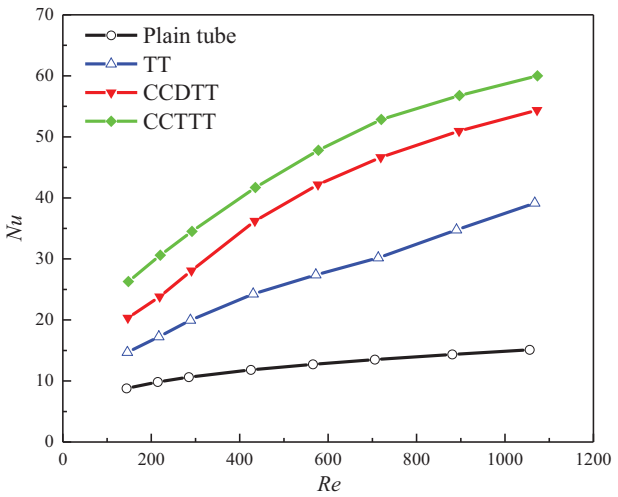


**FIGURE 5 |** Variation of the Nusselt number with the Reynolds number for FLiBe in the plain tube and the tube fitted with TT, CCDTT, and CCTTT ($y$ = 3).

factor in the tube fitted with CCTT is larger than those of the tube with TT and the plain tube under the same conditions. In the present studied range with twist ratio $y$ = 3, the friction factor of FLiBe in the tube with CCDTT and CCTTT are, respectively, 9.5–12.2 and 19.8–23.4 times of that in the plain tube and 2.22–2.32 and 4.26–4.83 times of that in the tube with TT.

The additional pressure drop of FLiBe flow with CCTT can be explained by following reasons: (1) the CCTTs provide greater partitioning and blockage on the tube cross-section, which accelerates flow velocity and reduces the hydraulic diameter; (2) the CCTTs remarkably increase the surface area of the tape; and (3) the swirl flow notably increases the near-wall velocity gradient, which results in higher pressure drop.

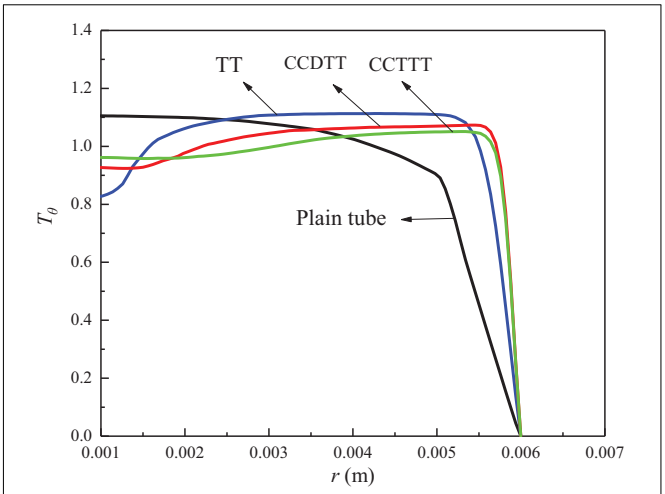


**FIGURE 6 |** The temperature profile of FLiBe in the plain tube and the tube fitted with TT, CCDTT, and CCTTT ($y$ = 3) at $l$ = 0.24 m, $Re$ = 720.

## Heat Transfer Coefficient and Effect on Temperature Profiles

The high friction is actually the price of enhancing the heat transfer of fluid. **Figure 5** shows the variation of the Nusselt number with the Reynolds number for FLiBe in the plain tube and the tube fitted with TT, CCDTT, and CCTTT, $y$ = 3. As expected, the tube fitted with CCTTs have better enhancement on the Nusselt number than those of the tube with TT and the plain tube under the same conditions. In the present studied range with twist ratio $y$ = 3, the Nusselt number of FLiBe in the tube with CCDTT and CCTTT are, respectively, 2.32–3.6 and 2.99–3.97 times of that in the plain tube and 1.38–1.39 and 1.53–1.79 times of that in the tube with TT.

In general, the disturbance on velocity profile can enable the CCTTs to mix the core flow with boundary flow, and therefore effectively affects the temperature distribution of FLiBe. To prove this expectation, the dimensionless temperature profiles of FLiBe in the plain tube and the tube fitted with TT, CCDTT, and CCTTT ($y$ = 3, $l$ = 0.24 m, $Re$ = 720) are compared in **Figure 6** in which the dimensionless temperature is defined as $T_\theta = (T_w - T) / (T_w - T_m)$.

**Figure 6** indicates that the twisted tape can significantly augment the near-wall temperature gradient of FLiBe and uniform the temperature distribution of core flow. This is because the blockage of twisted tape and centrifugal force induced by swirl flow can both accelerate the velocity of flow and therefore improve the near-wall temperature gradient and convective heat transfer. Moreover, the swirl flow also enables the core flow mix with boundary flow, which notably uniforms the temperature profile of core flow. As seen from the slope of the near-wall temperature, the CCTTs can produce a greater temperature gradient and a thinner thermal boundary layer than TT. In summary, the swirl flow's disturbance on the velocity field changes the temperature field and enhances the heat transfer.

It is also notable in **Figure 5** that the CCTTT has better augmentation on heat transfer than CCDTT while the trends of

the Nusselt number with the variation of the Reynolds number are similar for both tapes. This phenomenon indicates that CCDTT and CCTTT share the same mechanism of heat transfer enhancement whose effect would arise as more longitudinal vortices are generated (Guo et al., 2005).

Based on the above analysis of temperature profiles, the enhancement on heat transfer can be explained by three reasons: (1) the highly increased flow velocity enhances the convective of heat transfer; (2) more longitudinal vortices would induce considerable centrifugal force to mix core flow with boundary flow, and hence effectively uniform the temperature of core flow and make the thermal boundary layer thinner; and (3) the swirl flow increases the flow path.

### Overall Heat Transfer Performance

As analyzed in previous sections, the enhancement of heat transfer and flow resistance all increase with the twisted tape inserts. To evaluate the comprehensive effect of heat transfer augmentation under given pumping power, a performance evaluation criteria (PEC) (Fan et al., 2009) is employed and defined as follow:

$$PEC = \left(\frac{Nu}{Nu_0}\right) \Big/ \left(\frac{f}{f_0}\right)^{\frac{1}{6}} \tag{8}$$

where $Nu_0$ and $f_0$ are the Nusselt number and the friction factor of the plain tube, respectively. For power −1/6 in the equation, we apply the Darcy–Weisbach equation and Sieder-Tate equation for the friction factor and Nusselt number of laminar flow in a circular tube. Defining PEC under the constraint of pumping power satisfies the industrial need since how much heat transfer can be enhanced with the same pumping power provides better quantitative parameters than those concerned at the identical pressure drop. The variation of PEC with the Reynolds number for FLiBe in the tube fitted with TT, CCDTT, and CCTTT, $y = 3$ are displayed in **Figure 7**.

In general, the PEC value tends to rise with an increasing Reynolds number for all twisted tapes among which the CCTTs have much better heat transfer performance than TT. In the present studied range with twist ratio $y = 3$, the PEC of FLiBe in the tube with CCDTT and CCTTT are, respectively, 1.2–1.22 and 1.2–1.38 times of those in the tube with TT. Notably, the heat transfer performance of the tube fitted with CCTTT would decrease in a high Reynolds number near the transition regime. This is because with the increase of the Reynolds number, the increase of the friction factor of the tube with CCTTT is stronger than the enhancement of the Nusselt number. In the range of numerical simulation, the highest PEC 2.73 is obtained by CCTTT ($y = 2$) at a Reynolds number of 582.

## Comparison of Different Fluids

As mentioned in section "Introduction," though the CCTTs have prominent enhancement on laminar convective heat transfer of lubricating oil (Liu et al., 2017a,b, 2018), its variation of performance with different fluids is still unknown. To investigate whether the CCTTs are advantageous on heat transfer enhancement of high viscosity molten salt, the results of water and lubricating oil are presented and compared with FLiBe.

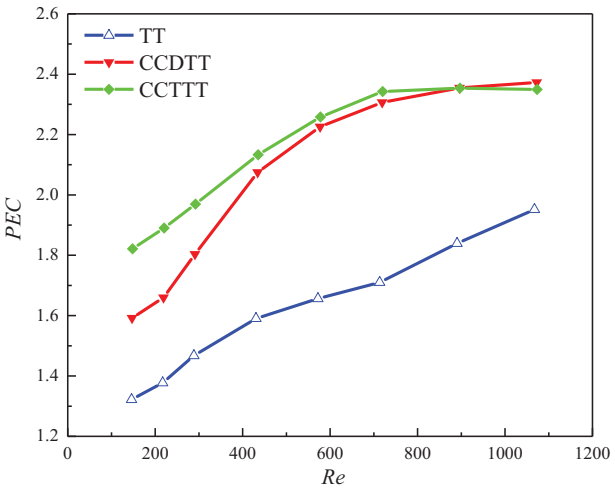


**FIGURE 7 |** Variation of PEC with the Reynolds number for FLiBe in the tube fitted with TT, CCDTT, and CCTTT ($y = 3$).

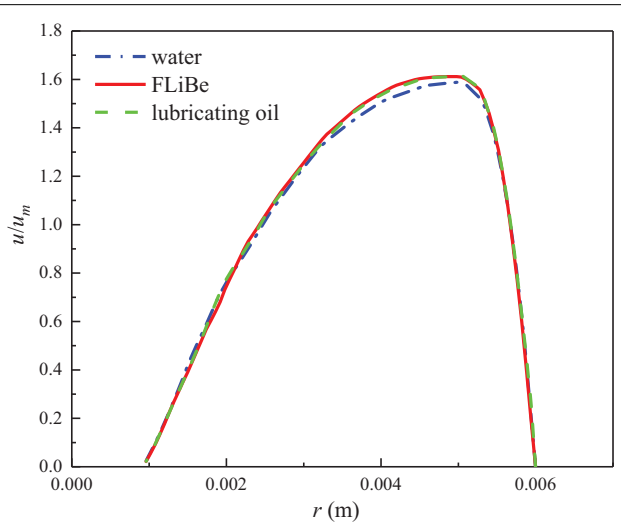


**FIGURE 8 |** The velocity profile of different fluids in the tube fitted with CCDTT ($y = 3$) at $l = 0.24$ m, $Re = 720$.

### Comparison of Velocity and Temperature Profiles

Various fluids' distinction on viscosity may induce a different level of the CCTTs' disturbance on the velocity and temperature profile, though most research (Kunlabud et al., 2017; Liu et al., 2017a,b, 2018; Saysroy and Eiamsa-Ard, 2017; Bahiraei et al., 2019; Khanmohammadi and Mazaheri, 2019) focused on one specific fluid. To investigate the effect, the velocity, and temperature profiles of FLiBe, water, and lubricating oil in the tube fitted with CCDTT are compared in **Figures 8**, **9**, respectively. The velocity profiles are normalized by each average velocity ($u_m$) to eliminate the differences among inlet velocity values. **Figure 8** indicates no obvious difference between the velocity profiles of various fluids, which demonstrates that the CCTTs can effectively disturb the velocity profile with the same

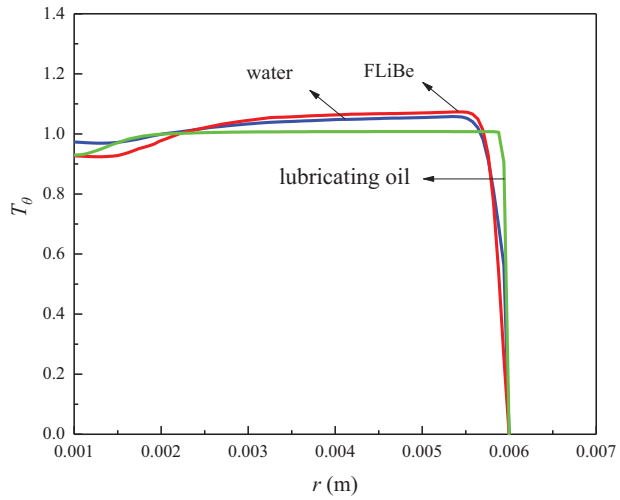


**FIGURE 9 |** Temperature profile of different fluids in the tube fitted with CCDTT ($y$ = 3) at $l$ = 0.24 m, $Re$ = 720.

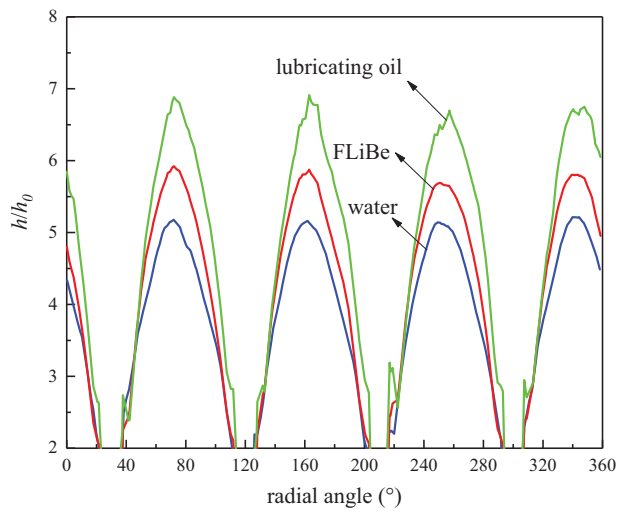


**FIGURE 10 |** Local heat transfer coefficient ratio of various working fluids in the tube fitted with CCDTT ($y$ = 3) at $l$ = 0.24 m, $Re$ = 720.

level for various working fluids at the laminar regime. This phenomenon testifies that the CCTTs are effective in affecting the velocity distribution even with high viscosity molten salt.

For the temperature profile, however, **Figure 9** indicates different level of CCTTs disturbance on various working fluids. The thermal boundary layer of lubricating oil is thinner than water and FLiBe. It can be attributed to the much higher Prandtl number of lubricating oil. A higher Prandtl number means a higher ratio of momentum diffusivity to the thermal diffusivity, and generally indicates a higher ratio of velocity boundary layer thickness to thermal boundary layer thickness.

The comparison between **Figures 8**, **9** shows that lubricating oil has a thinner thermal boundary layer than the other working fluids while the velocity boundary layer shows no difference.

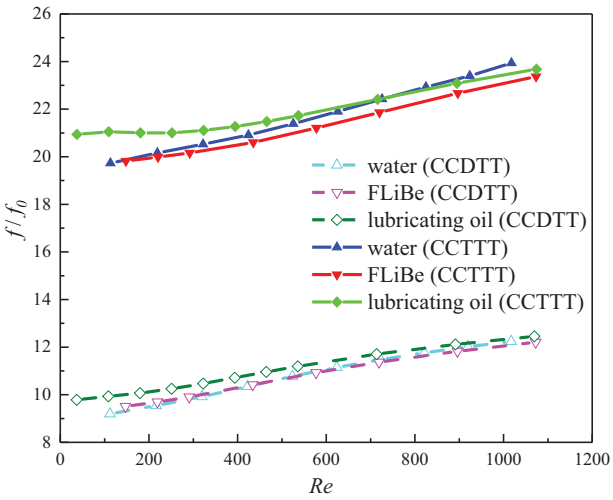


**FIGURE 11 |** Variation of friction factor ratio with the Reynolds number for various fluids in the tube fitted with CCDTT and CCTTT ($y$ = 3).

Since the fluids with higher viscosity would have thinner thermal boundary layers relative to the velocity boundary layer and CCTTs can induce the same level of disturbance on the velocity field, the thermal boundary layer of fluids with higher Prandtl numbers would be reduced much more, and hence the heat transfer enhancement is better. **Figure 10** indicates the local heat transfer coefficient ratio of various working fluids in a tube fitted with CCDTT ($y$ = 3, $l$ = 0.24 m, $Re$ = 720). It shows that lubricating oil and FLiBe have a higher ratio of heat transfer coefficient than water. In general, a thinner thermal boundary layer means a higher temperature gradient and heat transfer coefficient and **Figure 10** testifies that CCDTT has better enhancement on higher Prandtl number fluids.

In summary, CCTTs have better enhancement on the heat transfer of higher Prandtl number fluids, whose momentum diffusivity dominates the heat transfer behavior. It also indicates that the CCTTs have potential on the improvement of heat transfer of other high viscosity molten salts.

## Friction Factor and Nusselt Number Comparison

All the previous comparisons of results focus on the qualitative research at representative Reynolds numbers. To give a quantitative investigation of different fluids in the laminar flow regime, comparisons of friction factor ratio ($f/f_0$) and Nusselt number ratio ($Nu/Nu_0$) in the tube fitted with CCDTT and CCTTT ($y$ = 3) are presented in **Figures 11**, **12**, respectively. As **Figure 11** shows, the CCTTs have almost the same degree of increase in pressure drop for different fluids, which can be explained by the same level of velocity disturbance of different fluids in **Figure 8**. The similar velocity profile indicates a similar velocity gradient, and hence the increase of pressure drop, compared with the plain tube, should be approximate.

On the other hand, the increases in the heat transfer of different fluids show a prominent difference. **Figure 12** show that the CCTTs have better enhancement on the heat transfer

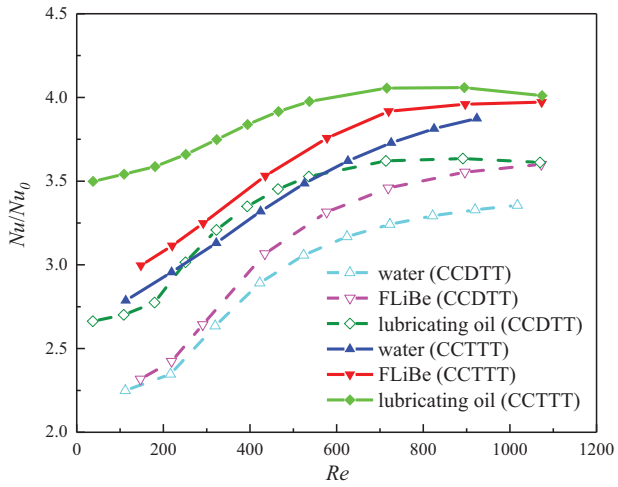


**FIGURE 12 |** Variation of Nusselt number ratio with the Reynolds number for different fluids in the tube fitted with CCDTT and CCTTT ($y$ = 3).

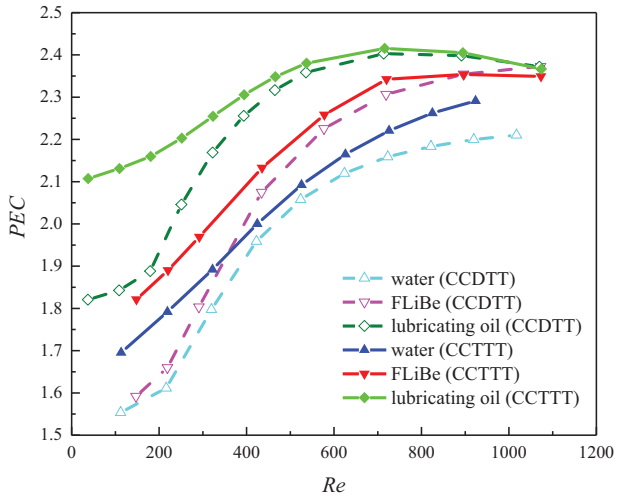


**FIGURE 13 |** Variation of PEC with the Reynolds number for different fluids in the tube fitted with CCDTT and CCTTT ($y$ = 3).

with higher Prandtl number fluids in the present range of the Reynolds number, which corresponds with previous analysis of the temperature profile. For exact comparison, the Nusselt number ratio of oil in the tube with CCDTT and CCTTT are, respectively, 1.047 and 1.035 times of that in FLiBe and 1.117 and 1.088 times of that in the water at $Re$ = 720. Higher Prandtl number fluids can have greater disturbance on a temperature profile from CCTTs since momentum diffusivity dominates the heat transfer behavior of viscous fluids.

### Overall Heat Transfer Performance Comparison

Coupling the results of the friction factor and heat transfer, the variation of PEC with the Reynolds number for different fluids in the tubes fitted with TT, CCDTT, and CCTTT ($y$ = 3) are displayed in **Figure 13**. From the analysis of the friction factor ratio and Nusselt number ratio among different fluids, it is easy to find that **Figure 13** has a similar trend to **Figure 12**. This is because the CCTTs can induce the same degree of disturbance on the velocity field (i.e., pressure drop increase) but a higher level of heat transfer augmentation in high viscosity fluids. It also implies that the differences in the thermophysical property have a stronger effect on the enhancement of heat transfer than pressure drop in the tube fitted with CCTTs. The higher the Prandtl number is, the better the heat transfer enhancement of CCTTs becomes. In other words, the CCTTs can have better overall heat transfer performance with a higher Prandtl number fluid. At $Re$ = 720, the PEC of oil in the tube with CCDTT and CCTTT are, respectively, 1.042 and 1.031 times of those in FLiBe and 1.113 and 1.088 times of those in water.

## CORRELATIONS OF NUSSELT NUMBER AND FRICTION FACTOR

### Analysis of the Correlations of Typical Twisted Tapes

Until now, many correlations have been developed for typical and modified twisted tapes (Garg et al., 2016). For TT, Manglik and Bergles developed their semi-empirical correlations of friction factor and Nusselt number ($Sw$ = 300–1400) (Manglik and Bergles, 1993a), as shown in Eqs 9 and 10:

$$fRe = 15.767\Psi^2\left(1 + 10^{-6}Sw^{2.55}\right)^{1/6}\varphi\left[1 + \left(\frac{\pi}{2y}\right)^2\right] \quad (9)$$

$$Nu = 4.612\left\{\left[\left(1 + 0.0951Gz^{0.894}\right)^{2.5} + 6.413 \times 10^{-9}\left(Sw \cdot Pr^{0.391}\right)^{3.835}\right]^2 + 2.132 \times 10^{-14}\left(Re_{ax} \cdot Ra\right)^{2.23}\right\}^{0.1}\left(\frac{\mu_f}{\mu_w}\right)^{0.14} \quad (10)$$

where $Sw$ is a dimensionless swirl parameter that accounts for centrifugal force effect (Eq. 13); $Gz$ is Graetz number ($Gz = MC_p/\lambda L$); $Pr$ is Prandtl number; $Re_{ax}$ is Reynolds number at axial velocity; $Ra$ is Rayleigh number that describes the buoyancy effect; $\varphi$ and $\psi$ are the cross section (Eq. 11) and hydraulic diameter parameters (Eq. 12); and $\mu_f$ and $\mu_w$ are the fluid dynamic viscosity at fluid and wall temperature.

These correlations were developed to comprehensively describe the TT's main effects on flow, including blockage, and swirl flow. One outstanding point is that these two effects were, respectively, correlated by the analytical solution and the experimental results since the blockage effect is numerically solvable, whereas swirl flow is mostly described by the empirical method.

### Blockage Effect

For the blockage effect, Manglik and Bergles applied the analytical solution of fully developed laminar flow in a semi-circular duct ($y = \infty$, $\delta = 0$) to solve the constant coefficient

15.767 as a numerical baseline solution of the friction factor. Concerning that the thickness of tape inserts will also decrease the cross-sectional area of the tube, and hence increase velocity and friction, two parameters that describe the tape thickness's effects on cross-sectional areas and hydraulic diameters were introduced. The first one is the cross-section parameter φ, as shown in Eq. 11:

$$\varphi = \frac{\text{plane tube cross sectional area}}{\text{tube with insert cross sectional area}} = \frac{\pi D^2/4}{\pi D^2/4 - \delta \cdot D} = \frac{\pi}{\pi - 4\delta/D} \tag{11}$$

The second one is the hydraulic diameter parameter, as shown in Eq. 12:

$$\Psi = \frac{\text{plane tube hydraulic diameter}}{\text{tube with insert hydraulic diameter}} = D \Big/ \left(4\frac{\pi D^2/4 - \delta \cdot D}{\pi D + 2D - 2\delta}\right) = \frac{\pi + 2 - 2\delta/D}{\pi - 4\delta/D} \tag{12}$$

To describe the effect of blockage on heat transfer, the constant coefficient 4.612 and a function of Graetz number (*Gz*, a dimensionless number that determines the length for thermally fully developed flow) were numerically solved under the analytical solution of a semi-circular duct model, which gave a good baseline solution of fully developed laminar flow's ($y = \infty$) Nusselt number. Having these coefficients and parameters derived from theoretical analysis can provide a simple and precise description of the blockage effect on fluids.

### Swirl Flow Effect

Besides the blockage effect, the twisted tapes also induce strong swirl flow, as shown in **Figure 2**. For the effect of swirl flow, the empirical correlating method was used to reveal the sophisticated helically rotating fluid flow. The swirl parameter that represents the balance of centrifugal, convective inertia, and viscous forces was defined to describe the intensity of swirl flow:

$$Sw = \frac{\left(\text{centrifugal force}\right)\left(\text{convective interia force}\right)}{\left(\text{viscous force}\right)^2} = \sqrt{\frac{\left(\rho u_s^2/H\right)\left(\rho u_s^2/D\right)}{\left(\mu u_s^2/D^2\right)^2}} = Re\varphi\sqrt{\left[1 + \left(\pi/2y\right)^2\right]/y} \tag{13}$$

where $u_s$ is the actual swirl velocity in the tube and defined as:

$$u_s = u\left(\frac{\pi D^2/4}{\pi D^2/4 - \delta \cdot D}\right)\sqrt{1 + \left(\pi/2y\right)^2} \tag{14}$$

Therefore, the characteristics of swirl flow were described by *Sw*, instead of *Re*, in the correlations of friction factor and Nusselt number. In the end, the blockage and swirl flow effect can be combined and correlated by the asymptotic matching method which yields Eqs 9 and 10.

## New Unified Correlations for Twisted Tapes and Coaxial Cross Twisted Tapes

Since CCTTs and TT have the alike geometry and the same mechanism of heat transfer improvement, it is reasonable to develop their correlations based on TT's correlations Eqs 9 and 10, proposed by Manglik and Bergles. For the blockage effect, parameters that describe the changes of the cross-sectional area and hydraulic diameter can be modified according to the geometry of CCTTs. The cross-section and hydraulic diameter parameters of CCDTT are defined in Eqs 15 and 16, respectively:

$$\varphi = \frac{\pi D^2/4}{\pi D^2/4 - 2\delta \cdot D + \delta^2} = \frac{\pi}{\pi - 8\delta/D + 4\delta^2/D^2} \tag{15}$$

$$\Psi = D/\left(4\frac{\pi D^2/4 - 2\delta \cdot D + \delta^2}{\pi D + 4D - 8\delta}\right) = \frac{\pi + 4 - 8\delta/D}{\pi - 8\delta/D + 4\delta^2/D^2} \tag{16}$$

The cross-section and hydraulic diameter parameters of CCTTT are defined in Eqs 17 and 18, respectively:

$$\varphi = \frac{\pi D^2/4}{\pi D^2/4 - 3\delta \cdot D + 1.5\sqrt{3}\delta^2} = \frac{\pi}{\pi - 12\delta/D + 6\sqrt{3}\delta^2/D^2} \tag{17}$$

$$\Psi = D/\left(4\frac{\pi D^2/4 - 3\delta \cdot D + 1.5\sqrt{3}\delta^2}{\pi D + 6D - \left(6\sqrt{3} + 6\right)\delta}\right) = \frac{\pi + 6 - \left(6\sqrt{3} + 6\right)\delta/D}{\pi - 12\delta/D + 6\sqrt{3}\delta^2/D^2} \tag{18}$$

For the concern of practical use, the cross section and hydraulic diameter parameters of TT, CCDTT, and CCTTT can be re-defined in a unified form where the second order term $\delta^2/D^2$ is omitted. The cross-section parameter is re-defined as:

$$\varphi = \frac{\pi}{\pi - 4n\delta/D} \tag{19}$$

The hydraulic diameter parameter is re-defined as:

$$\Psi = \frac{\pi + 2n - m\delta/D}{\pi - 4n\delta/D} \tag{20}$$

where *n* is the tape number and coefficient *m* shall be set 2, 8, or $6\sqrt{3} + 6$ for TT, CCDTT, or CCTTT, respectively.

For the swirl flow effect, the swirl parameter that describes the intensity of tape-twist induced swirl flow is defined as the same as Eq. 13 except that the cross-section parameter φ shall use the unified form in Eq. 19. In the heat transfer correlation, the numerical results show that the swirl flow effect surpasses the free convective effect, where $Gr << Sw^2$. This is because the flow in research has a low Grashof number, and therefore the effect of buoyancy force can be neglected in the correlation of heat transfer. Finally, the Nusselt number is developed as the function of *Sw*, *Gz,* and *Pr*. Based on the results of numerical simulations with FLiBe, water, and lubricating oil, the correlations of the Nusselt number and friction factor in the tube fitted with TT,

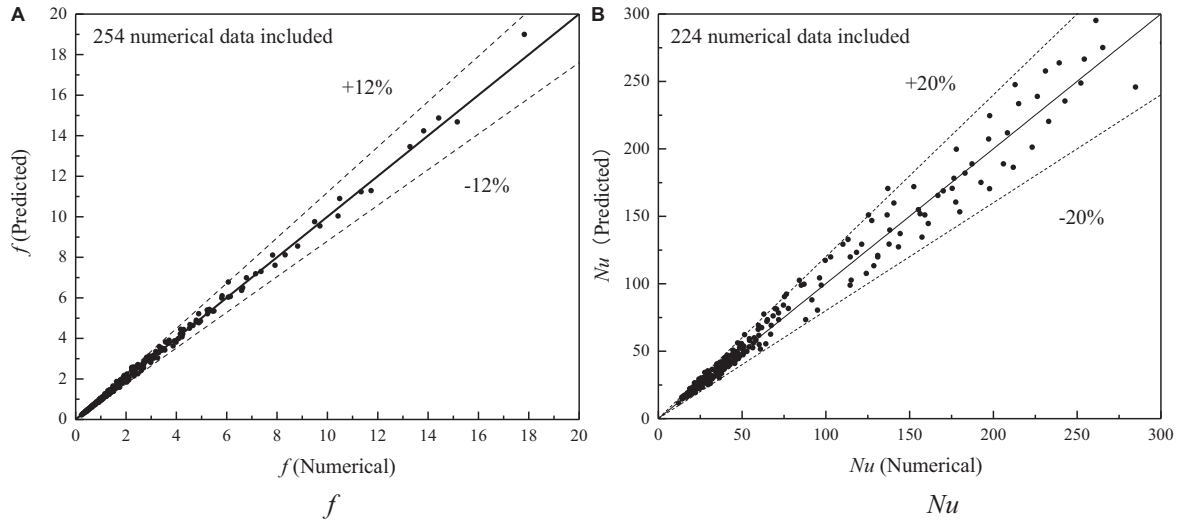


**FIGURE 14 |** Comparison of numerical results with predicted values of Nusselt number and friction factor. **(A)** *f*. **(B)** *Nu*.

CCDTT or CCTTT are uniformly developed and defined as follow:

$$fRe = A\varphi\Psi^2\left(1 + 1.348 \times 10^{-3} Sw^{1.09}\right)^{0.462}\left[1 + \left(\frac{\pi}{2y}\right)^2\right] \tag{21}$$

$$Nu = B[\left(1 + 0.2165Gz^{0.662}\right)^{0.251} + 3.87 \times 10^{-2}\left(Sw \cdot Pr^{0.4}\right)^{0.431}]^{2.06}\left(\frac{\mu_f}{\mu_w}\right)^{0.14} \tag{22}$$

where $A$ and $B$ are various constant coefficients for TT and CCTTs. As for TT, $A = 59.24$, $B = 3.81$; for CCDTT and CCTTT, $A = 47.38$, $B = 5.67$.

For Eqs 21 and 22, the range of Reynolds number, Prandtl number, and twist ratio are 100–1,100, 7–900, and 2–4, respectively. The comparison of numerical results with predicted values of the Nusselt number and friction factor are shown in **Figure 14**. The predicted values are in good agreement with the numerical simulations and deviations of $Nu$ and $f$ are within ± 20% and ± 12%, respectively.

## CONCLUSION

The characteristics of heat transfer and friction factor of laminar flow for various working fluids in a circular tube with coaxial cross twisted tape (CCTT) have been investigated numerically. The streamline, velocity profiles, temperature profiles, and performance evaluation criteria are all presented for analysis and the conclusion are summarized as follows:

(1) The velocity and temperature profiles of the tube fitted with different twisted tape reveal that the CCTTs can produce stronger swirl flow and improve the near-wall gradient of velocity and temperature. For FLiBe, the CCTTs are more effective in reducing the thermal boundary layer of FLiBe because of its thicker velocity boundary layer. For different fluids, the CCTTs' disturbance on velocity profiles is similar while the reduction on the thermal boundary layer would intensify with the increase of the Prandtl number.

(2) The numerical results show that the CCTTs can greatly enhance the heat transfer, though the pressure drop also increases. The plots of PEC ($y$ = 3) for FLiBe indicates that the overall performance of CCDTT and CCTTT are respectively 1.2-1.22 and 1.2-1.38 times of that in the tube with TT. The maximum PEC value 2.73 is obtained by CCTTT ($y$ = 2) at $Re$ = 582. For different fluids, the CCTTs provide better overall performance with higher Prandtl number fluids.

(3) The semi-empirical correlations of the Nusselt number and friction factor of various fluids for TT, CCDTT, and CCTTT are uniformly developed based on numerical results. The maximum discrepancy between the correlative results and numerical results for the Nusselt number and friction factor are found to be ± 20% and ± 12%, respectively.

## FUTURE WORK

The CCTTs heat transfer enhancement performance with FLiBe have been numerically studied and testified as a feasible method on high Prandtl number fluids, though further research could be done on experimental demonstration and geometry modification simulation. There are various types of geometry modifications that can be applied on the CCTTs, including alternative clockwise and counter-clockwise (Eiamsa-Ard and Promvonge, 2010), notched tape (Rahimi et al., 2009), multiple tapes (Piriyarungrod et al., 2018), and grooved tubes (Lu et al., 2015). These modifications could either periodically mix swirl flow in each channel or introduce perturbation near the wall so that heat transfer resistance is further reduced. Through

experimental demonstration, the semi-empirical correlation in this work could be testified and corrected based on measurement.

## DATA AVAILABILITY STATEMENT

The raw data supporting the conclusions of this article will be made available by the authors, without undue reservation, to any qualified researcher.

## AUTHOR CONTRIBUTIONS

This work was done during the undergraduate thesis of ZY under the instruction of XC and MD. The basic of new coaxial cross twisted tape performance has been previously researched by XL and she provided lots of help and insights to this work. ZG also helped ZY a lot on this work. All authors contributed to the article and approved the submitted version.

## REFERENCES


Abed, A. M., Hasan, S. M., Hussein, Z., Fadhil, D., and Abdulkadhim, A. (2018). Numerical analysis of flow and heat transfer enhancement in a horizontal pipe with P-TT and V-Cut twisted tape. *Case Stud. Ther. Engin.* 12, 749–758. doi: 10.1016/j.csite.2018.10.004

Agarwal, S., and Rao, M. R. (1996). Heat transfer augmentation for the flow of a viscous liquid in circular tubes using twisted tape inserts. *Int. J. Heat Mass Trans.* 39, 3547–3557. doi: 10.1016/0017-9310(96)00039-7

Amini, A., Miller, J., and Jouhara, H. (2017). An investigation into the use of the heat pipe technology in thermal energy storage heat exchangers. *Energy* 136, 163–172. doi: 10.1016/j.energy.2016.02.089

Bahiraei, M., Nima, M., Mehran, S. M., and Moayedi, H. (2019). Thermal performance of a new nanofluid containing biologically functionalized graphene nanoplatelets inside tubes equipped with rotating coaxial double-twisted tapes. *Int. Commun. Heat .Mass Trans.* 108:104305. doi: 10.1016/j.icheatmasstransfer.2019.104305

CD-adapco (2015). *STAR-CCM+User Guide Version (10.02)*. New York: CD-adapco.

Chang, C., Adriano, S., Zhiyong, W., Xin, L., Yongliang, L., Mingzhi, Z., et al. (2018). Enhanced heat transfer in a parabolic trough solar receiver by inserting rods and using molten salt as heat transfer fluid. *Appl. Energy* 220, 337–350. doi: 10.1016/j.apenergy.2018.03.091

Chen, Y.-S., Jian, T., Shen-De, S., Qiang, S., Yuan, F., Zhong-Feng, T., et al. (2017). Characteristics of the laminar convective heat transfer of molten salt in concentric tube. *Appl. Ther. Engin.* 125, 995–1001. doi: 10.1016/j.applthermaleng.2017.07.043

Chen, Y. S., Tian, J., Fu, Y., Tang, Z. F., Zhu, H. H., and Wang, N. X. (2018). Experimental study of heat transfer enhancement for molten salt with transversely grooved tube heat exchanger in laminar-transition-turbulent regimes. *Appl. Therm. Engin.* 132, 95–101. doi: 10.1016/j.applthermaleng.2017.12.054

Chiba, S., Shinya, C., Saburo, T., Kazuhisa, Y., and Akio, S. (2001). Heat transfer enhancement for a molten salt Flibe channel. *Fusion Technol.* 39 2P2, 779–783. doi: 10.13182/FST01-A11963333

Chiba, S.-Y., Kazuhisa, Y., Hidetoshi, H., Saburo, T., and Akio, S. (2006). Numerical research on heat transfer enhancement for high Prandtl-number fluid. *Fusion Engin. Design.* 81, 513–517. doi: 10.1016/j.fusengdes.2005.08.046

Dave, A., Sun, K., and Hu, L. (2018). Numerical simulations of molten salt pebble-bed lattices. *Ann. Nuclear Energy* 112, 400–410. doi: 10.1016/j.anucene.2017.10.037

Du, B.-C., Ya-Ling, H., Kun, W., and Han-Hui, Z. (2017). Convective heat transfer of molten salt in the shell-and-tube heat exchanger with segmental baffles. *Int. J. Heat Mass Trans.* 113, 456–465. doi: 10.1016/j.ijheatmasstransfer.2017.05.075

Eiamsa-Ard, S., and Promvonge, P. (2010). Performance assessment in a heat exchanger tube with alternate clockwise and counter-clockwise twisted-tape inserts. *Int. J. Heat Mass Trans.* 53, 1364–1372. doi: 10.1016/j.ijheatmasstransfer.2009.12.023

Fan, J., Ding, W. K., Zhang, J. F., He, Y. L., and Tao, W. Q. (2009). A performance evaluation plot of enhanced heat transfer techniques oriented for energy-saving. *Int. J. Heat Mass Trans.* 52, 33–44. doi: 10.1016/j.ijheatmasstransfer.2008.07.006

Garbrecht, O., Bieber, M., and Kneer, R. (2017). Increasing fossil power plant flexibility by integrating molten-salt thermal storage. *Energy* 118, 876–883. doi: 10.1016/j.energy.2016.10.108

Garg, M., Himanshu, N., Sourabh, K., and Shukla, M. K. (2016). Heat transfer augmentation using twisted tape inserts: A review. *Renew. Sustain. Energy Rev.* 63, 193–225. doi: 10.1016/j.rser.2016.04.051

Guo, Z.-Y., Tao, W.-Q., and Shah, R. (2005). The field synergy (coordination) principle and its applications in enhancing single phase convective heat transfer. *Int. J. Heat Mass Trans.* 48, 1797–1807. doi: 10.1016/j.ijheatmasstransfer.2004.11.007

He, Y., Li, L., Pengxiao, L., and Lianxiang, , M. (2018). Experimental study on heat transfer enhancement characteristics of tube with cross hollow twisted tape inserts. *Appl. Ther. Engin.* 131, 743–749. doi: 10.1016/j.applthermaleng.2017.12.029

Hosseinnezhad, R., Rahim, H., Omid, A. A., Hamid, H. A., Mohit, B., Ali, K., et al. (2018). Numerical study of turbulent nanofluid heat transfer in a tubular heat exchanger with twin twisted-tape inserts. *J. Therm. Analy. Calor.* 132, 741–759. doi: 10.1007/s10973-017-6900-5

Jianfeng, L., Shen, X., Ding, J., Peng, Q., and Wen, Y. (2013). Convective heat transfer of high temperature molten salt in transversely grooved tube. *Appl. Ther. Engin.* 61, 157–162. doi: 10.1016/j.applthermaleng.2013.07.037

Kearney, D., Kellyb, B., Herrmannc, U., Cabled, R., Pachecoe, J., Mahoneye, R., et al. (2004). Engineering aspects of a molten salt heat transfer fluid in a trough solar field. *Energy* 29, 861–870. doi: 10.1016/S0360-5442(03)00191-9

Khanmohammadi, S., and Mazaheri, N. (2019). Second law analysis and multi-criteria optimization of turbulent heat transfer in a tube with inserted single and double twisted tape. *Int. J. Ther. Sci.* 145:105998. doi: 10.1016/j.ijthermalsci.2019.105998

Kunlabud, S., Varesa, C., Vichan, K., Pitak, P., and Smith, E. (2017). Heat transfer in turbulent tube flow inserted with loose-fit multi-channel twisted tapes as swirl generators. *Theoret. Appl. Mechan. Lett.* 7, 372–378. doi: 10.1016/j.taml.2017.11.011

Liu, X., Chun, L., and Bian, H. (2017a). "Enhanced Heat Transfer And Resistance Performance Of New Complex Twisted Tapes For Highly-Viscous Fluid Flow Inside Tubes," in *17th international topical meeting on nuclear reactor thermal hydraulics*, (Harbin: Harbin Engineering University).

Liu, X., Liu, Q., and Bo, H. (2017b). "Numerical Study on Heat Transfer and Resistance of a Tube Fitted With New Twisted Tapes for Lubricating Oil," in *in 2017 25th International Conference on Nuclear Engineering*, (New York: American Society of Mechanical Engineers Digital Collection). doi: 10.1115/ICONE25-67766

Liu, X., Chun, L., Cao, X., and Yan, C. (2018). Numerical analysis on enhanced performance of new coaxial cross twisted tapes for laminar convective heat transfer. *Int. J. Heat Mass Trans.* 121, 1125–1136. doi: 10.1016/j.ijheatmasstransfer.2018.01.052

Lu, J., Jing, D., Tao, Y., and Xiangyang, S. (2015). Enhanced heat transfer performances of molten salt receiver with spirally grooved pipe. *Appl. Ther. Engin.* 88, 491–498. doi: 10.1016/j.applthermaleng.2014.09.020

Manglik, R., Agarwal, S. K., and Raja Rao, M. (1993). *Heat transfer enhancement of intube flows in process heat exchangers by means of twisted-tape inserts*. Troy, NY: Rensselaer Polytechnic Institute. Ph.D. thesis.

Manglik, R. M., and Bergles, A. E. (1993a). Heat transfer and pressure drop correlations for twisted-tape inserts in isothermal tubes: part I—laminar flows. *J. Heat Trans.* 115, 881–889. doi: 10.1115/1.2911383

Manglik, R. M., and Bergles, A. E. (1993b). Heat transfer and pressure drop correlations for twisted-tape inserts in isothermal tubes: Part II—Transition and turbulent flows. *J. Heat Trans.* 115, 890–896. doi: 10.1115/1.2911384

Meng, J.-A., Liang, X.-G., and Li, Z.-X. (2005). Field synergy optimization and enhanced heat transfer by multi-longitudinal vortexes flow in tube. *Int. J. Heat Mass Trans.* 48, 3331–3337. doi: 10.1016/j.ijheatmasstransfer.2005.02.035

Piriyarungrod, N., Manoj, K., Thianpongc, C., Pimsarnc, M., Chuwattanakulc, V., and Eiamsa-ard, S. (2018). Intensification of thermo-hydraulic performance in heat exchanger tube inserted with multiple twisted-tapes. *Appl. Therm. Engin.* 136, 516–530. doi: 10.1016/j.applthermaleng.2018.02.097

Promvonge, P. (2008). Thermal augmentation in circular tube with twisted tape and wire coil turbulators. *Energy Convers. Manag.* 49, 2949–2955. doi: 10.1016/j.enconman.2008.06.022

Rahimi, M., Shabanian, S. R., and Alsairafi, A. A. (2009). Experimental and CFD studies on heat transfer and friction factor characteristics of a tube equipped with modified twisted tape inserts. *Chem. Engin. Proc. Process Inten.* 48, 762–770. doi: 10.1016/j.cep.2008.09.007

Romatoski, R., and Hu, L. (2017). Fluoride salt coolant properties for nuclear reactor applications: A review. *Anna. Nucl. Energy* 109, 635–647. doi: 10.1016/j.anucene.2017.05.036

Ruengpayungsak, K., Saysroy, A., Wongcharee, K., and Eiamsa-Ard, S. (2019). Thermohydraulic performance evaluation of heat exchangers equipped with centrally perforated twisted tape: Laminar and turbulent flows. *J. Ther. Sci. Technol.* 14, JTST0002–JTST0002. doi: 10.1299/jtst.2019jtst0002

Sabharwall, P., Denis, C., Michael, G., Guiqiu, Z., Kumar, S., Mark, A., et al. (2014). Advanced heat exchanger development for molten salts. *Nucl. Engin. Design.* 280, 42–56. doi: 10.1016/j.nucengdes.2014.09.026

Saha, S., Gaitonde, U., and Date, A. (1989). Heat transfer and pressure drop characteristics of laminar flow in a circular tube fitted with regularly spaced twisted-tape elements. *Exper. Therm. Fluid Sci.* 2, 310–322. doi: 10.1016/0894-1777(89)90020-4

Saysroy, A., and Eiamsa-Ard, S. (2017). Enhancing convective heat transfer in laminar and turbulent flow regions using multi-channel twisted tape inserts. *Int. J. Therm. Sci.* 121, 55–74. doi: 10.1016/j.ijthermalsci.2017.07.002

Scarlat, R. O., and Peterson, P. F. (2014). The current status of fluoride salt cooled high temperature reactor (FHR) technology and its overlap with HIF target chamber concepts. *Nucl. Instr. Meth. Phys. Res. Sec. A Accele. Spectr. Detec. Assoc. Equip.* 733, 57–64. doi: 10.1016/j.nima.2013.05.094

Serrano-López, R., Fradera, J., and Cuesta-Lopez, S. (2013). Molten salts database for energy applications. *Chem. Engin. Process. Proc. Intens.* 73, 87–102. doi: 10.1016/j.cep.2013.07.008

Smithberg, E., and Landis, F. (1964). Friction and forced convection heat-transfer characteristics in tubes with twisted tape swirl generators. *J. Heat Trans.* 86, 39–48. doi: 10.1115/1.3687060

Sohal, M. S., Manohar, S., Ebner, M. A., Sabharwall, P., Sharpe, P., et al. (2010). *Engineering database of liquid salt thermophysical and thermochemical properties*. United States: Idaho National Laboratory (INL). doi: 10.2172/980801

Thorsen, R., and Landis, F. (1968). Friction and heat transfer characteristics in turbulent swirl flow subjected to large transverse temperature gradients. *J. Heat Trans.* 90, 87–97. doi: 10.1115/1.3597466

Toda, S., Shinya, C., Kazuhisa, Y., Masahiro, O., and Akio, S. (2002). Experimental research on molten salt thermofluid technology using a high-temperature molten salt loop applied for a fusion reactor Flibe blanket. *Fus. Engin. Des.* 63, 405–409. doi: 10.1016/S0920-3796(02)00195-3

Vignarooban, K., Xinhai, X., Arvayc, A., Hsua, K., and Kannan, A. M. (2015). Heat transfer fluids for concentrating solar power systems-a review. *Appl. Energy* 146, 383–396. doi: 10.1016/j.apenergy.2015.01.125

Watanabe, A., Shinji, E., Akio, S., and Hidetoshi, H. (2013). Evaluation of heat transfer characteristics of a sphere-packed pipe for Flibe blanket. *Fus. Engin. Des.* 88, 2357–2360. doi: 10.1016/j.fusengdes.2013.01.051

Wongcharee, K., and Eiamsa-Ard, S. (2011). Friction and heat transfer characteristics of laminar swirl flow through the round tubes inserted with alternate clockwise and counter-clockwise twisted-tapes. *Int. Commun. Heat Mass Trans.* 38, 348–352. doi: 10.1016/j.icheatmasstransfer.2010.12.007

Xiao, P., Guo, L., and Zhang, X. (2015). Investigations on heat transfer characteristic of molten salt flow in helical annular duct. *Appl. Ther. Engin.* 88, 22–32. doi: 10.1016/j.applthermaleng.2014.09.021

**Conflict of Interest:** The authors declare that the research was conducted in the absence of any commercial or financial relationships that could be construed as a potential conflict of interest.

## NOMENCLATURE

| | |
|---|---|
| $C_p$ | Specific heat at constant pressure, J/(kg·K) |
| $CR$ | Clearance ratio |
| $c$ | The clearance between twisted tape and tube wall, m |
| $D$ | Inner tube diameter, m |
| $f$ | Friction factor |
| $Gr$ | Grashof number, |
| $Gz$ | Graetz number, $MC_p/\lambda L$ |
| $H$ | 180-degree twist pitch, m |
| $h$ | Heat transfer coefficient, W/(m$^2$·K) |
| $L$ | Tube length, m |
| $l$ | Distance to the inlet, m |
| $M$ | Mass flow rate, kg/s |
| $m$ | Coefficient in hydraulic diameter parameter |
| $n$ | Coefficient in cross-section parameter for tape number |
| $Nu$ | Nusselt number |
| $p$ | Reference pressure, 101.325 kPa |
| $\Delta P$ | Pressure drop, Pa |
| PEC | Performance evaluation criteria |
| $Pr$ | Prandtl number |
| $r$ | Radial position, m |
| $R$ | Tube inner radius, m |
| $Ra$ | Rayleigh number |
| $Re$ | Reynolds number |
| $Sw$ | Swirl parameter |
| $T$ | Temperature, °C |
| $T_\theta$ | Dimensionless temperature |
| $U$ | Velocity, m/s |
| $u_s$ | Actual swirl velocity, m/s |
| $y$ | Twist ratio |
| *Greek symbols* | |
| $\delta$ | Tape thickness, m |
| $\lambda$ | Thermal conductivity, W/(m·K) |
| $\mu$ | Dynamic viscosity, Pa·s |
| $\mu_f$ | Dynamic viscosity at fluid mean temperature, Pa·s |
| $\rho$ | Density, kg/m$^3$ |
| $\varphi$ | Cross-section parameter |
| $\psi$ | Hydraulic diameter parameter |
| *Subscript* | |
| *0* | Plain tube |
| *ax* | Value at the axial flow |
| *m* | Mean value |
| *w* | Value at wall |

frontiers in Energy Research

BRIEF RESEARCH REPORT
published: 30 September 2020
doi: 10.3389/fenrg.2020.524445

# Scaling Design of the Pressure Response Experimental Facility for Pressure Suppression Containment

*Xinxing Liu, Zhaoming Meng*, Nan Zhang and Zhongning Sun*

*Fundamental Science on Nuclear Safety and Simulation Technology Laboratory, Harbin Engineering University, Harbin, China*

Pressure suppression containment has been adopted extensively in boiling water reactor design due to its remarkable pressure suppression capacity. To study the pressure response characteristics of the containment in the initial stage of the loss-of-coolant accident, it is necessary to build a scaling facility to simulate the prototype. Analysis of the steam mass and energy that are released from the break as well as of the steam condensation that occurs in the suppression pool is conducted, respectively, for the prototype pressurized water reactor. The suppression pipe system resistance is also scaled with a certain ratio. The length and diameter of the main pipe and the branch pipe as well as the orifice diameter are calculated. At last, the prototype and the experimental facility are modeled by MELCOR to analyze the steam mass and energy release. The results show that the containment pressure evolution trends of the prototype and the scaled experimental facility are consistent. The pressure difference exists at some times, with a maximum relative error of 4%.

**Keywords: pressure suppression containment, scaling experiment, pressure response, MELCOR, pipe resistance**

OPEN ACCESS

***Edited by:***
*Jinsuo Zhang,*
*Virginia Tech, United States*

***Reviewed by:***
*Khalil Ur Rahman,*
*Pakistan Nuclear Regulatory Authority, Pakistan*
*Zhitong Bai,*
*University of Michigan, United States*

****Correspondence:***
*Zhaoming Meng*
*mengzhaoming@hrbeu.edu.cn*

***Specialty section:***
*This article was submitted to Nuclear Energy, a section of the journal Frontiers in Energy Research*

***Received:*** *04 January 2020*
***Accepted:*** *27 August 2020*
***Published:*** *30 September 2020*

***Citation:***
*Liu X, Meng Z, Zhang N and Sun Z (2020) Scaling Design of the Pressure Response Experimental Facility for Pressure Suppression Containment. Front. Energy Res. 8:524445. doi: 10.3389/fenrg.2020.524445*

## INTRODUCTION

Different from the traditional large pressurized water reactor (PWR) nuclear power plants, small PWRs have been paid more and more attention due to their diversity of application and flexibility in site selection. When the loss-of-coolant accident (LOCA) happens, a large amount of high temperature and pressure coolant will be released to the containment from the break, which will cause the containment pressure to increase in a short time. In order to deal with this overpressure problem, large PWR nuclear power plants usually adopt large volume containment to slow down the pressure rise rate, while in small PWRs the containment pressure increases rapidly and reaches the safety limit value in a short time due to the compact containment vessel design. Besides, the active spray system and the passive cooling system cannot operate in time. Therefore, effective containment overpressure control measures should be introduced into the small PWR design.

Learning from the boiling water reactor (BWR) design experience, pressure suppression containment has an excellent effect in suppressing the short-term containment pressure increasing rate. Thus, the pressure suppression containment system can be adopted by small PWRs to make sure that the containment peak pressure is under the design safety limit value during severe accidents.

**Abbreviations:** LOCA, loss-of-coolant accident; PWR, pressurized water reactor; BWR, boiling water reactor; LUT, Lappeenranta University of Technology; RPC, rate of pressure change.

Due to the complex thermal hydrodynamic phenomenon of the suppression pool system, containment pressure response is influenced by many factors. Experiments should be conducted to verify whether pressure suppression containment can meet the demand for containment peak pressure suppression in the early stage of the LOCA.

Many research teams have carried out a lot of investigation work on the pressure suppression containment (Varzaly et al., 1978; Gamble et al., 2001; Yan and Bolger, 2010; Sawant and Khatib-Rahbar, 2011; Chen et al., 2012). The Marviken power plant in Sweden was originally designed and built as a boiling heavy water reactor (EPRI-NP, 1982; Marviken Power Station, 1977). Instead of being operated, the Marviken pressure suppression containment was used in performing full-scale blow-down experiments to study the containment response. Although the full-scale experiment can predict the real pressure evolution with the most limited deviation, such experiments are both costly and hard to operate. Therefore, the most acceptable methods of predicting pressure response in containment are through small-scale experimental facilities, using scaling laws to extrapolate small-scale results to full-scale conditions.

JAERI built a test facility to study containment response during LOCAs (Kukita et al., 1983), of which the lower portion of the test containment is a full-scale replica of one of the 20° sectors in an annular wetwell of a typical MARK II containment. The test facility features seven full-size vent pipes. The drywell and the primary system are represented in the same volumetric scale ratio (1:18) as the wetwell. Although the scale of the experiment is much smaller than the full-scale experiment, the same high-temperature and high-pressure of water as the BWR operating pressure and temperature are still needed in the experiment to simulate accident steam and mass release. It is still a challenge to perform such high-temperature and high-pressure experiments in the laboratory conditions.

Lappeenranta University of Technology in Finland conducted a series of experiments using PPOOLEX program to investigate suppression pool–related thermal hydraulic phenomena (Laine et al., 2013; Patel et al., 2014; Patel et al., 2016). The PPOOLEX test facility is a scaled-down test facility of Nordic type BWR containment. The 31-$m^3$ stainless steel containment consists of two main parts: the drywell compartment and the wetwell compartment, separated by an intermediate floor. The volume of the two parts and the diameter of the blow-down pipe were just simply scaled according to the Olkiluoto nuclear power plant prototype parameters, while more scaling parameters were not given in their reports. Therefore, it could not be concluded that the PPOOLEX facility is suitable for performing containment response experiments.

Anderson et al. (1978) conducted some fundamental experimental checks of the scaling laws originally put forward by Moody (1976), which mainly deal with small-scale modeling of the vent-clearing phase in which air flows into the suppression pool. The results showed that the dimensionless pressures were in excellent agreement if the four scaling parameters were held constant. Otherwise, the enthalpy flux must be scaled using an orifice to ensure that the pressure will scale. Although these scaling laws could give some guidance in scaling facility design analysis, the main assumptions of the derivation process were based on the vent-clearing phase, which is different from the steam blow-down experiments.

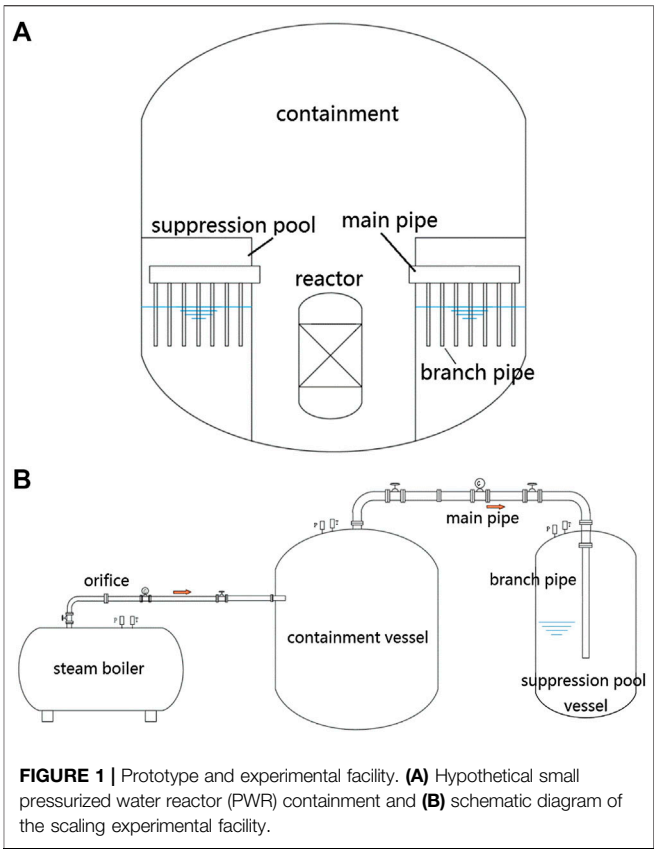


**FIGURE 1 |** Prototype and experimental facility. **(A)** Hypothetical small pressurized water reactor (PWR) containment and **(B)** schematic diagram of the scaling experimental facility.

In a word, the current experimental research of pressure suppression containment usually depends on large-scale facilities and prototype parameter steam source, which leads to difficulties in conducting the study in laboratory conditions. Therefore, it is meaningful to put forward some scaling laws to design a small-scale experimental facility, which contributes to the pressure suppression containment design and related analysis software validation.

In this article, a small PWR with pressure suppression containment is studied as a prototype. The break steam mass and energy release and the direct contact condensation process in the suppression pool are analyzed to obtain some main parameters that are dominant in containment pressure response. The scaled facility's geometrical dimensions are decided by these main parameters through overall consideration. The blow-down pipe resistance of the scaled facility is arranged to be the same as that of the prototype. At last, the prototype PWR and the scaled experimental facility are both simulated by using the severe accident analysis program MELCOR. The results are compared with each other to verify whether the scaling method put forward in this article is suitable for small-scale experimental facility design.

**TABLE 1 |** Main parameters of the prototype and scaling experimental facility.

| Parameter | Prototype | Scaled experiment |
|---|---|---|
| Primary circuit operating pressure (MPa) | 15 | 2 (steam boiler maximum operation pressure) |
| Primary circuit average temperature (°C) | 280 | 212 (steam boiler maximum operation temperature) |
| Containment initial pressure (MPa) | 0.1 | 0.1 |
| Containment initial temperature (°C) | 40 | 40 |
| Containment free volume ($m^3$) | 1,200 | 6 |
| Suppression pool total volume ($m^3$) | 600 | 3 |
| Suppression pool gas–water volume ratio | 2:1 | 2:1 |
| Suppression pool water initial temperature (°C) | 30 | 30 |
| Number of main pipes (N1) | 20 | 1 |
| Number of branch pipes of each blow-down pipe (N2) | 10 | 1 |
| Main pipe length (m) | 10 | 5 |
| Branch pipe length (m) | 2 | 3 |
| Blow-down pipe diameter (m) | 0.6 | – |
| Branch pipe diameter (m) | 0.1 | – |
| Suppression pool initial temperature (°C) | 30 | 30 |

## PRESSURE RESPONSE PROCESS IN THE CONTAINMENT

A hypothetical prototype small PWR pressure suppression containment is shown in **Figure 1A**. The reactor is located in the containment center, which is surrounded by the suppression pool. The containment and the suppression pool are connected by several large-diameter blow-down pipes (i.e., main pipes). Along the main pipe, there are several smaller diameter branch pipes, which are submerged in water.

For the scaling experimental facility, two stainless steel pressure vessels are used to simulate the containment and the suppression pool, respectively. The containment and the suppression pool are connected by one main pipe and one branch pipe. The steam mass and energy released from the break site during the LOCA is simulated by an electric steam boiler. A schematic diagram of the scaling experimental facility can be seen in **Figure 1B**. The main parameters of the prototype and some predetermined parameters of the scaling experimental facility before the scaling analysis are shown in **Table 1**.

Taking the free volume inside the containment as the control body, the heat absorption by the containment wall and the structure is ignored temporarily, which will be compensated in the scaling steam mass and energy release (see "Simulation Results and Discussion" section below). The only two primary items that affect containment pressure are considered, which are the energy from the break and the energy transported to the suppression pool. Therefore, the rate of pressure change equation is derived as (Brown, 1999)

$$\frac{V}{\gamma-1}\frac{dp}{dt} = \dot{m}_{brk}i_{brk} - \dot{m}_{in}i_{in}, \tag{1}$$

where $V$ refers to the containment free volume, $\gamma$ is the specific heat ratio, $p$ is the pressure of the containment, $\dot{m}_{brk}$ is the mass flow rate from the break, $\dot{m}_{in}$ represents the mass flow entered into the suppression pool, and $i_{brk}$ and $i_{in}$ are the specific enthalpy in the break and the containment.

By normalizing with appropriate reference values (i.e., $X^+ = X/X_{\mathrm{ref}}$), the variables in the above dimensional form of the rate of pressure change (RPC) equation can be put into the nondimensional form as follows:

$$\frac{1}{\gamma-1}\frac{dp^+}{dt} = \left\{\frac{\dot{m}_{brk}i_{brk}}{V\Delta p}\right\}_{ref}\frac{\dot{m}^+_{brk}i^+_{brk}}{V^+} - \left\{\frac{\dot{m}_{in}i_{in}}{V\Delta p}\right\}_{ref}\frac{\dot{m}^+_{in}i^+_{in}}{V^+} \tag{2}$$

The following two process-specific frequencies can be obtained from the coefficients of the above equation:

$$\omega_{cond} = \frac{\dot{m}_{in}i_{in}}{V\Delta p}; \quad \omega_{brk} = \frac{\dot{m}_{brk}i_{brk}}{V\Delta p} \tag{3}$$

Comparing the coefficients of both the prototype and the experiment, the scale ratio can be obtained as

$$r_{cond} = \frac{\left\{\frac{\dot{m}_{in}i_{in}}{V\Delta p}\right\}_P}{\left\{\frac{\dot{m}_{in}i_{in}}{V\Delta p}\right\}_m} = \frac{[\dot{m}_{in}]_R[i_{in}]_R}{[V]_R[\Delta p]_R}; \quad r_{brk} = \frac{\left\{\frac{\dot{m}_{brk}i_{brk}}{V\Delta p}\right\}_P}{\left\{\frac{\dot{m}_{brk}i_{brk}}{V\Delta p}\right\}_m} = \frac{[\dot{m}_{brk}i_{brk}]_R}{[V]_R[\Delta p]_R}. \tag{4}$$

If the pressure and the temperature response of the prototype and the experiment containment are ensured to be similar, which means $[\Delta p]_R = 1$ and $[i_{in}]_R = 1$, then

$$[\dot{m}_{in}]_R = [V]_R, \tag{5}$$

$$[\dot{m}_{brk}i_{brk}]_R = [V]_R. \tag{6}$$

If the volume scaling ratio of the prototype and the experimental containment is $[V]_R$ = 1:200, then $[\dot{m}_{in}]_R = 1:200$, $[\dot{m}_{brk}i_{brk}]_R = 1:200$. Because the blow-down pipe mass flow rate $\dot{m}_{in}$ is influenced by the pipe resistance and the direct contact condensation process in the suppression pool, the design parameters of the main pipe and branch pipe in the experiment can be obtained once the pipe resistance and the direct contact condensation process similarity between the prototype and the experiment is considered further. In the prototype, the steam mass and energy released from the break are due to the flash evaporation of the primary loop coolant. This process is influenced by the primary loop coolant parameters, such as pressure and temperature. The core decay heat transferred to the coolant and the cold water injected to the primary loop through the safety injection system will change the

primary loop coolant parameters, affecting the steam mass and energy release. However, in the experiment, only the steam boiler (nominal pressure 2 MPa) is used to simulate the steam mass and energy release during the break blow-down process, which cannot preserve the complex process that occurred in the prototype. Therefore, in order to ensure that the energy from the break satisfies the scale ratio, the experiment process is analyzed in advance by using MELCOR. Under the condition of ensuring the similarity of the pressure response between the prototype and the experiment, the steam boiler operation parameters and the orifice size in the blow-down pipe can be determined then.

## STEAM CONDENSATION PROCESS IN THE SUPPRESSION POOL

In the early stage of the LOCA, the water in the suppression pool is subcooled. The steam from the containment is supposed to be condensed completely in the suppression pool. For the direct contact condensation process in the suppression pool, the energy transfer process can be expressed as follows:

$$Q = NA_i h_{cond} \Delta T, \tag{7}$$

$$E = \dot{m}_{in} r_{fg}, \tag{8}$$

where $Q$ is the total heat transferred to the condensation pool water through condensation, $N$ is the total branch pipe number, $A_i$ is the gas bubble diameter, $h_{cond}$ is the condensation heat transfer coefficient, $\Delta T$ is the temperature difference of the water and gas, $E$ is the total energy discharged to the containment from the primary loop break, $\dot{m}_{in}$ is the gas mass flow rate in the blow-down pipe, and $r_{fg}$ is the latent heat of vaporization. In the scaled experiment, $h_{cond}$, $\Delta T$, and $r_{fg}$ can be considered to be approximately the same as the prototype. In order to assure the similarity of the condensation process, the energy relation can be expressed as the following equation:

$$\left[\frac{Q}{E}\right]_R = \left[\frac{NA_i}{\dot{m}_{in}}\right]_R = [N]_R [A_i]_R \frac{1}{[\dot{m}_{in}]_R} = 1. \tag{9}$$

The branch pipe number in the prototype and in the scaled experiment is 200 ($N_1 \times N_2 = 200$) and 1, respectively, which means $[N]_R = 200$. According to the relation between the bubble radius $R_b$ and the bubble surface area $A_i$, Eq. 10 can be gained:

$$[R_b]_R = \sqrt{[\dot{m}_{in}]_R \cdot \frac{1}{[N]_R}} = 1. \tag{10}$$

According to the research work of Gallego-Marcos et al. (2019), $R_b \propto \frac{m_i^{0.05} \cdot d^{0.9}}{\Delta T}$, where $m_i = \frac{\dot{m}_{in}}{N}$. The equation above is applied to the steam mass flow rate in the range of 80–233 kg/m$^2$ s, which covers the steam mass flow rate in the prototype. Therefore, the scale ratio of the pipe diameter and bubble radius can be expressed as the following equation:

$$[\mathrm{R}_b]_R = \left[\frac{\dot{m}_{in}}{N}\right]_R^{0.05} [d]_R^{0.9}. \tag{11}$$

Thus, $[d]_R = 1$, which means the branch pipe diameter of the scaled experiment is equal to that of the prototype.

## PIPE RESISTANCE IN THE BLOW-DOWN PIPE

The pressure difference between the containment and the suppression pool can be expressed as follows:

$$\Delta P = P_{Co} - P_{Sp} - \rho g H = \sum_i \left[\frac{f_i l_i}{d_i} + K_i\right] \frac{m_i^2}{2\rho A_i^2}, \tag{12}$$

where $P_{Co}$ is the pressure of the containment, $P_{Sp}$ is the air space pressure of the suppression pool, and ρgH is the gravity pressure drop from the pipe outlet to the water surface. On the right-hand side of the equation is the resistance term from the blow-down pipe inlet to the blow-down pipe outlet.

In order to ensure the pressure evolution similarity between the prototype and the scaled experiment, the total pressure drop inside the blow-down pipe should be kept equal. Thus,

$$[\Delta P]_R = \left[\sum_i \left[\frac{f_i l_i}{d_i} + K_i\right] \frac{m_i^2}{2\rho A_i^2}\right]_R = 1. \tag{13}$$

Because the diameter of the main pipe is much larger than that of the branch pipe, the loss due to frictional resistance of the main pipe in the prototype can be neglected. The mass flow rate in each branch pipe is assumed to be equal. Therefore, **Eq. 13** can be transferred to the following form:

$$\begin{aligned}\left[\left(\frac{f_{branch} l_{branch}}{d_{branch}} + K_{inlet}\right) \frac{\left(\dot{m}_{in}/(N_1 N_2)\right)^2}{(d_{branch})^4} + K_{shrink}^{cm} \frac{\left(\dot{m}_{in}/N_1\right)^2}{(d_{main})^4}\right]_P \\ = \left[\left(\frac{f_{main} l_{main}}{d_{main}} + K_{orifice} + K_{bend} + K_{shrink}^{cm}\right) \frac{(\dot{m}_{in})^2}{(d_{main})^4} \right. \\ \left. + \left(\frac{f_{branch} l_{branch}}{d_{branch}} + K_{shrink}^{mn}\right) \frac{(\dot{m}_{in})^2}{(d_{branch})^4}\right]_m,\end{aligned} \tag{14}$$

where $f$ is the frictional resistance coefficient, $l$ is the length of the pipe, and $d$ is the diameter of the pipe. Because the Re number in the blow-down pipe of the prototype and the scaled experiment is usually large ($\mathrm{Re} > 10^5$), the frictional resistance coefficient can be calculated as follows:

$$\begin{aligned}[f_{main}]_P &= 0.11 \times \left(\frac{0.046}{[d_{main}]_P}\right)^{0.25} = 0.0103, \\ [f_{main}]_m &= 0.11 \times \left(\frac{0.046}{[d_{main}]_m}\right)^{0.25} = 0.0146,\end{aligned} \tag{15}$$

$$\begin{aligned}[f_{branch}]_P &= 0.11 \times \left(\frac{0.046}{[d_{branch}]_P}\right)^{0.25} = 0.0161, \\ [f_{branch}]_{\mathrm{m}} &= 0.11 \times \left(\frac{0.046}{[d_{branch}]_{\mathrm{m}}}\right)^{0.25} = 0.0161.\end{aligned} \tag{16}$$

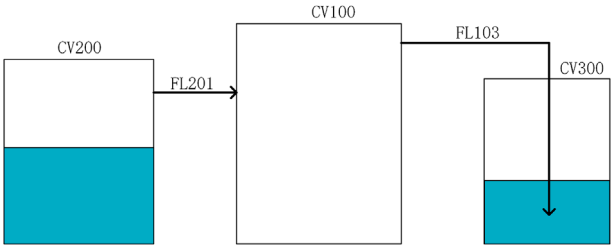


**FIGURE 2 |** MELCOR model nodalization of the experimental facility.

$K_{inlet}$ is the hydraulic head resistance coefficient of the main pipe and the branch pipe connection in the prototype. Based on the pipe dimensions and the research work by Lu et al. (2008), the $K_{inlet}$ is approximately equal to 1 in this study. $K_{shrink}^{cm}$ is the shrinkage resistance coefficient of the containment and main pipe connection. It can be calculated through $K_{shrink}^{cm} = 0.5\left[1 - \left(\frac{A_2}{A_1}\right)^2\right]$. $K_{\text{shrink}}^{mn}$ is the shrinkage resistance coefficient of the branch pipe and main pipe connection, which is approximately equal to 0.4. $K_{\text{bend}}$ is the bend resistance coefficient. $K_{\text{orifice}}$ is the orifice resistance coefficient used in the scaled experiment to keep the both sides equal in **Eq. 14**, which is approximately equal to 1.086 by calculation.

For the flat orifice, when the fluid Re number is larger than $10^5$, the orifice resistance coefficient can be calculated by **Eq. 17** (Idelchik, 1986):

$$K_{orifice} = \left\{\left(0.5 + \tau\sqrt{\left[1 - \left(\frac{[d_{orifice}]_m}{[d_{main}]_m}\right)^2\right]}\right)\left[1 - \left(\frac{[d_{orifice}]_m}{[d_{main}]_m}\right)^2\right] + \left[1 - \left(\frac{[d_{orifice}]_m}{[d_{main}]_m}\right)^2\right]^2\right\}\left(\frac{[d_{main}]_m}{[d_{orifice}]_m}\right)^4, \tag{17}$$

where $\tau$ is only related to orifice thickness $S$ and orifice bore diameter $D_h$. When $S/D_h = 0.2$, $\tau$ is equal to 1.22. Therefore, the orifice bore diameter $D_h = 0.123$ m and the orifice thickness $S = 24.6$ mm.

## SIMULATION RESULTS AND DISCUSSION

The prototype and the scaled experiment are simulated by using MELCOR, considering the heat absorption by the containment wall and the structure. The containment vessel and the suppression pool in the experiment are assumed to be well mixed due to the small volume compared to the volume of the prototype. Thus, both these parts are modeled with only one control volume. The MELCOR model nodalization of the experimental facility is shown in **Figure 2**. The steam boiler (CV200) and the containment vessel (CV100) are connected by a horizontal flow path (FL201). The suppression pipe (FL103) connects the containment vessel and the suppression pool vessel (CV300) and submerges below the water surface, with the bubble physics model activated to simulate the steam condensing process in the subcooled water. The main geometrical parameters and initial conditions of the FLs and CVs are listed in **Table 1**. The steam boiler operating parameters (water inventory and pressure) and the orifice bore diameter in the blow-down pipeline are adjusted to make the containment pressure evolution in the scaled experiment similar to that in the prototype. It turns out that the steam boiler operating pressure and the water inventory are 1 MPa and 2 $m^3$, respectively, according to the MELCOR simulation. Besides, according to **Eq. 17**, the blow-down rate is controlled by an orifice installed in the main pipe, of which the bore diameter is 67 mm and the thickness is 13.4 mm. The frictional pressure drops due to material flows contain contributions from both form loss and wall friction. The form loss contribution is based on user input coefficients. In this study, the form loss coefficient is set as 8.64, which consists of the effects of bends, orifice, and sudden area change near the connections between the pipe and the vessel. The wall friction terms are computed within MELCOR, based on segment lengths and roughness input by the user.

**Figure 3** shows the containment pressure response in the prototype and the scaled experiment. The containment pressure increases rapidly at first due to large amount of the coolant blow-down process. Then, the pressure increase rate gradually decreases after the suppression pool works. At last, the pressure maintains a stable value. The simulation result shows that the containment pressure in the scaled experiment matches well the pressure in the prototype to some extent. There is a safety injection system in the prototype, which is absent in the experimental facility. The operation of the safety injection cools the primary loop coolant and decreases steam release, resulting in a lower containment pressure in the prototype than in the experiment. Besides, the prototype blow-down process is accompanied by the core decay heat release. The continuous heat transferred to the primary coolant will change its thermal properties, such as pressure and

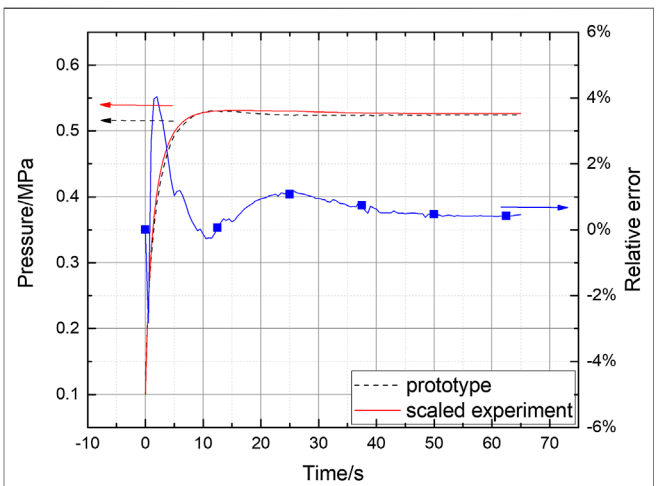


**FIGURE 3 |** Simulation results of containment pressure.

temperature, which has an influence on the steam mass and energy release. However, these complex opposite effects cannot be simulated in the experiment. These are supposed to be the main reasons for the pressure difference between the simulation results of the prototype and the scaled experiment.

## CONCLUSIONS

In this study, a scaling analysis of the pressure response of the experimental facility for the pressure suppression containment was conducted. Three aspects including the pressure response process in the containment, the steam condensation process in the suppression pool, and the resistance of the blow-down pipe were considered to obtain the main parameters for the scaled containment pressure response experimental facility. The main conclusions could be summarized as follows:

1) Compared to the full-scale or large-scale pressure response experiment of the pressure suppression containment, the small-scale experiment, which is mainly scaled by reasonable scaling laws, is much economically feasible. The results show that the containment pressure evolution trends of the prototype and the scaled experimental facility are consistent. The pressure difference exists at some times with a maximum relative error of 4%.
2) Because the pressure response in the containment and the steam condensation in the suppression pool are influenced by many different factors, it turns out to be impossible or impractical to achieve exact dynamic similarity between a small-scale system and a full-scale one.
3) The analytical method put forward in this article can guide the pressure suppression containment pressure response experiment design. But in the actual implementation process, the main reason that leads to the deviation should be considered and relevant measures should be adopted.

## DATA AVAILABILITY STATEMENT

The datasets generated for this study are available on request to the corresponding author.

## AUTHOR CONTRIBUTIONS

XL and ZM contributed to the entire scaling analysis process. NZ and ZS contributed to the background information. All authors contributed to the article and approved the submitted version.

## FUNDING

The financial supports of Heilongjiang Province Postdoctoral Fund (002150830605) and Fundamental Research Funds for Central University of Ministry of Education of China (3072020CF1503) are gratefully acknowledged.

## REFERENCES

Anderson, W. G., Hober, P. W., and Sonin, A. A. (1978). Final Report. Small scale modeling of hydrodynamic forces in pressure suppression systems.

Brown, W. L. (1999). "Scaling of the AP600 containment large scale test facility," in ICONE-7: Proceedings of the 7th international conference on nuclear engineering, Tokyo, Japan, April 19–23, 1999. Japan: Japan Society of Mechanical Engineers, 4252.

Chen, Y.-S., Yuann, Y.-R., and Dai, L.-C. (2012). Lungmen ABWR containment analyses during short-term main steam line break LOCA using Gothic. *Nucl. Eng. Des.* 247, 106–115. doi:10.1016/j.nucengdes.2012.02.012

EPRI-NP (1982). *The Marviken full-scale critical flow tests.* EPRI-NP-2370.

Gallego-Marcos, I., Kudinov, P., Villanueva, W., Puustinen, M., Räsänen, A., Tielinen, K., et al. (2019). Effective momentum induced by steam condensation in the oscillatory bubble regime. *Nucl. Eng. Des.* 350, 259–274. doi:10.1016/j.nucengdes.2019.05.011

Gamble, R. E., Nguyen, T. T., and Shiralkar, B. S. (2001). Pressure suppression pool mixing in passive advanced BWR plants. *Nucl. Eng. Des.* 204 (1–3), 321–336. doi:10.1016/s0029-5493(00)00363-0

Idelchik, I. E. (1986). *Handbook of hydraulic resistance*. 2nd Edn. Washington, DC: Hemisphere Publishing Corporation, translation.

Kukita, Y., Namatame, K., Takeshita, I., and Shiba, M. (1983). The noncondensable gas effects on loss-of-coolant accident steam condensation loads in boiling water reactor pressure suppression pool. *Nucl. Technol.* 63 (2), 337–346. doi:10.13182/nt83-a33292

Laine, J., Puustinen, M., and Raesaenen, A. (2013). *PPOOLEX experiments on the dynamics of free water surface in the blowdown pipe*. Finland: Nordisk Kernesikkerhedsforskning Roskilde.

Lu, F., Luo, Y.-h., and Yang, S.-m. (2008). Analytical and experimental investigation of flow distribution in manifolds for heat exchangers. *J. Hydrodyn.* 20 (2), 179–185. doi:10.1016/s1001-6058(08)60044-x

Marviken Power Station (1977). Report MXA-1-301. Sweden the Marviken full scale containment experiments. Containment response to a loss of coolant accident: summary report.

Moody, F. J. (1976). A systematic procedure for scale-modeling problems in unsteady fluid mechanics. General Electric Company, unpublished report.

Patel, G., Tanskanen, V., and Hujala, E. (2016). Direct contact condensation modeling in pressure suppression pool system. *Nucl. Eng. Des.* 321, 328–342. doi:10.1016/j.nucengdes.2016.08.026

Patel, G., Tanskanen, V., and Kyrki-Rajamäki, R. (2014). Numerical modelling of low-Reynolds number direct contact condensation in a suppression pool test facility. *Ann. Nucl. Energy* 71, 376–387. doi:10.1016/j.anucene.2014.04.009

Sawant, P., and Khatib-Rahbar, M. (2011). Modeling pressure suppression pool hydrodynamics in the ABWR containment. *Nucl. Eng. Des.* 241 (9), 3824–3838. doi:10.1016/j.nucengdes.2011.07.002

Varzaly, A. M., Grafton, W. A., and Seely, D. S. (1978). Confirmatory test program, full scale condensation and stratification phenomena-test series 5707 NEDE-21853-P. General Electric Report.

Yan, J., and Bolger, F. (2010). Evaluation of pool swell velocity during large break loss of coolant accident in boiling water reactor Mark III containment design. *Nucl. Eng. Des.* 240 (7), 1789–1794. doi:10.1016/j.nucengdes.2010.02.015

**Conflict of Interest:** The authors declare that the research was conducted in the absence of any commercial or financial relationships that could be construed as a potential conflict of interest.

frontiers in Energy Research

BRIEF RESEARCH REPORT
published: 20 November 2020
doi: 10.3389/fenrg.2020.584531

# Uncertainty Analysis on *k-ε* Turbulence Model in the Prediction of Subcooled Boiling in Vertical Pipes

*Xiang Zhang*[1], *Genglei Xia*[1]*, *Tenglong Cong*[2]*, *Minjun Peng*[1] *and Zhenhong Wang*[1]

[1]*Fundamental Science on Nuclear Safety and Simulation Technology Laboratory, Harbin Engineering University, Harbin, China,* [2]*School of Mechanical Engineering, Shanghai Jiao Tong University, Shanghai, China*

Computational fluid dynamics (CFD) has become an effective method for researching two-phase flow in reactor systems. However, the uncertainty analysis of Computational fluid dynamics simulation is still immature. The effects of uncertainties from two-phase models and boundary conditions have been analyzed in our previous work. In this work, the uncertainties from a turbulence model on the prediction of subcooled boiling flow were analyzed with the DEBORA benchmark experiments by a deterministic sampling method. Seven parameters in the standard *k-ε* model, which interrelated momentum, energy, turbulent kinetic energy, and dissipation rate, were studied as uncertainty sources, including $C_{\mu}$, $C_{\mu,g}$, $C_{1\varepsilon}$, $C_{2\varepsilon}$, $\sigma_k$, $\sigma_\varepsilon$, and $\mathrm{Pr}_t$. Radial parameters were calculated to study the effects of uncertainties from the turbulence model. The contributions of each uncertainty source on void fraction and liquid temperature were also analyzed. It was found that the models can simulate subcooled boiling flow accurately and uncertainty analysis by deterministic sampling can give a reference interval to increase the reliability of results. The $C_{2\varepsilon}$ and $C_{1\varepsilon}$, parameters in the production term and dissipation term of transport equations, dominate the radial distributions of void fraction and liquid temperature.

**Keywords: subcooled boiling, uncertainty analysis, deterministic sampling method, turbulence model, computational fluid dynamics**

OPEN ACCESS

***Edited by:***
*Jun Wang,*
*University of Wisconsin-Madison,*
*United States*

***Reviewed by:***
*Yacine Addad,*
*Khalifa University,*
*United Arab Emirates*
*Luteng Zhang,*
*Chongqing University, China*
*Han Bao,*
*Idaho National Laboratory (DOE),*
*United States*

***Correspondence:**
*Genglei Xia*
*xiagenglei@163.com*
*Tenglong Cong*
*tlcong@sjtu.edu.cn*

***Specialty section:***
*This article was submitted to Nuclear Energy and Policies, a section of the journal Frontiers in Energy Research*

***Received:*** *17 July 2020*
***Accepted:*** *08 October 2020*
***Published:*** *20 November 2020*

***Citation:***
*Zhang X, Xia G, Cong T, Peng M and Wang Z (2020) Uncertainty Analysis on k-ε Turbulence Model in the Prediction of Subcooled Boiling in Vertical Pipes. Front. Energy Res. 8:584531. doi: 10.3389/fenrg.2020.584531*

## INTRODUCTION

Subcooled boiling flow has received attention from industrial designers due to its high heat transfer coefficient. However, if the heat flux reaches a critical value a transient vapor film will appear on the heated wall due to the polymerization of bubbles. It may hinder the heat transfer and cause the wall temperature to rise.

In most Computational fluid dynamics (CFD) analysis on subcooled boiling flow, the boundary conditions and models are all treated as deterministic values. However, there might be some uncertainties from boundary condition measuring or the simplification of the model that needs to be considered for the numerical simulation of boiling flow (Bestion et al., 2016). The best estimated code plus uncertainty (BEPU) analysis method, which could obtain a set of output results by sampling a series of inputs of research targets, was suggested for the uncertainty analysis of nuclear safety in Pericas et al. (2017). The statistical parameters of outputs were analyzed to obtain the uncertainty quality. Traditionally, researchers have used random sampling, such as Monte Carlo random sampling and Latin Hypercube sampling, in uncertainty analysis (Chen et al., 2015; Rakhimov

et al., 2018). However, this type of analysis requires a large number of samples to be set as inputs, which consumes huge computing resources for CFD applications. Different to random sampling, the deterministic sampling (DS) method, reviewed by Bestion et al. (2016), describes the probability density function of uncertainty sources with deterministic points. These points must have the same statistical moments with uncertainty sources. This method has been used in uncertainty analysis with high computational costs, since the calculating cost can be reduced with a smaller sample size (Zhang et al., 2018a).

In two-phase flow simulations uncertainty analysis is significantly important due to the deficiency in two-phase flow theory and the measuring technique. Compared to the reality or truth value of interest, the errors in simulation results are divided into three parts by ASME V&V 20-2009 standards, which are simulation inputs, numerical methods, and modeling assumptions (McHale et al., 2009). Theoretically, the flow characteristics and heat transfer in two-phase flow are mainly described by the turbulence model and the two-phase model. The uncertainties of modeling assumptions in two-phase flow come from these models. The effects of two-phase model uncertainties and boundary condition uncertainties were analyzed systematically in our previous work by assuming that these errors are independent (Cong et al., 2018; Zhang et al., 2018c). On the other hand, the errors in the numerical solutions of equations can be reduced by grid sensitivity analysis and with a convergence check of the solver. Thus, we focus on the uncertainties from turbulence models in the current work.

The uncertainty brought by turbulence models for single phase flow and heat transfer has already attracted the attention of researchers (Platteeuw et al., 2008; Dunn et al., 2011; Hedberg and Hessling, 2015). Nevertheless, the turbulence model uncertainty in two-phase flow is still indistinct. These uncertainties may influence the distributions of key parameters, including void fraction, liquid temperature, and phase velocity. What is more, the $k$-$\varepsilon$ turbulence model, which was suggested by Zhang et al. (2015) for subcooled boiling flow simulation, was developed for single-phase flow decades ago. The parameters, which interrelated momentum, energy, turbulence kinetic energy, and dissipation rate, were summarized from common single phase experiments. For example, the value of coefficient $C_{2\varepsilon}$ in the dissipation term is usually derived from the experimental values of decay exponent, which was obtained in single-phase experiments (Mohamed and Larue, 1990). Thus, the parameters may need to be modified for two-phase flow in the future. The uncertainty analysis on the $k$-$\varepsilon$ turbulence model in this work assessed the sensitivity of model parameters to the subcooled boiling flow. The results can be used as a reference to modify the turbulence model for two-phase flow simulation in the future.

The uncertainty of two-phase models and boundary conditions have been analyzed in our previous work (Cong et al., 2018; Zhang et al., 2018c), as a series research, the uncertainty effects of the turbulence model on local parameters were studied by the DS method in this paper. The DEBORA subcooled boiling experiment (Garnier et al., 2001) was chosen as the benchmark and four different cases were calculated by Fluent to avoid experimental coincidence.

## MATHEMATICAL AND PHYSICAL MODELS

The Eulerian two-fluid model along with the RPI model has been widely used in subcooled boiling flow simulations. Their equations and the closure auxiliary models of the RPI model can be found in our previous work (Zhang et al., 2018b). The interphase momentum transfer is considered using drag force (Schiller and Naumann, 1935), lift force (Moraga et al., 1999), and turbulence dispersion force (Burns et al., 2004), and the interphase energy transfer is calculated by the Ranz-Marshall model (Ranz and Marshall, 1952).

The standard $k$-$\varepsilon$ model applied in this work is composed of the turbulent kinetic energy ($k$) transport equation and turbulent dissipation rate ($\varepsilon$) transport equation, which are:

$$\frac{\partial}{\partial t}(\rho k)+\frac{\partial}{\partial x_i}(\rho k u_i)=\frac{\partial}{\partial x_j}\left[\left(\mu+\frac{\mu_t}{\sigma_k}\right)\frac{\partial k}{\partial x_j}\right]+G_k+G_b-\rho\varepsilon \quad (1)$$

and

$$\frac{\partial}{\partial t}(\rho\varepsilon)+\frac{\partial}{\partial x_i}(\rho\varepsilon u_i)=\frac{\partial}{\partial x_j}\left[\left(\mu+\frac{\mu_t}{\sigma_\varepsilon}\right)\frac{\partial \varepsilon}{\partial x_j}\right]+C_{1\varepsilon}\frac{\varepsilon}{k}(G_k+C_{3\varepsilon}G_b)-C_{2\varepsilon}\rho\frac{\varepsilon^2}{k} \quad (2)$$

where $G_k$ and $G_b$ represent the turbulent kinetic energy generated by mean velocity gradients and buoyancy, respectively:

$$G_k=-\rho\overline{u_i u_j}\frac{\partial u_j}{\partial u_i} \quad (3)$$

$$G_b=-\frac{1}{\rho}\left(\frac{\partial \rho}{\partial T}\right)_p g_i\frac{\mu_t}{\mathrm{Pr}_t}\frac{\partial T}{\partial x_i} \quad (4)$$

where $g_i$ is the gravitation vector in the $i$ th direction. As shown in **Eq. (2)**, the $C_{1\varepsilon}$ concerns the production term with a default value of 1.44 and the $C_{2\varepsilon}$ influences the calculation of the dissipation term. The parameter $\sigma_k$ is the Prandtl number of turbulent kinetic energy. It represents the ratio of turbulent viscosity to turbulent kinetic energy diffusion. The turbulent viscosity is used to calculate the turbulent stress term in the momentum equation. Thus, the parameter $\sigma_k$ interrelates momentum and turbulent kinetic energy in the $k$-$\varepsilon$ model. Similarly, the parameter $\sigma_\varepsilon$ denotes the ratio of turbulent viscosity to turbulent dissipation rate diffusion and the energy Prandtl number $\mathrm{Pr}_t$ represents the ratio of turbulent viscosity to the thermal diffusion induced by turbulence.

The $\mu_t$ in transport equations is the turbulent viscosity. As mentioned before, it is a crucial step to determine the value of $\mu_t$, since it will be used to calculate the turbulent stress, which is an addition item induced by turbulent fluctuation in the momentum equation. It is different from single-phase flow where the bubbles induce additional turbulence in subcooled boiling flow. This

phenomenon can be described by adding a term to the turbulent viscosity (Sato and Sekoguchi, 1975), which is

$$\mu_t = C_\mu \rho \frac{k_l^2}{\varepsilon_l} + C_{\mu,g} \rho \alpha_g d_g \left| u_g - u_l \right| \tag{5}$$

where $C_\mu$ and $C_{\mu,g}$ are the empirical coefficient achieved by experimental results. Besides, the standard wall function is applied for the near-wall region.

The parameters, including $C_\mu$, $C_{\mu,g}$, $C_{1\varepsilon}$, $C_{2\varepsilon}$, $\sigma_k$, $\sigma_\varepsilon$, and $\mathrm{Pr}_t$, interrelated momentum, energy, turbulent kinetic energy, and dissipation rate in the standard k-ε model. The values significantly influence the applicability and accuracy of the *k-ε* model. These parameters have a set of default values in Fluent (Fluent, 2013), which were obtained from experimental results under special conditions. However, it still has some limitations. For example, the default value of parameter $C_\mu$ is obtained by the experiments which have a dynamic equilibrium between the production and the dissipation of pulsation kinetic energy in the boundary layer, while it may be not applicable to the flow that deviates from the dynamic equilibrium (Rodi, 1984). The uncertainties of these parameters can be transmitted to the CFD results. In consideration of the probability density, the functions of these parameters are indistinct for two-phase flow simulations, it is assumed that the parameters are independent and the distributions obey the normal distribution with a 5% relative error band for the $\pm 3\sigma$ interval which means that the relative uncertainty of the uncertainty sources is within ±5% at the 99.74% confidence level. The values recommended by Launder and Sharma (1974) and Sato and Sekoguchi (1975) are assumed as the mean value of distributions:

$$C_\mu = 0.09, C_{1\varepsilon} = 1.44, C_{2\varepsilon} = 1.92, \sigma_k = 1.0, \sigma_\varepsilon = 1.3, C_{\mu,g} = 0.6 \tag{6}$$

## DETERMINISTIC SAMPLING METHOD

In our previous work, the effects of two-phase model uncertainties and boundary condition uncertainties were analyzed by the Latin Hypercube sampling (LHS) method, respectively (Cong et al., 2018; Zhang et al., 2018c). However, the large number of samples (1,040 samples for two-phase model uncertainty analysis and 740 samples for boundary condition uncertainty analysis) shows poor efficiency in UQ calculations. It consumes huge computing resources which would be an issue for complex CFD simulations.

Thus, the DS method, which can reduce the number of samples substantially, was applied in this paper to predict the effects of turbulence model uncertainties on the simulation results. Unlike random sampling which characterizes the continuous probability density function of the sources, the DS method tries to represent them with a number of deterministic locations, known as sigma points (Bestion et al., 2016). These sigma points need to share the same statistical moments with the probability density function. The different sample methods could satisfy the different order of statistical moments. In order, the first four moments are mean, variance, skewness, and flatness. If we assume a parameter, $q$, and the number of samples, $N$, these statistical moments can be written as:

$$mean = \frac{1}{N}\sum_{n=1}^{N} q_n = \overline{q} \tag{7}$$

$$\mathrm{var} = \frac{1}{N}\sum_{n=1}^{N} \left(q_n - \overline{q}\right)^2 \tag{8}$$

$$skewness = \frac{1}{N}\sum_{n=1}^{N} \left(q_n - \overline{q}\right)^3 \Big/ \sigma^3 \tag{9}$$

$$flatness = \frac{1}{N}\sum_{n=1}^{N} \left(q_n - \overline{q}\right)^4 \Big/ \sigma^4 \tag{10}$$

$$x^{th}\ statistical\ moment = \frac{1}{N}\sum_{n=1}^{N} \left(q_n - \overline{q}\right)^x \Big/ \sigma^x \tag{11}$$

where $\sigma$ is the standard deviation. With the increase in the order of statistical moments satisfied, higher accuracy can be achieved but more samples are needed in the ensemble. And it is more difficult to calculate the sigma points if higher order statistical moments need to be satisfied. Besides, the different probability density functions of sources can also increase the difficulty of calculating the sigma points.

In the current work, the DS method with fourth order statistical moments, which is abbreviated to DS4, will be used and its results will be compared with the experimental data to provide a confidence interval for parameters. Besides, the contribution of each uncertainty source can be obtained by data analysis. As described in Hedberg and Hessling (2015), with the assumption that uncertainty sources are independent and all obey normal distributions, it will extract two circumjacent points and one central point for the ensemble:

$$q_{i1} = \mu_i - \sqrt{3}\sigma_i,\ q_{i2} = \mu_i,\ q_{i3} = \mu_i + \sqrt{3}\sigma_i \tag{12}$$

$$w_{i1} = \frac{1}{6},\ w_{i2} = \frac{4}{6},\ w_{i3} = \frac{1}{6} \tag{13}$$

where $i$ represents the $i$ th uncertainty source. In order to merge all the central points, the weights $w_{i2}$ need to be reset due to the fact that the sum of all weights should be one. The central point weight will then become:

$$w_c = \sum_{i=1}^{I} w_{i2} - (I - 1) \tag{14}$$

where $I$ is the number of uncertainty sources.

Then the fifteen samples extracted by DS4 are set as inputs in functions or codes, respectively. The outputs will be analyzed to quantify the effects propagated from the input uncertainty sources by statistical parameters, including mean value $\overline{\varphi}$, standard deviation $\delta\varphi$, and uncertainty bandwidth $UB$, which are:

$$\overline{\varphi} = \sum_{n=1}^{N} w_n f\left(S_n\right) \tag{15}$$

$$\delta\varphi = \sqrt{\sum_{n=1}^{N} w_n \left(f\left(S_n\right) - \overline{\varphi}\right)^2} \tag{16}$$

$$UB = 3\delta\varphi \tag{17}$$

The contributions of each uncertainty source can be evaluated by:

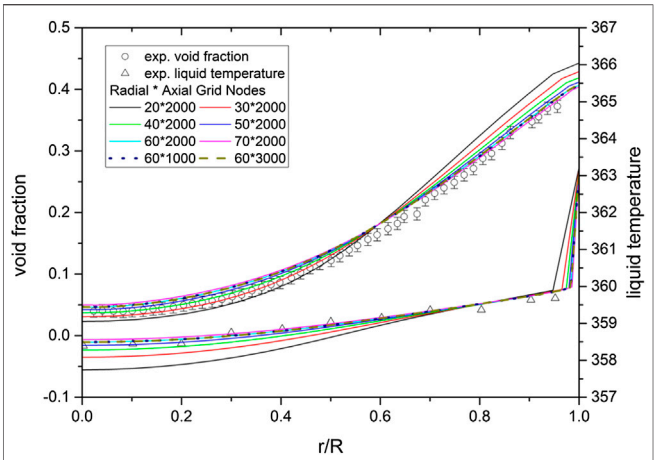


**FIGURE 1 |** Grid sensitivity analysis.

$$\delta\varphi_i = \sqrt{w_{2i-1}\left(f\left(S_{2i-1}\right)-\overline{\varphi}\right)^2 + w_{2i}\left(f\left(S_{2i}\right)-\overline{\varphi}\right)^2 - w_{2I+1}\left(f\left(S_{2I+1}\right)-\overline{\varphi}\right)^2 \Big/ I} \quad (18)$$

$$UB_i = 3\delta\varphi_i \quad (19)$$

$$C_i = UB_i \Big/ \sum_{i=1}^{I} UB_i \quad (20)$$

where $S_n$ represents the $n$ th group of samples, $\delta\varphi_i$ and $UB_i$ are the standard deviation and uncertainty bandwidth of the $i$ th uncertainty source, respectively, and $C_i$ is the contribution of the $i$ th source.

## BENCHMARK CASE AND NUMERICAL MODELING

The DEBORA experiment (Garnier et al., 2001) was selected as the benchmark case to analyze the uncertainty quality of the turbulence model. The R12 used as the working fluid in the DEBORA experiment has similar relevant non-dimensional numbers with water in high pressure when it works in relatively low pressure, which means the operation and measurement was easier. The fluid was heated in a vertical pipe with 3,500 mm length and 19.2 mm inner diameter. The tube was simplified into a 2D axial symmetry domain and the axisymmetric boundary was enabled in Fluent. Several parameters, such as void fraction, liquid temperature, and bubble diameter, were measured at the end of the heated tube. To avoid contingency, four experimental conditions of the DEBORA experiment were applied in this work, whose results can be extracted from public literature.

In order to avoid the error introduced by mesh, eight meshes with different radial and axial nodes were used to analyze the grid sensitivity with Case4. The radial distributions of void fraction and liquid temperature were compared and the results are presented in **Figure 1**. Finally, considering the computational accuracy and expense, the mesh with 60 × 2,000 nodes was employed in this work.

## RESULTS AND DISCUSSION

The samples of turbulence model parameters were set as computational inputs to analyze the uncertainty transition. The uncertainties of radial parameters in the DEBORA benchmark are presented and discussed in *Effects of Model Parameters Uncertainty on Subcooled Boiling*. For convenience of expression, the radial positions are processed into non-dimensional parameters by $r/R$, where $R$ is the radius of the heated pipe. Besides, the contribution of uncertainty sources is evaluated in *Contribution of Uncertainty Sources* with the computational data of DS4.

### Effects of Model Parameters Uncertainty on Subcooled Boiling

The distribution of radial parameters with uncertainties, including void fraction, liquid temperature, phase velocity, and bubble diameter, are presented in **Figure 2**. It is shown that the void fraction and liquid temperature agree well with the benchmark data while the bubble diameter deviates. The reason is that the bubble diameter model applied in this work is simplified to a function of the local subcooling, which do not consider the coalescence and break of bubbles. The results of vapor velocity perform the same trend with experiment data, but some differences exist in the values. This is because, on the one hand, the effect of the bubble diameter deviation on the momentum equation solving, on the other hand, the wall function in this work is developed based on single-phase fluid. It is indicated that a two-phase wall law based on bubble-equivalent surface roughness can improve the phase velocity adjacent to the boiling surface (Končar and Borut, 2010).

According to the results in **Figure 2**, the void fraction increases along the radial direction gradually, since the bubbles produced at the heated wall are spread from the near-wall region to the pipe center by the phase interaction forces. The uncertainty appears to be larger at the center and around of the pipe which means the void fraction is more sensitive to the turbulence model in these regions. This is different with the void fraction, the maximum value of the liquid temperature uncertainty bandwidth occurs only at the center of the pipe. Then the uncertainty bandwidth drops down along with the radial direction and finally the lower and the upper limit are almost overlapped at the near-wall region. This suggests that there is very little influence of turbulence model uncertainties on the liquid temperature near the wall. The distribution of bubble diameter uncertainty exhibits a similar property to the liquid temperature, due to the strong relationship between bubble diameter and liquid temperature which has been introduced above. Besides, we can find that the effects of turbulence model uncertainty to phase velocity are small, and occurs mainly in the region near $r/R$=0.6.

### Contribution of Uncertainty Sources

Based on the assumption that the parameters are independent from each other, the contributions of each uncertainty source to the radial

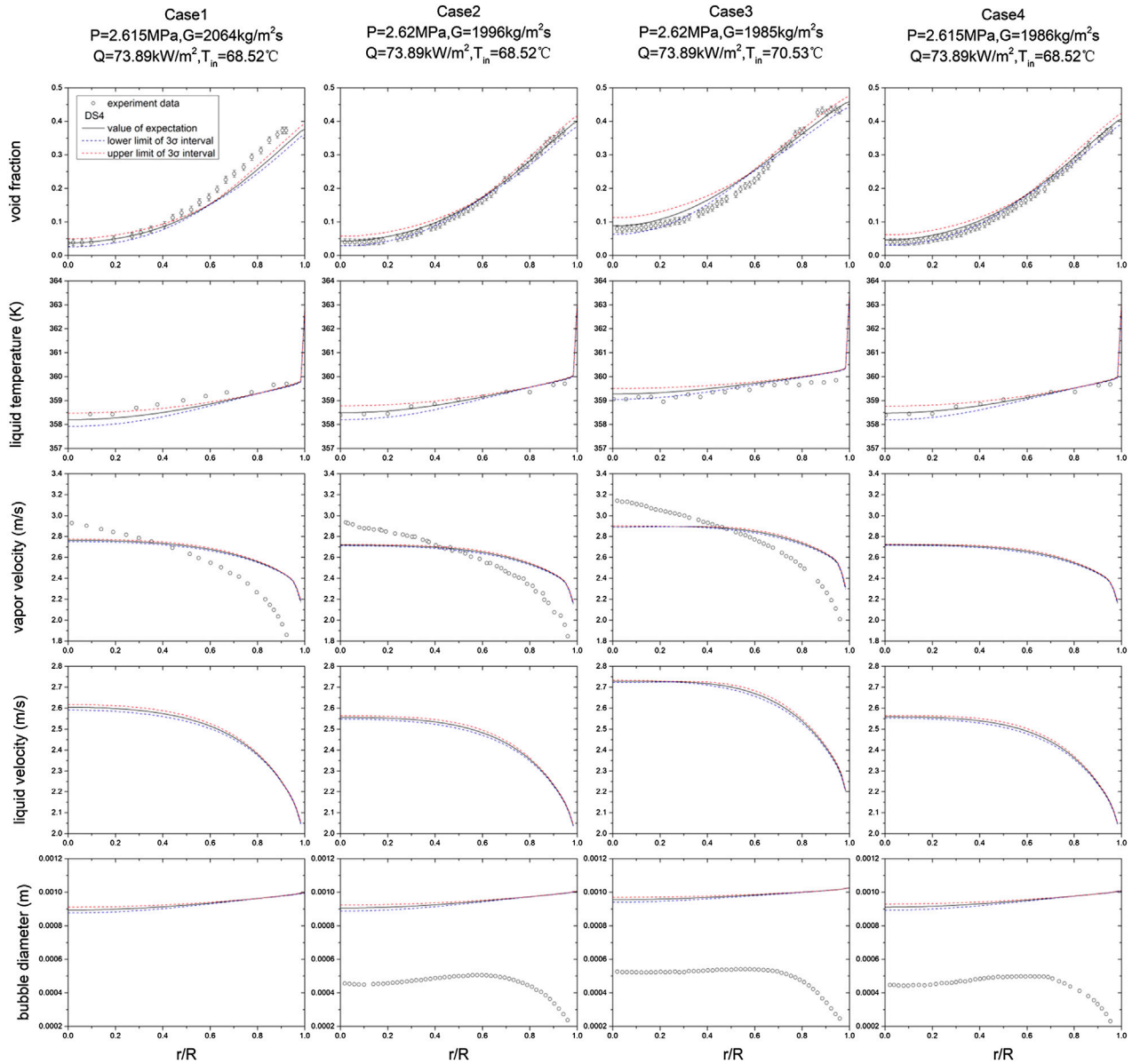


**FIGURE 2 |** Effects of model uncertainties on radial parameters (the experiment data of Case1 are extracted from Končar and Borut (2010) where the liquid velocity and bubble diameter are not given, the experiment data of Case2 and Case3 are extracted from Krepper and Rzehak (2011) where the liquid velocity are not given, the experiment data of Case4 are extracted from Yun et al. (2012) where the vapor velocity and liquid velocity are not given).

void fraction and radial liquid temperature can be calculated by using **Eq. (18) (19) (20)**.

As shown in **Figure 2**, the turbulence model uncertainties mainly influence the void fraction in partial regions, including the center of the pipe and the region close to the wall. Thus, several radial positions at the pipe exit, except the area around r/R=0.5, are selected to investigate the contribution of each uncertainty source along the radius. The results are given in **Figure 3**. And considering the same factors, parts of radial positions are selected for the contribution analysis of liquid temperature which is shown in **Figure 4**. A similar trend of contribution is presented by different cases, which avoid the accident of results. It is worth mentioning that the results of r/R=1 present the sources contribution to the maximum void fraction on the heated wall, which is a key parameter in critical heat flux prediction. It can be seen that the uncertainties of parameters $C_{2\varepsilon}$ and $C_{1\varepsilon}$ have a significant influence on the calculation of wall maximum void fraction. In addition, compared with the pipe center, the source contribution of $C_{\mu,g}$ to void fraction increases in the near-wall area. This means that the parameters $C_{2\varepsilon}$, $C_{1\varepsilon}$, and $C_{\mu,g}$ must be treated seriously in critical heat flux prediction. What is more, no matter the amount of void fraction or liquid temperature, the parameters $C_{2\varepsilon}$ and $C_{1\varepsilon}$ are always the most influential parameters

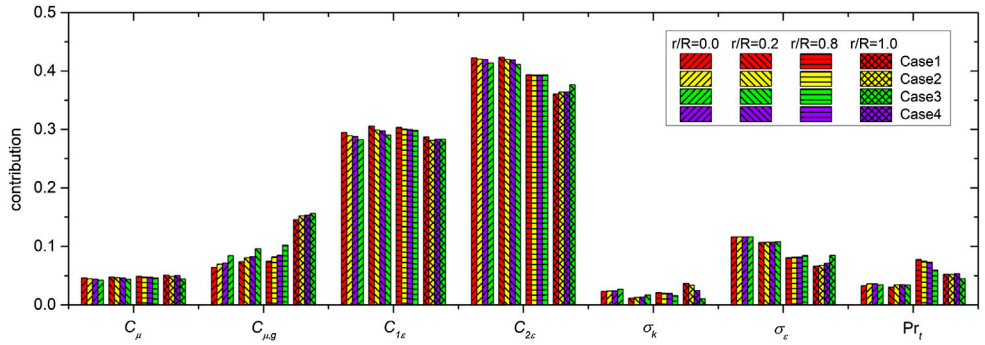


**FIGURE 3 |** Uncertainty sources contribution on void fraction.

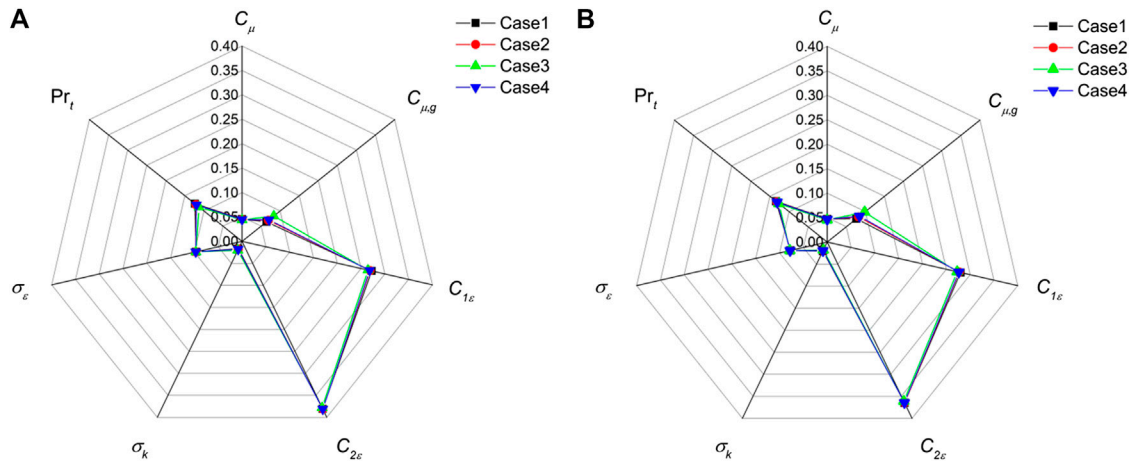


**FIGURE 4 |** Uncertainty sources contribution on liquid temperature.

in radial positions. This means that, to reasonably simulate subcooled boiling flow, the accurate value or probability density functions of $C_{2\varepsilon}$ and $C_{1\varepsilon}$ in the standard $k$-$\varepsilon$ model need to be investigated further. Compared to the results of void fraction, the $Pr_t$ contributes more in liquid temperature calculation. This is because turbulence will enhance the properties of thermal conduction, while $Pr_t$ is an important parameter for heat conductivity coefficient calculation.

## CONCLUSIONS

The uncertainty of two-phase models and boundary conditions has been analyzed using Latin Hypercube sampling in our previous work (Cong et al., 2018; Zhang et al., 2018c). As a series research, the effects of standard $k$-$\varepsilon$ model uncertainties in two-phase flow was analyzed using a more efficient and economical method, deterministic sampling, in this study. The DEBORA experiments were chosen as benchmarks. Seven parameters in the standard $k$-$\varepsilon$ model interrelated momentum, energy, turbulent kinetic energy, and dissipation rate were studied as uncertainty sources. The contribution of each uncertainty source was evaluated. In detail, the following conclusions can be drawn.

(1) Compared with the experiment data, a reasonable result within the confidence interval could be obtained. The results suggested that the models in our work can reasonably simulate the DEBORA experiments and the deterministic sampling can be a powerful tool for uncertainty quantification.
(2) The uncertainty band of radial parameters, including void fraction, liquid temperature, phase velocity, and bubble diameter, were obtained, which produced the sensitive parameter regions of the turbulence model.
(3) The contribution of each uncertainty source on different radial positions was analyzed. The parameters $C_{2\varepsilon}$ and $C_{1\varepsilon}$ always played predominant roles on the radial distributions of void fraction and liquid temperature, which specifies that these two parameters need to be treated carefully in further boiling flow simulations.

## DATA AVAILABILITY STATEMENT

The raw data supporting the conclusions of this article will be made available by the authors, without undue reservation.

## AUTHOR CONTRIBUTIONS

XZ contributed to the CFD simulation work and uncertainty analysis. GX contributed to the guidance of the deterministic sampling method. TC contributed to the guidance of Fluent. MP contributed to the guidance of the theory of numerical heat transfer. ZW contributed to the data processing

## ACKNOWLEDGMENTS

This work is supported by the National Natural Science Foundation of China (No. 11705035) and the Natural Science Foundation of Heilongjiang (No. LH2019A009), which are gratefully acknowledged.

## REFERENCES

Bestion, D., de Crécy, A., Camy, R., Barth, A., Bellet, S., Badillo, A., et al. (2016). *Review of uncertainty methods for computational fluid dynamics application to nuclear reactor thermal hydraulics*. Paris, France: Nuclear Safety NEA/CSNI R .

Burns, A. D., Frank, T., Hamill, I., and Shi, J.-M. (2004). "The Favre averaged drag model for turbulent dispersion in Eulerian multi-phase flows," *in* 5th International conference on multiphase flow (ICMF-5), Yokohama, Japan, May 30–June 4, (Japan Society of Multiphase Flow), 1–17

Chen, H., Fu, L., Jiong, G., and Lidong, W. (2015). Uncertainty and sensitivity analysis of filling fraction of pebble bed in pebble bed HTR. *Nucl. Eng. Des.* 292, 123–132. doi:10.1016/j.nucengdes.2015.05.032

Cong, T., Lv, X., Zhang, X., and Zhang, R. (2018). Investigation on the effects of model uncertainties on subcooled boiling. *Ann. Nucl. Energy* 121, 487–500. doi:10.1016/j.anucene.2018.08.001

Dunn, M. C., Shotorban, B., and Frendi, A. (2011). Uncertainty quantification of turbulence model coefficients via Latin hypercube sampling method. *J. Fluid Eng.* 133, 041402. doi:10.1115/1.4003762

Fluent, A. (2013). *ANSYS fluent theory guide 15.0*. Canonsburg, PA: ANSYS Inc. .

Garnier, J., Manon, E., and Cubizolles, G., (2001). Local measurements on flow boiling of refrigerant 12 in a vertical tube. *Multiphas. Sci. Technol.* 13, 1–111. doi:10.1615/multscientechn.v13.i1-2.10

Hedberg, P., and Hessling, P. (2015). "Use of Deterministic sampling for uncertainty quantification in CFD," in 16th International topical meeting on nuclear reactor thermal hydraulics-16 (NURETH-16), Chicago, Illinois, American Nuclear Society, 4907–4920

Končar, B., and Borut, M. (2010). Wall function approach for boiling two-phase flows. *Nucl. Eng. Des.* 240, 3910–3918. doi:10.1016/j.nucengdes.2010.08.004

Krepper, E., and Rzehak, R. (2011). CFD for subcooled flow boiling: simulation of DEBORA experiments. *Nucl. Eng. Des.* 241, 3851–3866. doi:10.1016/j.nucengdes.2011.07.003

Launder, B., and Sharma, B. I. (1974). Application of the energy-dissipation model of turbulence to the calculation of flow near a spinning disc. *Int. Commun. Heat Mass Tran.* 1, 131–137. doi:10.1016/0735-1933(74)90024-4

McHale, M., Friedman, J., and Karian, J. (2009). *Standard for verification and validation in computational fluid dynamics and heat transfer*. The American Society of Mechanical Engineers, ASME V&V

Mohamed, M. S., and Larue, J. C. (1990). The decay power law in grid-generated turbulence. *J. Fluid Mech.* 219, 195–214. doi:10.1017/s0022112090002919

Moraga, F. J., Bonetto, F. J., and Lahey, R. T. (1999). Lateral forces on spheres in turbulent uniform shear flow. *Int. J. Multiphas. Flow* 25, 1321–1372. doi:10.1016/s0301-9322(99)00045-2

Pericas, R., Ivanov, K., Reventós, F., and Batet, L. (2017). Comparison of best-estimate plus uncertainty and conservative methodologies for a PWR MSLB analysis using a coupled 3-D neutron-kinetics/thermal-hydraulic code. *Nucl. Technol.* 198 (2), 193–201. doi:10.1080/00295450.2017.1299493

Platteeuw, P., Loeven, G., and Bijl, H. (2008). "*Uncertainty quantification applied to the k-epsilon model of turbulence using the probabilistic collocation method,"* in 49th Structures, Structural Dynamics, and Materials Conference, Schaumburg,07 April–10 April,American Institute of Aeronautics and Astronautics, 2150. doi:10.2514/6.2008-2150

Rakhimov, A. C., Visser, D. C., and Komen, E. M. J. (2018). Uncertainty Quantification method for CFD applied to the turbulent mixing of two water layers. *Nucl. Eng. Des.* 333, 1–15. doi:10.1016/j.nucengdes.2018.04.004

Ranz, W., and Marshall, W. (1952). Evaporation from drops. *Chem. Eng. Prog.* 48, 141–146

Rodi, W. (1984). *Turbulence models and their application in hydraulics: a state of the art review*. The Netherlands: International Association for Hydraulic Research

Sato, Y., and Sekoguchi, K. (1975). Liquid velocity distribution in two-phase bubble flow. *Int. J. Multiphas. Flow* 2, 79–95. doi:10.1016/0301-9322(75)90030-0

Schiller, L., and Naumann, Z. (1935). A drag coefficient correlation. *Zeitschrift des Vereins Deutscher Ingenieure* 77, 318–320

Yun, B.-J., Splawski, A., Lo, S., and Song, C.-H. (2012). Prediction of a subcooled boiling flow with advanced two-phase flow models. *Nucl. Eng. Des.* 253, 351–359. doi:10.1016/j.nucengdes.2011.08.067

Zhang, R., Cong, T., Tian, W., Qiu, S., and Su, G. (2015). Effects of turbulence models on forced convection subcooled boiling in vertical pipe. *Ann. Nucl. Energy* 80, 293–302. doi:10.1016/j.anucene.2015.01.039

Zhang, H., Li, Y., Xiao, J., and Jordan, T. (2018a). Uncertainty analysis of condensation heat transfer benchmark using CFD code GASFLOW-MPI. *Nucl. Eng. Des.* 340, 308–317. doi:10.1016/j.nucengdes.2018.10.007

Zhang, X., Yu, T., Cong, T., and Peng, M. (2018b). Effects of interaction models on upward subcooled boiling flow in annulus. *Prog. Nucl. Energy* 105, 61–75. doi:10.1016/j.pnucene.2017.12.004

Zhang, X., Zhang, R., Lv, X., and Cong, T. (2018c). Investigation on the subcooled boiling in vertical pipe with uncertainties from boundary conditions by using FLUENT. *Frontiers in Energy Research* 6, 23. doi:10.3389/fenrg.2018.00023

**Conflict of Interest:** The authors declare that the research was conducted in the absence of any commercial or financial relationships that could be construed as a potential conflict of interest.

frontiers in Energy Research

BRIEF RESEARCH REPORT
published: 14 December 2020
doi: 10.3389/fenrg.2020.527598

# Experimental Study on the Natural Deposition Characteristics of Erosols in Containment

*Lin Tao Tian, Haifeng Gu*, Huiyu Yu and Junyan Chen*

*Nuclear Safety and Simulation Technology Key Laboratory of National Defense Disciplines, Harbin Engineering University, Harbin, China*

Against the background of the natural deposition of erosols in containment under severe accident conditions, a relevant experimental facility was designed and constructed to study the decay constant of the natural deposition of erosols. $TiO_2$ was used as the erosol medium, and the decay constant of erosols was studied. The results show that when erosol concentration is < 15,000/cm$^3$, the decay constant of erosols increases with the increase of the particle size. However, when it is ≥ 15,000/cm$^3$, because the agglomeration of small particles into larger particles accelerates the deposition of particles with smaller size, the decay constant of erosols decreases first and then increases with the increase of the particle size. In addition, the effect of electrostatic on the decay constant of the natural deposition of erosols was studied. When the electrostatic effect is present, the decay constant of erosols increases significantly. Finally, the natural deposition characteristics of erosols were obtained.

**Keywords: aerosol, natural deposition, polymerization, electrostatic effect, severe accident**

OPEN ACCESS

***Edited by:***
*Shripad T. Revankar, Purdue University, United States*

***Reviewed by:***
*Ivo Kljenak, Institut Jožef Stefan (IJS), Slovenia*
*Mingjun Wang, Xi'an Jiaotong University, China*
*Yen-Shu Chen, Institute of Nuclear Energy Research (INER), Taiwan*

****Correspondence:***
*Haifeng Gu*
*guhaifeng@hrbeu.edu.cn*

***Specialty section:***
*This article was submitted to Nuclear Energy, a section of the journal Frontiers in Energy Research*

***Received:*** *17 January 2020*
***Accepted:*** *10 November 2020*
***Published:*** *14 December 2020*

***Citation:***
*Tian LT, Gu H, Yu H and Chen J (2020) Experimental Study on the Natural Deposition Characteristics of Erosols in Containment. Front. Energy Res. 8:527598. doi: 10.3389/fenrg.2020.527598*

## INTRODUCTION

During the course of a severe accident at a nuclear power plant (NPP), like a loss-of-coolant accident (LOCA), a large amount of radioactive fission product is released into containment in the form of gases, vapors, and erosols. Erosol is the main carrier of radioactive fission products. A large amount of radioactive erosols pose a huge threat to the external environment. Erosols are suspended solid or liquid particles which are very small and highly dispersed in gas. The behavior of erosols in containment mainly includes collision, agglomeration, condensation/evaporation, sedimentation, and so on. This complicated behavior makes it difficult to study the natural deposition behavior characteristics of erosols. In a traditional NPP, the containment spray system can remove most of the erosol suspended in the containment space by spray droplets. However, in the third generation of an advanced pressurized-water reactor (AP) series NPP, the spray system was removed and a passive containment cooling system (PCCS) was used to remove erosol (Fu et al., 2017). Simultaneously, in the event of station blackout (SBO), the nuclear power plant loses off-site power and this can lead to a severe accident (Li et al., 2014). If that happens, the concentration and distribution of erosols in containment are mainly dependent on natural deposition. Therefore, it is necessary to study the natural deposition characteristics of erosols in containment.

**Abbreviations:** NPP, nuclear power plant; LOCA, loss-of-coolant accident; AP, advanced pressurized-water reactor; PCCS, passive containment cooling system.

Four different mechanisms affect the natural deposition of erosols in containment; gravitational sedimentation, Brownian diffusion, diffusiophoresis, and thermophoresis (Powers and Washington/SNL, 2017). Gravitational sedimentation is related to the particle size of the erosol. The velocity of sedimentation of erosols increases with increasing particle size. Brownian diffusion mainly refers to the random motion of particles. The smaller the size of the erosol particle, the more obvious the Brownian diffusion effect is. Thermophoresis is caused by the temperature difference between the space and the wall in containment. The temperature difference causes the erosol particle to move from a high temperature zone to a low temperature zone. Diffusiophoresis is caused by the concentration gradient between the space and the wall in containment. The concentration gradient causes the erosol particle to move from a high concentration zone to a low concentration zone.

Some research has tackled the natural deposition of erosols in containment. The European Joint Center studied the effects of four mechanisms on the natural deposition of erosols with the help of GRACE (Snepvangers and Van De Vate, 1987). The effect of various mechanisms on the natural deposition of erosols have been obtained. The results showed that the thermophoresis increased with the increase of the temperature difference between the gas and the wall surface. However, polydisperse erosols have been used to analyze the entire erosol spectrum without considering the deposition of different particle sizes. Later, the Atomic Energy Institute (China) conducted similar experiments, the experimental results showed that diffusiophoresis increased with the increase of the vapor condensation rate on the wall. At the same time, the experimental containers of the experiments were relatively small. A. Kontautas (Kontautas and Urbonavičius, 2009) studied the effects of erosol density and solubility on its natural deposition rate using a PHBEU facility. The result showed that the influence of the particle density on the deposition rate was not significant if the erodynamic mass median diameter was kept constant. A. Dehbi (Dehbi, 2004) used CFD particle tracking to predict erosol decay and deposition. The simulation results showed that 80–90% of the particle deposition occurred in the bottom section of containment, which was also consistent with experiments findings. J. M. Makynen (Yang and Jokiniemi, 1997) studied the effects of humidity on the natural deposition of erosols using an AHMED facility. Experiments were carried out by selecting erosols of different densities and different solubility. It was found that humidity had an effect on the natural deposition of erosols of different densities, and the natural deposition of hygroscopic erosols was more sensitive to humidity. In most studies, the agglomeration between particles and the effect of electrostatic interaction on the natural deposition of erosols were not considered. In other areas of research, Longbo Liu (Qiu et al., 2017) studied the effect of chamber erosol concentration on its natural settling. The results showed that when the erosol concentration was high and $10^4/cm^3$, the agglomeration between the erosols must be considered. Alvin C. K. Lai (Lai, 2006), in the background of an electrostatic precipitator, used the effect of an applied electric field to study the natural deposition of erosols. Their experiments showed that the presence of static electricity can affect the natural deposition of erosols. In general, there are relatively few studies on the natural deposition behavior characteristics of erosols in containment. Further research is necessary for the natural deposition of erosols in containment.

In the natural deposition process, erosol particles are deposited with an exponential decay law, so we usually use the decay constant to measure the natural deposition decay rate of erosol particles. As shown in this equation,

$$C(t) = C(0) \times e^{-\lambda t}$$

In the formula, $C(t)$ is the number concentration of erosol particles in the container at time t, t is the deposition time, and $\lambda$ is the natural erosol deposition decay constant.

In this study, the method of ion neutralization (Baskaran and Zhu, 2017) was used to remove static electricity from erosol particles. The effect of static electricity on the natural deposition of erosol was studied. At the same time, the natural deposition of erosols at different concentrations was studied. Finally, the natural deposition characteristics of erosols were obtained without static electricity and agglomeration.

# EXPERIMENTAL FACILITY AND METHOD

## Experimental Facility

The experimental facility (**Figure 1**) mainly included: a main experimental vessel, an erosol injection system, a sampling measurement system, a static electricity removal system, a spray system, and a sewage treatment system.

The main experimental vessel presented consisted of a closed cuboid vessel (1.5 $m^3$ volume, 1.5 m high, and 1 m length and width) made of plexiglass, which was transparent in order to visually observe the internal environment in the vessel in real time (Corno et al., 2017). The erosol was injected at the bottom of the vessel. An extraction system on the top of the vessel allowed us to discharge the erosol that had not been removed during the experimental process.

The erosols chosen in this experiment were polydisperse $TiO_2$ particles, which are safe and convenient to use, and its properties such as powder density, hygroscopicity, and count median diameter (CMD) are similar to those produced in a NPP. Erosol injection was performed using a Topas SAG 410 erosol generator. The generator used a special conveyance to distribute the erosol and we adjusted the erosol injection by controlling the speed of the conveyer belt and the pressure of the carrier gas. In addition, a drying tube was installed on the gas supply line of the erosol generator for drying the air and against the agglomeration of the erosol.

Erosol concentration and particle size distribution in the vessel was measured in real time using the WELAS granulometer that allowed for good repeatability of the initial test conditions (Marchand et al., 2006). In this experiment, the erosol particle size in the experimental data was not the actual particle size, but the optical particle size measured by the WELAS granulometer. The ten stainless steel sampling lines with a diameter of 6 mm were distributed at different positions in the vessel. The $TiO_2$ erosol selected for this experiment was measured for its size distribution which is shown in **Figure 2**. The erosol was distributed between 0.3 and 10 μm with a CMD of 0.67 μm.

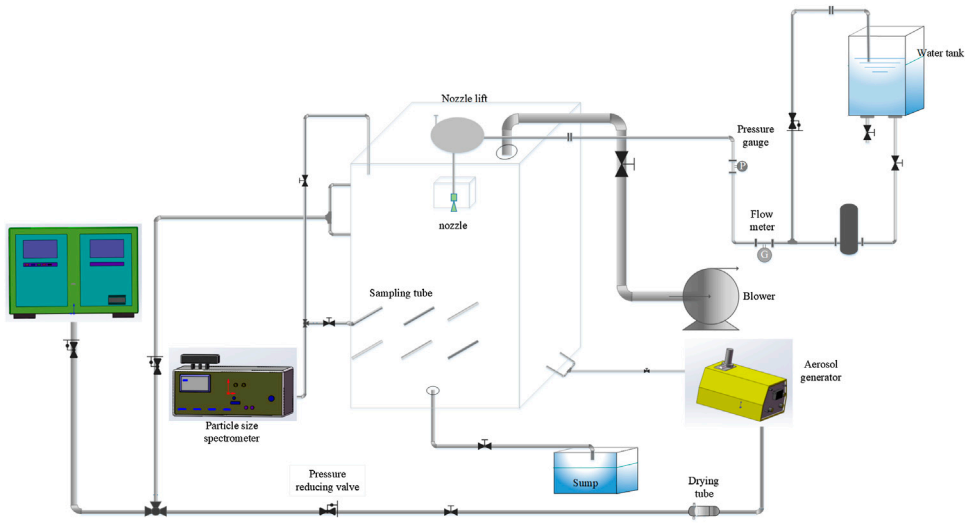


**FIGURE 1 |** Experimental facility.

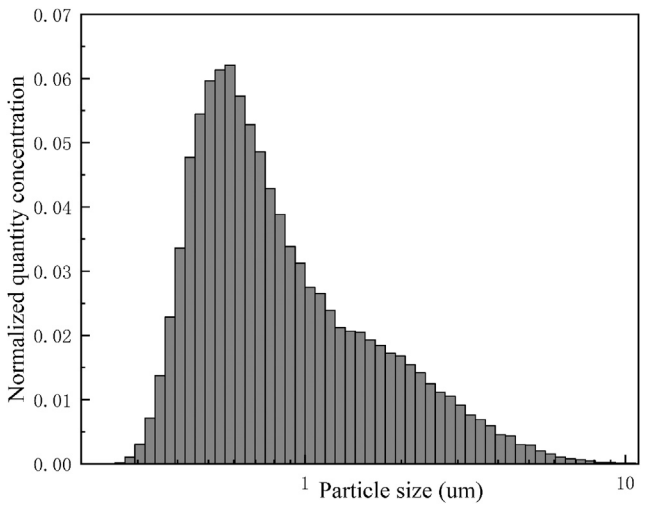


**FIGURE 2 |** Erosol particle size distribution.

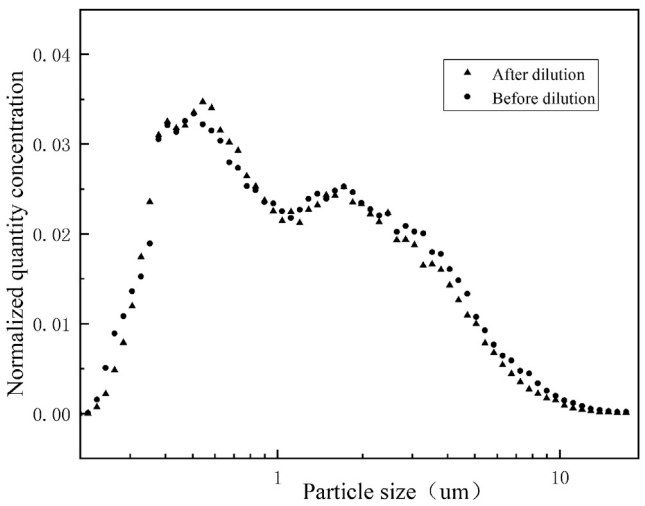


**FIGURE 3 |** Effect of the diluter on the measurement of experimental data.

During the erosol sampling measurement, the measure range of WELAS was between 0 and 8,000/cm$^3$, the actual concentration was much more than this order of magnitude in this experiment. Therefore, a high concentration of erosol was measured by dilution with a diluter. The diluter selected was the 3302 A erosol diluter produced by TSI, and its dilution factor can be 1–100 times. The dilution factor for this experiment was 25 times. A corresponding experiment was performed to verify the effect of the diluter on the sampling measurements. The measurement results are shown in **Figure 3**. The dilution factor of the multiple experimental diluter was maintained at 23–26 times. It can be seen that the use of the diluter had essentially no effect on the measurement of the experimental data.

## Removal of Static Electricity

Particles will generate static electricity during injection due to collisions and friction. In most studies of the natural deposition of erosols, the effects of electrostatic interaction on erosol deposition were not considered. In order to not only study the effect of the presence of static electricity on the natural deposition of erosols, and to also measure the effects of gravity sedimentation and Brownian diffusion on the natural deposition of erosols without static electricity, ion neutralization was used to eliminate static electricity from the erosol particles in this experiment. The principle of operation was to use positive and negative ions to neutralize the charge carried by the erosol particles. When the surface of the erosol particle was negatively charged, it attracted a

positive charge in the gas stream. When the charge of the erosol particle was positive, it attracted a negative charge in the gas stream. Thereby, the static electricity of the erosol particles was neutralized, and the purpose of eliminating static electricity was achieved.

In order to verify the effect of ion neutralization, relevant experiments were carried out. A plexiglass and a stainless steel sheet were placed horizontally in the vessel. The effect of neutralization on static removal was compared. When the ion neutralization was not used, during erosol injecting, the two plates placed in the vessel were observed afterward for a period of time. It was found that both the top and the bottom of the two plates deposited a large amount of erosol particles. The erosols deposited on the top surface of the plate were mainly caused by gravity sedimentation and Brownian diffusion, while the erosols on the bottom surface were mainly caused by electrostatic action and Brownian diffusion. The same experiment was performed using ion neutralization, it was found that the bottom surfaces of the two plates contained only a few erosol particles. The erosol on the top surface of the plate was mainly due to gravity sedimentation and the Brownian diffusion of erosol particles, those on the bottom were mainly caused by Brownian diffusion. Based on this, it was judged that the use of ion neutralization completely eliminated static electricity carried by the erosol. At the same time, the effect of ion neutralization time on static electricity removal was verified. The results showed that the ion neutralization method had no effect on the removal of static electricity, and that the static electricity on the surface of the particles was quickly removed (removal time was approximately 3 min).

## Experimental Procedure

The inside of the vessel was cleaned before the start of the experiment to ensure that the erosol in the vessel was close to the air background level. The $TiO_2$ erosol was then injected. In the injection process, depending on the purpose of the experiment, whether or not to remove the electrostatic was selected. After the erosol was injected, the measuring instrument WELAS was opened for erosol sampling. After the experiment was completed, data analysis was performed. In this experiment, the effects of electrostatic interaction and erosol concentration on the natural deposition of erosol were studied by setting different experimental conditions. At the same time, the effects of gravity sedimentation and Brownian diffusion on the natural deposition of erosols were studied after the removal of other disturbances. The whole experiment was carried out under a normal temperature and pressure. Considering the hydrophobicity of the TiO2 erosol, this experiment did not consider the influence of humidity on the natural deposition of erosols.

## Experimental Error Analysis

In this sort of experiment, a certain error usually occurs during the erosol sampling and measurement process. During the test, a 6 mm stainless steel tube was used for sampling, and the sampling tube was not bent. According to relevant experiments, the deposition of erosol particles on the inner wall of the sampling tube was less than 10%, resulting in sampling loss. At the same time, the data measurement error of the WELAS particle size spectrometer was within 5%.

# EXPERIMENTAL RESULTS AND ANALYSIS

## Effect of Static Electricity on the Natural Deposition Characteristics of Aerosols

First, the experiment was carried out in the presence of static electricity. After the start of the experiment, WELAS was used for real-time sampling measurements on the erosol size distribution in the vessel. It was found that the initial erosol particle size distribution changed greatly in a short period of time (approximately 5 min), as shown in **Figure 4**. It can be clearly seen that the proportion of erosols with a particle size smaller than 1 μm decreased, while erosols larger than 1 μm increased. This is mainly due to the interparticle agglomeration. Due to the presence of static electricity, smaller particles polymerized to form larger particles, resulting in a rapid right shift of the entire erosol particle size distribution after the start of the experiment. The same experiment was performed with static removal, as seen in **Figure 5**. It was found that the particle size distribution no longer changed significantly. During the period after the start of the experiment, the entire erosol size distribution remained essentially unchanged.

In addition to affecting the size distribution of erosol, the presence of electrostatic interaction also resulted in erosols being more easily deposited on the wall surface of the vessel. In **Figure 6**, when the electrostatic was removed, the decay constant of all of the particles decreased. This was mainly due to the presence of static electricity, which caused the electrostatically charged particles to be more easily absorbed on the wall surface of the vessel. It can be seen through these experiments that particles smaller than 2 μm were deposited more on the wall surface due to electrostaticity. When the particles size was larger than 2 μm, the electrostatic absorption was no longer significant. The presence of static electricity increased the deposition decay constant of particles between 0.3 and −4 μm by 10–35%.

## Characteristics of the Natural Deposition of Aerosols in Different Concentrations

The WELAS was used throughout the experiment to observe the particle size distribution of the erosol in the vessel in real time. Experiments were performed at different initial erosol concentrations. The results of the corresponding natural deposition experiments at small concentrations are shown in **Figure 7**. After the experiment, $1.5\times10^4/cm^3$ erosol particles were distributed into the vessel. It was found that the count median diameter (CMD) of the erosol gradually decreased as the experiment progressed. The erosol particle size range was determined by the gravity sedimentation control zone. Therefore, according to the calculation formula of gravity sedimentation, it was known that as the erosol particle size increased, the deposition rate would

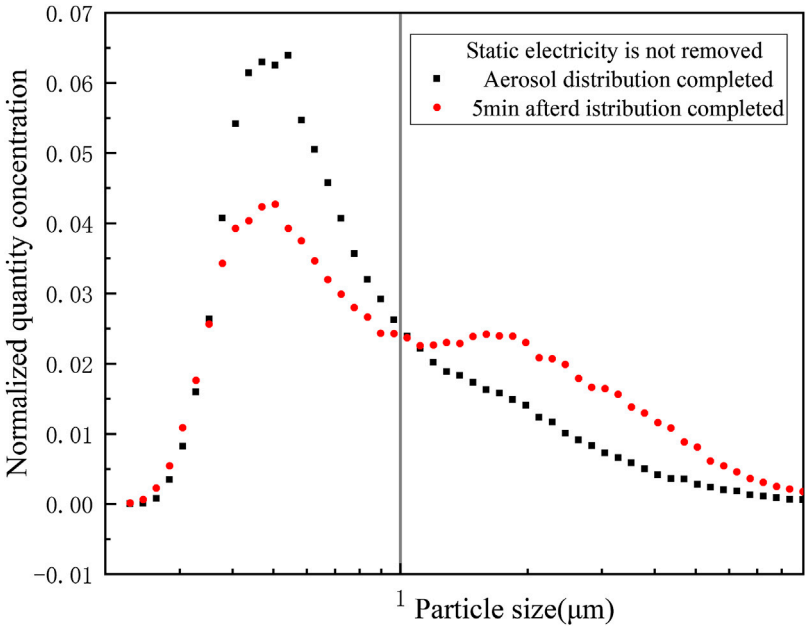


**FIGURE 4 |** Electrostatic effect on erosol distribution. Presence of electrostatic.

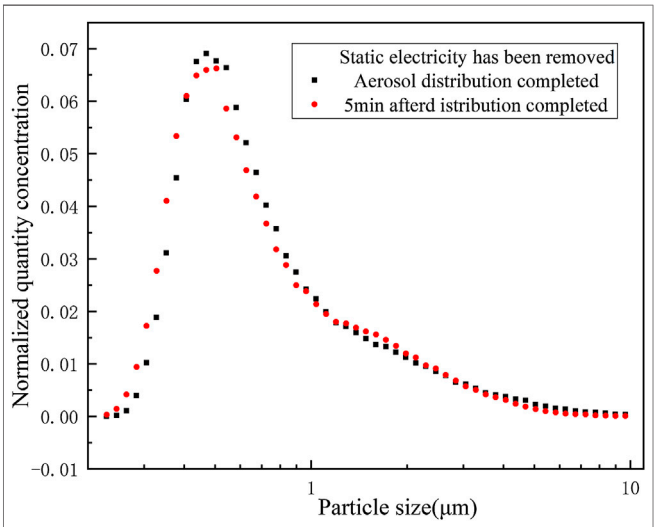


**FIGURE 5 |** Electrostatic effect on erosol distribution. Electrostatic removed.

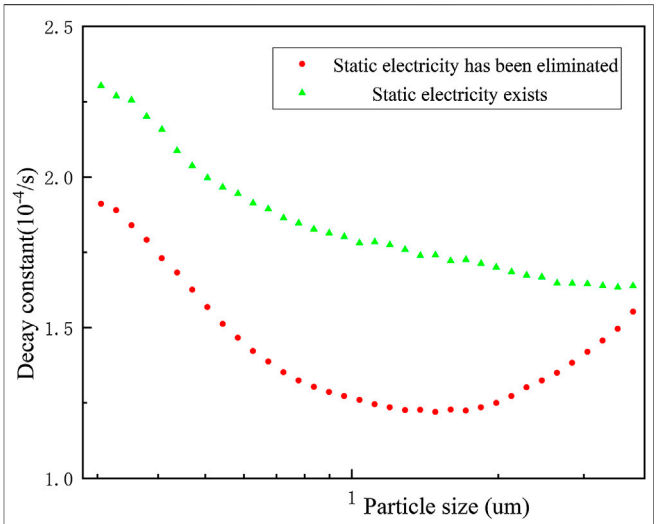


**FIGURE 6 |** Effect of static electricity on the decay constant of the natural deposition of erosols with different particle sizes.

increase. With the increase of the concentration of erosol in the vessel to some extent, it was found that the CMD of the erosol first increased and then decreased with time, as shown in **Figure 8**, The maximum CMD values was obtained at approximately 15,000 s. It was discovered that the change in CMD trend was mainly due to the agglomeration between particles. Due to the presence of agglomeration, the smaller erosol particles became larger, so that the removal rate of the smaller particles was faster than the larger particles, meaning that the CMD of the erosol increased. When the concentration of the erosol was deposited at a certain value, since the concentration of erosol in the vessel became smaller, the distance between the particles increased, so that the agglomeration between the particles was weakened. At this time, it was consistent with the experimental results when the concentration was small, and the CMD gradually became smaller as the experiment progressed. After multiple experiments, it was found that the erosol agglomeration

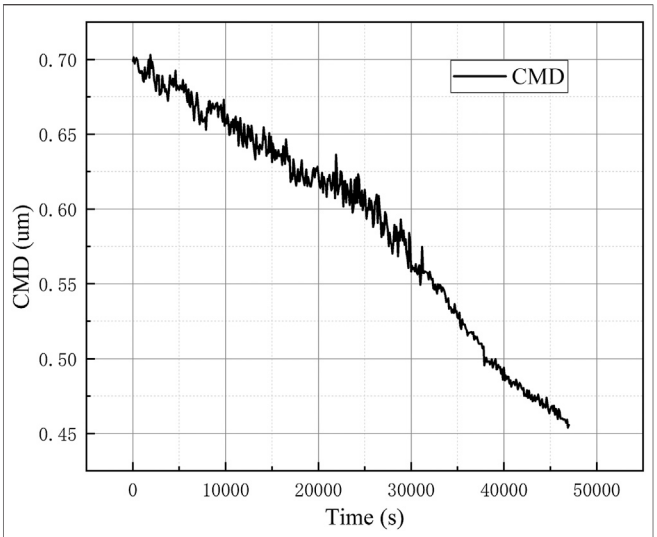


**FIGURE 7 |** CMD changes with time. CMD changes with time at lower concentrations.

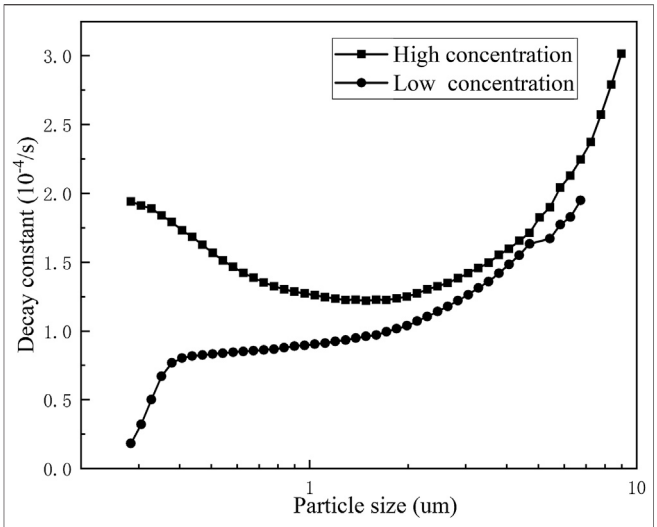


**FIGURE 9 |** Variation of decay constant with particle size. Electrostatic removal.

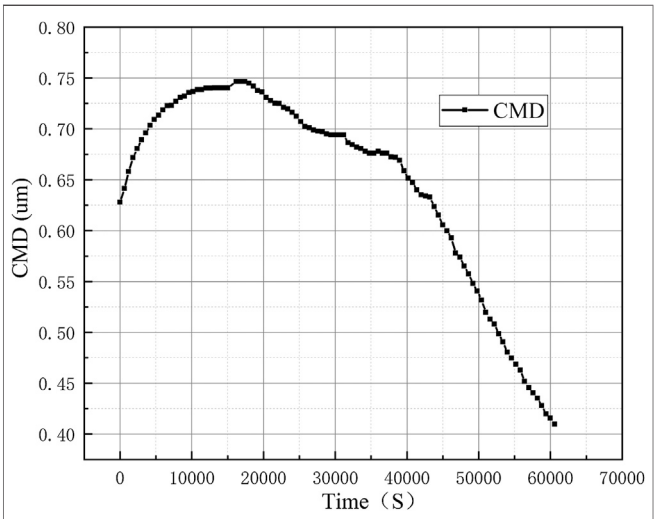


**FIGURE 8 |** CMD changes with time. CMD changes with time at higher concentrations.

concentration boundary was $1.5\times10^4/cm^3$. When the concentration of the erosol was less than $1.5\times10^4/cm^3$, the CMD gradually became smaller with deposition. When the concentration was greater than $1.5\times10^4/cm^3$, the CMD first increased and then decreased, and the highest point of increase, that also corresponded to erosol concentration, was $1.5\times10^4/cm^3$.

The experimentally obtained data were exponentially fitted to obtain the natural deposition decay constants of erosols of various particle sizes at different concentrations. It can be seen from **Figure 9**, when the erosol concentration number was $1.5\times10^5/cm^3$, as the erosol particle size became larger, the decay constant of the erosol decreased first and then increased. When the erosol concentration number was less than $1.5\times10^4/cm^3$, the decay constant increased with the increasing particle size. When the erosol concentration number was greater than $1.5\times10^4/cm^3$, there was agglomeration between the particles. It can be seen that the smaller the particle size, the more obvious the agglomeration was. As the particle size increased, the agglomeration became weaker. When the particle size was large to some extent, there was no longer any agglomeration between the particles. At this time, the natural deposition of the erosol particles was dominated by gravity sedimentation. As a result, the decay constants decreased first and then increased as the particle size of the erosol particle increased. This corresponded to the changing trend of CMD. At the same time, the effect of electrostatic action on the decay constant of each particle size was compared. In **Figure 10**, it was found that the concentration of erosol in the vessel was $1.47\times10^4/cm^3$ and the presence of electrostatic interaction had little effect on the decay constant of the erosol. At high concentrations, the decay constant of each particle size was significantly increased. At the same time, the erosol particle size corresponding to the lowest decay constant was significantly increased. This was mainly because the presence of static electricity enhanced the agglomeration between the particles. The agglomeration of the erosol in the vessel included the agglomeration resulting from the collision between the particles and the agglomeration resulting from the electrostatic interaction. When static electricity was present on the surface of the particles, it was affected by both electrostatic agglomeration and collision agglomeration. Moreover, the particle size range of the electrostatic agglomeration was wider, resulting in a right shift of the particle diameter corresponding to the lowest decay constant.

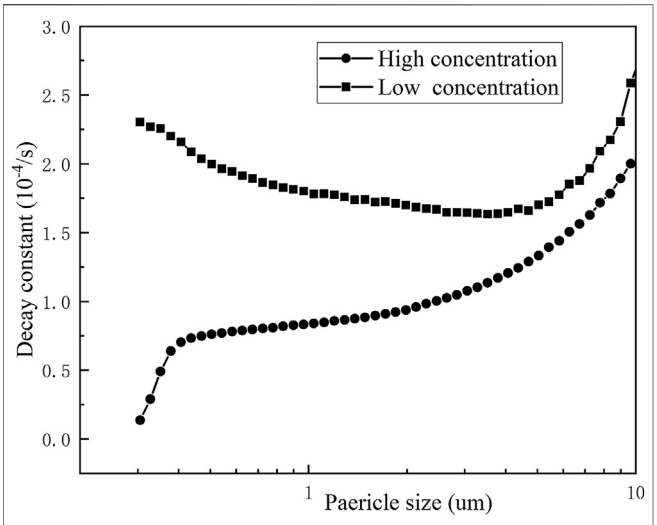


**FIGURE 10 |** Variation of decay constant with particle size. Presence of electrostatic.

## Characteristics of the Natural Deposition of Aerosols

It can be seen from the above related experiments that the electrostatic effect and the agglomeration between the particles had a certain affect on the natural deposition of the erosol. Therefore, a corresponding natural deposition experiment was carried out in the case where the erosol concentration was lower than $1.5\times10^4$/cm$^3$ and static electricity was removed. The erosol particle size distribution at different times and the natural deposition removed rate of erosols with different particles sizes was studied. The experiment lasted approximately 13 h. The change of the entire erosol particle size distribution with times was obtained, as shown in **Figure 11**. At that time, the natural deposition of erosol particles was only affected by gravity settling and Brownian diffusion. As time went by, the concentration number of all erosol particles decreased. After 45,600 s of natural deposition, the erosol removal rate of all particle sizes was above 80%. For erosols with a particle size greater than 0.4 μm, the removal rate was above 90%, and for erosols larger than 0.47 μm, the removal rate was above 96%. After the experiment, the erosol in the vessel was at the same level as the air background.

The concentration number of erosols with different particle sizes were obtained by an experiment. As shown in **Figure 12**, the quantitative concentration change of erosols with several particle sizes between 0.3 and 1.5 μm were obtained, and the change of real-time CMD was obtained. It can be clearly seen from **Figure 9** that as the particle size of the erosol increased, the natural deposition rate also increased accordingly. And the change of CMD also corresponded to the above. As the experiment progressed, CMD became smaller from 0.93 to 0.43 μm. It showed that when the erosol particle size was larger than 0.4 μm, the natural deposition mainly depended on gravity sedimentation, and the effect of Brownian diffusion was obviously smaller.

At the same time, the variation of the mass concentration and quantity concentration of the erosol in the vessel with time was obtained, as shown in **Figure 13**. It can be seen from the figure that the erosol mass concentration and quantity concentration gradually decreased with time and decreased with an exponential decay law. By fitting the curve, the decay constant of the mass concentration was $1.13\times10^{-4}$/s and the decay constant of the quantity concentration was $8.05^{*}10^{-5}$/s.

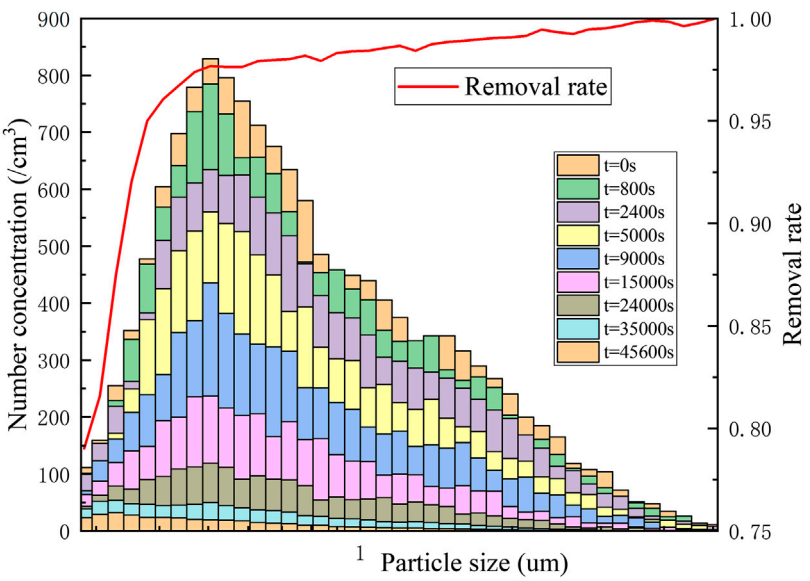


**FIGURE 11 |** Particle size distribution and removal rate of different particle sizes at different times.

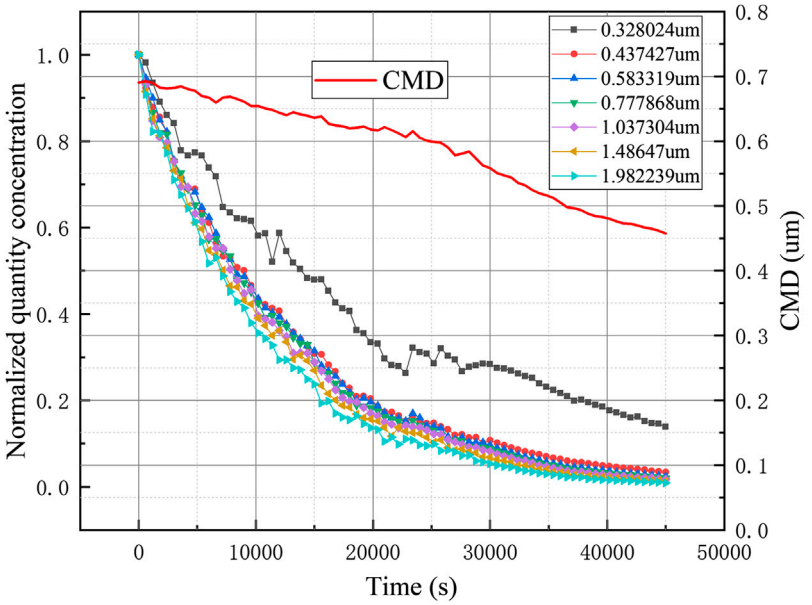


**FIGURE 12 |** Erosol concentration and particle CMD with time.

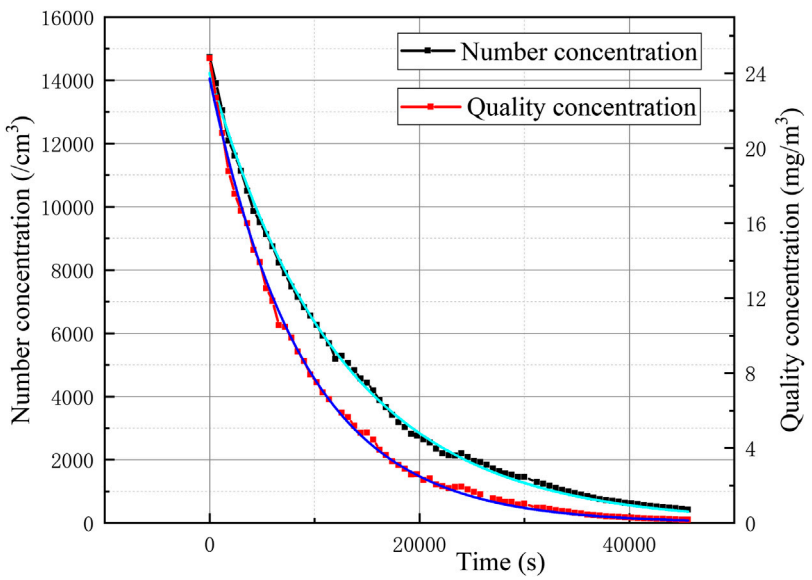


**FIGURE 13 |** Variations in mass concentrations over time.

## CONCLUSION

The presence of static electricity had a certain impact on the natural deposition of erosols: 1) the agglomeration of small particles at high concentration due to electrostatic and particle collision led to erosol particle size distribution shift after injection; 2) the presence of static electricity accelerated the natural deposition of the erosol, increasing the decay constant of erosols (0.3–4 μm) by 10%–35%.

When the concentration of the erosol was $\geq 1.5\times10^4/cm^3$, the agglomeration between the particles caused the decay constant to increase first and then decrease with the increase of particle size. When the concentration of the erosol was $<1.5\times10^4/cm^3$, there was no longer any agglomeration between the particles, and the decay constant of the erosol increased with the increase of the particle size. In addition, the presence of static electricity enhanced the agglomeration between particles.

The deposition of the erosol was naturally measured after the static electricity was removed and the concentration was less than $1.5\times10^4/cm^3$. At this time, the erosol mainly relied on gravity sedimentation and Brownian diffusion. It was found that after approximately 45,600 s, the removal rate of the erosols (0.3–10 μm) was above 80%. After approximately 45,600 s, the erosol concentration inside the container substantially settled back to the air background level. The overall mass concentration was small in terms of the exponential decay law, and its mass decay constant was $1.13\times10^{-4}/s$.

## DATA AVAILABILITY STATEMENT

The datasets generated for this study are available on request to the corresponding author.

## AUTHOR CONTRIBUTIONS

All authors listed have made a substantial, direct, and intellectual contribution to the work and approved it for publication.

## REFERENCES


Dehbi, A. (2004). "Tracking aerosols in large volumes with the help of CFD[C]," in 12th international conference on nuclear engineering, Arlington,Virginia USA, April 25–29, 2004 (New York, NY: American Society of Mechanical Engineers), 853–860.

Kontautas, A. and Urbonavičius, E. (2009). Analysis of aerosol deposition in PHEBUS containment during FPT-1 experiment. *Nucl. Eng. Des.* 239, 1267–1274. doi:10.1016/j.nucengdes.2009.03.012

Baskaran, Z. and Zhu, Y. (2017). *Static electricity and control measures*. Electronics World

Powers, D. A. and Washington/SNL, K. E. (2017). *A simplified model of aerosol removal by natural processes in reactor containments*. Tai yuan, China: Radiation Protection, 45–48.

Corno, A. D., Morandi, S., Parozzi, F., Araneo, L., and Casella, F. (2017). Experiments on aerosol removal by high-pressure water spray. *Nucl. Eng. Des.* 311, 28–34. doi:10.1016/j.nucengdes.2016.06.043

Fu, Y., Geng, J., and Sun, D. (2017). AP1000 aerosol natural removal analysis in the containment for AP1000 nuclear power point [J]. *Atomic Energy Sci. Technol.* 51 (4), 700–705. doi:10.7538/yzk.2017.51.04.0700

Yang, J. M. and Jokiniemi, J. K. (1997). AHMED experiments on hygroscopic and inert aerosol behaviour in LWR containment conditions: experimental results. *Nucl. Eng. Des.* 178, 45–59. doi:10.1016/S0029-5493(97)00174-X

Lai, A. C. K. (2006). Investigation of electrostatic forces on particle deposition in a test chamber. *Indoor Built Environ.* 15, 179–186. doi:10.1177/1420326x06063219

Snepvangers, L. J. M. and Van De Vate, F. (1987). *Diffusiophoresis of fission product aerosol in an lwr containment after core meltdown. nuclear science and technology*. Official Publications of the European Communities, 39.

Qiu, L., Zhang, Z., Wu, Y., Yang, W., Wu, S., and Zhang, L. (2017). Decay of high-concentration aerosol in a chamber. *Aerosol Sci. Eng.* 1, 155–159. doi:10.1007/s41810-017-0015-z

Marchand, D., Porcheron, E., Lemaitre, P., and Gréhan, G. (2006). Characterization of the washout of aerosols by spraying water for thermal hydraulic conditions representative of a severe accident in nuclear reactor containment[J]. *EMBO J.* 20 (17), 4923–4934.

Li, M., Wang, W., Su, G., and Qiu, S. (2014). Severe accident analysis for a typical PWR using the MELCOR code. *Prog. Nucl. Energy* 71, 30–38. doi:10.1016/j.pnucene.2013.10.014


**Conflict of Interest:** The authors declare that the research was conducted in the absence of any commercial or financial relationships that could be construed as a potential conflict of interest.

# Advantages of publishing in Frontiers

**OPEN ACCESS**
Articles are free to read for greatest visibility and readership

**FAST PUBLICATION**
Around 90 days from submission to decision

**HIGH QUALITY PEER-REVIEW**
Rigorous, collaborative, and constructive peer-review

**TRANSPARENT PEER-REVIEW**
Editors and reviewers acknowledged by name on published articles

**Frontiers**
Avenue du Tribunal-Fédéral 34
1005 Lausanne | Switzerland

**Visit us:** www.frontiersin.org
**Contact us:** frontiersin.org/about/contact

**REPRODUCIBILITY OF RESEARCH**
Support open data and methods to enhance research reproducibility

**DIGITAL PUBLISHING**
Articles designed for optimal readership across devices

**FOLLOW US**
@frontiersin

**IMPACT METRICS**
Advanced article metrics track visibility across digital media

**EXTENSIVE PROMOTION**
Marketing and promotion of impactful research

**LOOP RESEARCH NETWORK**
Our network increases your article's readership